frontiers | Research Topics

Symmetry and exact solutions of nonlinear mathematical physics equations

Edited by
Gangwei Wang, Xiangpeng Xin and
Samir A. El-Tantawy

Published in
Frontiers in Physics

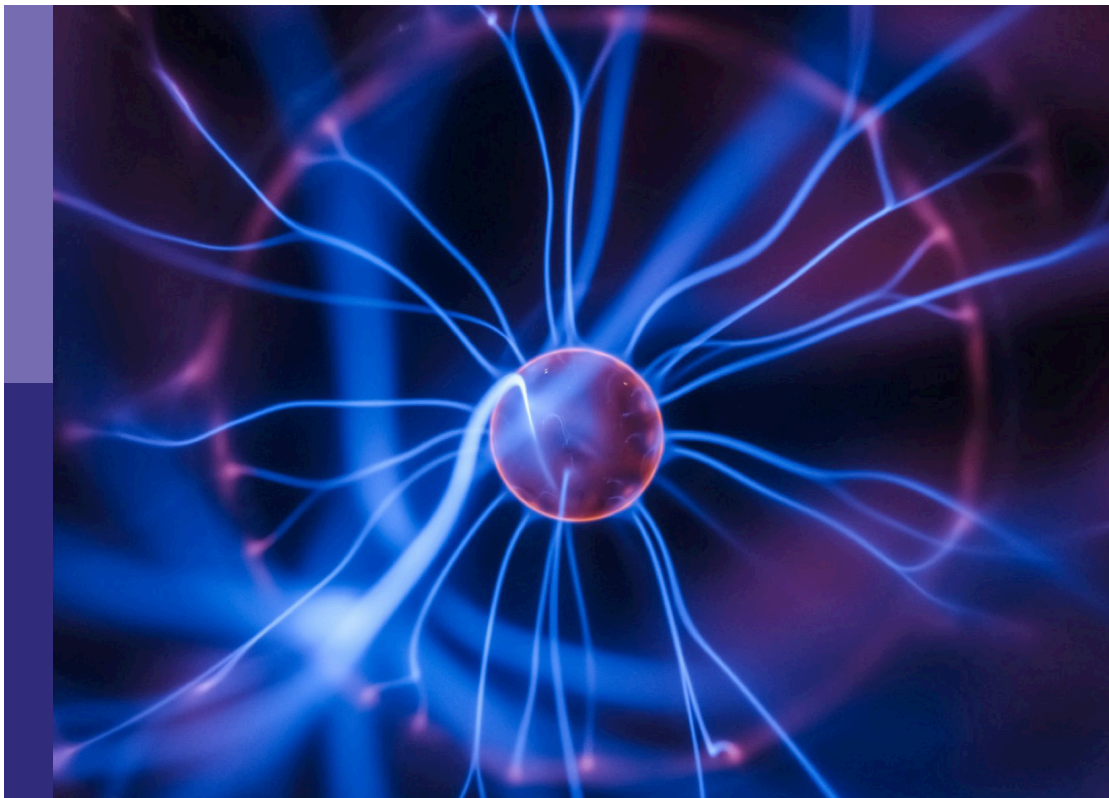

ISSN 1664-8714
ISBN 978-2-8325-5309-1
DOI 10.3389/978-2-8325-5309-1

About Frontiers

Frontiers is more than just an open access publisher of scholarly articles: it is a pioneering approach to the world of academia, radically improving the way scholarly research is managed. The grand vision of Frontiers is a world where all people have an equal opportunity to seek, share and generate knowledge. Frontiers provides immediate and permanent online open access to all its publications, but this alone is not enough to realize our grand goals.

Frontiers journal series

The Frontiers journal series is a multi-tier and interdisciplinary set of open-access, online journals, promising a paradigm shift from the current review, selection and dissemination processes in academic publishing. All Frontiers journals are driven by researchers for researchers; therefore, they constitute a service to the scholarly community. At the same time, the *Frontiers journal series* operates on a revolutionary invention, the tiered publishing system, initially addressing specific communities of scholars, and gradually climbing up to broader public understanding, thus serving the interests of the lay society, too.

Dedication to quality

Each Frontiers article is a landmark of the highest quality, thanks to genuinely collaborative interactions between authors and review editors, who include some of the world's best academicians. Research must be certified by peers before entering a stream of knowledge that may eventually reach the public - and shape society; therefore, Frontiers only applies the most rigorous and unbiased reviews. Frontiers revolutionizes research publishing by freely delivering the most outstanding research, evaluated with no bias from both the academic and social point of view. By applying the most advanced information technologies, Frontiers is catapulting scholarly publishing into a new generation.

What are Frontiers Research Topics?

Frontiers Research Topics are very popular trademarks of the *Frontiers journals series*: they are collections of at least ten articles, all centered on a particular subject. With their unique mix of varied contributions from Original Research to Review Articles, Frontiers Research Topics unify the most influential researchers, the latest key findings and historical advances in a hot research area.

Find out more on how to host your own Frontiers Research Topic or contribute to one as an author by contacting the Frontiers editorial office: frontiersin.org/about/contact

Symmetry and exact solutions of nonlinear mathematical physics equations

Topic editors

Gangwei Wang — Hebei University of Economics and Business, China

Xiangpeng Xin — Liaocheng University, China

Samir A. El-Tantawy — Port Said University, Egypt

Citation

Wang, G., Xin, X., El-Tantawy, S. A., eds. (2024). *Symmetry and exact solutions of nonlinear mathematical physics equations*. Lausanne: Frontiers Media SA.

doi: 10.3389/978-2-8325-5309-1

Table of contents

frontiers | Frontiers in Physics

TYPE Original Research
PUBLISHED 10 February 2023
DOI 10.3389/fphy.2023.1122592

OPEN ACCESS

EDITED BY
Samir A. El-Tantawy,
Port Said University, Egypt

REVIEWED BY
Alvaro Salas,
National University of Colombia, Colombia
Abdelhalim Ebaid,
University of Tabuk, Saudi Arabia

*CORRESPONDENCE
Yusry O. El-Dib,
yusryeldib52@hotmail.com

SPECIALTY SECTION
This article was submitted to Mathematical Physics, a section of the journal Frontiers in Physics

RECEIVED 13 December 2022
ACCEPTED 20 January 2023
PUBLISHED 10 February 2023

CITATION
El-Dib YO, Elgazery NS and Alyousef HA (2023), A heuristic approach to the prediction of a periodic solution for a damping nonlinear oscillator with the non-perturbative technique.
Front. Phys. 11:1122592.
doi: 10.3389/fphy.2023.1122592

A heuristic approach to the prediction of a periodic solution for a damping nonlinear oscillator with the non-perturbative technique

Yusry O. El-Dib[1]*, Nasser S. Elgazery[1] and Haifa A. Alyousef[2]

[1]Department of Mathematics, Faculty of Education, Ain Shams University, Cairo, Egypt, [2]Department of Physics, College of Science, Princess Nourah bint Abdulrahman University, Riyadh, Saudi Arabia

The present work attracts attention to obtaining a new result of the periodic solution of a damped nonlinear Duffing oscillator and a damped Klein–Gordon equation. It is known that the frequency response equation in the Duffing equation can be derived from the homotopy analysis method only in the absence of the damping force. We suggest a suitable new scheme successfully to produce a periodic solution without losing the damping coefficient. The novel strategy is centered on establishing an alternate equation apart from any difficulty in handling the influence of the linear damped term. This alternative equation was obtained with the rank upgrading technique. The periodic solution of the problem is presented using the non-perturbative method and validated by the modified homotopy perturbation technique. This technique is successful in obtaining new results toward a periodic solution, frequency equation, and the corresponding stability conditions. This methodology yields a more effective outcome of the damped nonlinear oscillators. With the help of this procedure, one can analyze many problems in the domain of physical engineering that involve oscillators and a linear damping influence. Moreover, this method can help all interested plasma authors for modeling different nonlinear acoustic oscillations in plasma.

KEYWORDS

damping nonlinear oscillator, non-perturbative technique, modified homotopy perturbation method, stability analysis, rank upgrade technique

1 Introduction

In the range of differential equations, various physical manifestations, such as acoustic waves in plasma physics, and many engineering problems are modeled. A lot of scientists have made magnificent efforts to evaluate the solution of these differential equations. Different techniques have been utilized to evaluate the corresponding solutions. Modeling different biological, physical, and biochemical engineering problem occurrences, in general, yields nonlinear partial differential equations (PDEs). Moreover, plasma physics is one of the most fertile fields for many researchers interested in studying nonlinear phenomena. To perform modeling, the nonlinear phenomena that propagate in different plasma systems and many ordinary and partial differential equations must be solved. For this purpose, different mathematical approaches have been introduced for modeling several physical problems. Recently, a damped nonlinear oscillator model has been widely considered in practical engineering, general physics, and in plasma physics. For mathematical scientists, an article on nonlinear PDEs, which are addressed in most engineering and science domains, is extremely important. Many authors have offered a survey of the literature with numerous references using various analytical techniques for dealing with the damped nonlinear oscillation problems.

Nonlinear systems remain a challenge, and its interest has fundamentally concentrated on specific changes in system instability and bifurcations.

Duffing oscillators are permanently connected with engineering and physical situations, especially plasma physics. The damping force is an impact on an oscillatory system that has the action of restricting, reducing, or averting its oscillation. Damping is created by operations of losing the energy stored in an oscillation. Examples include resistance in electronic oscillators, viscous pull in mechanical systems and plasma physics, osmosis, and expansion of light in visual oscillators. Damping, which did not build from vanishing energy, may be significant in other vibrating systems like those that subsist in some biological systems. A system's damping may be categorized as one of the following:

- **Overdamped**: The system reaches equilibrium as an exponential decay.
- **Critically damped**: The system reaches equilibrium as soon as possible without vibrating.
- **Underdamped**: The system vibrates with amplitude slowly lessening to zero (at low frequency compared to the nondamped case).
- **Undamped**: The system resonantly oscillates at its native frequency.

See [1] for additional instances for the aforementioned categories.

Over the current decades, a lot of physical phenomena have been described utilizing nonlinear ordinary differential equations (ODEs). One of the simplest of these oscillators called a Duffing equation has received significant interest in light of its classical applications in engineering, biology, plasma physics, and sciences. The history of nonlinear proceedings in engineering sciences has been observed since [2] employed the hardening spring model to investigate the vibration of the electromagnetic vibrating beam in 1918. Therefore, the Duffing equation has been extensively utilized in structural dynamics and in mathematics to determine the existence of oscillatory motions of second-order nonlinear PDEs. The oscillation/non-oscillation theorems of Meissner's equation were investigated by [3]. [4] utilized the multiple-scale perturbation approach to develop and calculate an analytic periodic solution of oscillating movements in damping Duffing oscillators. [5] used perturbation techniques for nonlinear structural vibrations using Duffing oscillators. Consequently, perturbation analysis is still used to obtain an analytic solution for oscillating movements. The HPM was first introduced by the famous mathematician [6]. Recently, it has been employed in numerous investigations in engineering and physics. In contrast, this technique failed in analyzing damping nonlinear oscillators [7]. There are many modifications made by many researchers to improve HPM to be a more functioning method. [8] employed the parameter-expanding technique as a modification to HPM in solving strongly nonlinear oscillators. [9] and [10] developed HPM by connecting it with Laplace transform for solving nonlinear oscillators. [11] obtained a periodic solution for the Fangzhu oscillator by HPM.

Next, several of the latest developments of this technique are briefly mentioned; for instance, the combination of the multiple-scale method and HPM [12–15], the parameterized HPM [16], and nonlinearities distribution HPM was applied to solve Troesch's problem [17]. Numerical and approximate techniques can be utilized for the treatment of nonlinear oscillators. Numerous estimates were used in trying to solve linear and nonlinear oscillators, for example, the reproducing kernel method [18]. Moreover, an iterative procedure is employed to evaluate a numerical solution of the optimal control issues of the Duffing oscillators [19]. Also, [20] applied the finite difference technique to investigate an oscillatory model. Furthermore, by substituting a suitable linear auxiliary operator for the linear operator in [21] analysis of nonlinear equations with restoring force, among other changes, they created a new version of HPM. By using the modified homotopy perturbation procedure, [22] also introduced an analytic solution for a nonconservative parametric quintic-cubic Duffing oscillator. A damped Mathieu equation was solved using a modulation for HPM by [23]. The Newell–Whitehead–Segel (NWS) equation's periodic solution was also estimated by [24] using the HPM. [25] introduced a simple frequency formulation to study a tangent oscillator. An analytic solution of Burgers' equation with time-fraction has been introduced by [26]. A variational principle for a nonlinear equation that appears in several micro-electro-mechanical systems was developed by [27]. Furthermore, a jerk Duffing oscillator was solved using the lowering rank approach by him and [28]. Luo and Jin have used the lower-order technique in numerical approaches [29]. Recently, [30] applied the non-perturbative technique to solve a damping Helmholtz–Rayleigh–Duffing oscillator.

It is common knowledge that some nonlinear differential equations do not have exact solutions. Then, the analysis of approximate solutions for some kinds of these systems plays a significant role in investigating nonlinear physical phenomena [31]. The damping Duffing oscillator refers to these kinds of equations, and it is represented by the following equation:

$$\ddot{y} + 2\mu\dot{y} + \omega_0^2 y + Qy^3 = 0;\ y = y(t) \tag{1}$$

It is thought to observe that a Duffing oscillator is a simple model which displays various kinds of vibrations, such as chaos and limit cycles. The term $\dot{y}(t)$ in Eq. 1 represents a damping oscillation, and μ refers to viscous damping. The part $(\omega_0^2 y + Qy^3)$ refers to a nonlinear restoring force acting as a hard spring (with ω_0^2 rules, the size of stiffness, and Q dominants, the size of nonlinearity). This equation illustrates a wonderful area of well-known nonlinear dynamical system behavior. It was used by a lot of scientists to illustrate such behaviors. Numerous problems in both engineering and physics drive to nonlinear Duffing oscillators (Eq. 1) from oscillations of a simple pendulum, including nonlinear electrical circuits. It has been approved in various applications in image processing [4, 5]. The approximate periodic response for the un-damped equation, obtained by various analytical methods, has been discussed in almost all textbooks on nonlinear vibration. Eq. 1, with a non-zero damping term, has received attention in many domains of physical engineering problems. The investigation of new techniques which drive the solution of the damped Duffing equation was of vital significance since these solutions can be used for a cubic Schrodinger/damping Klein–Gorden equation that has numerous uses in nonlinear optics, plasma physics, and fluid mechanics.

Other related works have been included in this study, yielding a good understanding of the present analysis. A fractionally damped beam has been analyzed by [32]. The influence of dispersion force and squeezed film damping was incorporated in the dynamic instability of the nanowire-fabricated sensor subjected to centrifugal and constant

acceleration [33, 34]. Even though Eq. 1 appears straightforward at a first glance, it contains several complex elements. The classical perturbation approach has a lot of drawbacks. Moreover, the following damping nonlinear Klein–Gorden equation has the same shortcoming when using the classical HPM:

$$y_{tt} + Py_{xx} + 2\mu y_t + 2\eta y_x + \sigma y = Qy^3; \quad y = y(x,t) \tag{2}$$

The real constant coefficients P, η, μ, σ, and Q can be defined as a second-order spatial derivative coefficient, spatial damped coefficient, temporal damped coefficient, natural frequency, and cubic stiffness parameter, respectively. The classical nonlinear Klein–Gordon equation, which appears in several scientific domains such as nonlinear optics, solid physics, fluid mechanics, quantum mechanics, and plasma physics, is derived from Eq. 2 when the values of the coefficients μ and η vanish. In addition to its applications in plasma physics, it can be used for modeling many nonlinear structures in plasma. It transforms into the one-dimensional time-nonlinear damped Klein–Gordon equation when $\mu > 0$ and $\eta = 0$ [35–38]. The aforementioned damping Klein–Gordon equation can be transformed into a damping Duffing oscillator by using the technique of the traveling wave approaches. Traveling waves engender multiple physical systems spontaneously, typically qualified by PDEs. Then, by including the following traveling wave's next variable $\zeta(x,t)$, one can create an alternative oscillatory form of Eq. 2.

$$\zeta(x,t) = 2\eta x + 2P\mu t. \tag{3}$$

Such transformation was applied to the nonlinear Klein–Gordon Eq. 2 without damping by [39]. According to the stated novel independent variable, one obtains

$$y_t = 2P\mu y'(\zeta), \quad y_x = 2\eta y'(\zeta), \quad y_{tt} = 4P^2\mu^2 y''(\zeta), \text{ and } y_{xx} = 4\eta^2 y''(\zeta), \tag{4}$$

where the prime denotes the total derivative concerning the variable ζ. By utilizing Eq. 4 with Eq. 2, it will be transformed into the following damping Duffing equation:

$$Py''(\zeta) + y'(\zeta) + \omega_0^2 y(\zeta) = Ry^3(\zeta), \tag{5}$$

where ω_0^2 and R are given through the subsequent notations:

$$\omega_0^2 = \frac{\sigma}{4(P\mu^2 + \eta^2)}, \text{ and } R = \frac{Q}{4(P\mu^2 + \eta^2)}. \tag{6}$$

The solution of Eq. 5 gives the traveling wave solution of the original nonlinear Klein–Gordon equation as given in Eq. 2. Suppose that Eq. 5 has been subjected to these initial conditions $y(0) = A$ and $y'(0) = 0$.

A fresh perturbation strategy is required to address the drawbacks. Unexpectedly, the flaw in Eq. 1 has been fixed by using the fractional derivative in conjunction with HPM [40, 41].

In the present research, a new suitable idea is presented successfully to produce a periodic solution for oscillators containing the damping coefficient without losing this damping force. The main idea is based on the rank upgrading technique by upgrading the linear operator to a higher order and using the original equation to replace what is equivalent to the linear damped term [42, 43]. The outcome is an alternative fourth-order differential equation devoid of any damping difficulties. The comparison between this alternative equation and the original equation showed that the obtained equation is corrected and can be used to perform the periodic solution. The periodic solution of the problem is presented using the non-perturbative method and validated by the modified homotopy perturbation technique.

2 Methodology

To overcome the difficulty in solving the damping nonlinear oscillator, one can employ the rank upgrading mechanism to annihilate the damping term "y'". This method is used for upgrading the order of the derivatives of Eq. 5 to become

$$Py''' + y'' + \omega_0^2 y' = 3Ry^2 y', \tag{7}$$

$$Py^{(4)} = -y''' + (3Ry^2 - \omega_0^2)y'' + 6Ryy'^2. \tag{8}$$

By removing y' from Eq. 7 with the help of Eq. 5 and replacing y''' in Eq. 8 yields

$$P^2 y^{(4)} - (1 + 2P(3Ry^2 - \omega_0^2))y'' - 6PRyy'^2 + (3Ry^2 - \omega_0^2) \times (Ry^2 - \omega_0^2)y = 0. \tag{9}$$

This is a fourth-order equation with cubic-quintic nonlinearity which represents an alternative form of the original damping Eq. 5. This new form will be subject to the initial conditions listed as follows:

$$y(0) = A, y'(0) = 0, y''(0) = \frac{A}{P}(RA^2 - \omega_0^2), \text{and } y'''(0) = -\frac{A}{P^2}(RA^2 - \omega_0^2). \tag{10}$$

It can be ensured that Eq. 9 represents an alternative form of the original Eq. 5 through the comparison of the numerical solutions.

3 Introducing the periodic solution

The periodic solution can be introduced from Eq. 9 analytically which can be illustrated as follows, with the non-perturbative approach and with the homotopy perturbation method:

It is noted that Eq. 9 can be rearranged in the following form:

$$y^{(4)} - g(y, y', y'') + f(y) = 0, \tag{11}$$

where the two odd functions $g(y, y', y'')$ and $f(y)$ are selected to have y'' and y as a common factor, respectively. Here,

$$\left.\begin{aligned} g(y, y', y'') &= \frac{1}{P^2}\left(1 + 2P(3Ry^2 - \omega_0^2) + 6PR\frac{yy'^2}{y''}\right)y'', \\ f(y) &= \frac{1}{P^2}(3Ry^2 - \omega_0^2)(Ry^2 - \omega_0^2)y. \end{aligned}\right\} \tag{12}$$

Consequently, Eq. 11 in the non-perturbative approach can be sought in the form

$$y^{(4)} - \beta^2 y'' + \varpi^4 y = 0. \tag{13}$$

The efficient frequency formula given by El-Dib [44–46] can be used to evaluate both β^2 and ϖ^4 as follows:

Introducing the trial solution to Eq. 13 in the form

$$\hat{y}(\zeta) = A\cos\omega\zeta, \tag{14}$$

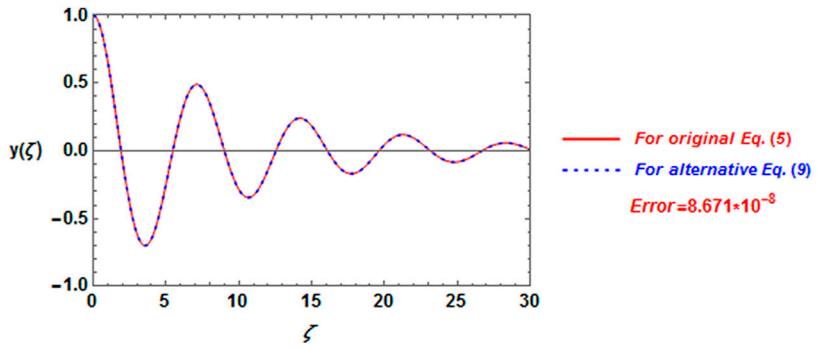

FIGURE 1
Comparison of the numerical solution between Eq. 5 and Eq. 9.

where A and ω represent the amplitude and the unknown frequency of the oscillation, respectively. Accordingly, both $\varpi^4(A)$ and $\beta^2(A)$ read

$$\varpi^4(A) = \frac{\int_0^T \hat{y}(\zeta) f(\hat{y}) d\zeta}{\int_0^T \hat{y}^2(\zeta) d\zeta} = \frac{1}{8P^2}\left(15A^4R^2 - 24A^2R\omega_0^2 + 8\omega_0^4\right); T = \frac{\pi}{2\omega}, \tag{15}$$

$$\beta^2(A) = \frac{\int_0^T \hat{y}''(\zeta) g(\hat{y}, \hat{y}', \hat{y}'') d\zeta}{\int_0^T \hat{y}''^2(\zeta) d\zeta} = \frac{1}{P^2}\left(1 + 3A^2PR - 2P\omega_0^2\right). \tag{16}$$

Employing Eq. 14 with the linear fourth-order Eq. 13 yields the frequency equation in the form

$$\omega^4 + \beta^2(A)\omega^2 + \varpi^4(A) = 0. \tag{17}$$

At this stage, the solution of Eq. 13 has the form

$$y(\zeta) = A\cos\omega\zeta, \tag{18}$$

with

$$\omega = \frac{1}{\sqrt{2}}\sqrt{-\beta^2 + \sqrt{\beta^4 - 4\varpi^4}}. \tag{19}$$

4 Validation with the homotopy perturbation approach

By utilizing the technique of the auxiliary equivalent [21, 40, 47, 48] by introducing $(P^2\omega^4 y)$ into Eq. 9 and then building the corresponding homotopy equation, one obtains

$$y^{(4)} - \omega^4 y = \frac{\rho}{P^2}\left[-P^2\omega^4 y + y'' - \left(3Ry^2 - \omega_0^2\right)\left(Ry^3 - \omega_0^2 y - Py''\right) + P\left(3Ry^2 - \omega_0^2\right)y'' + 6PRyy'^2\right]; \rho \in [0, 1]. \tag{20}$$

The new frequency parameter ω is unknown to determine the latter.

By operating both sides of Eq. 20 with the inverse $(D_\zeta^2 - \omega^2)$, one can reduce the artificial higher power and obtain

$$\left(D_\zeta^2 + \omega^2\right)y = \frac{\rho}{P^2\left(D_\zeta^2 - \omega^2\right)}\left[-P^2\omega^4 y + y'' - \left(3Ry^2 - \omega_0^2\right) \times\left(Ry^3 - \omega_0^2 y - Py''\right) + P\left(3Ry^2 - \omega_0^2\right)y'' + 6PRyy'^2\right]. \tag{21}$$

This equation is an alternative to Eq. 5; it is free of difficulty due to the linear damping effects. At this stage, the application of HPM is easy without any shortcomings. Typically, introducing the homotopy expansion [6], one finds

$$y(\zeta;\rho) = y_0(\zeta) + \rho y_1(\zeta) + \rho^2 y_2(\zeta) + ..., \tag{22}$$

where the unknowns $y_0(\zeta)$ and $y_1(\zeta)$ are given by substituting from Eq. 22 into Eq. 21; following the same procedure as given in HPM, the abovementioned unknowns may be determined by the simpler differential equations as follows:

$$y_0'' + \omega^2 y_0 = 0, \tag{23}$$

which is the linear harmonic equation having the general solution in the form

$$y_0(\zeta) = A\cos(\omega\zeta), \tag{24}$$

where A is the amplitude of the oscillation. Furthermore, we have

$$\left(D_\zeta^2 + \omega^2\right)y_1 = \frac{1}{P^2\left(D_\zeta^2 - \omega^2\right)}\left[-P^2\omega^4 y_0 + y_0'' - \left(3Ry_0^2 - \omega_0^2\right) \times\left(Ry_0^3 - \omega_0^2 y_0 - Py_0''\right) + P\left(3Ry_0^2 - \omega_0^2\right)y_0'' + 6PRy_0 y_0'^2\right]. \tag{25}$$

The zero-order solution Eq. 24 is introduced into Eq. 25, and the cancellation of the secular terms requires

$$P^2\omega^4 - \left(2P\omega_0^2 - 3PRA^2 - 1\right)\omega^2 + \omega_0^4 - 3R\omega_0^2A^2 + \frac{15}{8}R^2A^4 = 0. \tag{26}$$

Consequently, the frequency–amplitude equation is given by

$$\omega^2 = \frac{1}{2P^2}\left[\left(2P\omega_0^2 - 3PRA^2 - 1\right) \pm \sqrt{\frac{3}{2}P^2R^2A^4 - 4P\omega_0^2 + 6PRA^2 + 1}\right]. \tag{27}$$

It is noted that the frequency equation derived by the homotopy perturbation method is equivalent to that obtained before by the non-perturbative approach in Eq. 17.

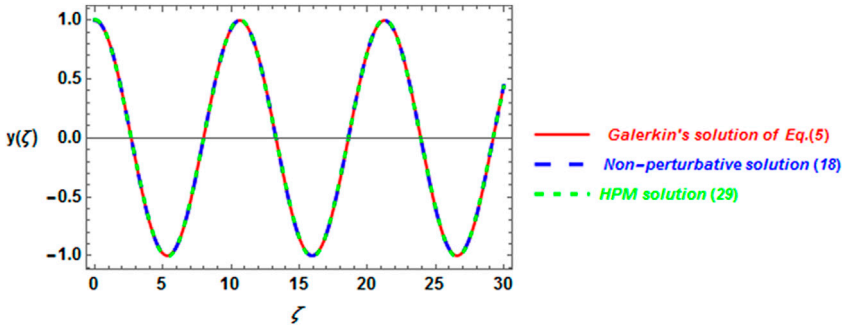

FIGURE 2
Comparison between the analytical periodic solutions by the non-perturbative and homotopy perturbation approaches (18) and (29), respectively, with Galerkin's solution (Eq. 32).

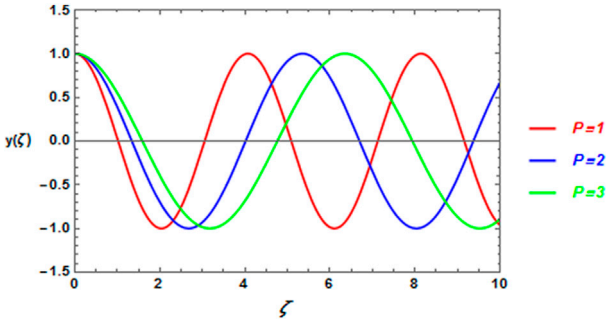

FIGURE 3
Influence of the parameter P on the periodic solution Eq. 32.

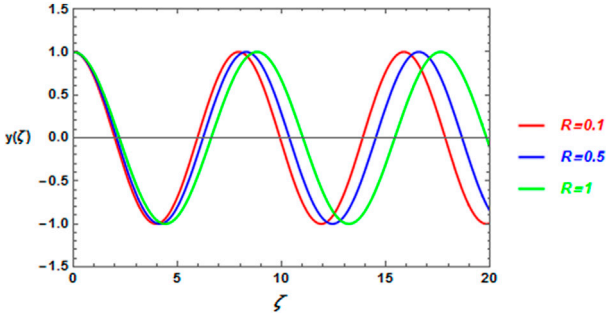

FIGURE 4
Influence of the parameter R on the periodic solution Eq. 32.

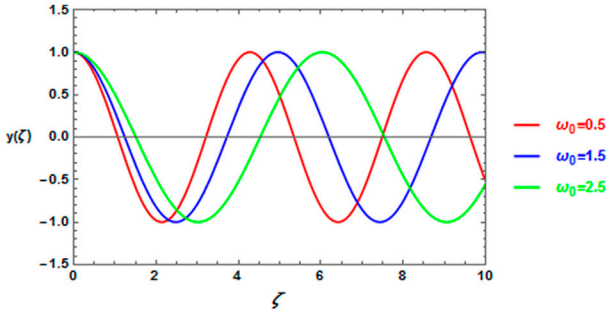

FIGURE 5
Influence of the parameter ω_0 on the periodic solution Eq. 32.

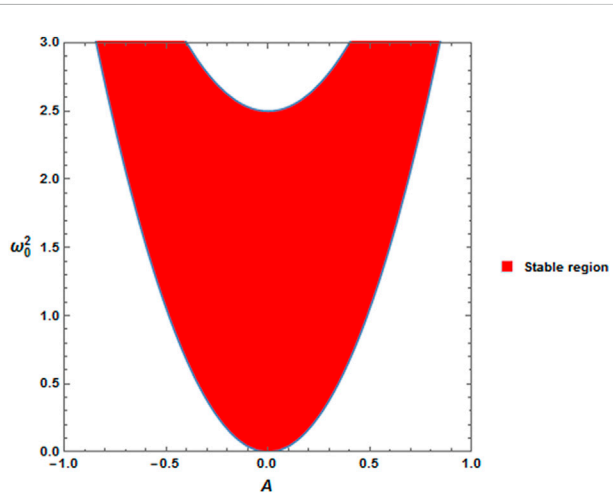

FIGURE 6
Stability distribution of the conditions for a system of $R = 2$ and $P = 0.1$.

Without secular terms, the solution of Eq. 25 arises in the form

$$y_1(\zeta) = \frac{RA^3}{80P^2\omega^4}\left(\omega_0^2 - 3P\omega^2 - \frac{15}{16}RA^2\right)\cos(3\omega\zeta) - \frac{R^2A^5}{3328P^2\Omega^4}\cos(5\omega\zeta). \quad (28)$$

Accordingly, the final first-order approximate solution gives

$$y(\zeta) = A\cos(\omega\zeta) + \frac{RA^3}{80P^2\omega^4}\left(\omega_0^2 - 3P\omega^2 - \frac{15}{16}RA^2\right)\cos(3\omega\zeta) - \frac{R^2A^5}{3328P^2\omega^4}\cos(5\omega\zeta). \quad (29)$$

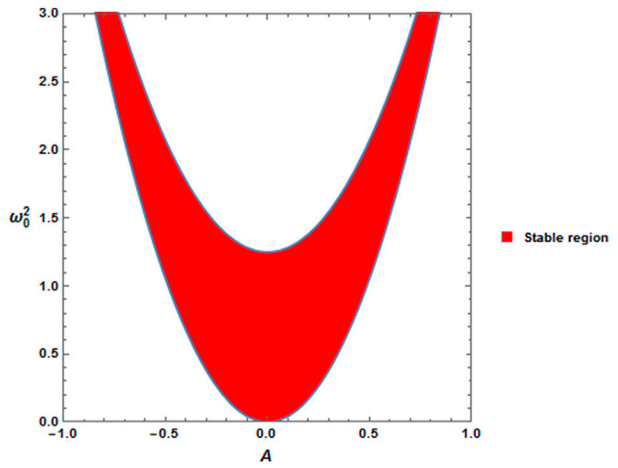

FIGURE 7
Stability distribution of the same system, as given in Figure 6, except that $P = 0.2$.

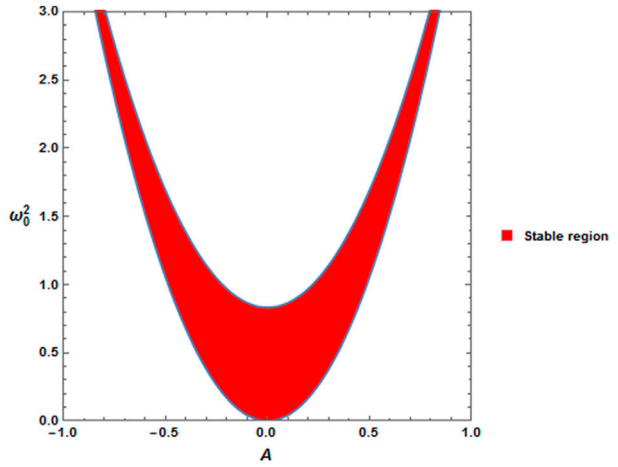

FIGURE 8
Stability distribution of the same system, as given in Figure 6, except that $P = 0.3$.

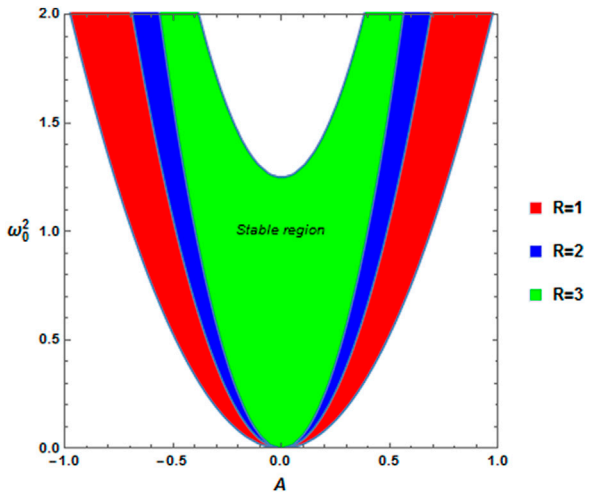

FIGURE 9
Stability distribution of the same system, as given in Figure 7, of $P = 0.2$.

It should be noted that solution Eq. 29 is superior to known asymptotic periodic solutions of Eq. 5. See, for illustration, the recent study demonstrated by [49]. In his work, he applied the Laplace Adomian decomposition method to a damping Duffing equation and obtained an asymptotic solution in terms of a power series. However, the abovementioned solution cannot be obtained using HPM without applying the rank upgrading technique.

The stability criteria of the frequency–amplitude Eq. 26 become

$$P\left(2\omega_0^2 - 3RA^2\right) > 1, \quad \omega_0^4 - 3R\omega_0^2 A^2 + \frac{15}{8}R^2A^4 > 0, \\ \text{and } \frac{3}{2}P^2R^2A^4 - 4P\omega_0^2 + 6PRA^2 + 1 > 0. \tag{30}$$

These criteria ensure the positivity of ω^2.

By employing the value of ζ as a function of x and y from Eq. 3 into the asymptotic solution of Eq. 29, consequently, this asymptotic solution is converted in terms of the original Klein–Gordon Eq. 2; therefore, one obtains

$$y(x,t) = A\cos\left(2\eta\omega x + 2P\mu\omega t\right) + \frac{RA^3}{80P^2\omega^4}\left(\omega_0^2 - 3P\omega^2 - \frac{15}{16}RA^2\right) \\ \times\cos\left(3\eta\omega x + 6P\mu\omega t\right) \quad - \frac{R^2A^5}{3328P^2\omega^4}\cos\left(10\eta\omega x + 10P\mu\omega t\right). \tag{31}$$

For more convenience, a numerical calculation will be represented to confirm the previous approximate analytic solution of the damping Duffing oscillator 5).

5 Numerical illustrations

In this section, the comparison between the numerical solutions for both the original Eq. 5 and alternative Eq. 9is explained. The Runge–Kutta approach built in Mathematica software will be used in this comparison. The numerical values of the parameters are selected in the form $P = 5, R = 0.1, \omega_0 = 2$ and $A = 1$. In Figure 1, the numerical solution for the original equation is represented by the solid red line, while the alternative equation is plotted with a blue dashed line. In this calculation, the error between these solutions is 8.671×10^{-8}. This means that the two curves are identical. This graph shows that Eq. 9 is another face of Eq. 5. This means that any solution of Eq. 9 represents a solution of Eq. 5. Therefore, the periodic solution obtained by the non-perturbative technique or that obtained by the modified HPM represents a periodic solution of the original Eq. 5.

It is worthwhile to observe that the periodic solution Eq. 18, that obtained by the non-perturbative method, and the periodic solution Eq. 29, performed by the modified homotopy perturbation approach, are required for comparing the periodic solution that can be produced from Eq. 5 directly. It is easy to employ the Galerkin's method directly to Eq. 5 to perform the following periodic solution:

$$y(\zeta) = A\cos\Omega\zeta, \tag{32}$$

where Ω is given by

$$\Omega = \frac{1}{2P}\left(-1 + \sqrt{1 - 3A^2PR + 4P\omega_0^2}\right). \quad (33)$$

Figure 2 represents the periodic solution obtained by three different methods. These are as follows: Galerkin's solution (Eq. 32), which is plotted by the solid red line; the non-perturbative solution (Eq. 18),which is represented by the blue dashed line; and the HPM solution (Eq. 29), which is represented by the dotted green curve. The calculations are made for the system having $P = 2.6, R = 1, \omega_0 = 1.5$, and $A = 1$. The investigation of this graph shows that there is an excellent agreement between the three curves. The relative error between the Galerkin solution (Eq. 32) and the non-perturbative solution (Eq. 18) is 0.0007843, while the error between the Galerkin solution (Eq. 32) and the HPM solution (Eq. 29) is found to be 0.004467. This comparison also shows that the non-perturbative solution (Eq. 18) is closer than the HPM solution (Eq. 29) to Galerkin's solution (Eq. 32).

The approximate solution, as given in Eq. 32, is sketched *versus* the parameter ζ for the amplitude $A = 1$ and $R = 0.1, P = 5\omega_0 = 2$. This calculation is displayed in Figures 3–5. These three graphs show a periodic solution for the damping Duffing Eq. 5. Moreover, the influence of the parameters P and R and the linear frequency ω_0 on the periodic solution is shown in these graphs. The growth in these coefficients reduces the time cycle of the wave solution.

The calculations are performed under the stability conditions that are given in Eq. 30. The stable distribution is located in the plane $(\omega_0^2 - A)$. The numerical outcomes are illustrated in Figures 6–9, where the stable region is colored in red. These stable regions have satisfied the three inequalities in Eq. 30. In Figure 6, the natural frequency ω_0^2 is plotted *versus* the amplitude A for the Duffing coefficient $R = 2$ at $P = 0.1$. When the parameter P was increased to the value of $P = 0.2$ (i.e., the damping coefficient is decreased), the stable region was decreased, as shown in Figure 7. The continued raise in P results in reducing the stable region, as shown in Figure 8, for $P = 0.3$. This shows the increase in the damping coefficient plays a stabilizing influence. This agreement is with those obtained in [11]. The examination of the increase in the Duffing coefficient is the subject of Figure 9. It is observed that as R increased, the width of the stable region decreased. This ensures that the nonlinear coefficient plays a destabilizing influence.

6 Conclusion

Away from the regular investigation of the nonlinear oscillators, the present article has been explained. This article deals with the nonlinear Duffing equation and obtains a new result of the periodic solution of a damped nonlinear Duffing oscillator and the damped Klein–Gordon equation by using a new technique named the rank upgrading technique. This technique first increases the order of the partial differential equation by differentiating the original differential equation. The alternative equation is obtained. The comparison between this alternative equation and the original equation shows that the obtained equation is corrected and can be used to perform the periodic solution. Its solution has been validated by applying the HPM to the alternative equation, in which the oscillation frequency obtained by the non-perturbative approach has been identical to that frequency obtained by the HPM. This frequency has been used to discuss stability behavior. A comparison of the periodic solutions' curves was obtained using three different methods. Non-perturbative, modified homotopy perturbation, and Galerkin solutions showed an excellent agreement. This comparison also shows that the non-perturbative solution is closer to Galerkin's solution than the HPM solution. Furthermore, this scheme is a new technique. Therefore, the present numerical method can be used for analyzing different acoustic waves and oscillations in plasma and different physical systems.

Data availability statement

The original contributions presented in the study are included in the article/Supplementary Materials, further inquiries can be directed to the corresponding author.

Author contributions

YE: conceptualization (equal), formal analysis (equal), investigation (equal), and methodology (equal). NE: conceptualization (equal), formal analysis (equal), investigation (equal), and methodology (equal). HA: conceptualization (equal), formal analysis (equal), investigation (equal), and methodology (equal).

Acknowledgments

The authors express their gratitude to Princess Nourah bint Abdulrahman University Researchers Supporting Project number (PNURSP2023R17), Princess Nourah bint Abdulrahman University, Riyadh, Saudi Arabia.

Conflict of interest

The authors declare that the research was conducted in the absence of any commercial or financial relationships that could be construed as a potential conflict of interest.

Publisher's note

All claims expressed in this article are solely those of the authors and do not necessarily represent those of their affiliated organizations, or those of the publisher, the editors, and the reviewers. Any product that may be evaluated in this article, or claim that may be made by its manufacturer, is not guaranteed or endorsed by the publisher.

References

1. Alciatore DG. *Introduction to mechatronics and measurement*. 3rd ed New York: McGraw-Hill (2007). ISBN 978-0-07-296305-2.

2. Duffing G. *Erzwunge Schweingungen bei Veränderlicher Eigenfrequenz*. Braunschweig): F. Viewig u. Sohn (1918).

3. Yamanaka Y, Yamaoka N. Oscillation and non-oscillation theorems for Meissner's equation. *Appl Math Comput* (2021) 388:125526. doi:10.1016/j.amc.2020.125526

4. Nayfeh AH. *Perturbation methods*. New York, USA: John Wily & Sons (1973).

5. Nayfeh AH, Mook DT. *Non-linear oscillations*. New York, USA: John Wily & Sons (1979).

6. He JH. Homotopy perturbation technique. *Comput Methods Appl Mech Eng* (1999) 178:257–62. doi:10.1016/s0045-7825(99)00018-3

7. He JH, El-Dib YO. Homotopy perturbation method with three expansions. *J Math Chem* (2021) 59:1139–50. doi:10.1007/s10910-021-01237-3

8. He JH. New interpretation of homotopy perturbation method. *Int J Mod Phys B* (2006) 20(18):2561–8. doi:10.1142/s0217979206034819

9. Liu ZJ, Adamu MY, Suleiman E, He JH. Hybridization of homotopy perturbation method and Laplace transformation for the partial differential equations. *Therm Sci* (2017) 21(4):1843–6. doi:10.2298/tsci160715078l

10. Filobello-Nino U, Vazquez-Leal H, Herrera-May AL, Ambrosio-Lazaro RC, Jimenez-Fernandez VM, Sandoval-Hernandez M, et al. The study of heat transfer phenomena by using modified homotopy perturbation method coupled by Laplace transform. *Therm Sci* (2020) 24(2B):1105–15. doi:10.2298/tsci180108204f

11. He JH, El-Dib YO. Homotopy perturbation method for Fangzhu oscillator. *J Math Chem* (2020) 58(10):2245–53. doi:10.1007/s10910-020-01167-6

12. El-Dib YO. Stability approach for periodic delay Mathieu equation by the He-multiple-scales method. *Alexandria Eng J* (2018) 57:4009–20. doi:10.1016/j.aej.2018.01.021

13. El-Dib YO. Modified multiple scale technique for the stability of the fractional delayed nonlinear oscillator. *Pramana - J Phys* (2020) 94:56. doi:10.1007/s12043-020-1930-0

14. El-Dib YO. Multiple scales homotopy perturbation method for Non-Linear Oscillators. *Nonlinear Sci Lett A* (2017) 8(4):352–64.

15. El-Dib YO. Periodic solution of the cubic nonlinear Klein–Gordon equation, and the stability criteria via the He-multiple-scales method. *Pramana - J Phys* (2019) 92:7. doi:10.1007/s12043-018-1673-3

16. Adamu MY, Ogenyi P. Parameterized homotopy perturbation method. *Nonlinear Science Letters A* (2017) 8(2):240–3.

17. Vazquez-Leal H. Non-linearities distribution homotopy perturbation method to find solution for Troesch problem. *Nonlinear Science Letters A* (2018) 9(3):279–91.

18. Akgül A, Ahmad H. Reproducing kernel method for Fangzhu's oscillator for water collection from air. *Math Methods Appl Sci* (2020). doi:10.1002/mma.6853

19. Liu C, Kuo C, Chang J. Solving the optimal control problems of nonlinear Duffing oscillators by using an iterative shape functions method. *Comp Model Eng Sci* (2020) 122(1):33–48. doi:10.32604/cmes.2020.08490

20. Liu X, Chen X, Kang R, Shen X, Ni B. A coupled cavitation model in an oscillatory oil squeeze film. *Comp Model Eng Sci* (2020) 123(1):129–52. doi:10.32604/cmes.2020.07836

21. Shen Y, El-Dib YO. A periodic solution of the fractional sine-Gordon equation arising in architectural engineering. *J Low Frequency Noise, Vibration Active Control* (2021) 40(2):683–91. doi:10.1177/1461348420917565

22. El-Dib YO, Elgazery NS, Mady AA, Alyousef HA. On the modeling of a parametric cubic-quintic non-conservative Duffing oscillator via the modified homotopy perturbation method. *Z für Naturforschung A* (2022) 77(5):475–86. doi:10.1515/zna-2021-0354

23. El-Dib YO, Elgazery NS. Damped Mathieu equation with a modulation property of the homotopy perturbation method. *J Sound Vibration* (2022) 56:21–36. doi:10.32604/sv.2022.014166

24. Elgazery NS. A periodic solution of the newell-whitehead-segel (NWS) wave equation via fractional calculus. *J Appl Comput Mech* (2020) 6(SI):1293–300.

25. He JH, Yang Q, He CH, Khan Y. A simple frequency formulation for the tangent oscillator. *Axioms* (2021) 10:320. doi:10.3390/axioms10040320

26. Shokhanda R, Goswami P, He JH, Althobaiti A. An approximate solution of the time-fractional two-mode coupled Burgers equation. *Fractal and Fractional* (2021) 5:196. doi:10.3390/fractalfract5040196

27. He JH, Anjum N, Skrzypacz P. A variational principle for a nonlinear oscillator arising in the microelectromechanical system. *J Appl Comput Mech* (2021) 7(1):78–83.

28. He JH, El-Dib YO. The reducing rank method to solve third-order Duffing equation with the homotopy perturbation. *Numer Methods Partial Differential Equations* (2021) 37(2):1800–8. doi:10.1002/num.22609

29. Luo Z, Jin S. A reduced-order extrapolated Crank–Nicolson collocation spectral method based on proper orthogonal decomposition for the two-dimensional viscoelastic wave equations. *Numer Methods Partial Differential Equations* (2020) 36:49–65. doi:10.1002/num.22397

30. El-Dib YO. The damping Helmholtz–Rayleigh–Duffing oscillator with the non-perturbative approach. *Mathematics Comput Simulation* (2022) 194:552–62. doi:10.1016/j.matcom.2021.12.014

31. He JH, El-Dib YO. The enhanced homotopy perturbation method for axial vibration of strings. *Fact universitatis, Ser Mech Eng* (2021) 19:735. doi:10.22190/FUME210125033H

32. Jena RM, Chakraverty S, Jena SK. Dynamic response analysis of fractionally damped beams subjected to external loads using homotopy analysis method. *J Appl Comput Mech* (2019) 5(2):355–66. doi:10.22055/jacm.2019.27592.1419

33. Atabak R, Sedighi HM, Reza A, Mirshekari E. Analytical investigation of air squeeze film damping for biaxial micro-scanner using eigenfunction expansion method. *Math Methods Appl Sci* (2020). doi:10.1002/mma.6658

34. Yekrangisendi A, Yaghobi M, Riazian M, Koochi A. Scale-dependent dynamic behavior of nanowire-based sensor in accelerating field. *J Appl Comput Mech* (2019) 5(2):486–97. doi:10.22055/jacm.2018.27302.1393

35. Lin Y, Cui M. A new method to solve the damped nonlinear Klein-Gordon equation. *Sci China Ser A: Math* (2008) 51:304–13. doi:10.1007/s11425-008-0030-2

36. Pang Y, Yang Y. A note on finite time blowup for dissipative Klein–Gordon equation. *Nonlinear Anal* (2020) 195:111729. doi:10.1016/j.na.2019.111729

37. Parka JY, Jeong U. Optimal control of damped Klein–Gordon equations with state constraints. *J Math Anal Appl* (2007) 334:11–27. doi:10.1016/j.jmaa.2006.12.042

38. Côte R, Martel Y, Yuan X. Long-time asymptotics of the one-dimensional damped nonlinear Klein–Gordon equation. *Archive Rational Mech Anal* (2021) 239(3):1837–74. doi:10.1007/s00205-020-01605-4

39. Dehghan M, Ghesmati A. Application of the dual reciprocity boundary integral equation technique to solve the nonlinear Klein–Gordon equation. *Comp Phys Commun* (2010) 181(8):1410–8. doi:10.1016/j.cpc.2010.04.008

40. El-Dib YO, Elgazery NS. Effect of fractional derivative properties on the periodic solution of the nonlinear oscillations. *Fractals* (2020) 28(4):2050095. doi:10.1142/S0218348X20500954

41. El-Dib YO. Stability approach of a fractional-delayed duffing oscillator. *Discontinuity, Nonlinearity, and Complexity* (2020) 9(3):367–76.

42. El-Dib YO. Homotopy perturbation method with rank upgrading technique for the superior nonlinear oscillation. *Math Comput Simulation* (2021) 182:555–65. doi:10.1016/j.matcom.2020.11.019

43. El-Dib YO, Matoog RT. The rank upgrading technique for a harmonic restoring force of nonlinear oscillators. *J Appl Comput Mech* (2021) 7(2):782–9.

44. El-Dib YO. Immediate solution for fractional nonlinear oscillators using the equivalent linearized method. *J Low Frequency Noise Vibration Active Control* (2022) 41(4):1411–25. doi:10.1177/14613484221098788

45. El-Dib YO. Insightful and comprehensive formularization of frequency amplitude formula for strong or singular nonlinear oscillators. *J Low Frequency Noise, Vibration Active Control* (2023) 146134842211181. doi:10.1177/14613484221118177

46. El-Dib YO, Elgazery NS, Gad NS. A novel technique to obtain a time-delayed vibration control analytical solution with simulation of He's formula. *J Low Frequency Noise* (2023). Vibration & Active Control. doi:10.1177/14613484221149518

47. He JH, El-Dib YO, Mady AA. Homotopy perturbation method for the fractal toda oscillator. *Fractal and Fractional* (2021) 5:93. doi:10.3390/fractalfract5030093

48. El-Dib YO. *Criteria of vibration control in delayed third-order critically damped Duffing oscillation. Archive of Applied Mechanics* (2021) 92(1):1–19. doi:10.1007/s00419-021-02039-4

49. Nnaji DU. *Application of Laplace adomian decomposition method (LADM) to duffing equation*. APLAMBERT Academic Publishing (2020).

frontiers | Frontiers in Physics

TYPE Original Research
PUBLISHED 14 February 2023
DOI 10.3389/fphy.2023.1114319

OPEN ACCESS

EDITED BY
Gangwei Wang,
Hebei University of Economics and Business, China

REVIEWED BY
Weipeng Hu,
Northwestern Polytechnical University, China
Zhonglong Zhao,
North University of China, China

*CORRESPONDENCE
Umair Ali,
umairkhanmath@gmail.com
Abdul Hamid Ganie,
a.ganie@seu.edu.sa

SPECIALTY SECTION
This article was submitted to Mathematical Physics, a section of the journal Frontiers in Physics

RECEIVED 02 December 2022
ACCEPTED 23 January 2023
PUBLISHED 14 February 2023

CITATION
Ali U, Naeem M, Alahmadi R, Abdullah FA, Khan MA and Ganie AH (2023), An investigation of a closed-form solution for non-linear variable-order fractional evolution equations *via* the fractional Caputo derivative.
Front. Phys. 11:1114319.
doi: 10.3389/fphy.2023.1114319

An investigation of a closed-form solution for non-linear variable-order fractional evolution equations *via* the fractional Caputo derivative

Umair Ali[1]*, Muhammad Naeem[2], Reham Alahmadi[3], Farah Aini Abdullah[4], Muhammad Asim Khan[5] and Abdul Hamid Ganie[3]*

[1]Department of Applied Mathematics and Statistics, Institute of Space Technology, Islamabad, Pakistan, [2]Department of Mathematics of Applied Sciences, Umm-Al-Qura University, Makkah, Saudi Arabia, [3]Department of Basic Sciences, College of Science and Theoretical Studies, Saudi Electronic University, Riyadh, Saudi Arabia, [4]School of Mathematical Sciences, Universiti Sains Malaysia, Penang, Malaysia, [5]Department of Mathematical Sciences, Faculty of Sciences, Universiti Teknologi Malaysia, Johor Bahru, Malaysia

Determining the non-linear traveling or soliton wave solutions for variable-order fractional evolution equations (VO-FEEs) is very challenging and important tasks in recent research fields. This study aims to discuss the non-linear space–time variable-order fractional shallow water wave equation that represents non-linear dispersive waves in the shallow water channel by using the Khater method in the Caputo fractional derivative (CFD) sense. The transformation equation can be used to get the non-linear integer-order ordinary differential equation (ODE) from the proposed equation. Also, new exact solutions as kink- and periodic-type solutions for non-linear space–time variable-order fractional shallow water wave equations were constructed. This confirms that the non-linear fractional variable-order evolution equations are natural and very attractive in mathematical physics.

KEYWORDS

space-time variable-order fractional shallow water wave equation, variable-order Caputo fractional derivative, Khater method, closed-form solution, graphical representation

1 Introduction

Fractional calculus is a generalization of traditional integer-order integration and derivation actions onto non-integer order. The idea of fractional calculus is as old as classical calculus; it was discussed for the first time by Leibniz and L'Hospital in 1965. The fractional- and variable-order VO fractional models gained more attention because these models describe the physical phenomenon properly as compared to integer-order differential models. The non-linear FEEs define different phenomena in various areas, such as signal preparation, medication, biology, and organic framework [1, 2]. Many strategies have been produced to solve integer/fractional-order problems. Various fractional-order literature works directed that the memory and/or

Abbreviations: ADI, alternating direction implicit scheme; EW, equal width; FPDE, fractional partial differential equation; GEW, generalized equal width; ODE, ordinary differential equation; SRLW, symmetric regularized long wave; VO, variable order; 2D, two-dimensional; 3D, three-dimensional.

non-locality of the system may change with time, space, or other conditions. So, here our focus is on VO fractional differential models, which describe the physical models that vary with time or space or space–time. For example, Akgül et al. [3] solved the VO FPDE numerically and presented numerical experiments to confirm the efficiency and feasibility. Katsikadelis [4] developed a numerical method for linear and non-linear VO FPDEs in the Caputo sense. The resultant numerical values demonstrated the accuracy of the proposed method. Sahoo et al. [5] reviewed the VO operator definitions and properties. They discussed the new transfer function and investigated the model of a dynamic viscoelastic oscillator. Sing et al. [6] suggested an SEIR model that modeled the 2014–2015 outbreak of the Ebola virus in Africa. They discussed the system of VO FDEs and estimated its parameters for one or more variables. Semary et al. [7] approximated the solution of Liouville–Caputo VO FPDEs with $0 < \alpha(t) \leq 1$ based on the Chebyshev function and discussed many linear and non-linear non-integer-order PDEs. Taghipour and Aminikhah [8] proposed the ADI numerical scheme for the fractional-order model and discussed the theoretical analysis. Other related studies can be seen in [9–16]. The effective analytical and closed-form solutions are studied in the recent literature. For example, Uddin et al. [17] considered the two important fractional-order models, namely, equal width and generalized equal width that describe the dispersive waves. They used the fractional derivative in the Riemann–Liouville sense and the $(\frac{G'}{G}, \frac{1}{G})$ expansion approach has been used, and they confirmed that the proposed approach is powerful, very convenient, and computationally efficient. Barman et al. [18] worked on a generalized Kudryashov method to provide a generic and inclusive closed-form solution. The proposed approach confirmed various shapes of waveform solutions such as kink-shaped, bell-shaped, singular, and flat in a 3D form. In another study, Barman et al. [19] proposed the same technique for Konopelchenko–Dubrovsky and Landau–Ginzburg–Higgs models. They obtained various varieties of analytical solutions for different parameters. The solutions are obtained in 2D and 3D forms, which demonstrated the efficiency and reliability of the proposed method. Roy et al. [20] solved the two significant types of models and implemented the new generalized G'/G expansion method. They constructed the solution in trigonometric, hyperbolic, and rational forms with different parameters. Kumar et al. [21] found out the exact solution for the higher-dimensional Fokas and breaking soliton models by the generalized exponential function method. The authors observed that the suggested method is effective and powerful. Ali et al. [22] investigated the exact solution for the VO fractional modified equal width equation based on the exp $(-\phi(\xi))$ method. The fractional derivative is obtained in the Caputo sense, and the obtained exact solution is new and somewhat natural in mathematical physics. Akhtar et al. [23] constructed exact and traveling wave solutions for the Konopelchenko–Dubrovsky model and used two types of integration schemes. The resultant solutions are dark, single, anti-kink forms having a wide range of applications in applied sciences. Islam et al. [24] worked on analytical techniques and found the solution for the fractional-order foam drainage equation and SRLW equation. They used the G'/G expansion method and investigated the traveling wave solution for the proposed models. Mamun et al. [25] discussed the double $(\frac{G'}{G}, \frac{1}{G})$ expansion approach for the breaking soliton and the (1 + 1)-dimensional classical Boussinesq equations and obtained different soliton solutions, such as kink, multi-periodic, single soliton, and periodic wave solutions for different values of parameters. The comprehensive study can be found in [26–35].

The aforementioned cited literature reported that so far only numerical studies have been discussed for VO models and no attempt has been made to find the closed form for such types of VO-FEEs. The objective of this paper is to discuss the closed-form solution of the non-linear VO-FEEs. Here, we solve the non-linear VO fractional shallow water wave equation with CFD using the Khater method. The VO fractional problems are more complex computationally than a constant fractional order, and the evolution of a system can be furthermore clearly and accurately described. This contribution seems natural and simple and models many systems with VO [36]. The traveling wave solutions for the VO physical models are not known to the authors.

2 The outline of the Khater method

The non-linear variable-order $\alpha(x, y, \ldots, t)$ FPDE is given as

$$\mathrm{H}\left(D_x^{\alpha(x,y,\ldots,t)}Y, D_x^{\alpha(x,y,\ldots,t)}D_t^{\alpha(x,y,\ldots,t)}Y, D_x^{\alpha(x,y,\ldots,t)}D_y^{2\alpha(x,y,\ldots,t)}Y, \ldots\right) = 0. \tag{1}$$

where H is a polynomial for $Y, Y_t, Y_x, D_t^{\alpha(x,y,\ldots,t)}, D_x^{\alpha(x,y,\ldots,t)}, D_y^{\alpha(x,y,\ldots,t)}$ and $D^{\alpha(x,y,\ldots,t)}$ represents Caputo fractional derivatives of the variable-order $\alpha(x, y, \ldots, t)$. The Caputo fractional derivative of the variable order for a function $Y(x,t)$ of order $\gamma(x,t)\epsilon(0,1]$ is defined as follows [22]:

$$D_t^{\gamma(x,t)}Y(x,t) = \begin{cases} \dfrac{1}{\Gamma(1+\gamma(x,t))}\displaystyle\int_0^t \frac{Y'(x,t)}{\Gamma(t-\xi)^{\gamma(x,t)}}d\xi, 0 < \gamma(x,t) < 1, \\ Y'(x,t), \gamma(x,t) = 1. \end{cases} \tag{2}$$

Also, the important property is given as follows:

$$D_t^{\gamma(x,t)}t^{\beta} = \frac{\Gamma(1-\beta)}{\Gamma(1-\beta+\gamma(x,t))}t^{\beta-\gamma(x,t)}, 0 < \gamma(x,t) < 1. \tag{3}$$

Eq. 1 involved the linear and non-linear highest-order derivatives. A brief explanation of the proposed method is as follows [37]:

Convert the variable-order FPDE into an ordinary differential equation (ODE) by taking the transformation as

$$\begin{aligned} Y(x,y,t) &= y(\xi), \xi \\ &= \frac{kx^{\alpha(x,y,\ldots,t)}}{\Gamma(1+\alpha(x,y,..,t))} + \frac{ly^{\alpha(x,y,\ldots,t)}}{\Gamma(1+\alpha(x,y,..,t))} + \cdots \\ &\quad - \frac{\omega t^{\alpha(x,y,\ldots,t)}}{\Gamma(1+\alpha(x,y,..,t))}. \end{aligned} \tag{4}$$

The obtained ODE is as follows:

$$\mathrm{H}(y, \omega y', ky'', ly''', \omega ly''', kly''', \ldots) = 0, \tag{5}$$

where k, l, m, and ω are constant parameters, if necessary, integrate Eq. 5. Next, we constructed a trial solution which can be expressed as

$$y(\xi) = \sum_{n=0}^{M} a_n a^{nf(\xi)}, \tag{6}$$

where a_n $(n = 1, 2, \ldots, M-1)$ can be zero and $a_M \neq 0$, and the function $f(\xi)$ satisfies the following second-order linear equation:

$$f'(\xi) = \frac{1}{\ln(a)}\left(\alpha a^{-f(\xi)} + \beta + \sigma a^{f(\xi)}\right). \tag{7}$$

The aforementioned equation has 27 possible solutions [33], which are derived by formulating various traveling wave solutions. Furthermore, the balancing principle is used to find M. Substituting Eq. 6 in Eq. 5 and Eq. 7, an equation involving the term $(a^{f(\xi)})$ is obtained. In the obtained system of equations, the same power of $(a^{f(\xi)})$ is equated to zero. The equations are solved simultaneously to find all unknown constants.

The solutions to Eq. 7:

When $\beta^2 - 4\alpha\sigma < 0$ and $\sigma \neq 0$,

$$a^{f(\xi)} = \frac{-\beta + \sqrt{4\alpha\sigma - \beta^2}\tan\left(\frac{\sqrt{4\alpha\sigma-\beta^2}}{2}\xi\right)}{2\sigma} \tag{8}$$

or

$$a^{f(\xi)} = \frac{-\beta - \sqrt{4\alpha\sigma - \beta^2}\cot\left(\frac{\sqrt{4\alpha\sigma-\beta^2}}{2}\xi\right)}{2\sigma}. \tag{9}$$

When $\beta^2 - 4\alpha\sigma > 0$ and $\sigma \neq 0$,

$$a^{f(\xi)} = \frac{-\beta - \sqrt{\beta^2 - 4\alpha\sigma}\tanh\left(\frac{\sqrt{\beta^2-4\alpha\sigma}}{2}\xi\right)}{2\sigma} \tag{10}$$

or

$$a^{f(\xi)} = \frac{-\beta - \sqrt{\beta^2 - 4\alpha\sigma}\coth\left(\frac{\sqrt{\beta^2-4\alpha\sigma}}{2}\xi\right)}{2\sigma}. \tag{11}$$

When $\beta^2 + 4\alpha^2 < 0$, $\sigma \neq 0$, and $\sigma = -p$,

$$a^{f(\xi)} = \frac{\beta - \sqrt{-(\beta^2 + 4\alpha^2)}\tan\left(\frac{\sqrt{-(\beta^2+4\alpha^2)}}{2}\xi\right)}{2\alpha} \tag{12}$$

or

$$a^{f(\xi)} = \frac{+\beta\sqrt{-(\beta^2 + 4\alpha^2)}\cot\left(\frac{\sqrt{-(\beta^2+4\alpha^2)}}{2}\xi\right)}{2\alpha}. \tag{13}$$

When $\beta^2 + 4\alpha^2 > 0$, $\sigma \neq 0$, and $\sigma = -\alpha$,

$$a^{f(\xi)} = \frac{\beta + \sqrt{(\beta^2 + 4\alpha^2)}\tanh\left(\frac{\sqrt{(q^2+4p^2)}}{2}\xi\right)}{2\alpha} \tag{14}$$

or

$$a^{f(\xi)} = \frac{\beta + \sqrt{(\beta^2 + 4\alpha^2)}\coth\left(\frac{\sqrt{(\beta^2+4\alpha^2)}}{2}\xi\right)}{2\alpha}. \tag{15}$$

When $\beta^2 - 4\,\alpha^2 < 0$ and $\sigma = \alpha$,

$$a^{f(\xi)} = \frac{-\beta + \sqrt{-(\beta^2 - 4\alpha^2)}\tanh\left(\frac{\sqrt{-(q^2-4p^2)}}{2}\xi\right)}{2\alpha} \tag{16}$$

or

$$a^{f(\xi)} = \frac{-\beta - \sqrt{-(\beta^2 - 4\alpha^2)}\coth\left(\frac{\sqrt{-(\beta^2-4\alpha^2)}}{2}\xi\right)}{2\alpha}. \tag{17}$$

When $\beta^2 - 4\alpha^2 > 0$ and $\sigma = \alpha$,

$$a^{f(\xi)} = \frac{-\beta - \sqrt{(\beta^2 - 4\alpha^2)}\tanh\left(\frac{\sqrt{(\beta^2-4\alpha^2)}}{2}\xi\right)}{2\alpha} \tag{18}$$

or

$$a^{f(\xi)} = \frac{-\beta - \sqrt{\beta^2 - 4\alpha^2}\,cot\,h\left(\frac{\sqrt{\beta^2-4\alpha^2}}{2}\xi\right)}{2\alpha}. \tag{19}$$

When $\beta^2 = 4\alpha\sigma$,

$$a^{f(\xi)} = -\frac{2 + \beta\xi}{2\sigma\xi}. \tag{20}$$

When $\sigma\alpha < 0$, $\beta = 0$, and $\sigma \neq 0$,

$$a^{f(\xi)} = -\sqrt{\frac{-\alpha}{\sigma}}\tanh\left(\sqrt{-\sigma\alpha}\,\xi\right) \tag{21}$$

or

$$a^{f(\xi)} = -\sqrt{\frac{-\alpha}{\sigma}}\,cot\,\mathrm{h}\left(\sqrt{-\sigma\alpha}\,\xi\right). \tag{22}$$

When $\beta = 0$ and $\alpha = -\sigma$,

$$a^{f(\xi)} = \frac{1 + e^{(-2\sigma\xi)}}{-1 + e^{(-2\sigma\xi)}}. \tag{23}$$

When $\alpha = \sigma = 0$,

$$a^{f(\xi)} = \cosh(\beta\xi) + \sinh(\beta\xi). \tag{24}$$

When $\alpha = \beta = k$ and $\sigma = 0$,

$$a^{f(\xi)} = e^{k\xi} - 1. \tag{25}$$

When $\beta = \sigma = k$ and $\alpha = 0$,

$$a^{f(\xi)} = \frac{e^{k\xi}}{1 - e^{k\xi}}. \tag{26}$$

When $\beta = \alpha + \sigma$,

$$a^{f(\xi)} = -\frac{1 - \alpha e^{(\alpha-\sigma)\xi}}{1 - \sigma e^{(\alpha-\sigma)\xi}}. \tag{27}$$

When $\beta = -(\alpha + \sigma)$,

$$a^{f(\xi)} = \frac{\alpha - e^{(\alpha-\sigma)\xi}}{\sigma - e^{(\alpha-\sigma)\xi}}. \tag{28}$$

When $\alpha = 0$,

$$a^{f(\xi)} = \frac{\beta\, e^{\beta\xi}}{1 - \sigma e^{\beta\xi}}. \tag{29}$$

When $\sigma = \beta = \alpha \neq 0$,

$$a^{f(\xi)} = \frac{1}{2}\left\{\sqrt{3}\;tan\left(\frac{\sqrt{3}}{2}\alpha\xi\right) - 1\right\}. \tag{30}$$

When $\sigma = \beta = 0$,

$$a^{f(\xi)} = \alpha\,\xi. \tag{31}$$

When $\alpha = \beta = 0$,

$$a^{f(\xi)} = \frac{-1}{\sigma\xi}. \tag{32}$$

When $\sigma = \alpha$ and $\beta = 0$,

$$a^{f(\xi)} = \tan(\alpha\xi). \tag{33}$$

When $\sigma = 0$,

$$a^{f(\xi)} = e^{\beta\xi} - \frac{\alpha}{\beta}. \tag{34}$$

The exact solutions for Eq. 1 are obtained by substituting unknown constants and Eq. 7 in Eq. 6.

3 Formulation for the solutions of shallow water wave equations

Shallow water waves arise in the ocean when the waves move from the center of the ocean to the shore or beach known as shallow water waves. Most of the ocean waves are produced by wind, tsunamis, earthquakes, tides, etc. [38], which carry energy. Tsunamis and tides are both shallow water waves. The shallow water wave equation has been derived from the Navier–Stokes equations. Here, we apply the proposed method to study the non-linear space–time fractional VO shallow water wave equation and construct a traveling wave solution based on the Khater method.

3.1 The non-linear space–time variable-order fractional shallow water wave equation

We consider the space–time VO fractional shallow water wave equation as follows [39]:

$$D_t^{2\gamma(x,t)}\left(D_x^{\delta(x,t)}Y\right) + 3D_x^{\delta(x,t)}Y\, D_t^{\delta(x,t)}Y - D_x^{\delta(x,t)}Y - D_t^{\gamma(x,t)}Y = 0. \tag{35}$$

Using the wave variable $\xi = \frac{kx^{\delta(x,t)}}{\Gamma(1+\delta(x,t))} - \frac{\omega t^{\gamma(x,t)}}{\Gamma(1+\gamma(x,t))}$, Eq. 35 simplified to

$$k\omega^2 y''' - 3k\omega\left(y'\right)^2 - ky' + \omega y' = 0. \tag{36}$$

By balancing the highest-order non-linear term $(y')^2$ and the highest-order linear term y''', we obtain $M = 1$. Therefore, the solution of Eq. 6 becomes

$$y = a_0 + a_1 a^{f(\xi)}. \tag{37}$$

Substituting Eq. 37 into Eq. 36 yields a polynomial equation for $(a^{f(\xi)})$. Equating the like powers of $(a^{f(\xi)})^n$, we attain a system of algebraic equations given as

$$\left(a^{f(\xi)}\right)^0: 2\alpha^2 k\omega^2\sigma a_1^2 - 3\alpha^2 k\omega a_1^4 + \alpha\beta^2 k\omega^2 a_1^2 - \alpha k a_1^2 + \alpha\omega a_1^2 = 0,$$
$$\left(a^{f(\xi)}\right)^1: 8\alpha\beta k\omega^2 a_1^2 - 6\alpha\beta k\omega a_1^4 + \beta^3 k\omega^2 a_1^2 - \beta k a_1^2 + \beta\omega a_1^2 = 0,$$
$$\left(a^{f(\xi)}\right)^2: 8\alpha k\omega^2\sigma^2 a_1^2 - 6\alpha k\omega a_1^4 + 7\beta^2 k\omega a_1^4 - k\sigma a_1^2 + \omega\sigma a_1^2 = 0,$$
$$\left(a^{f(\xi)}\right)^3: 12\beta k\omega^2\sigma^2 a_1^2 - 6\alpha\beta k\omega a_1^4 = 0,$$
$$\left(a^{f(\xi)}\right)^4: 6k\omega^2\sigma^3 a_1^2 - 3k\omega\sigma^2 a_1^4 = 0.$$

Solving the aforementioned system of algebraic equations by using computer algebra, we obtain

$$\textbf{Set 1}: a_0 = a_0, a_1 = \sqrt{\frac{\left(1+\sqrt{1-16\alpha k^2\sigma+4\beta^2k^2}\right)\sigma}{(4\alpha\sigma-\beta^2)k}}, \omega = \frac{1+\sqrt{1-16\alpha k^2\sigma+4\beta^2k^2}}{2(4\alpha\sigma-\beta^2)k}, \tag{38}$$

where ω, k, α, β, and σ are arbitrary constants. Substituting Eq. 38 into Eq. 37, we obtain

$$y_1 = a_0 + \sqrt{\frac{\left(1+\sqrt{1-16\alpha k^2\sigma+4\beta^2k^2}\right)\sigma}{(4\alpha\sigma-\beta^2)k}}\, a^{f(\xi)}. \tag{39}$$

Now, substituting the solutions of Eq. 7, we obtain the following 27 distinct traveling wave solutions for space–time fractional variable-order shallow water wave Eq. 35:

When $\beta^2 - 4\alpha\sigma < 0$ and $\sigma \neq 0$,

$$Y_1 = \frac{\left(\sqrt{4\alpha\sigma-\beta^2}\,\tan\left(\frac{1}{2}\sqrt{4\alpha\sigma-\beta^2}\left(\frac{kx^{\delta(x,t)}}{\Gamma(1+\delta(x,t))} - \frac{\omega t^{\gamma(x,t)}}{\Gamma(1+\gamma(x,t))}\right)\right) - \beta\right)\sqrt{-\frac{\left(1+\sqrt{1-16\alpha k^2\sigma+4\beta^2k^2}\right)\sigma}{(4\alpha\sigma-\beta^2)k}} + 2a_0\sigma}{2\sigma},$$

$$Y_2 = \frac{\left(-\sqrt{4\alpha\sigma-\beta^2}\,\cot\left(\frac{1}{2}\sqrt{4\alpha\sigma-\beta^2}\left(\frac{kx^{\delta(x,t)}}{\Gamma(1+\delta(x,t))} - \frac{\omega t^{\gamma(x,t)}}{\Gamma(1+\gamma(x,t))}\right)\right) - \beta\right)\sqrt{-\frac{\left(1+\sqrt{1-16\alpha k^2\sigma+4\beta^2k^2}\right)\sigma}{(4\alpha\sigma-\beta^2)k}} + 2a_0\sigma}{2\sigma}.$$

When $\beta^2 - 4\alpha\sigma > 0$ and $\sigma \neq 0$,

$$Y_3 = \frac{\left(-\sqrt{-4\alpha\sigma+\beta^2}\,\tanh\left(\frac{1}{2}\sqrt{-4\alpha\sigma+\beta^2}\left(\frac{kx^{\delta(x,t)}}{\Gamma(1+\delta(x,t))} - \frac{\omega t^{\gamma(x,t)}}{\Gamma(1+\gamma(x,t))}\right)\right) - \beta\right)\sqrt{-\frac{\left(1+\sqrt{1-16\alpha k^2\sigma+4\beta^2k^2}\right)\sigma}{(-4\alpha\sigma+\beta^2)k}} + 2a_0\sigma}{2\sigma},$$

$$Y_4 = \frac{\left(-\sqrt{-4\alpha\sigma+\beta^2}\,\coth\left(\frac{1}{2}\sqrt{-4\alpha\sigma+\beta^2}\left(\frac{kx^{\delta(x,t)}}{\Gamma(1+\delta(x,t))} - \frac{\omega t^{\gamma(x,t)}}{\Gamma(1+\gamma(x,t))}\right)\right) - \beta\right)\sqrt{-\frac{\left(1+\sqrt{1-16\alpha k^2\sigma+4\beta^2k^2}\right)\sigma}{(-4\alpha\sigma+\beta^2)k}} + 2a_0\sigma}{2\sigma}.$$

When $\beta^2 + 4\alpha^2 < 0$, $\sigma \neq 0$, and $\sigma = -p$,

$$Y_5 = \frac{\left(-\sqrt{-4\alpha^2-\beta^2}\,\tan\left(\frac{1}{2}\sqrt{-4\alpha^2-\beta^2}\left(\frac{kx^{\delta(x,t)}}{\Gamma(1+\delta(x,t))} - \frac{\omega t^{\gamma(x,t)}}{\Gamma(1+\gamma(x,t))}\right)\right) + \beta\right)\sqrt{-\frac{\left(1+\sqrt{1-16\alpha k^2\sigma+4\beta^2k^2}\right)\sigma}{(-4\alpha\sigma+\beta^2)k}} + 2a_0\sigma}{2\sigma},$$

$$Y_6 = \frac{\left(-\sqrt{-4\alpha^2-\beta^2}\,\cot\left(\frac{1}{2}\sqrt{-4\alpha^2-\beta^2}\left(\frac{kx^{\delta(x,t)}}{\Gamma(1+\delta(x,t))} - \frac{\omega t^{\gamma(x,t)}}{\Gamma(1+\gamma(x,t))}\right)\right) + \beta\right)\sqrt{-\frac{\left(1+\sqrt{1-16\alpha k^2\sigma+4\beta^2k^2}\right)\sigma}{(-4\alpha\sigma+\beta^2)k}} + 2a_0\sigma}{2\sigma}.$$

When $\beta^2 + 4\alpha^2 > 0$, $\sigma \neq 0$, and $\sigma = -p$,

$$Y_7 = \frac{\left(\sqrt{4\alpha^2+\beta^2}\,\tanh\left(\frac{1}{2}\sqrt{4\alpha^2+\beta^2}\left(\frac{kx^{\delta(x,t)}}{\Gamma(1+\delta(x,t))} - \frac{\omega t^{\gamma(x,t)}}{\Gamma(1+\gamma(x,t))}\right)\right) + \beta\right)\sqrt{-\frac{\left(1+\sqrt{1-16\alpha k^2\sigma+4\beta^2k^2}\right)\sigma}{(-4\alpha\sigma+\beta^2)k}} + 2a_0\sigma}{2\sigma},$$

$$Y_8 = \frac{\left(\sqrt{4\alpha^2+\beta^2}\,\coth\left(\frac{1}{2}\sqrt{4\alpha^2+\beta^2}\left(\frac{kx^{\delta(x,t)}}{\Gamma(1+\delta(x,t))} - \frac{\omega t^{\gamma(x,t)}}{\Gamma(1+\gamma(x,t))}\right)\right) + \beta\right)\sqrt{-\frac{\left(1+\sqrt{1-16\alpha k^2\sigma+4\beta^2k^2}\right)\sigma}{(-4\alpha\sigma+\beta^2)k}} + 2a_0\sigma}{2\sigma}.$$

When $\beta^2 - 4\alpha^2 < 0$ and $\sigma = \alpha$,

$$Y_9 = \frac{\left(\sqrt{4\alpha^2-\beta^2}\,\tan\left(\frac{1}{2}\sqrt{4\alpha^2-\beta^2}\left(\frac{kx^{\delta(x,t)}}{\Gamma(1+\delta(x,t))} - \frac{\omega t^{\gamma(x,t)}}{\Gamma(1+\gamma(x,t))}\right)\right) - \beta\right)\sqrt{-\frac{\left(1+\sqrt{1-16\alpha k^2\sigma+4\beta^2k^2}\right)\sigma}{(-4\alpha\sigma+\beta^2)k}} + 2a_0\sigma}{2\sigma},$$

$$Y_{10} = \frac{\left(-\sqrt{4\alpha^2-\beta^2}\,\cot\left(\frac{1}{2}\sqrt{4\alpha^2-\beta^2}\left(\frac{kx^{\delta(x,t)}}{\Gamma(1+\delta(x,t))} - \frac{\omega t^{\gamma(x,t)}}{\Gamma(1+\gamma(x,t))}\right)\right) - \beta\right)\sqrt{-\frac{\left(1+\sqrt{1-16\alpha k^2\sigma+4\beta^2k^2}\right)\sigma}{(-4\alpha\sigma+\beta^2)k}} + 2a_0\sigma}{2\sigma}.$$

When $q^2 - 4p^2 > 0$ and $r = p$,

$$Y_{11} = \frac{\left(-\sqrt{-4\alpha^2+\beta^2}\,\tanh\left(\frac{1}{2}\sqrt{-4\alpha^2+\beta^2}\left(\frac{kx^{\delta(x,t)}}{\Gamma(1+\delta(x,t))} - \frac{\omega t^{\gamma(x,t)}}{\Gamma(1+\gamma(x,t))}\right)\right) - \beta\right)\sqrt{-\frac{\left(1+\sqrt{1-16\alpha k^2\sigma+4\beta^2k^2}\right)\sigma}{(-4\alpha\sigma+\beta^2)k}} + 2a_0\sigma}{2\sigma},$$

$$Y_{12} = \frac{\left(-\sqrt{-4\alpha^2+\beta^2}\,\coth\left(\frac{1}{2}\sqrt{-4\alpha^2+\beta^2}\left(\frac{kx^{\delta(x,t)}}{\Gamma(1+\delta(x,t))} - \frac{\omega t^{\gamma(x,t)}}{\Gamma(1+\gamma(x,t))}\right)\right) - \beta\right)\sqrt{-\frac{\left(1+\sqrt{1-16\alpha k^2\sigma+4\beta^2k^2}\right)\sigma}{(-4\alpha\sigma+\beta^2)k}} + 2a_0\sigma}{2\sigma}.$$

When $q^2 = 4pr$,

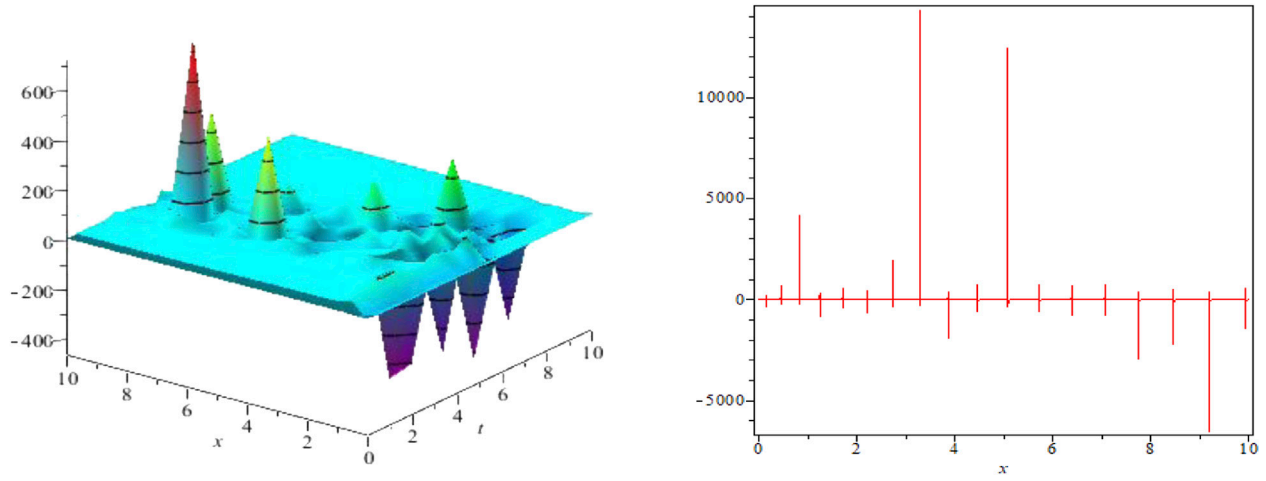

FIGURE 1
Periodic solution for Eq. 35 for Y_{12} at $\omega = \frac{1}{2}, k = 2, a_0 = 1, a_1 = -\frac{1}{2}, \gamma(x,t) = \frac{2\cos(xt)+(xt)}{56}, \delta(x,t) = \frac{2-\sin(xt)}{50}, \alpha = 4, \beta = 5, \sigma = -3, x = 4.5$.

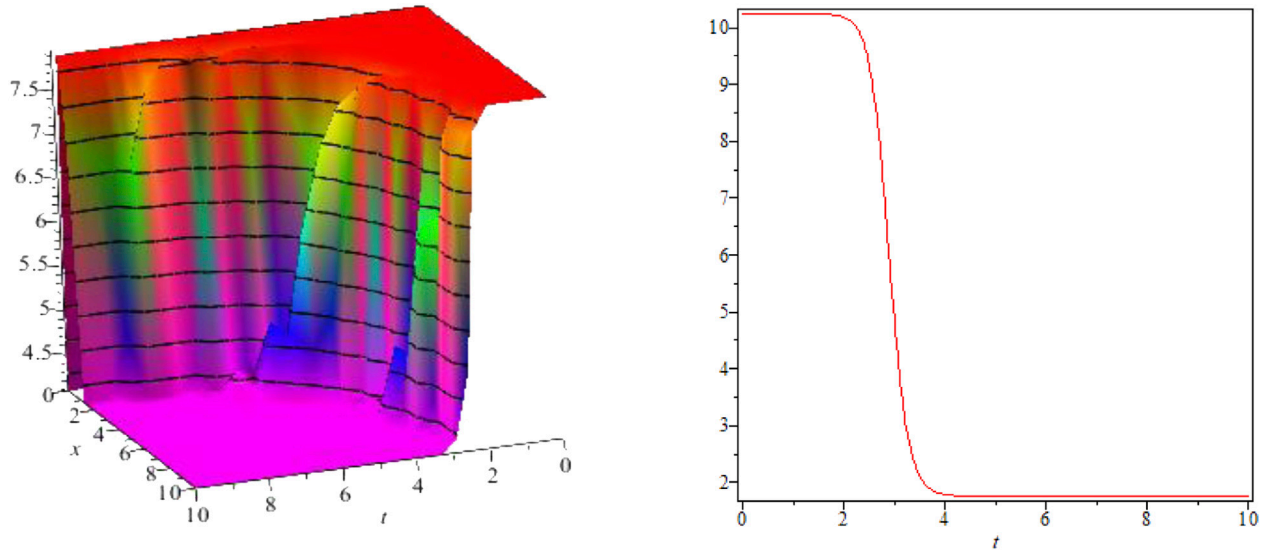

FIGURE 2
Kink-shaped solution for Eq. 35 for Y_5 at $\omega = 2, k = 3, a_0 = 5, a_1 = 5, \gamma(x,t) = \frac{2\cos(xt)+(xt)}{56}, \delta(x,t) = \frac{2-\sin(xt)}{50}, \alpha = 4, \beta = 5, \sigma = -30, x = 4$.

$$Y_{13} = \frac{\sqrt{-\frac{\left(1+\sqrt{1-16\alpha k^2\sigma+4\beta^2k^2}\right)\sigma}{(-4\alpha\sigma+\beta^2)k}}\left(-\beta\left(\frac{kx^{\delta(x,t)}}{\Gamma(1+\delta(x,t))}-\frac{\omega t^{\gamma(x,t)}}{\Gamma(1+\gamma(x,t))}\right)-2\right)+2a_0\sigma\left(\frac{kx^{\delta(x,t)}}{\Gamma(1+\delta(x,t))}-\frac{\omega t^{\gamma(x,t)}}{\Gamma(1+\gamma(x,t))}\right)}{2\sigma\left(\frac{kx^{\delta(x,t)}}{\Gamma(1+\delta(x,t))}-\frac{\omega t^{\gamma(x,t)}}{\Gamma(1+\gamma(x,t))}\right)}.$$

When $\sigma\alpha < 0$, $\beta = 0$, and $\sigma \neq 0$,

$$Y_{14} = -\sqrt{-\frac{\left(1+\sqrt{1-16\alpha k^2\sigma+4\beta^2k^2}\right)\sigma}{(-4\alpha\sigma+\beta^2)k}}\sqrt{-\frac{\alpha}{\sigma}}\tanh\left(\sqrt{-\alpha\sigma}\left(\frac{kx^{\delta(x,t)}}{\Gamma(1+\delta(x,t))}-\frac{\omega t^{\gamma(x,t)}}{\Gamma(1+\gamma(x,t))}\right)\right) + a_0,$$

$$Y_{15} = -\sqrt{-\frac{\left(1+\sqrt{1-16\alpha k^2\sigma+4\beta^2k^2}\right)\sigma}{(-4\alpha\sigma+\beta^2)k}}\sqrt{-\frac{\alpha}{\sigma}}\coth\left(\sqrt{-\alpha\sigma}\left(\frac{kx^{\delta(x,t)}}{\Gamma(1+\delta(x,t))}-\frac{\omega t^{\gamma(x,t)}}{\Gamma(1+\gamma(x,t))}\right)\right) + a_0.$$

When $\beta = 0$ and $\alpha = -\sigma$,

$$Y_{16} = \frac{\left(-e^{2\sigma\left(\frac{kx^{\delta(x,t)}}{\Gamma(1+\delta(x,t))}-\frac{\omega t^{\gamma(x,t)}}{\Gamma(1+\gamma(x,t))}\right)}-1\right)\sqrt{-\frac{\left(1+\sqrt{1-16\alpha k^2\sigma+4\beta^2k^2}\right)\sigma}{(-4\alpha\sigma+\beta^2)k}}}{e^{2\sigma\left(\frac{kx^{\delta(x,t)}}{\Gamma(1+\delta(x,t))}-\frac{\omega t^{\gamma(x,t)}}{\Gamma(1+\gamma(x,t))}\right)}-1} + a_0.$$

When $\alpha = \sigma = 0$,

$$Y_{17} = \left(\cosh\left(\frac{kx^{\delta(x,t)}}{\Gamma(1+\delta(x,t))}-\frac{\omega t^{\gamma(x,t)}}{\Gamma(1+\gamma(x,t))}\right)+\sinh\left(\frac{kx^{\delta(x,t)}}{\Gamma(1+\delta(x,t))}-\frac{\omega t^{\gamma(x,t)}}{\Gamma(1+\gamma(x,t))}\right)\right)\sqrt{-\frac{\left(1+\sqrt{1-16\alpha k^2\sigma+4\beta^2k^2}\right)\sigma}{(-4\alpha\sigma+\beta^2)k}} + a_0.$$

When $\alpha = \beta = k$ and $\sigma = 0$,

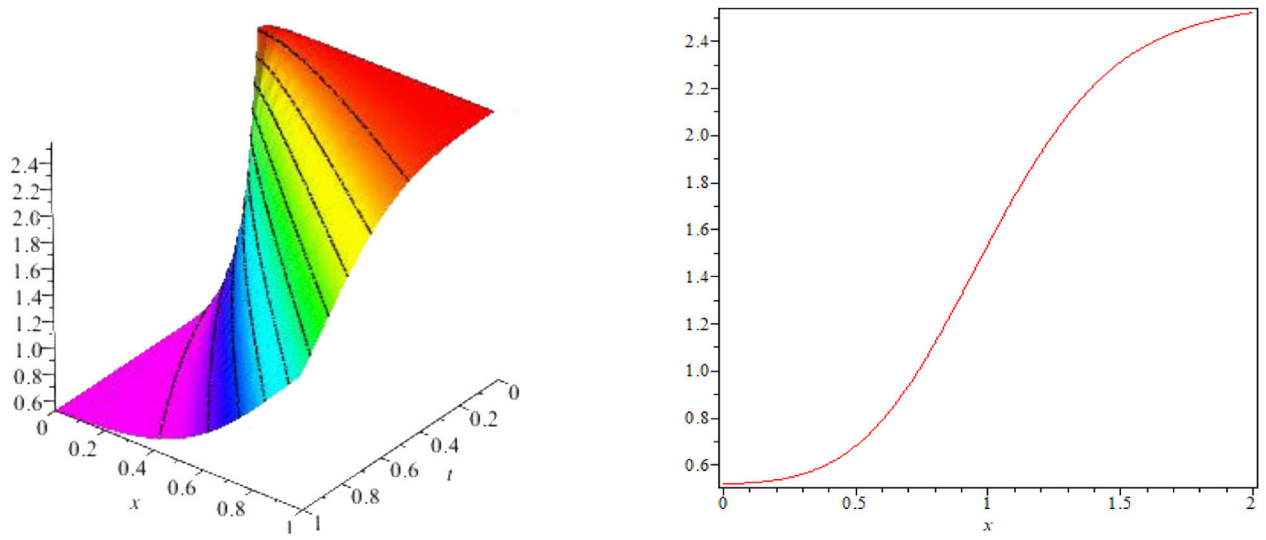

FIGURE 3
Kink-shaped solution for Eq. 35 for Y_7 at $\omega = 1, k = 1, a_0 = 1, a_1 = -\frac{1}{2}, \gamma(x,t) = \frac{20-(xt)^4}{50}, \delta(x,t) = \frac{15+\sin^6(xt)}{50}, \alpha = 4, \beta = 5, \sigma = -3, t = 1$.

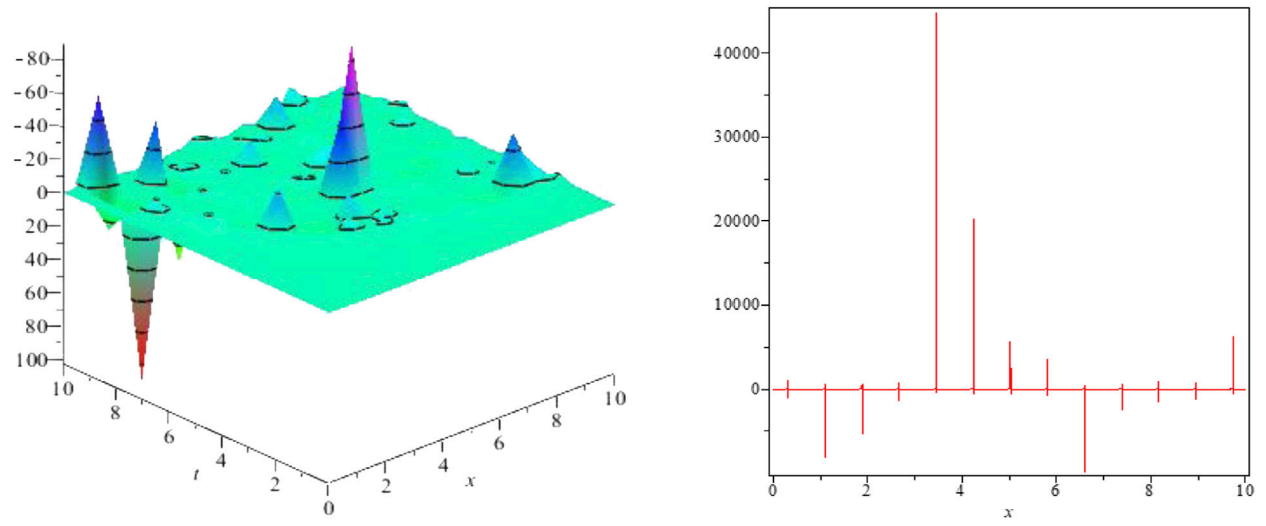

FIGURE 4
Kink-shaped solution for Eq. 35 for Y_{23} at $\omega = 1, k = 1, a_0 = 1, a_1 = -\frac{1}{2}, \gamma(x,t) = \frac{2\cos(xt)+(xt)}{56}, \delta(x,t) = \frac{2-\sin(xt)}{50}, \alpha = 4, \beta = 5, \sigma = -3, e = 2.7128, x = 3.5$.

$$Y_{18} = \left(-e^{\sigma\left(\frac{kx^{\delta(x,t)}}{\Gamma(1+\delta(x,t))} - \frac{\omega t^{\gamma(x,t)}}{\Gamma(1+\gamma(x,t))}\right)} - 1\right)\sqrt{-\frac{\left(1+\sqrt{1-16\alpha k^2\sigma+4\beta^2k^2}\right)\sigma}{(-4\alpha\sigma+\beta^2)k}} + a_0.$$

When $\beta = \sigma = z$ and $\alpha = 0$,

$$Y_{19} = \frac{-\sqrt{-\frac{\left(1+\sqrt{1-16\alpha k^2\sigma+4\beta^2k^2}\right)\sigma}{(-4\alpha\sigma+\beta^2)k}}e^{\sigma\left(\frac{kx^{\delta(x,t)}}{\Gamma(1+\delta(x,t))} - \frac{\omega t^{\gamma(x,t)}}{\Gamma(1+\gamma(x,t))}\right)}}{e^{\sigma\left(\frac{kx^{\delta(x,t)}}{\Gamma(1+\delta(x,t))} - \frac{\omega t^{\gamma(x,t)}}{\Gamma(1+\gamma(x,t))}\right)} - 1} + a_0.$$

When $\beta = \alpha + \sigma$,

$$Y_{20} = a_0 - \sqrt{-\frac{\left(1+\sqrt{1-16\alpha k^2\sigma+4\beta^2k^2}\right)\sigma}{(-4\alpha\sigma+\beta^2)k}}.$$

When $\beta = -(\alpha + \sigma)$,

$$Y_{21} = \frac{\sqrt{-\frac{\left(1+\sqrt{1-16\alpha k^2\sigma+4\beta^2k^2}\right)\sigma}{(-4\alpha\sigma+\beta^2)k}}\left(e^{\sigma\left(\frac{kx^{\delta(x,t)}}{\Gamma(1+\delta(x,t))} - \frac{\omega t^{\gamma(x,t)}}{\Gamma(1+\gamma(x,t))}\right)} - e^{\alpha\left(\frac{kx^{\delta(x,t)}}{\Gamma(1+\delta(x,t))} - \frac{\omega t^{\gamma(x,t)}}{\Gamma(1+\gamma(x,t))}\right)}\right)}{\sigma e^{\sigma\left(\frac{kx^{\delta(x,t)}}{\Gamma(1+\delta(x,t))} - \frac{\omega t^{\gamma(x,t)}}{\Gamma(1+\gamma(x,t))}\right)} - e^{\alpha\left(\frac{kx^{\delta(x,t)}}{\Gamma(1+\delta(x,t))} - \frac{\omega t^{\gamma(x,t)}}{\Gamma(1+\gamma(x,t))}\right)}} + a_0.$$

When $\alpha = 0$,

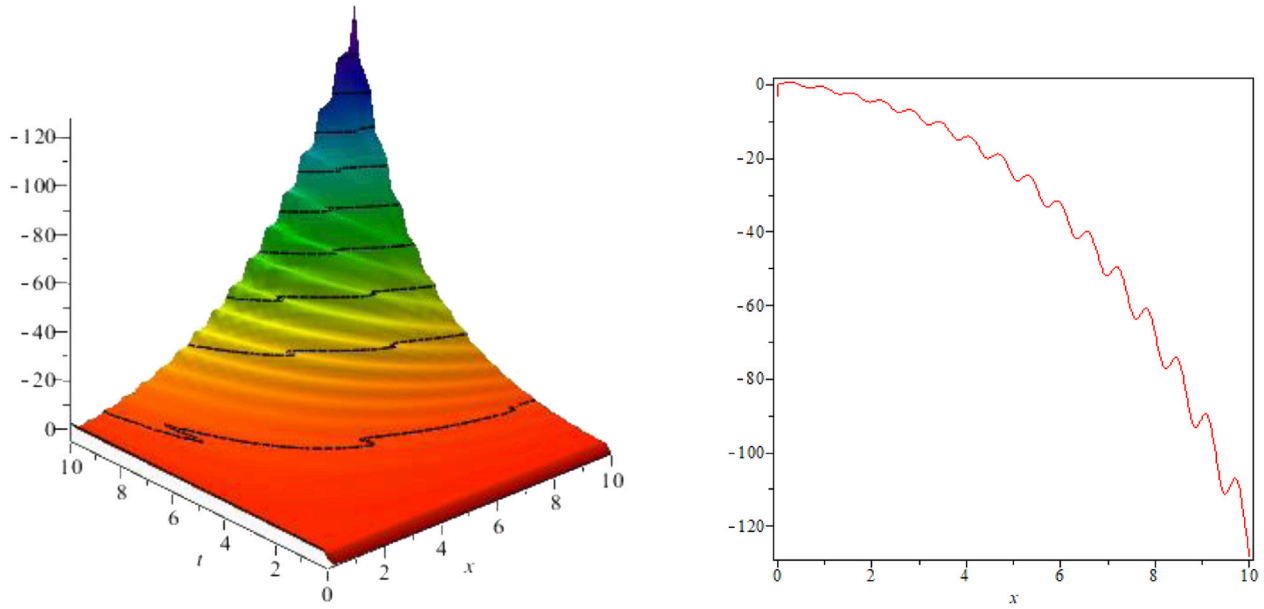

FIGURE 5
Kink-shaped solution for Eq. 35 for Y_{24} at $\omega = 1, k = 1, a_0 = 1, a_1 = -\frac{1}{2}, \gamma(x,t) = \frac{2\cos(xt)+(xt)}{56}, \delta(x,t) = \frac{2-\sin(xt)}{50}, \alpha = 4, \beta = 5, \sigma = -3, e = 2.7128, z = 1$.

$$Y_{22} = \frac{-\sqrt{-\frac{\left(1+\sqrt{1-16\alpha k^2\sigma+4\beta^2k^2}\right)\sigma}{(-4\alpha\sigma+\beta^2)k}}\beta e^{\beta\left(\frac{kx^{\delta(x,t)}}{\Gamma(1+\delta(x,t))}-\frac{\omega t^{\gamma(x,t)}}{\Gamma(1+\gamma(x,t))}\right)}}{\sigma e^{\sigma\left(\frac{kx^{\delta(x,t)}}{\Gamma(1+\delta(x,t))}-\frac{\omega t^{\gamma(x,t)}}{\Gamma(1+\gamma(x,t))}\right)}-1} + a_0.$$

When $\sigma = \beta = \alpha \neq 0$,

$$Y_{23} = a_o + \frac{1}{2}\sqrt{-\frac{\left(1+\sqrt{1-16\alpha k^2\sigma+4\beta^2k^2}\right)\sigma}{(-4\alpha\sigma+\beta^2)k}}\left(\tan\left(\frac{\sqrt{3}}{2}\alpha\left(\frac{kx^{\delta(x,t)}}{\Gamma(1+\delta(x,t))}-\frac{\omega t^{\gamma(x,t)}}{\Gamma(1+\gamma(x,t))}\right)\right)-1\right).$$

When $\sigma = \beta = 0$,

$$Y_{24} = a_o + \sqrt{-\frac{\left(1+\sqrt{1-16\alpha k^2\sigma+4\beta^2k^2}\right)\sigma}{(-4\alpha\sigma+\beta^2)k}}\alpha\left(\frac{kx^{\delta(x,t)}}{\Gamma(1+\delta(x,t))}-\frac{\omega t^{\gamma(x,t)}}{\Gamma(1+\gamma(x,t))}\right).$$

When $p = q = 0$,

$$Y_{25} = \frac{a_o\sigma\left(\frac{kx^{\delta(x,t)}}{\Gamma(1+\delta(x,t))}-\frac{\omega t^{\gamma(x,t)}}{\Gamma(1+\gamma(x,t))}\right)+\sqrt{-\frac{\left(1+\sqrt{1-16\alpha k^2\sigma+4\beta^2k^2}\right)\sigma}{(-4\alpha\sigma+\beta^2)k}}}{\sigma\left(\frac{kx^{\delta(x,t)}}{\Gamma(1+\delta(x,t))}-\frac{\omega t^{\gamma(x,t)}}{\Gamma(1+\gamma(x,t))}\right)}.$$

When $\sigma = \alpha$ and $\beta = 0$,

$$Y_{26} = a_o + \sqrt{-\frac{\left(1+\sqrt{1-16\alpha k^2\sigma+4\beta^2k^2}\right)\sigma}{(-4\alpha\sigma+\beta^2)k}}\tan\left(\alpha\left(\frac{kx^{\delta(x,t)}}{\Gamma(1+\delta(x,t))}-\frac{\omega t^{\gamma(x,t)}}{\Gamma(1+\gamma(x,t))}\right)\right).$$

When $r = 0$,

$$Y_{27} = \frac{1}{\beta}\left(e^{\beta\left(\frac{kx^{\delta(x,t)}}{\Gamma(1+\delta(x,t))}-\frac{\omega t^{\gamma(x,t)}}{\Gamma(1+\gamma(x,t))}\right)}-\alpha\right)\sqrt{-\frac{\left(1+\sqrt{1-16\alpha k^2\sigma+4\beta^2k^2}\right)\sigma}{(-4\alpha\sigma+\beta^2)k}} + a_0.$$

4 Graphical representation

This section focuses on the graphical representation of some specific findings. Marwan and Aminah [40] solved the generalized shallow water equation by the (G′/G)-expansion and constructed a new exact solution for the proposed method. Bagchi et al. [41] extended the elliptic function method and found the traveling wave solution for the generalized shallow water wave equation. The obtained solutions are in the form of singular and periodic soliton solutions. Here, in this study, the graphical results obtained for different values of VO $\gamma(x,t)$ and $\delta(x,t)$ are shown in Figures 1–5 for Eq. 35 in the form of 3D and 2D plots. Figure 1 and Figure 4 show the singleton soliton solution, and Figure 2, Figure 3, and Figure 5 represent the kink-shaped solution obtained using Maple 16 software.

5 Conclusion

In this paper, we solved the non-linear VO fractional evolution equation successfully in the Caputo fractional derivative sense and obtained new exact traveling wave solutions. The VO fractional evolution equation is discussed quite efficiently and accurately by using the Khater method.

Here, 27 exact solutions having Kink and singular soliton-type solutions are obtained for different values of VO $\gamma(x,t)$ and $\delta(x,t)$ for the proposed Caputo fractional VO equation. The different values of parameters examine different physical phenomena. This contribution is effective, instrumental, and evangelistic and seems more natural in the literature. This study can be extended to other types of VO FPDEs and can be solved by various analytical techniques.

Data availability statement

The raw data supporting the conclusion of this article will be made available by the authors, without undue reservation.

Author contributions

All authors listed have made a substantial, direct, and intellectual contribution to the work and approved it for publication.

Funding

The authors would like to thank the Deanship of Scientific Research at Umm Al-Qura University for supporting this work under grant code: 22UQU4310396DSR54.

Conflict of interest

The authors declare that the research was conducted in the absence of any commercial or financial relationships that could be construed as a potential conflict of interest.

Publisher's note

All claims expressed in this article are solely those of the authors and do not necessarily represent those of their affiliated organizations, or those of the publisher, the editors, and the reviewers. Any product that may be evaluated in this article, or claim that may be made by its manufacturer, is not guaranteed or endorsed by the publisher.

References

1. Bekir A, Güner Ö. The G′G-expansion method using modified Riemann–Liouville derivative for some space-time fractional differential equations. *Ain Shams Eng J* (2014) 5(3):959–65. doi:10.1016/j.asej.2014.03.006

2. Bin Z. (G′/G)-expansion method for solving fractional partial differential equations in the theory of mathematical physics. *Communic Theor Phys* (2012) 58:623–30. doi:10.1088/0253-6102/58/5/02

3. Akgül A, Baleanu D. On solutions of variable-order fractional differential equations. *Int J Optimization Control Theories Appl (Ijocta)* (2017) 7(1):112–6. doi:10.11121/ijocta.01.2017.00368

4. Katsikadelis JT. *Numerical solution of variable order fractional differential equations* (2018). Available at: https://arXiv.org/abs/preprint.arXiv:1802.00519.

5. Sahoo S, Saha Ray S, Das S, Bera RK. The formation of dynamic variable order fractional differential equation. *Int J Mod Phys C* (2016) 27(07):1650074. doi:10.1142/s0129183116500741

6. Singh AK, Mehra M, Gulyani S. Learning parameters of a system of variable order fractional differential equations. *Numer Methods Partial Differential Equations* (2021) num.22796. doi:10.1002/num.22796

7. Semary MS, Hassan HN, Radwan AG. The minimax approach for a class of variable order fractional differential equation. *Math Methods Appl Sci* (2019) 42(8):2734–45. doi:10.1002/mma.5545

8. Taghipour M, Aminikhah H. A new compact alternating direction implicit method for solving two-dimensional time fractional diffusion equation with Caputo-Fabrizio derivative. *Filomat* (2020) 34(11):3609–26. doi:10.2298/fil2011609t

9. Ali U, Sohail M, Usman M, Abdullah FA, Khan I, Nisar KS. Fourth-order difference approximation for time-fractional modified sub-diffusion equation. *Symmetry* (2020) 12(5):691. doi:10.3390/sym12050691

10. Ali U, Kamal R, Mohyud-Din ST. On nonlinear fractional differential equations. *Int J Mod Math Sci* (2012) 3:3., no.

11. Zhao Z, Yue J, He L. New type of multiple lump and rogue wave solutions of the (2+1)-dimensional Bogoyavlenskii–Kadomtsev–Petviashvili equation. *Appl Math Lett* (2022) 133:108294. doi:10.1016/j.aml.2022.108294

12. Zubair T, Usman M, Ali U, Mohyud-Din ST. Homotopy analysis method fa or system of partial differential equations. *Int J Mod Eng Sci* (2012) 1(2):67–79.

13. Zhao Z, He L. A new type of multiple-lump and interaction solution of the Kadomtsev–Petviashvili I equation. *Nonlinear Dyn* (2022) 109:1033–46. doi:10.1007/s11071-022-07484-6

14. Hu W, Deng Z, Han S, Zhang W. Generalized multi-symplectic integrators for a class of Hamiltonian nonlinear wave PDEs. *J Comput Phys* (2013) 235:394–406. doi:10.1016/j.jcp.2012.10.032

15. Hu W, Xu M, Song J, Gao Q, Deng Z. Coupling dynamic behaviors of flexible stretching hub-beam system. *Mech Syst Signal Process* (2021) 151:107389. doi:10.1016/j.ymssp.2020.107389

16. Zhao Z, He L. Lie symmetry, nonlocal symmetry analysis, and interaction of solutions of a (2+ 1)-dimensional KdV–mKdV equation. *Theor Math Phys* (2021) 206(2):142–62. doi:10.1134/s0040577921020033

17. Uddin MH, Khatun MA, Arefin MA, Akbar MA. Abundant new exact solutions to the fractional nonlinear evolution equation via Riemann-Liouville derivative. *Alexandria Eng J* (2021) 60(6):5183–91. doi:10.1016/j.aej.2021.04.060

18. Barman HK, Seadawy AR, Roy R, Akbar MA, Raddadi MH. Rational closed form soliton solutions to certain nonlinear evolution equations ascend in mathematical physics. *Results Phys* (2021) 27:104450. doi:10.1016/j.rinp.2021.104450

19. Barman HK, Akbar MA, Osman MS, Nisar KS, Zakarya M, Abdel-Aty AH, et al. Solutions to the Konopelchenko-Dubrovsky equation and the Landau-Ginzburg-Higgs equation via the generalized Kudryashov technique. *Results Phys* (2021) 24:104092. doi:10.1016/j.rinp.2021.104092

20. Roy R, Akbar MA, Seadawy AR, Baleanu D. Search for adequate closed form wave solutions to space–time fractional nonlinear equations. *Partial Differential Equations Appl Math* (2021) 3:100025. doi:10.1016/j.padiff.2021.100025

21. Kumar S, Niwas M, Osman MS, Abdou MA. Abundant different types of exact soliton solution to the (4+1)-dimensional Fokas and (2+1)-dimensional breaking soliton equations. *Commun Theor Phys* (2021) 73:105007. doi:10.1088/1572-9494/ac11ee

22. Ali U, Mastoi S, Othman WAM, Khater MM, Sohail M. Computation of traveling wave solution for nonlinear variable-order fractional model of modified equal width equation. *AIMS Math* (2021) 6(9):10055–69. doi:10.3934/math.2021584

23. Akhtar J, Seadawy AR, Tariq KU, Baleanu D. On some novel exact solutions to the time fractional (2+ 1) dimensional Konopelchenko–Dubrovsky system arising in physical science. *Open Phys* (2020) 18(1):806–19. doi:10.1515/phys-2020-0188

24. Islam T, Akbar MA, Azad AK. Traveling wave solutions to some nonlinear fractional partial differential equations through the rational (G′/G)-expansion method. *J Ocean Eng Sci* (2018) 3(1):76–81. doi:10.1016/j.joes.2017.12.003

25. Mamun Miah M, Shahadat Ali HM, Ali Akbar M, Majid Wazwaz A. Some applications of the (G′/G, 1/G)-expansion method to find new exact solutions of NLEEs. *The Eur Phys J Plus* (2017) 132(6):252–15. doi:10.1140/epjp/i2017-11571-0

26. Islam MS, Khan K, Akbar MA, Mastroberardino A. A note on improved F-expansion method combined with Riccati equation applied to nonlinear evolution equations. *R Soc Open Sci* (2014) 1(2):140038. doi:10.1098/rsos.140038

27. Hu W, Huai Y, Xu M, Feng X, Jiang R, Zheng Y, et al. Mechanoelectrical flexible hub-beam model of ionic-type solvent-free nanofluids. *Mech Syst Signal Process* (2021) 159:107833. doi:10.1016/j.ymssp.2021.107833

28. Hu W, Xu M, Zhang F, Xiao C, Deng Z. Dynamic analysis on flexible hub-beam with step-variable cross-section. *Mech Syst Signal Process* (2022) 180:109423. doi:10.1016/j.ymssp.2022.109423

29. Ali U, Ahmad H, Abu-Zinadah H. Soliton solutions for nonlinear variable-order fractional Korteweg–de Vries (KdV) equation arising in shallow water waves. *J Ocean Eng Sci* (2022). doi:10.1016/j.joes.2022.06.011

30. Gulalai SA, Rihan FA, Ullah A, Al-Mdallal QM, Akgul A. Nonlinear analysis of a nonlinear modified KdV equation under Atangana Baleanu Caputo derivative. *AIMS Math* (2022) 7(5):7847–65. doi:10.3934/math.2022439

31. Hu W, Wang Z, Zhao Y, Deng Z. Symmetry breaking of infinite-dimensional dynamic system. *Appl Math Lett* (2020) 103:106207. doi:10.1016/j.aml.2019.106207

32. Zayed Elsayed ME, Amer Yasser A, Shohib Reham MA. Exact traveling wave solution for nonlinear fractional partial differential equation using the improved (G'/G)-expansion method. *Int J Engin* (2014) 4(7):18–31.

33. Ali U, Ganie AH, Khan I, Alotaibi F, Kamran K, Muhammad S, et al. *Traveling wave solutions to a mathematical model of fractional order (2+ 1)-dimensional breaking soliton equation*. Fractals (2022). p. 2240124.

34. Hu W, Zhang C, Deng Z. Vibration and elastic wave propagation in spatial flexible damping panel attached to four special springs. *Commun Nonlinear Sci Numer Simulation* (2020) 84:105199. doi:10.1016/j.cnsns.2020.105199

35. Ali U, Ahmad H, Baili J, Botmart T, Aldahlan MA. Exact analytical wave solutions for space-time variable-order fractional modified equal width equation. *Results Phys* (2022) 33:105216. doi:10.1016/j.rinp.2022.105216

36. Hu W, Huai Y, Xu M, Deng Z. Coupling dynamic characteristics of simplified model for tethered satellite system. *Acta Mechanica Sinica* (2021) 37(8):1245–54. doi:10.1007/s10409-021-01108-9

37. Nayfeh AH, Balachandran B. *Applied nonlinear dynamics: Analytical, computational, and experimental methods*. John Wiley & Sons (2008).

38. Pushkarev AN, Zakharov VEE. Nonlinear amplification of ocean waves in straits. *Theor Math Phys* (2020) 203(1):535–546.

39. Rezazadeh H, Korkmaz A, Khater MM, Eslami M, Lu D, Attia RA. New exact traveling wave solutions of biological population model via the extended rational sinh-cosh method and the modified Khater method. *Mod Phys Lett B* (2019) 33(28):1950338. doi:10.1142/s021798491950338x

40. Clarkson PA, Mansfield EL. On a shallow water wave equation. *Nonlinearity* (1994) 7(3):975–1000. doi:10.1088/0951-7715/7/3/012

41. Bagchi B, Das S, Ganguly A. New exact solutions of a generalized shallow water wave equation. *Physica Scripta* (2010) 82(2):025003. doi:10.1088/0031-8949/82/02/025003

frontiers | Frontiers in Physics

TYPE Original Research
PUBLISHED 16 February 2023
DOI 10.3389/fphy.2023.1131007

OPEN ACCESS

EDITED BY
Gangwei Wang,
Hebei University of Economics and Business, China

REVIEWED BY
Weipeng Hu,
Northwestern Polytechnical University, China
Zhenli Wang,
Zaozhuang University, China
Cheng Chen,
Xi'an University of Posts and Telecommunications, China

*CORRESPONDENCE
Zenggui Wang,
wangzenggui@lcu.edu.cn

SPECIALTY SECTION
This article was submitted to Mathematical Physics, a section of the journal Frontiers in Physics

RECEIVED 24 December 2022
ACCEPTED 16 January 2023
PUBLISHED 16 February 2023

CITATION
Yang B, Song Y and Wang Z (2023), Lie symmetry analysis and exact solutions of the (3+1)-dimensional generalized Shallow Water-like equation.
Front. Phys. 11:1131007.
doi: 10.3389/fphy.2023.1131007

Lie symmetry analysis and exact solutions of the (3+1)-dimensional generalized Shallow Water-like equation

Ben Yang, Yunjia Song and Zenggui Wang*

School of Mathematical Sciences, Liaocheng University, Liaocheng, China

In this article, (3+1)-dimensional generalized Shallow Water-like (gSWl) equation is discussed. The infinitesimal generators of the equation are derived by using the Lie symmetry analysis method. The optimal system is obtained based on the adjoint table of the generators of the equation. Exact solutions of the equation are constructed by applying symmetry reduction, $\mathrm{Exp}(-\phi(\xi))$ expansion method, Exp-function expansion method, Riccati equation method, and (G'/G) expansion method. For analyzing the dynamical behavior of the solutions, we derive the physical structures of dark soliton, kink wave, and periodic solutions *via* numerical simulations.

KEYWORDS

(3+1)-dimensional gSWl equation, Lie symmetry analysis, Riccati equation method, exact solutions, (G′/G) expansion method

1 Introduction

Non-linear phenomena are widespread in the life of the world, such as marine engineering, hydrodynamics, chemical physics, etc [1–3]. To investigate exact solutions of any complex non-linear partial differential equations and examine the behavior of the solutions is very interesting. Many effective methods for constructing the exact solutions are proposed, including Bäcklund transformation method [4] (G'/G) expansion method [5, 6], Hirota bilinear method [7], Homogeneous balance method [8, 9], Lie symmetry method [10–12], Inverse scattering method [13], F-expansion method [14], Exp-function method [15, 16], Darboux transformation method [17], Riemann-Hilbert method [18, 19] and so on.

The following (3 + 1)-dimensional generalized Shallow Water equation

$$u_{xxxy} - 3u_{xx}u_y - 3u_xu_{xy} + u_{yt} - u_{xz} = 0, \tag{1.1}$$

has been studied by many approaches. Huang and Gao [20] derived the one-, two- and three-soliton solutions of the equation by the Hirota method, and deduced the propagation and interaction of the soliton solutions. In [21], Huang studied the stability of solitons by numerical methods and noticed that the soliton amplitude magnitude is affected by the spectral parameters. In [22], the closed-form solutions of the equation were derived by Lie symmetry, and the soliton solutions were found through the optimal system. Based on the auto-Bäcklund transformation, Li and Liu [23] constructed the multi-periodic solitons of Eq. 1.1 through the variable-coefficient homogeneous balance method and investigated the propagation and interactions of the solutions. In [24], Liu deduced the new periodic solitary solutions of Eq. 1.1 by the direct test function method, and the validity of the direct test function method was shown.

Liu and Zhu [25] investigated the variable coefficients of the gSW equation by the Hirota bilinear method and constructed a large number of breather wave solutions.

Tang, Ma and Xu [26] proposed the (3 + 1)-dimensional generalized Shallow Water-like (gSWl) equation

$$u_{xxxy} + 3u_{xx}u_y + 3u_xu_{xy} - u_{yt} - u_{xz} = 0, \tag{1.2}$$

which can be derived by rewriting Eq. 1.1 on the scale $x \to -x$. In [26], the Grammian and Pfaffian solutions of Eq. 1.2 were obtained and the equations were extended with the Pfaffianization method. Kumar et al. [27] derived the multi-stripe and breathing wave solutions of Eq. 1.2 by the bilinear method, combining the quadratic function and hyperbolic cosine method, the behavior between the one-block and multi-stripe solutions were obtained. Sadat et al. [28] applied symbolic calculations to yield lump-type and stripe solutions of Eq. 1.2. Zhang et al. [29] applied the generalized bilinear operator method and obtained the rational and lump solutions of Eq. 1.2.

The shallow water wave equation plays an essential role in marine engineering, environmental problems, and ecology, so it is valuable to derive the exact solutions of the shallow water wave equation. Employing the Lie symmetry method to yield exact solutions of the (3 + 1)-dimensional gSWl equation has not been studied. In this paper, the Lie symmetry analysis method is applied to investigate the solutions of Eq. 1.2. Lie symmetry method [30–34] has an important significance for solving partial differential equations (PDEs). Applying the Lie symmetry method, the symmetry group of the equation can be derived, furthermore, the equation can be similarly reduced and the new solutions of the equation can be yielded by the symmetry transformation. The Lie symmetry method can reduce the order of the equation when solving with higher order equations, which is difficult to accomplish by other methods.

The structure of the rest of the paper is as follows: In Sect 2, the infinitesimal generators are obtained by applying the Lie group transformation to the (3 + 1)-dimensional gSWl equation. In Sect 3, the optimal system for Eq. 1.2 is derived under the basis of the adjoint table. The periodic wave, kink wave and soliton solutions of the equation are derived by $\mathrm{Exp}(-\phi(\xi))$ expansion method, Exp-function expansion method, Riccati equation method, and (G'/G) expansion method in Sect 4. The dynamical behavior of the soliton wave solutions of the gSWl equation are analyzed in Sect 5. The conclusions are given in Sect 6.

2 Lie symmetry analysis for the (3 + 1) gSWl equation

The key step for solving non-linear PDEs by Lie symmetry group method is to obtain Lie algebra of the equation. Consider the following one-parameter Lie group transformation:

$$\begin{aligned}
\hat{x} &= x + \varepsilon\xi + O(\varepsilon^2),\\
\hat{y} &= y + \varepsilon\eta + O(\varepsilon^2),\\
\hat{z} &= z + \varepsilon\varphi + O(\varepsilon^2),\\
\hat{t} &= t + \varepsilon\tau + O(\varepsilon^2),\\
\hat{u} &= u + \varepsilon\phi + O(\varepsilon^2),
\end{aligned} \tag{2.1}$$

TABLE 1 Commutator table.

$[v_i, v_j]$	v_1	v_2	v_3	v_4	v_5	v_6
v_1	0	$-v_2$	0	0	0	0
v_2	v_2	0	0	0	0	0
v_3	0	0	0	$-3v_4$	$-v_5$	v_6
v_4	0	0	$3v_4$	0	0	0
v_5	0	0	v_5	0	0	0
v_6	0	0	$-v_6$	0	0	0

where ε is a parameter, and $\varepsilon \ll 1$. ξ, η, φ, τ, and ϕ are infinitesimal generators concerning x, y, z, t and u. The one-parameter vector field V of gSWl equation can be written as

$$V = \xi\frac{\partial}{\partial x} + \eta\frac{\partial}{\partial y} + \varphi\frac{\partial}{\partial z} + \tau\frac{\partial}{\partial t} + \phi\frac{\partial}{\partial u}. \tag{2.2}$$

The vector field V satisfies

$$pr^{(4)}V(\Delta)\big|_{\Delta=0} = 0, \tag{2.3}$$

in which $\Delta = u_{xxxy} + 3u_{xx}u_y + 3u_xu_{xy} - u_{yt} - u_{xz}$ and $pr^{(4)}$ is the fourth prolongation of V. The fourth prolongation of Eq. 1.2 can be derived as

$$pr^{(4)}V = V + \phi^x\frac{\partial}{\partial u_x} + \phi^y\frac{\partial}{\partial u_y} + \phi^{xx}\frac{\partial}{\partial u_{xx}} + \phi^{xz}\frac{\partial}{\partial u_{xz}} + \phi^{xy}\frac{\partial}{\partial u_{xy}} + \phi^{yt}\frac{\partial}{\partial u_{yt}} + \phi^{xxxy}\frac{\partial}{\partial u_{xxxy}}. \tag{2.4}$$

The invariant condition can be given as

$$\phi^{xxxy} + 3\phi^{xx}u_y + 3u_x\phi^{xy} - \phi^{yt} - \phi^{xz} + 3u_{xx}\phi^y + 3\phi^xu_{xy} = 0. \tag{2.5}$$

Based on Eq. 2.5, the system of determining equations can be given by

$$\begin{aligned}
&\phi_u = -\frac{1}{3}\tau_t,\ \phi_x = -\frac{1}{3}\eta_z - \frac{1}{3}\xi_t,\ \phi_y = -\frac{1}{3}\xi_z,\ \phi_t = 0,\\
&\tau_x = 0,\ \tau_y = 0,\ \tau_z = 0,\ \tau_{tt} = 0,\ \xi_u = 0,\ \xi_x = \frac{1}{3}\tau_t,\ \xi_y = 0,\\
&\eta_t = 0,\ \eta_u = 0,\ \eta_x = 0,\ \eta_y = \varphi_z - \frac{2}{3}\tau_t,\ \varphi_t = 0,\\
&\varphi_u = 0,\ \varphi_x = 0,\ \varphi_y = 0,\ \varphi_{zz} = 0,\ \xi_{tz} = -\frac{1}{2}\eta_{zz}.
\end{aligned} \tag{2.6}$$

By solving the above equations we can derive

$$\begin{aligned}
&\phi = -\frac{1}{3}c_3u - \frac{1}{6}\{F'_1(z) + 2F'_2(t)\}x + \frac{1}{6}\{F''_1(z)t - 2F'_3(z)\}y + F_4(z,t),\ \tau = c_3t + c_4,\\
&\xi = \frac{1}{3}c_3x + F_3(z) + F_2(t) - \frac{1}{2}tF'_1(z),\quad \eta = F_1(z) + \frac{1}{3}(3c_1 - 2c_3)y,\quad \varphi = c_1z + c_2,
\end{aligned} \tag{2.7}$$

where c_i and F_i $(i = 1, 2, 3, 4)$ are arbitrary constants and functions, respectively.

Assume that $F_1(z) = 0, F_2(t) = c_5, F_3(z) = 0, F_4(z,t) = c_6$. The infinitesimal generators have new forms

$$\xi = c_3x + c_5,\ \ \eta = (c_1 - 2c_3)y,\ \ \varphi = c_1z + c_2,\ \ \tau = 3tc_3 + c_4,\ \ \phi = -uc_3 + c_6. \tag{2.8}$$

TABLE 2 Adjoint table.

Ad	V_1	V_2	V_3	V_4	V_5	V_6
V_1	V_1	$e^{\varepsilon}V_2$	V_3	V_4	V_5	V_6
V_2	$V_1 - \varepsilon V_2$	V_2	V_3	V_4	V_5	V_6
V_3	V_1	V_2	V_3	$e^{3\varepsilon}V_4$	$e^{\varepsilon}V_5$	$e^{-\varepsilon}V_6$
V_4	V_1	V_2	$V_3 - 3\varepsilon V_4$	V_4	V_5	V_6
V_5	V_1	V_2	$V_3 - \varepsilon V_5$	V_4	V_5	V_6
V_6	V_1	V_2	$V_3 + \varepsilon V_6$	V_4	V_5	V_6

Thus, Lie algebras of infinitesimal symmetry of Eq. 1.2 can be spanned by the following six vector fields

$$v_1 = y\frac{\partial}{\partial y} + z\frac{\partial}{\partial z}, \quad v_2 = \frac{\partial}{\partial z}, \quad v_3 = x\frac{\partial}{\partial x} + 3t\frac{\partial}{\partial t} - 2y\frac{\partial}{\partial y} - u\frac{\partial}{\partial u},$$
$$v_4 = \frac{\partial}{\partial t}, \quad v_5 = \frac{\partial}{\partial x}, \quad v_6 = \frac{\partial}{\partial u}. \tag{2.9}$$

The commutator table derived for the gSWl equation by the action of Lie brackets is shown in Table 1, where $[v_i, v_j] = v_i v_j - v_j v_i$.

3 Optimal systems of one-dimensional subalgebras

Based on the Lie brackets, the optimal system of one-dimensional subalgebras of the equation can be deduced. By the linear combination of subalgebras, a new form is given by

$$V = a_1 v_1 + a_2 v_2 + a_3 v_3 + a_4 v_4 + a_5 v_5 + a_6 v_6. \tag{3.1}$$

By Olver theory [30], using symbolic calculations

$$Ad(\exp(\varepsilon V_i))V_j = V_j - \varepsilon[V_i, V_j] + \frac{1}{2}\varepsilon^2[V_i, [V_i, V_j]] - \cdots.$$

The adjoint table is shown in Table 2.

3.1 Construction of group invariants

The exchange and adjoint relations of the six-dimensional Lie algebras are given in Table 1 and Table 2, respectively. Assume that the vectors $V = \sum_{i=1}^{6} a_i v_i$ and $R = \sum_{i=1}^{6} s_i v_i$ satisfy

$$\begin{aligned}
&\mathrm{Ad}(\exp(\varepsilon R)V)\\
&= V - \varepsilon[R, V] + \frac{1}{2}\varepsilon^2[R, [R, V]] - \cdots\\
&= (a_1 v_1 + \cdots + a_6 v_6) - \varepsilon[s_1 v_1 + \cdots + s_6 v_6, a_1 v_1 + \cdots + a_6 v_6] + O(\varepsilon^2)\\
&= (a_1 v_1 + \cdots + a_6 v_6) - \varepsilon[k_1 v_1 + \cdots + k_6 v_6] + O(\varepsilon^2),
\end{aligned} \tag{3.2}$$

in which $k = k(a_1, \cdots a_6, s_1, \ldots, s_6)$ can be derived from Table 1. The values of k were calculated from Table 1 as follows

$$\begin{aligned}
&k_1 = 0, \quad k_2 = -a_2 s_1 + a_1 s_2, \quad k_3 = 0,\\
&k_4 = -3a_4 s_3 + 3a_3 s_4, \quad k_5 = -a_5 s_3 + a_3 s_5, \quad k_6 = a_6 s_3 - a_3 s_6.
\end{aligned} \tag{3.3}$$

For any s_j (j = 1, 2, 3, 4, 5, 6), it have required

$$k_1\frac{\partial \chi}{\partial a_1} + k_2\frac{\partial \chi}{\partial a_2} + k_3\frac{\partial \chi}{\partial a_3} + k_4\frac{\partial \chi}{\partial a_4} + k_5\frac{\partial \chi}{\partial a_5} + k_6\frac{\partial \chi}{\partial a_6} = 0. \tag{3.4}$$

Gather the coefficients containing s_j in the above equation, the following system of differential equations are deduced as

$$\begin{aligned}
&s_1\colon\ -a_2\frac{\partial \chi}{\partial a_2} = 0,\\
&s_2\colon\ a_1\frac{\partial \chi}{\partial a_2} = 0,\\
&s_3\colon\ -3a_4\frac{\partial \chi}{\partial a_4} - a_5\frac{\partial \chi}{\partial a_5} + a_6\frac{\partial \chi}{\partial a_6} = 0,\\
&s_4\colon\ 3a_3\frac{\partial \chi}{\partial a_4} = 0,\\
&s_5\colon\ a_3\frac{\partial \chi}{\partial a_5} = 0,\\
&s_6\colon\ -a_3\frac{\partial \chi}{\partial a_6} = 0.
\end{aligned} \tag{3.5}$$

After analyzing the above system of PDEs (3.5), it is not difficult to yield that the invariant function as $\chi(a_1, a_2, a_3, a_4, a_5, a_6) = F(a_1, a_3)$.

3.2 One-dimensional optimal system

For $J_n^{\varepsilon}\colon \dot{j} \to \dot{j}$ defined by $l \to \mathrm{Ad}(\exp(\varepsilon_i l_i)s)$ is a linear map [35], in which $n = 1, \ldots, 6$. The matrix M_n^{ε} of J_n^{ε} with respect to basis to $\{v_1, \ldots, v_6\}$ are deduced below

$$M_1^{\varepsilon} = \begin{bmatrix} 1&0&0&0&0&0\\ 0&e^{\varepsilon}&0&0&0&0\\ 0&0&1&0&0&0\\ 0&0&0&1&0&0\\ 0&0&0&0&1&0\\ 0&0&0&0&0&1 \end{bmatrix}, M_2^{\varepsilon} = \begin{bmatrix} 1&-\varepsilon_2&0&0&0&0\\ 0&1&0&0&0&0\\ 0&0&1&0&0&0\\ 0&0&0&1&0&0\\ 0&0&0&0&1&0\\ 0&0&0&0&0&1 \end{bmatrix}, M_3^{\varepsilon} = \begin{bmatrix} 1&0&0&0&0&0\\ 0&1&0&0&0&0\\ 0&0&1&0&0&0\\ 0&0&0&e^{3\varepsilon_3}&0&0\\ 0&0&0&0&e^{\varepsilon_3}&0\\ 0&0&0&0&0&e^{-\varepsilon_3} \end{bmatrix},$$
$$M_4^{\varepsilon} = \begin{bmatrix} 1&0&0&0&0&0\\ 0&1&0&0&0&0\\ 0&0&1&-3\varepsilon_4&0&0\\ 0&0&0&1&0&0\\ 0&0&0&0&1&0\\ 0&0&0&0&0&1 \end{bmatrix}, M_5^{\varepsilon} = \begin{bmatrix} 1&0&0&0&0&0\\ 0&1&0&0&0&0\\ 0&0&1&0&-\varepsilon_5&0\\ 0&0&0&1&0&0\\ 0&0&0&0&1&0\\ 0&0&0&0&0&1 \end{bmatrix}, M_6^{\varepsilon} = \begin{bmatrix} 1&0&0&0&0&0\\ 0&1&0&0&0&0\\ 0&0&1&0&0&\varepsilon_6\\ 0&0&0&1&0&0\\ 0&0&0&0&1&0\\ 0&0&0&0&0&1 \end{bmatrix}. \tag{3.6}$$

Then, the matrix M can be yielded by

$$M = M_1^{\varepsilon} * M_2^{\varepsilon} * M_3^{\varepsilon} * M_4^{\varepsilon} * M_5^{\varepsilon} * M_6^{\varepsilon}. \tag{3.7}$$

The matrix M can be written as

$$M = \begin{bmatrix} 1&-\varepsilon_2&0&0&0&0\\ 0&e^{\varepsilon_1}&0&0&0&0\\ 0&0&1&-3\varepsilon_4&-\varepsilon_5&\varepsilon_6\\ 0&0&0&e^{3\varepsilon_3}&0&0\\ 0&0&0&0&e^{\varepsilon_3}&0\\ 0&0&0&0&0&e^{-\varepsilon_3} \end{bmatrix}. \tag{3.8}$$

The adjoint transformation equation for Eq. 1.2 is

$$(\rho_1, \rho_2, \cdots, \rho_6) = (a_1, a_2, \ldots, a_6) \cdot M$$
$$= a_1 v_1 + (-a_1\varepsilon_2 + a_2 e^{\varepsilon_1}) v_2 + a_3 v_3 + (-3a_3\varepsilon_4 + a_4 e^{3\varepsilon_3}) v_4$$
$$+ (-a_3\varepsilon_5 + a_5 e^{\varepsilon_3}) v_5 + (a_3\varepsilon_6 + a_6 e^{-\varepsilon_3}) v_6. \tag{3.9}$$

By applying the invariants a_1 and a_3, discuss the situations of the following Lie algebras.

Case 1 Assume that $a_1 \neq 0$ and $a_3 = 0$. Let $a_1 = 1$. Making $\rho_2 = 0$, $\rho_3 = 0$ through

$$\varepsilon_1 = 0, \quad \varepsilon_2 = \frac{a_2}{a_1}, \quad \varepsilon_3 = 0, \tag{3.10}$$

and ε_4, ε_5, ε_6 are constants. In other words, all $v_1 + a_2 v_2 + a_3 v_3 + a_4 v_4 + a_5 v_5 + a_6 v_6$ can be replaced by $v_1 + \varsigma_4 v_4 + \varsigma_5 v_5 + \varsigma_6 v_6$, where ς_4, ς_5 and ς_6 are constants.

Case 2 Assume that $a_3 \neq 0$ and $a_1 = 0$. Let $a_3 = 1$. Making $\rho_1 = 0$, $\rho_4 = 0$, $\rho_5 = 0$, $\rho_6 = 0$ through

$$\varepsilon_1 = 0, \quad \varepsilon_3 = 0, \quad \varepsilon_4 = \frac{a_4}{3a_3}, \quad \varepsilon_5 = \frac{a_5}{a_3}, \quad \varepsilon_6 = -\frac{a_6}{a_3}, \tag{3.11}$$

and ε_2 is an arbitrary constant. In other words, all $a_1 v_1 + a_2 v_2 + v_3 + a_4 v_4 + a_5 v_5 + a_6 v_6$ can be replaced by $\varsigma_2 v_2 + v_3$, where ς_2 is a constant.

Case 3 Assume that $a_1 \neq 0$ and $a_3 \neq 0$. Let $a_1 = 1$ and $a_3 = 1$. Making $\rho_2 = 0$, $\rho_4 = 0$, $\rho_5 = 0$, $\rho_6 = 0$ through

$$\varepsilon_1 = 0, \quad \varepsilon_2 = \frac{a_2}{a_1}, \quad \varepsilon_3 = 0, \quad \varepsilon_4 = \frac{a_4}{3a_1}, \quad \varepsilon_5 = \frac{a_5}{a_1}, \quad \varepsilon_6 = -\frac{a_6}{a_1}. \tag{3.12}$$

In other words, all $v_1 + a_2 v_2 + v_3 + a_4 v_4 + a_5 v_5 + a_6 v_6$ can be replaced with $v_1 + v_3$.

Case 4 Replacing $a_1 = a_3 = 0$ into (3.9). By solving (3.9) for ε_i, we get $\varepsilon_1 = 0$, $\varepsilon_3 = 0$ and ε_2, ε_4, ε_5, ε_6 are arbitrary constants. In other words, all $v_1 + a_2 v_2 + v_3 + a_4 v_4 + a_5 v_5 + a_6 v_6$ can be replaced by $\varsigma_2 v_2 + \varsigma_4 v_4 + \varsigma_5 v_5 + \varsigma_6 v_6$, where ς_2, ς_4, ς_5 and ς_6 are constants.

Similarly, the other terms of the optimal system of Eq. 1.2 can be obtained by the above method. All of them are listed below.Single vector fields: v_1, v_2, v_3, v_4, v_5, v_6.Dual vector fields: $v_1 + v_3$, $v_1 + v_4$, $v_1 + v_5$, $v_1 + v_6$, $v_2 + v_3$, $v_2 + v_4$, $v_2 + v_5$, $v_2 + v_6$, $v_4 + v_5$, $v_4 + v_6$, $v_5 + v_6$.Triple vector fields: $v_1 + v_4 + v_5$, $v_1 + v_4 + v_6$, $v_1 + v_5 + v_6$, $v_2 + v_4 + v_5$, $v_2 + v_4 + v_6$, $v_4 + v_5 + v_6$.Quadruple vector fields: $v_1 + v_4 + v_5 + v_6$, $v_2 + v_4 + v_5 + v_6$.

4 Exact solutions of the gSWl equation

Next, the exact solutions of the gSWl equation are derived by employing the optimal system. The similarity solutions for arbitrary vector field v in the optimal system can be solved by the Lagrange's system.

$$\frac{dx}{\xi} = \frac{dy}{\eta} = \frac{dz}{\varphi} = \frac{dt}{\tau} = \frac{du}{\phi}. \tag{4.1}$$

4.1 Vector field v_1

The characteristic equation can be composed as

$$\frac{dx}{0} = \frac{dy}{y} = \frac{dz}{z} = \frac{dt}{0} = \frac{du}{0}. \tag{4.2}$$

(Eq. 4.2) has the following form similarity solution.

$U(x, y, z, t) = F(\alpha, \beta, \delta)$.in which $\alpha = x$, $\beta = \frac{y}{z}$, $\delta = t$.

Taking the above similarity solution into Eq. 1.2, the reduced NLPDE is given as

$$3F_{\alpha\alpha}F_\beta + 3F_\alpha F_{\alpha\beta} + F_{\alpha\alpha\alpha\beta} + \beta F_{\alpha\beta} - F_{\beta\delta} = 0. \tag{4.3}$$

Similarly, applying the Lie symmetry method, the infinitesimal generators of Eq. 4.3 can be derived

$$\xi_\alpha = \frac{1}{3}c_1\alpha + g_1(\delta), \quad \xi_\beta = -\frac{2}{3}c_1\beta + c_3, \quad \xi_\delta = c_1\delta + c_2,$$
$$\eta_F = -\frac{1}{3}c_1 F - \frac{1}{3}(c_3 + g_1(\delta)_\delta)\alpha + g_2(\delta). \tag{4.4}$$

Let $c_1 = 0, {}_1(\delta) = d, {}_2(\delta) = d$, $c_2 = d$, $c_3 = 3d$, and take these values into (4.4), we get

$$\frac{d\alpha}{d} = \frac{d\beta}{3d} = \frac{d\delta}{d} = \frac{dF}{-\alpha + d}, \tag{4.5}$$

which has the similarity solutions from

$$F(\alpha, \beta, \delta) = \alpha - \frac{1}{2}\alpha^2 + h(P, Q), \tag{4.6}$$

where $P = \alpha - \delta$ and $Q = 3\alpha - \beta$.

Putting it into Eq. 4.3, the following reduced equation can be yield

$$-3h_Q h_{PP} - 27h_Q h_{PQ} - 3h_P h_{PQ} + Qh_{PQ} - 54h_Q h_{QQ} - 9h_P h_{QQ}$$
$$+3Qh_{QQ} - 4h_{PQ} - 9h_{QQ} + 3h_Q - h_{PPPQ} - 9h_{PPQQ} - 27h_{PQQQ} - 27h_{QQQQ} = 0. \tag{4.7}$$

Repeating the above steps, we get

$$\xi_P = c_1, \quad \xi_Q = c_2, \quad \eta_h = \frac{1}{3}c_2 P + c_3. \tag{4.8}$$

Substituting $c_1 = d$, $c_2 = 3d$, $c_3 = d$ into (4.8). The new characteristic equation is given as

$$\frac{dP}{d} = \frac{dQ}{3d} = \frac{dh}{dP + 1}. \tag{4.9}$$

The new similarity solutions from

$$h(P, Q) = \frac{1}{2}P^2 + P + k(\varpi), \tag{4.10}$$

where $\varpi = 3P - Q$. Replacing (4.10) into Eq. 4.7, we get $3k_{\varpi\varpi} = 0$. The solution of Eq. 1.2 *via* the above method can be given as

$$u = 2x - t + \frac{1}{2}t^2 - xt + \frac{c_1 y}{z} - 3c_1 t + c_2, \tag{4.11}$$

in which c_1 and c_2 are constants.

4.2 Vector field v_3

The characteristic equation can be composed as

$$\frac{dx}{x} = \frac{dy}{-2y} = \frac{dz}{0} = \frac{dt}{3t} = \frac{du}{-u}. \tag{4.12}$$

The derived similarity solution has the form as.

$u(x, y, z, t) = F(\alpha, \beta, \theta)$.where $\alpha = \frac{x}{t^{\frac{1}{3}}}$, $\beta = yt^{\frac{2}{3}}$, $\theta = z$. Hence, the following (2 + 1)-dimensional equation can be given as

$$2\beta F_{\beta\beta} - 9F_{\alpha\alpha}F_{\beta} - 9F_{\alpha}F_{\alpha\beta} - 3F_{\alpha\alpha\alpha\beta} + F_{\beta} + 3F_{\alpha\theta} - \alpha F_{\alpha\beta} = 0. \quad (4.13)$$

Then, the new infinitesimal generators of Eq. 4.13 can be yielded

$$\xi_{\alpha} = c_3, \quad \xi_{\beta} = c_1\beta, \quad \xi_{\theta} = c_1\theta + c_2, \quad \eta_F = -\frac{1}{9}c_3\alpha + g_1(\theta). \quad (4.14)$$

Let $c_1 = 0$, $c_2 = 0$, $c_3 = 0$, $g_1(z) = \theta$, and take these values into (4.14), the corresponding characteristic equation is reduced as

$$\frac{d\alpha}{0} = \frac{d\beta}{\beta} = \frac{d\theta}{\theta} = \frac{dF}{\theta}, \quad (4.15)$$

which has the similarity solutions from

$$F(\alpha, \beta, \theta) = \theta + h(P, Q), \quad (4.16)$$

in which $P = \alpha$, $Q = \frac{\beta}{\theta}$. Substituting $F(\alpha, \beta, \theta)$ into Eq. 4.13 results

$$-9h_{PP}h_Q - 9h_Ph_{PQ} - Ph_{PQ} + 2Qh_{QQ} + h_Q - 3Qh_{PQ} - 3h_{PPPQ} = 0. \quad (4.17)$$

Equations 4.17 satisfies infinitesimal as follows

$$\xi_P = c_1, \quad \xi_Q = 0, \quad \eta_h = -P + c_2, \quad (4.18)$$

assume that $c_1 = 9$, $c_2 = 1$ and its characteristic equation is

$$\frac{dP}{9} = \frac{dQ}{0} = \frac{dh}{-P + 1}. \quad (4.19)$$

The similarity solution is

$$h(P, Q) = -\frac{1}{18}P^2 + \frac{P}{8} + k(\varpi), \quad (4.20)$$

where $\varpi = Q$. Then the ODE can be reduced as

$$2k_{\varpi} + 2\varpi k_{\varpi\varpi} = 0. \quad (4.21)$$

By solving the above equation, we get

$$u = \frac{z + \frac{x}{9t^{\frac{1}{3}}} - \frac{x^2}{18t^{\frac{2}{3}}} + c_2\ln\left(\frac{yt^{\frac{2}{3}}}{z}\right) + c_1}{t^{\frac{1}{3}}}. \quad (4.22)$$

4.3 Vector field $v_2 + v_5$

The characteristic equation can be composed as

$$\frac{dx}{1} = \frac{dy}{0} = \frac{dz}{1} = \frac{dt}{0} = \frac{du}{0}. \quad (4.23)$$

(4.23) has the following form similarity solution

$$u(x, y, z, t) = F(\alpha, \beta, \delta), \quad (4.24)$$

in which $\alpha = x - z$, $\beta = y$, $\delta = z$. Then Eq. 1.2 can be reduced to the following (2 + 1)-dimensional equation

$$F_{\alpha\alpha\alpha\beta} + 3F_{\alpha\alpha}F_{\beta} + 3F_{\alpha}F_{\alpha\beta} - F_{\beta\delta} + F_{\alpha\alpha} = 0. \quad (4.25)$$

The solution of Eq. 4.25 is more difficult to be derived, hence we use the $\mathrm{Exp}(-\phi(\xi))$ expansion method to find its solution. Considering the following traveling wave transformation

$$F(\alpha, \beta, \delta) = h(v), \quad v = k\alpha + l\beta + m\delta, \quad (4.26)$$

where k, l, m are constants. Replacing (4.26) into Eq. 4.25 and integrate the derived equation with respect to v once, we get

$$lk^3h_{vvv} + 3lk^2h_v^2 - lmh_v + k^2h_v = 0. \quad (4.27)$$

Suppose that Eq. 4.27 can be solved in the following form

$$h(v) = a_j(\exp(-\vartheta(v)))^j, \quad (4.28)$$

in which j can be determined later and ϑ satisfies

$$\vartheta'(v) = \exp(-\phi(v)) + \mu\exp(\vartheta(v)) + \lambda. \quad (4.29)$$

When $\lambda^2 - 4\mu > 0$ and $\mu \neq 0$, (4.29) has a solution given by

$$\vartheta(v) = \ln\left(\frac{-\sqrt{\lambda^2 - 4\mu}\tanh\left(\frac{\sqrt{\lambda^2 - 4\mu}}{2}(v + \varepsilon_0)\right) - \lambda}{2\mu}\right). \quad (4.30)$$

When $\lambda^2 - 4\mu < 0$, (4.29) has a solution given by

$$\vartheta(v) = \ln\left(\frac{\sqrt{4\mu - \lambda^2}\tan\left(\frac{\sqrt{4\mu - \lambda^2}}{2}(v + \varepsilon_0)\right) - \lambda}{2\mu}\right). \quad (4.31)$$

By balancing Eq. 4.27, $j = 1$. Hence (4.28) can be rewritten

$$h(v) = a_0 + a_1e^{-\vartheta(v)}. \quad (4.32)$$

Taking (4.32) along with Eq. 4.29 into Eq. 4.27, a series of algebraic equations about a_0, a_1, k, l and m can be deduced. Select a set from these to discuss the solution of the equations, we get

$$k = k, \quad l = \frac{k^2}{k^3\lambda^2 - 4k^3\mu - m}, \quad m = m, \quad a_0 = a_0, \quad a_1 = 2k. \quad (4.33)$$

If $\lambda^2 - 4\mu > 0$ and $\mu \neq 0$, the kink wave solution of Eq. 1.2 is

$$u = a_0 + \frac{4k\mu}{-\tanh\left(\frac{1}{2}c_1\sqrt{\lambda^2 - 4\mu} + \frac{1}{2}\left(mt + k(x - z) - \frac{k^2y}{k^3\lambda^2 - 4k^3\mu - m}\right)\sqrt{\lambda^2 - 4\mu}\right)\sqrt{\lambda^2 - 4\mu} - \lambda}. \quad (4.34)$$

If $\lambda^2 - 4\mu < 0$, the periodic wave solution of Eq. 1.2 can be given by

$$u = a_0 + \frac{4k\mu}{\tan\left(\frac{1}{2}c_1\sqrt{-\lambda^2 + 4\mu} + \frac{1}{2}\left(mt + k(x - z) - \frac{k^2y}{k^3\lambda^2 - 4k^3\mu - m}\right)\sqrt{-\lambda^2 + 4\mu}\right)\sqrt{-\lambda^2 + 4\mu} - \lambda}. \quad (4.35)$$

4.4 Vector field $v_4 + v_6$

The characteristic equation can be composed as

$$\frac{dx}{0} = \frac{dy}{0} = \frac{dz}{0} = \frac{dt}{1} = \frac{du}{1}. \quad (4.36)$$

We derive $u(x, y, z, t) = t + F(\alpha, \beta, \theta)$, where $\alpha = x$, $\beta = y$ and $\theta = z$ as the similarity variables. Taking it into Eq. 1.2, the following reduced equation can be obtained

$$F_{\alpha\alpha\alpha\beta} + 3F_{\alpha\alpha}F_{\beta} + 3F_{\alpha}F_{\alpha\beta} - F_{\alpha\theta} = 0. \tag{4.37}$$

In the following (G'/G) method is applied to solve Eq. 4.37. Considering the following traveling wave transform

$$F(\alpha, \beta, \theta) = h(v), \quad v = k\alpha + l\beta + m\theta, \tag{4.38}$$

in which k, l, m are constants. Putting (4.38) into Eq. 4.37 yields

$$lk^3h_{vvvv} + 6lk^2h_{vv}h_v - mkh_{vv} = 0, \tag{4.39}$$

then integrate once, we yield

$$k^3h_{vvv} + 3lk^2h_{vv} - mkh_v = 0. \tag{4.40}$$

Assume that Eq. 4.40 has solutions of the following form

$$h(v) = \sum_{j=0}^{p} \alpha_j \left(\frac{G'}{G}\right)^j, \tag{4.41}$$

in which b_j $(j = 0, \ldots, p)$ are constants which can be derived later and $h(v)$ satisfies the equation

$$G'' + \lambda G' + \mu G = 0. \tag{4.42}$$

Exploiting the principle of homogeneous balance, $p = 1$. Hence (4.41) can be rewritten as

$$h(v) = \alpha_0 + \alpha_1 \left(\frac{G'}{G}\right). \tag{4.43}$$

Substituting (4.42) and Eq. 4.43 into Eq. 4.40 and putting the same power combination of $(G'/G)^j$. Then make these coefficients be zero, and a series of algebraic equations about k, l, m, α_1, α_2 can be yielded. By solving the above equations, we obtain

$$k = k, \quad l = \frac{m}{k^2(\lambda - 4\mu)}, \quad m = m, \quad \alpha_0 = \alpha_0, \quad \alpha_1 = \alpha_1, \tag{4.44}$$

where $k \neq 0$ and $\lambda - 4\mu \neq 0$. With these parameters, we can yield the following forms of solutions:

For $\lambda^2 > 4\mu$,

$$u = \frac{k\sqrt{\lambda^2 - 4\mu}\,(c_1 \sinh\kappa) + c_2 \cosh\kappa}{c_1 \cosh\kappa + c_2 \sinh\kappa} - k\lambda + \alpha_0, \tag{4.45}$$

where $\kappa = \left(\frac{1}{2}\left(kx + \frac{my}{k^2(\lambda^2 - 4\mu)} + mz\right)\sqrt{\lambda^2 - 4\mu}\right)$ and c_1, c_2, α_0, k, λ, μ are constants.

For $\lambda^2 < 4\mu$,

$$u = \frac{k\sqrt{-\lambda^2 + 4\mu}\,(c_1 \sin\chi) + c_2 \cos\chi}{c_1 \cos\chi + c_2 \sin\varphi} - k\lambda + \alpha_0, \tag{4.46}$$

where $\chi = \left(\frac{1}{2}\left(kx + \frac{my}{k^2(\lambda^2 - 4\mu)} + mz\right)\sqrt{-\lambda^2 + 4\mu}\right)$ and c_1, c_2, α_0, k, λ, μ are constants.

4.5 Vector field $v_2 + v_4 + v_5 + v_6$

The characteristic equation can be composed as

$$\frac{dx}{1} = \frac{dy}{0} = \frac{dz}{1} = \frac{dt}{1} = \frac{du}{1}. \tag{4.47}$$

Solving (4.47), we derived the similarity solution

$$u(x, y, z, t) = F(\alpha, \beta, \theta), \tag{4.48}$$

in which $\alpha = x - t$, $\beta = y$ and $\theta = z - t$ are similarity variables. Taking (4.48) into Eq. 1.2, the (2 + 1)-dimensional equation can be yielded

$$F_{\alpha\alpha\alpha\beta} + 3F_{\alpha\alpha}F_{\beta} + 3F_{\alpha}F_{\alpha\beta} + F_{\alpha\beta} + F_{\beta\theta} - F_{\alpha\theta} = 0. \tag{4.49}$$

Next, applying the Riccati equation method, different forms of solutions of Eq. 4.49 can be deduced. Taking the following traveling wave transform

$$F(\alpha, \beta, \theta) = h(v), \quad v = k\alpha + l\beta + m\theta, \tag{4.50}$$

where k, l, m are constants. Substituting (Eq. 4.50) into Eq. 4.49 and integrating once yields

$$lk^3h_{vvv} + 3lk^2h_v^2 + lkh_v + lmh_v - mkh_v = 0. \tag{4.51}$$

Suppose that Eq. 4.51 has solutions of the following form

$$h(v) = \sum_{j=0}^{p} a_j \phi^j, \tag{4.52}$$

where a_j $(j = 1\ p)$ are constants which can be obtained later and $h(v)$ satisfies the equation

$$\phi' = \phi^2 + \omega, \tag{4.53}$$

in which ω is an constant. The form of the solutions of Eq. 4.53 are as follows

$$\phi = \begin{cases} -\sqrt{\omega}\tanh\left(\sqrt{-\omega}\,v\right), & \omega < 0, \\ -\dfrac{1}{v}, & \omega = 0, \\ \sqrt{\omega}\,\tan\left(\sqrt{\omega}\,v\right), & \omega > 0. \end{cases} \tag{4.54}$$

By balancing Eq. 4.51, we get $p = 1$. Hence, (Eq. 4.52) can be rewritten as

$$h = a_0 + a_1\phi. \tag{4.55}$$

Replacing (Eq. 4.53) along with Eq. 4.55 into Eq. 4.51, letting the same coefficients and a series of algebraic equations about a_0, a_1 and l can be yielded. Solving the above equations, we obtain

$$l = \frac{mk}{-4k^3\omega + m + k}, \quad k = k, \quad m = m, \quad a_0 = a_0, \quad a_1 = -2k. \tag{4.56}$$

On the basis of Eq. 4.56, we derive the solution of Eq. 1.2 as follows:

For $\omega < 0$,

$$u = t + 2k\sqrt{-\omega}\tanh\left(\sqrt{-\omega}\left(k(x - t) + \frac{mky}{-4k^3\omega + k + m} + m(z - t)\right)\right) + a_0, \tag{4.57}$$

where k, m, a_0, ω, y, z are constants.

For $\omega > 0$,

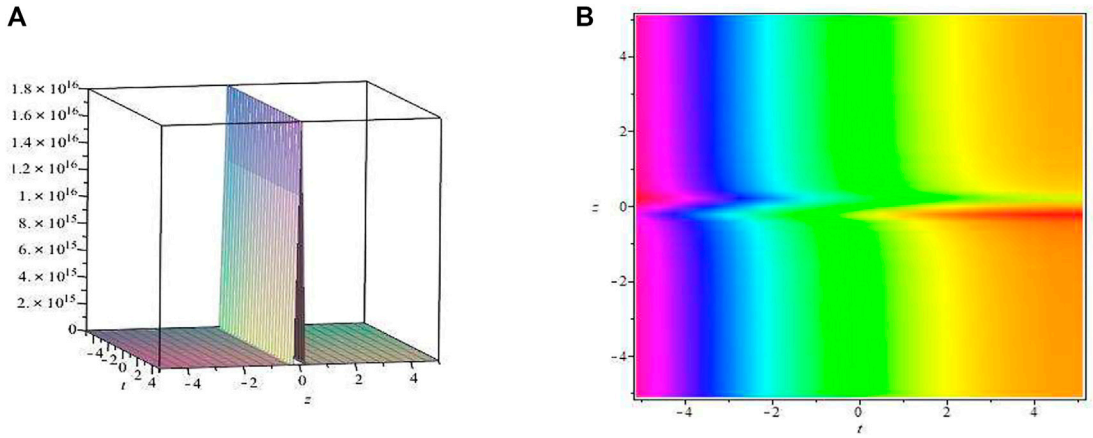

FIGURE 1
Singularity profile of (4.11).

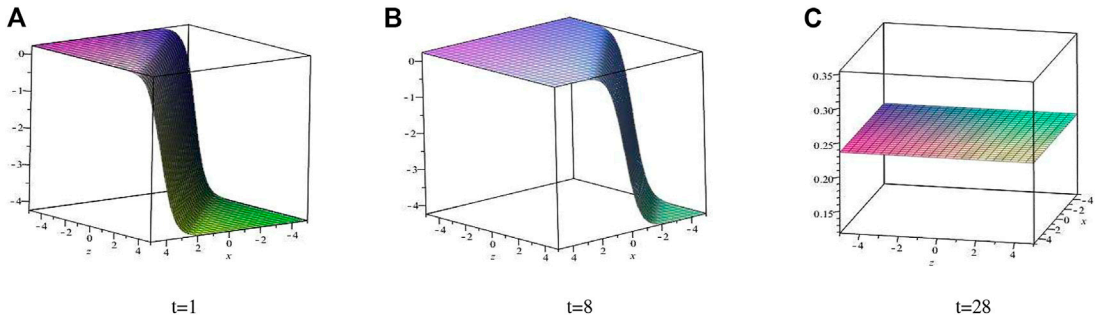

FIGURE 2
Annihilation of the kink wave solution of (4.34) at y =1.

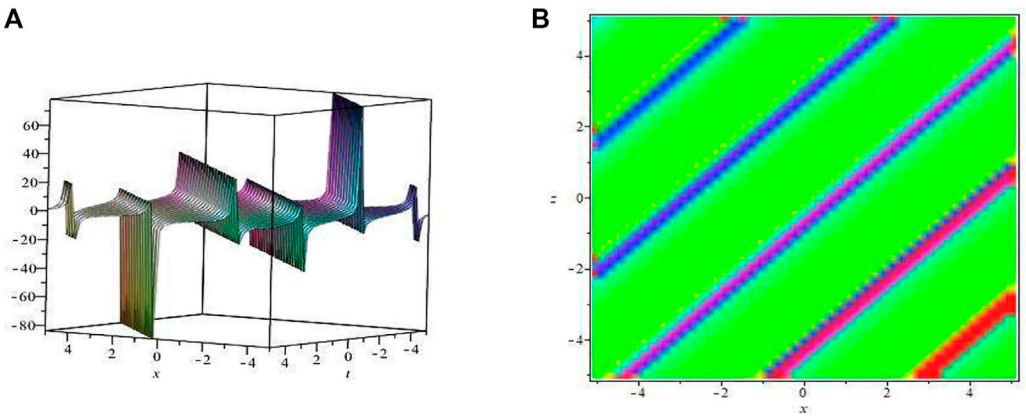

FIGURE 3
Multi period solution of (4.35).

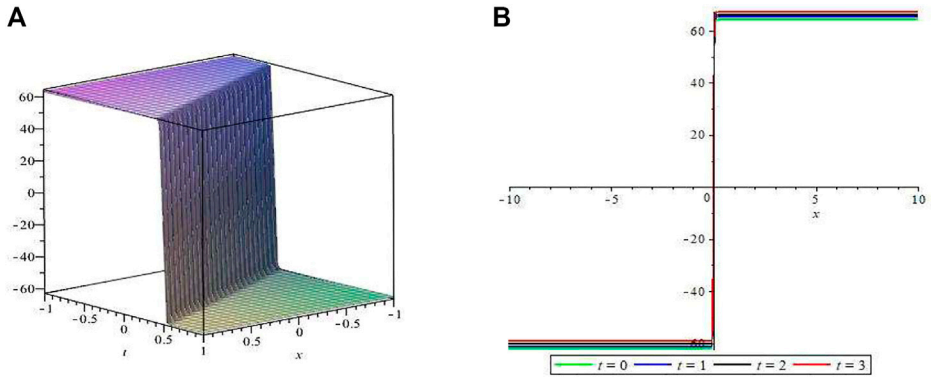

FIGURE 4
The kink wave solution of (4.57) at z =0.

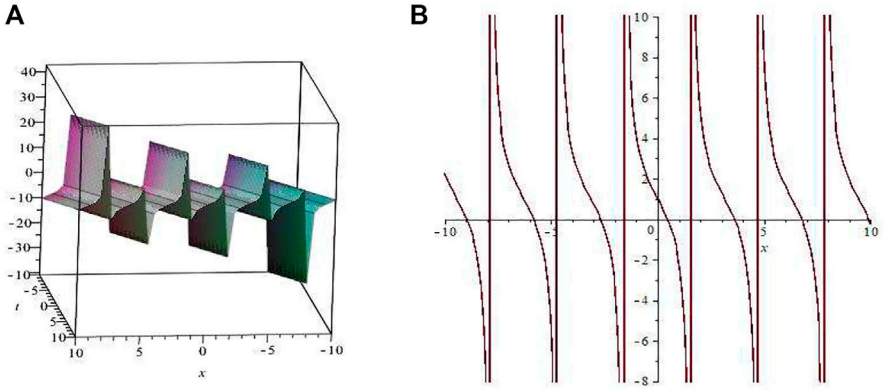

FIGURE 5
The periodic solution of (4.58) at z =0.

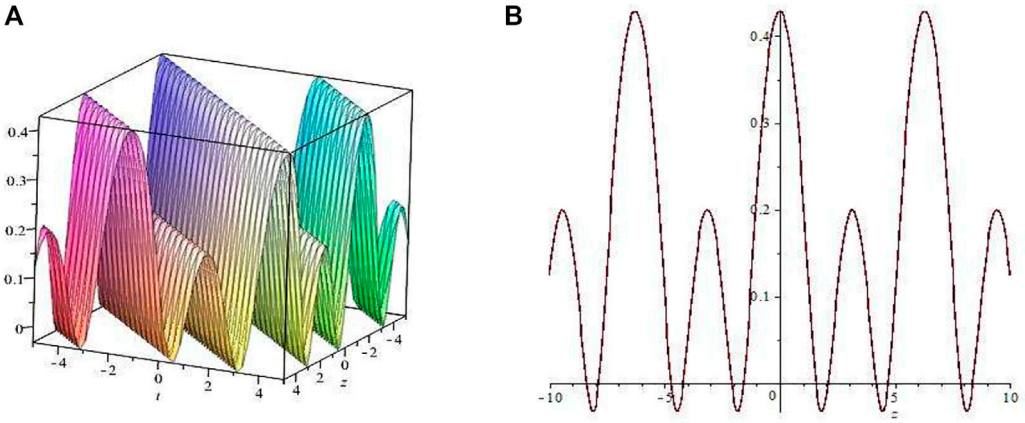

FIGURE 6
The symmetric two-periodic solution of (4.68).

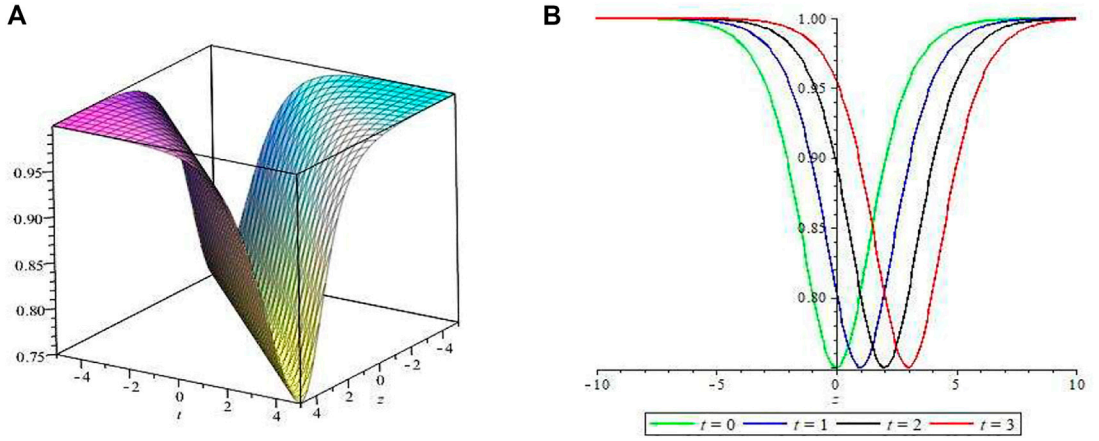

FIGURE 7
Dark soliton solution of (4.67).

$$u = t - 2k\sqrt{\omega}\tan\left(\left(k(x-t) + \frac{mky}{-4k^3\omega + k + m} + m(z-t)\right)\sqrt{\omega}\right) + a_0, \tag{4.58}$$

where k, m, a_0, ω, y, z are constants.

4.6 Vector field $v_2 + v_4$

The characteristic equation can be composed as

$$\frac{dx}{0} = \frac{dy}{0} = \frac{dz}{1} = \frac{dt}{1} = \frac{du}{0}. \tag{4.59}$$

Solving (Eq. 4.59), we derived the similarity solution

$$u(x, y, z, t) = F(\alpha, \beta, \theta), \tag{4.60}$$

where $\alpha = x$, $\beta = y$ and $\theta = z - t$ are similarity variables. Taking (Eq. 4.60) into Eq. 1.2, the (2 + 1)-dimensional equation can be obtained by

$$F_{\alpha\alpha\alpha\beta} + 3F_{\alpha\alpha}F_{\beta} + 3F_{\alpha}F_{\alpha\beta} + F_{\beta\theta} - F_{\alpha\theta} = 0. \tag{4.61}$$

Taking the traveling wave transform

$$F(\alpha, \beta, \theta) = h(v), \quad v = k\alpha + l\beta + m\theta, \tag{4.62}$$

where k, l and m are constants. Putting (Eq. 4.62) into Eq. 4.61 and integrate once, we derive

$$lk^3h_{vvv} + 3lk^2h_v{}^2 + lmh_v - mkh_v = 0. \tag{4.63}$$

Suppose the solution of Eq. 4.63 is given by

$$h(v) = \frac{\sum_{j=0}^{2p} s_j e^{iv}}{\sum_{j=0}^{2p} r_j e^{iv}}, \tag{4.64}$$

where s_j, r_j are constants to be obtained. By balancing Eq. 4.63, $p = 1$. Therefore, Eq. 4.64 is written as

$$h(v) = \frac{s_0 + s_1e^{v} + s_2e^{2v}}{r_0 + r_1e^{v} + r_2e^{2v}}. \tag{4.65}$$

Replacing (Eq. 4.63) along with Eq. 4.65 and making the same coefficient be zero, a family of algebraic equations about s_0, s_1, s_2, r_0, r_1, r_2, k, l and m can be yielded. Solving the above equations, we obtain:

$$k = 0, \quad l = 0, \ m = m, \ s_0 = s_0, \ s_1 = s_1, \ s_2 = s_2, \ r_0 = r_0, \ r_1 = r_1, \ r_2 = r_2. \tag{4.66}$$

Then the solution of Eq. 1.2 is given by:

$$u = \frac{s_0}{r_0 + r_1e^{(z-t)m} + r_2e^{((z-t)m)^2}} + \frac{s_1e^{(z-t)m}}{r_0 + r_1e^{(z-t)m} + r_2e^{((z-t)m)^2}} + \frac{s_2e^{((z-t)m)^2}}{r_0 + r_1e^{(z-t)m} + r_2e^{((z-t)m)^2}}, \tag{4.67}$$

where m, s_0, s_1, s_2, r_0, r_1 and r_2 are constants. Based on Eq. 4.67, replacing the parameter $k = ik$, $l = il$, $m = im$ and picking the real part, the following periodic wave solution can be given

$$u = \frac{s_0}{r_0 + r_1\cos((z-t)m) + r_2\cos(2(z-t)m)} + \frac{s_1\cos((z-t)m)}{r_0 + r_1\cos((z-t)m) + r_2\cos(2(z-t)m)} + \frac{s_2\cos(2(z-t)m)}{r_0 + r_1\cos((z-t)m) + r_2\cos(2(z-t)m)}. \tag{4.68}$$

5 Analysis and discussion

In this part, the geometric representation of the solution of Eq. 1.2 is discussed by employing graphical description. The physical phenomena of the solutions can be seen more obviously *via* numerical simulation. The solutions of the gSWl equation yielded from the above process include periodic, dark soliton, kink wave and annihilation structures of solutions. The dynamic structure of the solutions is investigated below.

Figure 1 depicts the physical structure of the singular solution when the parameter $c_1 = 1$, = 1, $x = 1$, $y = 1$. (B) Indicates the density plot of the corresponding solution.

Figure 2 describes the physical structure of the kink solution when $t = 1$, and the rest of the parameters take the value of $y = 1$, = 3, = 1, $k = 1$, $l = 1$, m = 1, = 1, = 1. When the time increases from $t = 1$

to $t = 28$, the energy of the wave is gradually depleted and eventually becomes a plane wave.

The physical structure of the antisymmetric periodic solution (4.35) is shown in Figure 3. The 3-D plot of the antisymmetric periodic solution is described when the parameter is taken as $z = 0$, $y = 0, = 1, = 1, k = 1, l = 1,$ m $= 1, = 1, = -1$. (B) show the density plot of the solution.

The dynamics structure of the kink wave solution at $z = 0$ is plotted in Figure 4. When $k = -10, c = 10, = 1, = -10, y = 1$. (A) shows the 3-D plot of the solution and (B) depicts the spread route of the solution along the x-axis when $t = 0$, $t = 1$, $t = 2$ and $t = 3$, respectively.

It is shown in Figure 5 and Figure 6 that the physical structure of the periodic wave solutions (4.58) and (4.68). (A) Is the corresponding 3D structure, (B) is the track of the solution along the x-axis, which is given when the parameter$k = 1, = -1, = 1, r = 1$, $y = 0$, $z = 0$ (4.68) shows the 3-D structure of the symmetric two-period wave solution, with the corresponding parameter $a_0 = 1, = 1, = 1, = 5, = 1, = 1,$ m $= 1$. (B) Depicts the spread route of the solution along the z-axis at $t = 0$.

A structure of the dynamics of the dark soliton (4.67) is depicted in Figure 7. The 3-D plot of the dark soliton is obtained when the parameter is selected as $a_0 = 1, = 1, = 1, = 1, = 2, = 1,$ m $= 1$. The spread route behavior of the dark soliton along the z-axis can be derived by choosing $t = 0$, $t = 1$, $t = 2$ and $t = 3$.

6 Conclusion

In summary, the (3 + 1)-dimensional generalized Shallow Water-like wave equation is shown in this paper which is studied based on the Lie symmetry method and the symbolic calculation. By the adjoint table of the infinitesimal generators, a one-dimensional optimal system is formulated. In terms of the optimal system, some new solutions of the gSWl equation are derived by $\mathrm{Exp}(-\phi(\xi))$ expansion method, Riccati equation method, Exp-function expansion method, and (G'/G) expansion method. In particular, the physical structures of the detected dark soliton, kink wave, and periodic solutions are investigated to make this study more credible.

In this work, a situation of the (3 + 1)-dimensional gSWl equation has been investigated based on the Lie symmetry method, and the rest of the latter cases are presented in other subsequent papers. More work needs to be done in the future. Firstly, in this paper, the exact solutions of the equation are derived richly with the Lie symmetry method, and other methods can be employed for the solutions of the equation, such as the numerical analysis method [36–38]. Secondly, the natural properties of the solutions to the equation can be investigated further in subsequent studies through the generalized multi-symplectic method and the structure-preserving method [39–42].

Data availability statement

The original contributions presented in the study are included in the article/Supplementary Material, further inquiries can be directed to the corresponding author.

Author contributions

BY: Conceptualization, Methodology, Investigation, Formal analysis, Writing–original draft. YS: Software, Formal analysis. ZW: Conceptualization, Funding acquisition, Resources, Supervision, Writing–review and editing.

Funding

This work was supported by Natural Science Foundation of Shandong Province (Grant ZR2021MA084), the Natural Science Foundation of Liaocheng University (318012025), and Discipline with Strong Characteristics of Liaocheng University—Intelligent Science and Technology (319462208).

Conflict of interest

The authors declare that the research was conducted in the absence of any commercial or financial relationships that could be construed as a potential conflict of interest.

Publisher's note

All claims expressed in this article are solely those of the authors and do not necessarily represent those of their affiliated organizations, or those of the publisher, the editors and the reviewers. Any product that may be evaluated in this article, or claim that may be made by its manufacturer, is not guaranteed or endorsed by the publisher.

References

1. Eslami M. Soliton-like solutions for the coupled Schrodinger-Boussinesq equation. *Optik* (2015) 126(23):3987–91. doi:10.1016/j.ijleo.2015.07.197

2. Eslami M, Mirzazadeh MA, Neirameh A. New exact wave solutions for Hirota equation. *Pramana* (2015) 84(1):3–8. doi:10.1007/s12043-014-0837-z

3. Gao XY, Guo YJ, Shan WR. Beholding the shallow water waves near an ocean beach or in a lake via a Boussinesq-Burgers system. *Chaos, Solitons & Fractals* (2021) 147: 110875. doi:10.1016/j.chaos.2021.110875

4. Lan ZZ, Gao YT, Yang JW, Su CQ, Solitons BQM. Solitons, Bäcklund transformation and Lax pair for a (2+1)-dimensional Broer-Kaup-Kupershmidt system in the shallow water of uniform depth. *Commun Nonlinear Sci Numer Simulation* (2017) 44:360–72. doi:10.1016/j.cnsns.2016.07.013

5. Iqbal MA, Wang Y, Miah MM, Osman MS. Study on date-Jimbo-Kashiwara-Miwa equation with conformable derivative dependent on time parameter to find the exact dynamic wave solutions. *Fractal and Fractional* (2021) 6(1):4. doi:10.3390/fractalfract6010004

6. Yokus A, Durur H, Ahmad H, Yao SW. Construction of different types analytic solutions for the Zhiber-Shabat equation. *Mathematics* (2020) 8(6):908. doi:10.3390/math8060908

7. Chen SJ, Ma WX, Lü X. Bäcklund transformation, exact solutions and interaction behaviour of the (3+1)-dimensional Hirota-Satsuma-Ito-like equation. *Commun Nonlinear Sci Numer Simulation* (2020) 83:105135. doi:10.1016/j.cnsns.2019.105135

8. Rady ASA, Osman ES, Khalfallah M. The homogeneous balance method and its application to the Benjamin-Bona-Mahoney (BBM) equation. *Appl Math Comput* (2010) 217(4):1385–90. doi:10.1016/j.amc.2009.05.027

9. Bhutani G, Brito-Parada PR. Analytical solution for a three-dimensional non-homogeneous bivariate population balance equation-A special case. *Int J Multiphase Flow* (2017) 89:413–6. doi:10.1016/j.ijmultiphaseflow.2016.11.005

10. Kumar S, Kumar D, Kumar A. Lie symmetry analysis for obtaining the abundant exact solutions, optimal system and dynamics of solitons for a higher-dimensional Fokas equation. *Chaos, Solitons & Fractals* (2021) 142:110507. doi:10.1016/j.chaos.2020.110507

11. Ghanbari B, Kumar S, Niwas M, Baleanu D. The Lie symmetry analysis and exact Jacobi elliptic solutions for the Kawahara-KdV type equations. *Results Phys* (2021) 23: 104006. doi:10.1016/j.rinp.2021.104006

12. Benoudina N, Zhang Y Y, Khalique CM. Lie symmetry analysis, optimal system, new solitary wave solutions and conservation laws of the Pavlov equation. *Commun Nonlinear Sci Numer Simulation* (2021) 94:105560. doi:10.1016/j.cnsns.2020.105560

13. Ma WX. Inverse scattering for nonlocal reverse-time nonlinear Schr*ddot*odinger equations. *Appl Math Lett* (2020) 102:106161. doi:10.1016/j.aml.2019.106161

14. Ali Akbar M, Ali NHM. The improved *F*-expansion method with Riccati equation and its applications in mathematical physics. *Cogent Math* (2017) 4(1):1282577. doi:10.1080/23311835.2017.1282577

15. Akbulut A, Kaplan M, Tascan F. The investigation of exact solutions of nonlinear partial differential equations by using exp method. *Optik* (2017) 132:382–7. doi:10.1016/j.ijleo.2016.12.050

16. Hafez MG. Exact solutions to the (3+1)-dimensional coupled Klein-Gordon-Zakharov equation using exp xi-expansion method. *Alexandria Eng J* (2016) 55(2): 1635–45. doi:10.1016/j.aej.2016.02.010

17. Li HM, Tian B, Xie XY, Chai J, Liu L, Gao YT. Soliton and rogue-wave solutions for a (2+1)-dimensional fourth-order nonlinear Schrodinger equation in a Heisenberg ferromagnetic spin chain. *Nonlinear Dyn* (2016) 86(1):369–80. doi:10.1007/s11071-016-2894-y

18. Peng WQ, Tian SF, Wang XB, Zhang TT, Fang Y. Riemann-Hilbert method and multi-soliton solutions for three-component coupled nonlinear Schrodinger equations. *J Geometry Phys* (2019) 146:103508. doi:10.1016/j.geomphys.2019.103508

19. Wang DS, Wang X. Long-time asymptotics and the bright N-soliton solutions of the Kundu–Eckhaus equation via the Riemann–Hilbert approach. *Nonlinear Anal Real World Appl* (2018) 41:334–61. doi:10.1016/j.nonrwa.2017.10.014

20. Huang QM, Gao YT, Jia SL, DengBilinear GF. Bilinear Bäcklund transformation, soliton and periodic wave solutions for a $$\varvec{(3 + 1)}$$ (3 + 1) -dimensional variable-coefficient generalized shallow water wave equation. *Nonlinear Dyn* (2017) 87(4):2529–40. doi:10.1007/s11071-016-3209-z

21. Huang QM, Gao YT. Bilinear form, bilinear Bäcklund transformation and dynamic features of the soliton solutions for a variable-coefficient (3+1)-dimensional generalized shallow water wave equation. *Mod Phys Lett B* (2017) 31(22):1750126. doi:10.1142/s0217984917501263

22. Kumar D, Kumar S. Some new periodic solitary wave solutions of (3+1)-dimensional generalized shallow water wave equation by Lie symmetry approach. *Comput Math Appl* (2019) 78(3):857–77. doi:10.1016/j.camwa.2019.03.007

23. Li YZ, Liu JG. Multiple periodic-soliton solutions of the (3+1)-dimensional generalised shallow water equation. *Pramana* (2018) 90(6):1–11.

24. Liu JG, He Y. New periodic solitary wave solutions for the (3+1)-dimensional generalized shallow water equation. *Nonlinear Dyn* (2017) 90(1):363–9. doi:10.1007/s11071-017-3667-y

25. Liu JG, Zhu WH. Breather wave solutions for the generalized shallow water wave equation with variable coefficients in the atmosphere, rivers, lakes and oceans. *Comput Math Appl* (2019) 78(3):848–56. doi:10.1016/j.camwa.2019.03.008

26. Tang YN, Ma WX, Xu W. Grammian and Pfaffian solutions as well as Pfaffianization for a (3+1)-dimensional generalized shallow water equation. *Chin Phys B* (2012) 21(7):070212. doi:10.1088/1674-1056/21/7/070212

27. Kumar D, Raju I, Paul GC, Ali ME, Haque MD. Characteristics of lump-kink and their fission-fusion interactions, rogue, and breather wave solutions for a (3+1)-dimensional generalized shallow water equation. *Int J Comp Math* (2022) 99(4): 714–36. doi:10.1080/00207160.2021.1929940

28. Sadat R, Kassem M, Ma WX. Abundant lump-type solutions and interaction solutions for a nonlinear (3+1)-dimensional model. *Adv Math Phys* (2018) 2018:1–8. doi:10.1155/2018/9178480

29. Zhang Y, Dong H, Zhang X, Yang H. Rational solutions and lump solutions to the generalized (3+1)-dimensional Shallow Water-like equation. *Comput Math Appl* (2017) 73(2):246–52. doi:10.1016/j.camwa.2016.11.009

30. Olver PJ. *Applications of Lie groups to differential equations*. Springer Science & Business Media (1993).

31. Ovsjannikov LV. *Group properties of differential equations*. Novosibirsk: Siberian Section of the Academy of Science of USSR (1962).

32. Wang GW. Symmetry analysis, analytical solutions and conservation laws of a generalized KdV-Burgers-Kuramoto equation and its fractional version. *Fractals* (2021) 29(04):2150101. doi:10.1142/s0218348x21501012

33. Wang GW. A new (3+1)-dimensional schrödinger equation: Derivation, soliton solutions and conservation laws. *Nonlinear Dyn* (2021) 104(2):1595–602. doi:10.1007/s11071-021-06359-6

34. Wang GW. A novel (3+1)-dimensional sine-gorden and a sinh-gorden equation: Derivation, symmetries and conservation laws. *Appl Math Lett* (2021) 113:106768. doi:10.1016/j.aml.2020.106768

35. Hu X, Li Y, Chen Y. A direct algorithm of one-dimensional optimal system for the group invariant solutions. *J Math Phys* (2015) 56(5):053504. doi:10.1063/1.4921229

36. Hu WP, Deng ZC, Han S, Zhang WR. Generalized multi-symplectic integrators for a class of Hamiltonian nonlinear wave PDEs. *J Comput Phys* (2013) 235:394–406. doi:10.1016/j.jcp.2012.10.032

37. Hu WP, Wang Z, Zhao YP, Deng ZC. Symmetry breaking of infinite-dimensional dynamic system. *Appl Math Lett* (2020) 103:106207. doi:10.1016/j.aml.2019.106207

38. Hu WP, Ye J, Deng ZC. Internal resonance of a flexible beam in a spatial tethered system. *J Sound Vibration* (2020) 475:115286. doi:10.1016/j.jsv.2020.115286

39. Hu WP, Zhang CZ, Deng ZC. Vibration and elastic wave propagation in spatial flexible damping panel attached to four special springs. *Commun Nonlinear Sci Numer Simulation* (2020) 84:105199. doi:10.1016/j.cnsns.2020.105199

40. Hu WP, Huai YL, Xu MB, Feng XQ, Jiang RS, Zheng YP, et al. Mechanoelectrical flexible hub-beam model of ionic-type solvent-free nanofluids. *Mech Syst Signal Process* (2021) 159:107833. doi:10.1016/j.ymssp.2021.107833

41. Hu WP, Huai YL, Xu MB, Deng ZC. Coupling dynamic characteristics of simplified model for tethered satellite system. *Acta Mechanica Sinica* (2021) 37(8): 1245–54. doi:10.1007/s10409-021-01108-9

42. Hu WP, Xu MB, Zhang F, Xiao C, Deng ZC. Dynamic analysis on flexible hub-beam with step-variable cross-section. *Mech Syst Signal Process* (2022) 180:109423. doi:10.1016/j.ymssp.2022.109423

frontiers | Frontiers in Physics

TYPE Original Research
PUBLISHED 28 February 2023
DOI 10.3389/fphy.2023.1150176

OPEN ACCESS

EDITED BY
Samir A. El-Tantawy,
Port Said University, Egypt

REVIEWED BY
Nadeem Sheikh,
City University of Science and Information Technology, Pakistan
Muhammad Khan,
University of Technology Malaysia, Malaysia

*CORRESPONDENCE
Ilyas Khan,
i.said@mu.edu.sa

SPECIALTY SECTION
This article was submitted to Mathematical Physics, a section of the journal Frontiers in Physics

RECEIVED 23 January 2023
ACCEPTED 08 February 2023
PUBLISHED 28 February 2023

CITATION
Khan RA, Taj S, Ahmed S, Khan I and Eldin SM (2023), Lie symmetry and exact homotopic solutions of a non-linear double-diffusion problem.
Front. Phys. 11:1150176.
doi: 10.3389/fphy.2023.1150176

Lie symmetry and exact homotopic solutions of a non-linear double-diffusion problem

R. A. Khan[1], S. Taj[2], S. Ahmed[1,3], Ilyas Khan[4]* and Sayed M. Eldin[5]

[1]School of Mechanical and Manufacturing Engineering (SMME), National University of Sciences and Technology (NUST), Islamabad, Pakistan, [2]College of Electrical and Mechanical Engineering, National University of Sciences and Technology (NUST), Islamabad, Pakistan, [3]Department of Mathematics and Statistics, Riphah International University I-14, Islamabad, Pakistan, [4]Department of Mathematics, College of Science, Majmaah University, Al-Majmaah, Saudi Arabia, [5]Center of Research, Faculty of Engineering, Future University in Egypt New Cairo, New Cario, Egypt

The Lie symmetry method is applied, and exact homotopic solutions of a non-linear double-diffusion problem are obtained. Additionally, we derived Lie point symmetries and corresponding transformations for equations representing heat and mass transfer in a thin liquid film over an unsteady stretching surface, using MAPLE. We used these symmetries to construct new (Lie) similarity transformations that are different from those that are commonly used for flow and mass transfer problems. These new (Lie) similarity transformations map the partial differential equations of a mathematical model under consideration to ordinary differential equations along with boundary conditions. Lie similarity transformations are shown to lead to new solutions for the considered flow problem. These solutions are obtained using the homotopy analysis method to analytically solve the ordinary differential equations that resulted from the reduction of considered flow equations through Lie similarity transformations. With the aid of these solutions, effects of various parameters on the flow and heat transfer are discussed and presented graphically in this study.

KEYWORDS

Lie similarity transformations, homotopy analysis method, symmetry, exact solutions, thin-film flow

1 Introduction

Fluid flow and heat transfer phenomena have a wide range of applications in engineering. By varying these transporters and enforcing various physical conditions, it is possible to produce a variety of industrial products at their best. As a result, it has drawn a significant amount of attention during the past several decades. The Navier–Stokes equations are used to quantitatively represent these heat and flow exchanges, with the appropriate circumstances. These are extremely non-linear partial differential equations (PDEs) of order two or higher. Such non-linearities lessen the likelihood of obtaining precise results. As a result, flow studies are related to approximation techniques and analytical solution schemes, and heat transfer techniques are frequently used.

The Runge–Kutta and shot method are combined for the derivation of the former type of solutions, whereas homotopy analysis and perturbation techniques are frequently used for the latter.

These problem-solving methods are not directly related to the PDEs that describe the flow problems. The system of ordinary differential equations (ODEs) relating to these flow issues is, nevertheless, solved using these methods. The similarity transformation is the technology that makes this kind of reduction possible. The dependent and/or independent variables of flow equations are reduced using these adjustments.

First, the fact that there are more established and diverse solution methods for ODEs than PDEs accounts for this reduction. Second, running ODEs through mathematical symbolic and numeric software requires less time and equipment compared to other approaches. Following the reduction of flow equations to ODEs *via* similarity transformations, one finds several applications of such solution algorithms in the literature.

With this procedure, the flow and heat transfers have been studied under different sets of conditions, for example, in a liquid film on an unsteady stretching surface [1, 2], under the effects of variable fluid properties and thermo capillarity [3], with Soret and Dufour effects on a viscoelastic fluid in three dimensions [4], in a rotating channel three-dimensional squeezing flow [5], in a three-dimensional flow of a nanofluid over a non-linearly stretching sheet [6], and for an Oldroyd-B nanofluid thin film over an unsteady stretching sheet [7]. Likewise, magnetohydrodynamic (MHD) flow and heat transfer have been studied for the following: thermosolutal Marangoni convection with heat generation [8], viscoelastic fluid flow over a vertical stretching sheet under the effects of Soret and Dufour [9], Jeffrey fluid over a stretching sheet considering the chemical reaction and thermal radiation [10], three-dimensional flow of an Oldroyd-B nanofluid on a radiative surface [11], thermally radiative flow in three dimensions of a Jeffrey nanofluid under internal heat generation [12], a shrinking sheet with thermal slip [13], a vertical stretching sheet under the effects of heat sink or source [14], mixed convection on the inclined stretching plate in the Darcy porous medium with a Soret effect considering variable surface conditions [15], and mixed convective flow of a Maxwell nanofluid past a porous vertical stretching sheet with a chemical reaction [16].

There are countless studies through an area of research known as the Lie symmetry method, which helps to accurately derive the analytical or approximate solutions for flow and heat transfer equations. For instance, Lie group theory has been employed to study the flow and heat transfer in a non-Newtonian fluid over a stretching surface with thermal radiation [17], MHD boundary layer flow over a stretching sheet with viscous dissipation and uniform heat source/sink [18], MHD mixed flow of unsteady convection on a vertical porous plate with radiation [19], MHD double-diffusion convection of a Casson nanofluid on a vertical stretching/shrinking surface under the effects of thermal radiation and chemical reaction [20], heat flux effect on MHD second slip flow past a stretching sheet along with heat generation [21], MHD Casson fluid flow near a stagnation point on a linearly stretching sheet taking variable viscosity and thermal conductivity into account [22], thermophysical properties of a magnetized Williamson fluid subject to porous/non-porous surfaces [23], two-parameter Lie scaling approach on an unsteady MHD Casson fluid over a porous rigid plate with a stagnation point flow [24], double-diffusive MHD tangent hyperbolic fluid flow on a stretching sheet [25], MHD thermally slip Carreau fluid subject to multiple flow regimes [26], and for a liquid film on an unsteady stretching sheet using Lie point symmetries [27].

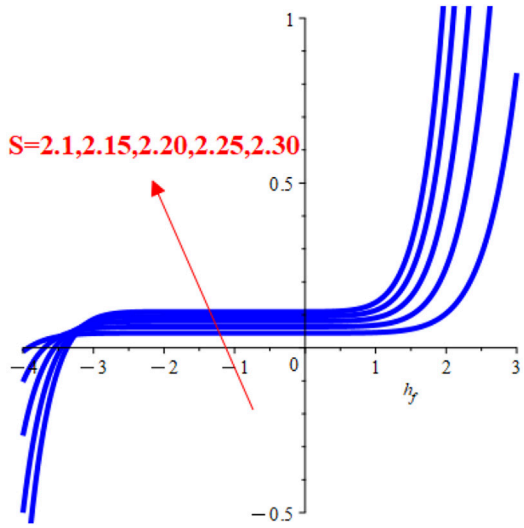

FIGURE 1
h_f-curves (S = 2.10 – 2.30).

The governing equations in the aforementioned flow models are non-linear. Therefore, numerous approaches are adopted to deal with the non-linearity of the governing equations. The Lie symmetry method is one of those that provide a systematic procedure to construct similarity transformation that is a pivotal component of solution schemes employed on fluid flows mentioned previously. Non-linear phenomena impose constraints on the studies conducted to analyze physical models appearing in numerous applications due to the availability of few techniques that are employed to deal with it. As far as the Lie approach is concerned, one may linearize the governing equations (28)–(31). There are many non-Lie procedures that are also available in the literature, for example, effective treatments of the non-linearity of differential equations have been reported in [32–34].

A Lie point symmetry transformation can be associated with a differential or an algebraic equation if it leaves it form invariant. It implies that a heat equation remains a heat equation after mapping it under its Lie point transformation. Every Lie point transformation possesses a Lie symmetry generator. For basic theory and the algebraic computations of the Lie symmetry generators and transformation, readers are referred to [35, 36]. MAPLE contains all these procedures to build symmetry transformations in the "PDEtools" package, which, on applying "Infinitesimals" on differential equations, reveals their symmetries. MAPLE is used to find out symmetry generators and corresponding transformations for flow problems that are being taken into consideration in this study.

We deduce Lie point symmetries for the momentum, energy, and concentration equations representing the flow problem under consideration. There exist nine Lie symmetries, and by using them,

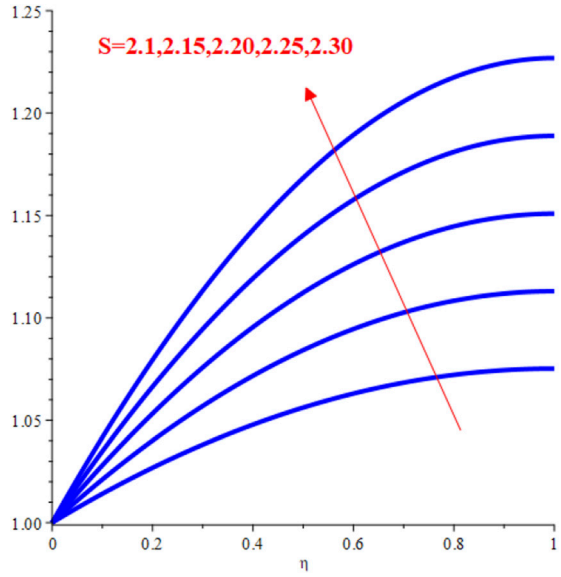

FIGURE 2
Velocity profiles (S = 2.10 – 2.30).

Lie similarity transformations are obtained. However, we employ only those symmetries which leave the associated boundary conditions in a particular form. Based on these constraints, we consider three linear combinations (that are also Lie point symmetries) of the derived Lie symmetries. In one of these, we combine two symmetries, while the remaining two consist of three symmetries. These three combinations provided a different type of similarity transformation which transformed flow equations into three different types of ODE systems. Arbitrary constants are used in the linear combinations of the Lie point symmetries, and these constants also appear in the resulting system of ODEs due to their presence in the Lie similarity transformations we construct. We use them to control the convergence of solutions of the flow model we are considering.

The outline of the paper is as follows. The second section is about flow equations and their Lie symmetries. The subsequent section is on similarity transformations and mapping of flow PDEs to ODEs. In the fourth section, analytical solutions are constructed and presented with graphs and tables. The last section is the conclusion.

2 Flow equations

The flow of heat and mass in a thin liquid film has been studied [37] on an unsteady stretching surface with thermosolutal capillarity and variable magnetic field. Here, we are considering the flow model without the magnetic field and thermosolutal capillarity. The governing equations for the flow of heat and mass transfer in a thin liquid film over an unsteady surface are given by the following system of PDEs:

$$\begin{aligned}
\frac{\partial u}{\partial x}+\frac{\partial v}{\partial y}&=0,\\
\frac{\partial u}{\partial t}+u\frac{\partial u}{\partial x}+v\frac{\partial u}{\partial y}-\nu\frac{\partial^2 u}{\partial y^2}&=0,\\
\frac{\partial T}{\partial t}+u\frac{\partial T}{\partial x}+v\frac{\partial T}{\partial y}-\kappa\frac{\partial^2 T}{\partial y^2}&=0,\\
\frac{\partial C}{\partial t}+u\frac{\partial C}{\partial x}+v\frac{\partial C}{\partial y}-D\frac{\partial^2 C}{\partial y^2}&=0,
\end{aligned} \tag{1}$$

subject to boundary conditions as follows:

$$u(t,x,y)=U_s(t,x),v(t,x,y)=0,T(t,x,y)=T_s(t,x),C(t,x,y)=C_s(t,x),\text{at}\,y=0,$$

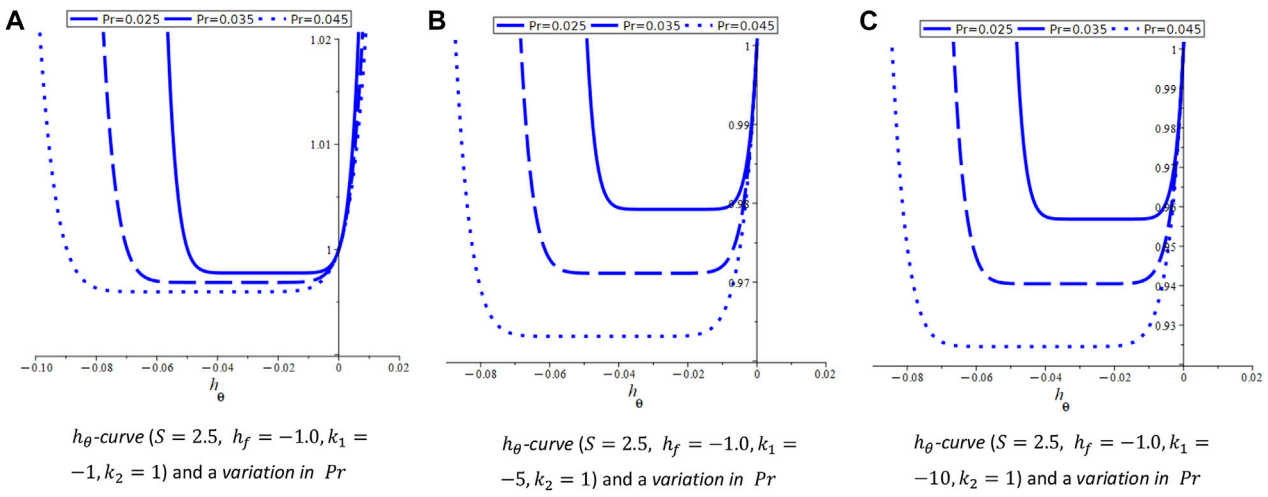

FIGURE 3
Different h-curves. **(A)** h_θ-curve (S = 2.5, h_f = –1.0, k_1 = –1, k_2 = 1) and a variation in Pr. **(B)** h_θ-curve (S = 2.5, h_f = –1.0, k_1 = –5, k_2 = 1) and a variation in Pr. **(C)** h_θ-curve (S = 2.5, h_f = –1.0, k_1 = –10, k_2 = 1) and a variation in Pr.

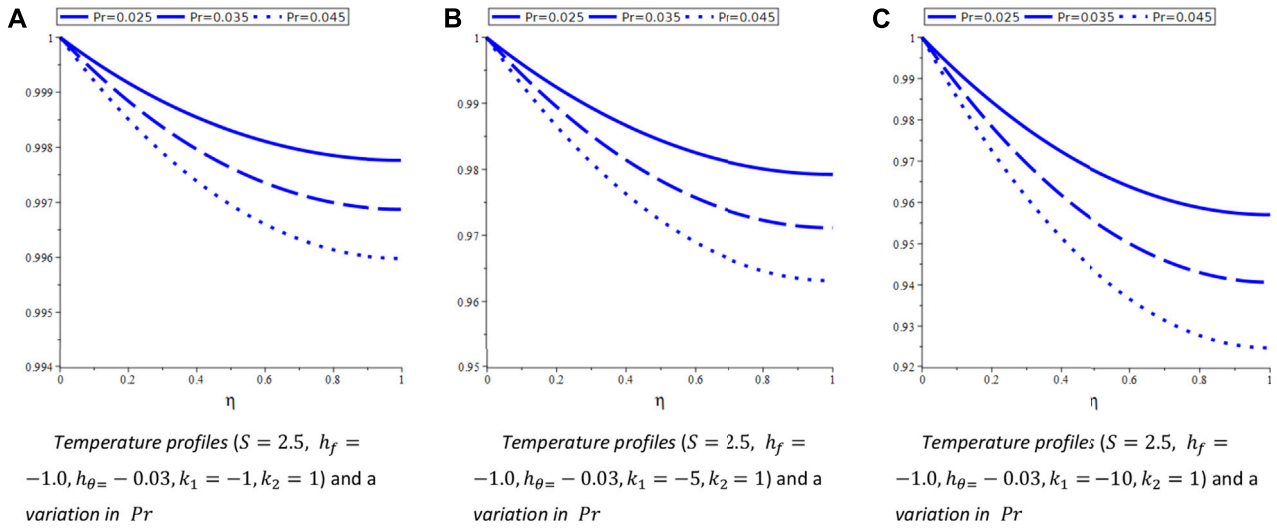

FIGURE 4
Different temperature profiles. **(A)** Temperature profiles ($S = 2.5, h_f = -1.0, h_{\theta=} - 0.03, k_1 = -1, k_2 = 1$) and a variation in Pr. **(B)** Temperature profiles ($S = 2.5, h_f = -1.0, h_{\theta=} - 0.03, k_1 = -5, k_2 = 1$) and a variation in Pr. **(C)** Temperature profiles ($S = 2.5, h_f = -1.0, h_{\theta=} - 0.03, k_1 = -10, k_2 = 1$) and a variation in Pr.

$$\frac{\partial u(t,x,y)}{\partial y} = 0, \frac{\partial T(t,x,y)}{\partial y} = 0, \frac{\partial C(t,x,y)}{\partial y} = 0, v(t,x,y) = \frac{dh}{dt}, \quad \text{at } y = h(t). \tag{2}$$

The Lie point symmetries of the flow mathematical model (Eq. 1) are derived by using the MAPLE "PDEtools" package and the built-in command "Infinitesimals."

$$\mathrm{X}_1 = \frac{\partial}{\partial t}, \mathrm{X}_2 = \frac{\partial}{\partial x}, \mathrm{X}_3 = \frac{\partial}{\partial T}, \mathrm{X}_4 = \frac{\partial}{\partial C}, \mathrm{X}_5 = t\frac{\partial}{\partial x} + \frac{\partial}{\partial u}, \mathrm{X}_6 = T\frac{\partial}{\partial T},$$
$$\mathrm{X}_7 = C\frac{\partial}{\partial C}, \mathrm{X}_8 = x\frac{\partial}{\partial x} + u\frac{\partial}{\partial u}, \mathrm{X}_9 = t\frac{\partial}{\partial t} + \frac{y}{2}\frac{\partial}{\partial y} - u\frac{\partial}{\partial u} - \frac{v}{2}\frac{\partial}{\partial v}. \tag{3}$$

However, for a detailed algebraic procedure to obtain symmetries of system (Eq. 1), the reader is referred to [27]. The Lie symmetry transformations corresponding to symmetry generators (Eq. 3) leave equations of system (Eq. 1) form invariant. These Lie transformations are given in Table 1. Furthermore, all the associated conditions (Eq. 2) should also remain invariant. For this purpose, we employ each

$$X_m^{[l]}(\zeta_n)|_{\zeta_n=0} = 0, \tag{4}$$

where l denotes the extension of the symmetry generator; here, we require the first extension of X_m, for $\mathrm{m} = 1, 2, \ldots, 9$, and ζ_n denotes the conditions (Eq. 2) for $n = 1, 2, \ldots, 8$, e.g., $\zeta_1 := u(t,x,0) = U_s(t,x)$, and *vice versa*.

3 Lie similarity transformations of flow equations

We construct the Lie similarity transformations corresponding to a few linear combinations for the derived Lie point symmetries $\mathbf{X}_1, \mathbf{X}_2, ..., \mathbf{X}_9$. These combinations are based on the unknown functions they determine for $U_s(t,x)$, $T_s(t,x)$, $C_s(t,x)$, and $h(t)$. In this work, only those cases are of interest in which all these functions remain dependent on their arguments. Hence, we consider the combination $k_1\mathbf{X}_8 + k_2\mathbf{X}_9$ of Lie symmetries in Case-I, $k_1\mathbf{X}_6 + k_2\mathbf{X}_7 + k_3\mathbf{X}_8$ in Case-II, and $k_1\mathbf{X}_6 + k_2\mathbf{X}_7 + k_3\mathbf{X}_9$ in Case-III, where k_1, k_2, and k_3 are any non-zero real numbers. All other symmetries from the list (Eq. 3) are not suitable in any form to construct the similarity transformations due to stretching sheet velocity and temperature obtained for these symmetries and their combinations. Hence, we consider only those linear combinations that are mentioned previously. These three linear combinations of symmetries leave both x and t in the stretching sheet velocity $U_s = U_s(t,x)$ and temperature $T_s = T_s(t,x)$; i.e., we want to keep them as functions of time t and space variable x. Moreover, $h(t)$ is also left as a function of t.

TABLE 1 Lie symmetry generators and transformations.

Generator	Transformation
X_1	$t = \bar{t} + \epsilon,\ x = \bar{x},\ y = \bar{y},\ u = \bar{u},\ v = \bar{v},\ T = \bar{T},\ C = \bar{C}$
X_2	$t = \bar{t},\ x = \bar{x} + \epsilon,\ y = \bar{y},\ u = \bar{u},\ v = \bar{v},\ T = \bar{T},\ C = \bar{C}$
X_3	$t = \bar{t},\ x = \bar{x},\ y = \bar{y},\ u = \bar{u},\ v = \bar{v},\ T = \bar{T} + \epsilon,\ C = \bar{C}$
X_4	$t = \bar{t},\ x = \bar{x},\ y = \bar{y},\ u = \bar{u},\ v = \bar{v},\ T = \bar{T},\ C = \bar{C} + \epsilon$
X_5	$t = \bar{t}e^{\epsilon},\ x = \bar{x},\ y = \bar{y},\ u = \bar{u} + \epsilon,\ v = \bar{v},\ T = \bar{T},\ C = \bar{C}$
X_6	$t = \bar{t},\ x = \bar{x},\ y = \bar{y},\ u = \bar{u},\ v = \bar{v},\ T = \bar{T}e^{\epsilon},\ C = \bar{C}$
X_7	$t = \bar{t},\ x = \bar{x},\ y = \bar{y},\ u = \bar{u},\ v = \bar{v},\ T = \bar{T},\ C = \bar{C}e^{\epsilon}$
X_8	$t = \bar{t},\ x = \bar{x}e^{\epsilon},\ y = \bar{y},\ u = \bar{u}e^{\epsilon},\ v = v,\ T = \bar{T},\ C = \bar{C}$
X_9	$t = \bar{t}e^{\epsilon},\ x = \bar{x},\ y = \bar{y}\sqrt{e^{\epsilon}},\ u = \bar{u}e^{-\epsilon},\ v = \frac{\bar{v}}{\sqrt{e^{\epsilon}}},\ T = \bar{T},\ C = \bar{C}$

The symmetry generator from (3) is applied to each of these conditions through the invariance criterion.

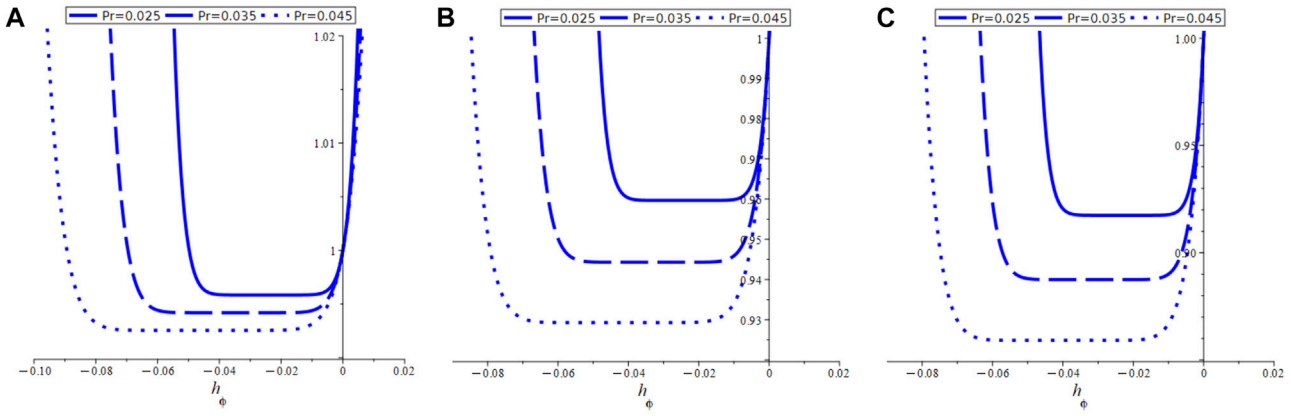

h_ϕ-curve ($S = 3.5,\ h_f = -1.0, k_1 = -1, k_2 = 1$) and a *variation in* Pr

h_ϕ-curve ($S = 3.5,\ h_f = -1.0, k_1 = -5, k_2 = 1$) and a *variation in* Pr

h_ϕ-curve ($S = 3.5,\ h_f = -1.0, k_1 = -10, k_2 = 1$) and a *variation in* Pr

FIGURE 5
Different h-curves.

In the study conducted earlier on this type of fluid and heat transports [38], both the said quantities are set to be dependent on both t and x.

3.1 Case-I: Similarity transformations for $k_1\mathbf{X}_8 + k_2\mathbf{X}_9$

These symmetry generators provided the similarity transformations

$$y = \beta\sqrt{\frac{\alpha\nu t}{b}}\eta, u = -\frac{bx}{\alpha t}\frac{df}{d\eta}, v = \beta\sqrt{\frac{b\nu}{\alpha t}}f(\eta), T = xt^{\frac{-k_1}{k_2}}\theta(\eta) - 1, \quad (5)$$
$$C = xt^{\frac{-k_1}{k_2}}\phi(\eta) - 1$$

which map the system of PDEs (Eq. 1) into the following system of ODEs:

$$\frac{d^3f}{d\eta^3} + \beta^2\left(S\frac{df}{d\eta} + \frac{S\eta}{2}\frac{d^2f}{d\eta^2} + \left(\frac{df}{d\eta}\right)^2 - f(\eta)\frac{d^2f}{d\eta^2}\right) = 0,$$
$$\frac{1}{P_r}\frac{d^2\theta}{d\eta^2} + \beta^2\left(\frac{df}{d\eta}\theta(\eta) - f(\eta)\frac{d\theta}{d\eta} + \frac{S\eta}{2}\frac{d\theta}{d\eta} + \frac{k_1}{k_2}S\theta(\eta)\right) = 0, \quad (6)$$
$$\frac{1}{S_c}\frac{d^2\phi}{d\eta^2} + \beta^2\left(\frac{df}{d\eta}\phi(\eta) - f(\eta)\frac{d\phi}{d\eta} + \frac{S\eta}{2}\frac{d\phi}{d\eta} + \frac{k_1}{k_2}S\phi(\eta)\right) = 0,$$

where η is the new independent variable. The associated boundary conditions are

$$f(0) = 0, \theta(0) = \phi(0) = 1, \frac{df(0)}{d\eta} = 1, f(1) = \frac{S}{2},$$
$$\frac{d^2f(1)}{d\eta^2} = \frac{d\theta(1)}{d\eta} = 0, \frac{d\phi(1)}{d\eta} = 0. \quad (7)$$

3.2 Case-II: Similarity transformations for $k_1\mathbf{X}_6 + k_2\mathbf{X}_7 + k_3\mathbf{X}_8$

In this case, the following similarity transformations are obtained:

$$y = \beta\sqrt{\frac{\alpha\nu(1+t)}{b}}\eta, u = -\frac{bx}{\alpha(1+t)}\frac{df}{d\eta}, v = \beta\sqrt{\frac{b\nu}{\alpha(1+t)}}f(\eta), \quad (8)$$
$$T = (1+t)x^{\frac{k_1}{k_3}}\theta(\eta), C = (1+t)x^{\frac{k_2}{k_3}}\phi(\eta).$$

These similarity transformations map the system of PDEs (Eq. 1) into the following system of ODEs:

$$\frac{d^3f}{d\eta^3} + \beta^2\left(S\frac{df}{d\eta} + \frac{S\eta}{2}\frac{d^2f}{d\eta^2} + \left(\frac{df}{d\eta}\right)^2 - f(\eta)\frac{d^2f}{d\eta^2}\right) = 0,$$
$$\frac{1}{P_r}\frac{d^2\theta}{d\eta^2} + \beta^2\left(\frac{k_1}{k_3}\frac{df}{d\eta}\theta(\eta) - f(\eta)\frac{d\theta}{d\eta} + \frac{S\eta}{2}\frac{d\theta}{d\eta} - S\theta(\eta)\right) = 0, \quad (9)$$
$$\frac{1}{S_c}\frac{d^2\phi}{d\eta^2} + \beta^2\left(\frac{k_2}{k_3}\frac{df}{d\eta}\phi(\eta) - f(\eta)\frac{d\phi}{d\eta} + \frac{S\eta}{2}\frac{d\phi}{d\eta} - S\phi(\eta)\right) = 0,$$

and the associated boundary conditions are given as follows:

$$f(0) = 0, \frac{df(0)}{d\eta} = \theta(0) = \phi(0) = 1,$$
$$f(1) = \frac{S}{2}, \frac{d^2f(1)}{d\eta^2} = \frac{d\theta(1)}{d\eta} = \frac{d\phi(1)}{d\eta} = 0. \quad (10)$$

3.3 Case-III: Similarity transformations for $k_1\mathbf{X}_6 + k_2\mathbf{X}_7 + k_3\mathbf{X}_9$

Here, we obtain the following similarity transformations:

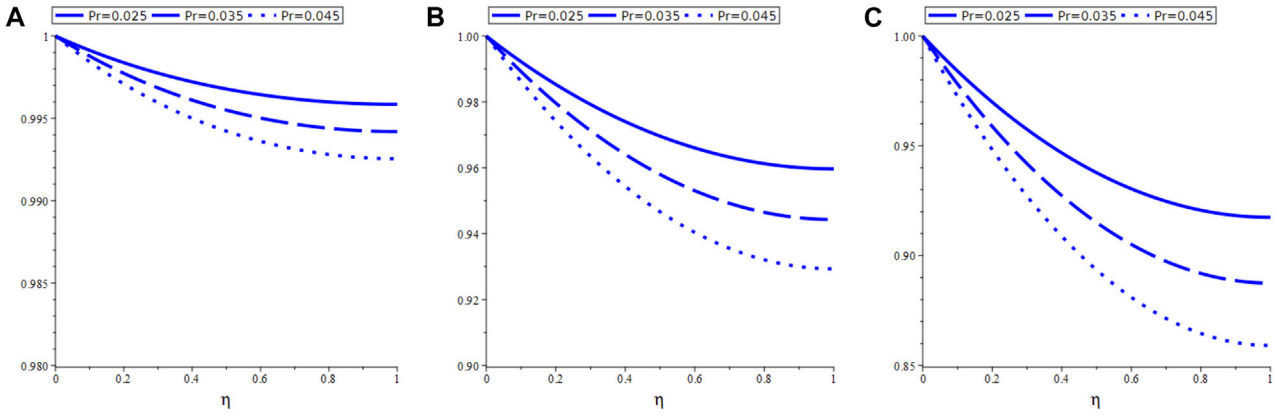

Concentration profiles ($S = 3.5,\ h_f = -1.0, h_\phi = -0.025, k_1 = -1, k_2 = 1$) and a *variation in* Pr

Concentration profiles ($S = 3.5,\ h_f = -1.0, h_\phi = -0.025, k_1 = -5, k_2 = 1$) and a *variation in* Pr

Concentration profiles ($S = 3.5,\ h_f = -1.0, h_\phi = -0.025, k_1 = -10, k_2 = 1$) and a *variation in* Pr

FIGURE 6
Different concentration profiles.

$$y = \beta\sqrt{\frac{\alpha\nu t}{b}}\eta, u = -\frac{b(1+x)}{\alpha t}\frac{df}{d\eta}, v = \beta\sqrt{\frac{b\nu}{\alpha t}}f(\eta),$$
$$T = (1+x)t^{\frac{k_1}{k_3}}\theta(\eta), C = (1+x)t^{\frac{k_2}{k_3}}\phi(\eta). \quad (11)$$

These similarity transformations map the system of PDEs (Eq. 1) into the following system of ODEs:

$$\frac{d^3f}{d\eta^3} + \beta^2\left(S\frac{df}{d\eta} + \frac{S\eta}{2}\frac{d^2f}{d\eta^2} + \left(\frac{df}{d\eta}\right)^2 - f(\eta)\frac{d^2f}{d\eta^2}\right) = 0,$$
$$\frac{1}{P_r}\frac{d^2\theta}{d\eta^2} + \beta^2\left(\frac{df}{d\eta}\theta(\eta) - f(\eta)\frac{d\theta}{d\eta} + \frac{S\eta}{2}\frac{d\theta}{d\eta} - \frac{k_1}{k_3}S\theta(\eta)\right) = 0, \quad (12)$$
$$\frac{1}{S_c}\frac{d^2\phi}{d\eta^2} + \beta^2\left(\frac{df}{d\eta}\phi(\eta) - f(\eta)\frac{d\phi}{d\eta} + \frac{S\eta}{2}\frac{d\phi}{d\eta} - \frac{k_2}{k_3}S\phi(\eta)\right) = 0.$$

The associated boundary conditions map to

$$f(0) = 0, \frac{df(0)}{d\eta} = \theta(0) = \phi(0) = 1,$$
$$f(1) = \frac{S}{2}, \frac{d^2f(1)}{d\eta^2} = \frac{d\theta(1)}{d\eta} = \frac{d\phi(1)}{d\eta} = 0. \quad (13)$$

4 Analytic solution by the homotopy analysis method

In this section, the velocity and temperature profiles are constructed with the aid of the analytical solution of order ten derived through the HAM. It has been observed that the first equation in all three cases that are under consideration here is the same. First, we draw h_f-curves that are presented graphically for $2.10 < S < 2.30$ in Figure 1. The reason to consider this range is the dimensionless film thickness which remains negative or zero for $S \leq 2.0$. Hence, all the velocity, temperature, and concentration profiles are presented here for $S > 2.0$. The dimensionless film thickness increases with an increase in S, under the conditions provided by Lie similarity conditions. This situation changes and opposite trends have been found in [39] using Lie similarity transformations with an introduction of a magnetic term. Figure 2 shows the velocity profiles for the same range of an unsteadiness parameter, which shows an increase in the velocity with this parameter. The temperature and concentration profiles are expected to be different in all three cases as, apparently, the second and third equations in the systems of ODEs (Eq. 6), (Eq. 9), and (Eq. 12) are different. Hence, they are written separately in the following cases to present the trends that are followed by these quantities under the influence of S, P_r, and S_c. Moreover, the constants k_1, k_2, and k_3 that are used in forming the linear combinations of the Lie symmetry generators (Eq. 3) also affect the temperature and concentration profiles. These are all present in the second and third equations of the systems in Case (3.1)–(3.3).

4.1 Velocity and concentration profiles for Case-I

For system (Eq. 6), we draw the h_θ-curves in Figures 3A–C, for $S = 2.5, h_f = -1.0, k_2 = 1$ and for three different values of $P_r = 0.25, 0.35, 0.45$. The h_θ-curves show a decline for $k_1 < 0$. From these curves, we select a value for $h_\theta = -0.003$ to construct the temperature profiles in Figures 4A–C, which also exhibit a decreasing trend with a decrease in the values of k_1. Likewise, we draw $h_\phi-$ curves in Figures 5A–C for $S = 3.5, h_f = -1.0, k_2 = 1$ and for multiple values of k_1. These figures show a decrease in the $h_\phi-$ curves with a decrease in k_1 and an increase in $P_r = 0.025, 0.035, 0.045$. The concentration profiles behave in a similar manner as $h_\phi-$ curves. Here, we present these profiles for

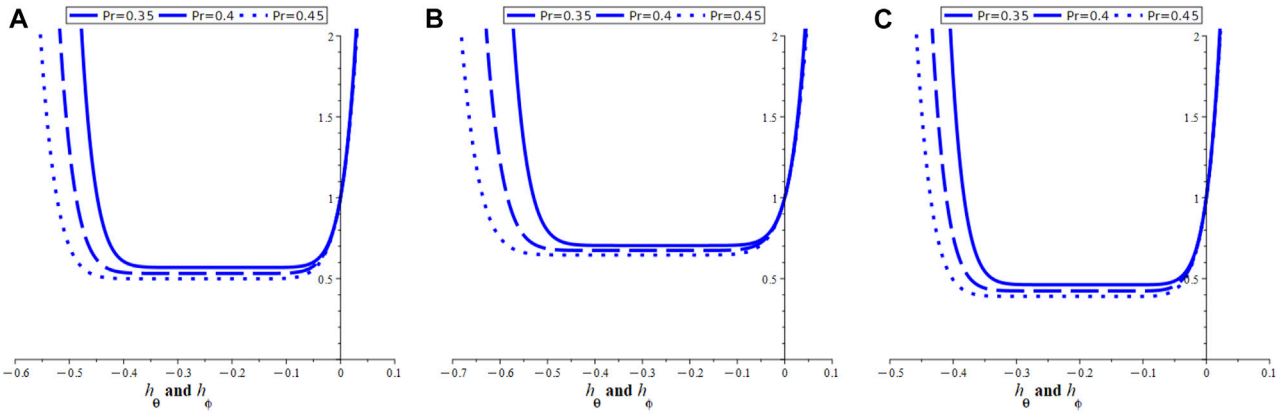

h_θ, h_ϕ-curve ($S = 3.0,\ h_f = -1.0, k_1 = 1, k_2 = 1, k_3 = -0.1$) and a *variation in* Pr

h_θ, h_ϕ-curve ($S = 3.0,\ h_f = -1.0, k_1 = 1, k_2 = 1, k_3 = -0.2$) and a *variation in* Pr

h_θ, h_ϕ-curve ($S = 4.0,\ h_f = -1.0, k_1 = 1, k_2 = 1, k_3 = -0.1$) and a *variation in* Pr

FIGURE 7
Different h-curves.

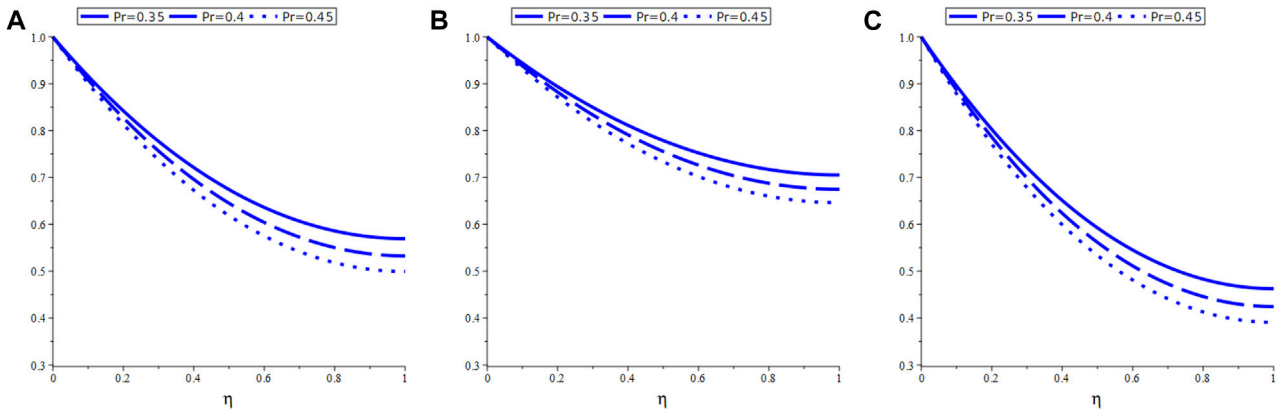

Temperature and concentration profiles ($S = 3.0,\ h_f = -1.0, h_\theta = -0.2, k_1 = 1, k_2 = 1, k_3 = -0.1$) and a *variation in* Pr

Temperature and concentration profiles ($S = 3.0,\ h_f = -1.0, h_\theta = -0.2, k_1 = 1, k_2 = 1, k_3 = -0.2$) and a *variation in* Pr

Temperature and concentration profiles ($S = 4.0,\ h_f = -1.0, h_\theta = -0.2, k_1 = 1, k_2 = 1, k_3 = -0.1$) and a *variation in* Pr

FIGURE 8
Different temperature and concentration profiles.

$S = 3.5, h_f = -1.0, h_\phi = -0.025, k_2 = 1$ and a variation in k_1 and $S_c = 0.025, 0.035, 0.045$. The temperature and concentration profiles follow the same trends as system (Eq. 6) equations for both are the same; however, we are presenting them here separately. In both the mentioned set of figures, we considered different values of the unsteadiness parameter S. It can be observed from these figures that the unsteadiness parameter and concentration are inversely proportional, i.e., $S \propto \frac{1}{T}$.

4.2 Velocity and concentration profiles for Case-II

System (Eq. 9) involves three arbitrary constants k_1, k_2, and k_3, which appear here due to the linear combination of Lie point symmetries we used to construct the corresponding Lie similarity transformation. We draw common curves for h_θ and h_ϕ as h-curves for this system in Figures 6A–C. These curves are

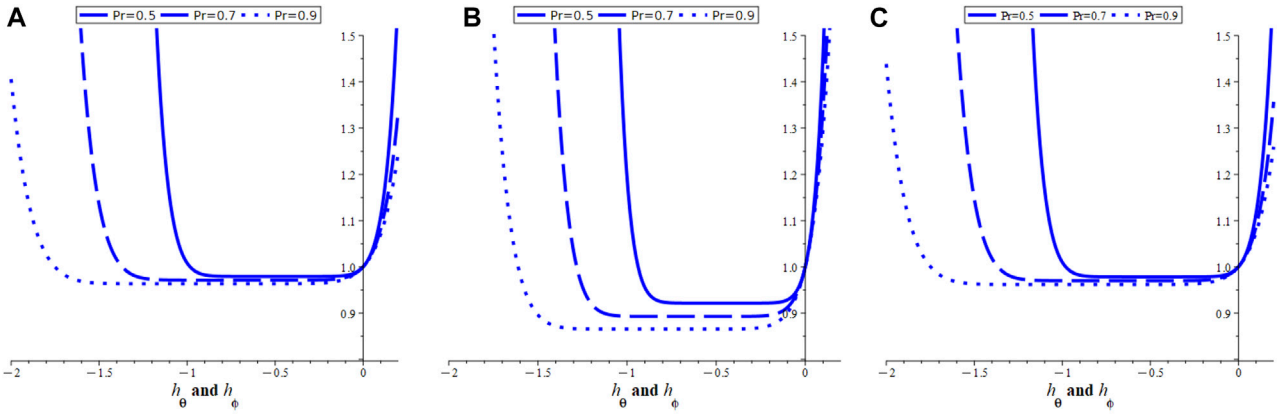

h_θ, h_ϕ-curve ($S = 3.5,\ h_f = -1.0, k_1 = 1, k_2 = 1, k_3 = 1.5$) and a *variation in* Pr

h_θ, h_ϕ-curve ($S = 3.5,\ h_f = -1.0, k_1 = 1, k_2 = 1, k_3 = 1$) and a *variation in* Pr

h_θ, h_ϕ-curve ($S = 4.5,\ h_f = -1.0, k_1 = 1, k_2 = 1, k_3 = 1.5$) and a *variation in* Pr

FIGURE 9
Different h-curves.

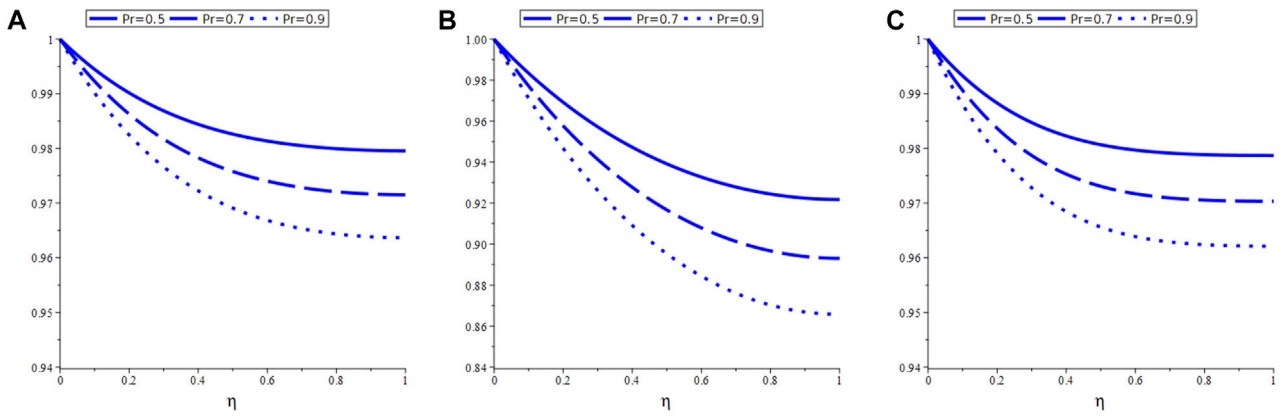

Temperature and concentration profiles ($S = 3.5,\ h_f = -1.0, h_\theta = -0.4, k_1 = 1, k_2 = 1, k_3 = 1.5$) and a *variation in* Pr

Temperature and concentration profiles ($S = 3.5,\ h_f = -1.0, h_\theta = -0.4, k_1 = 1, k_2 = 1, k_3 = 1$) and a *variation in* Pr

Temperature and concentration profiles ($S = 4.5,\ h_f = -1.0, h_\theta = -0.4, k_1 = 1, k_2 = 1, k_3 = 1.5$) and a *variation in* Pr

FIGURE 10
Different temperature and concentration profiles.

drawn for $h_f = -1.0, k_1 = 1, k_2 = 1$ and a variation in the unsteadiness parameter $S = 3.0$ and 4.0, $k_3 = -0.2$ and -0.1, and a range of $P_r = 0.35, 0.40, 0.45$ and $S_c = 0.35, 0.40, 0.45$. These curves and corresponding set of graphs for temperature and concentration show an increase when the unsteadiness parameter decreases from $S = 4.0$ to $S = 3.0$. Similar is the case when k_3 goes from -0.1 to -0.2, as shown in Figures 7A–C and Figures 8A–8C.

4.3 Velocity and concentration profiles for Case-III

System (Eq. 12) involves three arbitrary constants k_1, k_2, and k_3 that are also part of the associated Lie similarity transformation. Figures 9A–C show the h-curves for both h_θ and h_ϕ. These curves are constructed with the same values of h_f, k_1, k_2 as in the previous case and for a different value of the

unsteadiness parameter S. When the unsteadiness parameter decreases from 4.5 to 3.5, the h_θ- and h_ϕ-curves are decreasing. Similar behavior is shown by temperature and concentration profiles in Figures 10A–C; that is, for $1.0 < k_3 < 1.5$, the temperature and concentration are increasing. However, for $P_r = 0.5, 0.7, 0.9$, a decrease in the temperature and concentration is evident from these figures.

5 Conclusion

Lie point symmetries for heat and mass transfer in a thin liquid film on an unsteady stretching sheet are derived. These symmetries are used to construct Lie similarity transformations which map the PDEs representing the heat and flow model to ODE systems. We showed that there exist three different types of such reductions of the considered flow equations. In the Lie similarity transformation derivation, linear combinations of Lie symmetry generators are utilized. These linear combinations are derived with the help of arbitrary constants, which gives rise to multiple solutions of the flow and heat equations. We use the HAM to analytically solve the obtained non-linear ODEs with a 10^{th}-order of approximation. Velocity, temperature, and concentration profiles are drawn with the aid of these 10^{th}-order HAM solutions. These profiles are presented graphically with variations in the unsteadiness parameter S, Prandtl number P_r, Schmidt number S_c, and the arbitrary constants used in the linear combinations of the Lie point symmetries.

Data availability statement

The original contributions presented in the study are included in the article/Supplementary Material, further inquiries can be directed to the corresponding author.

Author contributions

RK designed and analyzed the results; ST prepared the figures and was involved in discussion; SA was responsible for software and coding; IK analyzed and wrote the manuscript and discussed the results; and SE was responsible for software and coding, supervised the research, and acquired funding.

Conflict of interest

The authors declare that the research was conducted in the absence of any commercial or financial relationships that could be construed as a potential conflict of interest.

Publisher's note

References

1. Andersson HI, Aarseth JB, Dandapat BS. Heat transfer in a liquid film on an unsteady stretching surface. *Int J Heat Mass Transfer* (2000) 43(1):69–74. doi:10.1016/s0017-9310(99)00123-4

2. Wang C. Analytic solutions for a liquid film on an unsteady stretching surface. *Heat Mass Transfer* (2006) 42(8):759–66. doi:10.1007/s00231-005-0027-0

3. Dandapat B, Santra B, Vajravelu K. The effects of variable fluid properties and thermocapillarity on the flow of a thin film on an unsteady stretching sheet. *Int J Heat Mass Transfer* (2007) 50(5-6):991–6. doi:10.1016/j.ijheatmasstransfer.2006.08.007

4. Hayat T, Safdar A, Awais M, Mesloub S. Soret and Dufour effects for three-dimensional flow in a viscoelastic fluid over a stretching surface. *Int J Heat Mass Transfer* (2012) 55(7-8):2129–36. doi:10.1016/j.ijheatmasstransfer.2011.12.016

5. Munawar S, Mehmood A, Ali A. Three-dimensional squeezing flow in a rotating channel of lower stretching porous wall. *Comput Math Appl* (2012) 64(6):1575–86. doi:10.1016/j.camwa.2012.01.003

6. Khan JA, Mustafa M, Hayat T, Alsaedi A. Three-dimensional flow of nanofluid over a non-linearly stretching sheet: An application to solar energy. *Int J Heat Mass Transfer* (2015) 86:158–64. doi:10.1016/j.ijheatmasstransfer.2015.02.078

7. Zhang Y, Zhang M, Bai Y. Flow and heat transfer of an Oldroyd-B nanofluid thin film over an unsteady stretching sheet. *J Mol Liquids* (2016) 220:665–70. doi:10.1016/j.molliq.2016.04.108

8. Zhang Y, Zheng L. Analysis of MHD thermosolutal Marangoni convection with the heat generation and a first-order chemical reaction. *Chem Eng Sci* (2012) 69(1):449–55. doi:10.1016/j.ces.2011.10.069

9. Rashidi MM, Ali M, Rostami B, Rostami P, Xie GN. Heat and mass transfer for MHD viscoelastic fluid flow over a vertical stretching sheet with considering Soret and Dufour effects. *Math Probl Eng* (2015) 2015:1–12. doi:10.1155/2015/861065

10. Narayana PS, Babu DH. Numerical study of MHD heat and mass transfer of a Jeffrey fluid over a stretching sheet with chemical reaction and thermal radiation. *J Taiwan Inst Chem Eng* (2016) 59:18–25. doi:10.1016/j.jtice.2015.07.014

11. Shehzad S, Abdullah Z, Abbasi F, Hayat T, Alsaedi A. Magnetic field effect in three-dimensional flow of an Oldroyd-B nanofluid over a radiative surface. *J Magnetism Magn Mater* (2016) 399:97–108. doi:10.1016/j.jmmm.2015.09.001

12. Shehzad S, Abdullah Z, Alsaedi A, Abbasi F, Hayat T. Thermally radiative three-dimensional flow of Jeffrey nanofluid with internal heat generation and magnetic field. *J Magnetism Magn Mater* (2016) 397:108–14. doi:10.1016/j.jmmm.2015.07.057

13. Ahmad S, Yousaf M, Khan A, Zaman G. Magnetohydrodynamic fluid flow and heat transfer over a shrinking sheet under the influence of thermal slip. *Heliyon* (2018) 4(10):e00828. doi:10.1016/j.heliyon.2018.e00828

14. Alarifi IM, Abokhalil A, Osman M, Lund L, Ayed M, Belmabrouk H, et al. MHD flow and heat transfer over vertical stretching sheet with heat sink or source effect. *Symmetry* (2019) 11(3):297. doi:10.3390/sym11030297

15. Mandal B, Bhattacharyya K, Banerjee A, Kumar Verma A, Kumar Gautam A. MHD mixed convection on an inclined stretching plate in Darcy porous medium with Soret effect and variable surface conditions. *Nonlinear Eng* (2020) 9(1):457–69. doi:10.1515/nleng-2020-0029

16. Dessie H, Fissha D. MHD mixed convective flow of Maxwell nanofluid past a porous vertical stretching sheet in presence of chemical reaction. *Appl Appl Math Int J* (2020) 15(1):31.

17. Tufail MN. Group theoretical analysis of non-Newtonian fluid flow, heat and mass transfer over a stretching surface in the presence of thermal radiation. *Appl Fluid Mech* (2016) 9:1515. doi:10.18869/acadpub.jafm.68.228.24069

18. Metri PG, Guariglia E, Silvestrov S. Lie group analysis for MHD boundary layer flow and heat transfer over stretching sheet in presence of viscous dissipation and uniform heat source/sink. *AIP Conf Proc* (2017) 1798:020096. doi:10.1063/1.4972688

19. Rajput GR, Patil V, Jadhav B. MHD mixed flow of unsteady convection with radiation over a vertical porous plate: Lie group symmetry analysis. *Appl Comput Mech* (2017) 11(2):1–12. doi:10.24132/acm.2017.380

20. Pal D, Roy N. Lie group transformation on MHD double-diffusion convection of a Casson nanofluid over a vertical stretching/shrinking surface with thermal radiation and chemical reaction. *Int J Appl Comput Math* (2018) 4(1):13–23. doi:10.1007/s40819-017-0449-7

21. Megahed AM, Abdel-Rahman RG. Lie group analysis of heat flux effect on MHD second slip flow for a slightly rarefied gas past a stretching sheet with heat generation. *Tech Sci* (2019) 22(1):45–59. doi:10.31648/ts.4347

22. Nazim Tufail M, Zaib F. Symmetry analysis of MHD Casson fluid flow for heat and mass transfer near a stagnation point over a linearly stretching sheet with variable viscosity and thermal conductivity. *Heat Transfer* (2021) 50(6):5418–38. doi:10.1002/htj.22131

23. Rehman KU, Shatanawi W, Abodayeh K. Thermophysical aspects of magnetized Williamson fluid flow subject to both porous and non-porous surfaces: A lie symmetry analysis. *Case Stud Therm Eng* (2021) 28:101688. doi:10.1016/j.csite.2021.101688

24. Saleem M, Tufail MN, Chaudhry QA. Unsteady MHD Casson fluid flow with heat transfer passed over a porous rigid plate with stagnation point flow: Two-parameter Lie scaling approach. *Pramana* (2021) 95(1):28–9. doi:10.1007/s12043-020-02054-0

25. Zeb S, Khan S, Ullah Z, Yousaf M, Khan I, Alshammari N, et al. Lie group analysis of double diffusive MHD tangent hyperbolic fluid flow over a stretching sheet. *Math Probl Eng* (2022) 2022:1–14. doi:10.1155/2022/9919073

26. Rehman KU, Shatanawi W, Abodayeh K. A group theoretic analysis on heat transfer in MHD thermally slip Carreau fluid subject to multiple flow regimes (MFRs). *Case Stud Therm Eng* (2022) 30:101787. doi:10.1016/j.csite.2022.101787

27. Safdar M, Ijaz Khan M, Taj S, Malik M, Shi QH. Construction of similarity transformations and analytic solutions for a liquid film on an unsteady stretching sheet using lie point symmetries. *Chaos, Solitons and Fractals* (2021) 150:111115. doi:10.1016/j.chaos.2021.111115

28. Soh CW, Mahomed F. Linearization criteria for a system of second-order ordinary differential equations. *J Int J Non-Linear Mech* (2001) 36(4):671–7. doi:10.1016/s0020-7462(00)00032-9

29. Maharaj A, Leach P. The method of reduction of order and linearization of the two-dimensional Ermakov system. *J Math Methods Appl Sci* (2007) 30(16):2125–45. doi:10.1002/mma.919

30. Ayub M, Khan M, Mahomed F. Algebraic linearization criteria for systems of ordinary differential equations. *J Nonlinear Dyn* (2012) 67(3):2053–62. doi:10.1007/s11071-011-0128-x

31. Dutt HM, Safdar M, Qadir A. Linearization criteria for two-dimensional systems of third-order ordinary differential equations by complex approach. *J Arabian J Math* (2019) 8(3):163–70. doi:10.1007/s40065-019-0238-8

32. Song L-M, Yang ZJ, Li XL, Zhang SM. Coherent superposition propagation of Laguerre–Gaussian and Hermite–Gaussian solitons. *J Appl Math Lett* (2020) 102:106114. doi:10.1016/j.aml.2019.106114

33. Shen S, Yang Z, Li X, Zhang S. Periodic propagation of complex-valued hyperbolic-cosine-Gaussian solitons and breathers with complicated light field structure in strongly nonlocal nonlinear media. *J Commun Nonlinear Sci Numer Simulation* (2021) 103:106005. doi:10.1016/j.cnsns.2021.106005

34. Shen S, Yang ZJ, Pang ZG, Ge YR. The complex-valued astigmatic cosine-Gaussian soliton solution of the nonlocal nonlinear Schrödinger equation and its transmission characteristics. *J Appl Math Lett* (2022) 125:107755. doi:10.1016/j.aml.2021.107755

35. Stephani H. *Differential equations: Their solution using symmetries*. Cambridge, United Kingdom: Cambridge University Press (1989).

36. Ibragimov NH. *CRC handbook of Lie group analysis of differential equations*. Florida, United States: CRC Press (1995).

37. Zhang Y, Zhang M, Qi S. Heat and mass transfer in a thin liquid film over an unsteady stretching surface in the presence of thermosolutal capillarity and variable magnetic field. *Math Probl Eng* (2016) 2016:8521580. doi:10.1155/2016/8521580

38. Wu Y, Zhang X, Zhang X. Simplified analysis of heat and mass transfer model in droplet evaporation process. *Appl Therm Eng* (2016) 99:938–43. doi:10.1016/j.applthermaleng.2016.01.020

39. Safdar M, Khan MI, Khan RA, Taj S, Abbas F, Elattar S, et al. Analytic solutions for the MHD flow and heat transfer in a thin liquid film over an unsteady stretching surface with Lie symmetry and homotopy analysis method. *Waves in Random Complex Media* (2022) 2022:1–19. doi:10.1080/17455030.2022.2073402

frontiers | Frontiers in Physics

TYPE Original Research
PUBLISHED 01 March 2023
DOI 10.3389/fphy.2023.1144175

OPEN ACCESS

EDITED BY
Gangwei Wang,
Hebei University of Economics and Business, China

REVIEWED BY
Abdul Hamid Kara,
University of the Witwatersrand, South Africa
Xiangpeng Xin,
Liaocheng University, China

*CORRESPONDENCE
Muhammad Khalid,
mkhalid_khan@yahoo.com

SPECIALTY SECTION
This article was submitted to Mathematical Physics, a section of the journal Frontiers in Physics

RECEIVED 13 January 2023
ACCEPTED 09 February 2023
PUBLISHED 01 March 2023

CITATION
Almas, Ata-ur-Rahman, Khalid M and Eldin SM (2023), Oblique propagation of arbitrary amplitude ion acoustic solitary waves in anisotropic electron positron ion plasma.
Front. Phys. 11:1144175.
doi: 10.3389/fphy.2023.1144175

Oblique propagation of arbitrary amplitude ion acoustic solitary waves in anisotropic electron positron ion plasma

Almas[1,2], Ata-ur-Rahman[1], Muhammad Khalid[3]* and Sayed M. Eldin[4]

[1]Department of Physics, Islamia College Peshawar, Peshawar, Pakistan, [2]Department of Physics, Abdul Wali Khan University Mardan, Mardan, Pakistan, [3]Department of Physics, Government Post Graduate College Mardan, Mardan, Pakistan, [4]Center of Research, Faculty of Engineering, Future University in Egypt, New Cairo, Egypt

The oblique propagation of arbitrary ion acoustic solitary waves (IASWs) in magnetized electron-positron-ion plasmas is investigated by employing Sagdeev pseudopotential approach. Ions are assumed to be adiabatic having anisotropic thermal pressure. Electrons and positrons are considered to be isothermal, following Maxwellian distribution. In terms of electrostatic potential, Sagdeev potential function is obtained and analyzed numerically in the context of relevant plasma configuration parameters. The existence region of solitary pulses is defined accurately. It is investigated how several plasma configuration parameters, such as the positron concentration, parallel, and perpendicular ion pressure affect soliton characteristics.

KEYWORDS

solitary waves, positrons, Sagdeev approach, pressure anisotropy, magnetized plasma

1 Introduction

To understand the fundamental processes in the Universe, most of the researchers have taken keen interest in the study of electron-positron-ion ($e-p-i$) plasma. Such plasmas are thought to have most probable appearance in the early Universe [1]. Other regions of space where such plasma is assumed to be found are atmospheres of Sun, neutron stars, active galactic nuclei and pulsar magnetosphere [2–4]. The existence of ions in astrophysical plasmas has some interior source, i.e., the processes of accretion, evaporation or seismic processes on the surface of stars might be a source of ions [5]. Moreover in matter, intense short laser pulse propagation can generate $e-p-i$ plasma [6]. In laboratory experiments, the production of such three component plasma is possible when positron were made to probe particle transport in tokamaks, in which case the two-component electron-ion ($e-i$) plasma becomes a three-component $e-p-i$ plasma [7, 8]. Clearly the wave motion behavior should be totally different in $e-p-i$ plasma compared to the two component electron-positron ($e-p$) and $e-i$ plasmas. The existence of ions is necessary for various low-frequency wave propagation which is other wise not possible in $e-p$ plasma [9].

The ion-acoustic (IA) waves are the low frequency waves which have been investigated in both linear and non-linear limits in $e-i$ plasma [10–13]. Several researchers have theoretically studied the linear as well as the non-linear wave phenomena in both magnetized and unmagnetized $e-p-i$ plasmas [14–18]. The IA solitary waves (IASWs) were first investigated in unmagnetized $e-p-i$ plasmas by Popel *et al.* [14]

by considering one dimensional perturbations. The solution of non-linear equations was obtained in the form of a solitary pulse or soliton. It was shown that positron concentration reduces the maximum amplitude of the solitons. The study of IASWs in magnetized $e - p - i$ plasmas was made by Mushtaq *et al.* [18]. In their research work, they found that the increase values of positron concentration leads to an increase in the amplitude of the solitary structure which is the opposite behavior to the previous study of these waves in an unmagnetized plasma [14].

Various techniques, such as the reductive perturbation and the Sagdeev pseudopotential are used to examine non-linear waves in plasma. Reductive perturbation technique (RPT) is applied to study small amplitude non-linear waves in unmagnetized/magnetized plasmas in the form of Korteweg-de Vries (KdV) equation, modified KdV equation and Zakharov-Kuznetsov (ZK) equation etc. For the very first time SWs in plasmas were studied by Washimi and Taniuti [19] through RPT and derived the KdV equation for IASWs [20]. However with this technique large amplitude excitations can not be studied. To overcome the limitation of small amplitude approximations, Sagdeev pseudo-potential method [21], usually called the mechanical-motion analog, provides an exact approach to the problem of finding arbitrary amplitude SWs. This method provides non-linear solutions for a plasma model which can be considered as candidates for SWs. The method basically modifies the Poisson's equation which results into general energy equation of the form

$$(d\phi/dx)^2 + 2G(\phi) = 0$$

The first term of the energy equation corresponds to kinetic energy, while the second term corresponds to potential energy. The equation basically represents a moving classical particle of unit mass in one dimensional potential $G(\phi)$ at time x. This method has been adopted for studying wave phenomena in various plasma environments like dusty plasmas, $e - p - i$ plasmas and magnetospheric plasmas [22, 23].

The presence of an external magnetic field causes the collisionless plasma to behave in an anisotropic manner. As a result, according to the Chew-Goldberger-Low (CGL) theory, pressure differs in directions that are parallel and perpendicular to the magnetic field [24]. Therefore two equations of states are necessary to evaluate ion pressure i.e., the parallel ion pressure $p_{\parallel}$ and perpendicular ion pressure $p_{\perp}$ relative to the external magnetic field. Magnetic compression and expansion generated by plasma convection in some space regions might be one of the reason of this anisotropic behavior of plasma [25]. The CGL theory can be applied to such anisotropic plasma in the case when, the coupling between degree of freedom is ignorable [26]. While in the isotropic plasma the strong coupling between the degree of freedom gives rise to a simplified description due to wave-particle interaction, and hence ionic pressure can be evaluated using single equation of state [25].

IASWs in magnetized $e - i$ plasma using Sagdeev pseudopotential method have been investigated by Chatterjee *et al.* [27]. They used quasi neutrality condition to discuss the existence conditions, shape and speed of SWs. The same approach was used by Sultana *et al.* [28] to analyze the oblique propagation of IASWs in a magnetized plasma in the presence of excess superthermal electrons. Oblique IA excitations in a magnetoplasma having κ-deformed Kaniadakis distributed electrons have also been discussed using Sagdeev's potential approach [29]. The same technique has also been used by various researchers to discuss the SWs in $e - p - i$ magnetoplasma [15, 30, 31].

The role of ion pressure anisotropy on the propagation characteristics of IA solitary structures in magnetized plasmas can not be ignored. Choi *et al.* used the Sagdeev potential approach and investigated the effect of anisotropy of ions on dust ion acoustic solitary waves (DIASWs) and double layer structures [32]. Adnan et al. [33] have examined the influence of pressure anisotropy on IASWs in superthermal magnetized $e - p - i$ plasma by applying RPT. It has been shown that the solitary structures are affected by superthermality of electrons and positrons, pressure anisotropy of ions as well as the positron concentration. Similarly pressure anisotropy effect on DIASWs in a nonthermal plasma in Ref. [34] have also been investigated. The oblique propagation of electrostatic SWs in non-Maxwellian $e - i$ plasma in the presences of ion pressure anisotropy with Sagdeev approach are studied in Ref. [35]. Khalid et al. [36] used Maxwellian electrons to investigate the modulation of multidimensional waves in anisotropic $e - i$ plasma. Similarly, Alyousef et al. have also used Sagdeev approach to study the IASWs in magnetoplasma [37]. In [38] Sagdeev approach is utilized and IASWs in magnetized e-i plasma in the presences of pressure anisotropy is discussed. The results have revealed that the model supports only positive potential non-linear structures. Furthermore, the effect of relevant plasma parameters on the characteristics of IA solitary structures is evaluated. However, to the best of authors knowledge, the non-linear IASWs in the presence of pressure anisotropy in magnetized $e - p - i$ plasma has not been explored, so for. We aim to considered anisotropic $e - p - i$ plasma with Maxwellian electrons and positrons to study these waves.

The following is a breakdown of how this paper is structured. The model equations are presented in Section 2. The linear wave analysis is covered in Section 3. The Sagdeev pseudopotential technique is used to analyze large-amplitude electrostatic excitations in Section 4. The soliton existence domain for propagation of IASWs is discussed in Section 5. In Section 6, a parametric investigation is carried out to examine the effect of various relevant parameters on the solitary wave characteristics. The summary of the present study is given in Section 7.

2 Basic equations

The goal of the present study is to propose a model for the propagation of IASWs in a magnetized plasma made up of Maxwellian electrons (n_e) and positrons (n_p) as well as adiabatically heated ions (n_i). The ions are considered to be inertial exhibiting pressure anisotropy relative to the external magnetic field. The external magnetic field is assumed to be uniform and is taken along x-axis, i.e., $B = B_0\hat{x}$. In the presence of ion pressure anisotropy, the ion fluid equations are,

$$\partial_t n_i + \nabla.(n_i \mathbf{u}_i) = 0, \tag{1}$$

$$\partial_t \mathbf{u}_i + (\mathbf{u}_i.\nabla)\mathbf{u}_i = -\frac{Ze}{m_i}\nabla\phi + \frac{Ze}{m_i c}(\mathbf{u}_i \times B_0\hat{x}) - \frac{1}{m_i n_i}\nabla.\tilde{\mathbf{P}}_i, \quad (2)$$

where $\mathbf{u}_i$, ϕ, m_i, e and Z stand for ion fluid velocity, electrostatic potential, ion mass, magnitude of electron charge and ionic charge state (for simplicity $Z = 1$ is chosen), respectively. Owing to the plasma anisotropy because of a strong external magnetic field B_0, the plasma behaves differently in the parallel and perpendicular direction (s). Thereby the pressure tensor $(\tilde{\mathbf{P}}_i)$ is divided into two components, i.e., the parallel $(p_{\parallel i})$ and perpendicular $(p_{\perp i})$ pressure components [24, 25], thus

$$\tilde{\mathbf{P}}_i = p_{\perp i}\hat{I} + (p_{\parallel i} - p_{\perp i})\hat{\mathbf{x}}\,\hat{\mathbf{x}}, \quad (3)$$

where $\hat{I}$ represents unit tensor and $\hat{x}$ shows the unit vector along B_0. The expressions for $p_{\parallel i}$ and $p_{\perp i}$ are

$$p_{\parallel i} = p_{\parallel i0}\left(\frac{n_i}{n_{i_0}}\right)^3 \text{ and } p_{\perp i} = p_{\perp i0}\left(\frac{n_i}{n_{i0}}\right). \quad (4)$$

In Eq. 4 $p_{\parallel i0} = n_{i0}k_B T_{i\parallel}$ and $p_{\perp i0} = n_{i0}k_B T_{i\perp}$ which are, respectively, the equilibrium values of parallel and perpendicular pressure functions, where n_{i0} is the unperturbed ion density. In case of ion pressure isotropy, we have $p_{\parallel i} = p_{\perp i}$ and $\nabla.\tilde{\mathbf{P}}_i = \nabla p_i$.

The electrons and positrons are assumed to follow the Boltzmann distributions under the electrostatic potential perturbation, and their number densities are given as

$$n_e = n_{e0}\exp\left(\frac{e\phi}{T_e}\right), \quad (5)$$

and

$$n_p = n_{p0}\exp\left(\frac{-e\phi}{T_p}\right). \quad (6)$$

The system of evolution equations is closed *via* Poisson's equation

$$\nabla^2\phi = 4\pi e\left(n_e - n_p - n_i\right), \quad (7)$$

where T_e and T_p are, respectively, the electron and positron temperatures, while n_{e0} (n_{p0}) is the unperturbed electron (positron) number density. We consider $n_{e0} = n_{i0} + n_{p0}$ at equilibrium i.e., the quasineutrality condition does hold.

2.1 Evolution equations

We have considered two dimensional perturbation in the xy-plane, by setting $\partial z = 0$. Thus, the above system of equations can be written as follows;

$$\partial_t n_i + \partial_x(n_i u_{ix}) + \partial_y\left(n_i u_{iy}\right) = 0, \quad (8)$$

$$\partial_t u_{ix} + \left(u_{ix}\partial_x + u_{iy}\partial_y\right)u_{ix} = -\frac{e}{m_i}\partial_x\phi - \frac{3p_{\parallel i0}}{m_i n_{io}^3}n_i\partial_x n_i, \quad (9)$$

$$\partial_t u_{iy} + \left(u_{ix}\partial + u_{iy}\partial_y\right)u_{iy} = -\frac{e}{m_i}\partial_y\phi + \mathbf{\Omega}_i u_{iz} - \frac{p_{\perp i0}}{m_i n_0 n_i}\partial_y n_i, \quad (10)$$

$$\partial_t u_{iz} + \left(u_{ix}\partial_x + u_{iy}\partial_y\right)u_{iz} = -\mathbf{\Omega}_i u_{iy}, \quad (11)$$

$$\partial_x^2\phi + \partial_y^2\phi = 4\pi e\left(n_e - n_p - n_i\right). \quad (12)$$

Here $\mathbf{\Omega}_i = \frac{eB_0}{m_i c}$ is ion gyro-frequency, while u_{ix}, u_{iy}, and u_{iz} denote the fluid velocity components.

2.2 Scaled evolution equations

To normalize the above system of equations, we normalize the number density variables n_s $(s = e, i, p)$ by the unperturbed ion density n_{i0}, the electrostatic potential ϕ by $T_e\varphi/e$, the ion fluid velocity components by the ion acoustic speed $(T_e/m_i)^{\frac{1}{2}}$. The time and space variables are scaled by the inverse ion plasma frequency $\omega_{pi}^{-1} = (4\pi n_{i0}e^2/m_i)^{\frac{1}{2}}$ and electron Debye radius $\lambda_{De} = (T_e/4\pi n_{e0}e^2)^{\frac{1}{2}}$, respectively. The normalized equations obtained by applying the mentioned normalization to Eqs 5, 6 and to Eqs 8–12 are:

$$\partial_t n_i + \partial_x(n_i u_{ix}) + \partial_y\left(n_i u_{iy}\right) = 0, \quad (13)$$

$$\partial_t u_{ix} + \left(u_{ix}\partial_x + u_{iy}\partial_y\right)u_{ix} = -\partial_x\varphi - p_\parallel n_i\partial_x n_i, \quad (14)$$

$$\partial_t u_{iy} + \left(u_{ix}\partial_x + u_{iy}\partial_y\right)u_{iy} = -\partial_y\varphi + \Omega u_{iz} - \frac{p_\perp}{n_i}\partial_y n_i, \quad (15)$$

$$\partial_t u_{iz} + \left(u_{ix}\partial_x + u_{iy}\partial_y\right)u_{iz} = -\Omega u_{iy}, \quad (16)$$

$$n_e = \exp(\varphi), \quad (17)$$

$$n_p = \exp(-\sigma\varphi), \quad (18)$$

$$\partial_x^2\varphi + \partial_y^2\varphi = \eta n_e - \gamma n_p - n_i. \quad (19)$$

Here $p_\parallel = \frac{3p_{\parallel i0}}{n_{io}T_e}$ and $p_\perp = \frac{p_{\perp i0}}{n_{io}T_e}$ represent the normalized parallel and perpendicular pressures, respectively, and are normalized by the thermal pressure in the relevant directions, with $\frac{\mathbf{\Omega}_i}{\omega_{pi}} = \Omega$ being the dimensionless parameter. Furthermore, $\sigma = \frac{T_e}{T_p}$, $\eta = \frac{n_{e0}}{n_{i0}}$, and $\gamma = \frac{n_{p0}}{n_{i0}}$ signify the electron to positron temperature ratio, unperturbed electron-to-ion density ratio and positron-to-ion density ratio, respectively. The over all charge neutrality in normalized form is $\eta - \gamma = 1$.

3 Linear wave analysis

To derive the dispersion relation (DR), we employ Poisson's Eq. 19 instead of plasma approximation, although plasma approximation will be used in Section 5 for non-linear analysis. The DR while using Eqs 13–19 is obtained as

$$\omega^4 - \left(\frac{k^2}{(k^2+\eta+\gamma\sigma)} + k_x^2 p_\parallel + k_y^2 p_\perp + \Omega^2\right)$$
$$\omega^2 + \left(p_\parallel + \frac{1}{(k^2+\eta+\gamma\sigma)}\right)\Omega^2 k_x^2 = 0, \quad (20)$$

where $k_x = k\cos\theta$ and $k_y = k\sin\theta$ are the wave numbers in the parallel and perpendicular directions to the magnetic field, re spectively, and $k_x^2 + k_y^2 = k^2$. It can be noticed from Eq. 20 that DR depends on the ion pressure anisotropy. Also, the magnetic field dependence is visible through the frequency ratio Ω. By solving Eq. 20, we get

$$\omega_\pm^2 = \frac{1}{2}\left[\left(\frac{k^2}{(k^2+\eta+\gamma\sigma)} + k_x^2 p_\parallel + k_y^2 p_\perp + \Omega^2\right)\right.$$
$$\left. \pm\sqrt{\left(\frac{k^2}{(k^2+\eta+\gamma\sigma)} + k_x^2 p_\parallel + k_y^2 p_\perp + \Omega^2\right)^2 - 4\left(p_\parallel + \frac{1}{(k^2+\eta+\gamma\sigma)}\right)\Omega^2 k_x^2}\right]. \quad (21)$$

Equation 21 gives two modes i.e., ω_- and ω_+, representing slow and fast electrostatic modes, respectively. An acoustic mode is

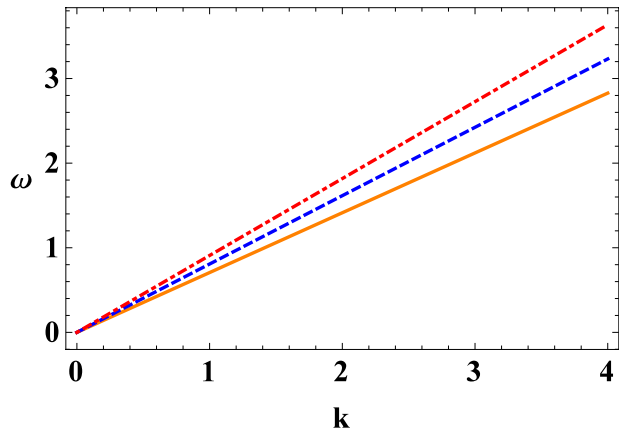

FIGURE 1
Plot of ω vs. k defined in Eq. 22 for different values of α i.e., α = 0.70 (solid curve), 0.80 (dashed curve) and 0.90 (dot-dashed curve) with $p_{\parallel}$ = 0.2, γ = 0.2 and σ = 0.1.

obtained by setting, $k_y \to 0$ and $k_x = k$ and considering $k \ll 1$. Thus, the phase speed parallel to the magnetic field is calculated as

$$\frac{\omega_-}{k} = \cos\theta\sqrt{\frac{1}{(\eta+\gamma\sigma)} + p_{\parallel}}. \tag{22}$$

This is called phase speed of acoustic mode which is independent of the magnetic field Ω and perpendicular pressure $p_{\perp}$. By inserting $\gamma = 0$ (i.e., in the absence of positron) and taking $p_{\parallel} = 0$, Eq. 22 reduces to the result of Ref. [29]. In Figure 1 Eq. 22 has been plotted for various values of obliqueness of the propagation direction, manifested *via* α (= $\cos\theta$). Increasing obliqueness (lowering α) results in a decrease in wave frequency and, consequently, in the phase speed of the magnetized IAW.

4 Arbitrary amplitude solitary wave analysis

We are now interested to investigate the existence of large amplitude solitary waves in Maxwellian plasmas with the inclusion of ion pressure anisotropy. The fluid variables in the evolution equations are considered to be transformed into a single variable *via* the transformation

$$\xi = \alpha x + \beta y - Mt, \tag{23}$$

to a moving frame (here M is the Mach number indicating the normalized pulse propagation velocity) where the solitary pulses are stationary. The parameters $\alpha = \frac{k_x}{k} = \cos\theta$ and $\beta = \frac{k_y}{k} = \sin\theta$, respectively, imply the direction cosines along $x-$ axis and y-axis subject to the condition that $\alpha^2 + \beta^2 = 1$. By utilizing Eq. 23 in Eqs 13–18 we obtain a set of dimensionless non-linear differential equations in the co-moving co-ordinate (ξ). The transformed equations can be expressed as,

$$-Md_\xi n_i + \alpha d_\xi(n_i u_{ix}) + \beta d_\xi\left(n_i u_{iy}\right) = 0, \tag{24}$$

$$\left(-M + \alpha u_{ix} + \beta u_{iy}\right)d_\xi u_{ix} + \alpha d_\xi\varphi + \alpha p_{\parallel} n_i d_\xi n_i = 0, \tag{25}$$

$$\left(-M + \alpha u_{ix} + \beta u_{iy}\right)d_\xi u_{iy} + \beta d_\xi\varphi - \Omega u_{iz} + \beta p_{\perp}\frac{1}{n_i}d_\xi n_i = 0, \tag{26}$$

$$\left(-M + \alpha u_{ix} + \beta u_{iy}\right)d_\xi u_{iz} + \Omega u_{iy} = 0. \tag{27}$$

By integrating Eqs 24–27 and implementing the appropriate boundary conditions, i.e., $n_i \to \eta - \gamma = 1$, $u_{ix,iy} \to 0$ and $\varphi \to 0$ at $\xi \to \pm\infty$, we obtain

$$\alpha u_{ix} + \beta u_{iy} = \frac{M(n_i - 1)}{n_i}, \tag{28}$$

$$u_{ix} = \frac{\alpha}{M}\left\{-\left(\eta + \frac{\gamma}{\sigma}\right) + \int n_i d\varphi + \frac{1}{3}p_{\parallel}\left(n_i^3 - 1\right)\right\}, \tag{29}$$

$$u_{iy} = \frac{M}{\beta}\frac{(n_i - 1)}{n_i} - \frac{\alpha^2}{M\beta}\left\{-\left(\eta + \frac{\gamma}{\sigma}\right) + \int n_i d\varphi + \frac{1}{3}p_{\parallel}\left(n_i^3 - 1\right)\right\}. \tag{30}$$

The combination of Eq. 28 with Eqs 26, 27 results in

$$-\frac{M}{n_i}d_\xi u_{iy} + \beta d_\xi\varphi - \Omega u_{iz} + \beta p_{\perp}\frac{1}{n_i}d_\xi n_i = 0, \tag{31}$$

$$-\frac{M}{n_i}d_\xi u_{iz} + \Omega u_{iy} = 0. \tag{32}$$

Substituting the value of u_{iy} from Eq. 30 into Eq. 32 one obtains

$$d_\xi u_{iz} = \frac{n_i\Omega}{\beta}\left(1 - \frac{1}{n_i}\right) - \frac{\alpha^2\Omega}{M^2\beta}\left\{-n_i\left(\eta + \frac{\gamma}{\sigma}\right) + n_i\int n_i d\varphi + \frac{1}{3}p_{\parallel}n_i\left(n_i^3 - 1\right)\right\}, \tag{33}$$

Differentiating Eq. 31 with respect to ξ and using Eqs 30 and 33 and after simplification, we have

$$d_\xi\left[d_\xi\left(\frac{M^2}{2}n_i^{-2} + \frac{\alpha^2 p_{\parallel}}{2}n_i^2 + \beta^2 p_{\perp}\log[n_i] + \varphi\right)\right] = \Omega^2\left[n_i\left(1 + \frac{\alpha^2}{M^2}\left(\eta + \frac{\gamma}{\sigma}\right)\right) - 1 - \frac{\alpha^2}{M^2}n_i\int n_i d\varphi - \frac{\alpha^2}{3M^2}p_{\parallel}n_i\left(n_i^3 - 1\right)\right] \tag{34}$$

Multiplying Eq. 34 by $d_\xi\left(\frac{M^2}{2}n_i^{-2} + \frac{\alpha^2 p_{\parallel}}{2}n_i^2 + \beta^2 p_{\perp}\log[n_i] + \varphi\right)$ and integrating once under the boundary conditions $\varphi \to 0$ and $d_\xi\varphi \to 0$ at $\xi \to \pm\infty$, we obtain the energy integral equation for the electrostatic potential φ, in the form

$$\frac{1}{2}(d_\xi\varphi)^2 + \psi(\varphi) = 0, \tag{35}$$

where $\psi(\varphi)$ is the Sagdeev pseudopotential, which is written as

$$\begin{aligned}\psi(\varphi) = \Omega^2\Bigg[&\varphi - \left\{1 + \frac{\alpha^2}{M^2}\left(\eta + \frac{\gamma}{\sigma}\right) + \frac{\alpha^2 p_{\parallel}}{3M^2}\right\}\delta_1(\varphi) \\ &+ \frac{\alpha^2}{2M^2}\delta_2(\varphi) - \left\{\frac{\alpha^4 p_{\parallel}}{3M^2} - \frac{\alpha^2 p_{\parallel}}{3M^2}\right\}\delta_3(\varphi) \\ &- \left\{M^2 + \alpha^2\left(\eta + \frac{\gamma}{\sigma}\right) + \frac{\alpha^2 p_{\parallel}}{3}\right\}\delta_4(\varphi) + \frac{M^2}{2}\delta_5(\varphi) - \alpha^2\varphi + \alpha^2\delta_6(\varphi) \\ &+ \frac{\alpha^2 p_{\parallel}}{3}\delta_7(\varphi) - \left\{\frac{\alpha^2 p_{\parallel}}{3} + \frac{\alpha^4 p_{\parallel}}{3M^2}\left(\eta + \frac{\gamma}{\sigma}\right) + \frac{\alpha^4 p_{\parallel}^2}{9M^2}\right\}\delta_8(\varphi) + \frac{\alpha^4 p_{\parallel}}{3M^2}\delta_9(\varphi) \\ &+ \frac{\alpha^4 p_{\parallel}^2}{18M^2}\delta_{10}(\varphi) - \left\{\beta^2 p_{\perp} + \frac{\alpha^2\beta^2 p_{\perp}}{M^2}\left(\eta + \frac{\gamma}{\sigma}\right) + \frac{\alpha^2\beta^2 p_{\perp}p_{\parallel}}{3M^2}\right\}\delta_{11}(\varphi) \\ &+ \beta^2 p_{\perp}\delta_{12}(\varphi) + \frac{\alpha^2\beta^2 p_{\perp}}{M^2}\delta_{13}(\varphi) - \frac{\alpha^2\beta^2 p_{\perp}}{M^2}\delta_{14}(\varphi) + \frac{\alpha^2\beta^2 p_{\perp}p_{\parallel}}{12M^2}\delta_{15}(\varphi)\Bigg] \\ &\times\left[1 - M^2\delta_{16}(\varphi) + \alpha^2 p_{\parallel}\delta_{17}(\varphi) + \beta^2 p_{\perp}\delta_{18}(\varphi)\right]^{-2}.\end{aligned} \tag{36}$$

Equation 35 is a well known pseudoenergy conservation equation of an oscillating particle of unit mass, with velocity $d_\xi\varphi$ and position φ in a potential well $\psi(\varphi)$. In Eq. 36 the potential functions $\delta_1(\varphi)$, $\delta_2(\varphi)\cdots\delta_{18}(\varphi)$ are given in the Appendix.

5 Soliton existence conditions

Solitary wave solutions are allowed by Eq. 35, if the following constraints are fulfilled [21]:

1. $\psi|_{\varphi=0} = d_\varphi\psi|_{\varphi=0} = d_\varphi\psi|_{\varphi=\varphi_m} = 0$,
2. $\psi(\varphi) < 0$ at $0 < \varphi < \varphi_m$,
3. $d_\varphi^2\psi|_{\varphi=0} < 0$

where φ_m represents the maximum amplitude of SWs. The origin at $\varphi = 0$ defines the equilibrium state, which should represent a local maximum of the Sagdeev pseudopotential $\psi(\varphi)$. From Eq. 36, it is clear that both $\psi|_{\varphi=0} = 0$ and $d_\varphi\psi|_{\varphi=0} = 0$ holds at equilibrium. We have to investigate $d_\varphi^2\psi|_{\varphi=0} < 0$, from which one can specify a range of velocity values in which SWs may occur. Using the procedure explained in Refs. [28, 39], the third condition takes the form

$$d_\varphi^2\psi|_{\varphi=0} = \Omega^2\frac{M^2 - M_1^2}{M^2\left(M^2 - M_2^2\right)} < 0, \tag{37}$$

with

$$M_1 = \mid \alpha \mid \sqrt{\frac{1}{\eta + \gamma\sigma} + p_\parallel} \leq 1, \tag{38}$$

and

$$M_2 = \sqrt{\frac{1}{\eta + \gamma\sigma} + \alpha^2 p_\parallel + (1 - \alpha^2)p_\perp}, \tag{39}$$

where M_1 and M_2 are the lower (threshold M_c) and the upper (maximum $M_{\max}$) limits of the Mach number. It is clear from Eq. 38 that the lower Mach number does not depends on $p_\perp$, while upper Mach number does depend on both $p_\parallel$ and $p_\perp$. While keeping $\alpha = 1$, both the equations reduce to the true acoustic phase speed of IAWs given in Eq. 22. Eq. 37 is satisfied for Mach number values in the range

$$M_1 < M < M_2, \tag{40}$$

i.e.,

$$\alpha < \frac{M}{M_2} < 1. \tag{41}$$

In other words, the inequality in Eq. 37 is valid if $\alpha = \cos\theta \leq 1$. Because we employed the neutrality hypothesis rather than Poisson's equation, our results are valid in the long wavelength limit. To examine the polarity of the non-linear structures, we have to check third derivative of Sagdeev potential $\psi(\varphi)$ at $\varphi = 0$ and $M = M_c$. If $d_\varphi^3\psi > 0$, then only positive structures (solitons or shocks) can exist otherwise, the plasma system can then support negative structures as well. It is found that,

$$d_\varphi^3\psi \mid_{\varphi=0, M=M_c} = \frac{\Omega^2\left(2 + \gamma(1+\sigma)\left(5 + \sigma + 3\gamma(1+\sigma)\right) + 4\left(\eta + \gamma\sigma\right)^3 p_\parallel\right)}{(1-\alpha^2)\left(1 + (\eta + \gamma\sigma)p_\parallel\right)\left(1 + (\eta + \gamma\sigma)p_\perp\right)}, \tag{42}$$

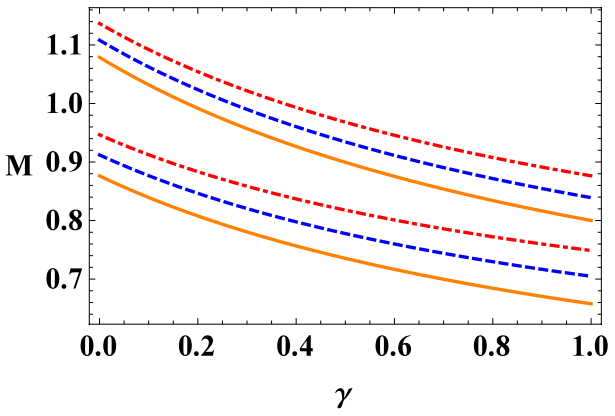

FIGURE 2
Variation of Mach number M vs. positron concentration γ for different values of $p_\parallel = 0.20$ (solid curve), 0.30 (dashed curve) and 0.40 (dot-dashed curve) with $\alpha = 0.80$, $p_\perp = 0.1$ and $\sigma = 0.1$.

which indicates that the current model can only support compressive (positive potential) solitary pulses. By keeping $\gamma = 0$ and neglecting $p_\parallel$ and $p_\perp$ we can retrieve the result of Ref. [29].

In order to emphasize the soliton existence region, we have plotted M_1 and M_2 in Figure 2 for different values of $p_\parallel = 0.20$ (solid curve), 0.30 (dashed curve) and 0.40 (dot-dashed curve). Considering, $p_\perp = 0.1$, $\alpha = 0.8$ and $\sigma = 0.1$, it can be seen that M decreases with the increasing values of γ while both limits of Mach numbers increase with increasing values of $p_\parallel$.

6 Parametric study

The Sagdeev potential $\psi(\varphi)$ depends on a number of important physical parameters in addition to the electric potential φ, including the excitation speed M, positron concentration γ, electron to positron temperature ratio σ, the obliqueness of propagation (*via* $\alpha = \cos\theta$), parallel ion pressure $p_\parallel$ and perpendicular ion pressure $p_\perp$. In this study, we specifically focus to assess the effect of γ, $p_\parallel$ and $p_\perp$. Therefore, the effect of these three parameters is studied on propagation characteristics of solitary structures.

In Figure 3, the variation of Sagdeev potential $\psi(\varphi)$, the resulting electrostatic potential φ and the associated electric field profile E have been shown for various values of positron concentration γ, while considering other fixed values $M = 0.9$, $\sigma = 0.1$, $\Omega = 0.3$, $\alpha = 0.8$, $p_\parallel = 0.2$ and $p_\perp = 0.1$. We note that as γ increases, the depth and root of the Sagdeev potential increases. It is clear from Figure 3B that, the amplitude of the solitary pulse increases while its width decreases with higher value of γ. Therefore, solitary structure gets taller and narrower with the increase of positron concentration in a magnetized anisotropic $e - p - i$ plasma. The same effect has been shown in Ref. [30] while studying these waves in unmagnetized isotropic plasma. It is clearly seen that in the absence of positron concentration $\gamma = 0$, the amplitude of solitary structure reduced as shown in Figure 3 by solid orange curve.

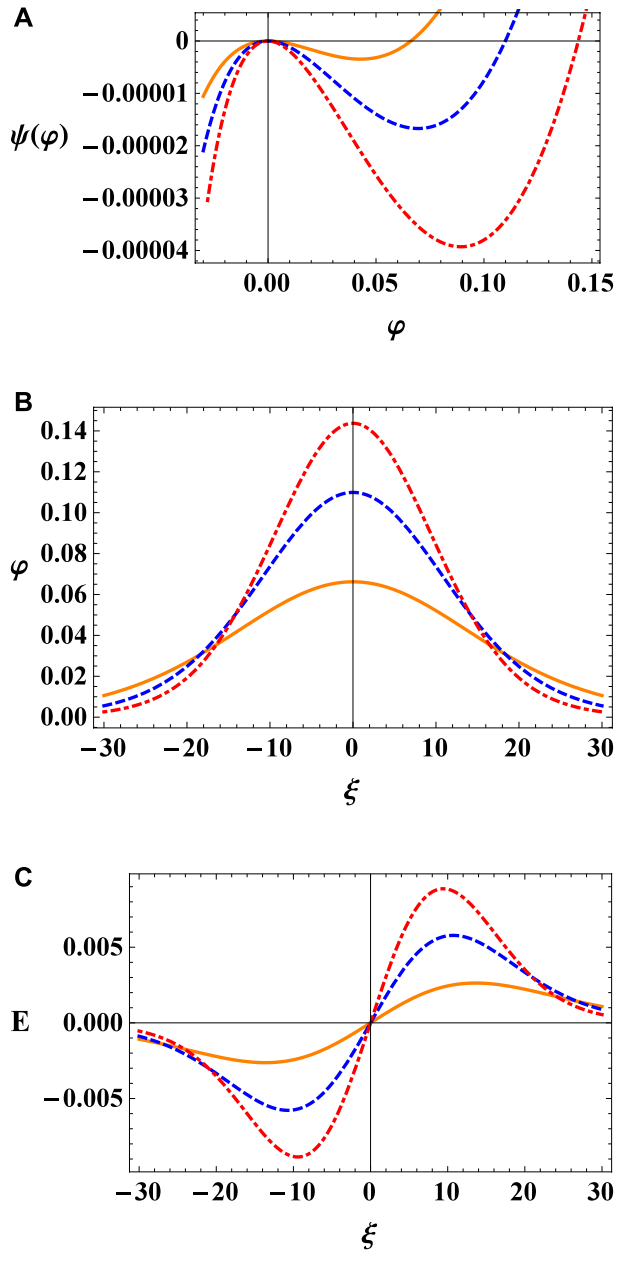

FIGURE 3
Plot of **(A)** Sagdeev potential $\psi(\varphi)$ vs. φ, **(B)** Electrostatic potential φ and **(C)** Electric field E for different values of γ = 0.00 (solid curve), 0.05 (dashed curve) and 0.10 (dot-dashed curve) with M = 0.9, Ω = 0.3, $p_{\parallel}$ = 0.2, $p_{\perp}$ = 0.1, α = 0.80, and σ = 0.1.

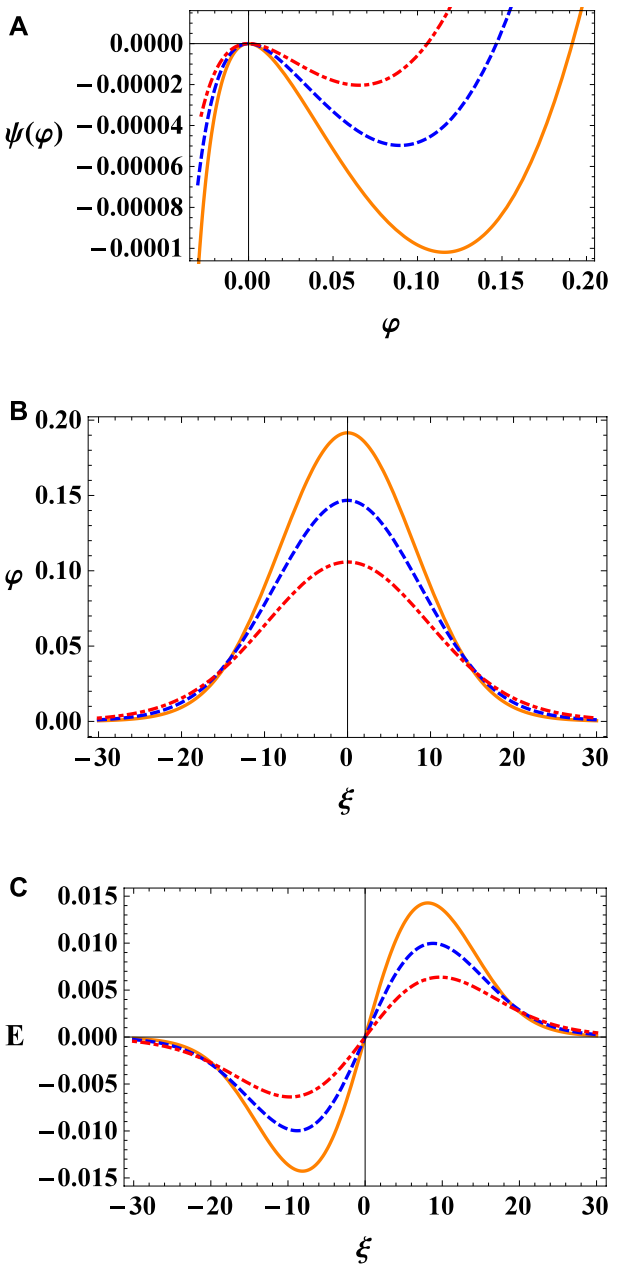

FIGURE 4
Plot of **(A)** Sagdeev potential $\psi(\varphi)$ vs. φ, **(B)** Electrostatic potential φ and **(C)** Electric field E for different values of $p_{\parallel}$ = 0.20 (solid curve), 0.25 (dashed curve) and 0.30 (dot-dashed curve) with M = 0.9, Ω = 0.3, γ = 0.2, $p_{\perp}$ = 0.1, α = 0.80, and σ = 0.1.

To study the effect of pressure anisotropy on the solitary waves, we have shown the variation of Sagdeev potential $\psi(\varphi)$ along with the corresponding electrostatic potential and electric field profiles with $p_{\parallel}$ = 0.20 (solid curve), 0.25 (dashed curve) and 0.30 (dot-dashed curve) while considering M = 0.9, γ = 0.2, Ω = 0.3, α = 0.8, σ = 0.1, and $p_{\perp}$ = 0.1in Figure 4. It has been noted that the ion parallel pressure $p_{\parallel}$ variation is quite effective (i.e., a minor change in $p_{\parallel}$ causes a significant changes in the Sagdeev potential). Thereby increasing values of $p_{\parallel}$ result in the decrease of depth and root of Sagdeev potential as well as in the amplitude of associated soliton pulses. The changing values of perpendicular ion pressure $p_{\perp}$ have no discernible influence on the amplitude of the solitary waves as shown in Figure 5. In Figure 6 we have considered three different cases, mainly $p_{\parallel} = p_{\perp} = 0$, $p_{\parallel} > p_{\perp}$ and $p_{\perp} > p_{\parallel}$ with fixed values of M = 0.85, γ = 0.1, Ω = 0.3, α = 0.8, σ = 0.1. For $p_{\parallel} > p_{\perp}$ the amplitude of solitary pulse decreases while in case of $p_{\perp} > p_{\parallel}$ the amplitude of solitary pulses is not significantly effected as compared to $p_{\parallel}$. In the absence of pressure anisotropy $p_{\parallel} = p_{\perp} = 0$, the amplitude of soliton increases as shown in Figure 6 by orange solid curve. We can infer from this Figure 6 that, in

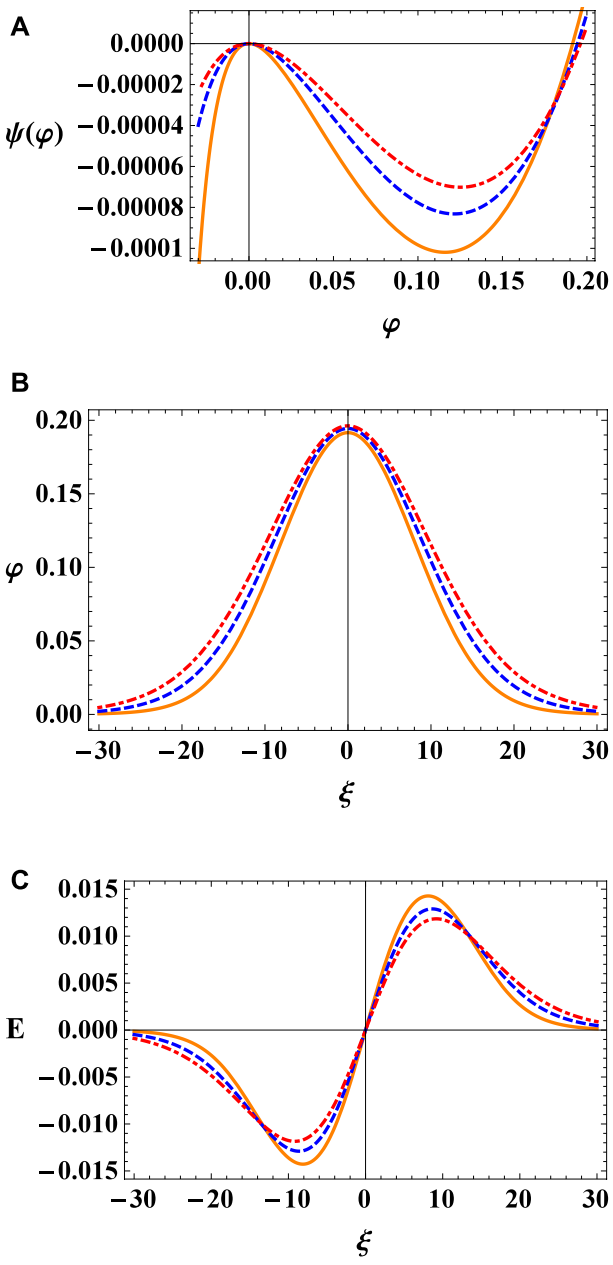

FIGURE 5
Plot of **(A)** Sagdeev potential $\psi(\varphi)$ vs. φ, **(B)** Electrostatic potential φ and **(C)** Electric field E for different values of $p_\perp = 0.1$ (solid curve), 0.5 (dashed curve) and 0.9 (dot-dashed curve) with $M = 0.9$, $\Omega = 0.3$, $\gamma = 0.2$, $p_\parallel = 0.2$, $\alpha = 0.80$, and $\sigma = 0.1$.

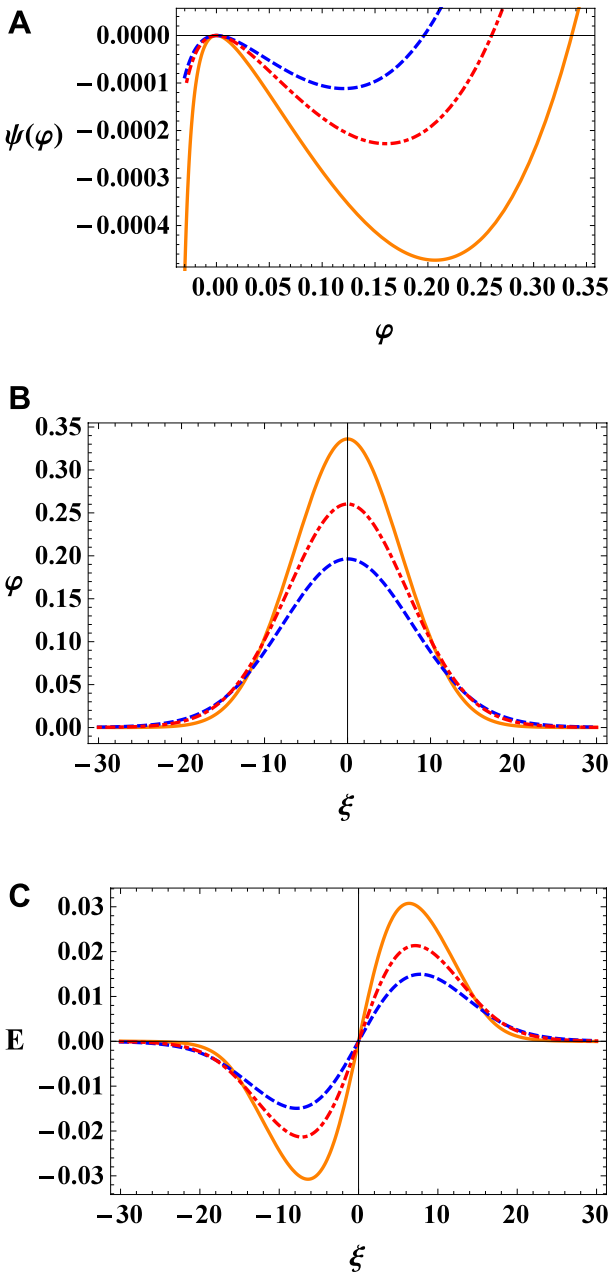

FIGURE 6
Plot of **(A)** Sagdeev potential $\psi(\varphi)$ vs. φ, **(B)** Electrostatic potential φ and **(C)** Electric field E for different pressure anisotropy cases $p_\parallel = p_\perp = 0$ (solid curve), $p_\parallel > p_\perp$ (dashed curve) and $p_\perp > p_\parallel$ (dot-dashed curve) with $M = 0.85$, $\Omega = 0.3$, $\gamma = 0.2$, $\alpha = 0.80$, and $\sigma = 0.1$.

comparison to $p_\perp$, the characteristics of IASWs are more sensitive to variations in $p_\parallel$ as compared to $p_\perp$. Similar results have been demonstrated in Ref. [35].

7 Conclusion

We have presented a study of the properties of arbitrary amplitude non-linear IASWs, propagating in a magnetized plasma characterized by anisotropic ions and Maxwellian distributed electrons and positrons. The linear analysis gives two modes, the IA and the ion-cyclotron modes, whose characteristics depends on the Maxwellian electron and positron and on the pressure anisotropy of the ions. We have shown that the frequency of the acoustic mode decreases with increasing obliqueness of propagation. In the non-linear regime, Sagdeev approach is used for the investigation of the properties of arbitrary amplitude IASWs. A parametric analysis was carried out for studying the characteristics of these waves, which can be summarize as follows.

- The amplitude of solitary pulses increases with rising values of positron concentration γ.
- The amplitude of solitary pulses reduced with higher values of parallel ion pressure $p_{\parallel}$.
- Finally, we found that the characteristics of IASWs are more sensitive to the parallel ion pressure $p_{\parallel}$ than perpendicular ion pressure $p_{\perp}$.

These results are general and might be applied to astrophysical plasma environments like the polar cups region of pulsars and near active galactic nuclei, where magnetized $e - p - i$ plasma and ions with aniotropic pressure can exist.

Data availability statement

The original contributions presented in the study are included in the article/Supplementary Material, further inquiries can be directed to the corresponding author.

Author contributions

All authors listed have made a substantial, direct, and intellectual contribution to the work and approved it for publication.

Conflict of interest

The authors declare that the research was conducted in the absence of any commercial or financial relationships that could be construed as a potential conflict of interest.

Publisher's note

References

1. Rees MJ, Gibbons GW, Hawking SW, Siklas S. *The very early universe*. Cambridge: Cambridge University Press (1983).

2. Kozlovsky B, Murphy RJ, Share GH. Positron-emitter production in solar flares from 3He reactions. *J Astrophy* (2004) 604:892–9. doi:10.1086/381969

3. Miller H, Witta P. *Active galactic nuclei*. Berlin: Springer-Verlag (1987).

4. Michel FC. Theory of pulsar magnetospheres. *Rev Mod Phys* (1982) 54:1–66. doi:10.1103/revmodphys.54.1

5. Zeba I, Moslem WM, Shukla PK. Ion solitary pulses in warm plasmas with ultrarelativistic degenerate electrons and positrons. *J Astrophy* (2012) 750:72. doi:10.1088/0004-637x/750/1/72

6. Berezhiani VI, Mahajan SM. Large amplitude localized structures in a relativistic electron-positron ion plasma. *Phys Rev Lett* (1994) 73:1110–3. doi:10.1103/physrevlett.73.1110

7. Surko CM, Murphy TJ. Use of the positron as a plasma particle. *Phys Fluids* (1990) 2:1372–5. doi:10.1063/1.859558

8. Surko CM, Leventhal M, Crane WS, Passner A, Wysocki F, Murphy TJ, et al. Use of positrons to study transport in tokamak plasmas (invited). *Rev Sci Instrum* (1986) 57:1862–7. doi:10.1063/1.1139154

9. Pakzad HR. Ion acoustic solitary waves in plasma with nonthermal electron and positron. *Phys Lett A* (2009) 373:847–50. doi:10.1016/j.physleta.2008.12.066

10. Krall NA, Trivelpiece AW. *Principles of plasm physics*. USA: McGraw-Hill (1973).

11. Hasegawa A. *Plasma instabilities and nonlinear effects*. New York: Springer (1975).

12. Davidson RC. *Methods in nonlinear plasma theory*. New York: Academic (1972).

13. Nicolson DR. *Introduction to plasma theory*. New York: Wiley (1983).

14. Popel SI, Vladimirov SV, Shukla PK. Ion-acoustic solitons in electron–positron–ion plasmas. *Phys Plasmas* (1995) 2:716–9. doi:10.1063/1.871422

15. Alinejad H, Mamun AA. Oblique propagation of electrostatic waves in a magnetized electron-positron-ion plasma with superthermal electrons. *Phys Plasmas* (2011) 18:112103. doi:10.1063/1.3656982

16. Ullah G, Saleem M, Khan M, Khalid M, Rahman A, Nabi S. Ion acoustic solitary waves in magnetized electron–positron–ion plasmas with Tsallis distributed electrons. *Contrib Plasma Phys* (2020) 60:e202000068. doi:10.1002/ctpp.202000068

17. Nejoh YN. The effect of the ion temperature on large amplitude ion-acoustic waves in an electron–positron–ion plasma. *Phys Plasmas* (1996) 3:1447–51. doi:10.1063/1.871734

18. Mahmood S, Mushtaq A, Saleem H. Ion acoustic solitary wave in homogeneous magnetized electron-positron-ion plasmas. *New J Phys* (2003) 5:28. doi:10.1088/1367-2630/5/1/328

19. Washimi H, Taniuti T. Propagation of ion-acoustic solitary waves of small amplitude. *Phys Rev Lett* (1966) 17:996–8. doi:10.1103/physrevlett.17.996

20. Kazeminezhad F, Kuhn S, Tavakoli A. Vlasov model using kinetic phase point trajectories. *Phys Rev E* (2003) 67:026704. doi:10.1103/physreve.67.026704

21. Sagdeev RZ. Cooperative phenomena and shock waves in collisionless plasmas. *Rev Plasma Phys* (1966) 4:23.

22. Berthomier M, Pottelette R, Malingre M. Solitary waves and weak double layers in a two-electron temperature auroral plasma. *J Geophys Res Space Phys* (1998) 103:4261–70. doi:10.1029/97ja00338

23. Verheest F. Nonlinear dust-acoustic waves in multispecies dusty plasmas. *Planet Space Sci* (1992) 40:1–6. doi:10.1016/0032-0633(92)90145-e

24. Chew GF, Goldberger ML, Low FE. The Boltzmann equation an d the one-fluid hydromagnetic equations in the absence of particle collisions. *Proc R Soc London, Ser A* (1956) 236:112–8.

25. Denton RE, Anderson BJ, Gary SP, Fuselier SA. Bounded anisotropy fluid model for ion temperatures. *J Geophys Res* (1994) 99:11225–41. doi:10.1029/94ja00272

26. Parks GK. *Physics of space plasmas*. USA: Perseus (1991).

27. Chatterjee P, Saha T, Ryu CM. Obliquely propagating ion acoustic solitary waves and double layers in a magnetized dusty plasma with anisotropic ion pressure. *Phys Plasmas* (2008) 15:123702. doi:10.1063/1.2996114

28. Sultana S, Kourakis I, Saini NS, Hellberg MA. Oblique electrostatic excitations in a magnetized plasma in the presence of excess superthermal electrons. *Phys Plasmas* (2010) 17:032310. doi:10.1063/1.3322895

29. Khalid M, El-Tantawy SA, Rahman AU. Oblique ion acoustic excitations in a magnetoplasma having κ-deformed Kaniadakis distributed electrons. *Astrophys Space Sci* (2020) 365:1–9.

30. El-Awady EI, El-Tantawy SA, Moslem WM, Shukla PK. Electron–positron–ion plasma with kappa distribution: Ion acoustic soliton propagation. *Phys Lett A* (2010) 374:3216–9. doi:10.1016/j.physleta.2010.05.053

31. Mahmood S, Akhtar N. Ion acoustic solitary waves with adiabatic ions in magnetized electron-positron-ion plasmas. *Eur Phys J D* (2008) 49:217–22. doi:10.1140/epjd/e2008-00165-4

32. Choi CR, Ryu CM, Lee DY, Lee NC, Kim YH. Dust ion acoustic solitary waves in a magnetized dusty plasma with anisotropic ion pressure. *Phys Lett A* (2007) 364: 297–303. doi:10.1016/j.physleta.2006.12.014

33. Adnan M, Williams G, Qamar A, Mahmood S, Kourakis I. Pressure anisotropy effects on nonlinear electrostatic excitations in magnetized electron-positron-ion plasmas. *Eur Phys J D* (2014) 68:247–15. doi:10.1140/epjd/e2014-50384-y

34. Adnan M, Mahmood S, Qamar A. Effect of anisotropic ion pressure on solitary waves in magnetized dusty plasmas. *Contrib Plasma Phys* (2014) 54:724–34. doi:10.1002/ctpp.201300061

35. Adnan M, Qamar A, Mahmood S, Kourakis I. On the characteristics of obliquely propagating electrostatic structures in non-Maxwellian plasmas in the presence of ion pressure anisotropy. *Phys Plasmas* (2017) 24:032114. doi:10.1063/1.4978613

36. Khalid M, Hadi F, Rahman A. Modulation of multi-dimensional waves in anisotropic magnetized plasma. *Eur Phys J Plus* (2021) 136:1061. doi:10.1140/epjp/s13360-021-02063-x

37. Alyousef H, Khalid M, Rahman A, Tantawy SA. Large amplitude electrostatic (Un)modulated excitations in anisotropic magnetoplasmas: Solitons and Freak waves. *Braz J Phys* (2022) 52:202. doi:10.1007/s13538-022-01199-0

38. Khalid M. Oblique ion-acoustic solitary waves in anisotropic plasma with Tsallis distribution. *EPL* (2022) 138:53003. doi:10.1209/0295-5075/ac6a08

39. Singh SV, Devanandhan S, Lakhina GS, Bharuthram R. Effect of ion temperature on ion-acoustic solitary waves in a magnetized plasma in presence of superthermal electrons. *Phys Plasmas* (2013) 20:012306. doi:10.1063/1.4776710

10.3389/fphy.2023.1144175

Appendix: Potential functions used in Eq. 36 are given as

$$\delta_1(\varphi) = \eta e^{\varphi} + \frac{\gamma}{\sigma} e^{-\sigma\varphi} - \left(\eta + \frac{\gamma}{\sigma}\right)$$

$$\delta_2(\varphi) = \left(\eta e^{\varphi} + \frac{\gamma}{\sigma} e^{-\sigma\varphi}\right)^2 - \left(\eta + \frac{\gamma}{\sigma}\right)^2$$

$$\delta_3(\varphi) = \left(\begin{array}{c} \frac{\eta^4}{4} e^{4\varphi} - \frac{4\eta^3\gamma}{3-\sigma} e^{(3-\sigma)\varphi} + \frac{6\eta^2\gamma^2}{2-2\sigma} e^{(2-2\sigma)\varphi} - \\ \frac{4\eta\gamma^3}{1-3\sigma} e^{(1-3\sigma)\varphi} - \frac{\gamma^4}{4\sigma} e^{-4\sigma\varphi} \end{array} \right) - \left(\frac{\eta^4}{4} - \frac{4\eta^3\gamma}{3-\sigma} + \frac{6\eta^2\gamma^2}{2-2\sigma} - \frac{4\eta\gamma^3}{1-3\sigma} - \frac{\gamma^4}{4\sigma}\right)$$

$$\delta_4(\varphi) = \left(\eta e^{\varphi} - \gamma e^{-\sigma\varphi}\right)^{-1} - (\eta - \gamma)^{-1}$$

$$\delta_5(\varphi) = \left(\eta e^{\varphi} - \gamma e^{-\sigma\varphi}\right)^{-2} - (\eta - \gamma)^{-2}$$

$$\delta_6(\varphi) = \left(\eta e^{\varphi} + \frac{\gamma}{\sigma} e^{-\sigma\varphi}\right)\left(\eta e^{\phi} - \gamma e^{-\sigma\varphi}\right)^{-1} - \left(\eta + \frac{\gamma}{\sigma}\right)(\eta - \gamma)^{-1}$$

$$\delta_7(\varphi) = \left(\eta e^{\varphi} - \gamma e^{-\sigma\varphi}\right)^2 - (\eta - \gamma)^2$$

$$\delta_8(\varphi) = \left(\eta e^{\varphi} - \gamma e^{-\sigma\varphi}\right)^3 - (\eta - \gamma)^3$$

$$\delta_9(\varphi) = \left(\eta e^{\varphi} - \gamma e^{-\sigma\varphi}\right)^3\left(\eta e^{\varphi} + \frac{\gamma}{\sigma} e^{-\sigma\varphi}\right) - (\eta - \gamma)^3\left(\eta + \frac{\gamma}{\sigma}\right)$$

$$\delta_{10}(\varphi) = \left(\eta e^{\varphi} - \gamma e^{-\sigma\varphi}\right)^6 - (\eta - \gamma)^6$$

$$\delta_{11}(\varphi) = \left(\eta e^{\varphi} - \gamma e^{-\sigma\varphi}\right) - (\eta - \gamma)$$

$$\delta_{12}(\varphi) = \log\left(\eta e^{\varphi} - \gamma e^{-\sigma\varphi}\right) - \log(\eta - \gamma)$$

$$\delta_{13}(\varphi) = \left(\eta e^{\varphi} - \gamma e^{-\sigma\varphi}\right)\left(\eta e^{\varphi} + \frac{\gamma}{\sigma} e^{-\sigma\varphi}\right) - (\eta - \gamma)\left(\eta + \frac{\gamma}{\sigma}\right)$$

$$\delta_{14}(\varphi) = \left(\frac{\eta^2 e^{2\varphi}}{2} - \frac{\gamma^2 e^{-2\sigma\varphi}}{2\sigma} - \frac{2\eta\gamma e^{(1-\sigma)\varphi}}{(1-\sigma)}\right) - \left(\frac{\eta^2}{2} - \frac{\gamma^2}{2\sigma} - \frac{2\eta\gamma}{(1-\sigma)}\right)$$

$$\delta_{15}(\varphi) = \left(\eta e^{\varphi} - \gamma e^{-\sigma\varphi}\right)^4 - (\eta - \gamma)^4$$

$$\delta_{16}(\varphi) = \left(\eta e^{\varphi} - \gamma e^{-\sigma\varphi}\right)^{-3}\left(\eta e^{\varphi} + \gamma\sigma e^{-\sigma\varphi}\right)$$

$$\delta_{17}(\varphi) = \left(\eta e^{\varphi} - \gamma e^{-\sigma\varphi}\right)\left(\eta e^{\varphi} + \gamma\sigma e^{-\sigma\varphi}\right)$$

$$\delta_{18}(\varphi) = \left(\eta e^{\varphi} - \gamma e^{-\sigma\varphi}\right)^{-1}\left(\eta e^{\varphi} + \gamma\sigma e^{-\sigma\varphi}\right)$$

frontiers | Frontiers in Physics

TYPE Original Research
PUBLISHED 07 March 2023
DOI 10.3389/fphy.2023.1123370

OPEN ACCESS

EDITED BY
Samir A. El-Tantawy,
Port Said University, Egypt

REVIEWED BY
Yasser Sharaby,
Suez University, Egypt
Xing Lu,
Beijing Jiaotong University, China

*CORRESPONDENCE
R. A. Alharbey,
rania.math@gmail.com

†These authors have contributed equally to this work

SPECIALTY SECTION
This article was submitted to Mathematical Physics, a section of the journal Frontiers in Physics

RECEIVED 14 December 2022
ACCEPTED 23 January 2023
PUBLISHED 07 March 2023

CITATION
Alharbey RA and Hassan SS (2023), Fractional critical slowing down in some biological models.
Front. Phys. 11:1123370.
doi: 10.3389/fphy.2023.1123370

Fractional critical slowing down in some biological models

R. A. Alharbey[1]* and S. S. Hassan[2†]

[1]Mathematics Department, Faculty of Science, King Abdulaziz University, Jeddah, Saudi Arabia, [2]Department of Mathematics, College of Science, University of Bahrain, Sakhir, Kingdom of Bahrain

The critical slowing down (CSD) phenomenon of the switching time in response to perturbation β ($0 < \beta < 1$) of the control parameters at the critical points of the steady state bistable curves, associated with two biological models (the spruce budworm outbreak model and the Thomas reaction model for enzyme membrane) is investigated within fractional derivative forms of order α ($0 < \alpha < 1$) that allows for memory mechanism. We use two definitions of fractional derivative, namely, Caputo's and Caputo-Fabrizio's fractional derivatives. Both definitions of fractional derivative yield the *same* qualitative results. The interplay of the two parameters α (as memory index) and β shows that the time delay τ_D can be reduced or increased, compared with the ordinary derivative case ($\alpha = 1$). Further, τ_D fits: (*i*) as function of β the scaling inverse square root formula $1/\sqrt{\beta}$ at fixed fractional derivative index ($\alpha < 1$) and, (*ii*) as a function of α ($0 < \alpha < 1$) an exponentially increasing form at fixed perturbation parameter β.

KEYWORDS

critical slowing down, Caputo's and Caputo-Fabrizio's fractional derivatives, switching timedelay, bistable behaviour, mathematical models in biology

1 Introduction

Bistable systems in many branches of sciences (physics, biology, . . .) and engineering are characterized by the co-existence of two stable states, where the system switches from one stable state to other state by means of changing one or some of the system control parameters [1–4]. The associated transient phenomena of lengthening the switching time between these two stable states, called critical slowing down (CSD), happens upon perturbing one of the parameters at the critical (switching-on or -off) points of the charactertistic bistable curve [5–8]. It has been suggested that, CSD may serve as a universal indicator of how a complex physical system (such as brain, ecosystems, climate and financial markets) approaches a threshold [9–12], and as well serving as an indicator of transitions in two-species biological models, which exhibit Hopf bifurcation or hysteresis transition [13]. For our specific current concern, the CSD phenomenon has recently been investigated by us in [14] for some biological bistable models, namely.

(a) The spruce budworm outbreak model [3, 4, 15];
(b) The Thomas-reaction (enzyme membrane) model [4, 16].

Specifically, our investigation in [14] was concerned with the nature of transition between the two stable states, and the verification of the inverse square root scaling law, for the switching time delay (τ_D) at the critical switching-on and -off points, independent of the type of non-linearity in the model rate equations. The model rate equation in model a) is of first order ordinary differential equation (ODE), while in model b) the model rate equations are coupled first order ODEs.On the other hand, fractional calculus, a field of mathematics that deals with the analysis of derivatives and integrals of fractional (or even complex) order, has its applications in diverse areas of science and engineering. The associated fractional

differential equations (FDEs) are widely and successfully used in mathematical modelling in a variety of fields. We refer the reader to the extensive list of major works and applications in the area of fractional calculus cited in ([17–20] and refs. therein). In ordinary calculus, the first order derivative of a function $f(t)$, namely $f'(t) = \frac{df}{dt}$ is the instantaneous rate of change of $f(t)$ over the infinitesimal time period, $t \to 0$, that is, local time effect. In fractional calculus, the physical meaning is non-local, as the time domain is manifested as a memory (or time delay) effect and the current state of the system depends on its earlier history. Moreover, in fitting with test data of various models of memory phenomena, the order of the fractional derivative serves as an index of memory [21, 22]. FDEs of arbitrary real order are not in general easy to solve analytically [23]. However, the numerical method based on Laplace transform technique is a basic one and applicable for a wide class of initial value problems for FDEs, [23–26]. Recent fundamental computational methods are found in [27, 28]; and refs, therein.

Experimentally speaking, fractional derivative models (FDMs) are in excellent agreement with experimental data in many branches of science and engineering. Two specific examples we quote.

1. A recent experimental study of viscoelastic properties of some soft biological tissues under harmonic mechanical loading shows that the FD Voigt model performed better, compared with integer order derivative models [29].
2. FDM (Maxwell's model) describing the viscoelastic Creep damage of some fruits is more efficient and well fitted with experimental data [30].

Further, CSD or more generally instability mechanism and chaos, have been investigated at large in fractional order dynamical systems in fields, like, fluid flow [31–35], neurology and biological phenomena ([36–38]; refs. therein) to account successfully for memory (time-delay) and special non-local effects. For example.

1. The Landau model that describes the fluid flow from laminar to turbulent has been examined within a fractional rate equation model [35] in order to account for memory effect. This transition to turbulence due to CSD shows that the turbulent fluctuations depend on memory of inverse power law decay in agreement with experiment [39]-slower than in the case of no memory (ordinary derivative case) of turbulent fluctuations decaying exponentially,
2. Capacitive memory due to fractional order cardiomyocyte dynamical model [37] alters the electrical signaling in cardiac cells in a manner that promote or suppress electrical instability (known as alternans).
3. The use of a fractional order mathematical model to study the signaling process in nerve cells (like, neuron) due to incorporated strong memory effects [36] has been interpreted as a neuronal disorder (Parkinson disease).

The concern of the present paper is to adopt the corresponding FDEs in both models a) [3, 4, 15] and b) [4, 16], referred to above, in order to incorporate for memory effects and examine effects of the fractional derivative order parameter (α), ($0 < \alpha < 1$) on the time delay (τ_D) associated with the CSD phenomena examined in the no-memory case [14]. We use and compare two definitions of fractional derivatives, namely, Caputo's [40] and Caputo-Fabrizio's [21, 22] definitions. Both definitions have the advantage of dealing with initial conditions of the variables and their integer derivatives suitable in most physical processes, like models a) [3, 4, 15] and b) [4, 16] referred to above. As a main result, it is found that Caputo's and Caputo-Fabrizio's definitions of fractional derivatives yield the *same* qualitative results of reduced time delay τ_D at fixed perturbation of the concerned control parameter, with smaller values of the fractional derivative order α. The small *quantitative difference* in τ_D is due to the different convoluted kernels (that model the memory or delay effect) in [21, 22, 40].This paper is presented as follows. In section 2), we present the model differential equations in both ordinary and Caputo's fractional derivative forms, for both models. In section 3), we present the computational results for the transient switching. Section 4) presents a summary of the results. In Supplementary Appendix A, a brief background of the model ODEs (eqa (1) and. 2) below) representing the two biological models referred to above is given, while Supplementary Appendix B presents a guideline for Euler's numerical method to solve fractional FDE.

2 The model equations

Here, we first present the model DEs of the two biological models (the Spruce-budworm and Thomas reaction models) in their ordinary derivative forms. (A brief background of these model ODEs are given in Supplementary Appendix A). Second, we present the corresponding fractional derivative forms, according to the two formulations of Caputo's [40] and Caputo-Fabrizio's definitions [21].

2.1 Ordinary derivative case

2.1.1 The spruce budworm Model

This model ([3, 4, 15]) provides a good example for understanding the dynamics of the interaction between trees and insects. The model rate equation for the insect (budworms) population has the form:

$$\begin{aligned}\frac{d}{d\tau}N(\tau) &= N(\tau)\left(1-\frac{N(\tau)}{K}\right) - FN^2(\tau)/\left(N^2(\tau)+B^2\right) \\ &\equiv f_o(N(\tau)),\end{aligned} \tag{1}$$

where $N(\tau)$ is the budworm's population, $\tau = rt$ is normalised time, r is the linear birth rate and K is the constant carrying capacity which is related to the foliage (food) available on the trees in the absence of birds. The constant $F = p_oA/r$ is the predation population with rate p_o and A is the (positive) predator attack rate and B is the threshold measure of the budworm population. The predation will approach an upper level value, $lim_{N\to\infty}FN^2/(N^2+B^2) = F$ as N increases.

2.1.2 The Thomas reaction model

The mechanism of this model is based on a basic reaction in an enzyme membrane, between the substrate oxygen and uric acid. The model equations of the system in a dimensionless form are [4, 16]:

$$\begin{aligned}\frac{du(\tau)}{d\tau} &= a - u(\tau) - \ell\frac{u(\tau)v(\tau)}{1+u(\tau)+ku^2(\tau)} \\ &\equiv f_1(u(\tau),v(\tau))\end{aligned} \tag{2a}$$

$$\begin{aligned}\frac{dv(\tau)}{d\tau} &= \gamma(b-v(\tau)) - \ell\frac{u(\tau)v(\tau)}{1+u(\tau)+ku^2(\tau)} \\ &\equiv f_2(u(\tau),v(\tau)).\end{aligned} \tag{2b}$$

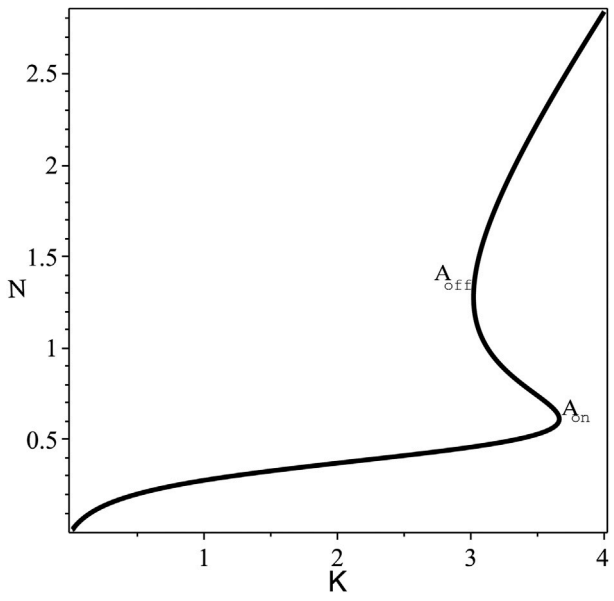

FIGURE 1
The steady state bistable curve of N against K, at fixed values of the parameters F =0.85, B =0.5. The switching-on and -off points: A_{on} =(3.6631,0.61299) and A_{off} =(3.0199,1.2793).

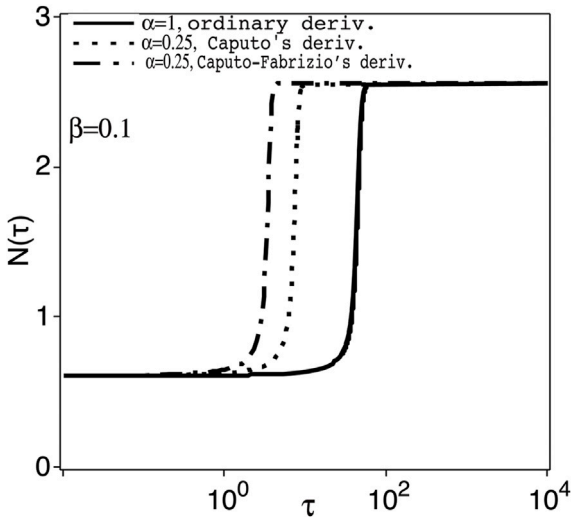

FIGURE 2
The transient population $N(\tau)$ *versus* the normalised time $\tau = \gamma t$ (as log scale), for control parameter with positive perturbation, $K = K_c + \beta$; K_c =3.6631 at the switching-on point, A_{on}, of Figure 1 and fixed β =0.1, and for α =1 (ordinary derivative) and 0.25 (Caputo's and Caputo-Fabrizio's fractional derivatives).

Here, u and v represent the uric acid and the oxygen being supplied at constant rates a and γb, respectively, where, a, ℓ, k, γ and b are all positive real constants. The factor $u(\tau)v(\tau)/\ (1+u(\tau)+ku^2(\tau))$ exhibits *substrate inhibition:* it increases (decreases) when u is small (large), with measure of inhibition's severity equal to k.

In [14], the model Equations 1, 2 were analysed in detail (theoretically and computationally) regarding regions of

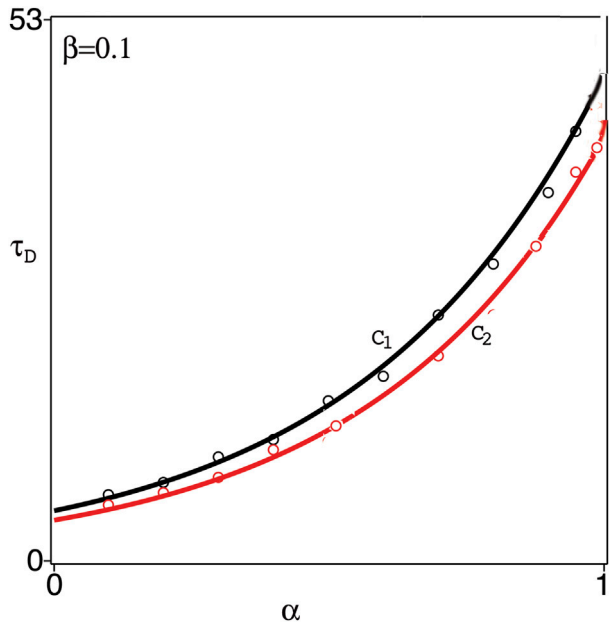

FIGURE 3
Time-delay, τ_D, *versus* the fractional derivative parameter α at fixed β =0.1. Circles represent the numerical results and the solid lines C_1, C_2 represent the exponential fitting, $4.9e^{2.2\alpha}$ in the case of Caputo's derivative, and $3.8e^{2.3\alpha}$ in the case of Caputo-Fabrizio's derivative, respectively.

bistability, the CSD phenomenon at the critical (switch-up and -down) points of the bistable curves and the verification of the inverse square root scaling law of the switching time delay [7, 41].

2.2 Fractional derivative cases

In this case, Equations 1, 2 take the following forms;

$$\frac{d^\alpha}{d\tau^\alpha}N(\tau) = f_o(N(\tau)), \tag{3}$$

and,

$$\frac{d^\alpha}{d\tau^\alpha}u(\tau) = f_1(u(\tau), v(\tau)), \tag{4a}$$

$$\frac{d^\alpha}{d\tau^\alpha}v(\tau) = f_2(u(\tau), v(\tau)), \tag{4b}$$

respectively, where $\frac{d^\alpha}{d\tau^\alpha}$ denotes the fractional derivative of order α ($0 < \alpha < 1$). There is no unique definition of fractional calculus (FC), derivatives and integrals. Definitions of FC are too many and still -up to date - increasing. Here, we use and compare two definitions of fractional derivatives of a continuous function $f(\tau)$ on $(0, \tau)$, namely, Caputo's [40] and Caputo-Fabrizio's [21] derivatives.

2.2.1 Caputo's fractional derivative [40]

Caputo's fractional derivative of $f(\tau)$ is defined as the convolution of the kernel power function $\tau^{-\alpha}$, $0 < \alpha < 1$ with the first order (ordinary derivative) $f'\tau)$ on the closed interval $[0, \tau]$,

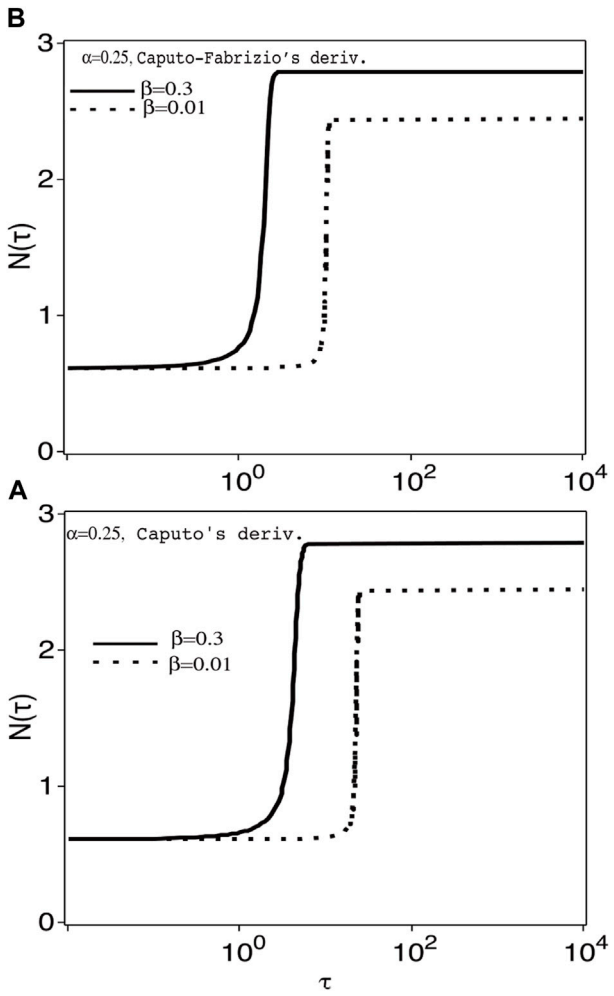

FIGURE 4
As Figure 2, but at fixed value of α =0.25, and different β =0.01,0.3 in the case of: **(A)** Caputo's, and **(B)** Caputo-Fabrizio's, fractional derivatives.

$$\left(\frac{d^{\alpha}}{d\tau^{\alpha}}f(\tau)\right)_{Cap} = \frac{1}{\Gamma(1-\alpha)}\int_0^{\tau}\frac{1}{(\tau-t')^{\alpha}}\frac{d}{dt'}f(t')dt', \quad (5)$$

with $\Gamma(x)$ is the gamma function.

2.2.2 Caputo-Fabrizio's derivative [21, 22]

This fractional derivative of $f(\tau)$ is defined as the convolution of the kernel exponential function $e^{-\alpha\tau/(1-\alpha)}$, $0 < \alpha < 1$, with $f'(\tau)$ on the closed interval $[0, \tau]$,

$$\left(\frac{d^{\alpha}}{d\tau^{\alpha}}f(\tau)\right)_{(Cap-Fab)} = \frac{1}{(1-\alpha)}\int_0^{\tau}e^{(-\alpha/(1-\alpha))(\tau-t')}\frac{d}{dt'}f(t')dt', \quad (6)$$

3 Transient switching and time delay

The switching time at the critical (switch-on and -off) points of the characteristic steady state bistable curves (N vs K) according to the FDE 3), or (u and v vs a) according to the FDEs 4) with both

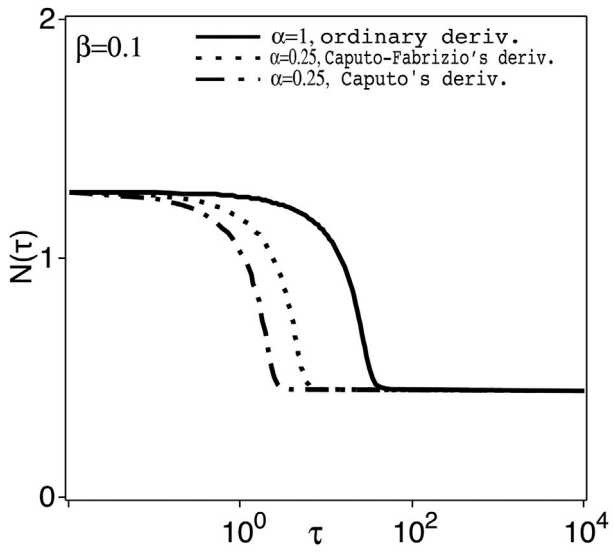

FIGURE 5
Data as in Figure 2, but with negative perturbation, $K_c - \beta$ at A_{off}, where K_c =3.0199.

Caputo's and Caputo-Fabrizio's fractional derivatives, Eqs. 5 and 6, respectively, are investigated by solving these FDEs numerically using the fractional Euler's method developed in [28, 48] (see Supplementary Appendix B for guidelines). This is done by replacing the control (input) parameter K in Equations 1–3) by $K_c \pm \beta$, or a in Equations 2, 4 by $a_c \pm \beta$, where β ($0 < \beta < 1$) is a small real perturbation of the relevant control parameter, and K_c, a_c are the initial (switch-on or switch-off) points of the bistable curves. Results are compared with the ordinary derivatives case ($\alpha = 1$) [14].

3.1 The spruce budworm model

The switching-on and off -points, A_{on} and A_{off}, respectively, of the steady state bistable curve (N vs. K) according to the ODE, Eq. 1, or the FDE; Eq. 3, i. e., $\frac{dN}{d\tau} = \frac{d^{\alpha}N}{d\tau^{\alpha}} = 0$, are shown in Figure 1, for fixed values of the parameters F and B (c.f [14]). For fixed positive perturbation parameter $\beta = 0.1$, the time delay τ_D to switch up to the upper branch of the bistable curve, Figure 2, is reduced in both cases of the fractional derivatives with smaller values of α, ($0 < \alpha < 1$), compared with the ordinary derivative case ($\alpha = 1$). This is confirmed in Figure 3 where for fixed $0 < \beta < 1$, τ_D vs. α best fits exponentially increasing function for $\alpha \in (0, 1)$ in both cases of fractional derivatives. Note in Figure 2, τ_D is slightly reduced in the case of Caputo-Fabrizio's fractional derivative, compared with Caputo's fractional derivative case. Further, for fixed fractional parameter $\alpha = 0.25$, for example, the lesser the perturbation parameter β, the larger is τ_D (i.e. slowing down)- Figures 4– like the case of $\alpha = 1$ [14]. For fixed negative value of perturbation- Figures 5– at the switching-off point A_{off} (in Figure 1), we have the same qualitative behaviour as in Figure 2, but with smooth delayed switching to the lower branch.

In both cases of positive and negative perturbations β) at the switching-on and -off points, A_{on} and A_{off}, respectively, the time delay

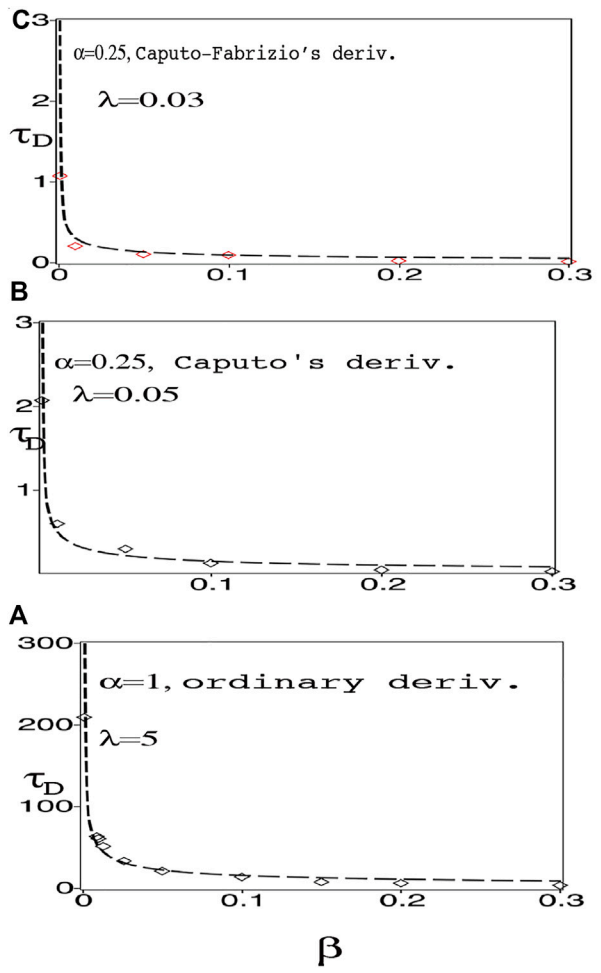

FIGURE 6
Time-delay, τ_D, *versus* the perturbation parameter β at the switching-on point A_{on} in Figure 1. Circles represent the numerical results and the dashed lines represent the corresponding fittings, $\lambda/\sqrt{\beta}$. **(A)** The case of ordinary derivative (α =1). **(B)** The case of Caputo's fractional derivative (α =0.25). **(C)** As **(B)** but with Caputo-Fabrizio's fractional derivative.

formula $\tau_D \sim|\beta|^{-1/2}$ (inverse square root scaling law) essentially holds in the both cases of Caputo's and Caputo-Fabrizio's fractional derivatives ($0 < \alpha < 1$), Figure 6, similar to the ordinary derivative case ($\alpha = 1$) [14], but with different proportionality factor.

3.2 The Thomas reaction model

The steady state bistable curves for the Oxygen and uric acid concentrations u, v, respectively, against the supplied rate a, according to Eq. 2 or 4) are shown in Figure 7, for fixed values of other system parameters [14]. For positive perturbation β in the ordinary derivative case ($\alpha = 1$) at the switching-on point, A_{on} in Figure 7, the transient oxygen concentration $u(\tau)$, Figure 8, shows similar qualitative behaviour of reducing τ_D in both cases of Caputo's and Caputo-Fabrizio's fractional derivatives, but with smaller quantitive difference. The same behaviour occurs with negative perturbation at the switching-off point A_{off} in Figure 7. Similar qualitative behaviour is

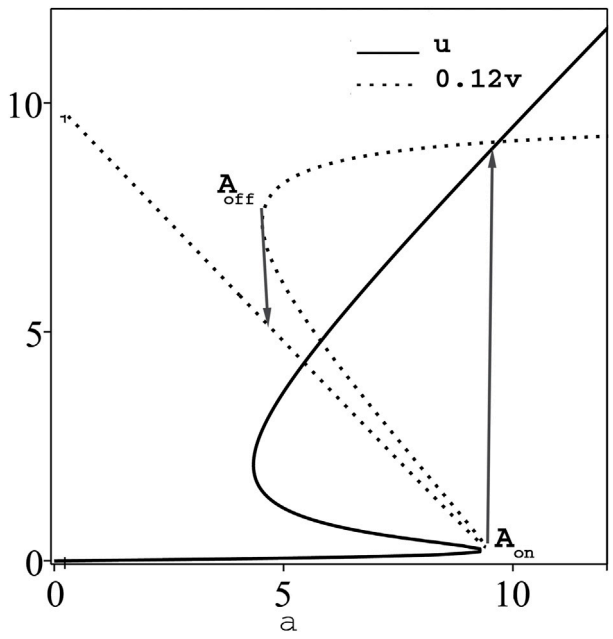

FIGURE 7
The steady state bistable curves, u and $0.12v$, *versus* the control parameter, a, for fixed parameters K =20, B =100, $\gamma = l$ =1.

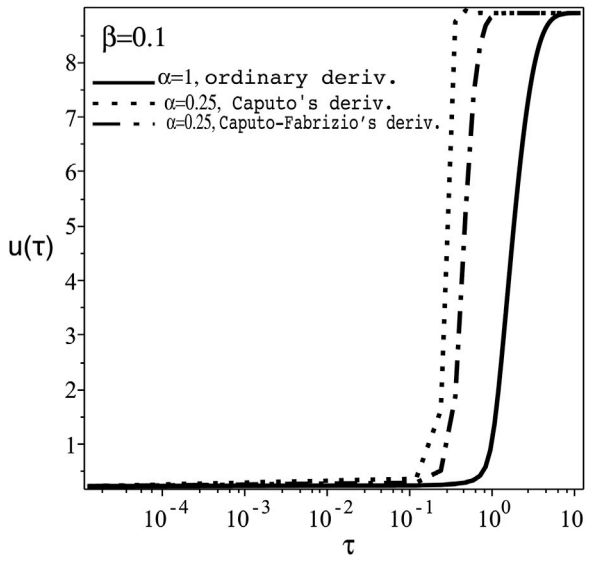

FIGURE 8
The transient Oxygen concentration, $u(\tau)$, *versus* the normalised time, τ with positive perturbation, $\kappa = a_c + \beta$, a_c =9.3643, at the switching-on point A_{on} of Figure 7 with fixed β =0.1 for α =1 (ordinary derivative) and 0.25 (Caputo's and Caputo-Fabrizio's fractional derivatives).

also exhibited for the transient uric acid concentration $v(t)$ for $\alpha = 1$ [14] and $\alpha < 1$. The time delay τ_D in both cases of $u(\tau)$ and $v(\tau)$ against the fractional parameter α and the perturbation parameter β shows similar qualitative behaviour as in Figures 3, 6, respectively.

4 Summary

Fractional order mathematical models generalise the concept of ordinary differentiation to incorporate memory (time delay) and spatial non-local effects, and hence provide extra fractional parameters to interpret/predict the dynamical behaviour of the concerned model and capture more of its details.In this paper, we have investigated the switching time response at the critical switching-on and -off points of the bistable curves related to two biological models, namely, the spruce budworm outbreak model [3, 4, 15] and the Thomas reaction model for enzyme membrane [4, 16] within fractional order models. Two definitions of fractional derivatives of order α, $(0 < \alpha < 1)$ have been used, namely, Caputo's [40] and Caputo-Fabrizio's [21, 22] fractional derivatives. Our study shows the following.

(i) The two definitions use convolution kernels of different variability that model the memory effect, namely, as power function [40] and as exponential function [21]. Both definitions yield the *same* qualitative results, (ii)-(iv) below, for the two biological models referred to above. The small quantitative variance in the results is due to the different mathematical forms for the memory or delay effect.

(ii) The switching time τ_D due to the perturbation in the control (input) parameter, at the critical points of the bistable curves, is reduced further in the fractional derivative case $(0 < \alpha < 1)$, compared with the ordinary derivative case $(\alpha = 1)$ [14],

(iii) For fixed perturbation β, τ_D as a function of the fractional derivative parameter, α, $(0 < \alpha < 1)$ fits an exponential form, i.e., τ_D is reduced with strong memory index $(\alpha \ll 1)$ and,

(iv) The switching time τ_D as a function of the perturbation parameter β fits the scaled inverse square root law $\frac{1}{\sqrt{\beta}}$ at fixed fractional derivative index $(\alpha < 1)$ as in the ordinary derivative case $(\alpha = 1)$ [14]. This is a further indication of the universality of this inverse square root law in both cases of ordinary and fractional derivative formulations. Experimental affirmation of this law in optical bistable models within ordinary derivative formation was reported in [42].

In general, fractional order models provide deeper insight into the system dynamics with memory taken, into effect and further motivate for experimental observation.Finally, we refer to some very recent works [43, 44] on biological models of COVID-19. In [43], the authors investigated various parameter estimation methods of COVID-19 incubation period using lognormal and Gamma distribution assumptions. The expressions for the maximum likelihood estimation, expectation maximisation algorithm and newly proposed algorithm [43] are termed as double or single (Riemann) integrals: these integral expressions can be converted to fractional integrals (i.e usual Riemann integral with memory or non-local, convolution kernel of fractional index, e.g. [23]), and so to have extra fractional order parameter. The other biological model of COVID-19 [44] is concerned with the stability and sensitivity analysis, and optimal control strategies of a suggested epidemic control of COVID-19. The adopted model of ODEs can be converted to FDEs and so to investigate the memory effect in this epidemic model. The formulation of the models in [43, 44] within fractional calculus will certainly add details concerning memory/non-local effects.

Data availability statement

The original contributions presented in the study are included in the article/Supplementary Material, further inquiries can be directed to the corresponding author.

Author contributions

RA: Conceptualization, Methodology, Software SH: Data curation, Writing- Original draft preparation. RA: Visualization, Investigation. SH: Supervision: RA: Software, Validation: SH: Writing- Reviewing and Editing. All authors contributed to the article and approved the submitted version.

Funding

The authors received the fund by the Deanship of Scientific Research (DSR), King Abdulaziz University, Jeddah under grant No. (G-184-247-1443).

Conflict of interest

The authors declare that the research was conducted in the absence of any commercial or financial relationships that could be construed as a potential conflict of interest.

Publisher's note

Supplementary material

The Supplementary Material for this article can be found online at: https://www.frontiersin.org/articles/10.3389/fphy.2023.1123370/full#supplementary-material

References

1. Gibbs HM. Optical bistability: Controling light with light. In: *Quantum electronics-principles and applications*. Massachusetts, United States: Academic Press (1985).

2. Mandel P, Erneux T. Nonlinear control in optical bistability. *IEEE J Quan Electron* (1985) 21:1352–5. doi:10.1109/jqe.1985.1072832

3. May RM. Thresholds and break points in ecosystems with a multiplicity of stable states. *Nature* (1977) 289:471–7. doi:10.1038/269471a0

4. Murray JD. *Mathematical biology: I. An introduction*. 3rd ed. Berlin, Germany: Springer (2002).

5. Cribier S, Giacobino E, Grynberg G. Quantitative investigation of critical slowing down in all-optical bistability. *Opt Commun* (1983) 47:170–2. doi:10.1016/0030-4018(83)90109-8

6. Garmire E, Marburger JH, Allen SD, Winful HG. Transient response of hybrid bistable optical devices. Appl. *Phys Lett* (1979) 34:374–6.

7. Shu Q, Rand SC. Critical slowing down and dispersion of avalanche upconversion dynamics. *Phys Rev B* (1997) 55:8776–83. doi:10.1103/physrevb.55.8776

8. Boettner C, Boers N. Critical slowing down in dynamical systems driven by nonstationary correlated noise. *Phys Rev Res* (2022) 4:013230–7. doi:10.1103/physrevresearch.4.013230

9. Wolchover N. Nature's critical warning system (2015). Available at https://www.quantamagazine.org/20151117-natures-critical-warning-system/ Accessed 2015.

10. Carpenter SR, Brock WA. Rising variance: A leading indicator of ecological transition. *Ecol Lett* (2006) 9:311–8. doi:10.1111/j.1461-0248.2005.00877.x

11. Dakos V, Scheffer M, van Nes EH, Brovkin V, Petoukhov V, Held H. Slowing down as an early warning signal for abrupt climate change. *Proc Natl Acad Sci* (2008) 105:14308–12. doi:10.1073/pnas.0802430105

12. Ditlevsen PD, Johnsen SJ. Tipping points: Early warning and wishful thinking. *Geophys Res Lett* (2010) 37:L19703. doi:10.1029/2010gl044486

13. Chisholm RA, Filotas E. Critical slowing down as an indicator of transitions in two-species models. *J Theor Biol* (2009) 257:142–9. doi:10.1016/j.jtbi.2008.11.008

14. Alharbey RA, Nejad LAM, Lynch S, Hassan SS. Critical slowing down in biological bistable models. *Int J. Pure Appl. Math.* (2014) 93:581–602. doi:10.12732/ijpam.v93i4.8

15. Ludwig D, Jones DD, Holling CS. Qualitative analysis of insect outbreak systems: The spruce budworm and forest. *J Anim Ecol* (1978) 47:315–32. doi:10.2307/3939

16. Thomas D. Artificial enzyme membranes, transport, memory and oscillation. In: D Thomas JP Kernevez, editors. *Analysis and control of immobilized enzyme systems*. Berlin Heidelberg New York: Springer (1975). p. pp115–150.

17. Machado JAT, Kiryakova V, Mainardi F. Recent history of fractional calculus. Commun. *Nonlinear Sci Numer Simulat* (2011) 16:1140–53.

18. Du M, Wong Z, Hu H. Measuring memory with the order of fractional derivative. *Scientific Rep* (2013) 3:3431–3. doi:10.1038/srep03431

19. De Oliveira, Edmundo CapelasJos Antnio Tenreiro Machado. A review of definitions for fractional derivatives and integral. *Math Probl Eng* (2014) 2014:1–6. doi:10.1155/2014/238459

20. Teodoro GS, Machado JT, De Oliveira EC. A review of definitions of fractional derivatives and other operators. *J Comput Phys* (2019) 388:195–208. doi:10.1016/j.jcp.2019.03.008

21. Caputo M, Fabrizio's M. A new definition of fractional derivative without singular kernel. *Progr Fract Differ Appl* (2015) 2:73–85.

22. Caputo M, Fabrizio M. Applications of new time and spatial fractional derivatives with exponential kernels. *Progr Fract Differ Appl* (2016) 2:1–11. doi:10.18576/pfda/020101

23. Podlubny I. *Fractional differential euqations*. Massachusetts, United States: Academic Press (1999).

24. Caputo M, Mainardi F. A new dissipation model based on memory mechanism. *Pure Appl Geophys* (1971) 91:134–47. doi:10.1007/bf00879562

25. Anastasio TJ. The fractional-order dynamics of brainstem vestibulo-oculomotor neurons. *Biol Cybernet* (1994) 72:69–79. doi:10.1007/bf00206239

26. Magin RL. *Fractional calculus in engineering*. USA: Begell House Publishers (2006).

27. Sweilam NH, Khader MM, Mahdy AMS. Computational methods for fractional differential equations generated by optimization problem. *J Fractional Calculus Appl* (2012) 3:1–12.

28. Tong P, Feng Y, Lv H. Euler's method for fractional differential equations. *WSEAS Transaction Maths* (2013) 12:1146–53.

29. Meral FC, Royston TJ, Magin R. Fractional calculus in viscoelasticity: An experimental study. *Commun Nonlinear Sci Numer Simulation* (2010) 15:939–45. doi:10.1016/j.cnsns.2009.05.004

30. Xu Z, Chen W. A fractional-order model on new experiments of linear viscoelastic Creep of hami melon. *Comput Maths Appl* (2013) 66:677–81. doi:10.1016/j.camwa.2013.01.033

31. Scheidegger AE, Johnson EF. The statistical behavior of instabilities in displacement processes in porous media. *Can J Phys* (1961) 39:326–34. doi:10.1139/p61-031

32. Verma AP. Statistical behavior of fingering in a displacement process in heterogeneous porous medium with capillary pressure. *Can J Phys* (1969) 47:319–24. doi:10.1139/p69-042

33. Bhathawala PH, Parveen S. Analytic study of three phase flow through porous media. *J Indian Acad Math* (2001) 23:17–24.

34. Prajapati JC, Patel AD, Pathak KN, Shukla AK. Fractional calculus approach in the study of instability phenomenon in fluid dynamics. *Palestine J Maths* (2012) 2:95–105.

35. West BJ, Turalska M. The fractional Landau model. *IEEE/CAA J Automatica Sinica.* (2016) 3:257–60.

36. Joshi H, Jha BK. Fractional-order mathematical model for calcium distribution in nerve cells. *Comput Appl Maths* (2020) 39:56–22. doi:10.1007/s40314-020-1082-3

37. Comlekoglu T, Weinberg SH. Memory in a fractional-order cardiomyocyte model alters voltage-and calcium-mediated instabilities. *Commun Nonlinear Sci Numer Simulation* (2020) 89:105340. doi:10.1016/j.cnsns.2020.105340

38. Ionescu C, Lopes A, Copot D, Machado JT, Bates JH. The role of fractional calculus in modeling biological phenomena: A review. *Commun Nonlinear Sci Numer Simulation* (2017) 51:141–59. doi:10.1016/j.cnsns.2017.04.001

39. Cooperputting NG. Design into turbulence. *los alamos Sci Technol Mag* (2009) 1663:10–5.

40. Caputo M. Linear models of dissipation whose Q is almost frequency independent, Part II. *J Roy Astr Soc* (1967) 13:529–39.

41. Alistair Steyn-Ross D, Steyn-Ross M. Modeling phase transition in the brain, *Springer series in computational neuroscience*, Springer, NewYork, NY, 2010.

42. Al-Attar HA, MacKenzie HA, Firth WJ. Critical slowing-down phenomena in an InSb optically bistable etalon. *JOSA B* (1986) 3:1157–63. doi:10.1364/josab.3.001157

43. Yin MZ, Zhu QW, L X. Parameter estimation of the incubation period of COVID-19 based on the doubly interval-censored data model. *Nonlinear Dyn* (2021) 106:1347–58. doi:10.1007/s11071-021-06587-w

44. L X, Hui HW, Liu F, Bai YL. Stability and optimal control strategies for a novel epidemic model of COVID-19. *Nonlinear Dyn* (2021) 106:1491–507. doi:10.1007/s11071-021-06524-x

45. Fowler AC. *Mathematical models in the applied sciences*. Cambridge, United Kingdom: Cambridge University Press (1997).

46. Barbotin JN, Thomas D. Electron microscopic and kinetic studies dealing with an artificial enzyme membrane. Application to a cytochemical model with the horseradish peroxidase-3,3'-diaminobenzidine system. *J Histochem Cytochem* (1974) 11:1048–59. doi:10.1177/22.11.1048

47. Chan YH, Boxer SG. Model membrane systems and their applications. *Curr Opin Chem Biol* (2007) 11:581–7. doi:10.1016/j.cbpa.2007.09.020

48. Zaid M. Odibat and shaher momani, an algorithm for the numerical solution of differential equations of fractional order. *J Appl Math Inform* (2008) 26(1-2):15–27.

frontiers | Frontiers in Physics

TYPE Original Research
PUBLISHED 10 March 2023
DOI 10.3389/fphy.2023.1133754

OPEN ACCESS

EDITED BY
Xiangpeng Xin,
Liaocheng University, China

REVIEWED BY
Jian Li,
Shanghai University, China
Haifeng Wang,
Jimei University, China

*CORRESPONDENCE
Liangji Sun,
ljsunuzz@163.com
Lihua Zhang,
zzlh100@163.com

SPECIALTY SECTION
This article was submitted to Mathematical Physics, a section of the journal Frontiers in Physics

RECEIVED 29 December 2022
ACCEPTED 26 January 2023
PUBLISHED 10 March 2023

CITATION
Wang Z, Sun L, Hua R, Su L and Zhang L (2023), Time-fractional generalized fifth-order KdV equation: Lie symmetry analysis and conservation laws. *Front. Phys.* 11:1133754. doi: 10.3389/fphy.2023.1133754

Time-fractional generalized fifth-order KdV equation: Lie symmetry analysis and conservation laws

Zhenli Wang[1], Liangji Sun[1]*, Rui Hua[1], Lingde Su[1] and Lihua Zhang[2]*

[1]School of Mathematical and Statistics, Zaozhuang University, Zaozhuang, China, [2]School of Mathematical and Statistics, Hebei University of Economics and Business, Shijiazhuang, China

The purpose of this study is to apply the Lie group analysis method to the time-fractional order generalized fifth-order KdV (TFF-KdV) equation. We examine applying symmetry analysis to the TFF-KdV equation with the Riemann–Liouville (R–L) derivative, employing the G'/G-expansion approach to yield trigonometric, hyperbolic, and rational function solutions with arbitrary constants. The discovered solutions are unique and have never been studied previously. For solving non-linear fractional partial differential equations, we find that the G'/G-expansion approach is highly effective. Finally, conservation laws for the equation are well-built with a full derivation based on the Noether theorem.

KEYWORDS

Lie group analysis, Riemann–Liouville derivative, time-fractional generalized fifth-order KdV (TFF-KdV) equation, G'/G-expansion method, conservation laws

1 Introduction

The soliton solutions of non-linear evolution equations have has a significant impact on the flesh and have been widely used in wide ranges of physical and biological sciences, such as non-linear optics, plasma physics, fluid dynamics, biochemistry, and mathematical chemistry. In recent years, fractional partial differential equations (FPDEs) have attracted great attention and have been extensively investigated. The non-linear FPDEs can be found in different fields of science and engineering problems, such as signal processing, mechanics, plasma physics, finance, electricity, stochastic dynamical system, control theory, economics, and electrochemistry [1–6]. Several efficient methods have been presented to solve FPDEs of interest. It is necessary to point out that some methods used for solving non-linear FPDEs are actually to construct numerical and analytical methods, such as the fractional sub-equation method [7–10], tanh-function method [11–13], Adomian decomposition method [14–17], variational iteration method [18–20], trial equation method [21, 22], homotopy perturbation method [23, 24], exponential rational function method [25], Riccati sub-equation method [26], and rational G'/G-expansion method [27], which have been applied to handle the non-linear evolution equations.

As far as we know, the fractional differentiation and integration operators have a variety of definitions so that we can mention them, like the Riemann–Liouville definition [3, 28] and the Caputo definition [29]. Recently, [30] proposed a new simple definition of the fractional derivative named the conformable fractional derivative, which can redress shortcomings of many definitions.

In this paper, we consider the following time-fractional generalized fifth-order KdV (TFF-KdV) equation:

$$u_t^\alpha + u^2 u_x - u u_{xxx} + u_{xxxxx} = 0. (0 < \alpha < 1), \tag{1.1}$$

where $0 < \alpha \le 1, D_t^\alpha = \partial^\alpha u/\partial t^\alpha$.When $\alpha = 1$, Eq. 1 can be reduced to a generalized fifth-order KdV equation of general meaning.

Some of the researchers have investigated different kinds of exact solutions for different orders of KdV equations. For example, Wang [31] has found some new exact solutions of the fifth-order KdV equation with the Lie point symmetry group method, while Abdel-Salam A B and Al-Muhiameed Z I A [32] have provided the exact solutions for the KdV–mKdV equation by applying the analytic solution method. Recently, an efficient numerical scheme has been developed to solve a linearized time-fractional KdV equation by Zhang [33].

Our aim in the present work is to investigate many new closed-form solutions of the TFF-KdV equation by using Lie group analysis and the G'/G-expansion method with the Riemann–Liouville (R–L) derivative. These algebraic methods can be regarded as the most concise and the most efficient methods for searching the closed-form solutions of the non-linear FPDEs.

The rest of the article is organized as follows: the basic definitions and properties of the fractional calculus are being considered in terms of the Riemann–Liouville derivative in Section 2. In Section 3, we briefly give an account of the Lie symmetry analysis method for the TFF-KdV equation. We perform the Lie group classification on the TFF-KdV equation and investigate the symmetry reductions of the TFF-KdV equation. The main steps of the improved G'/G-expansion method are given, and the exact solutions of the TFF-KdV equation are obtained in Section 4. In Section 5, conservation laws of the TFF-KdV equation are constructed by using the Noether theorem. Finally, in Section 6 of this paper, we will discuss the results obtained.

2 Foreword

As to the fractional derivative operators, various definitions which are not necessarily equivalent to each other exist. In this paper, we would like to consider the most common definition that is named after the Riemann and Liouville derivative, which is the natural generalization of the Cauchy formula for the n-fold primitive of a function $f(x)$. The Riemann–Liouville (R–L) fractional derivative is defined as follows [34]:

$$D_t^\alpha f = \begin{cases} \dfrac{d^n f}{dt^n} I^{n-\alpha} f(t), & 0 \le n-1 < \alpha < n, \\ \dfrac{d^n f}{dt^n}, & \alpha = n, \end{cases}, \tag{2.1}$$

where $n \in \mathbb{N}$ and $I^\mu f(t)$ is the R–L fractional integral of order μ, namely,

$$I^\mu f(t) = \frac{1}{\Gamma(\mu)} \int_0^t (t-\xi)^{\mu-\alpha} f(\xi) d\xi, \ \mu > 0$$
$$I^0 f(t) = f(t),$$

and $\Gamma(z)$ is the standard Gamma function.

Definition 1. The R–L fractional partial derivative is defined by

$$D_t^\alpha f = \begin{cases} \dfrac{1}{\Gamma(n-\alpha)} \dfrac{\partial}{\partial t^n} \displaystyle\int_0^t (t-\xi)^{n-\alpha-1} u(\xi, x) d\xi, & 0 \le n-1 < \alpha < n, \\ \dfrac{\partial f}{\partial t^n}, & \alpha = n. \end{cases} \tag{2.2}$$

If it exists, $\partial_t^n$is the usual partial derivative of the integer order n [31, 35].

In [34], some useful formulas and properties are provided. Here, we only mention the following:

$$D_t^\alpha t^\gamma = \frac{\Gamma(\gamma+1)}{\Gamma(\gamma+1-\alpha)} t^{\gamma-\alpha}, \gamma > 0, \tag{2.3}$$

$$D_t^\alpha [u(t) v(t)] = u(t) D_t^\alpha v(t) + v(t) D_t^\alpha u(t), \tag{2.4}$$

$$D_t^\alpha [(f(u(t)))] = f'_u [u(t)] D_t^\alpha v(t) = D_u^\alpha f[u(t)] (u_t')^\alpha. \tag{2.5}$$

Definition 2. The generalized Leibnitz rule [36, 37] is defined by

$$D_t^\alpha [u(t) v(t)] = \sum_{n=0}^{\infty} \binom{\alpha}{n} D_t^{\alpha-n} u(t) D_t^n v(t), \ \alpha > 0, \tag{2.6}$$

where

$$\binom{\alpha}{n} = \frac{(-1)^{n-1} \alpha \Gamma(n-\alpha)}{\Gamma(1-\alpha)\Gamma(n+1)}. \tag{2.7}$$

Definition 3. Considering the generalization of the chain rule [31]for composite functions, we have

$$\frac{d^m f(g(t))}{dt^m} = \sum_{k=1}^{m} \sum_{r=0}^{k} \binom{k}{r} \frac{1}{k!} [-g(t)]^r \frac{d^m}{dt^m} [g(t)^{k-r}] \frac{d^k f(g)}{dt^k}. \tag{2.8}$$

3 Lie symmetry analysis for fractional partial differential equations

In this section, we consider the time-fractional differential equations as the form:

$$D_t^\alpha (u) = G(x, t, u, u_x, u_{xx}, \ldots), \ (0 < \alpha < 1), \tag{3.1}$$

where $u = u(x,t), u_x = \partial u/\partial x$, and $D_t^\alpha u$ is a fractional derivative of u with respect to t. Subject to the Lie theory, if Eq. 3.1 is a invariant under a one-parameter Lie group of point transformations, then

$$\begin{aligned} t^\star &= t + \varepsilon\tau(x,t,u) + O(\varepsilon^2), x^\star = x + \varepsilon\varsigma(x,t,u) + O(\varepsilon^2), \\ u^\star &= u + \varepsilon\eta(x,t,u) + O(\varepsilon^2), \\ \frac{\partial u^\star}{\partial t^\star} &= \frac{\partial^\alpha u}{\partial t^\alpha} + \varepsilon\eta_\alpha^0(x,t,u) + O(\varepsilon^2), \\ \frac{\partial u^\star}{\partial x^\star} &= \frac{\partial u}{\partial x} + \varepsilon\eta^x(x,t,u) + O(\varepsilon^2), \\ &\vdots \\ \frac{\partial^5 u^\star}{\partial x^{\star 5}} &= \frac{\partial^5 u}{\partial x^5} + \varepsilon\eta^{xxxxx}(x,t,u) + O(\varepsilon^2), \end{aligned} \tag{3.2}$$

where $\varepsilon \ll 1$ is a small parameter, and

$$\begin{aligned} \eta^x &= D_x(\eta) - u_x D_x(\varsigma) - u_t D_x(\tau), \\ \eta^{xx} &= D_x(\eta^x) - u_{xt} D_x(\tau) - u_{xx} D_x(\varsigma), \\ \eta^{xxx} &= D_x(\eta^{xx}) - u_{xxt} D_x(\tau) - u_{xxx} D_x(\varsigma), \\ \eta^{xxxx} &= D_x(\eta^{xxx}) - u_{xxxt} D_x(\tau) - u_{xxxx} D_x(\varsigma), \\ \eta^{xxxxx} &= D_x(\eta^{xxxx}) - u_{xxxxt} D_x(\tau) - u_{xxxxx} D_x(\varsigma). \end{aligned} \tag{3.3}$$

Here, D_x denotes the total derivative.

$$D_x = \frac{\partial}{\partial x} + u_x\frac{\partial}{\partial u} + u_{xx}\frac{\partial}{\partial u_x} + \cdots, \tag{3.4}$$

and the vector field associated with the aforementioned group of transformations can be written as

$$\mathrm{V} = \varsigma(x,t,u)\frac{\partial}{\partial x} + \tau(x,t,u)\frac{\partial}{\partial t} + \eta(x,t,u)\frac{\partial}{\partial u}. \tag{3.5}$$

If the vector field Eq. 3.5 generates a symmetry of Eq. 3.1, then V must satisfy Lie's symmetry condition.

$$\mathrm{Pr}^{(n)}\mathrm{V}\Delta\big|_{\Delta=0} = 0, \tag{3.6}$$

where $\Delta = D_t^\alpha(u) - G(x,t,u,u_x,u_{xx},\ldots)$.

Conversely, the corresponding group transformations (Eq. 3.2) to a known operator (Eq. 3.6) are found by solving the Lie equations.

$$\begin{aligned}\frac{d(\bar{x}(\varepsilon))}{d\varepsilon} &= \varsigma(\bar{x}(\varepsilon),\bar{t}(\varepsilon),\bar{u}(\varepsilon)),\ \bar{x}(0) = x,\\ \frac{d(\bar{u}(\varepsilon))}{d\varepsilon} &= \eta(\bar{x}(\varepsilon),\bar{t}(\varepsilon),\bar{u}(\varepsilon)),\ \bar{u}(0) = u.\end{aligned} \tag{3.7}$$

It is not different to observe that Eq. 3.2 conserves the structure of the fractional derivative infinitesimal operator Eq. 2.1. As the lower limit of the integral is constant, it should be in variant with respect to Eq. 3.2. Therefore, we can arrive at

$$\tau(x,t,u)|_{t=0} = 0. \tag{3.8}$$

For the R–L fractional time derivative [31, 35, 38], Eq. 3.8 can be changed into

$$\begin{aligned}\eta_\alpha^0 &= D_t^\alpha(\eta) + \varsigma D_t^\alpha(u_x) - D_t^\alpha(\varsigma u_x) + D_t^\alpha(D_t(\tau)u) - D_t^{\alpha+1}(\tau u)\\ &\quad + \tau D_t^{\alpha+1}(u).\end{aligned} \tag{3.9}$$

By means of the generalized Leibnitz rule (Eq.2.6), Eq.3.9 can be read as

$$\begin{aligned}\eta_\alpha^0 &= D_t^\alpha(\eta) - \alpha D_t(\tau)\frac{\partial^\alpha u}{\partial t^\alpha} - \sum_{n=1}^{k}\binom{\alpha}{n}D_t^n(\varsigma)D_t^{\alpha-n}(u_x)\\ &\quad - \sum_{n=1}^{\infty}\binom{\alpha}{n+1}D_t^{n+1}(\tau)D_t^{\alpha-n}(u).\end{aligned} \tag{3.10}$$

Furthermore, by applying the chain rule in Eq. 2.8 and the generalized Leibnitz rule in Eq. 3.10 with $f(t) = 1$, we can arrive at

$$\eta_t^\alpha = \frac{\partial^\alpha\eta}{\partial t^\alpha} + \eta_u\frac{\partial^\alpha u}{\partial t^\alpha} - u\frac{\partial^\alpha\eta_u}{\partial t^\alpha} + \sum_{n=1}^{\infty}\binom{\alpha}{n}\frac{\partial^n\eta_u}{\partial t^n}D_t^{\alpha-n}(u) + \mu, \tag{3.11}$$

where

$$\begin{aligned}\mu &= \sum_{n=2}^{\infty}\sum_{m=2}^{n}\sum_{k=2}^{m}\sum_{r=o}^{k-1}\binom{\alpha}{n}\binom{n}{m}\\ &\quad\times\binom{k}{r}\frac{1}{k!}\frac{t^{n-\alpha}}{\Gamma(n+1-\alpha)}(-u)^r\frac{\partial^m}{\partial t^m}\left(u^{k-r}\right)\frac{\partial^{n-m+k}\eta}{\partial t^{n-m}\partial u^k}.\end{aligned} \tag{3.12}$$

It should be noted that we have $\mu = 0$ when the infinitesimal η is linear of the variable u, considering the existence of the derivatives $\frac{\partial^k\eta}{\partial u^k}, k \geq 2$ in the aforementioned expression. To sum up the aforementioned reasonings, the explicit form of $\eta^{\alpha,t}$ is obtained.

$$\begin{aligned}\eta^{\alpha,t} &= \frac{\partial^\alpha\eta}{\partial t^\alpha} + (\eta_u - \alpha D_t(\tau))\frac{\partial^\alpha u}{\partial t^\alpha} - u\frac{\partial^\alpha\eta_u}{\partial t^\alpha}\\ &\quad + \mu + \sum_{n=1}^{\infty}\left[\binom{\alpha}{n}\frac{\partial^\alpha\eta_u}{\partial t^\alpha} - \binom{\alpha}{n+1}D_t^{n+1}(\tau)\right]\times D_t^{\alpha-n}(u)\\ &\quad - \sum_{n=1}^{\infty}\binom{\alpha}{n}D_t^n(\varsigma)D_t^{\alpha-n}(u_x).\end{aligned} \tag{3.13}$$

According to the Lie theory, we have the following theorems:

Theorem 1. The function $u = \phi(x, t)$ is an invariant solution of Eq. 3.1 if and only if

(i)$\mathrm{V}\phi = 0 \Leftrightarrow (\varsigma(x,t,u)\frac{\partial}{\partial x} + \tau(x,t,u)\frac{\partial}{\partial t} + \eta(x,t,u)\frac{\partial}{\partial u})\phi = 0$, and

(ii)$u = \phi(x, t)$ is the solution of FDPEs, as in Eq. 3.1.

4 The time-fractional fifth-order KdV equation

In the previous section, we have elaborated some definitions and formulas of the Lie symmetry analysis method of FPDEs. Now in this part, we are going to deal with the invariance properties of the TFF-KdV equation. Next, we will give some exact and explicit solutions to the TFF-KdV equation.

4.1 Lie symmetry of the TFF-KdV equation

By using the Lie group theory, we can derive the corresponding system of the symmetry equations as

$$\eta_\alpha^0 + 2u^2\eta^x + 4u\eta u_x - \eta u_{xxx} - u\eta^{xxx} + \eta^{xxxxx} = 0. \tag{4.1}$$

By solving Eq. 3.1 with the help of Eq. 3.3, we can obtain

$$\varsigma = c_1x + c_2, \tau = \frac{5c_1}{\alpha}t, \eta = -2c_1u, \tag{4.2}$$

where c_1 and c_2 are arbitrary constants. Furthermore, the corresponding operator can be arrived at

$$\mathrm{V} = (c_1x + c_2)\frac{\partial}{\partial x} + \frac{5c_1t}{\alpha}\frac{\partial}{\partial t} - 2c_1u\frac{\partial}{\partial u}. \tag{4.3}$$

Similarly, the Lie algebra of infinitesimal symmetries of Eq. 1.1 is spanned by the two vector fields:

$$\mathrm{V}_1 = \frac{\partial}{\partial x}, \mathrm{V}_2 = x\frac{\partial}{\partial x} + \frac{5t}{\alpha}\frac{\partial}{\partial t} - 2u\frac{\partial}{\partial u}. \tag{4.4}$$

It is easy to check that the vector fields are closed under the Lie bracket, respectively,

$$[\mathrm{V}_1,\mathrm{V}_2] = 2\mathrm{V}_1,\ [\mathrm{V}_2,\mathrm{V}_1] = -2\mathrm{V}_1. \tag{4.5}$$

In order to obtain the similarity variables for V_2, we have to solve the corresponding characteristic equations.

$$\frac{dx}{x} = \frac{\alpha dt}{5t} = \frac{du}{-2u}. \tag{4.6}$$

Thus, we derive the group-invariant solution and group-invariant as follows:

$$\theta = xt^{-\frac{\alpha}{5}},\ u = t^{-\frac{2\alpha}{5}} g(\theta). \tag{4.7}$$

It is not difficult to observe that Eq. 1.1 is reduced to a non-linear ordinary differential equation (NODE). We derived a theorem as follows:

Theorem 2. The TFF-KdV equation Eq. 1.1 can be reduced into a NODE of fractional order by transformation in Eq. 4.7 as follows:

$$\left(P_{\frac{5}{\alpha}}^{1-\frac{7\alpha}{5},\alpha} g\right)(\theta) = g^2 g_\theta - g g_{\theta\theta\theta} + g_{\theta\theta\theta\theta\theta}, \tag{4.8}$$

with the Erdelyi–Kober (EK) fractional differential operator $P_\beta^{\tau,\alpha}$ of order [34].

$$\left(P_\beta^{\tau^2,\alpha} g\right) := \prod_{j=0}^{n-1}\left(\tau^2 + j - \frac{1}{\beta}\theta\frac{d}{d\theta}\right)\left(K_\beta^{\tau^2+\alpha,n-\alpha} g\right)(\theta), \tag{4.9}$$

$$n = \begin{cases} [\alpha]+1, & \alpha \neq \mathbb{N}, \\ \alpha & \alpha \in \mathbb{N}, \end{cases} \tag{4.10}$$

where

$$\left(K_\beta^{\tau^2,\alpha} g\right) := \begin{cases} \dfrac{1}{\Gamma(\alpha)}\displaystyle\int_1^\infty (u-1)^{\alpha-1} u^{-\left(\tau^2+\alpha\right)} g\left(\theta u^{\frac{1}{\beta}}\right) du, & \alpha > 0, \\ g(\theta), & \alpha = 0, \end{cases} \tag{4.11}$$

is the EK fractional integral operator [39, 40].

Let $n-1 < \alpha < n$, $n = 1, 2, 3, \ldots$. Based on the R–L fractional derivative for the similarity transformation (Eq. 4.7), we have

$$\frac{\partial^\alpha u}{\partial t^\alpha} = \frac{\partial^n}{\partial t^n}\left[\frac{1}{\Gamma(n-\alpha)}\int_0^t (t-s)^{n-\alpha-1} s^{\frac{-2\alpha}{5}} g\left(x s^{\frac{-\alpha}{5}}\right) ds\right]. \tag{4.12}$$

Taking $v = t/s$, one can obtain $ds = -\frac{t}{v^2} dv$. Then Eq. 4.12, can be written as

$$\frac{\partial^\alpha u}{\partial t^\alpha} = \frac{\partial^n}{\partial t^n}\left[t^{n-\frac{7\alpha}{5}} \frac{1}{\Gamma(n-\alpha)}\int_1^\infty (v-1)^{n-\alpha-1} v^{-n+\frac{7\alpha}{5}-1} g\left(\theta v^{\frac{\alpha}{5}}\right) dv\right]. \tag{4.13}$$

If we use the definition of the EK fractional integral operator (Eq. 4.11), then Eq. 4.13 will be

$$\frac{\partial^\alpha u}{\partial t^\alpha} = \frac{\partial^n}{\partial t^n}\left[t^{n-\frac{7\alpha}{5}}\left(K_{\frac{5}{\alpha}}^{1-\frac{2\alpha}{5},n-\alpha} g\right)(\theta)\right]. \tag{4.14}$$

Now, we attempt to simplify the right hand side of Eq. 4.14. Taking into account $\theta = xt^{-\frac{\alpha}{5}}, \rho \in C^1(0,\infty)$, we can obtain

$$t\frac{\partial}{\partial t}\rho(\theta) = tx\left(-\frac{\alpha}{5}\right) t^{-\frac{\alpha}{5}-1}\rho'(\theta) = -\frac{\alpha}{5}\theta\frac{\partial}{\partial\theta}\rho(\theta). \tag{4.15}$$

One can arrive at

$$\begin{aligned} &\frac{\partial^n}{\partial t^n}\left[t^{n-\frac{7\alpha}{5}}\left(K_{\frac{5}{\alpha}}^{1-\frac{2\alpha}{5},n-\alpha} g\right)(\theta)\right] \\ &= \frac{\partial^{n-1}}{\partial t^{n-1}}\left[\frac{\partial}{\partial t}\left(t^{n-\frac{7\alpha}{5}}\left(K_{\frac{5}{\alpha}}^{1-\frac{2\alpha}{5},n-\alpha} g\right)(\theta)\right)\right] \\ &= \frac{\partial^{n-1}}{\partial t^{n-1}}\left[t^{n-\frac{7\alpha}{5}}\left(n - \frac{7\alpha}{5} - \frac{\alpha}{5}\theta\frac{\partial}{\partial\theta}\left(K_{\frac{5}{\alpha}}^{1-\frac{2\alpha}{5},n-\alpha} g\right)(\theta)\right)\right]. \end{aligned} \tag{4.16}$$

Through repeating the same procedure $n-1$ times, we obtain the following equation:

$$\begin{aligned} &\frac{\partial^n}{\partial t^n}\left[t^{n-\frac{7\alpha}{5}}\left(K_{\frac{5}{\alpha}}^{1-\frac{2\alpha}{5},n-\alpha} g\right)(\theta)\right] \\ &= \frac{\partial^{n-1}}{\partial t^{n-1}}\left[\frac{\partial}{\partial t}\left(t^{n-\frac{7\alpha}{5}}\left(K_{\frac{5}{\alpha}}^{1-\frac{2\alpha}{5},n-\alpha} g\right)(\theta)\right)\right] \\ &= \frac{\partial^{n-1}}{\partial t^{n-1}}\left[t^{n-\frac{7\alpha}{5}}\left(n - \frac{7\alpha}{5} - \frac{\alpha}{5}\theta\frac{\partial}{\partial\theta}\left(K_{\frac{5}{\alpha}}^{1-\frac{2\alpha}{5},n-\alpha} g\right)(\theta)\right)\right] \\ &\vdots \\ &= t^{-\frac{7\alpha}{5}}\prod_{j=0}^{n-1}\left(1 - \frac{7\alpha}{5} + j - \frac{\alpha}{5}\theta\frac{\partial}{\partial\theta}\right)\left(K_{\frac{5}{\alpha}}^{1-\frac{2\alpha}{5},n-\alpha} g\right)(\theta). \end{aligned} \tag{4.17}$$

Then, by using Eq. 4.9, we find that

$$\frac{\partial^n}{\partial t^n}\left[t^{n-\frac{7\alpha}{5}}\left(K_{\frac{5}{\alpha}}^{1-\frac{2\alpha}{5},n-\alpha} g\right)(\theta)\right] = t^{-\frac{7\alpha}{5}}\left(P_{\frac{5}{\alpha}}^{1-\frac{7\alpha}{5},\alpha} g\right)(\theta). \tag{4.18}$$

Substituting Eq. 4.18 into Eq. 4.14, the following expression for the time-fractional derivative is obtained:

$$\frac{\partial^\alpha u}{\partial t^\alpha} = t^{-\frac{7\alpha}{5}}\left(P_{\frac{5}{\alpha}}^{1-\frac{7\alpha}{5},\alpha} g\right)(\theta). \tag{4.19}$$

Thus, the TFF-KdV equation Eq. 1.1 can be reduced into a fractional-order ODE as follows:

$$\left(P_{\frac{5}{\alpha}}^{1-\frac{7\alpha}{5},\alpha} g\right)(\theta) = g^2 g_\theta - g g_{\theta\theta\theta} + g_{\theta\theta\theta\theta\theta}. \tag{4.20}$$

By this mean, the proof of theorem 2 is completed.

4.2 The G'/G-expansion method for the non-linear FPDEs

A general non-linear conformable time FPDE can be written as follows:

$$P\left(u, u_t^\alpha, u_x, u_t^{2\alpha}, u_{xx}, \ldots\right) = 0,\ (0 < \alpha < 1), \tag{4.21}$$

where u is an unknown function of independent variables x and t, and P is a polynomial in $u = u(x, t)$ and its partial fractional derivatives, where the highest order derivatives and non-linear terms are involved.

Next, we will illustrate the major steps of the G'/G-expansion method [41].

Step 1. Combining the independent variables x and t into one variable $\xi = kx + l\frac{t^\alpha}{\alpha}$, it is supposed that

$$u(x,t) = \phi(\xi), \xi = kx + l\frac{t^\alpha}{\alpha}, \tag{4.22}$$

where k, l are constants that will be determined later.

The traveling wave variable in Eq. 4.22 permits us to reduce Eq. 4.21 to an ODE for $u(x, t) = \phi(\xi)$,

$$P\left(\phi, -l\phi', k\phi', l^2\phi'', k^2\phi'', \ldots\right) = 0. \tag{4.23}$$

Step 2. Assuming that the exact solution of Eq. 4.23 can be expressed by the polynomial in (ω/G) and ω, G satisfies the following relation

$$\left(\frac{\omega}{G}\right)' = a + b\left(\frac{\omega}{G}\right) + c\left(\frac{\omega}{G}\right)^2, \tag{4.24}$$

namely,

$$\omega' G - \omega G' = aG^2 + b\omega G + c\omega^2, \tag{4.25}$$

where a, b, c are arbitrary constants. Now, let us have a careful examination on Eq. 4.24. If choosing $\omega = G'$, $a = -\mu$, $= -\lambda$, $c = -1$, then $u(\xi)$ can be expressed as

$$u(\xi) = \sum_{i=0}^{m} a_i \left(\frac{G'}{G}\right)^i, \tag{4.26}$$

where G satisfies the second-order LODE in the form

$$G'' + \lambda G' + \mu G = 0. \tag{4.27}$$

In here, the general solutions of Eq. 4.27 are as follows:

$$\frac{G'(\xi)}{G(\xi)} = \begin{cases} \frac{-\lambda}{2} + \frac{\sqrt{\lambda^2 - 4\mu}}{2}\left(\frac{C_1 \sinh\left(\frac{\sqrt{\lambda^2-4\mu}}{2}\xi\right) + C_2 \cosh\left(\frac{\sqrt{\lambda^2-4\mu}}{2}\xi\right)}{C_1 \cosh\left(\frac{\sqrt{\lambda^2-4\mu}}{2}\xi\right) + C_2 \sinh\left(\frac{\sqrt{\lambda^2-4\mu}}{2}\xi\right)}\right) & \lambda^2 - 4\mu > 0, \\ \frac{-\lambda}{2} + \frac{C_2}{C_1 + C_2 \xi} & \lambda^2 - 4\mu = 0, \\ \frac{-\lambda}{2} + \frac{\sqrt{\lambda^2 - 4\mu}}{2}\left(\frac{-C_1 \sin\left(\frac{\sqrt{\lambda^2-4\mu}}{2}\xi\right) + C_2 \cos\left(\frac{\sqrt{\lambda^2-4\mu}}{2}\xi\right)}{C_1 \cos\left(\frac{\sqrt{\lambda^2-4\mu}}{2}\xi\right) + C_2 \sin\left(\frac{\sqrt{\lambda^2-4\mu}}{2}\xi\right)}\right) & \lambda^2 - 4\mu < 0. \end{cases} \tag{4.28}$$

This is just the G'/G-expansion method that Wang et al [42] have proposed recently.

Furthermore, if we put $\omega = \tanh\xi, g = 1, a = 1, b = 0, c = -1$, then $u(\xi)$ turns to be $u(\xi) = \sum_{i=0}^{m} a_i (\tanh\xi)^i$, which is the tanh-function expansion method.

Step 3. Substituting Eq. 4.24 into Eq. 4.23 and using second-order LODE, collecting all terms with the same order of G'/G together, we will obtain the system of algebraic equations for $a_m \cdots\cdots$, l, λ, and μ.

Step 4. Substituting the results obtained in the aforementioned steps into Eq. 4.26.

4.3 The application to the TFF-KdV equation using the G'/G-expansion method

Considering the TFF-KdV equation as follows:

$$u_t^\alpha + u^2 u_x - u u_{xxx} + u_{xxxxx} = 0. (0 < \alpha < 1). \tag{4.29}$$

Eq. 4.29 has been investigated in [31] by using the Lie symmetry analysis. Now, we will use the G'/G-expansion method to find the closed-form solutions to the TFF-KdV equation. For this purpose, we will apply the traveling wave transformation as follows:

$$u(x,t) = \phi(\xi), \xi = x + l\frac{t^\alpha}{\alpha}, \tag{4.30}$$

where l is the constant that will be determined later. The transformation of Eq. 4.29 and Eq. 4.30 leads to the following equation:

$$l\phi' + \phi^2\phi' - \phi\phi''' + \phi^{'''''} = 0. \tag{4.31}$$

Eq. 4.31 is integrable; thus, once integrating with respect to ξ, we can obtain the following result:

$$l\phi + \frac{1}{3}\phi^3 + \phi\phi'' - \frac{1}{2}(\phi')^2 + \phi^{''''} + C = 0, \tag{4.32}$$

where C is the integral constant that will be determined later.

Considering the homogeneous balance between ϕ^3 and ϕ'''' in Eq. 4.32, $3m = m + 4$ gives $m = 2$. Thus, we can write Eq. 4.32 as

$$\phi = a_0 + a_1\left(\frac{g'}{g}\right) + a_2\left(\frac{g'}{g}\right)^2. \tag{4.33}$$

By substituting Eqs 4.33 and 4.27 into Eq. 4.32 and collecting all terms with the same power of $(\frac{G'}{G})$ together, the left-hand side of Eq. 4.32 is converted into another polynomial in $(\frac{G'}{G})$. Equating the coefficients of this polynomial to zero yields a set of simultaneous algebraic equations for a_2, a_1, a_0, l, λ, μ and C. Solving the algebraic equations, we obtain

$$\begin{aligned} &a_2 = -12,\ a_1 = -12\lambda,\ a_0 = -1 - 3\lambda^2, \\ &\lambda = \lambda, \mu = \frac{\lambda^2 + 1}{4}, l = \frac{1}{2}\left(48\mu^2 - 24\mu\lambda^2 + 3\lambda^2 - 5\right), \end{aligned} \tag{4.34}$$

where λ, μ and a_0 are arbitrary constants.

We substitute Eq. 4.34 with Eq. 4.28 into Eq. 4.32 and obtain the closed-form solutions of Eq. 4.32as three types, which are as follows:

When $\lambda^2 - 4\mu > 0$, we can obtain the hyperbolic function solutions as follows:

$$\begin{aligned} \phi(\xi) &= -\left[(1 + 3\lambda^2) + 12\lambda\left(\frac{g'}{g}\right) + 12\left(\frac{g'}{g}\right)^2\right] \\ &= -\left[1 + 3\left(\lambda^2 - 4\mu\right)\left(\frac{C_1 \sinh\left(\frac{\sqrt{\lambda^2-4\mu}}{2}\xi\right) + C_2 \cosh\left(\frac{\sqrt{\lambda^2-4\mu}}{2}\xi\right)}{C_1 \cosh\left(\frac{\sqrt{\lambda^2-4\mu}}{2}\xi\right) + C_2 \sinh\left(\frac{\sqrt{\lambda^2-4\mu}}{2}\xi\right)}\right)^2\right], \end{aligned} \tag{4.35}$$

where $\xi = x + \frac{1}{2}\left(48\mu^2 - 24\mu\lambda^2 + 3\lambda^2 - 5\right)\left(\frac{t^\alpha}{\alpha}\right)$, and C_1 and C_2 are arbitrary constants.

Taking C_1 and C_2 special values, then different known solutions can be deduced from Eq. 4.35.

For example,

(i) If $C_1 = 0$ and $C_2 \neq 0$, we have

$$\phi(\xi) = -\left[1 + 3\left(\lambda^2 - 4\mu\right)\coth^2\left(\frac{\sqrt{\lambda^2 - 4\mu}}{2}\xi\right)\right]. \tag{4.36}$$

(ii) If $C_1 \neq 0$ and $C_2 = 0$, we have

$$\phi(\xi) = -\left[1 + 3\left(\lambda^2 - 4\mu\right)\tanh^2\left(\frac{\sqrt{\lambda^2 - 4\mu}}{2}\xi\right)\right]. \tag{4.37}$$

(iii) If $C_1 \neq 0$ and ${C_2}^2 < {C_1}^2$, we have

$$\phi(\xi) = -\left[1 + 3\left(\lambda^2 - 4\mu\right)\tanh^2\left(\xi_0 + \frac{\sqrt{\lambda^2 - 4\mu}}{2}\xi\right)\right]. \tag{4.38}$$

(iv) If $C_2 \neq 0$ and ${C_1}^2 < {C_2}^2$, we have

$$\phi(\xi) = -\left[1 + 3\left(\lambda^2 - 4\mu\right)\coth^2\left(\xi_0 + \frac{\sqrt{\lambda^2 - 4\mu}\,\xi}{2}\right)\right]. \tag{4.39}$$

Here, $\xi_0 = \tanh^{-1}\left(\frac{C_1}{C_2}\right)$.

However, if $\lambda^2 - 4\mu < 0$, we obtain the trigonometric function solutions:

$$\phi(\xi) = -\left[1 + 3\left(\lambda^2 - 4\mu\right)\left(\frac{-C_1 \sin\left(\frac{\sqrt{\lambda^2-4\mu}\,\xi}{2}\right) + C_2 \cos\left(\frac{\sqrt{\lambda^2-4\mu}\,\xi}{2}\right)}{C_1 \cos\left(\frac{\sqrt{\lambda^2-4\mu}\,\xi}{2}\right) + C_2 \sin\left(\frac{\sqrt{\lambda^2-4\mu}\,\xi}{2}\right)}\right)^2\right], \tag{4.40}$$

where $\xi = x + \frac{1}{2}\left(48\mu^2 - 24\mu\lambda^2 + 3\lambda^2 - 5\right)\left(\frac{t^\alpha}{\alpha}\right)$, and C_1 and C_2 are arbitrary constants.

Remark 1. Taking C_1 and C_2 as special values, various known solutions can be found from Eq. 4.40. Here, we do not list them for simplicity.

However, if $\lambda^2 - 4\mu = 0$, the following rational function solutions can be obtained:

$$\phi(\xi) = -\left[1 + 12\left(\frac{C_1}{C_2 + C_1\xi}\right)^2\right], \tag{4.41}$$

where $\xi = x + \frac{1}{2}\left(48\mu^2 - 24\mu\lambda^2 + 3\lambda^2 - 5\right)\left(\frac{t^\alpha}{\alpha}\right)$, and C_1 and C_2 are arbitrary constants.

Remark 2. When $\omega = \tanh\xi$, which is the tanh-function expansion method. This is similar to the $\left(\frac{G'}{G}\right)$ method, which is omitted here.

Remark 3. Inc, M and B Kilic [43] have investigated exact solutions for the KdV-like equation using Kudryashov, Exp-function, and Jacobi elliptic rational expansion methods. From the aforementioned procedure, the G'/G-expansion method is very powerful for FPDEs. As far as we know, the solutions obtained therefrom under this study have never been reported previously, and are newly generated.

Remark 4. Recently, many scholars put forward the Riemann–Hilbert method [44, 45], and its application in FPDEs is also worthy of further study.

5 Conservation laws of the TFF-KdV equation

In this part, we have obtained the conservation laws for the TFF-KdV equation by applying Eq. 4.4 of Lie point symmetry.

Based on the definition of the conserved vector for inter-order PDEs, a conserved vector $C(C^t, C^x)$ for Eq. 1.1 admits the following conservation equation:

$$D_t\left(C^t\right) + D_x(C^x)|_{(TFF-KdV)} = 0. \tag{5.1}$$

It should be noted that the TFF-KdV equation might be written in the form of the conservation law as Eq. 5.1.

$$C_0^t = D_0^{\alpha-1}u, C_0^x = u^2u_x - uu_{xxx} + u_{xxxxx}. \tag{5.2}$$

We also study the conservation laws with the adjoint equation [46] and symmetries of the TFF-KdV equation. As to Eq. 1.1, the adjoint equation can be written in the following form:

$$\varpi_t^\alpha + u^2\varpi_x - u\varpi_{xxx} + \varpi_{xxxxx} = 0, \tag{5.3}$$

and the Lagrangian can be written in the symmetrized form as follows:

$$L = \varpi\left(u_t^\alpha + u^2u_x - uu_{xxx} + u_{xxxxx}\right), \tag{5.4}$$

where $\varpi(t, x)$ is a new dependent variable. The adjoint equation of Eq. 1.1 is written as

$$W^* = \frac{\delta L}{\delta u} = 0, \tag{5.5}$$

where $\frac{\delta}{\delta u}$ is the Euler–Lagrange operator we defined by

$$\frac{\delta}{\delta u} = \frac{\partial}{\partial u} + \left(D_t^\alpha\right)^*\frac{\partial}{\partial D_t^\alpha u} - D_x\frac{\partial}{\partial u_x} + D_x^2\frac{\partial}{\partial u_{xx}} - D_x^3\frac{\partial}{\partial u_{xxx}} + D_x^4\frac{\partial}{\partial u_{xxxx}} - D_x^5\frac{\partial}{\partial u_{xxxxx}}, \tag{5.6}$$

where $\left(D_t^\alpha\right)^*$ is the adjoint operator of D_t^α. As to the Riemann–Liouville fractional differential operators, we have

$$\left(D_t^\alpha\right)^* = (-1)^n\mathrm{K}_T^{n-\alpha}\left(D_t^n\right) = \left(D_T^\alpha\right)_t^C, \tag{5.7}$$

where

$$\mathrm{K}_T^{n-\alpha}f(t,x) = \frac{1}{\Gamma(n-\alpha)}\int_t^T \frac{f(\tau,x)}{(\tau-t)^{1+\alpha-n}}d\tau, n = [\alpha] + 1 \tag{5.8}$$

is the right-sided Caputo operator of the fractional differentiation of order α.

Through the substitution of Eq. 5.4 into Eq. 5.5, it can lead to the adjoint equation of Eq. 1.1 admitting the following expression:

$$W^* = \left(D_t^\alpha\right)^*\varpi + u^2\varpi_x + u\varpi_{xxx} + \varpi_{xxxxx} = 0. \tag{5.9}$$

The TFF-KdV equation arrives at the following conservation law in [44].

$$D_t\left(C_i^t\right) + D_x\left(C_i^x\right) = 0, \tag{5.10}$$

where the conserved vector $C(C^t, C^x)$ has a new form.

$$C_i^x = \mathrm{X}_i\frac{\delta L}{\delta u_x} + D_x\left(\mathrm{X}_i\right)\frac{\delta L}{\delta u_{xx}} + D_x^2\left(\mathrm{X}_i\right)\frac{\delta L}{\delta u_{xxx}} + D_x^3\left(\mathrm{X}_i\right)\frac{\delta L}{\delta u_{xxxx}} + D_x^4\left(\mathrm{X}_i\right)\frac{\delta L}{\delta u_{xxxxx}}, \quad C_i^t = \sum_{k=0}^{n-1}(-1)^k D_t^{\alpha-1-k}\left(\mathrm{X}_i\right)D_t^k\left[\frac{\partial L}{\partial\left(D_t^\alpha u\right)}\right] - (-1)^n S\left[\mathrm{X}_i, D_t^n\left(\frac{\partial L}{\partial\left(D_t^\alpha u\right)}\right)\right], n = [\alpha] + 1, \tag{5.11}$$

where $\mathrm{X}_i = \eta_i - \varsigma_i u_x - \tau_i u_t$, and S is the integral.

$$S(f,g) = \frac{1}{\Gamma(n-\alpha)}\int_0^t\int_t^T \frac{f(p,x)g(q,x)}{(q-p)^{\alpha+1-n}}dqdp. \tag{5.12}$$

Using the symmetries$\mathrm{V}_1 = \frac{\partial}{\partial x}, \mathrm{V}_2 = x\frac{\partial}{\partial x} + \frac{5t}{\alpha}\frac{\partial}{\partial t} - 2u\frac{\partial}{\partial u}$, we have

$$\mathrm{X}_1 = -u_x, \mathrm{X}_2 = -xu_x - \frac{5t}{\alpha}u_t - 2u. \tag{5.13}$$

Substituting Eq.5.4 and Eq.5.13 into Eq. 5.11, we obtain the following conserved vectors for the TFF-KdV equation.

Case 1: By using the symmetry $X_1 = -u_x$, we find an additional conserved vector as follows:

$$C_1^x = X_1\left[\frac{\partial L}{\partial u_x} + (-1)^n D_x^{n-1}\frac{\partial L}{\partial u_{nx}}\right] + D_x^{n-1}(X_1)\frac{\partial L}{\partial u_{nx}},$$
$$C_1^t = -K_t^{1-\alpha}(-X_1)\psi - S(-X_1, \psi_t). \tag{5.14}$$

Case 2: By using the symmetry$X_2 = -xu_x - \frac{5t}{\alpha}u_t - 2u$, we find an additional conserved vector:

$$C_2^x = X_2\left[\frac{\partial L}{\partial u_x} + (-1)^n D_x^{n-1}\frac{\partial L}{\partial u_{nx}}\right] + D_x^{n-1}(X_2)\frac{\partial L}{\partial u_{nx}},$$
$$C_2^t = K_t^{1-\alpha}(-X_2)\psi + S(-X_2, \psi_t). \tag{5.15}$$

According to the aforementioned detailed analysis, we have

Theorem 3. The TFF-KdV equation has the following conservation laws:

$$D_t(C_i^t) + D_x(C_i^x) = 0, i = 1, 2, \tag{5.16}$$

where C_i^t is shown in Eq.5.2, Eq.5.14, and Eq. 5.15.

6 Conclusion

In this research, it was considered the symmetry analysis, explicit solutions to the TFF-KdV equations with Riemann-Liouville derivative. The TFF-KdV equation was reduced to a non-linear ordinary differential equation (ODE) of fractional order. The G'/G-expansion method was obtained to work out the TFF-KdV equation in the sense of the Riemann–Liouville derivative. There were three types of exact solutions that originated in the aspect of hyperbolic, trigonometric, and rational functions with some parameters, which have great potential for further research. All solutions derived in this study were checked utilizing Maple by incorporating them into Eq. 1.1. At last, considering the advantages of the G'/G-expansion method such as efficiency, conciseness, and briefness, the method can be applied to several other higher-order non-linear FPDEs arising in mathematical physics, plasma, hydrodynamics, engineering, and other fields of applied sciences. Finally, based on the Noether theorem, the conservation laws of the equation are well-constructed with detailed derivation. Additionally, it is clear from Lie symmetry analysis that this approach is relatively well-organized and can be used to solve many different non-linear FPDEs from natural sciences.

Data availability statement

The original contributions presented in the study are included in the article/Supplementary Material, further inquiries can be directed to the corresponding authors.

Author contributions

ZW: conceptualization, methodology, investigation, formal analysis, and writing—original draft. LJS, RH, and LDS: software and formal analysis. LZ: conceptualization, funding acquisition, resources, supervision, and writing—review and editing.

Funding

This research was funded by the National Natural Science Foundation of China (No. 12105073), the Science and Technology Program of Colleges and Universities in Hebei Province (No. QN2020144), the Scientific Research and Development Program Fund Project of Hebei University of Economics and Business (No. 2020YB15), the Youth Team Support Program of Hebei University of Economics and Business, the Doctoral Research Start-up Fund project of Zaozhuang University (No. 1020708), and Natural Science Foundation of Shandong Province (ZR2022MA081).

Conflict of interest

The authors declare that the research was conducted in the absence of any commercial or financial relationships that could be construed as a potential conflict of interest.

Publisher's note

References

1. Oldham K, Spanier J. *The fractional calculus theory and applications of differentiation and integration to arbitrary order. vol.111*. Amsterdam, Netherlands: Elsevier (1974).

2. Miller KS, Ross B. *An introduction to the fractional calculus and fractional differential equations*. New York: Wiley (1993).

3. Samko SG, Kilbas AA, Marichev OI. Fractional integrals and derivatives: Theory and applications. *Minsk ; Nauka I Tekhnika* (1993) 3:397–414.

4. Hilfer R. *Applications of fractional calculus in physics*. Singapore: World Scientific (2000).

5. Podlubny I. *Fractional differential equations, volume 198 of mathematics in science and engineering*. Cambridge, MA, USA: Academic Press (1999).

6. West B, Bologna M, Grigolini P. *Physics of fractal operators*. Berlin, Germany: Springer Science & Business Media (2012).

7. Tang B, He Y, Wei L, Zhang X. A generalized fractional sub-equation method for fractional differential equations with variable coefficients. *Phys Lett A* (2012) 376: 2588–90. doi:10.1016/j.physleta.2012.07.018

8. Guo S, Mei L, Li Y, Sun YF. The improved fractional sub-equation method and its applications to the space-time fractional differential equations in fluid mechanics. *Phys Lett A* (2012) 376:407–11. doi:10.1016/j.physleta.2011.10.056

9. Meng F. A new approach for solving fractional partial differential equations. *J Appl Math* (2013) 2013:1–5. doi:10.1155/2013/256823

10. Bekir A, Aksoy E, Cevikel AC. Exact solutions of nonlinear time fractional partial differential equations by sub-equation method. *Math Meth App Sci* (2015) 38:2779–84. doi:10.1002/mma.3260

11. Parkes E, Duffy B. Travelling solitary wave solutions to a compound KdV-Burgers equation. *Phys Lett A* (1997) 229:217–20. doi:10.1016/s0375-9601(97)00193-x

12. Raslan K, Ali KK, Shallal MA. The modified extended tanh method with the Riccati equation for solving the space-time fractional EW and MEW equations. *Chaos, Solitons Fractals.* (2017) 103:404–9. doi:10.1016/j.chaos.2017.06.029

13. Tariq H, Akram G. New approach for exact solutions of time fractional CahnCAllen equation and time fractional Phi-4 equation. *Phys A* (2017) 473:352–62.

14. El-Sayed A, Gaber M. The Adomian decomposition method for solving partial differential equations of fractal order in finite domains. *Phys Lett A* (2006) 359:175–82. doi:10.1016/j.physleta.2006.06.024

15. Hu Y, Luo Y, Lu Z. Analytical solution of the linear fractional differential equation by Adomian decomposition method. *J Comput Appl Math* (2008) 215:220–9. doi:10.1016/j.cam.2007.04.005

16. El-Sayed A, Behiry S, Raslan W. Adomians decomposition method for solving an intermediate fractional advectionCdispersion equation. *Comput Math Appl* (2010) 59:1759–65.

17. Yang XJ, Zhang Y. A new Adomian decomposition procedure scheme for solving local fractional Volterra integral equation. *Adv Inf Technol Manage* (2012) 1:158–61.

18. Inc M. The approximate and exact solutions of the space-and time-fractional Burgers equations with initial conditions by variational iteration method. *J Math Anal Appl* (2008) 345:476–84. doi:10.1016/j.jmaa.2008.04.007

19. Odibat Z, Momani S. The variational iteration method: An efficient scheme for handling fractional partial differential equations in fluid mechanics. *Comput Math Appl* (2009) 58:2199–208. doi:10.1016/j.camwa.2009.03.009

20. Wu GC, Lee E. Fractional variational iteration method and its application. *Phys Lett A* (2010) 374:2506–9. doi:10.1016/j.physleta.2010.04.034

21. Pandir Y, Gurefe Y, Misirli E. The extended trial equation method for some time fractional differential equations. *Discrete Dyn Nat Soc* (2013) 6:85–8.

22. Odabasi M, Misirli E. On the solutions of the nonlinear fractional differential equations via the modified trial equation method. *Math Meth App Sci* (2015) 41:904. doi:10.1002/mma.3533

23. Sezer SA, Yildirim A, Mohyud-Din ST. Hes homotopy perturbation method for solving the fractional KdV-Burgers-Kuramoto equation. *Int J Numer Methods Heat Fluid Flow* (2011) 21:448–58. doi:10.1108/09615531111123119

24. Gepreel KA. The homotopy perturbation method applied to the nonlinear fractional Kolmogorov-Petrovskii-Piskunov equations. *Appl Math Lett* (2011) 24:1428–34. doi:10.1016/j.aml.2011.03.025

25. Mohyud-Din ST, Bibi S. Exact solutions for nonlinear fractional differential equations using exponential rational function method. *Opt Quant Electron* (2017) 49:64. doi:10.1007/s11082-017-0895-9

26. Khodadad FS, Nazari F, Eslami M, Rezazadeh H. Soliton solutions of the conformable fractional Zakharov-Kuznetsov equation with dual-power law nonlinearity. *Opt Quant Electron* (2017) 49:384. doi:10.1007/s11082-017-1225-y

27. Islam T, Akbar MA, Azad AK. Traveling wave solutions to some nonlinear fractional partial differential equations through the rational G'/G-expansion methods. *J Ocean Eng Sci* (2018) 3:76. doi:10.1016/j.joes.2017.12.003

28. Jumarie G. Table of some basic fractional calculus formulae derived from a modified Riemann-Liouville derivative for non-differentiable functions. *Appl Math Lett* (2009) 22:378–85. doi:10.1016/j.aml.2008.06.003

29. Podlubny I. *Fractional differential equations: An introduction to fractional derivatives, fractional differential equations, to methods of their solution andsome of their applications. Vol. 198*. Cambridge, MA, USA: Academic Press (1998).

30. Khalil R, Horani MA, Yousef A, Sababheh M. A new definition of fractional derivative. *J Comput Appl Math* (2014) 264:65–70. doi:10.1016/j.cam.2014.01.002

31. Wang GW, Liu XQ, Zhang YY. Lie symmetry analysis to the time fractional generalized fifth-order KdV equation. *Commun.Nonlinear Sci Numer Simul* (2013) 18:2321–6. doi:10.1016/j.cnsns.2012.11.032

32. Abdel-Salam AB, Al-Muhiameed ZIA. Analytic solutions of the space-time fractional combined KdV-mKdV equation. *Math Probl Eng* (2015) 2:1–6. doi:10.1155/2015/871635

33. Zhang Q, Zhang J, Jiang S, Zhang Z. Numerical solution to a linearized time fractional KdV equation on unbounded domains. *Math Comput* (2017) 87(310):693–719. doi:10.1090/mcom/3229

34. Jumarie G. Modied Riemann-Liouville derivative and fractional Taylor series of non-differentiable functions further results. *Comput Math Appl* (2006) 51:1367–76.

35. Gazizov RK, Kasatkin AA, Lukashchuk SY. Continuous transformation groups of fractional differential equations. *Vestnik, USATU* (2007) 9:125–35.

36. Podlubny I. *Fractional differential equations*. San Diego, CA: Academic Press (1999).

37. Kiryakova V. *Generalized fractional calculus and applications*. Pitman Res. Notesin Math (1994).

38. Sahadevan R, Bakkyaraj T. Invariant analysis of time fractional generalized Burgers and Korteweg-de Vries equations. *J Math Anal Appl* (2012) 393:341–7. doi:10.1016/j.jmaa.2012.04.006

39. Wang GW, Wazwaz AM. On the modified Gardner type equation and its time fractional form. *Chaos, Solitons and Fractals* (2022) 155:111694. doi:10.1016/j.chaos.2021.111694

40. Jefferson GF, Carminati J. FracSym: Automated symbolic computation of Lie symmetries of fractional differential equations. *Comput Phys Commun* (2014) 185:430–41. doi:10.1016/j.cpc.2013.09.019

41. Li W, Chen J, Zhang G. The (ω/g)-expansion method and its application to Vakhnenko equation. *Chin Phys B* (2009) 18(2):400–4. doi:10.1088/1674-1056/18/2/004

42. Wang M, Li X, Zhang J. The(G'/G)-expansion method and travelling wave solutions of nonlinear evolution equations in mathematical physics. *Phys Lett A* (2008) 372:417–23.

43. Inc M, Kilic B. Classification of traveling wave solutions for time-fractional fifth-order KdV-like equation. *Waves in Random & Complex Media* (2014) 24(4):393–403. doi:10.1080/17455030.2014.927083

44. Wang HF, Zhang YF. Application of Riemann–Hilbert method to an extended coupled nonlinear Schrödinger equations. *J Comput Appl Math* (2023) 420:114812. doi:10.1016/j.cam.2022.114812

45. Li J, Xia TC. A Riemann-Hilbert approach to the Kundu-nonlinear Schrödinger equation and its multi-component generalization. *J Math Anal Appl* (2021) 500:125109. doi:10.1016/j.jmaa.2021.125109

46. Ibragimov NH. A new conservation theorem. *J Math Anal Appl* (2007) 333:311–28. doi:10.1016/j.jmaa.2006.10.078

frontiers | Frontiers in Physics

TYPE Original Research
PUBLISHED 21 March 2023
DOI 10.3389/fphy.2023.1133550

OPEN ACCESS

EDITED BY
Samir A. El-Tantawy,
Port Said University, Egypt

REVIEWED BY
Md. Golam Hafez,
Chittagong University of Engineering & Technology, Bangladesh
Noreen Sher Akbar,
National University of Sciences and Technology (NUST), Pakistan

*CORRESPONDENCE
Muhammad Sohail,
muhammad_sohail111@yahoo.com
Sayed M. Eldin,
sayed.eldin22@fue.edu.eg

SPECIALTY SECTION
This article was submitted to Mathematical Physics, a section of the journal Frontiers in Physics

RECEIVED 29 December 2022
ACCEPTED 22 February 2023
PUBLISHED 21 March 2023

CITATION
Sohail M, Nazir U, Mukdasai K, Singh M, Singh A, Mohan CR, Galal AM and Eldin SM (2023), Transportation of Fe_3O_4-SiO_2-Al_2O_3/EO and SiO_2-Al_2O_3/EO nanoparticles in magnetized Reiner–Philippoff liquid, including modified fluxes *via* Galerkin algorithm: Significance of EMHD. *Front. Phys.* 11:1133550. doi: 10.3389/fphy.2023.1133550

Transportation of Fe_3O_4-SiO_2-Al_2O_3/EO and SiO_2-Al_2O_3/EO nanoparticles in magnetized Reiner–Philippoff liquid, including modified fluxes *via* Galerkin algorithm: Significance of EMHD

Muhammad Sohail[1]*, Umar Nazir[2], Kanit Mukdasai[2], Manoj Singh[3], Abha Singh[4], Chandika Rama Mohan[5], Ahmed M. Galal[6,7] and Sayed M. Eldin[8]*

[1]Institute of Mathematics, Khwaja Fareed University of Engineering & Information Technology, Rahim Yar Khan, Pakistan, [2]Department of Mathematics, Faculty of Science, Khon Kaen University, Khon Kaen, Thailand, [3]Department of Mathematics, Faculty of Science, Jazan University, Jazan, Saudi Arabia, [4]Department of Basic Sciences, College of Sciences and Theoretical Studies, Dammam-branch, Saudi Electronic University, Riyadh, Saudi Arabia, [5]Clinical Nutrition Department Applied Medical Science College Jazan University, Jizan, Saudi Arabia, [6]Mechanical Engineering Department, College of Engineering, Prince Sattam Bin Abdulaziz University, Wadi Addawaser, Saudi Arabia, [7]Production Engineering and Mechanical Design Department, Faculty of Engineering, Mansoura University, Mansoura, Egypt, [8]Faculty of Engineering and Technology, Future University in Egypt New Cairo, New Cairo, Egypt

This developing study is focused on mass diffusion and thermal energy enhancement in Reiner–Philippoff martial across a vertical-surface under an exposed Lorentz force. Characterization of the thermal energy and mass diffusion are modified utilizing non-Fourier's theory in the presence of a heat source. Three types of nanoparticles—Al_2O_3, titanium dioxide, and TiO_2—in engine oil are inserted for production of heat energy. Darcy's Forchheimer theory is used to analyze behavior flow and heat energy. Moreover, effects related to Dufour and Soret are added. A transformed system of ODEs is achieved regarding the developed model using similarity variables. Numerically developing models in the form of ODEs are handled with the aid of the finite element method (FEM). Fluidic thermal energy is augmented against upshot values of time relaxation number. Fluidic concentration declines against changes in Schmidt number and chemical reaction number.

KEYWORDS

EMHD, three-phase simulations, buoyancy forces, thermal properties, two-dimensional plate, Galerkin algorithm

1 Introduction

Non-Newtonian fluids have numerous applications and are used extensively in many materials. This investigation deals with Sutterby nanofluid boundary-layer flow in a stretched cylinder by including updated models for mass and heat transfers and applying the Cattaneo–Christov theory. Boundary-layer analysis leads to the creation of a mathematical

model. By utilizing conservation principles, the physical phenomena are first generated in terms of PDEs. The penetrating medium is influenced by the advanced Darcy's law. The suggested model's non-linear equations are optimally and dynamically investigated. By establishing the conservation rules for mass, momentum, energy, and concentration, non-linear partial differential equations (PDEs) are created. The OHAM is adopted and aims to develop numerical solutions for non-linear systems, as previously discussed [1]. Nanofluids are the newest category of fluids, and Choi first described them at the beginning of 1995. Akbar et al. [2] formulated a model of peristaltic transport in the presence of thermal conductive using variable viscosity-based temperature with carbon nanoparticles; the authors found the exact solution of the developed model. Akram et al. [3] utilized curved microchannels to investigate heat transfer and flow behavior in the presence of titanium dioxide in Carneau fluid rheology; the authors estimated the motion of nanoparticles using mechanisms of thermophoretic and Brownian motion *via* an exact solution technique. Maraj et al. [4] discovered the consequences of Lorentz force, including CNTs and thermal deposition in the channel, utilizing exact closed-form solutions involving radiation and magnetic field. Akram et al. [5] studied thermal features of peristaltic transport involving Lorentz force and electroosmosis with SWCNTs in aqueous diagrams. Multiple industrial and technological implications, including wire drawing, glass fiber production, assembly of particularly elastic sheets, and cooling of concerning metallic plates are among the pertinent themes investigated previously [6] regarding the study of fluid attributes in multiple mathematical models. When a fixed magnetic field was supplied, Bhandari and Husain carefully examined the combined impacts particularly of rotating viscosity and magnetized force subjected to a 2D Ferro hydrodynamic non-conductor nanoliquid flow across a stretched surface. To explore the hybrid nanomaterials' flow demeanor when subjected to a stretched sheet, Gul et al. presented a computer model. Fractional calculus ideas have been widely used in different areas in recent years. This topic has recently expanded in several different directions, including fractional-order multipoles influenced by electromagnetism and in the field of electrochemistry. Moreover, tracer is used within the fluid flow demeanor, the neuron model in the field of biology, finance, and signal processing. The Riemann–Liouville and Caputo fractional derivatives are the most popular applications discussed by Shah and Khan [7]. Biomedical engineering and medical care greatly benefit from the radiation and magnetic field impacts appertaining to nanofluids. Khan et al. [8] examined gold particle performance toward the blood flow demeanor (Sisko fluid flow) through a penetrating, slick, curvy surface. Partial slip impacts were considered in thoroughly analyzing the properties referring to nanofluidic flow. After Choi's original study, a significant advancement in this field was made. In an experimental study, Eastman et al. examined heat transfer in the presence of Al_2O_3 and CuO particles, synthesized using ethylene glycol and water, respectively. Investigation based on blood flow demeanor in small arteries involves many variable features. Understanding the rheological behavior of blood and other biological fluids, namely urine, spermatozoa, and eye drops, requires accounting for heat conductivity and viscosity change. In the current work, which was motivated by these applications, we describe the peristaltic flow demeanor—particularly Ree–Eyring liquid *via* a uniform compliant channel—while accounting for the influence of varying thermal conductivity and viscosity, as described previously [9]. Recent studies have shown a particular interest in dusty fluid model flows due to their two-phase nature. This effect occurs when solid particles are dispersed in fluid (gas or liquid) flows. As an example, consider the chemical process that results in droplet formation when relatively small dust particles agglomerate, leading to high dusty-air velocity. Cosmic dust, a mixture of gas and dust particles, is the essential precursor for planetary systems, as expressed previously [10]. In tabular and graphical formats, Khan and Pop [11] examined fluctuation in declining Nusselt and reduced Sherwood numbers. Falkner–Skan flow is one of the most well-known motives for investigating magnetohydrodynamics, on account of its applications in the field of fluid dynamics and heat transfer. In the scientific community, conventional flow behavior, specifically Newtonian and non-Newtonian fluids subjected to a moving wedge, is very popular right now. Lin et al. investigated the properties of heat transmission within the static wedge flow demeanor. The authors examined the model particularly for every conceivable finite Prandtl number value. Watanabe and Watanabe and Pop, respectively, researched forced and free-convection Falkner–Skan flow. Akbar et al. [12] discussed investigations into shape factors associated with SiO_2/MoS_2 nanoparticles in a base fluid in a channel including a temperature gradient (oscillatory). Convection may occur in three different ways in heat transfer flows: naturally, forcibly, and mixed. The last of these has uses in a variety of industrial and natural phenomena, including nuclear reactor cooling, electronic systems, and heat exchangers used to heat or cool fluids in the food industry and in compact heat exchangers, as studied previously [13]. In numerous systems pertaining to heating and cooling, fluids including water and kerosene oil, ethylene, and glycol are frequently utilized. Most of these fluids, which are sometimes referred to as the basic fluids, are poor heat conductors. We must address the issues caused by these systems' weak conductivities in order to improve their performance. Nowadays, a relatively novel approach is being used to increase thermal conductivity and other thermal characteristics. Habib et al. [14] discussed a new discovery regarding nanofluid behavior in clinical isolates of *Staphylococcus aureus* using gold nanoparticles. Alghamdi et al. [15] favored adopting non-linear stretching sheets. These crucial industrial applications drove researchers to carefully examine boundary-layer flow demeanor over linear and non-linear prolonged sheets of a range of geometric thicknesses. Micropolar nanofluidic flow demeanor embedded with buoyancy force, along with magnetic field subjected to an enclosure, has been studied for its heat and mass transmission mechanism. The proposed mathematical model needed to assess effectiveness, particularly nanoparticle thermal efficiency, must be built using mass and energy and must be within the momentum equations. This study aims to increase the effectiveness of heat and mass transmission within the heat transport machinery and heat-ameliorated units used in engineering and industrial operations. The proposed dimensionless 2D model given the significance of dimensional analysis analyzed previously [16]. The substandard thermal conductivity of operating liquids, which constrains high solidity and performance appertaining to thermal production within heat exchanges, is currently a serious worldwide problem. Most frequently, ethanol and water, as well as an acetone and an ethylene–glycol combination, are used as working fluids, as discussed previously [17]. Additionally, in response to this issue, numerous scientists and engineers have demonstrated the essential principles of improving thermal properties, specifically for energy-

transported liquids, and efficiency, particularly of heat transfer in industrial appliances.

Examining entropy production in catalytic and non-linear thermal radiative impacts involves assessing the hydromagnetic stagnation point flow demeanor of a micropolar nanofluid. A water nanofluid is created by mixing in the magnetite nanoparticles. The time-independent, significant 2D flow demeanor is supposed to start with a vertically stretchable sheet. When creating the governing equations for the relevant issue, the Joule heating and viscous dissipation impacts are considered, as described previously [18]. Using updated heat and mass flux models, the entropy production approach is subjected to Maxwell nanofluid incorporated with gyrotactic microorganisms influenced by homogeneous–heterogeneous processes. Amended models are provided using the dual diffusive theory and the generalized Fick's equation. According to boundary-layer theory, derived equations that depict the flow situation under consideration are modeled as PDEs. An appropriate transformation is then applied to alter the resulting PDEs toward the transformed ODEs and is subsequently solved using a powerful technique called the optimal homotopy analysis approach. Special instances of certain previously published research are in close accordance with our findings. Graphs are used to describe the effects, specifically of physical factors within the velocity, as well as temperature, concentration, reaction rate, the concentration of motile bacteria, and entropy production, as examined in an earlier study [19]. Based on the three-dimensional and steady power-law for nanofluidic flow demeanor close to the stagnation point area, the MHD and non-linear thermal radiative impacts included in penetrable material are applied to conduct an entropy generation study. The heat transformation phenomena inside the boundary layer configured by the stretchy moving disc are investigated and accompanied by non-uniformly thermal radiative heat source/sink exposed to convective boundary circumstances. The basic fluid ethylene glycol ($C_2H_6O_2$) is combined with multi-wall carbon nanotubes (MWCNTs). The suggested fluid flow issue is analytically modeled, as discussed previously [20]. Incompressible viscous hybrid nanofluid flow is analyzed in three dimensions in a rotating frame. The basic liquid is ethylene glycol, and the nanoparticles are copper and silver. Fluid flows within the dual parallel surfaces, with the bottom surface extending linearly. Since fluid conducts, a consistent magnetic field is applied. We consider the viscous dissipation impacts and Joule heating and non-linear thermal radiations. The Nusselt number and surface drag force are addressed as interesting quantities. Xia et al. [21] examined the rate of entropy formation. Because of their significant industrial applications and high heat transfer rates, nanofluids are of great importance to scientists. Hybrid nanofluids, a brand-new form of nanofluid, have lately been employed to accelerate heat transfer even further. The current phenomena focus particularly on the investigation of SWCNT–MWCNT/water hybrid nanofluidic flow demeanor and on heat transmission subjected to a moving wedge. The flow demeanor in the porosity media is described by the Darcy–Forchheimer relationship. In addition, Ahmad et al. [22] covered in depth the effect of varying viscosity and velocity, as well as thermal slip, thermal radiation, and heat production. By performing a theoretical study, peculiarly viscous three-dimensional fluid flow demeanor incorporated with gyrotactic microorganisms across a non-linear stretchy surface, heat mechanisms, and mass transmission may be understood. To regulate the flow of fluid, the fluctuating magnetic field is thought to be normal toward the stretchy surface. The varying thermal conductivity prompts a discussion of thermal transportation. Mass transportation incorporates chemical processes and variable mass diffusion properties. The porous medium is defined using the Darcy–Forchheimer equation. To improve diffusion, Abdelsalam and Sohail [23] included Brownian motion and thermophoresis. The current study investigates viscous fluid flow in three dimensions when specific heat (PHF) and concentration (PCF) fluxes are present. Chemical reactions, viscosity dissipation, and Joule heating impacts are all considered when the mathematical formulation is being constructed. Fluid becomes electrically conductive when influenced by the applied magnetic field, whereas the non-linear system referring to ordinary differential equations is obtained by appropriate transformations. The resultant non-linear system determines the solution. To investigate the effects, particularly the physical factors, of the temperature and concentration distributions, graphs are plotted. Maraj et al. [24] estimated rotational flow and motion of hybrid nanoparticles with Hall currents in a vertical channel using conditions of thermal periodic and velocity slip *via* closed-form solutions. Saleem et al. [25] adopted FEM for statistical solutions, referring to a set of ODEs. Damaged arteries with stenosis have reduced blood flow; the accumulation of plaque within the artery walls, brought on by fats and oils, leads to the development of this stenosis. Multiple stenoses may exist in an artery that has severe stenosis. Multiple stenoses cause the artery to narrow, which restricts blood flow across it. Many academics have recently been interested in examining this particular kind of stenotic artery. Blood flows through tiny channels, with non-Newtonian behavior in big vessels and Newtonian behavior in smaller vessels. Owing to various peculiarities, particularly blood circulation along with the mechanical characteristics of the vessel walls, it is essential to examine the blood flow through a stenotic channel. Shahzad et al. [26] determined the location of stenosis on the vessel wall and the flow behavior through sick blood arteries by observing blood flow across a stenotic artery. In this investigation, the contributions of viscous dissipation and thermophoresis, as well as Brownian motion, gravitational effects, and stratification impacts, were examined. Physical events are derived as linked systems of partial differential equations. An appropriate transformation converts the model's equation system into straightforward ordinary differential equations (ODEs). Naz et al. [27] used an ideal homotopy analysis approach and an improvised system that relies on coupled non-linear ODEs solved in Mathematica. Due to its use in several sectors, heat transfer is crucial. Hybrid nanofluidic flow, a novel manner of nanofluids with a greater heat exponent in comparison to the nanofluids, is being utilized to improve the ability of regular fluids to transport heat. In a base fluid, two-element nanoparticles are known as hybrid nanofluids (HNFs). Jamshed et al. [28] demonstrated the properties of steady hybrid nanofluidic flow and thermal transfer over a slippery surface. Convection, whether forced or natural, is more significant in the context of fluid dynamics than the other two well-known heat transfer processes, conduction and radiation. It happens because of differences in the thermal energy that is applied differently to various parts of the fluid under examination. Akram et al. [29] discussed theoretical investigations of thermal transfer based on Au and Ag hybrid water-based nanoparticles induced by electroosmotic pumping in a microchannel. Due to their poor heat

conductivity, pure liquids like water and oil have proven to be problematic in this respect. To improve heat transmission and modify the carrier fluid's thermal characteristics, nanoparticles with an approximate diameter of less than 100 nm, materials with intensified thermal conductivities, are mixed along with the fluid, as discussed previously [30]. This analysis emphasizes the importance of radiation and Joule heating effects, particularly for Casson liquid-boundary layer flow (BLF) configured by a linearly elongating surface, as well as the properties of momentum and entropy production. Likewise, species and thermal dissemination are also considered. Thermal conductivity and mass diffusion coefficient models that vary with temperature are used to provide thermal and species transportation. Emerging issues take the non-linear partial differential equations form, in opposition to the principles governing the movement of mass, momentum, heat, and species. The exhibited issue may be transformed into ordinary differential equations with the proper modification. Sohail et al. [31] used the optimal homotopy analysis method (OHAM) as a competent and dependable approach for obtaining numerical solutions, specifically for upgraded boundary-layer ordinary differential equations (ODEs). Due to its applicability, heat transfer analysis in two-dimensional flows has drawn the interest of several academics in recent years. Akram et al. [32] derived features of electroosmotic flow by inserting silver nanoparticles and solving using two various approaches. Applications like drawing wire, making plastic and rubber sheets, cooling electric plates enclosed by a bath, melt spinning, and hot rolling, among others, all benefit from fluid passage over elongating sheets. Because a plate expands at a specific rate, Sakiadis was the first to examine fluid flow. Crane then concentrated on the laminar flow demeanor, specifically two-dimensional, incompressible, and viscous fluid subjected to a stretching plate. There is a precise closed-form solution to this problem. Following the above-mentioned studies, many researchers (see, for instance, [33]) concentrated on fluid flow caused by stretched plates. These researchers investigated flow demeanor across an exponentially stretching sheet with the impacts of MHD and radiation, and discovered that the magnetic and radiation parameters are what reduce the heat transmission rate. The authors looked across the Eyring–Powell fluid boundary-layer fluid flow configured by a linearly stretching sheet and computed the findings for velocity profiles using the collocation method.

2 Mathematical analysis

Two-dimensional consequences of mass diffusion and thermal fields of a complex fluid (Reiner–Philippoff) were investigated under conditions of EMHD on a vertical plate. Three phases of hybrid nanomaterial are implemented in the presence of engine oil. Fields associated with mass diffusion and thermal conductivity are carried out by heat sink and non-Fourier's theory, as well as variable properties pertaining to mass diffusion and thermal conductivity. A flow diagram with boundary conditions and suspension of ternary hybrid nanoparticles is shown in Figure 1. Conservation laws have been implemented to obtain distributions for motion, concentration, and thermal conductivity, as listed below. The thermophysical properties of different used materials are depicted in Table 1.

The reduced form of PDEs [34–36] is derived as

$$\frac{\partial \nu_1}{\partial x}+\frac{\partial \nu_2}{\partial y}=0,$$

$$\nu_1\frac{\partial \nu_1}{\partial x}+\nu_2\frac{\partial \nu_1}{\partial y}+\frac{\nu_{THnf}}{k^*}f\nu_1=\frac{1}{\rho_{Thnf}}\frac{\partial \boldsymbol{\tau}}{\partial y}-\frac{\sigma_{THnf}}{\rho_{Thnf}}{B_0}^2\nu_1 +\frac{B_0^2(x)}{\rho_{Thnf}}EB-G(\beta_1)_{Thnf}(T-T_\infty), \tag{1}$$

$$-\frac{f}{(k^*)^{12}}{\nu_1}^2-G(\beta_2)_{Thnf}(C-C_\infty), \tag{2}$$

$$\nu_1\frac{\partial T}{\partial x}+\nu_2\frac{\partial T}{\partial y}+\gamma_1\left[\begin{array}{l}{\nu_1}^2\frac{\partial^2 T}{\partial x^2}+{\nu_2}^2\frac{\partial^2 T}{\partial y^2}+2\nu_1\nu_2\frac{\partial^2 T}{\partial x\partial y}+\left(\nu_1\frac{\partial \nu_1}{\partial x}+\nu_2\frac{\partial \nu_1}{\partial x}\right)\frac{\partial T}{\partial x}\\ +\left(\nu_1\frac{\partial \nu_2}{\partial x}+\nu_2\frac{\partial \nu_2}{\partial x}\right)\frac{\partial T}{\partial y}-\frac{Q_0}{(\rho C_p)_{hnf}}\left(\nu_1\frac{\partial T}{\partial x}+\nu_2\frac{\partial T}{\partial y}\right)\end{array}\right] =\frac{1}{(\rho C_p)_{hnf}}\frac{\partial}{\partial y}\left(k^T_{Thnf}\frac{\partial T}{\partial y}\right)+\frac{Q_0}{(\rho C_p)_{Thnf}}(T-T_\infty), \tag{3}$$

$$\nu_1\frac{\partial C}{\partial x}+\nu_2\frac{\partial C}{\partial y}+\gamma_2\left[\begin{array}{l}{\nu_1}^2\frac{\partial^2 C}{\partial x^2}+{\nu_2}^2\frac{\partial^2 C}{\partial y^2}++2\nu_1\nu_2\frac{\partial^2 C}{\partial x\partial y}+\left(\nu_1\frac{\partial \nu_1}{\partial x}+\nu_2\frac{\partial \nu_1}{\partial x}\right)\frac{\partial C}{\partial x}\\ +\left(\nu_1\frac{\partial \nu_2}{\partial x}+\nu_2\frac{\partial \nu_2}{\partial x}\right)\frac{\partial C}{\partial y}-K_M\left(\nu_1\frac{\partial C}{\partial x}+\nu_2\frac{\partial C}{\partial y}\right)\end{array}\right] =K_M(C-C_\infty)+\frac{\partial}{\partial y}\left(D_{Thnf}\frac{\partial C}{\partial y}\right) \tag{4}$$

and subjected to the desired boundary conditions

$$\begin{aligned}&\nu_1=ax^{\frac{1}{3}},C=C_w,\nu_2=0,T=T_w:\\ &y=0,C\to C_\infty,\nu_1\to 0,T\to T_\infty:\ y\to\infty\ .\end{aligned} \tag{5}$$

Similarity, the variables of temperature-dependent concentration and temperature-dependent thermal conductivity are defined as

$$\varphi=\frac{C-C_w}{C_w-C_\infty},\eta=\frac{y}{x^{1/3}}\left(\frac{a}{\nu_f}\right)^{1/2},\psi=x^{2/3}\left(a\nu_f\right)^{1/2},\tau=\rho_f\left(a^3\nu_f\right)^{1/2},$$

$$\theta=\frac{T-T_w}{T_w-T_\infty}, \tag{6}$$

$$k^t_{Thnf}=k_{Thnf}\left[1+\epsilon_1\left(\frac{T-T_\infty}{T_w-T_\infty}\right)\right], \tag{7}$$

$$D^c_{Thnf}=D_{Thnf}\left[1+\epsilon_2\left(\frac{T-T_\infty}{T_w-T_\infty}\right)\right]. \tag{8}$$

The system of ODEs [34] is formulated as

$$D_1G-F''\frac{G^2+\lambda\Upsilon^2}{G^2+\Upsilon^2}=0, \tag{9}$$

$$G'-D_1\frac{1}{3}F'^2+D_1\frac{2}{3}FF''-\frac{\sigma_{Thnf}}{\sigma_f}MF'+D_1\lambda_1\theta-\epsilon F'-D_1F_rF'^2 +D_1\lambda_2\varphi+\frac{\sigma_{Thnf}}{\sigma_f}ME_1=0, \tag{10}$$

$$(1+\epsilon_1\theta)\theta''+\epsilon_1(\theta')^2+Pr\,\Gamma\frac{k_f\left(\rho C_p\right)_{Thnf}}{k_{Thnf}\left(\rho C_p\right)_f}\left[FF'\theta'+\eta F^2\theta''-H_tF\theta'\right] +\frac{k_f\left(\rho C_p\right)_{Thnf}}{k_{Thnf}\left(\rho C_p\right)_f}\frac{2}{3}PrF\theta'+\frac{k_f}{k_{Thnf}}H_tPr\,\theta=0, \tag{11}$$

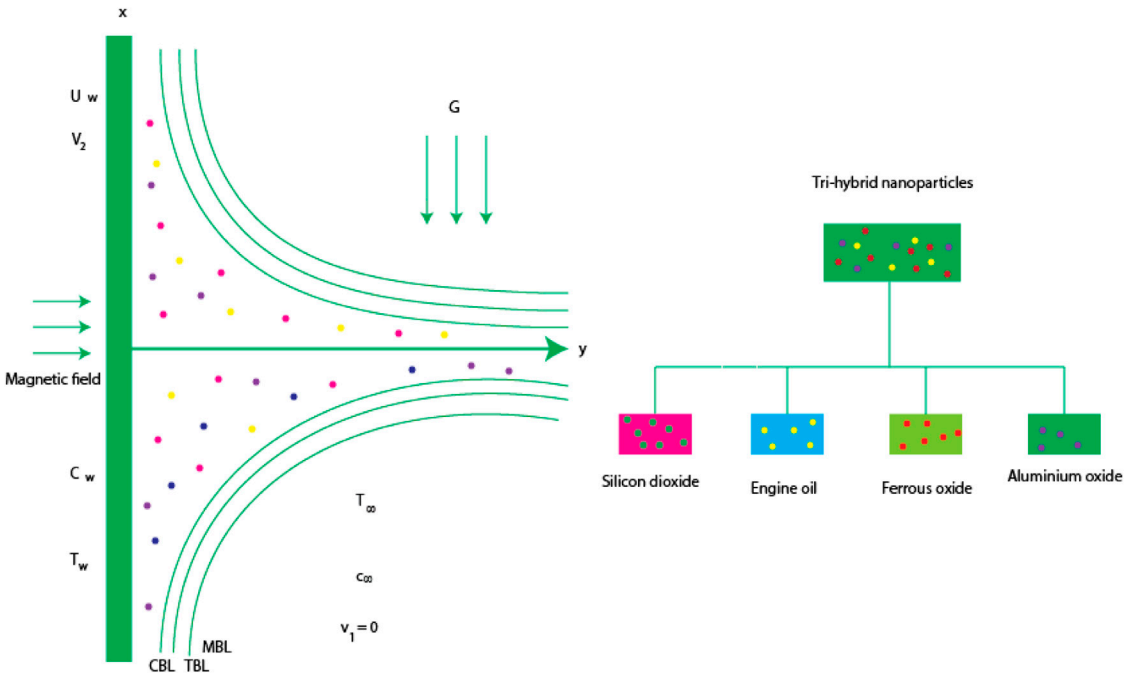

FIGURE 1
Physical configuration of the model.

$$(1+\epsilon_2\varphi)\varphi'' + \epsilon_2\varphi'\theta' + \frac{2}{3D_2}PrF\varphi' + \frac{Sc\Gamma_1}{D_2}\left[FF'\varphi' + \eta F^2\varphi'' - K_cF\varphi'\right] - \frac{K_cSc}{D_2}\varphi = 0. \quad (12)$$

Equation 5 in dimensionless form [34] is defined as

$$F(0) = 0, F'(0) = 1, \theta(0) = 1, \varphi(0) = 1, F(\infty) \to 0, \theta(\infty) \to 0, \varphi(\infty) \to 0. \quad (13)$$

The defined correlations associated with tri-hybrid nanoparticles [36] are

$$\rho_{Thnf} = (1-\Phi_1)\left\{(1-\Phi_2)\left[(1-\Phi_3)\rho_f + \Phi\Phi_3\rho_3\right] + \Phi_2\rho_2\right\} + \Phi\Phi_1\rho_1, \quad (14)$$

$$\frac{K_{hnf}}{K_{nf}} = \frac{K_2 + 2K_{nf} - 2\Phi_1\left(K_{nf} - K_2\right)}{K_2 + 2K_{nf} + \Phi_2\left(K_{nf} - K_2\right)},$$
$$D_2 = (1-\Phi_3)^{1.5}(1-\Phi_1)^{1.5}(1-\Phi_2)^{1.5}, \quad (15)$$
$$\frac{K_{Thnf}}{K_{hnf}} = \frac{K_1 + 2K_{hnf} - 2\Phi_1\left(K_{hnf} - K_1\right)}{K_1 + 2K_{hnf} + \Phi_1\left(K_{hnf} - K_1\right)},$$
$$\frac{K_{nf}}{K_f} = \frac{K_3 + 2K_f - 2\Phi_3\left(K_f - K_3\right)}{K_3 + 2K_f + \Phi_3\left(K_f - K_3\right)}, \quad (16)$$
$$\frac{\sigma_{Tnf}}{\sigma_{hnf}} = \frac{\sigma_1(1+2\Phi_1) - \Phi_{hnf}(1-2\Phi_1)}{\sigma_1(1-\Phi_1) + \sigma_{hnf}(1+\Phi_1)},$$
$$\frac{\sigma_{nf}}{\sigma_f} = \frac{\sigma_3(1+2\Phi_3) + \Phi_f(1-2\Phi_3)}{\sigma_3(1-\Phi_3) + \sigma_f(1+\Phi_3)},$$

$$\mu_{Thnf} = \frac{\mu_f}{(1-\Phi_3)^{2.5}(1-\Phi_2)^{2.5}(1-\Phi_1)^{2.5}}, \quad (17)$$

$$D_1 = \frac{\left[(1-\Phi_2)\left\{(1-\Phi_1) + \Phi_1\frac{\rho_{s1}}{\rho_f}\right\}\right] + \Phi_2\frac{\rho_{s2}}{\rho_f}}{(1-\Phi_1)^{-2.5}(1-\Phi_2)^{-2.5}},$$
$$\frac{\sigma_{hnf}}{\sigma_{nf}} = \frac{\sigma_2(1+2\Phi_2) + \Phi_{nf}(1-2\Phi_2)}{\sigma_2(1-\Phi_2) + \sigma_{nf}(1+\Phi_2)}. \quad (18)$$

The mathematical expressions of Sherwood number and temperature gradient [34] are

$$Nu = \frac{-xk_{Thnf}\frac{\partial T}{\partial y}\big|_{y=0}}{(T_w - T_\infty)k_f}, (R_e)^{-1/2}N^*u = -\frac{k_{Thnf}}{k_f}\theta'(0), \quad (20)$$

$$Sh = \frac{-xQ_t}{D_{Thnf}(C - C_\infty)}, (Re)^{-1/2}S^*h = -\frac{1}{D_2}\varphi'(0), \quad (21)$$

where (Reynolds number) $Re\left(=\frac{U_w x}{\nu_f}\right)$.

3 Numerical procedure

The current model in terms of ODEs is numerically handled by a finite element approach based on the following steps:

$$\int_{\eta_e}^{\eta_{e+1}} wet_1\left(F' - T\right)d\eta = 0, \quad (22)$$

$$\int_{\eta_e}^{\eta_{e+1}} wet_2\begin{bmatrix} G' - D_1\frac{1}{3}T^2 + D_1\frac{2}{3}FT' - \frac{\sigma_{hnf}}{\sigma_f}MT + D_1\lambda_1\theta \\ -\epsilon T - D_1F_rT^2 + D_1\lambda_2\varphi + \frac{\sigma_{hnf}}{\sigma_f}ME_1 \end{bmatrix}d\eta = 0, \quad (23)$$

$$\int_{\eta_e}^{\eta_{e+1}} wet_3 \begin{bmatrix} (1+\epsilon_1\theta)\theta'' + \epsilon_1(\theta')^2 + + \dfrac{k_f(\rho C_p)_{Thnf}}{k_{Thnf}(\rho C_p)_f}\dfrac{2}{3}PrF\theta' + \dfrac{k_f}{k_{hnf}}H_tPr\,\theta \\ +Pr\,\Gamma\dfrac{k_f(\rho C_p)_{Thnf}}{k_{hnf}(\rho C_p)_f}\left[FT\theta + \eta F^2\theta'' + H_tF\theta\right] \end{bmatrix} d\eta = 0, \tag{24}$$

$$\int_{\eta_e}^{\eta_{e+1}} wet_4 \begin{bmatrix} \dfrac{Sc\Gamma_1}{D_2}\left(FT\varphi' + \eta F^2\varphi'' + K_cF\varphi'\right) - \dfrac{K_cSc}{D_2}\varphi \\ (1+\epsilon_2\varphi)\varphi'' + \epsilon_2\varphi\theta \end{bmatrix} d\eta = 0. \tag{25}$$

3.1 Discretization

The computational form domain has been discretized into elements, and weighted residuals are derived as

$$K_{ij}^{11} = 0, K_{ij}^{13} = 0, K_{ij}^{14} = 0, K_{ij}^{12} = -\int_{\eta_e}^{\eta_{e+1}} \left(\psi_j\psi_i\right)d\eta, B_i^1 = 0, \tag{26}$$

$$K_{ij}^{22} = \int_{\eta_e}^{\eta_{e+1}} \begin{bmatrix} -\left(\dfrac{\bar{G}^2+\lambda\Upsilon^2}{\bar{G}^2+\lambda\Upsilon^2}\right)'\dfrac{d\psi_j}{d\eta}\dfrac{d\psi_j}{d\eta} - D_1\dfrac{1}{3}\bar{T}\psi_j\psi_i + D_1\dfrac{2}{3}\bar{F}\psi_i\dfrac{d\psi_j}{d\eta} - \dfrac{\sigma_{hnf}}{\sigma_f}M\psi_j\psi_i \\ -\epsilon\psi_j\psi_i - D_1F_r\bar{H}\psi_i\dfrac{d\psi_j}{d\eta} \end{bmatrix} d\eta, \tag{27}$$

$$K_{ij}^{23} = \int_{\eta_e}^{\eta_{e+1}} \left[D_1\lambda_1\psi_j\psi_i\right]d\eta, K_{ij}^{24} = \int_{\eta_e}^{\eta_{e+1}} \left[D_1\lambda_2\psi_j\psi_i\right]d\eta, B_i^2 = \frac{\sigma_{hnf}}{\sigma_f}ME_1, K_{ij}^{21} = 0, \tag{28}$$

$$K_{ij}^{33} = \int_{\eta_e}^{\eta_{e+1}} \begin{bmatrix} -\left(1+\epsilon_1\theta + Pr\,\Gamma\dfrac{k_f(\rho C_p)_{Thnf}}{k_{hnf}(\rho C_p)_f}\bar{F}^2\right)\dfrac{d\psi_j}{d\eta}\dfrac{d\psi_j}{d\eta} + \epsilon_1\overline{\theta'}\psi_i\dfrac{d\psi_j}{d\eta} + \dfrac{k_f}{k_{hnf}}H_tPr\psi_j\psi_i \\ \dfrac{k_f(\rho C_p)_{Thnf}}{k_{Thnf}(\rho C_p)_f}\dfrac{2}{3}Pr\bar{F}\psi_i\dfrac{d\psi_j}{d\eta} + r\Gamma\dfrac{k_f(\rho C_p)_{Thnf}}{k_{hnf}(\rho C_p)_f}\left(\bar{F}\bar{T}\psi_i\dfrac{d\psi_j}{d\eta} + H_t\bar{F}\psi_i\dfrac{d\psi_j}{d\eta}\right) \end{bmatrix} d\eta, \tag{29}$$

$$K_{ij}^{44} = \int_{\eta_e}^{\eta_{e+1}} \begin{bmatrix} -\left(1+\epsilon_2\bar{\varphi} + \eta\bar{F}^2\right)\dfrac{d\psi_j}{d\eta}\dfrac{d\psi_j}{d\eta} + \epsilon_2\overline{\varphi'}\psi_i\dfrac{d\psi_j}{d\eta} + \dfrac{2}{3}Sc\bar{F}\psi_i\dfrac{d\psi_j}{d\eta} - \dfrac{K_cSc}{D_2}\psi_j\psi_i \\ \dfrac{Sc\Gamma_1}{D_2}\left(\bar{F}\bar{T}\psi_i\dfrac{d\psi_j}{d\eta} + K_c\bar{F}\psi_i\dfrac{d\psi_j}{d\eta}\right) \end{bmatrix} d\eta, \tag{30}$$

$$K_{ij}^{31} = 0, K_{ij}^{41} = 0, K_{ij}^{32} = 0, K_{ij}^{42} = 0, K_{ij}^{34} = 0, K_{ij}^{43} = 0, B_i^3 = 0, B_i^4 = 0. \tag{31}$$

3.2 Assembly process

The assembly process is implemented to derive a global stiffness matrix. In this step, the boundary vector, source vector, and stiffness matrix are obtained as.

3.3 Investigations of error and convergence

Error analysis is estimated as

$$Er = \left|\Omega^j - \Omega^{j-1}\right|. \tag{32}$$

Table 2 shows mesh-free simulations and convergence analysis, while criteria regarding convergence are defined as

TABLE 1 Thermal properties of engine oil, silicon dioxide, and aluminum oxide [36, 37].

Engine oil	Aluminum oxide	Silicon dioxide	Fe_3O_4
$k(0.144)$	$k(32.9)$	$k(1.4013)$	$k(80)$
$\sigma(0.125\times10^{-11})$	$\sigma(5.96\times10^{7})$	$\sigma(3.5\times10^{6})$	$\sigma(0.112\times10^{-6})$
ρ (884)	ρ (6310)	ρ (2270)	ρ (5180)

$$Max\left|\Omega^j - \Omega^{j-1}\right| < 10^{-8}. \tag{33}$$

3.4 Validation of works

The code for FEM was designed in MAPLE 18. Table 3 illustrates the present validation in view of temperature gradient, with an already-published study [38] having different values of Υ in the absence of tri-hybrid nanoparticles, variable properties, heat sink, and non-Fourier's law. It was noticed that the present results were obtained by the finite element method while the present simulations, obtained by the finite element method, are compared with a shooting approach termed the RK4-method (see Table 3).

4 Results and discussion

The development of a two-dimensional model is formulated in view of Reiner–Philippoff toward a surface involving buoyancy forces and electric field. Energy transfer and mass species are carried out in the presence. Dispersions of tiny nanoparticles are incorporated using generalized theory. Mass diffusion (variable) and thermal conductivity (variable) are inserted into the concentration and energy equations. A finite element scheme has been utilized to simulate numerical study of the present problem. Graphical explanations regarding flow, solute, and thermal energy *versus* various parameters are displayed in the following sections.

4.1 Study of fluidic motion

In this subsection, graphs related to velocity curves are plotted *versus* electric magnetic (E_1) number, Forchheimer number (F_r), and fluid parameter (γ). Comparative study of tri-hybrid nanofluid and hybrid nanoparticles on a velocity field is conducted *versus* parameters, shown in Figures 2–4. It is evident that solid curves are generated to represent the role of nanoparticles (tri-hybrid), and dash–dot lines are plotted to sketch the estimation of hybrid nanomaterials. Figure 2 predicts the behavior of E_1 on the velocity field. Here, E_1 is electric field number, and velocity increases *versus* enhancement in E_1. Here, the parameter related to E_1 is known as the electric magnetic number; it is modeled using the electric magnetic number in the momentum equation. Mathematically, a parameter regarding E_1 is based on $(\frac{\sigma_{Thnf}}{\sigma_f}ME_1)$ and appears in

TABLE 2 Analysis of the grid-independent study carried out for 300 elements for concentration, velocity, and temperature profiles.

Number of elements	$F'\left(\frac{\eta_{max}}{2}\right)$	$\theta\left(\frac{\eta_{max}}{2}\right)$	$\varphi\left(\frac{\eta_{max}}{2}\right)$
30	0.03739643693	0.007435435051	0.009773428084
60	0.03652941667	0.003617569756	0.004548750392
90	0.03623026090	0.002433140864	0.002959697248
120	0.03607872439	0.001849791306	0.002192563678
150	0.03598713063	0.001500248584	0.001740935198
180	0.03592576537	0.001266406353	0.001443441685
210	0.03588178671	0.001098466029	0.001232702583
240	0.03584874587	0.0009717300891	0.001075606893
270	0.03582297916	0.0008725175218	0.0009539964889
300	0.03580234563	0.0007926265239	0.0008570696942

TABLE 3 Validation of present works for Nusselt number with different values of Υ when $\epsilon_1 = 0, \Gamma = 0, \Phi_1 = \Phi_3 = \Phi_2 = 0, H_t = 0$.

Υ	Sajid et al. [38] (Shooting method)	present works (Finite element approach)
0.1	0.130909	0.001232702583
0.2	0.109284	0.001232702583
0.3	0.085161	0.001232702583

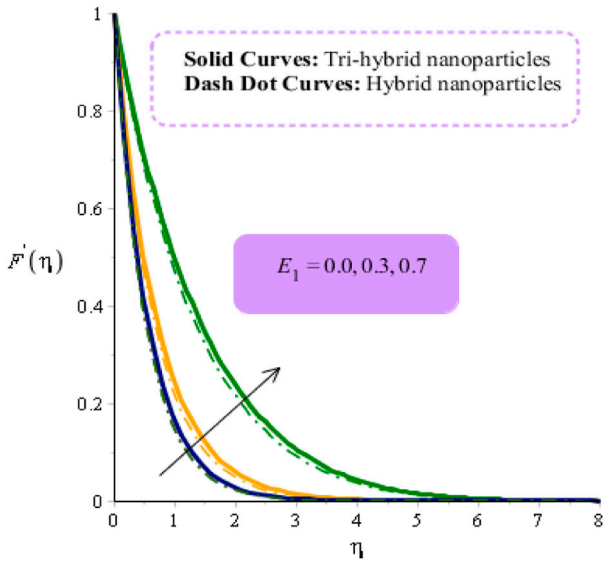

FIGURE 2
Effect of E_1 on velocity curves.

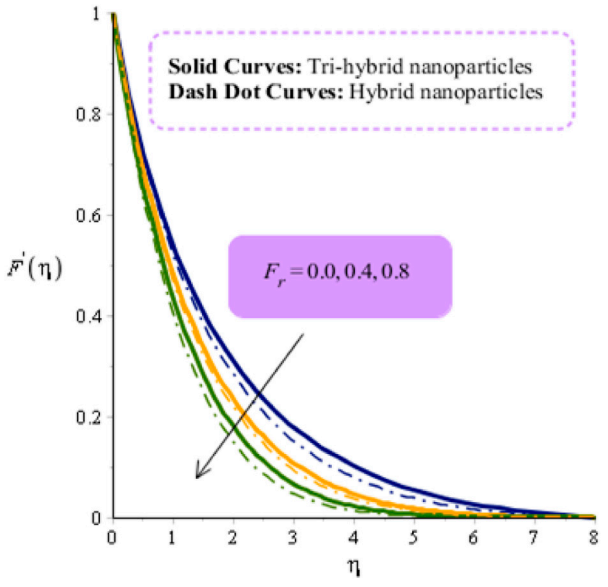

FIGURE 3
Effect of F_r on velocity curves.

the dimensionless momentum equation. Direct proportional relations have been estimated among velocity and E_1. Therefore, velocity increases against $E_1 > 0$. The physical reason behind this increasing trend is the appearance of a Lorentz force because forces (electromagnetic) behave in the same direction during the flow of nanoparticles. Furthermore,

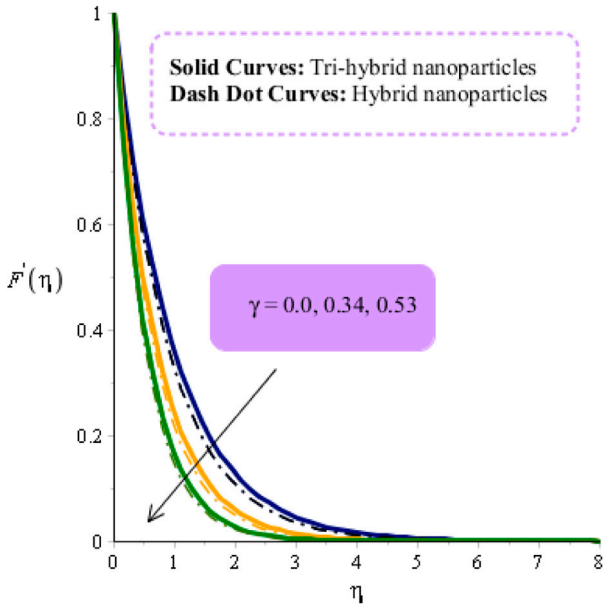

FIGURE 4
Effect of ϒ on velocity curves.

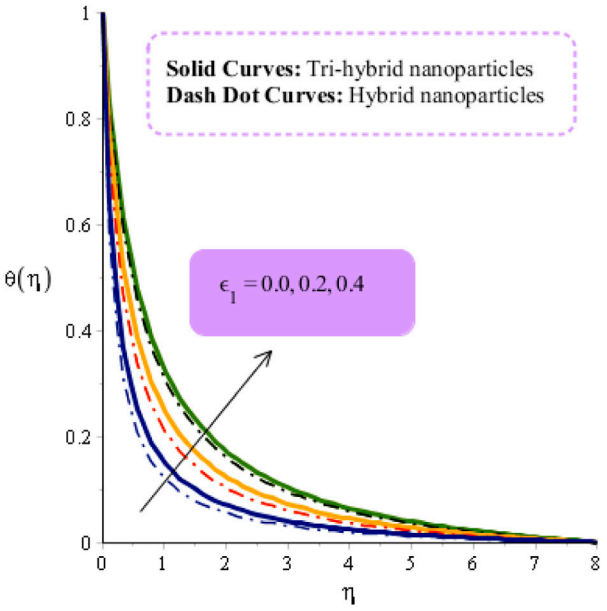

FIGURE 6
Effect of ϵ_1 on thermal energy curves.

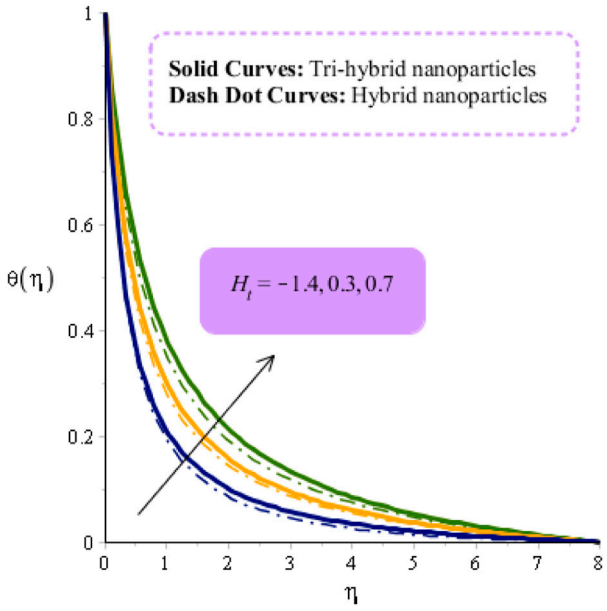

FIGURE 5
Effect of H_t on thermal energy curves.

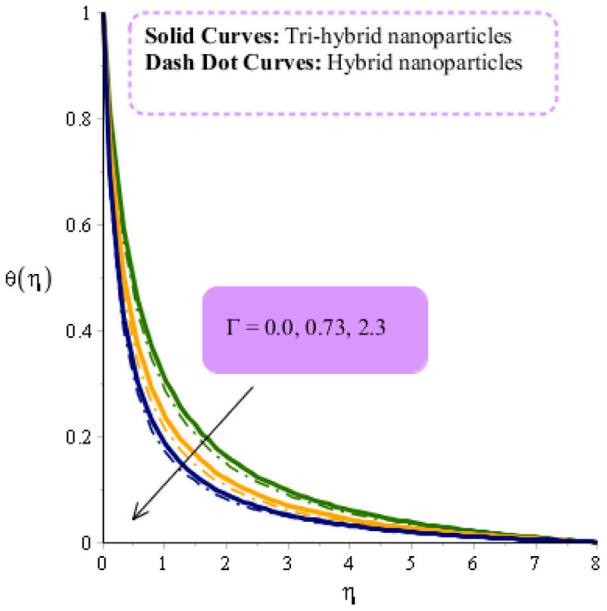

FIGURE 7
Effect of Γ on thermal energy curves.

drag force declines when E_1 is enhanced. Thickness in view of momentum layers is increased against magnified values of E_1. Figure 3 predicts the influence of F_r on fluidic motion. Momentum layers are based on variation in F_r. It is mentioned that a retardation motion is created in motion regarding particles, which creates a resistance force in fluidic particles. Momentum layers are also reduced using higher values of F_r. Physical, numerous pores are placed at the surface. Therefore, velocity field is reduced when F_r is increased. Moreover, F_r is known as a Forchheimer porous medium, which is related to resistive force on the flow. It is a non-linear function *versus* velocity, while it experiences retardation force. Mathematically, the direct proportional relation among drag force and F_r is increased when F_r is enhanced. Thickness

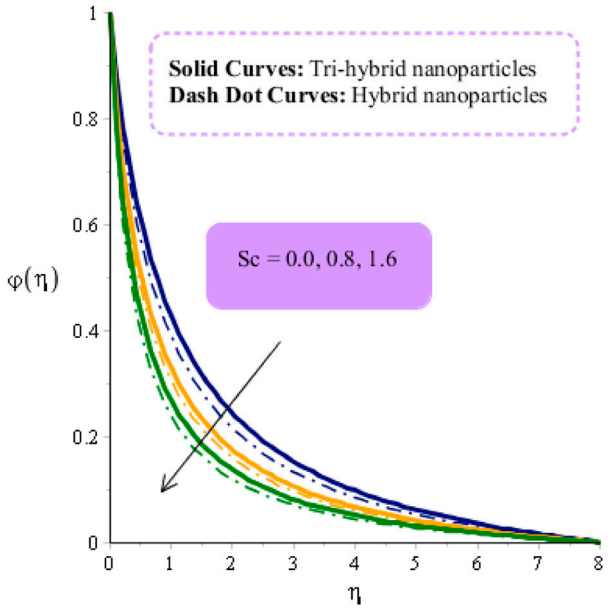

FIGURE 8
Effect of *Sc* on concentration curves.

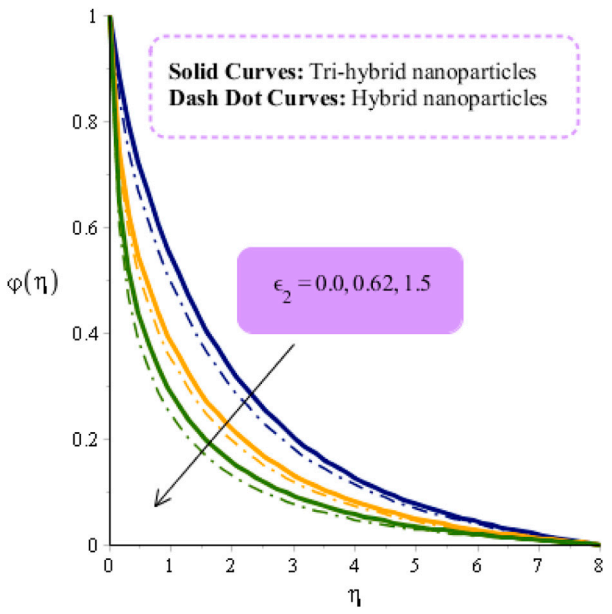

FIGURE 9
Effect of ϵ_2 on concentration curves.

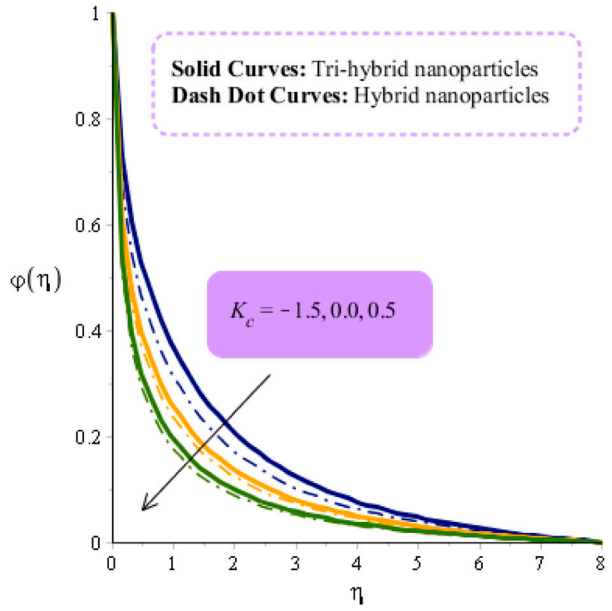

FIGURE 10
Effect of K_c on concentration curves.

TABLE 4 Change in H_t, M, Sc, and K_c on Sherwood and Nusselt numbers with Al_2O_3-SiO_2-Fe_3O_4/EO.

		Al_2O_3-SiO_2-Fe_3O_4/EO	
		$(R_e)^{-1/2}Nu$	$(R_e)^{-1/2}Sh$
−1.5	1.4439048872	2.354043674	
H_t	0.3	1.4341150491	2.216220131
1.5	1.4187348974	2.203340433	
0.0	1.9949244290	2.1300114046	
M	0.4	1.7986367522	2.3872299315
0.8	1.5886139807	2.3766813849	
0.0	1.4825160433	2.8766813849	
Sc	0.7	1.5201264396	2.8430450127
1.4	1.5621956263	2.8103801176	
−1.8	1.5621956263	2.7661353542	
K_c	0.2	1.5621956263	2.9319543998
1.8	1.5621956263	2.9872274152	

based on momentum layers declines *versus* enhancement of F_r. This drag force reduces flow on the surface. Figure 4 shows the behavior of Υ on velocity curves. This is a dimensionless parameter that is modeled due to the appearance of Reiner–Philippoff liquid in the momentum. It is evident that fluidic motion is decreased when Υ increases. Moreover, thickness based on momentum layers declines with higher impacts of Υ. Mathematically, an inverse proportional relation has been observed among Υ and velocity. Therefore, an increase in Υ results in flow decreases on the surface. γ is a dimensional parameter also called the Bingham number; it is a ratio among viscous stress and yield stress. Apparent viscosity has a direct proportional relation with increasing shear rate. Consequently, flow increases when shear rate is enhanced.

TABLE 5 Change in $H_t, M, Sc,$ and K_c on Sherwood and Nusselt numbers with SiO_2-Fe_3O_4/EO.

		SiO_2-Fe_3O_4/EO	
		$(R_e)^{-1/2}N^*u$	$(R_e)^{-1/2}S^*h$
	−1.5	0.4808393951	0.9899124392
H_t	0.3	0.4781358091	0.9610303301
	1.5	0.4466081794	0.9411023305
	0.0	0.9175509096	0.1347447593
M	0.4	0.9476944663	0.2613222183
	0.8	0.9666081791	0.2899124392
	0.0	0.4547368979	0.9899124392
Sc	0.7	0.4603960486	1.4199335063
	1.4	0.4718914433	1.4823116160
	−1.8	0.2703851806	1.0261973903
K_c	0.2	0.2887116869	1.6702558152
	1.8	0.2946886834	1.9525223760

4.2 Study of fluidic temperature

Figures 5–7 show the role of fluidic temperature against changes in H_t, ϵ_1, and λ_1. The solid lines are plotted to sketch the role of tri-hybrid nano-structures, while dash–dot lines are plotted to measure the role of hybrid nanoparticles. Figure 5 represents behavior among fluidic temperature and H_t. Fluidic temperature is increased by applying an external heat source at the wall. Mathematically, heat sink (H_t) is directly proportional to $(T - T_\infty)$, whereas temperature difference increases when H_t is increased. In Figure 5, two types of heat transfer are experienced based on heat generation and heat absorption. Furthermore, heat absorption is numerically predicted by $H_t < 0$, and heat generation is predicted by $H_t > 0$. Physically, the heat source (external) is implemented at the surface and is utilized to control thermal thickness. Thermal layer thickness for $H_t < 0$ is higher than for $H_t > 0$. The characteristic of ϵ_1 on thermal layers is shown in Figure 6. The appearance ϵ_1 is created due to the appearance of variable thermal conductivity. In the current investigation, thermal conductivity is considered as a function of thermal energy. Mathematically, thermal conductivity is based on temperature, whereas ϵ_1 is based on $(T_w - T_\infty)$. An increase in ϵ_1 enhances the temperature difference. Mathematically, ϵ_1 is a function of temperature difference. Consequently, temperature difference is based on ϵ_1. Hence, temperature increases against increases in thermal conductivity. Moreover, the thickness of thermal layers for $\epsilon_1 = 0$ is less than the thickness (of thermal layers) for $\epsilon_1 \neq 0$. Whether an involvement of the time relaxation parameter is created due to the appearance of a generalized mechanism of heat transmission is investigated. Γ denotes relaxation time number, and Γ reveals production regarding time related to migration of heat energy through a heated surface. Physically, fluid particles need more time in the case of transfer of thermal energy toward neighboring particles. This reason declines in thermal energy, as depicted in Figure 7.

4.3 Investigation of fluidic concentration

Figures 8–10 determine the characterizations of fluidic concentration *versus* impacts of Sc, K_c, and ϵ_2 upon inserting a tri-hybrid nanofluid. Solid lines are the sketched behavior of tri-hybrid nanofluid, while dash–dot lines are sketched for hybrid nanofluid. Figure 8 reveals the role of Sc on fluidic concentration in the presence of hybrid and tri-hybrid nanofluids. Physically, it is the division of momentum and mass diffusion diffusivities. Hence, an inverse proportional relation of mass diffusion is found *versus* Sc. Therefore, an increase in Sc resulting form higher mass diffusivity is observed. Moreover, mass diffusion for tri-hybrid nanofluids is higher than the amount of mass diffusion for hybrid nano-structures. This reduction of $\varphi(\eta)$ occurs when mass diffusivity decreases against higher values of Sc. Thickness related to concentration can be managed through numerical values of Sc. Furthermore, the amount of mass diffusion for $Sc = 0$ is less than the amount of mass diffusion for $Sc \neq 0$. Figure 9 demonstrates the relationship between mass diffusion and variable mass diffusion number; it shows that the appearance of ϵ_2 on mass diffusion is created due to the implication of variable mass diffusion. Furthermore, variable mass diffusion is based on temperature difference. Therefore, mass diffusion declines when ϵ_2 is increased. From Eq. 8, it was shown that ϵ_2 is a function of temperature difference. Consequently, ϵ_2 is also based on concentration difference, while mass diffusion increases when ϵ_2 is increased. An illustration of the chemical reaction parameter on mass diffusion is shown in Figure 10. Two kinds of chemical reactions are generated for positive or negative numerical values of the chemical reaction parameters. For both cases, mass diffusion declines when K_c is increased. Here, three cases of chemical reactions based on chemical parameters have been observed. It is estimated that $K_c < 0$ when solute particles have been generated, while $K_c > 0$ when solute particles are utilized in the chemical reaction and $K_c = 0$ when no chemical reaction has occurred. As Figure 10 shows, increasing concentrations can be controlled by generative chemical reactions, whereas destructive chemical reactions are performed for increasing concentration tendency.

4.4 Study of Sherwood number and Nusselt number

The impact of Al_2O_3-SiO_2-Fe_3O_4/EO and SiO_2-Fe_3O_4/EO on the Sherwood number and temperature gradient *versus* magnetic number, Schmidt number, H_t, and K_c are observed. Numerical outcomes among Al_2O_3-SiO_2-Fe_3O_4/EO and SiO_2-Fe_3O_4/EO are

recorded in Tables 4, 5. It was observed that temperature gradient and Sherwood number decline with various values of H_t and M. However, the opposite trend was estimated for Sherwood number and temperature gradient. Essentially, the thermal rate and Sherwood number are greater for Al_2O_3-SiO_2-Fe_3O_4/EO than for SiO_2-Fe_3O_4/EO (see Tables 4, 5).

5 Conclusion

Features of fluidic motion, fluidic thermal energy, and fluidic concentration are determined in a two-dimensional model under non-Fourier's law with variable properties. A heat source and chemical reactions are also taken out into a mixture of nanoparticles. A strong scheme, termed a finite element method, is utilized. The main findings of the problem are summarized as follows:

- ➢ Velocity field has been enhanced against changes in H_t, but the opposite behavior is observed *versus* M and F_r.
- ➢ Heat energy increases against changes in relaxation number, heat source number, and variable thermal conductivity parameter.
- ➢ Fluidic concentration declines against changes in Schmidt number and chemical reaction parameter.
- ➢ The cooling process can be improved by adding ternary hybrid nano-structures rather than other nanoparticles.
- ➢ The highest production of thermal energy can be achieved utilizing tri-hybrid nanoparticles as compared with hybrid nanofluids and nanofluids.
- ➢ Thermal gradient and mass diffusion gradient are higher for Al_2O_3-SiO_2-Fe_3O_4/EO than for SiO_2-Fe_3O_4/EO.

Data availability statement

The raw data supporting the conclusion of this article will be made available by the authors, without undue reservation.

Author contributions

All authors listed have made a substantial, direct, and intellectual contribution to the work and approved it for publication.

Funding

This study was supported by funding from Prince Sattam bin Abdulaziz University (project number PSAU/2023/R/1444).

Conflict of interest

The authors declare that the research was conducted in the absence of any commercial or financial relationships that could be construed as a potential conflict of interest.

Publisher's note

All claims expressed in this article are solely those of the authors and do not necessarily represent those of their affiliated organizations, or those of the publisher, the editors, and the reviewers. Any product that may be evaluated in this article, or claim that may be made by its manufacturer, is not guaranteed or endorsed by the publisher.

References

1. Sohail M, Naz R. Modified heat and mass transmission models in the magnetohydrodynamic flow of Sutterby nanofluid in stretching cylinder. *Physica A: Stat Mech its Appl* (2020) 549:124088. doi:10.1016/j.physa.2019.124088

2. Akbar NS, Maraj EN, Noor NFM, Habib MB. Exact solutions of an unsteady thermal conductive pressure driven peristaltic transport with temperature-dependent nanofluid viscosity. *Case Stud Therm Eng* (2022) 35:102124. doi:10.1016/j.csite.2022.102124

3. Akram J, Akbar NS, Alansari M, Tripathi D. Electroosmotically modulated peristaltic propulsion of TiO2/10W40 nanofluid in curved microchannel. *Int Commun Heat Mass Transfer* (2022) 136:106208. doi:10.1016/j.icheatmasstransfer.2022.106208

4. Maraj EN, Akbar NS, Iqbal Z, Azhar E. Framing the MHD mixed convective performance of CNTs in rotating vertical channel inspired by thermal deposition: Closed form solutions. *J Mol Liquids* (2017) 233:334–43. doi:10.1016/j.molliq.2017.03.041

5. Akram J, Akbar NS, Tripathi D. Electroosmosis augmented MHD peristaltic transport of SWCNTs suspension in aqueous media. *J Therm Anal Calorim* (2022) 147(3):2509–26. doi:10.1007/s10973-021-10562-3

6. Saeed A, Bilal M, Gul T, Kumam P, Khan A, Sohail M. Fractional order stagnation point flow of the hybrid nanofluid towards a stretching sheet. *Scientific Rep* (2021) 11(1):20429–15. doi:10.1038/s41598-021-00004-3

7. Shah NA, Khan I. Heat transfer analysis in a second grade fluid over and oscillating vertical plate using fractional Caputo–Fabrizio derivatives. *The Eur Phys J C* (2016) 76(7):362–11. doi:10.1140/epjc/s10052-016-4209-3

8. Khan U, Zaib A, Ishak A. Magnetic field effect on Sisko fluid flow containing gold nanoparticles through a porous curved surface in the presence of radiation and partial slip. *Mathematics* (2021) 9(9):921. doi:10.3390/math9090921

9. Rajashekhar C, Mebarek-Oudina F, Vaidya H, Prasad KV, Manjunatha G, Balachandra H. Mass and heat transport impact on the peristaltic flow of a Ree–Eyring liquid through variable properties for hemodynamic flow. *Heat Transfer* (2021) 50(5):5106–22. doi:10.1002/htj.22117

10. Rehman SU, Fatima N, Ali B, Imran M, Ali L, Shah NA, et al. The Casson dusty nanofluid: Significance of Darcy–forchheimer law, magnetic field, and non-Fourier heat flux model subject to stretch surface. *Mathematics* (2022) 10(16):2877. doi:10.3390/math10162877

11. Khan WA, Pop I. Boundary-layer flow of a nanofluid past a stretching sheet. *Int J Heat mass transfer* (2010) 53(11-12):2477–83. doi:10.1016/j.ijheatmasstransfer.2010.01.032

12. Akbar NS, Iqbal Z, Ahmad B, Maraj EN. Mechanistic investigation for shape factor analysis of SiO_2/MoS_2–ethylene glycol inside a vertical channel influenced by oscillatory temperature gradient. *Can J Phys* (2019) 97(9):950–8. doi:10.1139/cjp-2018-0717

13. Laouira H, Mebarek-Oudina F, Hussein AK, Kolsi L, Merah A, Younis O. Heat transfer inside a horizontal channel with an open trapezoidal enclosure subjected to a heat source of different lengths. *Heat Transfer—asian Res* (2020) 49(1):406–23. doi:10.1002/htj.21618

14. Habib MB, Akbar NS. New trends of nanofluids to combat *Staphylococcus aureus* in clinical isolates. *J Therm Anal Calorim* (2021) 143(3):1893–9. doi:10.1007/s10973-020-09502-4

15. Alghamdi M, Wakif A, Thumma T, Khan U, Baleanu D, Rasool G. Significance of variability in magnetic field strength and heat source on the radiative-convective motion of sodium alginate-based nanofluid within a Darcy-Brinkman porous structure bounded vertically by an irregular slender surface. *Case Stud Therm Eng* (2021) 28:101428. doi:10.1016/j.csite.2021.101428

16. Batool S, Rasool G, Alshammari N, Khan I, Kaneez H, Hamadneh N. Numerical analysis of heat and mass transfer in micropolar nanofluids flow through lid driven cavity: Finite volume approach. *Case Stud Therm Eng* (2022) 37:102233. doi:10.1016/j.csite.2022.102233

17. Khan U, Zaib A, Shah Z, Baleanu D, Sherif ESM. Impact of magnetic field on boundary-layer flow of Sisko liquid comprising nanomaterials migration through radially shrinking/stretching surface with zero mass flux. *J Mater Res Technol* (2020) 9(3):3699–709. doi:10.1016/j.jmrt.2020.01.107

18. Ishtiaq B, Zidan AM, Nadeem S, Alaoui MK. Analysis of entropy generation in the nonlinear thermal radiative micropolar nanofluid flow towards a stagnation point with catalytic effects. *Physica Scripta* (2022) 97(8):085204. doi:10.1088/1402-4896/ac79d7

19. Sohail M, Naz R, Abdelsalam SI. On the onset of entropy generation for a nanofluid with thermal radiation and gyrotactic microorganisms through 3D flows. *Physica Scripta* (2020) 95(4):045206. doi:10.1088/1402-4896/ab3c3f

20. Ghaffari A, Mustafa I, Muhammad T, Altaf Y. Analysis of entropy generation in a power-law nanofluid flow over a stretchable rotatory porous disk. *Case Stud Therm Eng* (2021) 28:101370. doi:10.1016/j.csite.2021.101370

21. Xia WF, Hafeez MU, Khan MI, Shah NA, Chung JD. Entropy optimized dissipative flow of hybrid nanofluid in the presence of non-linear thermal radiation and Joule heating. *Scientific Rep* (2021) 11(1):16067–16. doi:10.1038/s41598-021-95604-4

22. Ahmad S, Nadeem S, Ullah N. Entropy generation and temperature-dependent viscosity in the study of SWCNT–MWCNT hybrid nanofluid. *Appl Nanoscience* (2020) 10(12):5107–19. doi:10.1007/s13204-020-01306-0

23. Abdelsalam SI, Sohail M. Numerical approach of variable thermophysical features of dissipated viscous nanofluid comprising gyrotactic micro-organisms. *Pramana* (2020) 94(1):67–12. doi:10.1007/s12043-020-1933-x

24. Maraj EN, Zehra I, SherAkbar N. Rotatory flow of MHD (MoS_2-SiO_2)/H_2O hybrid nanofluid in a vertical channel owing to velocity slip and thermal periodic conditions. *Colloids Surf A: Physicochemical Eng Aspects* (2022) 639:128383. doi:10.1016/j.colsurfa.2022.128383

25. Saleem S, Gopal D, Shah NA, Feroz N, Kishan N, Chung JD, et al. Modelling entropy in magnetized flow of eyring–powell nanofluid through nonlinear stretching surface with chemical reaction: A finite element method approach. *Nanomaterials* (2022) 12(11):1811. doi:10.3390/nano12111811

26. Shahzad MH, Awan AU, Akhtar S, Nadeem S. Entropy and stability analysis on blood flow with nanoparticles through a stenosed artery having permeable walls. *Sci Prog* (2022) 105(2):003685042210960. doi:10.1177/00368504221096000

27. Naz R, Noor M, Shah Z, Sohail M, Kumam P, Thounthong P. Entropy generation optimization in MHD pseudoplastic fluid comprising motile microorganisms with stratification effect. *Alexandria Eng J* (2020) 59(1):485–96. doi:10.1016/j.aej.2020.01.018

28. Jamshed W, Prakash M, Hussain SM, Eid MR, Nisar KS, Muhammad T, et al. Entropy amplified solitary phase relative probe on engine oil based hybrid nanofluid. *Chin J Phys* (2022) 77:1654–81. doi:10.1016/j.cjph.2021.11.009

29. Akram J, Akbar NS, Tripathi D. A theoretical investigation on the heat transfer ability of water-based hybrid (Ag–Au) nanofluids and Ag nanofluids flow driven by electroosmotic pumping through a microchannel. *Arabian J Sci Eng* (2021) 46(3):2911–27. doi:10.1007/s13369-020-05265-0

30. Alsabery AI, Hashim I, Hajjar A, Ghalambaz M, Nadeem S, Saffari Pour M. Entropy generation and natural convection flow of hybrid nanofluids in a partially divided wavy cavity including solid blocks. *Energies* (2020) 13(11):2942. doi:10.3390/en13112942

31. Sohail M, Shah Z, Tassaddiq A, Kumam P, Roy P. Entropy generation in MHD Casson fluid flow with variable heat conductance and thermal conductivity over non-linear bi-directional stretching surface. *Scientific Rep* (2020) 10(1):12530–16. doi:10.1038/s41598-020-69411-2

32. Akram J, Akbar NS, Tripathi D. Analysis of electroosmotic flow of silver-water nanofluid regulated by peristalsis using two different approaches for nanofluid. *J Comput Sci* (2022) 62:101696. doi:10.1016/j.jocs.2022.101696

33. Sohail M, Ali U, Al-Mdallal Q, Thounthong P, Sherif ESM, Alrabaiah H, et al. Theoretical and numerical investigation of entropy for the variable thermophysical characteristics of couple stress material: Applications to optimization. *Alexandria Eng J* (2020) 59(6):4365–75. doi:10.1016/j.aej.2020.07.042

34. Xiu W, Saleem S, Weera W, Nazir U. Cattaneo-Christove thermal flux in Reiner–Philippoff martial under action of variable Lorentz force employing tri-hybrid nanomaterial approach. *Case Stud Therm Eng* (2022) 38:102267. doi:10.1016/j.csite.2022.102267

35. Hou E, Wang F, Nazir U, Sohail M, Jabbar N, Thounthong P. Dynamics of tri-hybrid nanoparticles in the rheology of pseudo-plastic liquid with dufour and soret effects. *Micromachines* (2022) 13(2):201. doi:10.3390/mi13020201

36. Nazir U, Saleem S, Al-Zubaidi A, Shahzadi I, Feroz N. Thermal and mass species transportation in tri-hybridized Sisko martial with heat source over vertical heated cylinder. *Int Commun Heat Mass Transfer* (2022) 134:106003. doi:10.1016/j.icheatmasstransfer.2022.106003

37. Nazir U, Mukdasai K. Combine influence of Hall effects and viscous dissipation on the motion of ethylene glycol conveying alumina, silica and titania nanoparticles using the non-Newtonian Casson model. *AIMS Maths* (2023) 8(2):4682–99. doi:10.3934/math.2023231

38. Sajid T, Sagheer M, Hussain S. Impact of temperature-dependent heat source/sink and variable species diffusivity on radiative Reiner–Philippoff fluid. *Math Probl Eng* (2020) 2020:9701860. doi:10.1155/2020/9701860

Nomenclature

v_1 and v_2 velocity components
ν dynamic viscosity
$\boldsymbol{\tau}$ vector tensor
G gravitational acceleration
T fluidic temperature
C concentration
Q_0 heat source
C_p specific heat capacitance
k thermal conductivity
γ_2 and γ_1 time relaxation parameters
C_w wall concentration
ψ stream function
PDEs partial differential equations
σ electrical conductivity
Pr Prandtl fluid
Φ_1, Φ_2, and Φ_3 volume fractions
U_w wall difference
EO engine oil
a stretching ratio number along the x-direction
E_1 electric field parameter
ϵ porous number
θ dimensionless temperature
Γ and Γ_1 time relaxation parameters
nf nanofluid
Nu Nusselt number
MHD magneto-hydrodynamics
FEM finite element method
Sc Schmidt number
$wet_4, wet_3, wet_1, and\ wet_2$ weight functions
x and y space coordinates
f permeability
B_0 magnetic field
β_2 and β_1 buoyancy parameters
T_∞ ambient temperature
C_∞ ambient concentration
ρ density
D mass diffusion
K_M chemical reaction number
T_w wall temperature
η independent variable
ϵ_1 and ϵ_2 very small numbers
λ fluid number
F_r Forchheimer number
φ concentration
Re Reynolds number
ODEs ordinary differential equations
H_t heat sink
Υ fluid number
E electric field
F and G dimensionless velocity
EO engine oil
$Thnf$ tri-hybrid nanofluid
s_1, s_3, and s_2 solid nanoparticles
Sh Sherwood number
EMHD electric magneto-hydrodynamic
K_c chemical reaction number
Q_t wall flux

frontiers | Frontiers in Physics

TYPE Original Research
PUBLISHED 22 March 2023
DOI 10.3389/fphy.2023.1149019

OPEN ACCESS

EDITED BY
Gangwei Wang,
Hebei University of Economics and Business, China

REVIEWED BY
Xinyue Li,
Shandong University of Science and Technology, China
Zenggui Wang,
Liaocheng University, China

*CORRESPONDENCE
Muhammad Mobeen Munir,
mmunir.math@pu.edu.pk

SPECIALTY SECTION
This article was submitted to Mathematical Physics, a section of the journal Frontiers in Physics

RECEIVED 20 January 2023
ACCEPTED 03 March 2023
PUBLISHED 22 March 2023

CITATION
Mobeen Munir M, Bashir H and Athar M (2023), Lie symmetries and reductions *via* invariant solutions of general short pulse equation.
Front. Phys. 11:1149019.
doi: 10.3389/fphy.2023.1149019

Lie symmetries and reductions *via* invariant solutions of general short pulse equation

Muhammad Mobeen Munir[1]*, Hajra Bashir[2] and Muhammad Athar[2]

[1]Department of Mathematics, University of Punjab, Lahore, Pakistan, [2]Department of Mathematics, Division of Science and Technology, University of Education, Lahore, Pakistan

Around 1880, Lie introduced an idea of invariance of the partial differential equation (PDE) under one-parameter Lie group of transformation to find the invariant, similarity, or auto-model solutions. Lie symmetry analysis (LSA) provides us an algorithm to search for point symmetries for solving related linear systems for infinitesimal generators. Actually, point symmetries lead us to one-parameter family of solutions from a known solution. LSA is a program that provides us the exact solutions for the non-linear differential equations (DEs) in analogy of the program designed by Galois for algebraic polynomial equations. In this paper, we have carried out the LSA for computing the similarity solutions (symmetries) of the non-linear short pulse equation (SPE) for the cases when $h(u) = e^{u}$, $k(u) = u_{xx}$, $h(u) = e^{u^n}$, and $k(u) = u_{xx}$. In addition, an optimal system of one-dimensional sub-algebra has been set up. The reductions and invariant solutions for the generalized SPE are calculated corresponding to this optimal system as well. Reductions reduce the non-linear PDE or system of PDEs into non-linear reduced ordered ODE or system of PDEs. This helps to solve these systems of PDEs to reduced form. Graphical behavior of the transformed points of the 1-parameter solution functions have drawn.

KEYWORDS

short pulse equation, Lie point symmetry analysis, optimal system for lie subalgebras, reductions, invariant solutions

1 Introduction

Galois used the group theory to discuss the solvability of algebraic polynomial equations. Sophus Lie used the same idea foe differential equations and devised a comprehensive program now known as Lie symmetry analysis (LSA). In his attempt, he also developed the theory of Lie groups with broad applications in many areas of mathematics, physics, and in applied sciences [1, 2]. [3] have explained the procedure of symmetry reductions and exact solutions for the non-linear PDEs using three different methods that are direct, classical, and non-classical. [4] used LSA for systems of non-linear PDEs including the solutions, for system of non-linear coupled PDEs in real physical application, for the unsteady liquid and gas flow in long pipelines, for approximated long wave equations in shallow water and for the general dispersive long-wave equation.

Non-linear short pulse equation (SPE) represents the propagation of ultra-short pulses (light pulses) in optical fibers of silica [5]. Propagation of pulses in optical fibers was first depicted by the cubic non-linear Schrodinger equation (NLSE) which are used to provide the actual fiber connections and refer new systems of fiber communication to attain very high

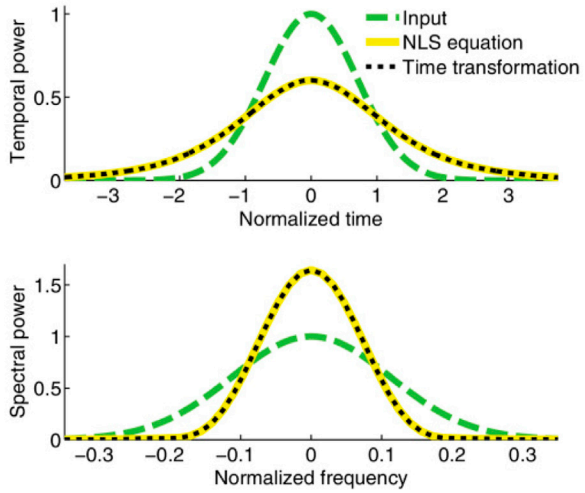

FIGURE 1
Pulse propagation in NL-dispersive optics.

data transmission [6, 7]. Research studies on a large scale have been performed for the propagation of ultra-short pulses (very narrow pulses) that permit high quality fast data transmission [6, 8]. In case of short pulses (or ultra-short pulses), the rationality of NLSE lacks due to the breakdown, [9]. Also, the higher order terms that are involved in cubic NLSE cause difficulties, see Figure 1, for the behavior of NLSE as an output [10]. Therefore, determined the SPE which provides more accurate approximation of the solution of Maxwell's equation in non-linear media rather than the NLSE [6]. The SPE has vast applications in many applied fields such as systems of impulse, mechanics, neural networks, and in many other fields of sciences. Determined the symmetries of SPE and travelling wave solution by parametric representation and power series process, respectively, [11]. Evaluated the symmetry reductions and conservation laws by using the direct method for SPE, [12]. Authors also determined the Lie symmetries for SPE through the non-local system. Established the results for well-posedness of solutions which are bounded for homogenous IBVP and Cauchy problem connected with SPE, [5]. Matsuno constructed multiple exact solutions by using the direct method for three novel PDEs related with generalizations of SPE that are integrable, [13]. He gave the parametric representation of multi-soliton solutions of generalized SPE. LSA has been used by many mathematicians to explore the results related to the exact solutions of non-linear PDEs which depict physical phenomena [14]. Discussed the class of non-linear PDEs having an arbitrary order [15]. Authors estimated the determining equations for non-classical symmetries by using compatibility of original equations with invariant surface conditions.

In this article, we have discussed the LSA for one of the modified form of SPE and see graphical behavior of the functions depending upon 1-parameter (ϵ) Lie groups. The non-linear SPE is as follows:

$$u_{xt} = \alpha u + \frac{1}{3}\beta\left(u^3\right)_{xx}, \tag{1}$$

where $u(x, t)$ is the magnitude of electric field. α and β are the real parameters. Considering the SPE of the following form

$$u_{xt} = \alpha h(u) + \frac{1}{3}\beta k^3(u), \tag{2}$$

where we let the general functions $h(u)$ and $k(u)$ as:

- $h(u) = e^u$ and $k(u) = u_{xx}$,
- $h(u) = e^{u^n}$ for $n \in N$, $(n > 1)$ and $k(u) = u_{xx}$.

It is worth mentioning that the case $h(u) = u^n$ and $k(u) = u_{xx}$ for Eq. 2 has been recently discussed in the article [16]. We will find Lie point symmetries corresponding to the aforementioned cases and the optimal system with reductions and see their graphical behavior corresponding to the Lie symmetries.

2 Results

In the present section, we give our main results with computations.

2.1 Lie symmetries of SPE for the case of $h(u) = e^u$ and $k(u) = u_{xx}$

Eq. 2 becomes

$$u_{xt} = \alpha e^u + \frac{1}{3}\beta u_{xx}^3, \tag{3}$$

Consider the one parameter Lie group of point transformations for Eq. 3.

$$\begin{aligned} x^* &= x + \epsilon\lambda(x,t,u) + O(\epsilon^2),\\ t^* &= t + \epsilon\mu(x,t,u) + O(\epsilon^2),\\ u^* &= u + \epsilon\nu(x,t,u) + O(\epsilon^2), \end{aligned} \tag{4}$$

where $\epsilon \in R$ is the group parameter.The group generator of (4) is defined in the following vector form as:

$$W = \lambda(x,t,u)\frac{\partial}{\partial x} + \mu(x,t,u)\frac{\partial}{\partial t} + \nu(x,t,u)\frac{\partial}{\partial u}, \tag{5}$$

where λ, μ and ν are infinitesimal functions of group variables. The second prolongation of the infinitesimal generator along with coefficients has the following form:

$$\begin{aligned} Pr^{(2)}W &= W + \nu^x\frac{\partial}{\partial u_x} + \nu^t\frac{\partial}{\partial u_t} + \nu^{xx}\frac{\partial}{\partial u_{xx}} + \nu^{xt}\frac{\partial}{\partial u_{xt}} + \nu^{tt}\frac{\partial}{\partial u_{tt}},\\ \nu^{xx} &= D_xD_x\left(\nu - \lambda u_x - \mu u_t\right) + \lambda u_{xxx} + \mu u_{xxt},\\ \nu^{xt} &= D_xD_t\left(\nu - \lambda u_x - \mu u_t\right) + \lambda u_{xtx} + \mu u_{xtt}. \end{aligned} \tag{6}$$

where D_x and D_t are the total derivatives.

Apply the second prolongation of the infinitesimal generator Eq. 5 onto Eq. 3. Then, in order to calculate symmetry of Eq. 3, we have the equation of the following form:

$$Pr^{[2]}W\left(u_{xt} - \alpha e^u - \frac{1}{3}\beta u_{xx}^3\right)\Big|_{u_{xt}=\alpha e^u+\frac{1}{3}\beta u_{xx}^3} = 0. \tag{7}$$

Solving this equation

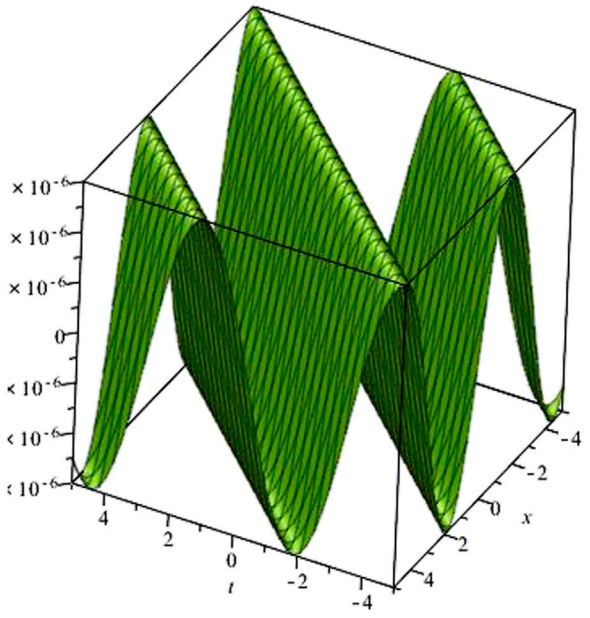

FIGURE 2
For $u^{(1)} = -\frac{6}{5}\epsilon[\cos(e^{-\frac{1}{5}\epsilon}x + e^{-\epsilon}t)]$ and ϵ =0.000005.

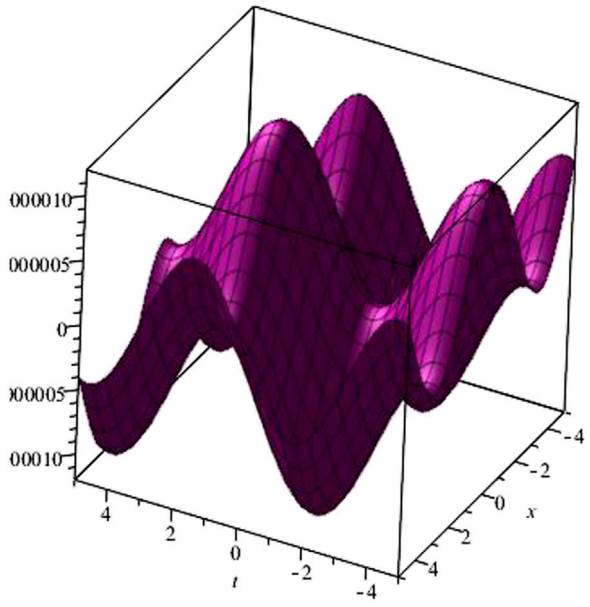

FIGURE 3
For $u^{(1^*)} = -\frac{6}{5}\epsilon[\cos(\epsilon^{-\frac{1}{5}\epsilon}x) + \sin(e^{-\epsilon}t)]$ and ϵ = 0.000005.

$$\left[-\alpha\nu e^{u} - \beta\nu^{xx}\left(u^{2}\right)_{xx} + \nu^{xt}\right]|_{u_{xt}=\alpha e^{u}+\frac{1}{3}\beta u^{3}_{xx}} = 0. \tag{8}$$

Substitute the values of ν^{xx}, ν^{xt} and Eq. 3 which leads to an under-determined system of equations given as:

$$\begin{aligned}
&\mu_{xx} = 0, \quad \mu_{xu} = 0, \quad \mu_{uu} = 0, \quad \lambda_{uu} = 0, \quad \mu_{u} = 0, \quad \lambda_{u} = 0,\\
&\lambda_{tu} = 0, \quad \mu_{x} = 0, \quad \nu_{uu} = 0, \quad \nu_{xu} = 0, \quad \nu_{xx} = 0, \quad \nu_{tu} = 0,\\
&\lambda_{t} = 0, \quad \lambda_{xx} = 0,\\
&\quad -\alpha\nu e^{u} + \nu_{xt} + \alpha\left(\nu_{u} - \lambda_{x} - \mu_{t}\right)e^{u} = 0,\\
&\quad -\frac{2}{3}\nu_{u} + \frac{5}{3}\lambda_{x} - \frac{1}{3}\mu_{t} = 0.
\end{aligned} \tag{9}$$

The solution of the aforementioned determining equations gives the coefficient functions in the form of

$$\begin{aligned}
\lambda(x) &= \frac{1}{5}c_1' x + c_3',\\
\mu(t) &= c_1' t + c_2',\\
\nu(x,t,u) &= -\frac{6}{5}c_1'.
\end{aligned} \tag{10}$$

c_1', c_2' and c_3' are arbitrary constants. Thus, the Lie algebra of the infinitesimal symmetries for the case $n = 1$ is

$$\begin{aligned}
W_1 &= \frac{1}{5}x\partial_x + t\partial_t - \frac{6}{5}\partial_u,\\
W_2 &= \partial_t,\\
W_3 &= \partial_x.
\end{aligned} \tag{11}$$

Theorem 3.1 The set of these generators is closed under the one parameter Lie groups H_i^{ϵ} which are generated by infinitesimal generators W_i for i = 1, 2, and 3 are given in the following table. The entries give the transformed points $\exp(\epsilon W_i)(x, t, u) = (x^*, t^*, u^*)$.

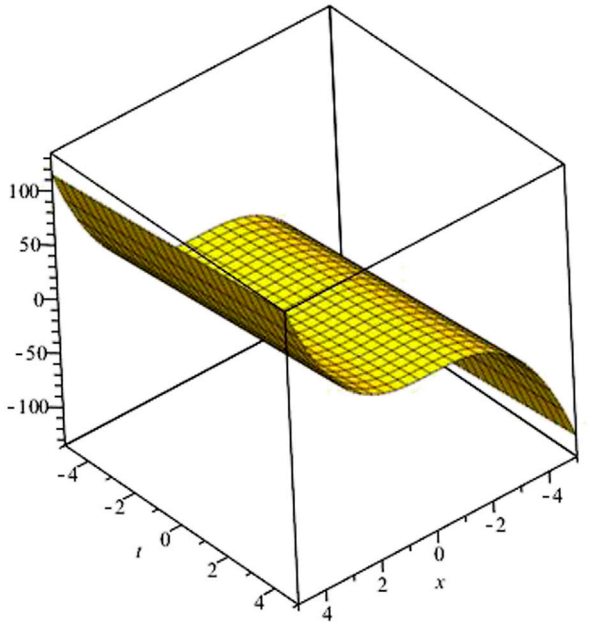

FIGURE 4
For $u^{(2)} = x^3 + 2(t - \epsilon)$ and ϵ = 0.000005.

$$\begin{aligned}
H_1^{\epsilon} &: (x,t,u) \to \left(e^{\frac{1}{5}\epsilon}x, e^{\epsilon}t, u - \frac{6}{5}\epsilon\right),\\
H_2^{\epsilon} &: (x,t,u) \to (x, t+\epsilon, u),\\
H_3^{\epsilon} &: (x,t,u) \to (x+\epsilon, t, u).
\end{aligned} \tag{12}$$

where $\epsilon \in R$ is the group parameter.**Theorem 3.2** If $u = \mathbb{B}(x,t)$ satisfies Eq. 3, then, $u^{(i)}(i$ = 1, 2, and 3) are solutions of Eq. 3:

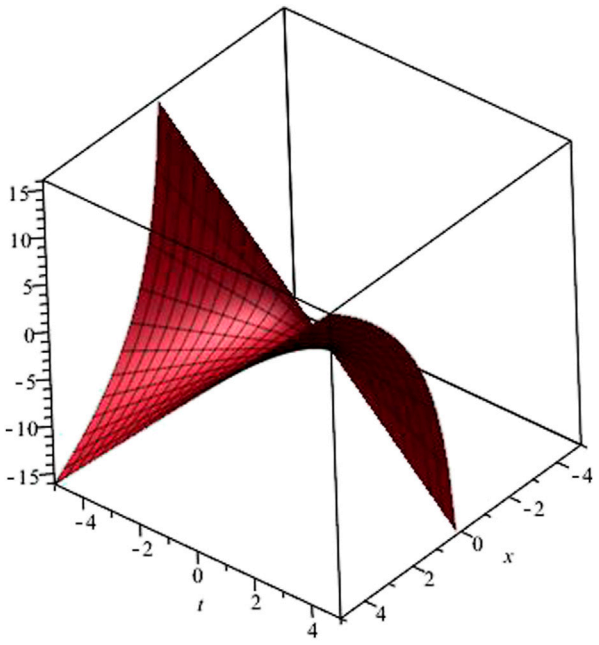

FIGURE 5
For $u^{(3)}=2t\ln(x-\epsilon)$.

$$\begin{aligned} u^{(1)} &= -\frac{6}{5}\epsilon\mathbb{B}\left(e^{-\frac{1}{5}\epsilon}x, e^{-\epsilon}t\right), \\ u^{(2)} &= \mathbb{B}(x, t-\epsilon), \\ u^{(3)} &= \mathbb{B}(x-\epsilon, t). \end{aligned} \tag{13}$$

where $u^i = H_i^{\epsilon}.\mathbb{B}^i(x,t)$, (i = 1,2, and 3), $\epsilon \ll 1$ is any positive number.

The Eq. 13 provides a class of solutions for Eq. 3 depending upon the parameter ϵ and general function $\mathbb{B}^i$ where $(i = 1, 2, 3)$. The Figures 2–5 show the graphical view of the functions u^i, $(i = 1, 2, 3)$ where u^i attained from Lie symmetry groups W_i. These graphs are formed by letting different general functions in place of $\mathbb{B}^i$ in Eq. 13. The graphs are constructed from the maple.

For first equation in Eq. 13, letting the general trigonometric function in place of $\mathbb{B}(x,t)$

$$u^{(1)} = -\frac{6}{5}\epsilon\left[\cos\left(e^{-\frac{1}{5}\epsilon}x + e^{-\epsilon}t\right)\right], \tag{14}$$

along-with $\epsilon = 0.000005$ and abscissa $x = -5$ to 5, ordinate $t = -5$ to 5.

$$u^{(1)} = -0.000006\left[\cos\left(e^{-0.000001}x + e^{-0.000005}t\right)\right]. \tag{15}$$

Figure 2 shows the graphical behavior of Eq. 15.letting another general value of function $\mathbb{B}(x,t) = \cos(\epsilon^{-\frac{1}{5}\epsilon}x) + \sin(e^{-\epsilon}t)$. The function becomes

$$u^{(1^*)} = -0.000006\left[\cos\left(e^{-0.000001}x\right) + \sin\left(e^{-0.000005}t\right)\right]. \tag{16}$$

Figure 3 shows the graphical view of Eq. 16.

For second equation of Eq. 13, considering a general function $\mathbb{B}(x,t) = x^3 + 2(t-\epsilon)$ for the same values of $\epsilon = 0.000005$ and aforementioned coordinates for Eq. 14.

$$u^{(2)} = x^3 + 2(t - 0.000005), \tag{17}$$

[.,.]	W_1	W_2	W_3
W_1	0	0	0
W_2	W_2	0	0
W_3	$\frac{1}{5}W_3$	0	0

Adj	W_1	W_2	W_3
W_1	W_1	W_2	W_3
W_2	$W_1 - \epsilon W_2$	W_2	W_3
W_3	$W_1 - \frac{1}{5}\epsilon W_3$	W_2	W_3

Figure 4 shows its graphical view.

For last equation of Eq. 13, we let a general logarithmic function $\mathbb{B} = 2t\ln(x-\epsilon)$ and for similar values of ϵ, x, and t coordinates.

$$u^{(3)} = 2t\ln(x - 0.000005). \tag{18}$$

Its graph is in Figure 5.

2.2 Optimal system of subalgebras

In this part, we will find the optimal system of one dimensional Lie subalgebras for Eq. 3 by using the adjoint representation. The corresponding commutator table and the adjoint table are as follows: Commutator Table: Adjoint Table:

Let us take a generator

$$W = \beta_1 W_1 + \beta_2 W_2 + \beta_3 W_3, \tag{19}$$

Case No.1 For $\beta_1 \neq 0$, the generator turns to

$$W = W_1 + \beta_2 W_2 + \beta_3 W_3. \tag{20}$$

Applying $Adj_{e^{\beta_2 W_2}}$ on Y gives

$$W' = W_1 + \beta_3 W_3, \tag{21}$$

furthermore, proceeding in the same way

$$W'' = Adj_{e^{5\beta_3 W_3}}(W_3) = W_1, \tag{22}$$

which successively makes the coefficients β_2 and β_3 equal to 0and implies that $W \simeq W_1$.**Case No.2** Without loss of generality, here we take $\beta_1 = 0$ and $\beta_2 = 1$, the generator becomes

$$W = W_2 + \beta_3 W_3, \tag{23}$$

Now, act $Adj_{e^{\beta_3 W_3}}$ on the aforementioned W,

$$W' = W_2 + \beta_3 W_3, \tag{24}$$

Subcase No.2.1 If $\beta_3 < 0$, then

$$W' = W_2 - W_3. \tag{25}$$

Subcase No.2.2 If $\beta_3 > 0$, then

$$W' = W_2 + W_3. \tag{26}$$

Case No.3 For $\beta_1 = \beta_2 = 0$ and $\beta_3 = 1$. Thus, in the meanwhile we have $W \simeq W_3$.**Case No.4** Let consider $\beta_1 = 0 = \beta_3$ and $\beta_2 \neq 0$. In this case, the generator is $W \simeq W_2$.

The optimal system of one-dimensional subalgebras admitted by Eq. 3) is as follows:

$$W = \begin{cases} W_1, \\ W_2, \\ W_3, \\ W_2 \pm W_3. \end{cases} \tag{27}$$

2.3 Reductions and invariant solutions

2.3.1 Reduction by W_2

The invariants for corresponding characteristic equation are as follows:

$$x = a, \quad u = b, \tag{28}$$

where a and b are arbitrary constants.

The invariant solution can be written in the form of $b = f(a)$, implies that

$$u = f(a), \tag{29}$$

substituting this value in Eq. 3), we obtain

$$\Rightarrow \beta\left(f''(a)\right)^3 + 3\alpha e^{f(a)} = 0. \tag{30}$$

The solution of this reduced equation for $\beta = 1$ is given in the form of solution set as.

$$\int^{f(a)} \frac{\mp 1}{\sqrt{6(-3\alpha e^b) - k_1}} db - x - k_2 = 0,$$

$$\mp 6k_1 \arctan\left(\sqrt{-3I3^{\frac{5}{6}} - 33^{\frac{1}{3}}(-\alpha e^{f(a)})^{\frac{1}{3}} + \frac{1}{k_1^2}}k_1\right) - x - k_2 = 0,$$

$$\mp 6k_1 \arctan\left(\sqrt{3I3^{\frac{5}{6}} - 33^{\frac{1}{3}}(-\alpha e^{f(a)})^{\frac{1}{3}} - \frac{1}{k_1^2}}k_1\right) - x - k_2 = 0.$$

2.3.2 Reduction by W_3

The corresponding characteristic equation to this generator is as follows:

$$\frac{dx}{1} = \frac{dt}{0} = \frac{du}{0}, \tag{31}$$

this gives two invariants

$$t = a_1, \quad u = b_1, \tag{32}$$

where a_1 and b_1 are arbitrary constants. It implies

$$u = f(t), \tag{33}$$

putting this in Eq. 3, we obtain

$$\alpha e^u = 0, \tag{34}$$

which gives a trivial solution for $u = f(x)$.

2.3.3 Reduction by W_1

The characteristic equation is

$$5\frac{dx}{x} = \frac{dt}{t} = -\frac{5}{6}du, \tag{35}$$

solving this, we obtain corresponding invariants of the form

$$r = \frac{t}{x^5}, \quad s = e^u x^6, \tag{36}$$

from this

$$u = \ln\left[x^{-6} f\left(tx^{-5}\right)\right], \tag{37}$$

where we obtain

$$\begin{aligned} u_x &= -\frac{1}{xf(r)}\left[5rf'(r) + 6f(r)\right], \\ u_{xx} &= \frac{f(r)\left[25r^2 f''(r) + 6f(r) + 30rf'(r)\right] - 25r^2 f'^2(r)}{x^2 f^{2(r)}}, \\ u_{xt} &= \frac{f(r)\left[-5rf''(r) - 5f'(r)\right] + 5rf'^2(r)}{x^6 f^2(r)}. \end{aligned} \tag{38}$$

substituting these derivatives into Eq. 3, we obtain

$$\begin{aligned} &3f^5(r)\left[-5rf''(r) - 5rf'(r)\right] + 15rf^4(r)f'^2(r) - 3\alpha f^7(r) \\ &+\beta\left[f(r)\left[6f(r) + 25r^2 f''(r) + 30rf'(r)\right] - 25r^2 f'^2(r)\right]^3 \\ &= 0. \end{aligned} \tag{39}$$

Thus, non-linear PDE (3) reduces to a non-linear ODE.

2.3.4 Reduction by $W_2 + W_3$

The invariants that we gain by solving characteristic equation are as follows:

$$a_3 = x - t, \quad u = b_3, \tag{40}$$

a_3 and b_3 are arbitrary constants. The invariant solution corresponding to them is $u = f(a_3)$. Inserting this solution into Eq. 3 will give us a non-linear ODE of the form

$$3f''(a_3) + \beta\left(f''(a_3)\right)^3 + 3\alpha e^{f(a_3)} = 0. \tag{41}$$

2.3.5 Reduction by $W_2 - W_3$

The invariants corresponding to characteristic equation for this case are $a_4 = x + t$ and $b_4 = u$. Furthermore, its invariant solution is given as $u = f(a_4)$. Therefore, the Eq. 3 will be converted into an ODE of the form

$$3f''(a_4) - \beta\left(f''(a_4)\right)^3 - 3\alpha e^{f(a_4)} = 0. \tag{42}$$

2.4 Determining lie symmetry of SPE for the case $h(u) = e^{u^n}$ and $k(u) = u_{xx}$ $(n > 1)$

The equation becomes

$$u_{xt} = \alpha e^{u^n} + \frac{1}{3}\beta u_{xx}^3. \tag{43}$$

The one-parameter Lie group of transformations and the second prolongation with coefficients are given in Eqs 4, 6, respectively for Eq. 43. Let the generator be

$$Z = \lambda(x,t,u)\partial_x + \mu(x,t,u)\partial_t + \nu(x,t,u)\partial_u, \tag{44}$$

[.,.]	Z_1	Z_2
Z_1	0	0
Z_2	0	0

Adj	Z_1	Z_2
Z_1	Z_1	Z_2
Z_2	Z_1	Z_2

Therefore, we have

$$Pr^{[2]}Z\left(u_{xt} - \alpha e^{u^n} - \frac{1}{3}\beta u_{xx}^3\right)|_{u_{xt}=\alpha e^{u^n}+\frac{1}{3}\beta u_{xx}^3} = 0, \tag{45}$$

simplification gives the following equation:

$$-\alpha n v e^{u^n} u^{n-1} - \beta v^{xx} u_{xx}^2 + v^{xt} = 0, \tag{46}$$

which is solved for the values of v^{xx} and v^{xt}, will give us the equation involving derivatives of infinitesimals with respect to dependent and independent variables and also the derivatives of dependent variable w.r.to independent variables. Substituting Eq. 43 and comparing the values of coefficients on both sides gives an under-determined system of equations

$$\begin{gathered}\mu_{xx} = 0 \quad \mu_{xu} = 0, \quad \mu_{uu} = 0, \quad \lambda_{uu} = 0, \quad \mu_u = 0, \quad \lambda_u = 0,\\ \lambda_{tu} = 0, \quad \mu_x = 0, \quad v_{uu} = 0, \quad v_{xu} = 0, \quad v_{xx} = 0, \quad v_{tu} = 0,\\ \lambda_t = 0, \quad \lambda_{xx} = 0, \quad -\frac{2}{3}v_u + \frac{5}{3}\lambda_x - \frac{1}{3}\mu_t = 0,\\ -\alpha n v e^{u^n} u^{n-1} + v_{xt} + \alpha\left(v_u - \lambda_x - \mu_t\right)e^{u^n} = 0.\end{gathered} \tag{47}$$

To solve this system, we consider v as:

$$v = L(t)x + Mu + N(t), \tag{48}$$

which satisfies the aforementioned equations and then by solving the aforementioned system, we obtain

$$\begin{aligned}\lambda(x) &= c_2,\\ \mu(t) &= c_1,\\ v(x,t,u) &= 0.\end{aligned} \tag{49}$$

c_1 and c_2 are any arbitrary constants. The infinitesimal generators for the one-parameter of Lie groups of transformations admitted in Eq. 43) are given by

$$\begin{aligned}Z_1 &= \partial_t,\\ Z_2 &= \partial_x.\end{aligned} \tag{50}$$

These symmetry generators give us the symmetry groups Q_i^ϵ for i = 1, 2:

$$\begin{aligned}Q_1^\epsilon &= (x, t+\epsilon, u),\\ Q_2^\epsilon &= (x+\epsilon, t, u).\end{aligned} \tag{51}$$

If u = R (x,t) is a solution of Eq. 43), then u^i for i = 1, 2, and 3 and $\epsilon \ll 1$ also satisfies Eq. 43,

$$\begin{aligned}u^{(1)} &= R(x, t-\epsilon),\\ u^{(2)} &= R(x-\epsilon, t).\end{aligned} \tag{52}$$

Commutator Table:also,
Adjoint Table.

Proposition 5.1: The generators $Z_1 = \partial_t$ and $Z_2 = \partial_x$ form a two-dimensional abelian Lie symmetry algebra.

2.5 Optimal system, reductions and invariant solutions

Considering a generator $Z = b_1Z_1 + b_2Z_2$. This generator will established a set of optimal system comprising of Lie algebra

$$Z = \{Z_1, Z_2, b_1Z_1 + b_2Z_2\} \tag{53}$$

where b_1, and b_2 are arbitrary constants. The reduction of PDE Eq. 39 by using the generator Z_1 leads to an invariant solution $u = f(c_1)$. The reduced non-linear ODE will be

$$3\alpha e^{u^n} + \beta u'^3 = 0 \tag{54}$$

The reduction through Z_2 generates a trivial case for Eq. 39.

3 Conclusion

In this paper, we have carried out the LSA for computing the similarity solutions (symmetries) of the non-linear SPE for the cases when $h(u) = e^u$ and $k(u) = u_{xx}$ and $h(u) = e^{u^n}$ and $k(u) = u_{xx}$ in SPE (2). In addition, an optimal system of one-dimensional subalgebra has been set up. The reductions and invariant solutions for the generalized SPE are calculated corresponding to this optimal system as well. The graphs are formed by the maple for the functions obtained from the transformed points of one-parameter Lie groups.

Data availability statement

The original contributions presented in the study are included in the article/Supplementary Material; further inquiries can be directed to the corresponding author.

Author contributions

Article has been concieved by MM, drafted by HB and MA. All authors contributed to the article and approved the submitted version.

Conflict of interest

The authors declare that the research was conducted in the absence of any commercial or financial relationships that could be construed as a potential conflict of interest.

Publisher's note

References

1. Oliveri F. Lie symmetries of differential equations: Classical results and recent contributions. *Symmetry* (2010) 2(2):658–706. doi:10.3390/sym2020658

2. Knight JC, Broeng J, Birks TA, Russell PSJ. Photonic band gap guidance in optical fibers. *Science* (1998) 282(5393):1476–8. doi:10.1126/science.282.5393.1476

3. Clarkson PA, Ludlow DK, Priestley TJ. The classical, direct, and nonclassical methods for symmetry reductions of nonlinear partial differential equations. *Methods Appl Anal* (1997) 4(2):173–95. doi:10.4310/maa.1997.v4.n2.a7

4. Liu H, Zhang L. Symmetry reductions and exact solutions to the systems of nonlinear partial differential equations. *Physica Scripta* (2018) 94(1):015202. doi:10.1088/1402-4896/aaeeff

5. Coclite GM, di Ruvo L. Well-posedness results for the short pulse equation. *Z für Angew Mathematik Physik* (2015) 66(4):1529–57. doi:10.1007/s00033-014-0478-6

6. Schäfer T, Wayne CE. Propagation of ultra-short optical pulses in cubic nonlinear media. *Physica D: Nonlinear Phenomena* (2004) 196(1-2):90–105. doi:10.1016/j.physd.2004.04.007

7. Agrawal GP. Nonlinear fiber optics. In: *Nonlinear science at the dawn of the 21st century*. Berlin, Heidelberg: Springer (2000). p. 195–211.

8. Karasawa N, Nakamura S, Nakagawa N, Shibata M, Morita R, Shigekawa H, et al. Comparison between theory and experiment of nonlinear propagation for a-few-cycle and ultrabroadband optical pulses in a fused-silica fiber. *IEEE J Quan Electron* (2001) 37(3):398–404. doi:10.1109/3.910449

9. Moloney JV, Newell AC. Nonlinear optics. *Physica D: Nonlinear Phenomena* (1990) 44(1-2):1–37. doi:10.1016/0167-2789(90)90045-q

10. Xiao Y, Maywar DN, Agrawal GP. New approach to pulse propagation in nonlinear dispersive optical media. *JOSA B* (2012) 29(10):2958–63. doi:10.1364/josab.29.002958

11. Liu H, Li J. Lie symmetry analysis and exact solutions for the short pulse equation. *Nonlinear Anal Theor Methods Appl* (2009) 71(5-6):2126–33. doi:10.1016/j.na.2009.01.075

12. Fakhar K, Wang G, Kara AH. Symmetry reductions and conservation laws of the short pulse equation. *Optik* (2016) 127(21):10201–7. doi:10.1016/j.ijleo.2016.08.013

13. Matsuno Y. Parametric solutions of the generalized short pulse equations. *J Phys A: Math Theor* (2020) 53(10):105202. doi:10.1088/1751-8121/ab6f18

14. Ali AT. New generalized Jacobi elliptic function rational expansion method. *J Comput Appl Math* (2011) 235(14):4117–27. doi:10.1016/j.cam.2011.03.002

15. El-Sabbagh MF, Ali AT. New generalized Jacobi elliptic function expansion method. *Commun Nonlinear Sci Numer Simulation* (2008) 13(9):1758–66. doi:10.1016/j.cnsns.2007.04.014

16. Zhao W, Munir MM, Bashir H, Ahmad D, Athar M. Lie symmetry analysis for generalized short pulse equation. *Open Phys* (2022) 20(1):1185–93. doi:10.1515/phys-2022-0212

frontiers | Frontiers in Physics

TYPE Original Research
PUBLISHED 28 March 2023
DOI 10.3389/fphy.2023.1160391

OPEN ACCESS

EDITED BY
Gangwei Wang,
Hebei University of Economics and Business, China

REVIEWED BY
Guofu Yu,
Shanghai Jiao Tong University, China
Junchao Chen,
Lishui University, China

*CORRESPONDENCE
Gaizhu Qu,
qugaizhu.hi@163.com
Shoufeng Shen,
mathssf@zjut.edu.cn

SPECIALTY SECTION
This article was submitted to Mathematical Physics, a section of the journal Frontiers in Physics

RECEIVED 07 February 2023
ACCEPTED 22 February 2023
PUBLISHED 28 March 2023

CITATION
Qu G, Wang M and Shen S (2023), Applications of the invariant subspace method on searching explicit solutions to certain special-type non-linear evolution equations.
Front. Phys. 11:1160391.
doi: 10.3389/fphy.2023.1160391

Applications of the invariant subspace method on searching explicit solutions to certain special-type non-linear evolution equations

Gaizhu Qu[1]*, Mengmeng Wang[2] and Shoufeng Shen[3]*

[1]School of Mathematics and Physics, Weinan Normal University, Weinan, China, [2]Department of Mathematics, Hangzhou Zhongce Vocational School Qiantang, Hangzhou, China, [3]Department of Applied Mathematics, Zhejiang University of Technology, Hangzhou, China

We extend the invariant subspace method (ISM) to a class of Hamilton–Jacobi equations (HJEs) and a family of third-order time-fractional dispersive PDEs with the Caputo fractional derivative in this letter. More precisely, the complete classification is presented for such HJEs that admit invariant subspaces governed by solutions of the second-order and third-order linear ordinary differential equations (ODEs). Meanwhile, some concrete equations are derived for the construction of new exact solutions $u(x,t)=\sum_{i=1}^{n}C_i(t)f_i(x)$. Then a set of invariant subspaces of the considered third-order time-fractional non-linear dispersive equations are obtained. Based on the Laplace transform method (LTM) and applying several properties of the well known Mitta-Leffer (ML) function, the different types of explicit solutions of a family of third-order time-fractional dispersive PDEs are finally derived.

KEYWORDS

exact solution, Hamilton–Jacobi equation, complete classification, invariant subspace method, Laplace transform

1 Introduction

One of the recently invented methods to derive the explicit solution of NPDE is ISM, which was initiated by Galaktionov and Svirshchevskii in [1] and many researchers have illustrated its applicability in Refs. [2–6]. Specifically, Refs. [2, 3, 5, 6] have addressed the basic question of the dimension of invariant subspaces, which in addition to ISM is also relevant to Lie-Bäcklund symmetry (LBS) and the conditional Lie-Bäcklund symmetry (CLBS) [7–14]. Very recently, Refs. [15–23] generalized this method to resolve fractional non-linear partial differential equations (fNPDEs). It is verified that by applying ISM, a fNPDE can be reduced to a system of fractional non-linear ordinary differential equations (fNODEs), which can be solved by known analytical approaches.

In this paper, we analyze the following two families of special-type non-linear evolution equations.

1.1 Hamilton–Jacobi equations

Hamilton–Jacobi equations (HJEs) can be regarded as models for various processes in theoretical physics, quantum mechanics and contemporary problems of control, etc. In Refs. [24–28], the authors analyzed HJEs in different directions. References [29–32] have also indicated that these equations can be used to depict several properties including blow up behavior and the long time action of non-linear diffusion equations. We will consider the following HJEs

$$u_t = u_x^{m+2} + p(x)B(u)u_x^{m+1} + Q(x,u),\ t \in \mathbb{R}^+,\ x \in \mathbb{R}, \tag{1.1}$$

where $u = u(t, x)$ and $p(x)$, $B(u)$, $Q(x, u)$ are sufficiently smooth functions of indicated variables. Here we suppose that $m \neq -1, -2$. This assumption means that Eq. 1.1 is a fully non-linear HJE. In Ref. [7], Qu showed that Eq. 1.1 preserves the second-order CLBS with $\eta = u_{xx} + H(u)u_x^2 + G(u)u_x + F(u)$ and classified the solutions for Eq. 1.1.

1.2 Third-order time-fractional dispersive PDEs

The concept of fractional order derivative was initiated with the half-order derivative as considered by Leibniz and L'Hopital and many authors have generalized it to an arbitrary order derivative. Different concepts of fractional derivatives were proposed in [33–36]. Now fNPDEs have gained much attention because they can be utilized to represent a large number of physical processes. Some techniques have been employed to solve fNPDEs, but the study of fNPDEs has been still handicapped due to the limitations on dealing with more complex fNODEs.

We will study a family of third-order time-fractional dispersive PDEs

$$\frac{\partial^\alpha}{\partial t^\alpha}\left[u - \delta^2\frac{\partial^2 u}{\partial x^2}\right] + \sigma\frac{\partial u}{\partial x} + \gamma\frac{\partial^3 u}{\partial x^3} = F[u] = \frac{\partial}{\partial x}\left[b_1 u^2 + b_2\left(\frac{\partial u}{\partial x}\right)^2 + b_3 u\frac{\partial^2 u}{\partial x^2}\right], \tag{1.2}$$

where $u = u(t, x)$, $0 < \alpha \leq 1$, $t > 0$, and $\frac{\partial^\alpha u}{\partial t^\alpha}$ is the Caputo fractional derivative of u with respect to t. The ordinary case $\alpha = 1$ of Eq. 1.2 was first introduced in [37] and has been discussed in depth by many researchers [38, 39]. In fact, when $\alpha = 1$, $\delta = b_2 = b_3 = 0$, Eq. 1.2 becomes the KdV equation. If we take $\alpha = \delta^2 = b_3 = 1, b_1 = -\frac{3}{2}, b_2 = \frac{1}{2}$, Eq. 1.2 becomes the Camassa–Holm equation [40]:

$$u_t + \sigma u_x + \gamma u_{xxx} - u_{xxt} + 3uu_x = 2u_x u_{xx} + uu_{xxx}. \tag{1.3}$$

If $\alpha = \delta^2 = b_2 = b_3 = -\frac{b_1}{2} = 1, \sigma = \gamma = 0$, Eq. 1.2 is the Degasperis–Procesi equation [41, 42]:

$$u_t - u_{xxt} + 4uu_x = 3u_x u_{xx} + uu_{xxx}. \tag{1.4}$$

If $\alpha = \delta^2 = 2b_2 = b_3 = 1$, $\sigma = \gamma = b_1 = 0$, Eq. 1.2 becomes the Hunter-Saxton equation [1]:

$$u_t - u_{xxt} = 2u_x u_{xx} + uu_{xxx}. \tag{1.5}$$

These equations arise as asymptotic models in the theory of shallow water waves. Many authors have concentrated on studying the above special cases of Eq. 1.2.

The major contents of this paper are as follows. We recall the method of the invariant subspace, and also introduce several definitions and fundamental theorems on fractional derivatives and integrals in Section 2. In Section 3 we obtain the complete invariant subspace classification of Eq. 1.1 and derive the reductions and explicit solutions of several examples by utilizing ISM. In Section 4, combined with LTM and inspired by several properties of the well known ML function, we investigate exact solutions of different cases for Eq. 1.2. In the last section, we make some concluding remarks.

2 Preliminaries

First, we introduce ISM. Then, we give several definitions and properties.

2.1 Invariant subspace method

Now, we will present brief details of ISM for a kth-order NPDE

$$u_t = F(x, u, u_x, \ldots, u_{kx}) \equiv F[u], \tag{2.1}$$

where $u_{jx} = \frac{\partial^j u}{\partial x^j}$ $(j = 1, \ldots, k)$.

In [15], Gazizov and Kasatkin demonstrated that ISM can be used to reduce a fNPDE to a system of fNODEs.

We focus on the fNPDE of the form

$$\frac{\partial^\alpha u}{\partial t^\alpha} = F(x, u, u_x, \ldots, u_{kx}) \equiv F[u], \tag{2.2}$$

where $\frac{\partial^\alpha}{\partial t^\alpha}$ is the time-fractional Caputo derivative. Let $f_1(x), f_2(x), \ldots, f_n(x)$ be linearly independent functions and their linear span over $\mathbb{R}$ be W_n, namely,

$$W_n = \mathcal{L}\{f_1(x), f_2(x), \ldots, f_n(x)\} \equiv \left\{\sum_{i=1}^n C_i f_i(x),\ C_i \in \mathbb{R}\right\}.$$

Definition 2.1. If differential operator F satisfies $F[W_n] \subseteq W_n$, the subspace W_n is invariant under F.

Let us suppose Eq. 2.2 preserves the subspace W_n, then

$$F\left[\sum_{i=1}^n C_i f_i(x)\right] = \sum_{i=1}^n \Psi_i(C_1, C_2, \ldots, C_n) f_i(x)$$

$(C_1, C_2, \ldots, C_n) \in \mathbb{R}^n$. Thus Eq. 2.2 has the solution

$$u(x,t) = \sum_{i=1}^n C_i(t) f_i(x),$$

$\{C_i(t), (i = 1, 2, \ldots, n)\}$ satisfy the n-dimensional dynamical system

$$\frac{\partial^\alpha C_i(t)}{\partial t^\alpha} = \Psi(C_1(t), C_2(t), \ldots, C_n(t)), \quad i = 1, 2, \ldots, n.$$

Observing that the subspace W_n is determined by a basic solution set of a linear nth-order ODE,

$$L[y] \equiv y^{(n)} + a_{n-1}(x)y^{(n-1)} + \cdots + a_1(x)y' + a_0(x)y = 0. \quad (2.3)$$

Therefore, the invariant condition F is

$$L[F[u]]_{[H]} = 0. \quad (2.4)$$

2.2 Some results on fractional calculus

Definition 2.2. The Riemann–Liouville fractional integral operator of order $\alpha > 0$ is represented as the following expression:

$$I^{\alpha}_{a^+} f(t) = \frac{1}{\Gamma(\alpha)} \int_a^t (t-\tau)^{\alpha-1} f(\tau) d\tau, \quad t > a. \quad (2.5)$$

Where $\Gamma(p) = \int_0^{\infty} e^{-x} x^{p-1} dx$ is the Euler Gamma function. Note that $I^0_{a^+} f(t) = f(t)$.

Definition 2.3. The Caputo fractional differential operator of order $\alpha > 0$ is represented as the following expression:

$$D^{\alpha}_{a^+} f(t) = I^{n-\alpha}_{a^+} D^n f(t) = \begin{cases} \frac{1}{\Gamma(n-\alpha)} \int_a^t (t-\tau)^{n-\alpha-1} f^{(n)}(\tau) d\tau, & \alpha \in (n-1, n),\ n \in \mathbb{N}, \\ f^{(n)}(t), & \alpha = n \in \mathbb{N}. \end{cases} \quad (2.6)$$

When $\alpha = 0, D^{\alpha}_{a^+} f(t) = f(t)$.

We can replace operators $D^{\alpha}_{0^+} f(t)$ and $I^{\alpha}_{0^+} f(t)$ by $D^{\alpha} f(t)$ and $I^{\alpha} f(t)$ respectively. The following properties are true for fractional integral and derivative:

$$\begin{aligned} &D^{\alpha}[f(t) + g(t)] = D^{\alpha} f(t) + D^{\alpha} g(t), \\ &D^{\alpha} I^{\alpha} f(t) = f(t), \\ &I^{\alpha} D^{\alpha} f(t) = f(t) - \sum_{k=0}^{n-1} \frac{f^{(k)}(0)}{k!} t^k, \ \alpha > 0, \ t > 0, \\ &I^{\alpha} t^{\beta} = \frac{\Gamma(\beta+1)}{\Gamma(\beta+\alpha+1)} t^{\beta+\alpha}, \ \alpha > 0, \ t > 0, \ \beta > -1, \\ &D^{\alpha} t^{\beta} = \frac{\Gamma(\beta+1)}{\Gamma(\beta-\alpha+1)} t^{\beta-\alpha}, \ \beta > 0. \end{aligned}$$

When $\alpha \in (0, 1]$, the LT of Caputo fractional derivative has the following expression

$$\mathrm{L}\left\{\frac{d^{\alpha} f(t)}{dt^{\alpha}}\right\} = s^{\alpha} \bar{f}(s) - s^{\alpha-1} f(0),$$

where $\bar{f}(s) = \int_0^{\infty} e^{-st} f(t) dt$.

Definition 2.4. A ML function is

$$E_{\alpha,\beta}(z) = \sum_{k=0}^{\infty} \frac{z^k}{\Gamma(\alpha k + \beta)}, \quad \mathrm{Re}(\alpha) > 0, \ \mathrm{Re}(\beta) > 0.$$

Also, $E_{\alpha,1}(z) = E_{\alpha}(z)$.

We can see the γth order Caputo derivatives of the ML function are:

$$\begin{aligned} &D^{\gamma}\left[t^{\beta-1} E_{\alpha,\beta}(at^{\alpha})\right] = t^{\beta-\gamma-1} E_{\alpha,\beta-\gamma}(at^{\alpha}), \\ &D^{\gamma}\left[E_{\alpha}(at^{\alpha})\right] = a E_{\alpha}(at^{\alpha}), \end{aligned}$$

$a \in \mathbb{R}, \gamma > 0, \alpha > 0$, and the following presentation gives the LT of function $t^{\alpha k+\beta-1} E^{(k)}_{\alpha,\beta}(\pm at^{\alpha})$, that is

$$\begin{aligned} \mathrm{L}\left\{t^{\alpha k+\beta-1} E^{(k)}_{\alpha,\beta}(\pm at^{\alpha})\right\} &= \int_0^{\infty} t^{\alpha k+\beta-1} e^{-st} E^{(k)}_{\alpha,\beta}(\pm at^{\alpha}) dt \\ &= \frac{k! s^{\alpha-\beta}}{(s^{\alpha} \mp a)^{k+1}}, \ \mathrm{Re}(s) > |a|^{\frac{1}{\alpha}}. \end{aligned}$$

3 Exact solutions of HJEs

3.1 Invariant subspace classification of Eq. 1.1

For Eq. 1.1, we write it in the form $u_t = F[u] = u_x^{m+2} + p(x)B(u)u_x^{m+1} + Q(x,u)$. By the maximal dimension $n \le 2k+1$, we consider the following cases for $n = 2, 3$.

We investigate $n = 2$ first. After a straightforward calculation, we obtain that

$$J_1 u_x^{m+3} + J_2 u_x^{m+2} + J_3 u_x^{m+1} + J_4 u_x^m + J_5 u_x^{m-1} + J_6 u_x^2 + J_7 u_x + J_8 = 0, \quad (3.1)$$

where $J_i (i = 1, 2, \ldots, 8)$ have the following expressions:

$$\begin{aligned} J_1 &= pB'', \\ J_2 &= (m+1)(m+2)a_1^2 - (m+1)a_0 - (m+2)a_1' \\ &\quad + 2p'B' - 2(m+1)pa_1B', \\ J_3 &= p''B - (2m+3)pa_0B'u - (2m+1)a_1p'B \\ &\quad + [m(m+1)a_1^2 - (m+1)a_1' - ma_0]pB \\ &\quad + 2(m+1)(m+2)a_1a_0u - (m+2)a_0'u, \\ J_4 &= (m+1)[(m+2)a_0^2u + (2ma_1a_0 - a_0')pB - 2a_0p'B]u, \\ J_5 &= m(m+1)pa_0^2u^2B, \\ J_6 &= Q_{uu}, \\ J_7 &= 2Q_{xu}, \\ J_8 &= a_0Q + a_1Q_x - a_0uQ_u + Q_{xx}. \end{aligned} \quad (3.2)$$

Observing the above expression Eq. 3.1, we shall discuss four possibilities: $m = -3, 1, 2$ and $m \neq -3, 1, 2$. For the case of $m = -3$, we derive the following system

$$\begin{aligned} &2a_0 + 2a_1^2 + a_1' + 2(p' + 2a_1p)B' = 0, \\ &p''B + 5a_1p'B + (3a_0 + 6a_1^2 + 2a_1')pB \\ &\quad + (3a_0pB' + 4a_0a_1 + a_0')u = 0, \\ &a_0^2u + (a_0' + 6a_0a_1)pB + 2a_0p'B = 0, \\ &pa_0^2B = 0, \\ &Q_{xu} = 0, \\ &Q_{uu} = 0, \\ &pB'' + a_0Q + a_1Q_x - a_0uQ_u + Q_{xx} = 0. \end{aligned} \quad (3.3)$$

From the first equation of Eq. 3.3, it is apparent that $B(u) = b_1u + b_2$. By solving the fifth and sixth equations of Eq. 3.3, we obtain $Q(x, u) = q_1u + Q_1(x)$, where b_1, b_2 and q_1 are arbitrary constants and $Q_1(x)$ is a function of x. Inserting $B(u) = b_1u + b_2$ and $Q(x, u) = q_1u + Q_1(x)$ into system Eq. 3.3, we have

$$\begin{aligned} &2a_1^2 + 4b_1a_1p + a_1' + 2a_0 + 2b_1p' = 0, \\ &6b_1a_1^2p + (4a_0 + 5b_1p')a_1 + 2b_1a_1'p + 6b_1a_0p + a_0' + b_1p'' = 0, \\ &6b_2a_1^2p + 5b_2a_1p' + 2b_2a_1'p + 3b_2a_0p + b_2p'' = 0, \\ &6b_1a_0a_1p + a_0^2 + 2b_1a_0p' + b_1a_0'p = 0, \\ &6b_2a_0a_1p + 2b_2a_0p' + b_2a_0'p = 0, \\ &b_1a_0^2p = 0, \\ &b_2a_0^2p = 0. \\ &a_1Q_1' + a_0Q_1 + Q_1'' = 0. \end{aligned} \quad (3.4)$$

TABLE 1 Classifications of W_2 governed by linear ODEs (2.3) of Eq. 1.1.

No.	Eq. 1.1	ODE (2.3)	W_2
1	$u_t = u_x^{-1} + p_1(b_1u + b_2)u_x^{-2} + q_1u + q_2x + q_3$	$y'' = 0$	$W\{1, x\}$
2	$u_t = u_x^{-1} + \frac{p_1}{x}(b_1u + b_2)u_x^{-2} + q_1u + q_2\sqrt{x} + q_3$	$y'' + \frac{1}{2x}y' = 0$	$W\{1, \sqrt{x}\}$
3	$u_t = u_x^{-1} + \frac{1}{3x}(-u + 3p_1b_2)u_x^{-2} + q_1u + q_2\sqrt[3]{x} + q_3$	$y'' + \frac{2}{3x}y' = 0$	$W\{1, \sqrt[3]{x}\}$
4	$u_t = u_x^3 + \frac{1}{p_1}(b_1u + b_2)u_x^2 + q_1u + q_2x + q_3$	$y'' = 0$	$W\{1, x\}$
5	$u_t = u_x^3 + \frac{2}{p_1(2x-a_1)}(b_1u + b_2)u_x^2 + q_1u + q_2$	$y'' - \frac{1}{2x-a_1}y' = 0$	$W\left\{1, \sqrt[3]{(x - \frac{1}{2}a_1)^2}\right\}$
6	$u_t = u_x^3 + \frac{1}{p_1(x+a_1)}(b_1u + b_2)u_x^2 + q_1u \pm \frac{2\sqrt{2}}{3}q_2(x + a_1)^{\frac{3}{2}} + q_3$	$y'' - \frac{1}{2(x+a_1)}y' = 0$	$W\left\{1, (x + a_1)^{\frac{3}{2}}\right\}$
7	$u_t = u_x^3 + \frac{1}{p_1(x+2a_1)}(-3p_1u + b_2)u_x^2 + q_1u + q_2$	$y'' - \frac{2}{x+2a_1}y' = 0$	$W\left\{1, (x + 2a_1)^3\right\}$
8	$u_t = u_x^3 + (p_1x + p_2)b_2u_x^2 + q_1u + q_2x + q_3$	$y'' = 0$	$W\{1, x\}$
9	$u_t = u_x^3 - (x^2 + p_1x + p_2)u_x^2 + q_1u^2 + q_2u + q_3x + q_4$	$y'' = 0$	$W\{1, x\}$
10	$u_t = u_x^3 + p_1(b_1u + b_2)u_x^2 + q_1u + q_2x + q_3$	$y'' = 0$	$W\{1, x\}$
11	$u_t = u_x^3 + (p_1\sqrt{x} + \frac{p_2}{x})b_2u_x^2 + q_1u + q_2x^{\frac{3}{2}} + q_3$	$y'' - \frac{1}{2x}y' = 0$	$W\left\{1, x^{\frac{3}{2}}\right\}$
12	$u_t = u_x^3 - \frac{4}{9}(q_1x^2 + p_1\sqrt{x} + \frac{p_2}{x})u_x^2 + q_1u^2 + q_2u + q_3x^{\frac{3}{2}} + q_4$	$y'' - \frac{1}{2x}y' = 0$	$W\left\{1, x^{\frac{3}{2}}\right\}$
13	$u_t = u_x^3 + \frac{p_1}{x}(b_1u + b_2)u_x^2 + q_1u + q_2x^{\frac{3}{2}} + q_3$	$y'' - \frac{1}{2x}y' = 0$	$W\left\{1, x^{\frac{3}{2}}\right\}$
14	$u_t = u_x^3 + (\frac{p_1}{x} + \frac{p_2}{x^4})(-\frac{3}{p_1}u + b_2)u_x^2 + q_1u + q_2x^3 + q_3$	$y'' - \frac{2}{x}y' = 0$	$W\{1, x^3\}$
15	$u_t = u_x^3 + \frac{27}{x^3}u^3 + q_1u + x^{\frac{3}{2}}[q_2\sin(\frac{3\sqrt{3}}{2}\ln x) + q_3\cos(\frac{3\sqrt{3}}{2}\ln x)]$	$y'' - \frac{2}{x}y' + \frac{9}{x^2}y = 0$	$W\{x^{\frac{3}{2}}\sin(\frac{3\sqrt{3}}{2}\ln x), x^{\frac{3}{2}}\cos(\frac{3\sqrt{3}}{2}\ln x)\}$
16	$u_t = u_x^3 + \frac{9}{4}(p_1x^2 + \frac{1}{x})uu_x^2 - \frac{27}{16}(3p_1 + \frac{1}{x^3})u^3 + q_1u + q_2x^{\frac{3}{2}} + q_3x^{-\frac{3}{2}}$	$y'' + \frac{1}{x}y' - \frac{9}{4x^2}y = 0$	$W\left\{x^{\frac{3}{2}}, x^{-\frac{3}{2}}\right\}$
17	$u_t = u_x^3 - \frac{27}{8x}uu_x^2 + \frac{729}{128x^3}u^3 + q_1u + q_2x^{\frac{3}{2}} + q_3x^{\frac{9}{4}}$	$y'' - \frac{11}{4x}y' + \frac{27}{8x^2}y = 0$	$W\left\{x^{\frac{3}{2}}, x^{\frac{9}{4}}\right\}$
18	$u_t = u_x^3 + \frac{1}{x}(-\frac{9}{2}u + b_2)u_x^2 + \frac{27}{2x^3}u^3 - \frac{9}{4x^3}b_2u^2 + q_1u + q_2x^{\frac{3}{2}} + q_3x^3$	$y'' - \frac{7}{2x}y' + \frac{9}{2x^2}y = 0$	$W\left\{x^{\frac{3}{2}}, x^3\right\}$
19	$u_t = u_x^3 + \frac{1}{3x}(a_0 - 9)uu_x^2 + \frac{1}{3x^3}a_0^2u^3 + q_1u$	$y'' - \frac{2}{x}y' + \frac{a_0}{x^2}y = 0$	$W\left\{x^{\frac{3+\sqrt{9-4a_0}}{2}}, x^{\frac{3-\sqrt{9-4a_0}}{2}}\right\}$
20	$u_t = u_x^3 + \frac{3}{4x}(1 + 2a_1)uu_x^2 - \frac{1}{16x^3}(1 + 2a_1)^3u^3 + q_1u + q_2x^{\frac{3}{2}} + q_3x^{-a_1-\frac{1}{2}}$	$y'' + \frac{a_1}{x}y' - \frac{3}{4x^2}(2a_1 + 1)y = 0$	$W\left\{x^{\frac{3}{2}}, x^{-a_1-\frac{1}{2}}\right\}$
21	$u_t = u_x^4 + p_1(b_1u + b_2)u_x^3 + q_1u + q_2x + q_3$	$y'' = 0$	$W\{1, x\}$
22	$u_t = u_x^4 + \frac{3}{p_1(3x-a_1)}(b_1u + b_2)u_x^3 + q_1u + q_2$	$y'' - \frac{1}{3x-a_1}y' = 0$	$W\left\{1, (x - \frac{1}{3}a_1)^{\frac{4}{3}}\right\}$
23	$u_t = u_x^4 + \frac{1}{p_1(x-a_1)}(-2p_1u + b_2)u_x^3 + q_1u + q_2$	$y'' - \frac{1}{x-a_1}y' = 0$	$W\left\{1, (x - a_1)^2\right\}$
24	$u_t = u_x^4 + (p_1x + p_2)u_x^3 + q_1u^2 + q_2xu + q_3u + q_4x + q_5$	$y'' = 0$	$W\{1, x\}$
25	$u_t = u_x^4 + (b_1u + b_2)u_x^3 + q_1u^2 + q_2xu + q_3u + q_4x + q_5$	$y'' = 0$	$W\{1, x\}$
26	$u_t = u_x^4 + x^{-\frac{4}{3}}(b_1u + b_2)u_x^3 + q_1u^2 + q_2x^{\frac{4}{3}}u + q_3u + q_4x^{\frac{4}{3}} + q_5$	$y'' - \frac{1}{3x}y' = 0$	$W\left\{1, x^{\frac{4}{3}}\right\}$
27	$u_t = u_x^4 - (p_1x^{4a_1} + p_2x^{3a_1+1} + 1)u_x^3 + q_1u^2 + q_2x^{1-a_1}u + q_3u + q_4x^{1-a_1} + q_5$	$y'' + \frac{a_1}{x}y' = 0$	$W\left\{1, x^{1-a_1}\right\}$
28	$u_t = u_x^4 - u_x^3 + q_1x^{1-a_1}u + q_2u + q_3x^{\frac{1-a_1+\sqrt{(a_1-1)^2-4a_0}}{2}} + q_4x^{\frac{1-a_1-\sqrt{(a_1-1)^2-4a_0}}{2}}$	$y''' + \frac{a_1}{x}y'' + \frac{a_0}{x}y = 0$	$W\left\{x^{\frac{1-a_1+\sqrt{(a_1-1)^2-4a_0}}{2}}, x^{\frac{1-a_1-\sqrt{(a_1-1)^2-4a_0}}{2}}\right\}$
29	$u_t = u_x^{m+2} + p_1(b_1u + b_2)u_x^{m+1} + q_1u + q_2x + q_3$	$y'' = 0$	$W\{1, x\}$
30	$u_t = u_x^{m+2} + \frac{m+1}{p_1[(m+1)x-a_1]}(b_1u + b_2)u_x^{m+1} + q_1u + q_2$	$y'' - \frac{1}{(m+1)x-a_1}y' = 0$	$W\left\{1, (x - \frac{a_1}{m+1})^{\frac{m+2}{m+1}}\right\}$
31	$u_t = u_x^{m+2} + \frac{1}{p_1(x+a_1)}(b_1u + b_2)u_x^{m+1} + q_1u + \frac{q_2}{m+2}[(m + 1)(x + a_1)]^{\frac{m+2}{m+1}} + q_3$	$y'' - \frac{1}{(m+1)(x+a_1)}y' = 0$	$W\left\{1, (x + a_1)^{\frac{m+2}{m+1}}\right\}$

(Continued on following page)

TABLE 1 (*Continued*) Classifications of W_2 governed by linear ODEs (2.3) of Eq. 1.1.

No.	Eq. 1.1	ODE (2.3)	W_2
32	$u_t = u_x^{m+2} + \frac{-(m+2)p_1u+mb_2}{p_1(mx-2a_1)}u_x^{m+1} + q_1u + q_2$	$y'' - \frac{2}{mx-2a_1}y' = 0$	$W\left\{1, (x-\frac{2a_1}{m})^{\frac{m+2}{m}}\right\}$
33	$u_t = u_x^{m+2} + \frac{-(m+2)p_1u+mb_2}{mp_1(x+a_1)}u_x^{m+1} + q_1u + \frac{2^{-\frac{2}{m}}q_2}{m+2}[m(x+a_1)]^{\frac{m+2}{m}} + q_3$	$y'' - \frac{2}{m(x+a_1)}y' = 0$	$W\left\{1, (x+a_1)^{\frac{m+2}{m}}\right\}$

TABLE 2 Classifications of W_3 governed by linear ODEs (2.3) of Eq. 1.1.

No.	Eq. 1.1	ODE (2.3)	W_2
1	$u_t = u_x^2 + p_1u_x + q_1u + q_2x^2 + q_3x + q_4$	$y''' = 0$	$W\{1, x, x^2\}$
2	$u_t = u_x^2 + p_1u_x + a_1u^2 + q_2u + q_3\cos(\sqrt{a_1}x) + q_4\sin(\sqrt{a_1}x)$	$y''' + a_1y' = 0 (a_1 > 0)$	$W\{1, \cos(\sqrt{a_1}x), \sin(\sqrt{a_1}x)\}$
3	$u_t = u_x^2 + p_1u_x + a_1u^2 + q_2u + q_3e^{\sqrt{-a_1}x} + q_4e^{-\sqrt{-a_1}x}$	$y''' + a_1y' = 0 (a_1 < 0)$	$W\{1, e^{\sqrt{-a_1}x}, e^{-\sqrt{-a_1}x}\}$
4	$u_t = u_x^2 + \frac{4}{3}a_2uu_x + \frac{4}{9}a_2^2u^2 + q_2u + q_3e^{-\frac{1}{3}a_2x} + q_4e^{-\frac{2}{3}a_2x}$	$y''' + a_2y'' + \frac{2}{9}a_2^2y' = 0$	$W\{1, e^{-\frac{1}{3}a_2x}, e^{-\frac{2}{3}a_2x}\}$

Taking into account the assumption $p(x) \neq 0$ and solving the system (3.4), the corresponding classifying equations and two-dimensional invariant subspaces are listed as the first three lines in Table 1 with the case $m = -3$. The cases of $m = 1, 2$ and $m \neq -3, 1, 2$ can be dealt in a similar way; therefore, we obtain the invariant subspace classification results, which are presented in Table 1.

When $n = 3$, we find there is only one case: $m = 0$, and the corresponding results are listed in Table 2.

3.2 Applications

In this section, we provide a further discussion for addressing with the explicit solutions using the above classification results.

Example 1: The equation

$$u_t = u_x^3 + \frac{9}{4x}uu_x^2 - \frac{27}{16x^3}u^3 + q_1u \tag{3.5}$$

admits the two-dimensional invariant subspace $W\left\{x^{\frac{3}{2}}, x^{-\frac{3}{2}}\right\}$ generated by ODE

$$y'' + \frac{1}{x}y' - \frac{9}{4x^2}y = 0.$$

As a result, we derive that

$$u(x,t) = C_1(t)x^{\frac{3}{2}} + C_2(t)x^{-\frac{3}{2}},$$

Substituting the above solution into Eq. 3.5, we obtain

$$C_1' = q_1C_1 + \frac{27}{4}C_1^3,$$
$$C_2' = -\frac{81}{4}C_1^2C_2 + q_1C_2,$$

For $q_1 = 0$, we can see that

$$C_1 = \frac{2}{\sqrt{4c_1 - 54t}},$$
$$C_2 = c_2(27t - 2c_1)^{\frac{3}{2}}.$$

For $q_1 \neq 0$, we have

$$C_1 = \frac{2}{\sqrt{4c_1q_1e^{-2q_1t} - 27}},$$
$$C_2 = c_2\left(4c_1q_1e^{-2q_1t} - 27\right)^{\frac{3}{2}}e^{4q_1t}.$$

The corresponding solution shown in Figure 1

Example 2: The equation

$$u_t = u_x^4 + q_1u \tag{3.6}$$

admits the invariant subspace $W\left\{1, (x-\frac{1}{3}a_1)^{\frac{4}{3}}\right\}$ governed by ODE

$$y'' - \frac{1}{3x - a_1}y' = 0.$$

Then, we arrive at

$$u(x,t) = C_1(t) + C_2(t)\left(x - \frac{1}{3}a_1\right)^{\frac{4}{3}},$$

Inserting the above solution into Eq. 3.6, we obtain

$$C_1' = q_1C_1,$$
$$C_2' = \frac{256}{81}C_2^4 + q_1C_2,$$

For $q_1 = 0$, we obtain

$$C_1 = c_1,$$
$$C_2 = \frac{3}{\sqrt[3]{27c_2 - 256t}}.$$

For $q_1 \neq 0$, we have

$$C_1 = c_1e^{q_1t},$$
$$C_2 = 3\sqrt[3]{\frac{3q_1}{81c_2q_1e^{-3q_1t} - 256}}.$$

The corresponding solution shown in Figure 2

Example 3: The equation

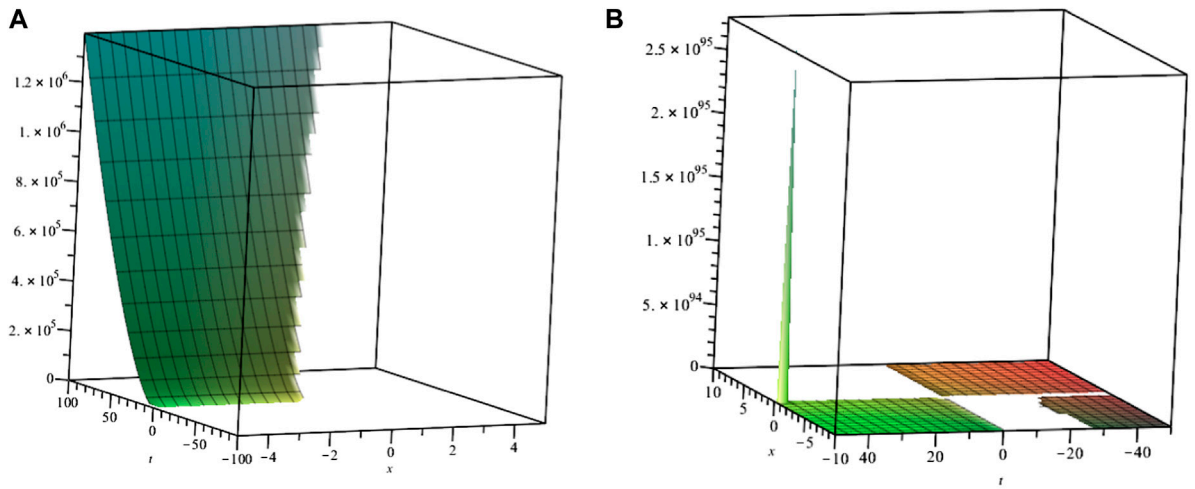

FIGURE 1
Solution profile of Eq. 3.5.

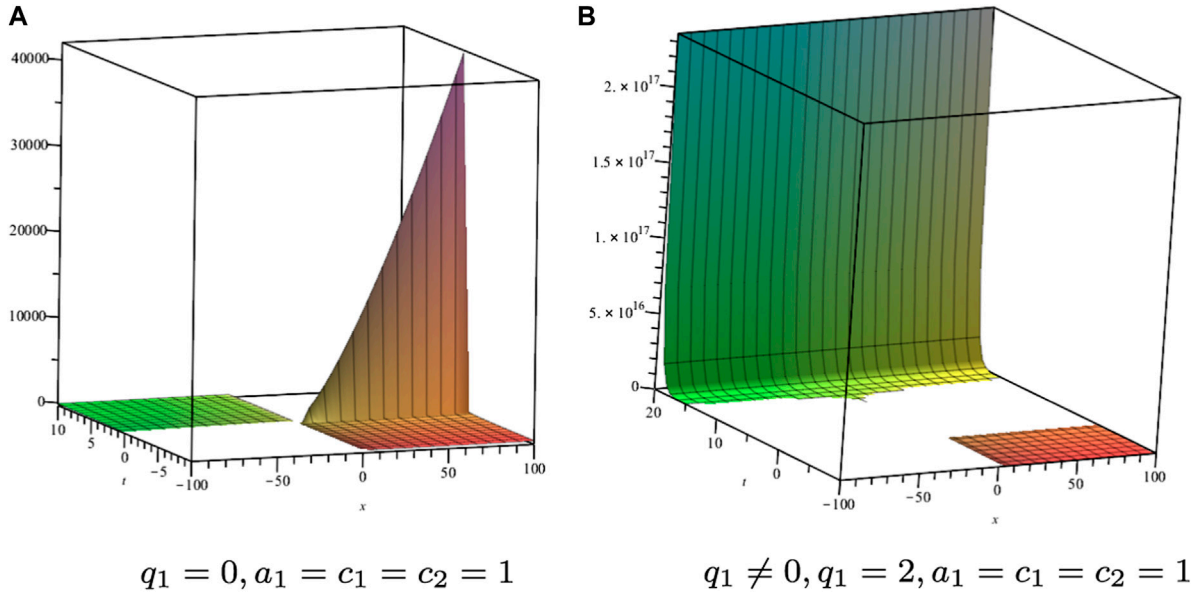

FIGURE 2
Solution profile of Eq. 3.6.

$$u_t = u_x^{m+2} - \frac{m+2}{mx} u u_x^{m+1} \tag{3.7}$$

admits the two-dimensional invariant subspace $W\left\{1, x^{\frac{m+2}{m}}\right\}$ governed by ODE

$$y'' - \frac{2}{mx} y' = 0.$$

Then we arrive at

$$u(x,t) = C_1(t) + C_2(t) x^{\frac{m+2}{m}},$$

Inserting the above solution into Eq. 3.7, we obtain

$$C_1' = 0,$$
$$C_2' = -\left(\frac{m+2}{m}\right)^{m+2} C_1 C_2^{m+1},$$

we can see that

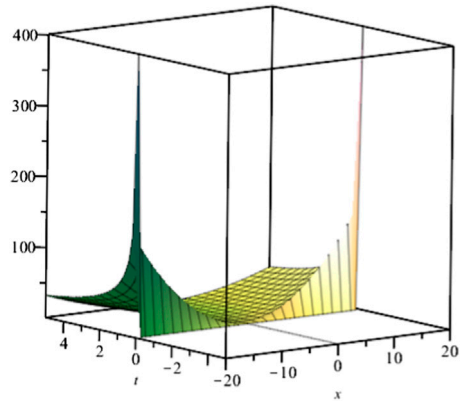

FIGURE 3
Solution profile of Eq. 3.7 with $m = 2$, $c_1 = c_2 = 1$.

$$C_1 = c_1,$$
$$C_2 = \frac{1}{\sqrt[m]{m\left(\frac{m+2}{m}\right)^{m+2} c_1 t + c_2}}.$$

The corresponding solution shown in Figure 3

Example 4: The equation

$$u_t = u_x^2 + \frac{4}{3}a_2 u u_x + \frac{4}{9}a_2^2 u^2 + q_2 u \tag{3.8}$$

admits the three-dimensional trigonometric invariant subspace $W\left\{1, e^{-\frac{1}{3}a_2 x}, e^{-\frac{2}{3}a_2 x}\right\}$ governed by ODE

$$y''' + a_2 y'' + \frac{2}{9}a_2^2 y' = 0.$$

Then we arrive at

$$u(x,t) = C_1(t) + C_2(t)e^{-\frac{1}{3}a_2 x} + C_3(t)e^{-\frac{2}{3}a_2 x},$$

Inserting the above solution into Eq. 3.8, we obtain

$$C_1' = \frac{4}{9}a_2^2 C_1^2 + q_2 C_1,$$
$$C_2' = \frac{4}{9}a_2^2 C_1 C_2 + q_2 C_2,$$
$$C_3' = \frac{1}{9}a_2^2 C_2^2 + q_2 C_3,$$

For $q_2 = 0$, we can see that

$$C_1 = \frac{9}{9c_1 - 4a_2^2 t},$$
$$C_2 = \frac{c_2}{9c_1 - 4a_2^2 t},$$
$$C_3 = \frac{c_2^2}{36\left(9c_1 - 4a_2^2 t\right)} + c_3.$$

For $q_2 \neq 0$, we have

$$C_1 = \frac{9q_2}{9c_1 q_2 e^{-q_2 t} - 4a_2^2},$$
$$C_2 = \frac{c_2}{9c_1 q_2 e^{-q_2 t} - 4a_2^2},$$
$$C_3 = \left[\frac{a_2^2 c_2^2}{81c_1 q_2^2\left(9c_1 q_2 e^{-q_2 t} - 4a_2^2\right)} + c_3\right]e^{q_2 t}.$$

The corresponding solution shown in Figure 4

4 Exact solutions of a family of third-order time-fractional dispersive PDEs

Now, we will investigate the different invariant subspaces of non-linear differential operator $F[u]$ and discuss explicit solutions of Eq. 1.2, see the following discussions.

Case 1. Let us consider the following equation

$$\frac{\partial^\alpha u}{\partial t^\alpha} + \gamma\frac{\partial^3 u}{\partial x^3} - \delta^2\frac{\partial^2}{\partial x^2}\left(\frac{\partial^\alpha u}{\partial t^\alpha}\right) = F[u] = \frac{\partial}{\partial x}\left[b_1 u^2 + b_2\left(\frac{\partial u}{\partial x}\right)^2 + b_3 u\frac{\partial^2 u}{\partial x^2}\right]. \tag{4.1}$$

Here $\alpha \in (0,1) - \left\{\frac{1}{2}\right\}$, Eq. 4.1 admits the invariant subspace $W_2 = \mathcal{L}\{1, x\}$, the reason is that

$$F[C_1 + C_2 x] = 2b_1 C_1 C_2 + 2b_1 C_2^2 x \in W_2.$$

This means that Eq. 4.1 has the following explicit solution:

$$u(x,t) = C_1(t) + C_2(t)x,$$

Substituting the solution into Eq. 4.1, we have

$$\frac{d^\alpha C_1(t)}{dt^\alpha} = 2b_1 C_1(t) C_2(t), \tag{4.2}$$
$$\frac{d^\alpha C_2(t)}{dt^\alpha} = 2b_1 C_2^2(t). \tag{4.3}$$

Eqs 4.2, 4.3 provide

$$C_2(t) = \frac{1}{2b_1}\frac{\Gamma(1-\alpha)}{\Gamma(1-2\alpha)}t^{-\alpha},$$

and

$$C_1(t) = t^{-\alpha}.$$

Then

$$u(x,t) = t^{-\alpha} + \frac{1}{2b_1}\frac{\Gamma(1-\alpha)}{\Gamma(1-2\alpha)}t^{-\alpha}x.$$

The corresponding solution shown in Figure 5

Case 2. We consider the equation

$$\frac{\partial^\alpha u}{\partial t^\alpha} + \sigma\frac{\partial u}{\partial x} + \gamma\frac{\partial^3 u}{\partial x^3} - \delta^2\frac{\partial^2}{\partial x^2}\left(\frac{\partial^\alpha u}{\partial t^\alpha}\right) = F[u] = \frac{\partial}{\partial x}\left[-a_1^2(b_2 + b_3)u^2 + b_2\left(\frac{\partial u}{\partial x}\right)^2 + b_3 u\frac{\partial^2 u}{\partial x^2}\right], \tag{4.4}$$

$\alpha \in (0, 1]$, Eq. 4.4 preserves invariant subspace $W_2 = \mathcal{L}\{1, e^{-a_1 x}\}$, since

$$F[C_1 + C_2 e^{-a_1 x}] = a_1^3(2b_2 + b_3)C_1 C_2 e^{-a_1 x} \in W_2,$$

which means that Eq. 4.4 has the solution

$$u(x,t) = C_1(t) + C_2(t)e^{-a_1 x}.$$

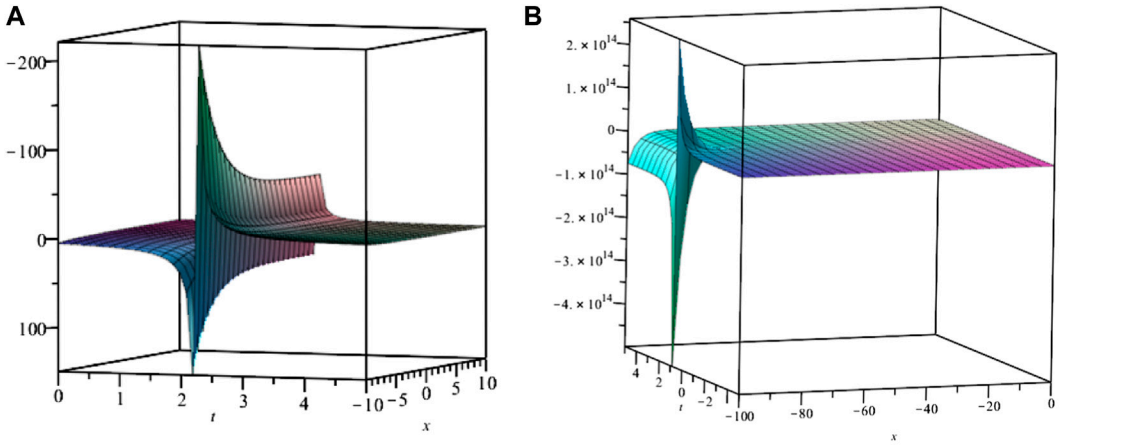

FIGURE 4
Solution profile of Eq. 3.8.

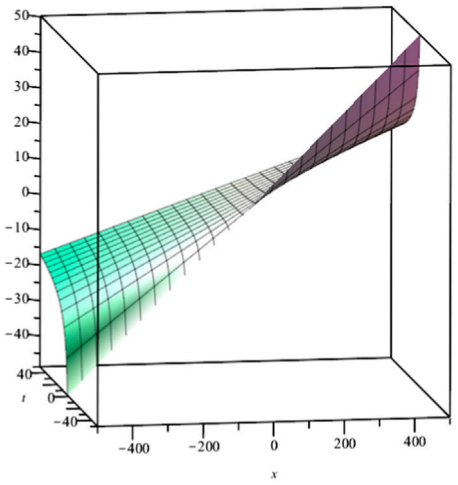

FIGURE 5
Solution profile of Eq. 4.1 with $\alpha = 1/3$, $b_1 = 2$.

Plugging the solution into Eq. 4.4, we find

$$\frac{d^\alpha C_1(t)}{dt^\alpha} = 0, \tag{4.5}$$

$$\left(1 - a_1^2\delta^2\right)\frac{d^\alpha C_2(t)}{dt^\alpha} = a_1\left(\sigma + \gamma a_1^2\right)C_2(t) + a_1^3(2b_2 + b_3)C_1(t)C_2(t). \tag{4.6}$$

Solving Eq. 4.5, $C_1(t) = c_1$, c_1 is an arbitrary constant, and when $a_1^2\delta^2 \neq 1$, letting

$$\mu = \frac{a_1\left[\sigma + \gamma a_1^2 + a_1^2(2b_2 + b_3)c_1\right]}{1 - a_1^2\delta^2}.$$

Therefore, Eq. 4.6 becomes

$$\frac{d^\alpha C_2(t)}{dt^\alpha} = \mu C_2(t). \tag{4.7}$$

Applying the LT to Eq. 4.7, we have

$$s^\alpha \mathrm{L}\{C_2(t)\} - s^{\alpha-1}C_2(0) = \mu \mathrm{L}\{C_2(t)\},$$

namely,

$$\bar{C}_2(s) = \mathrm{L}\{C_2(t)\} = a\frac{s^{\alpha-1}}{s^\alpha - \mu}.$$

Here $C_2(0) = a$, its inverse LT is

$$C_2(t) = aE_{\alpha,1}(\mu t^\alpha), \quad \alpha \in (0, 1].$$

where $E_{\alpha,1}(.)$ is the ML function

$$E_{\alpha,1}(\mu t^\alpha) = \sum_{k=0}^{\infty}\frac{(\mu t^\alpha)^k}{\Gamma(\alpha k + 1)}.$$

Hence, we derive that

$$u(x,t) = c_1 + aE_{\alpha,1}(\mu t^\alpha)e^{-a_1 x}.$$

In the case of $\alpha = 1$, it is a traveling wave solution

$$u(x,t) = c_1 + ae^{\mu t - a_1 x}.$$

The corresponding solution shown in Figure 6

Case 3. We consider the equation

$$\begin{aligned}\frac{\partial^\alpha u}{\partial t^\alpha} + \sigma\frac{\partial u}{\partial x} + \gamma\frac{\partial^3 u}{\partial x^3} - \delta^2\frac{\partial^2}{\partial x^2}\left(\frac{\partial^\alpha u}{\partial t^\alpha}\right) &= F[u] \\ &= \frac{\partial}{\partial x}\left[a_0(b_2 + b_3)u^2 + b_2\left(\frac{\partial u}{\partial x}\right)^2 + b_3 u\frac{\partial^2 u}{\partial x^2}\right],\end{aligned} \tag{4.8}$$

$\alpha \in (0, 1]$, Eq. 4.8 admits the two-dimensional invariant subspace $W_2 = \mathcal{L}\{\cos(\sqrt{a_0}\,x), \sin(\sqrt{a_0}\,x)\}$, since

$$F\left[C_1\cos\left(\sqrt{a_0}\,x\right) + C_2\sin\left(\sqrt{a_0}\,x\right)\right] = 0 \in W_2.$$

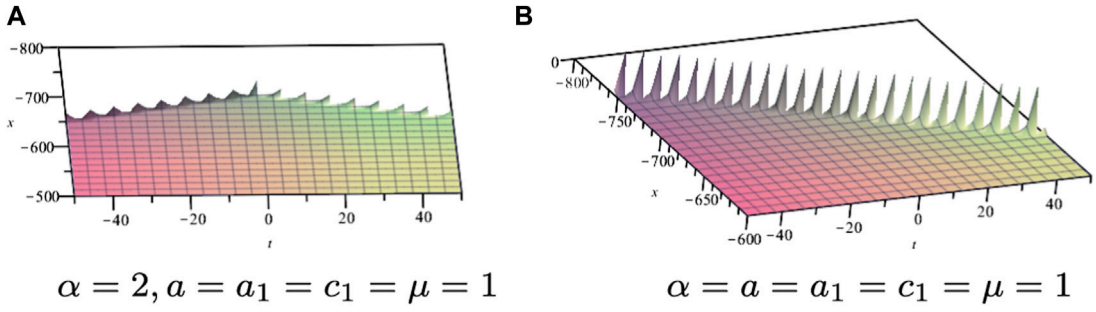

FIGURE 6
Solution profile of Eq. 4.4.

This indicates that Eq. 4.8 has the solution

$$u(x,t) = C_1 \cos\left(\sqrt{a_0}\, x\right) + C_2 \sin\left(\sqrt{a_0}\, x\right).$$

Substituting the solution into Eq. 4.8, we have

$$\frac{d^\alpha C_1(t)}{dt^\alpha} = \lambda C_2(t), \tag{4.9}$$

$$\frac{d^\alpha C_2(t)}{dt^\alpha} = -\lambda C_1(t). \tag{4.10}$$

Here, $\lambda = \frac{\sqrt{a_0}(\sigma - a_0\gamma)}{1+a_0\delta^2}$. By applying the time-fractional derivative $\frac{d^\alpha}{dt^\alpha}$ to Eq. 4.9, we derive that

$$\frac{d^\alpha}{dt^\alpha}\frac{d^\alpha C_1(t)}{dt^\alpha} = -\lambda^2 C_1(t).$$

Now we discuss the following Cauchy problem:

$$\begin{cases} \dfrac{d^\alpha}{dt^\alpha}\dfrac{d^\alpha C_1(t)}{dt^\alpha} = -\lambda^2 C_1(t), \\ C_1(0) = a, \\ \dfrac{d^\alpha C_1(t)}{dt^\alpha}\Big|_{t=0} = 0. \end{cases} \tag{4.11}$$

Then, define $g(t) = \frac{d^\alpha C_1(t)}{dt^\alpha}$, and utilizing the LT to this equation, we can see

$$\bar{g}(s) = s^\alpha \bar{C}_1(s) - a s^{\alpha-1}. \tag{4.12}$$

At the same time, applying LT to the first equation of Eq. 4.11, we obtain

$$\mathrm{L}\left\{\frac{d^\alpha}{dt^\alpha}\frac{d^\alpha C_1(t)}{dt^\alpha}\right\} = \mathrm{L}\left\{\frac{d^\alpha g(t)}{dt^\alpha}\right\} = s^\alpha \bar{g}(s) - s^{\alpha-1} g(0), \tag{4.13}$$

Inserting Eq. 4.12 into Eq. 4.13, we find

$$\bar{C}_1(s) = a\frac{s^{2\alpha-1}}{s^{2\alpha}+\lambda^2}.$$

whose inverse LT is

$$C_1(t) = aE_{2\alpha,1}\left(-\lambda^2 t^{2\alpha}\right), \quad \alpha \in (0,1]. \tag{4.14}$$

where $E_{2\alpha,1}(.)$ is the ML function

$$E_{2\alpha,1}\left(-\lambda^2 t^{2\alpha}\right) = \sum_{k=0}^{\infty} \frac{(-1)^k \lambda^{2k} t^{2\alpha k}}{\Gamma(2\alpha k+1)}.$$

Substituting Eq. 4.14 in Eq. 4.10, we get

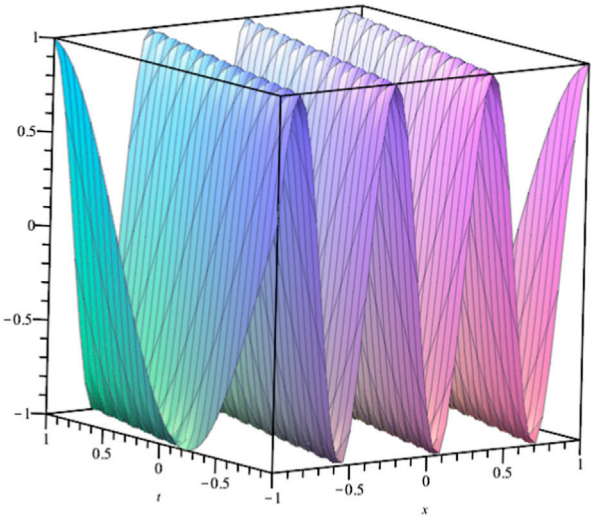

FIGURE 7
Solution profile of Eq. 4.8 with $a_0 = 100$, $\sigma = \gamma = 1$, $\delta = 2$.

$$\frac{d^\alpha C_2(t)}{dt^\alpha} = -\lambda a E_{2\alpha,1}\left(-\lambda^2 t^{2\alpha}\right). \tag{4.15}$$

By applying I^α on both sides of Eq. 4.15, we obtain

$$C_2(t) = -a\lambda t^\alpha E_{2\alpha,\alpha+1}\left(-\lambda^2 t^{2\alpha}\right).$$

For the sake of simplicity, we set the integration constant to zero. Assuming $a = 1$, the solution of Eq. 4.8 is

$$u(x,t) = E_{2\alpha,1}\left(-\lambda^2 t^{2\alpha}\right)\cos\left(\sqrt{a_0}\, x\right) - \lambda t^\alpha E_{2\alpha,\alpha+1}\left(-\lambda^2 t^{2\alpha}\right)\sin\left(\sqrt{a_0}\, x\right).$$

Note that for $\alpha = 1$,

$$E_{2,1}\left(-\lambda^2 t^2\right) = \sum_{k=0}^{\infty} \frac{\left(-\lambda^2 t^2\right)^k}{\Gamma(2k+1)} = \cos(\lambda t),$$

$$\lambda t E_{2,2}\left(-\lambda^2 t^2\right) = \lambda t \sum_{k=0}^{\infty} \frac{\left(-\lambda^2 t^2\right)^k}{\Gamma(2k+2)} = \sin(\lambda t),$$

and the solution becomes

$$u(x,t) = \cos(\lambda t)\cos\left(\sqrt{a_0}\,x\right) - \sin(\lambda t)\sin\left(\sqrt{a_0}\,x\right)$$
$$= \cos\left(\lambda t + \sqrt{a_0}\,x\right).$$

The corresponding solution shown in Figure 7

Case 4. We consider the equation

$$\frac{\partial^\alpha u}{\partial t^\alpha} - \frac{4}{9}\gamma a_1^2\frac{\partial u}{\partial x} + \gamma\frac{\partial^3 u}{\partial x^3} - \delta^2\frac{\partial^2}{\partial x^2}\left(\frac{\partial^\alpha u}{\partial t^\alpha}\right) = F[u]$$
$$= \frac{\partial}{\partial x}\left[-\frac{1}{9}a_1^2u^2 - \frac{3}{4}\left(\frac{\partial u}{\partial x}\right)^2 + u\frac{\partial^2 u}{\partial x^2}\right], \tag{4.16}$$

$\alpha \in (0, 1]$, Eq. 4.16 admits the two-dimensional invariant subspace $W_2 = \mathcal{L}\left\{e^{-\frac{1}{3}a_1x}, e^{-\frac{2}{3}a_1x}\right\}$, since

$$F\left[C_1e^{-\frac{1}{3}a_1x} + C_2e^{-\frac{2}{3}a_1x}\right] = \frac{1}{18}a_1^3C_1^2e^{-\frac{2}{3}a_1x} \in W_2.$$

This means that the explicit solution has the following form

$$u(x,t) = C_1(t)e^{-\frac{1}{3}a_1x} + C_2(t)e^{-\frac{2}{3}a_1x}.$$

Substituting the solution into Eq. 4.16, we have

$$\frac{d^\alpha C_1(t)}{dt^\alpha} = \lambda_1 C_1(t), \tag{4.17}$$
$$\frac{d^\alpha C_2(t)}{dt^\alpha} = \lambda_2[C_1(t)]^2, \tag{4.18}$$

where $\lambda_1 = \frac{a_1^3\gamma}{a_1^2\delta^2-9}, \lambda_2 = \frac{a_1^3}{18-8a_1^2\delta^2}$. Setting $C_1(0) = 1$ and employing the LT of both sides of Eq. 4.17, we have

$$\bar{C}_1(s) = \frac{s^{\alpha-1}}{s^\alpha - \lambda_1}.$$

Its inverse LT is

$$C_1(t) = E_{\alpha,1}(\lambda_1 t^\alpha), \quad \alpha \in (0,1].$$

Utilizing $C_1(t)$ in Eq. 4.18, we obtain

$$\frac{d^\alpha C_2(t)}{dt^\alpha} = \lambda_2\left(E_{\alpha,1}(\lambda_1 t^\alpha)\right)^2.$$

However, while the ML function does not fulfill the following composition property

$$E_\alpha(x)E_\alpha(y) \neq E_\alpha(x+y),$$

it should be noted that

$$E_\alpha(x^\alpha) = \sum_{k=0}^{\infty}\frac{x^{\alpha k}}{\Gamma(\alpha k+1)}$$

which satisfies the composition property, that is,

$$E_\alpha(x^\alpha)E_\alpha(y^\alpha) = E_\alpha\left((x+y)^\alpha\right), \quad \alpha > 0.$$

Thus, we find

$$\frac{d^\alpha C_2(t)}{dt^\alpha} = \lambda_2 E_{\alpha,1}(\lambda_1(2t)^\alpha)). \tag{4.19}$$

Taking I^α on Eq. 4.19 and applying the integration of the ML function relation, we derive the following result:

$$C_2(t) = \lambda_2(2t)^\alpha E_{\alpha,\alpha+1}(\lambda_1(2t)^\alpha)).$$

Here, we set $C_2(0) = 0$. Hence, the exact solution of Eq. 4.16 associated with $W_2 = \mathcal{L}\left\{e^{-\frac{1}{3}a_1x}, e^{-\frac{2}{3}a_1x}\right\}$ reads

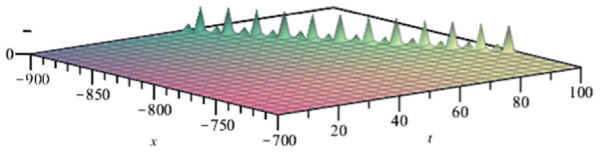

FIGURE 8
Solution profile of Eq. 4.16 with $a_1 = 1$, $\lambda_1 = 1$, $\lambda_2 = 2$, $\delta = 2$.

$$u(x,t) = E_{\alpha,1}(\lambda_1 t^\alpha)e^{-\frac{1}{3}a_1x} + \lambda_2(2t)^\alpha E_{\alpha,\alpha+1}(\lambda_1(2t)^\alpha))e^{-\frac{2}{3}a_1x}.$$

Note that for $\alpha = 1$,

$$E_{1,1}(\lambda_1 t) = \sum_{k=0}^{\infty}\frac{(\lambda_1 t)^k}{\Gamma(k+1)} = e^{\lambda_1 t},$$
$$E_{1,2}(\lambda_1(2t)) = \sum_{k=0}^{\infty}\frac{(2\lambda_1 t)^k}{\Gamma(k+2)} = \frac{e^{2\lambda_1 t}-1}{2\lambda_1 t},$$
$$u(x,t) = e^{\lambda_1 t - \frac{1}{3}a_1x} + \frac{\lambda_2}{\lambda_1}\left(e^{2\lambda_1 t}-1\right)e^{-\frac{2}{3}a_1x}.$$

The corresponding solution shown in Figure 8

Case 5. We consider the equation

$$\frac{\partial^\alpha u}{\partial t^\alpha} + \sigma\frac{\partial u}{\partial x} + \gamma\frac{\partial^3 u}{\partial x^3} - \delta^2\frac{\partial^2}{\partial x^2}\left(\frac{\partial^\alpha u}{\partial t^\alpha}\right) = F[u]$$
$$= \frac{\partial}{\partial x}\left[(b_2+b_3)u^2 + b_2\left(\frac{\partial u}{\partial x}\right)^2 + b_3u\frac{\partial^2 u}{\partial x^2}\right], \tag{4.20}$$

$\alpha \in (0, 1]$, Eq. 4.20 admits the three-dimensional invariant subspace $W_3 = \mathcal{L}\{1, \cos x, \sin x\}$, since

$$F[C_1 + C_2\cos x + C_3\sin x] = (2b_2+b_3)C_1C_3\cos x$$
$$-(2b_2+b_3)C_1C_2\sin x \in W_3.$$

This means that the exact solution has the following form:

$$u(x,t) = C_1(t) + C_2(t)\cos x + C_3(t)\sin x.$$

Substituting the solution into Eq. 4.20, we obtain

$$\frac{d^\alpha C_1(t)}{dt^\alpha} = 0, \tag{4.21}$$
$$(1+\delta^2)\frac{d^\alpha C_2(t)}{dt^\alpha} = (\gamma-\sigma)C_3(t) + (2b_2+b_3)C_1(t)C_3(t), \tag{4.22}$$
$$(1+\delta^2)\frac{d^\alpha C_3(t)}{dt^\alpha} = (\sigma-\gamma)C_2(t) - (2b_2+b_3)C_1(t)C_2(t). \tag{4.23}$$

Solving Eq. 4.21, we obtain $C_1(t) = c_1$, inserting it into Eq. 4.22 and Eq. 4.23, we find

$$\frac{d^\alpha C_2(t)}{dt^\alpha} = \lambda C_3(t),$$
$$\frac{d^\alpha C_3(t)}{dt^\alpha} = -\lambda C_2(t),$$

where $\lambda = \frac{\gamma-\delta+c_1(2b_2+b_3)}{1+\delta^2}$, Following the procedure described in case 3, we obtain the exact solution

$$u(x,t) = c_1 + E_{2\alpha,1}\left(-\lambda^2t^{2\alpha}\right)\cos x - \lambda t^\alpha E_{2\alpha,\alpha+1}\left(-\lambda^2t^{2\alpha}\right)\sin x.$$

Note that for $\alpha = 1$,

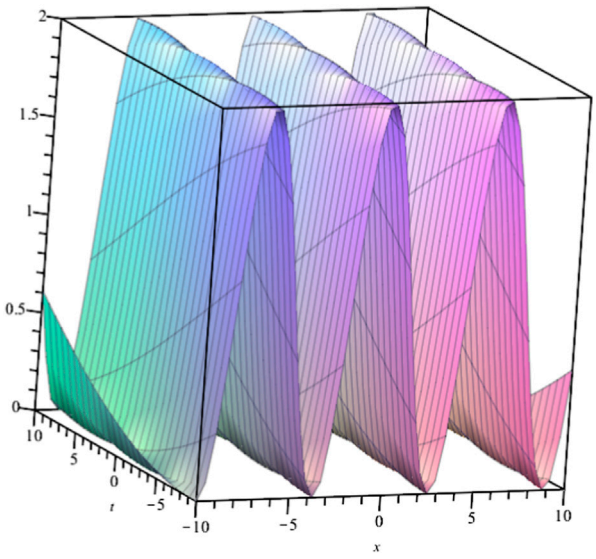

FIGURE 9
Solution profile of Eq. 4.20 with $\alpha = \gamma = b_2 = b_3 = c_1 = 1$, $\delta = 10$.

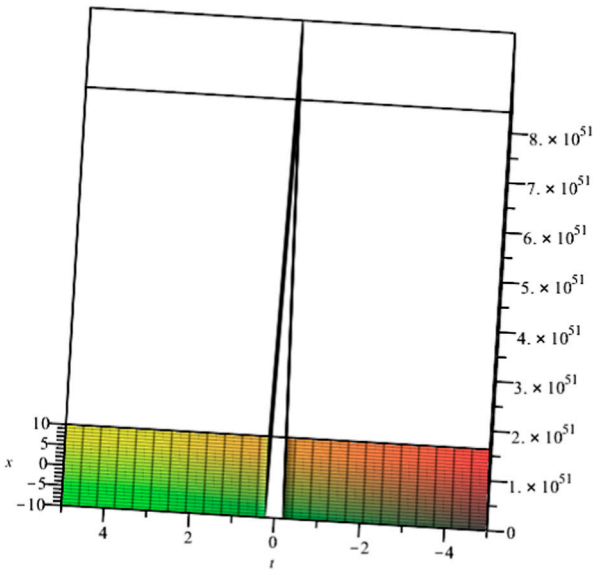

FIGURE 10
Solution profile of Eq. 4.24 with $\alpha = 1/3$, $b_2 = b_3 = 1$, $\delta = 10$.

$$E_{2,1}\left(-\lambda^2 t^2\right) = \sum_{k=0}^{\infty} \frac{(-1)^k (\lambda t)^{2k}}{\Gamma(2k+1)} = \cos(\lambda t),$$
$$\lambda t E_{2,2}\left(-\lambda^2 t^2\right) = \lambda t \sum_{k=0}^{\infty} \frac{(-1)^k (\lambda t)^{2k+1}}{\Gamma(2k+1)} = \sin(\lambda t),$$

and the solution is

$$u(x,t) = c_1 + \cos(\lambda t)\cos x - \sin(\lambda t)\sin x = c_1 + \cos(\lambda t + x),$$

which is a compacton solution.

The corresponding solution shown in Figure 9

Case 6. We consider the equation

$$\frac{\partial^\alpha u}{\partial t^\alpha} - \delta^2 \frac{\partial^2}{\partial x^2}\left(\frac{\partial^\alpha u}{\partial t^\alpha}\right) = F[u] = \frac{\partial}{\partial x}\left[b_2\left(\frac{\partial u}{\partial x}\right)^2 + b_3 u \frac{\partial^2 u}{\partial x^2}\right], \quad (4.24)$$

$\alpha \in (0,1) - \left\{\frac{1}{2}\right\}$, Eq. 4.24 admits the four-dimensional invariant subspace $W_4 = \mathcal{L}\{1, x, x^2, x^3\}$, since

$$\begin{aligned} F\left[C_1 + C_2 x + C_3 x^2 + C_4 x^3\right] = {} & 6b_3 C_1 C_4 + (4b_2 + 2b_3) C_2 C_3 \\ & + \left[(8b_2 + 4b_3) C_3^2 + 12(b_2 + b_3) C_2 C_4\right] x \\ & + 12(3b_2 + 2b_3) C_3 C_4 x^2 \\ & + 12(3b_2 + 2b_3) C_4^2 x^3 \in W_4. \end{aligned}$$

This means that the exact solution has the following form

$$u(x,t) = C_1(t) + C_2(t)x + C_3(t)x^2 + C_4(t)x^3.$$

Substituting the solution into (4.24), we have

$$\begin{aligned} &\frac{d^\alpha C_1(t)}{dt^\alpha} - 2\delta^2 \frac{d^\alpha C_3(t)}{dt^\alpha} = 6b_3 C_1(t) C_4(t) + (4b_2 + 2b_3) C_2(t) C_3(t), \\ &\frac{d^\alpha C_2(t)}{dt^\alpha} - 6\delta^2 \frac{d^\alpha C_4(t)}{dt^\alpha} = (8b_2 + 4b_3) C_3^2(t) + 12(b_2 + b_3) C_2(t) C_4(t), \\ &\frac{d^\alpha C_3(t)}{dt^\alpha} = 12(3b_2 + 2b_3) C_3(t) C_4(t), \\ &\frac{d^\alpha C_4(t)}{dt^\alpha} = 12(3b_2 + 2b_3) C_4^2(t). \end{aligned}$$

Solving this system, we derive that

$$\begin{aligned} C_1(t) &= \frac{2(3b_2 + 2b_3)}{2b_2 + b_3}\delta^2 t^{-\alpha} + \frac{16}{3}(3b_2 + 2b_3)^2 \left[\frac{\Gamma(1-2\alpha)}{\Gamma(1-\alpha)}\right]^2 t^{-\alpha}, \\ C_2(t) &= \left[\frac{\delta^2}{2(2b_2 + b_3)} \frac{\Gamma(1-\alpha)}{\Gamma(1-2\alpha)} + 4(3b_2 + 2b_3) \frac{\Gamma(1-2\alpha)}{\Gamma(1-\alpha)}\right] t^{-\alpha}, \\ C_3(t) &= t^{-\alpha}, \\ C_4(t) &= \frac{1}{12(3b_2 + 2b_3)} \frac{\Gamma(1-\alpha)}{\Gamma(1-2\alpha)} t^{-\alpha}. \end{aligned}$$

Thus, Eq. 4.24 has the solution

$$\begin{aligned} u(x,t) = {} & (3b_2 + 2b_3)\left[\frac{2}{2b_2 + b_3}\delta^2 + \frac{16}{3}(3b_2 + 2b_3)\eta^2\right] t^{-\alpha} \\ & + \left[4(3b_2 + 2b_3)\eta + \frac{1}{2(2b_2 + b_3)\eta}\delta^2\right] t^{-\alpha} x + t^{-\alpha} x^2 \\ & + \frac{1}{12(3b_2 + 2b_3)\eta} t^{-\alpha} x^3. \end{aligned}$$

where $\eta = \frac{\Gamma(1-2\alpha)}{\gamma(1-\alpha)}$.

The corresponding solution shown in Figure 10

5 Conclusion

In this work, a class of HJEs (1.1) and a family of third-order time-fractional dispersive PDEs (1.2) are investigated by utilizing ISM. All invariant subspaces for the considered HJEs are derived and displayed in Table 1 and Table 2. Meanwhile, some exact solutions to the equations are obtained due to the corresponding symmetry reductions. For the third-order time-fractional dispersive PDEs, the right-hand side of Eq. 1.2 is the derivative of a quadratic differential polynomial, therefore they preserve more than one invariant subspace, each of which generates a solution. Then, by employing the LT method and applying several properties of the

well known ML function, the different kinds of explicit solutions of Eq. 1.2 are derived.

There are still some important problems to be considered. For instance, how does one use ISM to resolve initial value problems? How can we develop this method to investigate higher-dimensional nonlinear equations and their discrete versions? This will be considered in the future. Moreover, in the extended version of this work, we will discuss more complicated fractional differential equations by using ISM.

Data availability statement

The original contributions presented in the study are included in the article/supplementary material, further inquiries can be directed to the corresponding authors.

Author contributions

GQ: Investigation, methodology, software, writing—original draft. MW: Writing—review and editing, software. SS: Formal analysis, writing—review and editing, supervision. All authors contributed to the article and approved the submitted version.

Funding

The work was supported by the National Natural Science Foundation of China (Grant No. 11501419), the Natural Science Foundation of Shaanxi Province, China (Grant No. 2021JM-521) and the Key Research Foundation of Weinan City, China (Grant No. 2019ZDYF-JCYJ-118).

Conflict of interest

The authors declare that the research was conducted in the absence of any commercial or financial relationships that could be construed as a potential conflict of interest.

Publisher's note

All claims expressed in this article are solely those of the authors and do not necessarily represent those of their affiliated organizations, or those of the publisher, the editors and the reviewers. Any product that may be evaluated in this article, or claim that may be made by its manufacturer, is not guaranteed or endorsed by the publisher.

References

1. Galaktionov VA, Svirshchevskii SR. *Exact solutions and invariant subspaces of nonlinear partial differential equations in mechanics and physics*. London: Chapman and Hall/CRC (2007).

2. Qu CZ, Zhu CR. Classification of coupled systems with two-component nonlinear diffusion equations by the invariant subspace method. *J Phys A Math Theor* (2009) 42: 475201. [27pp]. doi:10.1088/1751-8113/42/47/475201

3. Zhu CR, Qu CZ. Maximal dimension of invariant subspaces admitted by nonlinear vector differential operators. *J Math Phys* (2011) 52:043507. [15pp]. doi:10.1063/1.3574534

4. Ma WX. A refined invariant subspace method and applications to evolution equations. *Sci China Math* (2012) 55:1769–78. doi:10.1007/s11425-012-4408-9

5. Song JQ, Shen SF, Jin YY, Zhang J. New maximal dimension of invariant subspaces to coupled systems with two-component equations. *Commun Nonlinear Sci Numer Simulat* (2013) 18:2984–92. doi:10.1016/j.cnsns.2013.03.019

6. Shen SF, Qu CZ, Jin YY, Ji LN. Maximal dimension of invariant subspaces to systems of nonlinear evolution equations. *Chin Ann Math Ser B* (2012) 33:161–78. doi:10.1007/s11401-012-0705-4

7. Qu CZ. Conditional Lie Bäcklund symmetries of Hamilton-Jacobi equations. *Nonlinear Anal* (2009) 71:e243–e258.doi:10.1016/j.na.2008.10.045

8. Svirshchevskii SR. Lie Bäcklund symmetries of linear ODEs and generalized separation of variables in nonlinear equations. *Phys Lett A* (1995) 99:344–8.

9. King JR. Exact polynomial solutions to some nonlinear diffusion equations. *Phys D* (1993) 64:35–65. doi:10.1016/0167-2789(93)90248-y

10. Fokas AS, Liu QM. Nonlinear interaction of traveling waves of nonintegrable equations. *Phys Rev Lett* (1994) 72:3293–6. doi:10.1103/physrevlett.72.3293

11. Zhdanov RZ. Conditional Lie-Bäcklund symmetry and reductions of evolution equations. *J Phys A Math Gen* (1995) 28:3841–50.

12. Qu CZ. Group classification and generalized conditional symmetry reduction of the nonlinear diffusion-convection equation with a nonlinear source. *Stud Appl Math* (1997) 99:107–36. doi:10.1111/1467-9590.00058

13. Qu CZ. Exact solutions to nonlinear diffusion equations obtained by a generalized conditional symmetry method. *IMA J Appl Math* (1999) 62:283–302. doi:10.1093/imamat/62.3.283

14. Ji LN, Qu CZ. Conditional Lie Bäcklund symmetries and solutions to (n+1)-dimensional nonlinear diffusion equationscklund symmetries and solutions to $(n + 1)$-dimensional nonlinear diffusion equations. *J Math Phys* (2007) 48:103509. doi:10.1063/1.2795216

15. Gazizov RK, Kasatkin AA. Construction of exact solutions for fractional order differential equations by invariant subspace method. *Comput Math Appl* (2013) 66: 576–84.doi:10.1016/j.camwa.2013.05.006

16. Sahadevan R, Bakkyaraj T. Invariant subspace method and exact solutions of certain nonlinear time fractional partial differential equations. *Fract Calc Appl Anal* (2015) 18:146–62. doi:10.1515/fca-2015-0010

17. Harris PA, Garra R. Analytic solution of nonlinear fractional Burgers-type equation by invariant subspace method. *Nonlinear Stud* (2013) 20:471–81. doi:10.48550/arXiv.1306.1942

18. Prakash P, Priyendhu KS, Lakshmanan M. Invariant subspace method for $(m+1)$-dimensional non-linear time-fractional partial differential equations. *Commun Nonlinear Sci Numer Simulat* (2022) 111:106436.doi:10.1016/j.cnsns.2022.106436

19. Prakash P, Priyendhu KS, Anjitha KM. Initial value problem for the (2+1)-dimensional time-fractional generalized convection-reaction-diffusion wave equation: invariant subspace and exact solutions. *Comput Appl Math* (2022) 41:1–55.

20. Sahadevan R, Prakash P. Exact solutions and maximal dimension of invariant subspaces of time fractional coupled nonlinear partial differential equations. *Commun Nonlinear Sci Numer Simulat* (2017) 42:158–77. doi:10.1016/j.cnsns.2016.05.017

21. Rui WG. Idea of invariant subspace combined with elementary integral method for investigating exact solutions of time-fractional NPDEs. *Appl Math Comput* (2018) 339:158–71. doi:10.1016/j.amc.2018.07.033

22. Feng W, Zhao SL. Time-fractional inhomogeneous nonlinear diffusion equation: Symmetries, conservation laws, invariant subspaces, and exact solutions. *Mod Phys Lett B* (2018) 32:1850401. doi:10.1142/s0217984918504018

23. Choudhary S, Prakash P, Varsha DG. Invariant subspaces and exact solutions for a system of fractional PDEs in higher dimensions. *Comput Appl Math* (2019) 38:126. doi:10.1007/s40314-019-0879-4

24. Crandall MG, Lions PL. Viscosity solutions of Hamilton-Jacobi equations. *Trans Amer Math Soc* (1983) 277:1–42. doi:10.1090/s0002-9947-1983-0690039-8

25. Crandall MG, Evans LC, Lions PL. Some properties of viscosity solutions of Hamilton-Jacobi equations. *Trans Amer Math Soc* (1984) 282:487–502. doi:10.1090/s0002-9947-1984-0732102-x

26. Crandall MG, Lions PL. On existence and uniqueness of solutions of Hamilton-Jacobi equations. *Nonlinear Anal TMA* (1986) 10:353–70. doi:10.1016/0362-546x(86)90133-1

27. Evans LC. Partial differential equations. In: *Graduate studies in mathematics*. Providence, RI: American Mathematical Society (1998).

28. Wei QL. Viscosity solution of the Hamilton-Jacobi equation by a limiting minimax method. *Nonlinearity* (2014) 27:17–41. doi:10.1088/0951-7715/27/1/17

29. Galaktionov VA. *Gemetric sturmian theory of nonlinear parabolic equations and applications*. Boca Raton, FL: Chapman and Hall/CRC (2004).

30. Galaktionov VA. Vȧzquez jl. A stability technique for evolution partial differential equations. In: *A dynamical systems approach*. Boston, MA: Birkhauser Boston, Inc (2004).

31. Galaktionov VA, Vazquez JL. Blow-up for quasilinear heat equations described by means of nonlinear Hamilton–Jacobi equationszquez JL. Blow-Up for quasilinear heat equations described by means of nonlinear Hamilton-Jacobi equations. *J Differential Equations* (1996) 127:1–40. doi:10.1006/jdeq.1996.0059

32. Galaktionov VA, Vazquez JL. Geometrical properties of the solutions of one-dimensional nonlinear parabolic equationszquez JL. Geometrical properties of the solutions of one-dimensional nonlinear parabolic equations. *Math Ann* (1995) 303: 741–69. doi:10.1007/bf01461014

33. Podlubny I. *Fractional differential equations: An introduction to fractional derivatives, fractional differential equations, to methods of their solution and some of their applications*. New York: Academic Press (1999).

34. Oldham KB, Spanier J. *The fractional calculus*. New York: Academic Press (1974).

35. Miller KS, Ross B. *An introduction to the fractional calculus and fractional differential equations*. New York: John Wiley and Sons (1993).

36. Kilbas AA, Trujillo JJ, Srivastava HM. *Theory and applications of fractional differential equations*. Amsterdam: Elseiver (2006).

37. Degasperis A, Holm DD, Hone ANW. A new integrable equation with peakon solutions. *Theor Math Phys* (2002) 133:1463–74. doi:10.48550/arXiv.nlin/0205023

38. Rui WG, He B, Long Y, Chen C. The integral bifurcation method and its application for solving a family of third-order dispersive PDEs. *Nonlinear Anal* (2008) 69:1256–67. doi:10.1016/j.na.2007.06.027

39. Johnson RS. Camassa-Holm, Korteweg-de Vries and related models for water waves. *J Fluid Mech* (2002) 455:63–82. doi:10.1017/s0022112001007224

40. Camassa R, Holm D. An integrable shallow water equation with peaked solitons. *Phys Rev Lett* (1993) 71:1661–4. doi:10.1103/physrevlett.71.1661

41. Chen C, Tang M. A new type of bounded waves for Degasperis-Procesi equation. *Chaos Soliton Fract* (2006) 27:698–704. doi:10.1016/j.chaos.2005.04.040

42. Coclite GM, Karlsen KH. On the well-posedness of the Degasperis-Procesi equation. *J Funct Anal* (2006) 233:60–91. doi:10.1016/j.jfa.2005.07.008

frontiers | Frontiers in Physics

TYPE Original Research
PUBLISHED 31 March 2023
DOI 10.3389/fphy.2023.1179961

OPEN ACCESS

EDITED BY
Xiangpeng Xin,
Liaocheng University, China

REVIEWED BY
Junchao Chen,
Lishui University, China
Xiaoen Zhang,
South China University of Technology, China

*CORRESPONDENCE
Yunqing Yang,
yqyang@amss.ac.cn

SPECIALTY SECTION
This article was submitted to Mathematical Physics, a section of the journal Frontiers in Physics

RECEIVED 05 March 2023
ACCEPTED 16 March 2023
PUBLISHED 31 March 2023

CITATION
Shi X and Yang Y (2023), Exact solutions and Darboux transformation for the reverse space–time non-local fifth-order non-linear Schrödinger equation. *Front. Phys.* 11:1179961. doi: 10.3389/fphy.2023.1179961

Exact solutions and Darboux transformation for the reverse space–time non-local fifth-order non-linear Schrödinger equation

Xinrui Shi[1,2] and Yunqing Yang[1,2]*

[1]School of Information Engineering, Zhejiang Ocean University, Zhoushan, China, [2]Key Laboratory of Oceanographic Big Data Mining and Application of Zhejiang Province, Zhoushan, China

In this paper, the non-local reverse space–time fifth-order non-linear Schrödinger(NLS) equation has been investigated, which is proposed by the non-local reduction of Ablowitz–Kaup–Newell–Segur (AKNS) scattering problems. The determinant representation of the Nth Darboux transformation for the non-local reverse space–time fifth-order NLS equation is obtained. Some interesting non-linear wave solutions, including soliton, complexiton, and rogue wave solutions, are derived by the Darboux transformation. Moreover, the dynamics of non-linear wave solutions are illustrated with the corresponding evolution plots, and the results show that the non-local fifth-order NLS equation has new different properties from the local case.

KEYWORDS

non-local fifth-order non-linear Schrödinger equation, Darboux transformation, soliton, rogue wave, integrable system

1 Introduction

Integrable systems play an important role in non-linear science fields such as non-linear optics [1, 2], ocean physics [3], Bose–Einstein condensates [4], and even financial markets [5]. The investigation of various physically meaningful non-linear wave solutions is still one of the active areas of research in the field of integrable systems. In the past decades, many powerful methods and techniques have been proposed to construct various non-linear wave solutions and to study their underlying dynamics, such as Darboux transformation [6, 7], inverse scattering [8, 9], bilinear transformation [10], and Riemann–Hilbert approaches [11, 12]. Recently, Ablowitz and Musslimani proposed a new integrable non-local non-linear Schrödinger (NLS) equation under a reduction of the Ablowitz–Kaup–Newell–Segur (AKNS) system, and some non-linear wave solutions are constructed by the inverse scattering method [13]. Subsequently, much more non-local integrable systems including reverse space–time and reverse time cases are further investigated [14]. At the same time, the physical background of non-local integrable equations is also investigated from various related fields, such as multi-place systems [15], magnetic structures [16], nanomagnetic artificial materials [17], and loop quantum cosmology [18] [19, 20].

The NLS equation [21] is a fundamental prototype and plays a pivotal role in many fields of physics, such as fluid mechanics [22], plasmas [23], Bose–Einstein condensates [24], and deep water waves [25]. However, the NLS equation only contains the lowest-order dispersion term and the lowest-order non-linear effect. Under the necessary physical conditions, various higher-order dispersions and non-linear effects must be taken into account, such as ultrashort pulses in optical fibers [26], where the effects of higher-order dispersions should

be considered. Therefore, some higher-order NLS equations, including Hirota [27], Lakshmanan–Porsezian–Daniel (LPD) [21, 28], and quintic NLS equations [29], have been constructed, and their corresponding integrable properties and dynamics have been studied.

In this paper, we consider the scattering problem as follows:

$$\begin{aligned}\Phi_x &= U\Phi,\\ \Phi_t &= V\Phi = (\lambda U + V_0 + \alpha L + \omega M + \delta N)\Phi,\end{aligned} \tag{1}$$

where $\Phi = (\phi_1(x,t), \phi_2(x,t))^T$, λ is the spectral parameter, and U, V_0, L, M, and N are given by

$$\begin{aligned}U &= \begin{bmatrix} i\lambda & ir \\ iq & -i\lambda \end{bmatrix}, V_0 = \frac{1}{2}\begin{bmatrix} -iqr & r_x \\ -q_x & iqr \end{bmatrix}\\ L &= -4\left(\lambda^2 U + \lambda V_0\right) + L_0, M = 2\lambda L + M_0, N = -2\lambda M + N_0,\end{aligned} \tag{2}$$

where

$$\begin{aligned}L_0 &= \begin{bmatrix} qr_x - rq_x & i\left(2r^2q + r_{xx}\right) \\ i\left(2q^2r + q_{xx}\right) & rq_x - qr_x \end{bmatrix},\\ M_0 &= \begin{bmatrix} m_1 & m_2 \\ m_3 & -m_1 \end{bmatrix}, N_0 = \begin{bmatrix} n_1 & n_2 \\ n_3 & -n_1 \end{bmatrix},\\ m_1 &= i\left(-3q^2r^2 - qr_{xx} + q_xr_x - rq_{xx}\right),\\ m_2 &= 6qrr_x + r_{xxx},\\ m_3 &= -6qrq_x - q_{xxx},\\ n_1 &= qr_{xxx} - rq_{xxx} + q_{xx}r_x - q_xr_{xx} + 6qr\left(qr_x - rq_x\right),\\ n_2 &= ir_{xxxx} + 2ir^2q_{xx} + 8iqrr_{xx} + 4irr_xq_x + 6iqr_x^2 + 6ir^3q^2,\\ n_3 &= iq_{xxxx} + 2iq^2r_{xx} + 8iqrq_{xx} + 4iqr_xq_x + 6irq_x^2 + 6iq^3r^2.\end{aligned} \tag{3}$$

Under the symmetry reduction $q(x,t) = r^*(x,t)$, the generalized integrable fifth-order NLS equation [30],

$$iq_t + S(q,r) - i\alpha H(q,r) + \omega P(q,r) - i\delta Q(q,r) = 0, \tag{4}$$

where

$$\begin{aligned}S(q,r) &= \frac{1}{2}q_{xx} + q^2r,\\ H(q,r) &= q_{xxx} + 6qq_xr,\\ P(q,r) &= q_{xxxx} + 8qrq_{xx} + 6q^3r^2 + 4qq_xr_x + 6q_x^2r + 2q^2r_{xx},\\ Q(q,r) &= q_{xxxxx} + 10qrq_{xxx} + 10\left(qq_xr_x\right)_x + 20rq_xq_{xx} + 30q^2r^2q_x,\end{aligned}$$

can be obtained from the compatibility condition of the linear spectral problem (1), i.e., the zero-curvature equation, $U_t - V_x + [U,V] = 0$. However, a new integrable reverse space–time non-local fifth-order NLS equation,

$$\begin{aligned}&ir(-x,-t)_t + S(-r(-x,-t), r(x,t)) - i\alpha H(-r(-x,-t), r(x,t))\\ &+\omega P(-r(-x,-t), r(x,t)) - i\delta Q(-r(-x,-t), r(x,t)) = 0,\end{aligned} \tag{5}$$

can be obtained under the symmetry reduction,

$$q(x,t) = -r(-x,-t). \tag{6}$$

Considering the importance of such non-local equations in multi-place physical systems [15], it is significant and has far-reaching importance in constructing exact solutions to the equations and aids in studying the dynamical properties of the solutions. To the best of our knowledge, such reverse space–time non-local equations have not been investigated. This paper is organized as follows: in Section 2, the one-fold and N-fold Darboux transformation of Eq. 5 are presented; in Section 3, soliton, complexiton, and rogue wave solutions are derived through the Darboux transformation and their corresponding dynamical properties and evolutions are discussed; and in Section 4, some conclusions and discussions are drawn.

2 Darboux transformation for the reverse space–time non-local fifth-order NLS equation

The Darboux transformation method is a very effective tool for constructing exact solutions of integrable non-linear equations in the soliton theory. In order to derive the Darboux transformation of the reverse space–time non-local fifth-order NLS in Eq. 5, we first introduce a gauge transformation of the linear spectral problem (1),

$$\Phi^{[1]} = T^{[1]}\Phi, \tag{7}$$

under which the linear spectral problem (1) can be deformed as follows:

$$\begin{aligned}\Phi_x^{[1]} &= U^{[1]}\Phi^{[1]} = \left(T_x^{[1]} + T^{[1]}U\right)\left(T^{[1]}\right)^{-1}\Phi^{[1]},\\ \Phi_t^{[1]} &= V^{[1]}\Phi^{[1]} = \left(T_t^{[1]} + T^{[1]}V\right)\left(T^{[1]}\right)^{-1}\Phi^{[1]}.\end{aligned} \tag{8}$$

The next pivotal step is to construct the Darboux matrix $T^{[1]}$ in such a form that $U^{[1]}, V^{[1]}$ in Equation 8 have the same form as U and V in (1) and the old potentials r and q are replaced by the new potentials $r^{[1]}, q^{[1]}$. Suppose

$$T^{[1]} = \lambda I + B^{[1]} = \begin{pmatrix} \lambda + b_{11}^{[1]} & b_{12}^{[1]} \\ b_{21}^{[1]} & \lambda + b_{22}^{[1]} \end{pmatrix}, \tag{9}$$

where $b_{ij}^{[1]}\ (i,j = 1,2)$ are functions of x and t. Substituting Eq. 9 into Eq. 8, it is evident that the relationships between two potentials in the two linear spectral problems (1, 8) can be given as

$$\begin{aligned}r^{[1]} &= r - 2b_{12}^{[1]},\\ q^{[1]} &= q + 2b_{21}^{[1]}.\end{aligned} \tag{10}$$

In addition, combined with symmetry reduction (6), there is

$$b_{12}^{[1]}(x,t) = b_{21}^{[1]}(-x,-t). \tag{11}$$

We see that $f(\lambda_j) = (f_1(\lambda_j), f_2(\lambda_j))^T$ and $g(\lambda_j) = (g_1(\lambda_j), g_2(\lambda_j))^T$ are two eigenfunctions corresponding to the eigenvalue $\lambda = \lambda_j\ (j = 1, 2)$. From the gauge transformation, there exist constants $\gamma_j, j = (1,2)$ such that

$$\begin{aligned}\lambda_j + b_{11}^{[1]} + \sigma_j b_{12}^{[1]} &= 0,\\ b_{21}^{[1]} + \sigma_j\left(\lambda_j + b_{22}^{[1]}\right) &= 0,\end{aligned} \tag{12}$$

where

$$\sigma_j = \frac{f_2\left(\lambda_j\right) + \gamma_j g_2\left(\lambda_j\right)}{f_1\left(\lambda_j\right) + \gamma_j g_1\left(\lambda_j\right)}, \quad (j = 1,2). \tag{13}$$

Then, the gauge transformation $T^{[1]}$ can be given as follows:

$$T^{[1]} = \begin{pmatrix} \lambda & 0 \\ 0 & \lambda \end{pmatrix} + \frac{1}{\sigma_2 - \sigma_1}\begin{pmatrix} \lambda_2\sigma_1 - \lambda_1\sigma_2 & \lambda_1 - \lambda_2 \\ \sigma_1\sigma_2(\lambda_2 - \lambda_1) & \lambda_1\sigma_1 - \lambda_2\sigma_2 \end{pmatrix}, \tag{14}$$

where $\sigma_j, (j = 1,2)$ can satisfy

$$
\begin{aligned}
\sigma_{jx} &= -2i\sigma_j\lambda_j - ir\sigma_j^2 + iq,\\
\sigma_{jt} &= \Big(\big(-2ir^2q_{xx} - 4irq_xr_x - 6iqr_x^2 - ir_{xxxx}\big)\delta + 2\chi_d r_{xxx} - \frac{\chi_d}{2}r_{xx}\\
&\quad + \big(12qr\chi_d + 2\chi_c\big)r_x + 4i\chi_a r\big)\sigma_j^2 + \big(\big(4rq^2r_x - 4r^2qq_x + 2rq_{xxx}\\
&\quad - 2qr_{xxx} - 2q_{xx}r_x + 2q_xr_{xx}\delta - 4irq_{xx}\chi_d - 4iqr_{xx}\chi_d\big)\\
&\quad + \big(4ir_x\chi_d - ir\chi_b\big)q_x + iqr_x\chi_b - 12ir^2q^2\chi_d + 8i\lambda_j^2\chi_c - 4iqr\chi_c\sigma_j\\
&\quad + 2\big(2iq^2r_{xx} + 4iqr_xq_x + 6irq_x^2 + iq_{xxxx}\big)\delta\\
&\quad + 2\chi_d q_{xxx} + \frac{\chi_d}{2}q_{xx} + \big(12qr\chi_d + 2\chi_c\big)q_x - 4iq\chi_a,
\end{aligned}
\tag{15}
$$

along with

$$
\begin{aligned}
\chi_a &= -\frac{3\delta q^2r^2}{2} - 4\delta\lambda_j^4 + 2\omega\lambda_j^3 + \alpha\lambda_j^2 - \frac{\lambda_j}{4} - \frac{\big(-4\delta\lambda_j^2 + 2\omega\lambda_j + \alpha\big)qr}{2},\\
\chi_b &= 4i\lambda_j\omega + 2i\alpha + 16iqr\delta - 8i\delta\lambda_j^2,\\
\chi_c &= -4\delta\lambda_j^3 + 2\omega\lambda_j^2 + \alpha\lambda_j - \frac{1}{4},\\
\chi_d &= \delta\lambda_j - \frac{\omega}{2}, \quad j = 1, 2.
\end{aligned}
\tag{16}
$$

By tedious calculations and using the identities (15), it can be verified that $U^{[1]}, V^{[1]}$ have the same forms as U and V under the symmetry reduction (6). To construct the N-fold Darboux transformation of Eq. 5, a more generalized higher-order gauge transformation can be given as follows:

$$
\Phi^{[N]} = T_N\Phi, \tag{17}
$$

where

$$
T_N = \prod_{k=1}^{N} T^{[k]} = \prod_{k=1}^{N}\big(\lambda I + B^{[k]}\big) = \prod_{k=1}^{N}\begin{pmatrix} \lambda + b_{11}^{[k]} & b_{12}^{[k]} \\ b_{21}^{[k]} & \lambda + b_{22}^{[k]} \end{pmatrix}, \tag{18}
$$

from which the following relationships can be obtained:

$$
\begin{aligned}
r^{[N]}(x,t) &= r(x,t) - 2\sum_{k=1}^{N} b_{12}^{[k]}(x,t),\\
q^{[N]}(x,t) &= q(x,t) + 2\sum_{k=1}^{N} b_{21}^{[k]}(x,t).
\end{aligned}
\tag{19}
$$

Combined with symmetry reduction (6), there is

$$
b_{12}^{[k]}(x,t) = b_{21}^{[k]}(-x,-t). \tag{20}
$$

Similar to the case of one-fold Darboux transformation, we construct the following equations:

$$
\begin{aligned}
\big((T_N)_{11} + \sigma_j(T_N)_{12}\big)\big|_{\lambda=\lambda_j} &= 0,\\
\big((T_N)_{21} + \sigma_j(T_N)_{22}\big)\big|_{\lambda=\lambda_j} &= 0,
\end{aligned}
\tag{21}
$$

with

$$
\sigma_j = \frac{f_2\big(\lambda_j\big) + \gamma_j g_2\big(\lambda_j\big)}{f_1\big(\lambda_j\big) + \gamma_j g_1\big(\lambda_j\big)}, \quad j = 1, 2, \ldots, 2N. \tag{22}
$$

From algebraic Eq. 21, the determinant representation of the N-fold Darboux matrix T_N can be derived by Cramer's rule, from which the determinant representations of $r^{[N]}$ and $q^{[N]}$ can be given as follows:

$$
r^{[N]} = r - 2\frac{W_{2N}}{Q_{2N}}, \qquad q^{[N]} = q + 2\frac{\hat{W}_{2N}}{Q_{2N}}. \tag{23}
$$

Here,

$$
Q_{2N} = \begin{bmatrix}
1 & \sigma_1 & \lambda_1 & \lambda_1\sigma_1 & \ldots & \lambda_1^{N-1} & \sigma_1\lambda_1^{N-1}\\
1 & \sigma_2 & \lambda_2 & \lambda_2\sigma_2 & \ldots & \lambda_2^{N-1} & \sigma_2\lambda_2^{N-1}\\
1 & \sigma_3 & \lambda_3 & \lambda_3\sigma_3 & \ldots & \lambda_3^{N-1} & \sigma_3\lambda_3^{N-1}\\
1 & \sigma_4 & \lambda_4 & \lambda_4\sigma_4 & \ldots & \lambda_4^{N-1} & \sigma_4\lambda_4^{N-1}\\
\vdots & \vdots & \vdots & \vdots & \ddots & \vdots & \vdots\\
1 & \sigma_{2N-1} & \lambda_{2N-1} & \lambda_{2N-1}\sigma_{2N-1} & \ldots & \lambda_{2N-1}^{N-1} & \sigma_{2N-1}\lambda_{2N}^{N-1}\\
1 & \sigma_{2N} & \lambda_{2N} & \lambda_{2N}\sigma_{2N} & \ldots & \lambda_{2N}^{N-1} & \sigma_{2N}\lambda_{2N}^{N-1}
\end{bmatrix}, \tag{24}
$$

$$
W_{2N} = \begin{bmatrix}
1 & \sigma_1 & \lambda_1 & \lambda_1\sigma_1 & \ldots & \lambda_1^{N-1} & -\lambda_1^{N}\\
1 & \sigma_2 & \lambda_2 & \lambda_2\sigma_2 & \ldots & \lambda_2^{N-1} & -\lambda_2^{N}\\
1 & \sigma_3 & \lambda_3 & \lambda_3\sigma_3 & \ldots & \lambda_3^{N-1} & -\lambda_3^{N}\\
1 & \sigma_4 & \lambda_4 & \lambda_4\sigma_4 & \ldots & \lambda_4^{N-1} & -\lambda_4^{N}\\
\vdots & \vdots & \vdots & \vdots & \ddots & \vdots & \vdots\\
1 & \sigma_{2N-1} & \lambda_{2N-1} & \lambda_{2N-1}\sigma_{2N-1} & \ldots & \lambda_{2N-1}^{N-1} & -\lambda_{2N-1}^{N}\\
1 & \sigma_{2N} & \lambda_{2N} & \lambda_{2N}\sigma_{2N} & \ldots & \lambda_{2N}^{N-1} & -\lambda_{2N}^{N}
\end{bmatrix}, \tag{25}
$$

$$
\hat{W}_{2N} = \begin{bmatrix}
1 & \sigma_1 & \lambda_1 & \lambda_1\sigma_1 & \ldots & -\lambda_1^{N}\sigma_1 & \sigma_1\lambda_1^{N-1}\\
1 & \sigma_2 & \lambda_2 & \lambda_2\sigma_2 & \ldots & -\lambda_2^{N}\sigma_2 & \sigma_2\lambda_2^{N-1}\\
1 & \sigma_3 & \lambda_3 & \lambda_3\sigma_3 & \ldots & -\lambda_3^{N}\sigma_3 & \sigma_3\lambda_3^{N-1}\\
1 & \sigma_4 & \lambda_4 & \lambda_4\sigma_4 & \ldots & -\lambda_4^{N}\sigma_4 & \sigma_4\lambda_4^{N-1}\\
\vdots & \vdots & \vdots & \vdots & \ddots & \vdots & \vdots\\
1 & \sigma_{2N-1} & \lambda_{2N-1} & \lambda_{2N-1}\sigma_{2N-1} & \ldots & -\lambda_{2N-1}^{N}\sigma_{N-1} & \sigma_{2N-1}\lambda_{2N-1}^{N-1}\\
1 & \sigma_{2N} & \lambda_{2N} & \lambda_{2N}\sigma_{2N} & \ldots & -\lambda_{2N}^{N}\sigma_N & \sigma_{2N}\lambda_{2N}^{N-1}
\end{bmatrix}. \tag{26}
$$

This is the N-fold Darboux transformation of Eq. 5. Moreover, the existence of the symmetry reduction condition Eq. 6 implies that the Darboux transformation of the non-local reverse space–time fifth-order NLS Eq. 5 is very different from the Darboux transformation of the classical fifth-order NLS Eq. 4, although both of them have the same form.

3 Non-linear wave solutions of the reverse space–time non-local fifth-order NLS equation

3.1 One-soliton solutions from zero seed solution

To construct a soliton solution of the non-local Eq. 5, we take a zero seed solution, under which the corresponding eigenfunctions of the linear spectral problem (1) can be given as follows:

$$
\begin{aligned}
f^{[1]}(\lambda) &= \begin{pmatrix} e^{i\lambda x - i\lambda^2\left(-16\delta\lambda^3 + 8\omega\lambda^2 + 4\alpha\lambda - 1\right)t} \\ 0 \end{pmatrix},\\
g^{[1]}(\lambda) &= \begin{pmatrix} 0 \\ e^{-i\lambda x + i\lambda^2\left(-16\delta\lambda^3 + 8\omega\lambda^2 + 4\alpha\lambda - 1\right)t} \end{pmatrix}.
\end{aligned}
\tag{27}
$$

Then, the following relationships can be obtained:

$$
\sigma_j = \gamma_j e^{\xi_j} \qquad (j = 1, 2), \tag{28}
$$

$$
b_{12}^{[1]}(x,t) = \frac{\lambda_1 - \lambda_2}{\gamma_2 e^{\xi_2} - \gamma_1 e^{\xi_1}}, \quad b_{21}^{[1]}(x,t) = \frac{(\lambda_2 - \lambda_1)\gamma_1\gamma_2 e^{\xi_1 + \xi_2}}{\gamma_2 e^{\xi_2} - \gamma_1 e^{\xi_1}}, \tag{29}
$$

$$
\xi_j = 8i\Big(-4\delta\lambda_j^4 t + 2\lambda_j^3\omega t + \alpha\lambda_j^2 t - \frac{1}{4}\lambda_j t - \frac{1}{4}x\Big)\lambda_j, \tag{30}
$$

under which the conditions for symmetry reduction (6) can be obtained as follows:

$$
\gamma_1\left(\gamma_2^2 - 1\right) = 0, \gamma_2\left(1 - \gamma_1^2\right) = 0. \tag{31}
$$

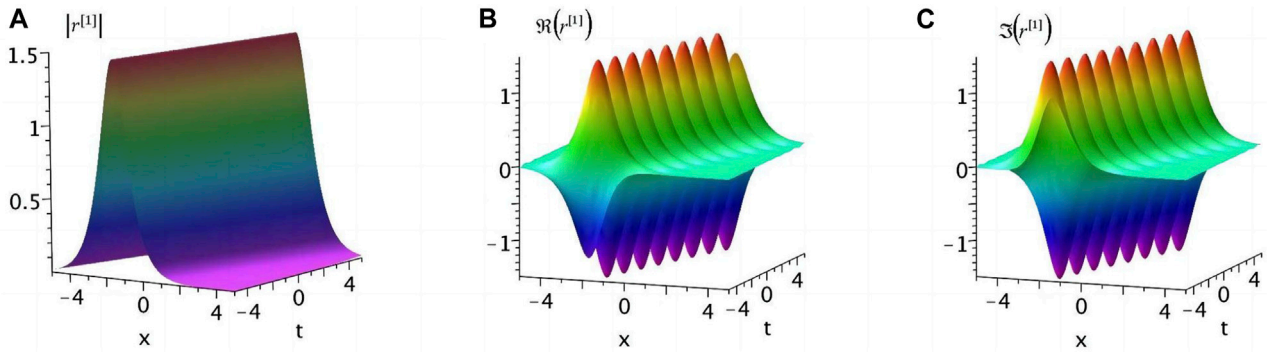

FIGURE 1
(Color online). **(A)** Density evolution of the one-soliton solution; **(B)** evolution of the real part; **(C)** evolution of the imaginary part of the soliton solution (34) under the parameters $\alpha = \frac{1}{2}$, $\delta = \frac{1}{5}$, $\omega = \frac{1}{3}$, $k_1 = -\frac{1}{5}$, $w_1 = -\frac{3}{4}$, $(\delta k_1^4 - \frac{2k_1^3\omega}{5} + (-2w_1^2\delta - \frac{3\alpha}{20})k_1^2 + (\frac{2w_1^2\omega}{5} + \frac{1}{40})k_1 + \frac{w_1^2(w_1^2\delta+\frac{\alpha}{4})}{5}) < 0$.

Without the loss of generality, we take $\gamma_1 = -1$ and $\gamma_2 = 1$ and $\lambda_j = k_j + iw_j$, $(j = 1, 2)$, and the solution can be simplified as follows:

$$r^{[1]} = -((k_1 - k_2) + i(w_1 - w_2))\mathrm{sech}\Big(\frac{1}{2}((\xi_{1R} - \xi_{2R}) + i(\xi_{1I} - \xi_{2I}))\Big)e^{-\frac{1}{2}((\xi_{1R}+\xi_{2R})+i(\xi_{1I}+\xi_{2I}))}, \tag{32}$$

where

$$\xi_{jR} = \Re(\xi_j) = 160w_j\Big(\Big(\delta k_j^4 - \frac{2k_j^3\omega}{5} + \Big(-2w_j^2\delta - \frac{3\alpha}{20}\Big)k_j^2 + \Big(\frac{2w_j^2\omega}{5} + \frac{1}{40}\Big)k_j + \frac{w_j^2\Big(w_j^2\delta + \frac{\alpha}{4}\Big)}{5}\Big)t + \frac{x}{80}\Big),$$

$$\xi_{jI} = \Im(\xi_j) = \Big(8\Big(k_j^3 - 3k_jw_j^2\Big)\alpha + 32\Big(10k_j^3 - k_j^5 - 5k_jw_j^4\Big)\delta + 16\Big(k_j^4 - 6k_j^2w_j^2 + w_j^4\Big)\omega 2w_j^2 - 2k_j^2)t - 2xk_j. \tag{33}$$

The soliton solution can be obtained as follows:

$$r^{[1]} = \frac{-2iw_1e^{2i\left(16k_1^5\delta - 160\delta k_1^3w_1^2 + 80\delta k_1w_1^4 - 8k_1^4\omega + 48\omega k_1^2w_1^2 - 8w_1^4\omega - 4\alpha k_1^3 + 12\alpha k_1w_1^2 + k_1^2 - w_1^2\right)t + 2ik_1x}}{\cosh\Big(160w_1\Big(\Big(\delta k_1^4 - \frac{2k_1^3\omega}{5} + \Big(-2w_1^2\delta - \frac{3\alpha}{20}\Big)k_1^2 + \Big(\frac{2w_1^2\omega}{5} + \frac{1}{40}\Big)k_1 + \frac{w_1^2\left(w_1^2\delta + \frac{\alpha}{4}\right)}{5}\Big)t + \frac{x}{80}\Big)\Big)}. \tag{34}$$

This is under the condition that $k_1 = k_2$ and $w_1 = -w_2$. Evidently, the propagation direction of a soliton (34) is determined by the value of $(\delta k_1^4 - \frac{2k_1^3\omega}{5} + (-2w_1^2\delta - \frac{3\alpha}{20})k_1^2 + (\frac{2w_1^2\omega}{5} + \frac{1}{40})k_1 + \frac{w_1^2(w_1^2\delta+\frac{\alpha}{4})}{5})$. In Figure 1A, the evolution of a soliton solution (34) is illustrated, and the corresponding evolution profiles of the real and imaginary parts are shown in Figures 1B, C, which exhibit the characteristics of a breather. On the other hand, by taking $k_2 = -2k_1$ and $w_2 = 0$, the complexiton solution can be given as follows:

$$r^{[1]} = (-3k_1 - iw_1)\mathrm{sech}\Big(\frac{1}{2}(\xi_{1R} + i(\xi_{1I} - \xi_{2I}))\Big)e^{-\frac{1}{2}(\xi_{1R}+i(\xi_{1I}+\xi_{2I}))}, \tag{35}$$

where

$$\begin{aligned}\frac{1}{2}i(\xi_{1I} - \xi_{2I}) &= i\big(-\big(12w_1^2k_1 - 36k_1^3\big)\alpha - \big(528k_1^5 - 160k_1^3w_1^2 + 80k_1w_1^4\big)\delta - \big(-3k_1^2 - w_1^2\big) - \big(120k_1^4 + 48k_1^2w_1^2 - 8w_1^4\big)\omega\big)t - 3ixk_1,\\ -\frac{1}{2}i(\xi_{1I} + \xi_{2I}) &= -i\big(\big(-28k_1^3 - 12k_1w_1^2\big)\alpha + \big(496k_1^5 + 160k_1^3w_1^2 - 80k_1w_1^4\big)\delta + \big(w_1^2 - 5k_1^2\big) + \big(136k_1^4 - 48k_1^2w_1^2 + 8w_1^4\big)\omega\big)t - ik_1x.\end{aligned} \tag{36}$$

It can be seen from Figure 2A that the solution (35) propagates to the left along the x-axis under the condition that $(\delta k_1^4 - \frac{2k_1^3\omega}{5} + (-2w_1^2\delta - \frac{3\alpha}{20})k_1^2 + (\frac{2w_1^2\omega}{5} + \frac{1}{40})k_1 + \frac{w_1^2(w_1^2\delta+\frac{\alpha}{4})}{5}) > 0$. Figures 2B, C show the evolution characteristics of the real and imaginary parts of the solution (35). The propagation states of the solution (35) at three different times are shown in Figure 2D.

3.2 Two-soliton solutions from zero seed solution

Two-fold exact solutions of Eq. 5 can be derived from the Darboux transformation (23) by taking $N = 2$. In order to satisfy the constraint condition (20), we take $\gamma_1 = -1$, $\gamma_2 = 1$, $\gamma_3 = -1$, and $\gamma_4 = 1$ and consider the case that the eigenvalues are two pairs of conjugate complexes, i.e., $\lambda_1 = \lambda_2^* = k_1 + iw_1, \lambda_3 = \lambda_4^* = k_2 + iw_2$. Then, the solution can be obtained as

$$r^{[2]} = \frac{G_1(x,t)}{H_1(x,t)}, \tag{37}$$

where

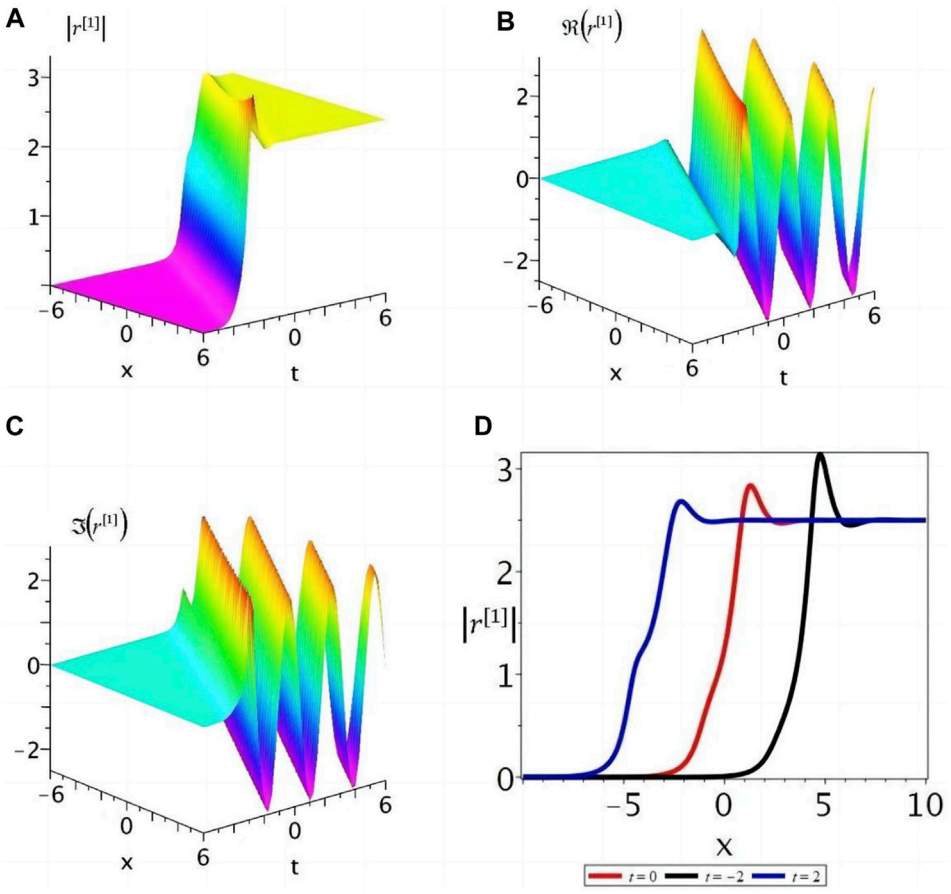

FIGURE 2
(Color online). **(A)** Density evolution of the complexiton solution; **(B)** evolution of the real part; **(C)** evolution of the imaginary part; **(D)** three evolution states at t =−2,0,2 for the solution (35) under the parameters $\alpha = -\frac{1}{5}, \delta = \frac{1}{4}, \omega = \frac{1}{2}, k_1 = \frac{1}{3}, w_1 = -\frac{3}{4}$, $(\delta k_1^4 - \frac{2k_1^3\omega}{5} + (-2w_1^2\delta - \frac{3\alpha}{20})k_1^2 + (\frac{2w_1^2\omega}{5} + \frac{1}{40})k_1 + \frac{w_1^2(w_1^2\delta+\frac{\alpha}{4})}{5}) > 0$.

$$
\begin{aligned}
G_1(x,t) = 4i\Bigg(&\left(\frac{w_1^2}{2} - \frac{w_2^2}{2} + \frac{(k_1-k_2)^2}{2}\right)\cosh(\xi_{2R}) \\
&+ iw_2(k_1-k_2)\sinh(\xi_{2R})\Bigg)w_1 e^{-i\xi_{1I}} \\
&- 4i\Bigg(\left(\frac{w_1^2}{2} - \frac{w_2^2}{2} - \frac{(k_1-k_2)^2}{2}\right)\cosh(\xi_{1R}) \\
&+ iw_1(k_1-k_2)\sinh(\xi_{1R})\Bigg)w_2 e^{-i\xi_{2I}},
\end{aligned} \tag{38}
$$

$$
\begin{aligned}
H_1(x,t) = {} & 2w_1w_2\cos(\xi_{1I} - \xi_{2I}) - (w_1^2 + w_2^2 + (k_1-k_2)^2) \\
& \cosh(\xi_{1R})\cosh(\xi_{2R}) + 2w_1w_2\sinh(\xi_{1R})\sinh(\xi_{2R}),
\end{aligned}
$$

and ξ_{jR} and ξ_{jI} are defined by (33) previously. In Figure 3A, the two-soliton solution behaves as an interaction of two bright solitons; after that, they stably propagate with original shapes and velocities. The corresponding evolutions of real and imaginary parts of the solution are shown in Figures 3B, C, which are all two-order breather solutions.

3.3 One-soliton solutions from non-zero seed solution

In order to construct the rogue wave solution of Eq. 5 by the Darboux transformation (10), the seed solution is taken as the plane wave solution,

$$
r = -ice^{-i(ax+\eta t)}, q = ice^{i(ax+\eta t)}, \tag{39}
$$

where a and c are an arbitrary constant and $\eta = (-a^3 + 6ac^2)\alpha + (a^5 - 20a^3c^2 + 30ac^4)\delta + (-a^4 + 12a^2c^2 - 6c^4)\omega + \frac{a^2}{2} - c^2$, respectively. Substituting the seed solution (39) into the linear spectral problem (1) with $\lambda = \frac{a}{2} - ic$ or $\lambda = \frac{a}{2} + ic$, the eigenfunctions can be obtained as follows:

$$
\Phi(\lambda) = \begin{pmatrix} (C_1(cx - \Delta_1 t + 1) + cC_2)e^{\frac{i}{2}(ax+\eta t)} \\ (C_1(-cx + \Delta_1 t) - cC_2)e^{-\frac{i}{2}(ax+\eta t)} \end{pmatrix}, \tag{40}
$$

or

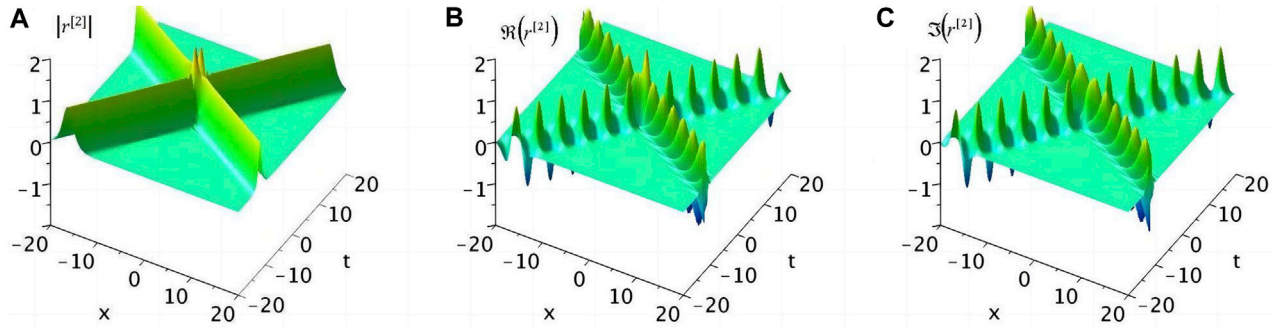

FIGURE 3
(Color online). **(A)** Density evolution of the two-soliton solution; **(B)** evolution of the real part; **(C)** evolution of the imaginary part of the solution (37) under the parameters $k_1 = -\frac{1}{2}, w_1 = -\frac{1}{2}, k_2 = \frac{11}{20}, w_2 = \frac{11}{20}, \alpha = \frac{1}{2}, \delta = -\frac{3}{10}, \omega = \frac{3}{10}$.

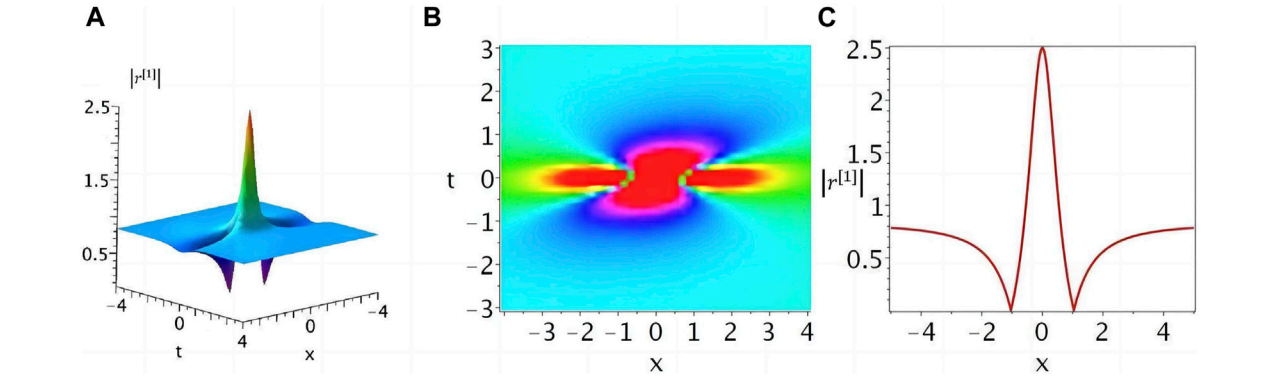

FIGURE 4
(Color online). The rogue wave solution given by (45) with $a = -\frac{9}{10}, c = -\frac{5}{6}, \alpha = -\frac{1}{4}, \delta = -\frac{1}{6}, \omega = \frac{1}{6}$: **(A)** density evolution; **(B)** 2D contour plot; **(C)** amplitude $|r^{[1]}|$ profile with $t = 0$ of the rogue wave.

$$\Phi(\lambda) = \begin{pmatrix} (C_3(-cx + \Delta_2 t + 1) - cC_4)e^{\frac{i}{2}(ax+\eta t)} \\ (C_3(-cx + \Delta_2 t) - cC_4)e^{-\frac{i}{2}(ax+\eta t)} \end{pmatrix}, \tag{41}$$

where

$$\begin{aligned} \Delta_1 &= -c(-3a^2 + 6c^2)\alpha - c(5a^4 - 60a^2c^2 + 30c^4)\delta - c(-4a^3 + 24ac^2)\omega - ac \\ &\quad + ic^2(20a^3\delta - 60ac^2\delta - 12\omega a^2 + 12c^2\omega - 6a\alpha + 1), \\ \Delta_2 &= -c(-3a^2 + 6c^2)\alpha - c(5a^4 - 60a^2c^2 + 30c^4)\delta - c(-4a^3 + 24ac^2)\omega - ac \\ &\quad - ic^2(20a^3\delta - 60ac^2\delta - 12\omega a^2 + 12c^2\omega - 6a\alpha + 1), \end{aligned} \tag{42}$$

and C_1, C_2, C_3, and C_4 are arbitrary constants. For simplicity, taking $\{C_1 = 1, C_2 = -\frac{1}{c}\}$ and $\{C_3 = -1, C_4 = -\frac{1}{c}\}$ and considering their relationship (13), we have the following:

$$\begin{aligned} \sigma_1 &= \left(-1 + \frac{1 + \gamma_1}{1 + (cx - \Delta_1 t)(\gamma_1 + 1)}\right)e^{-i(ax+\eta t)}, \\ \sigma_2 &= \left(1 + \frac{\gamma_2 - 1}{1 + (cx - \Delta_2 t)(\gamma_2 - 1)}\right)e^{-i(ax+\eta t)}. \end{aligned} \tag{43}$$

To satisfy the constraint condition (11), we take $\gamma_1 = 1$ and $\gamma_2 = -1$. Then, the rogue wave solution can be given as follows:

$$r^{[1]} = ice^{i(ax+\eta t)}\left(1 + \frac{G_2(x,t)}{H_2(x,t)}\right), \tag{44}$$

where

$$\begin{aligned} G_2(x,t) &= -4 + i(8c^2 + 160a^3c^2\delta - 480ac^4\delta - 96a^2c^2\omega - 48a\alpha c^2 \\ &\quad + 96c^4\omega)t, \\ H_2(x,t) &= 4c^2\left((a^4 + 4c^4)\alpha^2 + (30(a^6 + 6a^4c^2 \right. \\ &\quad - 6a^2c^4 + 12c^6)\delta + 24(a^5 - 2a^3c^2 + 6ac^4)\omega)\alpha - 6a^3\alpha \\ &\quad + 25(a^8 - 8a^6c^2 + 60a^4c^4 + 36c^8)\delta^2 + 40a^3(-a^4 + 6a^2c^2 \\ &\quad - 30c^4)\omega\delta + 10a(a^4 - 8a^2c^2 - 6c^4)\delta + 16(a^6 - 3a^4c^2 \\ &\quad + 18a^2c^4 + 9c^6)\omega^2 + 8(-a^4 + 3a^2c^2 + 3c^4)\omega + a^2 + c^2)t^2 \\ &\quad + (24c^2(2c^2 - a^2)\alpha + 40c^2\left((6c^2 - a^2)^2 - 30c^4\right)\delta \\ &\quad + 32ac^2(6c^2 - a^2)\omega + 8ac^2)xt + 4c^2x^2 + 1. \end{aligned} \tag{45}$$

The density evolution and 2D contour plots for the rogue wave solution (45) under appropriate parameters are shown in Figures 4A, B, and the typical amplitude $|r^{[1]}|$ profile with $t = 0$ is illustrated in Figure 4C.

4 Conclusion

In this paper, the reverse space–time non-local fifth-order NLS Eq. 5 is studied by Darboux transformations. Based on the scattering problem, the N-fold Darboux transformation of the equation is constructed. By selecting different seed solutions, we have presented soliton, complexiton, and rogue wave solutions of Eq. 5, whose non-linear dynamics and evolutions are discussed. However, the computational effort increases rapidly due to the increase of the order of the Darboux transformation and the presence of the symmetric reduction condition; so, more interesting and physically meaningful non-linear wave solutions are difficult to be derived, such as breather and higher-order rogue wave solutions. At the same time, whether the equation has other integrable properties, such as Bäcklund transformations, Hamilton structures, and infinite conservation laws, will be studied in the near future.

Data availability statement

The raw data supporting the conclusion of this article will be made available by the authors, without undue reservation.

Author contributions

XS: conceptualization, formal analysis, investigation, methodology, and writing—original draft. YY: conceptualization, methodology, and writing—review and editing. All authors contributed to the article and approved the submitted version.

Funding

This work is supported by the Zhoushan Science and Technology Program (No. 2021C21023).

Conflict of interest

The authors declare that the research was conducted in the absence of any commercial or financial relationships that could be construed as a potential conflict of interest.

Publisher's note

References

1. Soli DR, Ropers C, Koonath P, Jalali B. Optical rogue waves. *Nature* (2007) 450: 1054–7. doi:10.1038/nature06402

2. Hasegawa A. *Optical soliton theory and its applications in communication*. Berlin: Springer (2003).

3. Li J, Xu T, Meng XH, Zhang YX, Zhang HQ, Tian B. Lax pair, Bäcklund transformation and N-soliton-like solution for a variable-coefficient Gardner equation from nonlinear lattice, plasma physics and ocean dynamics with symbolic computation. *J Math Anal Appl* (2007) 336:1443–55. doi:10.1016/j.jmaa.2007.03.064

4. Yan ZY, Konotop VV, Akhmediev N. Three-dimensional rogue waves in nonstationary parabolic potentials. *Phys Rev E* (2010) 82:036610. doi:10.1103/PhysRevE.82.036610

5. Yan ZY. Vector financial rogue waves. *Phys Lett A* (2011) 375:4274–9. doi:10.1016/j.physleta.2011.09.026

6. Li YS, Zhang JE. Darboux transformations of classical Boussinesq system and its multi-soliton solutions. *Phys Lett A* (2001) 284:253–8. doi:10.1016/S0375-9601(01)00331-0

7. Feng BF, Ling LM. Darboux transformation and solitonic solution to the coupled complex short pulse equation. *Physica D: Nonlinear Phenomena* (2022) 437:133332. doi:10.1016/j.physd.2022.133332

8. Weng WF, Zhang GQ, Zhou ZJ, Yan ZY. Semi-rational vector rogon–soliton solutions of the five-component Manakov/NLS system with mixed backgrounds. *Appl Maths Lett* (2022) 125:107735. doi:10.1016/j.aml.2021.107735

9. Ma WX. Inverse scattering and soliton solutions of nonlocal complex reverse-spacetime mKdV equations. *J Geometry Phys* (2020) 157:103845. doi:10.1016/j.geomphys.2020.103845

10. Hu XB, Ma WX. Application of hirota's bilinear formalism to the toeplitz lattice—Some special soliton-like solutions. *Phys Lett A* (2002) 293:161–5. doi:10.1016/S0375-9601(01)00850-7

11. Geng XG, Wu JP. Riemann–Hilbert approach and N-soliton solutions for a generalized Sasa–Satsuma equation. *Wave Motion* (2016) 60:62–72. doi:10.1016/j.wavemoti.2015.09.003

12. Xu J, Fan EG. A Riemann-Hilbert approach to the initial-boundary problem for derivative nonlinear Schrödinger equation. *Acta Mathematica Scientia* (2014) 34: 973–94. doi:10.1016/S0252-9602(14)60063-1

13. Ablowitz MJ, Musslimani ZH. Integrable nonlocal nonlinear schrödinger equation. *Phys Rev Lett* (2013) 110:064105. doi:10.1103/PhysRevLett.110.064105

14. Ablowitz MJ, Musslimani ZH. Integrable nonlocal nonlinear equations. *Stud Appl Maths* (2017) 139:7–59. doi:10.1111/sapm.12153

15. Lou SY. Alice-Bob systems, P̂-T̂-Ĉ symmetry invariant and symmetry breaking soliton solutions. *J Math Phys* (2018) 59:083507. doi:10.1063/1.5051989

16. Gadzhimuradov TA, Agalarov AM. Towards a gauge-equivalent magnetic structure of the nonlocal nonlinear Schrödinger equation. *Phys Rev A* (2016) 93: 062124. doi:10.1103/PhysRevA.93.062124

17. Rybakov FN, Borisov AB, Blügel S, Kiselev NS. New type of stable particlelike states in chiral magnets. *Phys Rev Lett* (2015) 115:117201. doi:10.1103/PhysRevLett.115.117201

18. Dantas CC. An inhomogeneous space-time patching model based on a nonlocal and nonlinear Schrödinger equation. *Foundations Phys* (2016) 46:1269–92. doi:10.1007/s10701-016-0019-6

19. Tang XY, Liang ZF, Hao XZ. Nonlinear waves of a nonlocal modified KdV equation in the atmospheric and oceanic dynamical system. *Commun Nonlinear Sci Numer Simulation* (2018) 60:62–71. doi:10.1016/j.cnsns.2017.12.016

20. Zhang XE, Chen Y, Zhang Y. Breather, lump andXsoliton solutions to nonlocal KP equation. *Comput Maths Appl* (2017) 74:2341–7. doi:10.1016/j.camwa.2017.07.004

21. Lakshmanan M, Porsezian K, Daniel M. Effect of discreteness on the continuum limit of the Heisenberg spin chain. *Phys Lett A* (1988) 133:483–8. doi:10.1016/0375-9601(88)90520-8

22. Wen XY, Yan ZY. Higher-order rational solitons and rogue-like wave solutions of the (2 + 1)-dimensional nonlinear fluid mechanics equations. *Commun Nonlinear Sci Numer Simulation* (2017) 43:311–29. doi:10.1016/j.cnsns.2016.07.020

23. Moslem WM. Langmuir rogue waves in electron-positron plasmas. *Phys Plasmas* (2011) 18:032301. doi:10.1063/1.3559486

24. He JS, Charalampidis E, Kevrekidis P, Frantzeskakis D. Rogue waves in nonlinear Schrödinger models with variable coefficients: Application to Bose–Einstein condensates. *Phys Lett A* (2014) 378:577–83. doi:10.1016/J.PHYSLETA.2013.12.002

25. Benney DJ, Newell AC. The propagation of nonlinear wave envelopes. *J Maths Phys* (1967) 46:133–9. doi:10.1002/sapm1967461133

26. Dudley JM, Tarlor JR. *Supercontinuum generation in optical fibers*. Cambridge: Cambridge University Press (2010).

27. Li LJ, Wu ZW, Wang LH, He JS. High-order rogue waves for the Hirota equation. *Ann Phys* (2013) 334:198–211. doi:10.1016/j.aop.2013.04.004

28. Yang YQ, Suzuki T, Cheng XP. Darboux transformations and exact solutions for the integrable nonlocal Lakshmanan–Porsezian–Daniel equation. *Appl Maths Lett* (2020) 99:105998. doi:10.1016/j.aml.2019.105998

29. Yang YQ, Wang X, Cheng XP. Higher-order rational solutions for a new integrable nonlocal fifth-order nonlinear Schrödinger equation. *Wave Motion* (2018) 77:1–11. doi:10.1016/j.wavemoti.2017.10.012

30. Chowdury A, Kedziora DJ, Ankiewicz A, Akhmediev N. Soliton solutions of an integrable nonlinear Schrödinger equation with quintic terms. *Phys Rev E* (2014) 90:032922. doi:10.1103/PhysRevE.90.032922

frontiers | Frontiers in Physics

TYPE Original Research
PUBLISHED 10 April 2023
DOI 10.3389/fphy.2023.1189447

OPEN ACCESS

EDITED BY
Xiangpeng Xin,
Liaocheng University, China

REVIEWED BY
Bo Ren,
Zhejiang University of Technology, China
Xzhong Liu,
Shaoxing University, China

*CORRESPONDENCE
Xueping Cheng,
chengxp2005@126.com

SPECIALTY SECTION
This article was submitted to Mathematical Physics, a section of the journal Frontiers in Physics

RECEIVED 19 March 2023
ACCEPTED 29 March 2023
PUBLISHED 10 April 2023

CITATION
Zhang L, Cheng X, Yang W and Zhao Z (2023), Non-local residual symmetry and soliton-cnoidal periodic wave interaction solutions of the KdV6 equation. *Front. Phys.* 11:1189447. doi: 10.3389/fphy.2023.1189447

Non-local residual symmetry and soliton-cnoidal periodic wave interaction solutions of the KdV6 equation

Luwei Zhang[1], Xueping Cheng[1,2]*, Wei Yang[1] and Zhangxuan Zhao[1]

[1]School of Information Engineering, Zhejiang Ocean University, Zhoushan, China, [2]Key Laboratory of Oceanographic Big Data Mining & Application of Zhejiang Province, Zhoushan, China

The residual symmetry of the KdV6 equation is obtained by the Painlevé truncate expansion. Since the residual symmetry is non-local, five field quantities are introduced to localize it into the local one. Besides, the interaction solutions between solitons and cnoidal periodic waves of the KdV6 equation are constructed by making use of the consistent tanh expansion method. As an illustration, a specific interaction solution in the form of tanh function and Jacobian elliptic function is discussed both analytically and graphically.

KEYWORDS

the KdV6 equation, non-local residual symmetry, consistent tanh expansion method, soliton-cnoidal periodic wave interaction solution, localization

1 Introduction

Due to the wide applications in explaining physical phenomena, seeking exact solutions of non-linear equations becomes one of the most important tasks in non-linear science. In fact, finding solutions of non-linear evolution equations is not an easy thing, and only in few special cases one may write down the explicit analytical solutions. Despite of this fact, kinds of non-linear excitations such as the solitons, conoidal periodic waves, Painlevé waves have been found. However, although the non-linear waves or even the interactions among solitons have been well studied, the research on the interactions among different types of non-linear waves is still a thorny issue. Recently, Lou discovered that, starting from the non-local symmetries of non-linear equations, the interactions, such as the soliton-Painlevé wave, soliton-cnoidal periodic wave, soliton-KdV wave, *etc.*, can be established [1-6]. Moreover, recent researches have also shown that the interaction solutions between solitons and other non-linear excitations can also be obtained by the consistent tanh expansion (CTE) method, which is evolved from the classical tanh function expansion method [7-9].

In Ref. [10], K^{2}S^{2}T [A. Karasu-Kalkanlı, A. Karasu, A. Sakovich, S. Sakovich, R. Turhan] introduced the Painlevé test for integrability of partial differential equation to the sixth-order non-linear wave equation

$$u_{xxxxxx} + \alpha_1 u_x u_{xxxx} + \alpha_2 u_{xx} u_{xxx} + \alpha_3 u_x^2 u_{xx} + \alpha_4 u_{tt} + \alpha_5 u_{xxxt} + \alpha_6 u_x u_{xt} + \alpha_7 u_t u_{xx} = 0, \tag{1}$$

where α_i ($i = 1, 2, \ldots, 7$) are arbitrary parameters. They found that there were four cases of relations between the parameters that pass the Painlevé test. Three of those cases correspond to the known integrable equations, the bidirectional Sawada–Kotera equation (11)–(15), the

bidirectional Kaup-Kupershmidt equation (11), (12) and (16) and the Drinfeld-Sokolov-Satsuma-Hirota system [17-19], whereas the fourth one

$$\left(\partial_x^2 + 8u_x\partial_x + 4u_{xx}\right)\left(u_t + u_{xxx} + 6u_x^2\right) = 0 \tag{2}$$

turns out to be new. This new integrable case is associated with the same spectral problem as of the potential KdV equation, so Eq. 2 is also called the KdV6 equation. In Ref. [10], K^{2}S^{2}T also showed the Lax pair, auto-Bäcklund transformation, traveling wave solutions, and third-order generalized symmetries of the KdV6 equation. In fact, since K^{2}S^{2}T first derived the KdV6 equation, there has been a growing interest in finding its exact solutions, conservation laws and various integrable properties [20-24]. However, as far as we know, the research on the interaction solution of this equation is still lacking.

In present paper, we shall focus on investigating the non-local residual symmetry and the interactions between solitons and cnoidal periodic waves for the KdV6 equation. The paper is organized as follows: In Section 2, the non-local residual symmetry of the KdV6 equation is derived. To constitute a local symmetry, five dependent variables are brought in, thus the non-local symmetry is localized into the Lie point symmetry of the enlarged KdV6 system. In Section 3, with the aid of the CTE method, the interaction solutions between solitons and cnoidal periodic waves of the KdV6 equation are acquired. According to these explicit solutions, the dynamical properties of the interaction solutions are investigated. Finally, the main results are summarized in Section 4.

2 Non-local residual symmetry and its localization

By the transformation $v = u_x$, $w = u_t + u_{xxx} + 6u_x^2$, Eq. 2 is equivalent to

$$v_t + v_{xxx} + 12vv_x - w_x = 0, \qquad w_{xxx} + 8vw_x + 4wv_x = 0. \tag{3}$$

Since the KdV6 Eq. 3 possesses Painlevé property, we formulate the truncated Painlevé expansion as

$$v = \frac{p_2}{\phi^2} + \frac{p_1}{\phi} + p_0, \qquad w = \frac{q_2}{\phi^2} + \frac{q_1}{\phi} + q_0, \tag{4}$$

where p_2, p_1, p_0, q_2, q_1 and q_0 are undetermined functions depending on $\{x, t\}$. Substituting the expansion 4) into Eq. 3 and collecting the terms with the same power of ϕ, we get the expressions

$$\begin{aligned}
&p_2 = -\phi_x^2, \quad p_1 = \phi_{xx}, \quad p_0 = -\frac{1}{4}\frac{\phi_{xxx}}{\phi_x} + \frac{1}{8}\frac{\phi_{xx}^2}{\phi_x^2} + \lambda,\\
&q_2 = -12\lambda\phi_x^2 - \phi_x\phi_{xxx} + \frac{3}{2}\phi_{xx}^2 - \phi_x\phi_t,\\
&q_1 = 12\lambda\phi_{xx} + \phi_{xxxx} + \phi_{xt} - \frac{3\phi_{xx}\phi_{xxx}}{\phi_x} + \frac{3}{2}\frac{\phi_{xx}^3}{\phi_x^2},\\
&q_0 = \frac{9\lambda\phi_{xx}^2}{\phi_x^2} + \frac{1}{2}\frac{\phi_{xx}\phi_{xt}}{\phi_x^2} - \frac{2\lambda\phi_t}{\phi_x} - \frac{8\lambda\phi_{xxx}}{\phi_x} - \frac{1}{2}\frac{\phi_{xxxxx}}{\phi_x} + \frac{3}{2}\frac{\phi_{xxx}^2}{\phi_x^2}
\end{aligned} \tag{5}$$

with λ being a free integral constant. In this case, Eq. 3 can be represented as its Schwartzian form

$$8\lambda\left(\frac{\phi_t}{\phi_x}\right)_x + 3\{\phi;x\}\{\phi;x\}_x + 20\lambda\{\phi;x\}_x + \{\phi;x\}_t + \{\phi;x\}_{xxx} = 0 \tag{6}$$

with the Schwartzian derivative $\{\phi;x\} = \frac{\phi_{xxx}}{\phi_x} - \frac{3}{2}\frac{\phi_{xx}^2}{\phi_x^2}$. The Schwartzian form (6) is form invariant under the Möbious transformation

$$\phi \to \frac{a + b\phi}{c + d\phi}, \quad (ad \neq bc) \tag{7}$$

which implies that Eq. 6 possesses the symmetry

$$\sigma^\phi = d_1 + d_2\phi + d_3\phi^2 \tag{8}$$

with d_i $(i = 1, 2, 3)$ being three random constants.

In view of the expansion 4), it is found that $\{p_0, q_0\}$ is just the solution of the KdV6 equation, so the following non-auto-Bäcklund transformation theorem is true.

Non-auto-Bäcklund transformation theorem. If ϕ satisfies the Schwartzian Equation 6, then

$$\begin{aligned}
v &= -\frac{1}{4}\frac{\phi_{xxx}}{\phi_x} + \frac{1}{8}\frac{\phi_{xx}^2}{\phi_x^2} + \lambda,\\
w &= \frac{9\lambda\phi_{xx}^2}{\phi_x^2} + \frac{1}{2}\frac{\phi_{xx}\phi_{xt}}{\phi_x^2} - \frac{2\lambda\phi_t}{\phi_x} - \frac{8\lambda\phi_{xxx}}{\phi_x} - \frac{1}{2}\frac{\phi_{xxxxx}}{\phi_x} + \frac{3}{2}\frac{\phi_{xxx}^2}{\phi_x^2}
\end{aligned} \tag{9}$$

constitutes a solution of the KdV6 Eq. 3.

In addition, the substituting of the expansion 4) into Eq. 3 also tells us that the residues p_1 and q_1, taking the form as Eq. 5, exactly satisfy the symmetry equations of the KdV6 equation, i.e.,

$$\begin{aligned}
&\sigma_t^v + \sigma_{xxx}^v + 12\sigma^v v_x + 12v\sigma_x^v - \sigma_x^w = 0,\\
&\sigma_{xxx}^w + 8\sigma^v w_x + 8v\sigma^w + 4\sigma^w v_x + 4w\sigma_x^v = 0.
\end{aligned} \tag{10}$$

Thus $\{p_1, q_1\}$ is then named as the residual symmetry of the KdV6 equation. Clearly, seen from Eq. 5, the residual symmetry $\{p_1, q_1\}$ contains the space and time derivatives of ϕ, which means that this symmetry is non-local. We turn now to the task of localizing it into a local one such that one can use Lie's first principle to recover the original Bäcklund transformation. To this end, the following five field quantities have to be introduced

$$\phi_1 = \phi_x, \quad \phi_2 = \phi_{1x}, \quad g = \phi_t, \quad g_1 = \phi_{1t}, \quad h = v_x. \tag{11}$$

As a result, the residual symmetry $\{p_1, q_1\}$ of the KdV6 equation is converted into the Lie point symmetry

$$\begin{aligned}
&\left\{\sigma^v, \sigma^w, \sigma^\phi, \sigma^{\phi_1}, \sigma^{\phi_2}, \sigma^g, \sigma^{g_1}, \sigma^h\right\}^T\\
&= \left\{\phi_2, -4\phi_1 h + 4v\phi_2 + 8\lambda\phi_2 + g_1, -\phi^2, -2\phi\phi_1, -2\phi_1^2 - 2\phi\phi_2,\right.\\
&\left. -2\phi g, -2\phi_1 g - 2\phi g_1, -\frac{8v\phi_1^2 - 8\lambda\phi_1^2 - \phi_2^2}{2\phi_1}\right\}^T
\end{aligned} \tag{12}$$

of the enlarged KdV6 system {3), 6), 9), (11)}.

As is known, symmetry reduction [25, 26] is one of the most powerful methods to study exact explicit solutions for non-linear equations. Based on the Lie point symmetry (12), one may continue to explore more abundant symmetry reduction solutions for the KdV6 equation. The details on this topic might be reported in our future research work.

3 CTE solvability of the KdV6 equation and its soliton-cnoidal wave interaction solutions

In this section, we would like to obtain the soliton-cnoidal wave interaction solutions for the KdV6 Eq. 3. In the frame of the CTE method, by balancing the highest order non-linearity and dispersive term of the KdV6 equation, we take v and w in the following generalized truncated tanh function expansion

$$\begin{aligned} v &= v_2 \tanh^2 f + v_1 \tanh f + v_0, \\ w &= w_2 \tanh^2 f + w_1 \tanh f + w_0, \end{aligned} \tag{13}$$

where v_i, w_i $(i = 0, 1, 2)$, being six real-valued functions of (x, t), are to be determined from the requirement for solutions v and w to satisfy Eq. 3. Inserting Eq. 13 into the KdV6 equation and requiring the coefficients of all powers of $\tanh f$ to be zeros yield twelve overdetermined partial differential equations. After a few detail calculations, we can conclude that

$$\begin{aligned} v &= -f_x^2 \tanh^2 f + f_{xx} \tanh f - \frac{1}{4}\frac{f_{xxx}}{f_x} + \frac{1}{8}\frac{f_{xx}^2}{f_x^2} + \frac{1}{2}f_x^2 + \lambda, \\ w &= \left(2f_x^4 - 12\lambda f_x^2 - f_x f_{xxx} + \frac{3}{2}f_{xx}^2 - f_x f_t\right)\tanh^2 f \\ &\quad + \left[f_{xxxx} - \frac{3f_{xx}f_{xxx}}{f_x} + f_{xt} + \frac{3f_{xx}^3}{2f_x^2} - \left(6f_x^2 - 12\lambda\right)f_{xx}\right]\tanh f \\ &\quad - \frac{1}{2}\frac{f_{xxxxx}}{f_x} + \frac{2f_{xx}f_{xxxx}}{f_x^2} - \frac{1}{2}\frac{f_{xxt}}{f_x} + \frac{3}{2}\frac{f_{xxx}^2}{f_x^2} + \frac{1}{2}\frac{f_{xx}f_{xt}}{f_x^2} \\ &\quad - \left(\frac{21}{4}\frac{f_{xx}^2}{f_x^3} - 4f_x + \frac{8\lambda}{f_x}\right)f_{xxx} + \frac{9}{4}\frac{f_{xx}^4}{f_x^4} + \left(\frac{3}{2} + \frac{9\lambda}{f_x^2}\right)f_{xx}^2 \\ &\quad + \left(f_x - \frac{2\lambda}{f_x}\right)f_t - 2f_x^4 + 16\lambda f_x^2 - 24\lambda^2, \end{aligned} \tag{14}$$

and the expansion function f is determined by

$$\begin{aligned} &\frac{1}{4}\frac{f_{xxxxxx}}{f_x} - \frac{3}{2}\frac{f_{xx}f_{xxxxx}}{f_x^2} + \frac{1}{4}\frac{f_{xxxt}}{f_x} - \left(\frac{5}{2}\frac{f_{xxx}}{f_x^2} - \frac{45}{8}\frac{f_{xx}^2}{f_x^3} + \frac{5}{2}f_x - \frac{5\lambda}{f_x}\right)f_{xxxx} \\ &\quad - \frac{3}{4}\frac{f_{xxt}f_{xx}}{f_x^2} + \frac{15}{2}\frac{f_{xxx}^2 f_{xx}}{f_x^3} - \left(\frac{1}{4}\frac{f_{xt}}{f_x^2} + \frac{15f_{xx}^3}{f_x^4} + \frac{20\lambda f_{xx}}{f_x^2}\right)f_{xxx} + \frac{45}{8}\frac{f_{xx}^5}{f_x^5} \\ &\quad + \left(\frac{3}{4}\frac{f_{xx}^2}{f_x^3} - f_x + \frac{2\lambda}{f_x}\right)f_{xt} + \frac{15\lambda f_{xx}^3}{f_x^3} - \left(\frac{2\lambda f_t}{f_x^2} - 6f_x^3 + 20\lambda f_x\right)f_{xx} = 0 \end{aligned} \tag{15}$$

with λ being an arbitrary integral constant.

In order to obtain the interaction solutions between solitons and other non-linear excitations for the KdV6 equation, the expansion function in Eq. 15 may be assumed in the form

$$f = \frac{x - \omega_1 t}{b_1} + W\left(\frac{x - \omega_0 t}{b_0}\right) \equiv \frac{x - \omega_1 t}{b_1} + W(\xi), \tag{16}$$

where ω_1 and ω_0 describe the velocities of the soliton and its surrounding W-wave, b_1 and b_0 are two quantities referring to the widths of the soliton and W-wave, respectively. Specially, if $W(\xi) = 0$ is taken, the solution (14) with Eq. 16 reduces to the trivial traveling wave solution.

Inserting the ansatz (16) into Eq. 15 and introducing the abbreviation

$$W_\xi(\xi) = W_1, \tag{17}$$

it follows that Eq. 15 becomes the equation satisfied by the elliptic function

$$W_{1\xi}^2 = a_4 W_1^4 + a_3 W_1^3 + a_2 W_1^2 + a_1 W_1 + a_0 \tag{18}$$

with coefficients a_1, a_4 and ω_1 taking the form

$$\begin{aligned} a_1 &= \frac{a_0 b_1}{b_0} + \frac{b_0 a_2}{b_1} - \frac{a_3 b_0^2}{b_1^2} + \frac{4b_0^3}{b_1^3}, \quad a_4 = 4, \\ \omega_1 &= \frac{\left(2b_0^2 b_1^2\omega_0 + a_2 b_1^2 - 3a_3 b_0 b_1 + 24b_0^2\right)\left(a_0 b_1^4 - a_2 b_0^2 b_1^2 + 2a_3 b_0^3 b_1 - 12b_0^4\right)}{16 b_0^6 b_1^4 \lambda} \\ &\quad + \frac{2b_0^4 b_1^2\omega_0 - 5a_0 b_1^4 + 5a_2 b_0^2 b_1^2 - 10a_3 b_0^3 b_1 + 60b_0^4}{2b_0^4 b_1^2}. \end{aligned} \tag{19}$$

Hence, the corresponding relation between the solution of the KdV6 equation and that of Eq. 18 is established. Given any one solution of Eq. 18, the associated interaction solution of the KdV6 system can be realized. According to Ref. [27], Eq. 18 has varieties of solutions in the form of Jacobian elliptic functions, which gives us a chance to look for the physically relevant soliton-cnoidal periodic wave interaction solutions for the KdV6 equation. As a representative example, we suppose now that Eq. 18 owns the solution

$$W_1 = \frac{c_0 CD}{1 - c_1 S^2}, \tag{20}$$

where c_0 and c_1 are two real constants, $S \equiv \mathrm{sn}(\xi, m)$, $C \equiv \mathrm{cn}(\xi, m)$ and $D \equiv \mathrm{dn}(\xi, m)$ represent the Jacobian elliptic sine function, Jacobian elliptic cosine function and Jacobian elliptic function of the third kind, respectively, and m is known as the modulus of the Jacobian elliptic functions. Substituting the solution (20) into Eq. 18 and eliminating the coefficients of different powers of Jacobian elliptic functions, we obtain after a brief calculation

$$\begin{aligned} &a_0 = m^3 + 2m^2 + m, \quad a_2 = -m^2 - 6m - 1, \\ &a_3 = 0, \quad b_0 = \frac{1}{2}b_1\delta(m+1), \quad c_0 = \delta\sqrt{m}, \quad c_1 = m, \\ &\omega_1 = \left(1 - \frac{(m-1)^2}{b_1^2\lambda(m+1)^2}\right)\omega_0 + \frac{20(m-1)^2}{b_1^2(m+1)^2} - \frac{2\left(5m^2 + 6m + 5\right)(m-1)^2}{b_1^4\lambda(m+1)^4}. \end{aligned} \tag{21}$$

Next integrating the notation (17), the expression for the cnoidal periodic wave can be written as

$$W = -\delta \mathrm{arctanh}\left(m^{1/2}S\right) + c_2 \tag{22}$$

with an integral constant c_2. Substituting this into Eq. 16, we form now the formula for the expansion function

$$f = -\delta \mathrm{arctanh}\left(m^{1/2}S\right) - \frac{\omega_1 t}{b_1} + \frac{x}{b_1} + c_2. \tag{23}$$

Therefore, after inserting Eq. 23 into the solution (14), the soliton-cnoidal periodic wave interaction solution of the KdV6 equation is constructed. Here we omit the lengthy formulas for the sake of simplicity.

As pointed out in our pervious work [2, 7], soliton-cnoidal wave interaction solutions can be regarded as dressed solitons, namely, solitons dressed by cnoidal periodic waves. After taking the limit $\tanh(f) = \pm 1$ in the solution (14), i.e., removing the soliton cores of v and w, only the cnoidal periodic wave parts remain. To illustrate the soliton-cnoidal periodic wave structure in more detail, it is exhibited in a graphical way with the parameters $c_2 = 0$, $\delta = b_1 = \lambda = 1$, $\omega_0 = 2$ and $m = 0.01$; Figures 1A,B display the profiles of the soliton-cnoidal wave structures at $t = 0$; Figures 1C,D depict the soliton cores of v

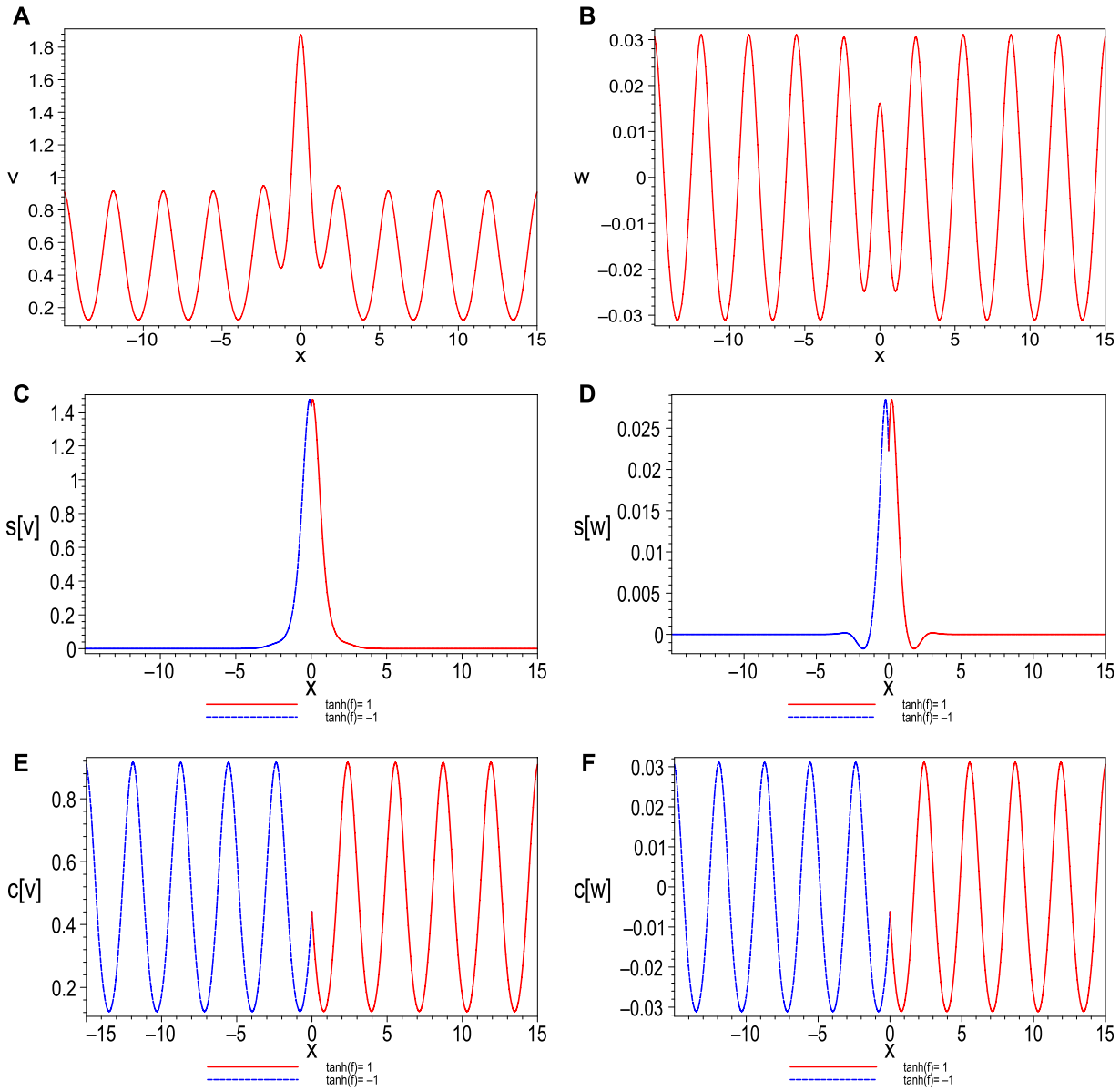

FIGURE 1
(A) and **(B)**: Profiles of the soliton-cnoidal periodic wave interaction solutions with parameters c_2=0, $\lambda = \delta = b_1$=1, ω_0=2 and m =0.01. **(C)** and **(D)**: Soliton cores of the interaction solutions. **(E)** and **(F)**: Background periodic waves of the interaction solutions.

and w, where the dashed lines show the left parts of the solitons, i.e., taking $\tanh(f) = -1$ in the solution (14), and the right parts are displayed by the solid lines. Figures 1E,F show the corresponding cnoidal periodic wave structures. As is expected, apart from the soliton cores, the solutions v and w rapidly tend to the cnoidal periodic waves propagating along the x direction.Furthermore, we would like to illustrate how to control the profiles of the soliton-cnoidal periodic waves and analyze their dynamical behaviors. First, the designable of the velocity of the cnoidal periodic wave is to be considered. Figure 2 exhibits the time-space evolutions of the soliton-cnoidal periodic wave solution (14). The overtaking collision processes between solitons and cnoidal waves are shown in Figure 2A, B. Here both the solitons and the cnoidal waves are right-moving, but the velocity of cnoidal waves, selected as $\omega_0 = 2$, is slower than the velocity of solitons $\omega_1 = 7.96$, which is calculated from Eq. 19. As time evolves, the soliton collide with every peak of cnoidal wave, and both the amplitudes and the widths of solitons and cnoidal periodic waves are unchanged except for a phase shift; Figure 2C, D show the interactions between solitons and cnoidal waves with zero velocity. In this situation, the cnoidal waves can be viewed as the standing waves. The right-going solitons collide with the standing periodic waves during their propagations. It is also shown that the collisions between solitons and cnoidal waves are elastic with a slight phase shift. The head-on collision between

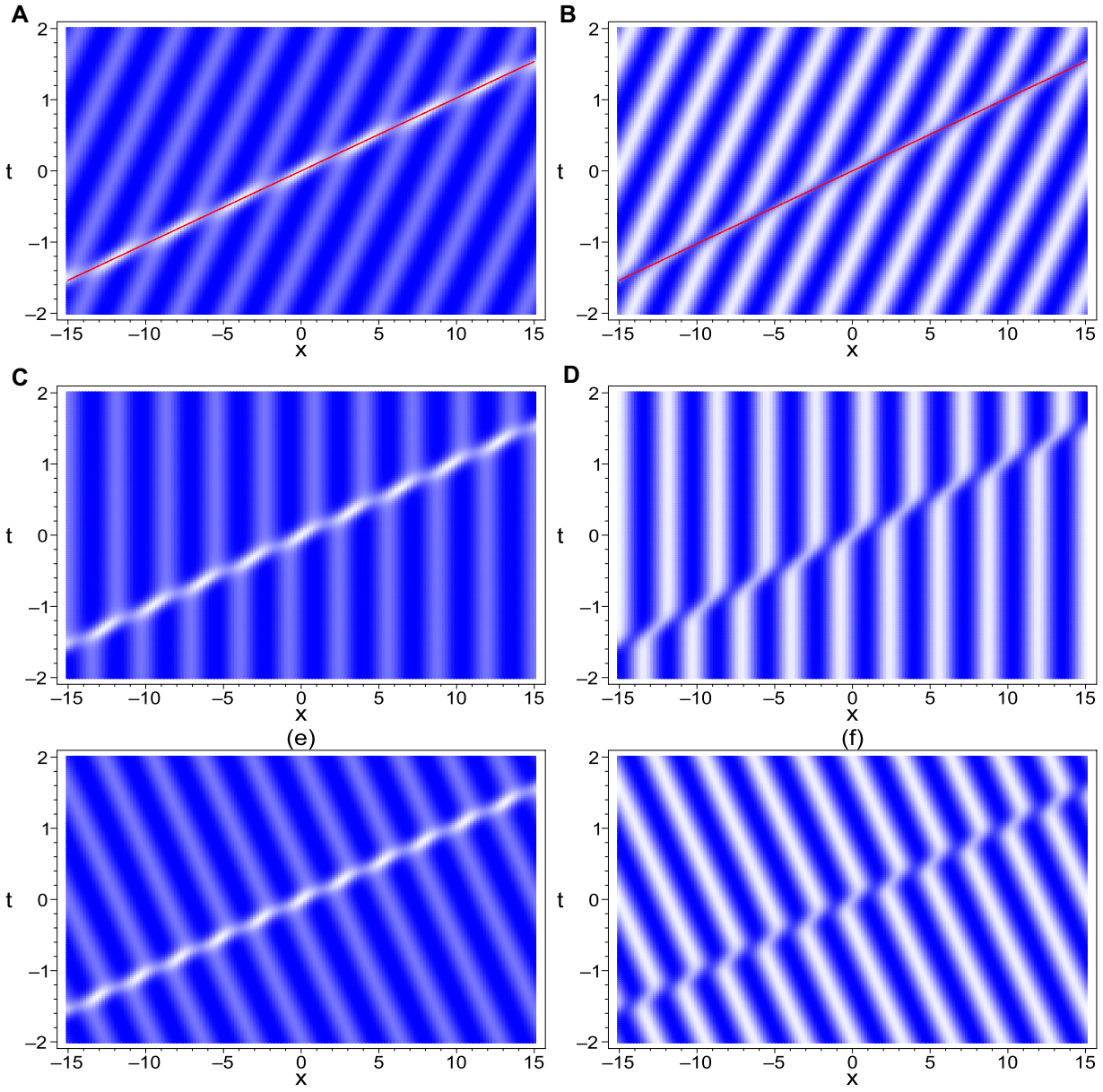

FIGURE 2
Density profiles of the soliton-cnoidal periodic wave with the parameters **(A)** and **(B)**ω_0=2; **(C)** and **(D)**: ω_0=0; **(E)** and **(F)**: ω_0=−2. Other parameters are the same as those in Figure 1.

solitons and cnoidal waves can be observed from Figure 2E, F, which display the right-going solitons colliding with the left-going cnoidal waves ($\omega_0 = -2$). In addition, the straight line that the soliton propagates along is $x = \omega_1 t - b_1 c_2$, determined by Eq. 23, which is drawn in Figure 2A, B by solid lines.

As shown in Eq. 21, the wave parameter m indicates not only the modulus of the Jacobian elliptic function, but also the amplitude of Jacobian elliptic function. With the increasing of m, the amplitude of the cnoidal periodic wave trends to decrease. In particular, under the asymptotic condition $m \to 0$, the soliton profiles go to be the classical KdV6 solitons, and the surrounding cnoidal periodic waves are non-zero and with a slight amplitude periodic wave, which is displayed in Figure 3.

4 Summary and discussion

In this paper, by making use of the truncated Painlevé expansion, the residual symmetry of the KdV6 equation was derived. To eliminate the non-locality of the residual symmetry, we introduced five new field quantities ϕ_1, ϕ_2, g, g_1 and h to localize it into the local Lie point symmetry of the enlarged KdV6 system {(3), (6), (9), (11)}. Besides, the

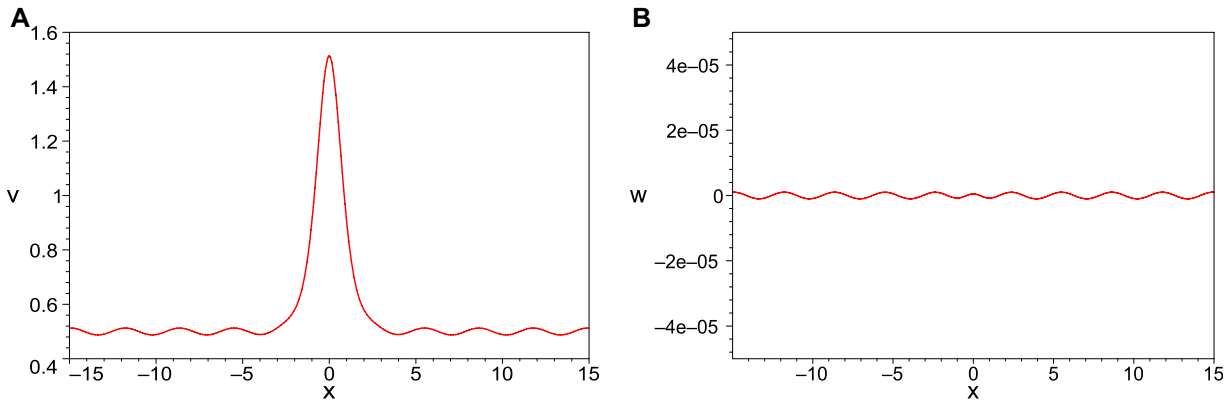

FIGURE 3
2D plots of the soliton-cnoidal periodic wave interaction solutions **(A)** v and **(B)** w with m = 0.00001, and other parameters are chosen as those in Figure 1.

CTE method was applied to the KdV6 equation to get its soliton-cnoidal wave interaction solutions. In the process of solving the equation that the expansion function f satisfies, an intimate connection between this equation and the equation satisfied by the elliptic functions was constructed. By choosing any one elliptic function solution, the corresponding interaction solutions of the KdV6 equation can be acquired. To show the interaction solution more concretely, the Jacobian elliptic wave solution (20) of Eq. 18 was introduced. The results show that the soliton-cnoidal wave interaction solutions of the KdV6 equation can be viewed as the solitons dressed by the cnoidal periodic waves. Once the cnoidal wave backgrounds are taken away, only the soliton cores are left. The results also exhibit that the shapes of the soliton-cnoidal wave interaction solutions of the KdV6 equation are designable by selecting different values of wave parameters. In particular, how to design the velocities and amplitudes of the cnoidal periodic waves were demonstrated, and the dynamical behaviors of the soliton-cnoidal periodic wave interaction solutions were analyzed. In addition, we believe that the method used for getting non-local residual symmetry in this paper can also be applied to complex functional equations, such as the non-linear Schrödinger type equations, and their abundant soliton-nonlinear wave interaction solutions can also be obtained by symmetry reduction method. More studies regarding the soliton-nonlinear wave interaction solutions for other partial differential equations will be reported in our future research work.

Data availability statement

The original contributions presented in the study are included in the article/Supplementary Material, further inquiries can be directed to the corresponding author.

Author contributions

LZ: Methodology, Software, Formal analysis, Writing–original draft. XC: Conceptualization, Funding acquisition, Resources, Supervision, Writing–review and editing. WY: Investigation, Formal analysis. ZZ: Software, Formal analysis.

Funding

This work is supported by the National Natural Science Foundation of China (Grant Nos. 11975204 and 12075208), the Project of Zhoushan City Science and Technology Bureau (Grant No. 2021C21015) and the Training Program for Leading Talents in Universities of Zhejiang Province.

Conflict of interest

The authors declare that the research was conducted in the absence of any commercial or financial relationships that could be construed as a potential conflict of interest.

Publisher's note

All claims expressed in this article are solely those of the authors and do not necessarily represent those of their affiliated organizations, or those of the publisher, the editors and the reviewers. Any product that may be evaluated in this article, or claim that may be made by its manufacturer, is not guaranteed or endorsed by the publisher.

References

1. Hu XR, Lou SY, Chen Y. Explicit solutions from eigenfunction symmetry of the Korteweg-de Vries equation. *Phys Rev E* (2012) 85:056607. doi:10.1103/physreve.85.056607

2. Cheng XP, Chen CL, Lou SY. Interactions among different types of nonlinear waves described by the Kadomtsev-Petviashvili equation. *Wave Motion* (2014) 51:1298–308. doi:10.1016/j.wavemoti.2014.07.012

3. Cheng XP, Yang YQ, Ren B, Wang JY. Interaction behavior between solitons and (2+1)-dimensional CDGKS waves. *Wave Motion* (2016) 86:150–61. doi:10.1016/j.wavemoti.2018.08.008

4. Ren B. Symmetry reduction related with nonlocal symmetry for Gardner equation. *Commun Nonlinear Sci Numer Simul* (2017) 42:456–63. doi:10.1016/j.cnsns.2016.06.017

5. Xia YR, Yao RX, Xin XP. Residual symmetry, Bäcklund transformation, and soliton solutions of the higher-order Broer-Kaup system. *Adv Math Phys* (2021) 2021:1–10. doi:10.1155/2021/9975303

6. Liu XZ, Yu J. Solitons and symmetry reduction solutions of a nonlocal two-mode Korteweg-de Vries equation. *Math Method Appl Sci* (2022) 45:11423–32. doi:10.1002/mma.8458

7. Lou SY, Cheng XP, Tang XY. Dressed dark solitons of the defocusing nonlinear Schrödinger equation. *Chin Phys Lett* (2014) 31:070201. doi:10.1088/0256-307X/31/7/070201

8. Lou SY. Consistent riccati expansion for integrable systems. *Stud Appl Math* (2015) 134:372–402. doi:10.1111/sapm.12072

9. Wu JW, Cai YJ, Lin J. Residual symmetries, consistent Riccati expansion integrability, and interaction solutions of a new (3+1)-dimensional generalized Kadomtsev-Petviashvili equation. *Chin Phys B* (2022) 31:030201. doi:10.1088/1674-1056/ac1f08

10. Karasu-Kalkanl A, Karasu A, Sakovich A, Sakovich S, Turhan R. A new integrable generalization of the Korteweg-de Vries equation. *J Math Phys* (2008) 49:073516. doi:10.1063/1.2953474

11. Dye JM, Parker A. On bidirectional fifth-order nonlinear evolution equations, Lax pairs, and directionally dependent solitary waves. *J Math Phys* (2001) 42:2567–89. doi:10.1063/1.1354642

12. He JS, Cheng Y, Roemer RA. Solving bi-directional soliton equations in the KP hierarchy by gauge transformation. *J High Energ Phys.* (2006) 2006:103. doi:10.1088/1126-6708/2006/03/103

13. Ma YL, Geng XG. Darboux and Bäcklund transformations of the bidirectional Sawada-Kotera equation. *Appl Math Comput* (2012) 218:6963–5. doi:10.1016/j.amc.2011.12.077

14. Lai XJ, Cai XO. Adomian decomposition method for approximating the solutions of the bidirectional Sawada-Kotera equation. *Z Naturforsch A* (2010) 65:658–64. doi:10.1515/zna-2010-8-906

15. Dong JJ, Li B, Yuen MW. Soliton molecules and mixed solutions of the(2+1)-dimensional bidirectional Sawada-Kotera equation. *Commun Theor Phys* (2020) 72:025002. doi:10.1088/1572-9494/ab6184

16. Dye JM, Parker A. A bidirectional Kaup-Kupershmidt equation and directionally dependent solitons. *J Math Phys* (2002) 43:4921–49. doi:10.1063/1.1503866

17. Karasu-Kalkanlı A, Sakovich SY. Bäcklund transformation and special solutions for the Drinfeld-Sokolov-Satsuma-Hirota system of coupled equations. *J Phys A: Math Gen* (2001) 34:7355–8. doi:10.1088/0305-4470/34/36/315

18. Heris JM, Lakestani M. Exact solutions for the integrable sixth-order Drinfeld-Sokolov-Satsuma-Hirota system by the analytical methods. *Int Sch Res Notices* (2014) 2014:1–8. doi:10.1155/2014/840689

19. Huang LL, Chen Y. Nonlocal symmetry and similarity reductions for the Drinfeld-Sokolov-Satsuma-Hirota system. *Appl Math Lett* (2017) 64:177–84. doi:10.1016/j.aml.2016.09.010

20. Li JB, Zhang Y. The geometric property of soliton solutions for the integrable KdV6 equations. *J Math Phys* (2010) 51:043508–967. doi:10.1063/1.3359002

21. Kupershmidt BA. Kdv6: An integrable system. *Phys Lett A* (2008) 372:2634–9. doi:10.1016/j.physleta.2007.12.019

22. Lin RL, Yao HS, Zeng YB. Restricted flows and the soliton equation with self-consistent sources. *Symmetry Integr Geom* (2006) 2:096. doi:10.3842/SIGMA.2006.096

23. Zhao ZL, Chen Y, Han B. On periodic wave solutions of the KdV6 equation via bilinear Bäcklund transformation. *Optik* (2017) 140:10–7. doi:10.1016/j.ijleo.2017.04.016

24. Bruzon MS, Garrido TM. Symmetries and conservation laws of a KdV6 equation. *Discrete Contin Dyn Syst* (2018) 11:631–41. doi:10.3934/dcdss.2018038

25. Yang B, Song YJ, Wang ZG. Lie symmetry analysis and exact solutions of the (3+1)-dimensional generalized shallow water-like equation. *Front Phys* (2023) 11:1131007. doi:10.3389/fphy.2023.1131007

26. Liu N. Invariant solutions and conservation laws of the variable-coefficient Heisenberg ferromagnetic spin chain equation. *Front Phys* (2020) 8:260. doi:10.3389/fphy.2020.00260

27. Liu SK, Liu SD. *Nonlinear equations in physics*. Beijing: Peking University Press (2000).

frontiers | Frontiers in Physics

TYPE Original Research
PUBLISHED 10 May 2023
DOI 10.3389/fphy.2023.1169012

OPEN ACCESS

EDITED BY
Xiangpeng Xin,
Liaocheng University, China

REVIEWED BY
Muhammad Mujtaba Shaikh,
Mehran University of Engineering and Technology, Pakistan
Ibrahim Mahariq (2 PhDs),
American University of the Middle East, Kuwait

*CORRESPONDENCE
Enxiang Qu,
03318@qqhru.edu.cn

RECEIVED 18 February 2023
ACCEPTED 10 April 2023
PUBLISHED 10 May 2023

CITATION
Qu E, Qi H, Guo J, Yuan S and Lv C (2023), Fuzzy response to SH guided-wave scattering by semicircular depressions on the boundary of a ribbon-shaped elastic plate.
Front. Phys. 11:1169012.
doi: 10.3389/fphy.2023.1169012

Fuzzy response to SH guided-wave scattering by semicircular depressions on the boundary of a ribbon-shaped elastic plate

Enxiang Qu [1]*, Hui Qi[2], Jing Guo[2], Shangqi Yuan[2] and Chun Lv[1]

[1]School of Architecture and Civil Engineering, Qiqihar University, Qiqihar, China, [2]School of Aerospace and Civil Engineering, Harbin Engineering University, Harbin, China

In this paper, the fuzzy scattering problem with semicircular depressions on the boundary of a band-shaped elastic plate with steady SH guided wave incident is studied and an analytical solution is given. First, the SH guided wave is constructed by the guided wave expansion method, and then the scattered wave satisfying the free condition of the boundary stress of the strip domain is constructed by the cumulative mirror method. Finally, a definite solution equation is obtained based on the fact that the shear stress at the edge of the semi-circular recessed hole is zero. In this paper, the ambiguity of the number of waves and the width of the bands is taken into account. In order to avoid the irreversibility of interval algorithm and the difficulty of solving non-linear equations, the membership function of fuzzy quantity is segmented to make the membership degree and fuzzy quantity correspond respectively. A deterministic problem that translates into piecewise processing. Two numerical examples are given to examine the changes in fuzzy response of different numbers of fuzzy waves and fuzzy thicknesses to the dynamic stress concentration factor of the hoop at the collapse limit.

KEYWORDS

semicircular depressions, fuzzy scattering, SH guided wave, membership function, fuzzy thicknesses

1 Introduction

The scattering theory of elastic waves is widely used in the fields of earthquake engineering, ocean engineering and geological exploration. The research and application of elastic wave scattering are very extensive, and rich results have been achieved. For the study of elastic wave scattering problems, several parameters are uncertain. This is due to the ambiguity of its own objective attributes, the approximate processing of mathematical modeling, and the use of random parameters as deterministic parameters. Since the American cybernetics expert Professor Zadeh proposed fuzzy sets in 1965, the research direction of fuzzy mathematics has become more extensive, such as fuzzy reliability, fuzzy control, fuzzy optimization, fuzzy calculus equations and so on. Tong et al. [1] investigated the adaptive fuzzy output-feedback backstepping control design problem for uncertain strict-feedback non-linear systems in the presence of unknown virtual and actual control gain functions and immeasurable states. Shi et al. [2] proposed the issue of the reliable asynchronous sampled-data filtering of Takagi-Sugeno (T-S) fuzzy delayed neural networks with stochastic intermittent faults, randomly occurring time-varying parameter

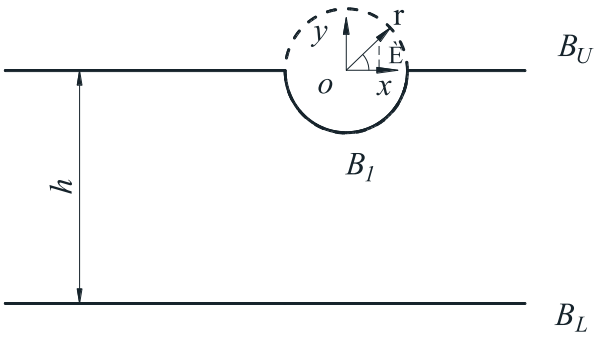

FIGURE 1
Theoretical model of steady-state scattering of SH waves by semi-cylindrical depressions in elastic ribbon domains.

uncertainties and controller gain fluctuation. Zhao et al. [3] solved the problem of asymptotic tracking control for a class of uncertain switched non-linear systems under fuzzy approximation framework. Shi et al. [4] dealt with the non-fragile memory filtering issue of T-S fuzzy delayed neural networks with randomly occurring time-varying parameter uncertainties and variable sampling rates. Liu et al. [5] proposed the concept of q-rung orthopair fuzzy sets (q-ROFSs) to be able to describe more complex fuzzy uncertainty information effectively. Sun et al. [6] researched the issue of fuzzy adaptive control for a class of strict-feedback non-linear systems with non-affine nonlinear faults. Hu et al. [7] explored the performance of fuzzy system-based medical image processing for predicting the brain disease. Zhu et al. [8] investigated the event-triggered control problem for stochastic non-linear systems with unmeasured states and unknown backlash-like hysteresis. Lin et al. [9] proposed a novel picture fuzzy multi-criteria decision making (MCDM) model to solve the site selection problem for car sharing stations. Zhang et al. [10] studied the fault detection problem for continuous-time fuzzy semi-Markov jump systems (FSMJSs) by employing an interval type-2 (IT2) fuzzy approach. Wang et al. [11] presented a fault-tolerant tracking control strategy for Takagi-Sugeno fuzzy model-based non-linear systems which combines integral sliding mode control with adaptive control technique. Garg H et al. [12] introduced a novel multi-attribute decision making (MADM) method under interval-valued intuitionistic fuzzy (IVIF) set environment by integrating a Technique for Order Preference by Similarity to Ideal Solution (TOPSIS) method. Pan et al. [13] developed a novel risk analysis approach by merging interval-valued fuzzy sets (IVFSs), improved Dempster-Shafer (D-S) evidence theory, and fuzzy Bayesian networks (BNs), acting as a systematic decision support approach for safety insurance for the entire life cycle of a complex system under uncertainty. In other numerical applications, spectral elemental methods are also effectively applied by researchers [14-15]. Mahariq I et al. [16] explored the on-resonance and off-resonance optical response of dielectric cylinders excited by normal incident plane waves. Mahariq I et al. [17] also studied photonic nanojets resulting from corrugated cylinders (with irregular boundaries) under normally incident plane-wave illumination.

SH waves are the most fundamental elastic waves, propagating in a direction perpendicular to the direction of vibration. The SH wave has only one inverse plane vibration displacement (out-of-plane displacement). Compared to P and SV waves, SH waves have the simplest elastodynamic behaviour. For elastic dynamics problems with complex initial boundary conditions, P and SV waves can be difficult to find solutions for. For SH waves, however, such problems can be easily solved to obtain further analytical solutions. There are a lot of ambiguity factors in the elastic wave scattering problem, such as seismic intensity, wave speed, medium shear modulus, medium density, amplitude and frequency of incident waves, *etc.*, all of which are typical ambiguities with randomness and ambiguity. In this paper, the ambiguity of the number of waves and plate thickness ambiguity of SH guided wave scattering are studied for the semicircular depression on the boundary of the band-shaped elastic plate, and the membership function is segmented so that the ambiguity and the membership function correspond respectively. This method can avoid the appearance of interval numbers and combine the decomposition theorem of fuzzy numbers well. In this paper, a new theoretical method is given to deal with fuzzy dynamics knowledge, and the curve of dynamic stress concentration factor of semicircular sag boundary with membership degree of fuzzy quantity is discussed in detail, and a valuable reference conclusion for practical engineering is obtained.

2 Theoretical model and analysis

2.1 Theoretical model

In this paper, the classical model in the reference [18] is used as an example to further illustrate the use of fuzzy mathematics in solving the scattering problem for defects in thin plates. As shown in Figure 1, the thickness of the infinitely long strip-shaped domain is h, the upper boundary is B_U, the lower boundary is B_L, the center of the depression is o, and the radius is r. The shear modulus and density of the medium are μ and ρ, respectively. The right-hand plane rectangular coordinate system (o, x, y) is established with the center of a circle o as the origin, where the X-axis is parallel to the length direction of the belt shape domain, and the Y-axis is parallel to the thickness direction. At the same time, taking the center of the circle as the pole, a plane polar coordinate system (O, r, θ) is established. Introduce complex variables $z = x + iy = re^{i\theta}$; $\bar{z} = x - iy = re^{-i\theta}$, of which $i = \sqrt{-1}$, and establish complex plane $(z, \bar{z})$. When the SH wave propagates in the plate, the out-of-plane direction is the vibration direction of the particle, and the amplitude w is only a function of the coordinates (x, y, t) or (r, θ, t).

2.2 Control equation

According to the theoretical model shown in Figure 1, the control equations satisfying the upper and lower boundary stress freedom can be obtained. According to reference [19], the control equation for the anti-plane dynamics problem can be obtained. The governing equation of the elasto-dynamic inverse plane problem is the scalar wave Eq. 1:

$$\mu \Delta w = \rho \frac{\partial^2 w}{\partial t^2} \tag{1}$$

In the formula: Δ is the two-dimensional Laplace operator. In this chapter, the steady-state SH wave is analyzed. According to the separation variable method, after separating the space variable and the time variable, the time harmonic factor $e^{-i\omega t}$ is omitted, and the Helmholtz equation, which is the governing equation of Eq. 2 is obtained:

$$\Delta w + k^2 w = 0 \tag{2}$$

Where: $k = \omega/c_s$ is the wave number of the anti-plane shear wave, ω is the circular frequency, and $c_s = \sqrt{\mu/\rho}$ is the phase velocity. In the complex plane, the Helmholtz equation and the stress-strain relationship can be expressed as:

$$4\frac{\partial w}{\partial z \partial \bar{z}} + k^2 w = 0 \tag{3}$$

$$\begin{cases} \tau_{xz} = \mu\left(\dfrac{\partial w(z,\bar{z})}{\partial z} + \dfrac{\partial w(z,\bar{z})}{\partial \bar{z}}\right) \\ \tau_{yz} = \mu i\left(\dfrac{\partial w(z,\bar{z})}{\partial z} - \dfrac{\partial w(z,\bar{z})}{\partial \bar{z}}\right) \end{cases} \tag{4}$$

$$\begin{cases} \tau_{rz} = \mu\left[\dfrac{\partial w(z,\bar{z})}{\partial z}e^{i\theta} + \dfrac{\partial w(z,\bar{z})}{\partial \bar{z}}e^{-i\theta}\right] \\ \tau_{\theta z} = \mu i\left[\dfrac{\partial w(z,\bar{z})}{\partial z}e^{i\theta} - \dfrac{\partial w(z,\bar{z})}{\partial \bar{z}}e^{-i\theta}\right] \end{cases} \tag{5}$$

2.3 Incident wave

Establish a global coordinate system at any point of the upper boundary B_U of the belt domain, and satisfy the stress freedom condition (6) of the upper and lower boundaries of the belt domain. The SH guided wave expression is Eq. 7, where $\exp[i(k_m x - \omega t)]$ is the propagation term in the x-direction. m is the guided wave order and its physical meaning is the number of nodes of the interference term in the y-axis direction. w_m^1 and w_m^2 are the amplitudes of the corresponding propagating guided waves. When m is an even number $w_m^1 = 0$. When m is an odd number $w_m^2 = 0$.

q_m satisfies Eq. 8, k_m is the apparent wave-number in the x-axis direction, and q_m satisfies Eq. 9. Only when k_m is a real number, $\exp[i(k_m x - wt)]$ can represent a propagating traveling wave in the direction of the x-axis. Considering the issues discussed in this chapter, the study of non-propagating waves has no meaning. Therefore, when the m-order SH guided wave is incident, the wave number is required to satisfy $k > m\pi/h$.

$$\mu \left.\frac{\partial w}{\partial y}\right|_{y=-h,0} = 0 \tag{6}$$

$$w_m = w_m^1 \sin\left[q_m\left(y + \frac{h}{2}\right)\right] + w_m^2 \cos\left[q_m\left(y + \frac{h}{2}\right)\right] \exp[i(k_m x - \omega t)] \tag{7}$$

$$q_m = \frac{m\pi}{h} \tag{8}$$

$$q_m^2 = k^2 - k_m^2 \tag{9}$$

Using the superposition method to superimpose the guided waves of each order, all the displacement waves in the strip-shaped medium satisfying the stress freedom of the upper and lower boundaries can be obtained:

$$w^i = \sum_{m=0}^{+\infty} w_m = \sum_{m=0}^{+\infty} f_m(y)\exp[i(k_m x - \omega t)] \tag{10}$$

In this chapter, the steady-state SH wave is discussed, and the time harmonic factor $e^{-i\omega t}$ is omitted. When the incident guided wave is of order m, the expressions of displacement and stress are as follows:

$$w^{(i)} = \left\{w_m^1 \cdot \sin\left[q_m\left(y + \frac{h}{2}\right)\right] + w_m^2 \cdot \cos\left[q_m\left(y + \frac{h}{2}\right)\right]\right\} \cdot \exp(ik_m x) \tag{11}$$

$$\begin{cases} \tau_{xz}^{(i)} = i\mu k_m \cdot \left\{w_m^1 \cdot \sin\left[q_m\left(y + \frac{h}{2}\right)\right] + w_m^2 \cdot \cos\left[q_m\left(y + \frac{h}{2}\right)\right]\right\} \cdot \exp(ik_m x) \\ \tau_{yz}^{(i)} = q_m\left\{w_m^1 \cdot \cos\left[q_m\left(y + \frac{h}{2}\right)\right] - w_m^2 \cdot \sin\left[q_m\left(y + \frac{h}{2}\right)\right]\right\} \cdot \exp(ik_m x) \end{cases} \tag{12}$$

$$\begin{cases} \tau_{rz}^{(i)} = \tau_{xz}^{(i)}\cos(\theta) + \tau_{yz}^{(i)}\sin(\theta) \\ \tau_{\theta z}^{(i)} = -\tau_{xz}^{(i)}\sin(\theta) + \tau_{yz}^{(i)}\cos(\theta) \end{cases} \tag{13}$$

2.4 Scattered waves

Under the action of incident SH waves, the concave will produce scattered waves. By using the method of repeated mirror image, the semi-cylindrical depression B_1 is extended to the medium into a whole circle, which is named as the circular hole $\overline{B_1}$. According to the wave function expansion method, the displacement and stress of all-space scattered waves generated by the boundary of a circular hole satisfy:

$$w^{(s)}{}_0^0(z) = w_0 \sum_{n=-\infty}^{+\infty} A_n H_n^{(1)}(k|z|)\left(\frac{z}{|z|}\right)^n \tag{14}$$

$$\tau_{rz\ 0}^{(s)\ 0}(z) = \frac{k\mu}{2}\sum_{n=-\infty}^{+\infty} A_n\left[H_{n-1}^{(1)}(k|z|)\cdot\left(\frac{z}{|z|}\right)^{(n-1)} e^{i\theta} - H_{n+1}^{(1)}(k|z|)\cdot\left(\frac{z}{|z|}\right)^{(n+1)} e^{-i\theta}\right] \tag{15}$$

$$\tau_{\theta z\ 0}^{(s)\ 0}(z) = \frac{ik\mu}{2}\sum_{n=-\infty}^{+\infty} A_n\left[H_{n-1}^{(1)}(k|z|)\cdot\left(\frac{z}{|z|}\right)^{(n-1)} e^{i\theta} + H_{n+1}^{(1)}(k|z|)\cdot\left(\frac{z}{|z|}\right)^{(n+1)} e^{-i\theta}\right] \tag{16}$$

The scattered wave $w^{(s)}{}_0^0$ generated by the circular hole $\bar{B}$ is reflected for the first time at the boundaries B_U and B_L of the band domain, respectively. This reflected wave can be represented by the mirror images $w^{(s)}{}_1^1$ and $w^{(s)}{}_2^1$ of the scattered wave $w^{(s)}{}_0^0$ to the boundaries B_U and B_L, which is called the first mirror scattered wave. The first reflected wave will have a second reflection on the boundaries B_U and B_L of the strip domain, respectively. The reflected wave can be

represented by the mirror images ${w^{(s)}}_1^2$ and ${w^{(s)}}_2^2$ of the first mirror scattered waves ${w^{(s)}}_1^1$ and ${w^{(s)}}_2^1$ on the boundaries B_U and B_L, known as the secondary mirror scattering wave.

Repeating this, the displacements of the P-th mirror scattered waves are ${w^{(s)}}_1^P$ and ${w^{(s)}}_2^P$, and the corresponding stresses are $\tau_{rz\ 1}^{(s)P}$, $\tau_{\theta z\ 1}^{(s)P}$, $\tau_{rz\ 2}^{(s)P}$ and $\tau_{\theta z\ 2}^{(s)P}$. Among them, P is the number of mirror images and the subscripts 1 and 2 represent the mirror faces of B_U and B_L, respectively.

$$ {w^{(s)}}_1^P(z) = w_0 \sum_{n=-\infty}^{+\infty} A_n H_n^{(1)}\left(k\left|z_1^p\right|\right)\left(\frac{z_1^p}{\left|z_1^p\right|}\right)^{(-1)^P n} \tag{17} $$

$$ \tau_{rz\ 1}^{(s)P}(z) = \frac{k\mu}{2}\sum_{n=-\infty}^{+\infty} A_n\left[H_{n-1}^{(1)}\left(k\left|z_1^p\right|\right)\cdot\left(\frac{z_1^p}{\left|z_1^p\right|}\right)^{(-1)^P(n-1)} e^{(-1)^P i\theta} - H_{n+1}^{(1)}\left(k\left|z_1^p\right|\right)\cdot\left(\frac{z_1^p}{\left|z_1^p\right|}\right)^{(-1)^P(n+1)} e^{(-1)^{(p+1)}i\theta}\right] \tag{18} $$

$$ \tau_{\theta z\ 1}^{(s)P}(z) = (-1)^P\frac{ik\mu}{2}\sum_{n=-\infty}^{+\infty} A_n\left[H_{n-1}^{(1)}\left(k\left|z_1^p\right|\right)\cdot\left(\frac{z_1^p}{\left|z_1^p\right|}\right)^{(-1)^P(n-1)} e^{(-1)^P i\theta} + H_{n+1}^{(1)}\left(k\left|z_1^p\right|\right)\cdot\left(\frac{z_1^p}{\left|z_1^p\right|}\right)^{(-1)^P(n+1)} e^{(-1)^{(p+1)}i\theta}\right] \tag{19} $$

$$ {w^{(s)}}_2^P(z) = w_0 \sum_{n=-\infty}^{+\infty} A_n H_n^{(1)}\left(k\left|z_2^p\right|\right)\left(\frac{z_2^p}{\left|z_2^p\right|}\right)^{(-1)^P n} \tag{20} $$

$$ \tau_{rz\ 2}^{(s)P}(z) = \frac{k\mu}{2}\sum_{n=-\infty}^{+\infty} A_n\left[H_{n-1}^{(1)}\left(k\left|z_2^p\right|\right)\cdot\left(\frac{z_2^p}{\left|z_2^p\right|}\right)^{(-1)^P(n-1)} e^{(-1)^P i\theta} - H_{n+1}^{(1)}\left(k\left|z_2^p\right|\right)\cdot\left(\frac{z_2^p}{\left|z_2^p\right|}\right)^{(-1)^P(n+1)} e^{(-1)^{(p+1)}i\theta}\right] \tag{21} $$

$$ \tau_{\theta z\ 2}^{(s)P}(z) = (-1)^P\frac{ik\mu}{2}\sum_{n=-\infty}^{+\infty} A_n\left[H_{n-1}^{(1)}\left(k\left|z_2^p\right|\right)\cdot\left(\frac{z_2^p}{\left|z_2^p\right|}\right)^{(-1)^P(n-1)} e^{(-1)^P i\theta} + H_{n+1}^{(1)}\left(k\left|z_2^p\right|\right)\cdot\left(\frac{z_2^p}{\left|z_2^p\right|}\right)^{(-1)^P(n+1)} e^{(-1)^{(p+1)}i\theta}\right] \tag{22} $$

In the above formula:

$$ z_1^p = z - i\left[\frac{(-1)^P h + h}{2} + (p-1)h\right] \tag{23} $$

$$ z_2^p = z + i\left[h + \frac{(-1)^{p+1} h + h}{2} + (p-1)h\right] \tag{24} $$

Using the superposition method, the scattered waves obtained by each mirror image are accumulated together, and the displacement of the scattered waves generated by the circular hole $\bar{B}$ that can satisfy the stress freedom of the upper and lower boundaries of the strip domain can be obtained as Eq. 25, and the stress is expressed as Eq. 26 and 27.

$$ w^{(s)}(z) = {w^{(s)}}_0^0(z) + \sum_{P=1}^{+\infty}\left({w^{(s)}}_1^P(z) + {w^{(s)}}_2^P(z)\right) \tag{25} $$

$$ \tau_{rz}^{(s)}(z) = \tau_{rz\ 0}^{(s)0}(z) + \sum_{P=1}^{+\infty}\left(\tau_{rz\ 1}^{(s)P}(z) + \tau_{rz\ 2}^{(s)P}(z)\right) \tag{26} $$

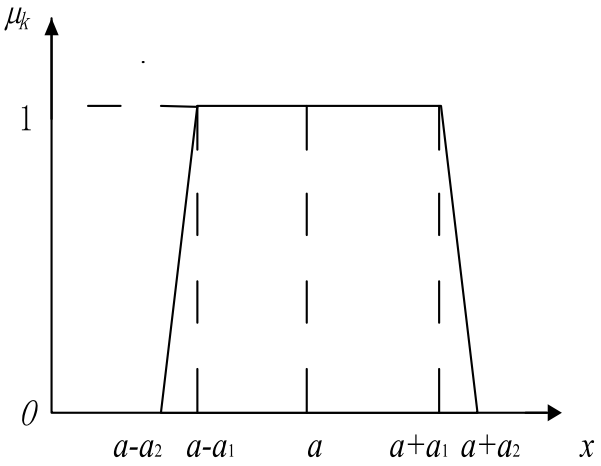

FIGURE 2
Trapezoidal distribution.

$$ \tau_{\theta z}^{(s)}(z) = \tau_{\theta z\ 0}^{(s)0}(z) + \sum_{P=1}^{+\infty}\left(\tau_{\theta z\ 1}^{(s)P}(z) + \tau_{\theta z\ 2}^{(s)P}(z)\right) \tag{27} $$

2.5 Definite solution conditions

The incident wave and scattered wave constructed according to the above method have already satisfied the condition that the shear stress at the boundary B_U and B_L is zero, so that the condition of stress freedom at the concave boundary B_1 becomes the definite solution condition of the whole problem. The resulting coefficients A_n on the scattered wave function level are the set of Eq. 28. Firstly, the coordinate translation technique is used to translate the stress expressions solved in other coordinate systems into the complex plane $(z, \bar{z})$. Then, the Fourier expansion method is used, and both ends of the formula are multiplied by $e^{-im\theta_j}$ at the same time, and then the infinite algebraic equations with coefficient A_n are integrated on the interval $(-\pi, 0)$. Finally, the truncated finite terms are solved.

$$ \tau_{rz}^{(i)}(z) + \tau_{rz}^{(s)}(z) = 0, z \in B \tag{28} $$

2.6 Dynamic stress concentration factor

Under the action of steady-state SH wave, the dynamic stress concentration factor characterizes the degree of dynamic stress concentration. Define Eq. 29 as the dynamic stress concentration factor of the recessed edge.

$$ \gamma = \frac{|\tau_{\theta z}|}{|\tau_0|} \tag{29} $$

Where: $\tau_{\theta z}$ is the angular stress on the edge of the depression and $\tau_0 = \mu k w_0$ is the maximum amplitude of the incident stress.

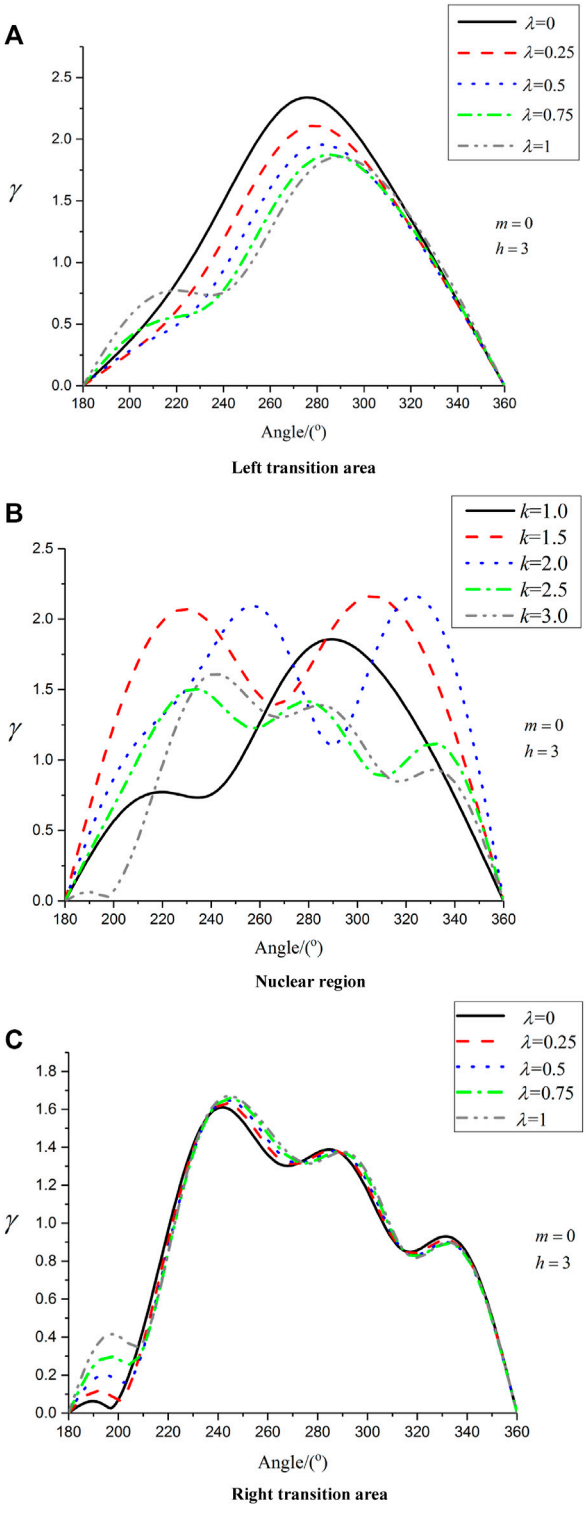

FIGURE 3
Distribution of hoop dynamic stress concentration factor of semi-circular depression when the thickness of the ribbon domain is h = 3. **(A–C)** represent the results of these three subsets: Left transition area, Nuclear region and Right transition area.

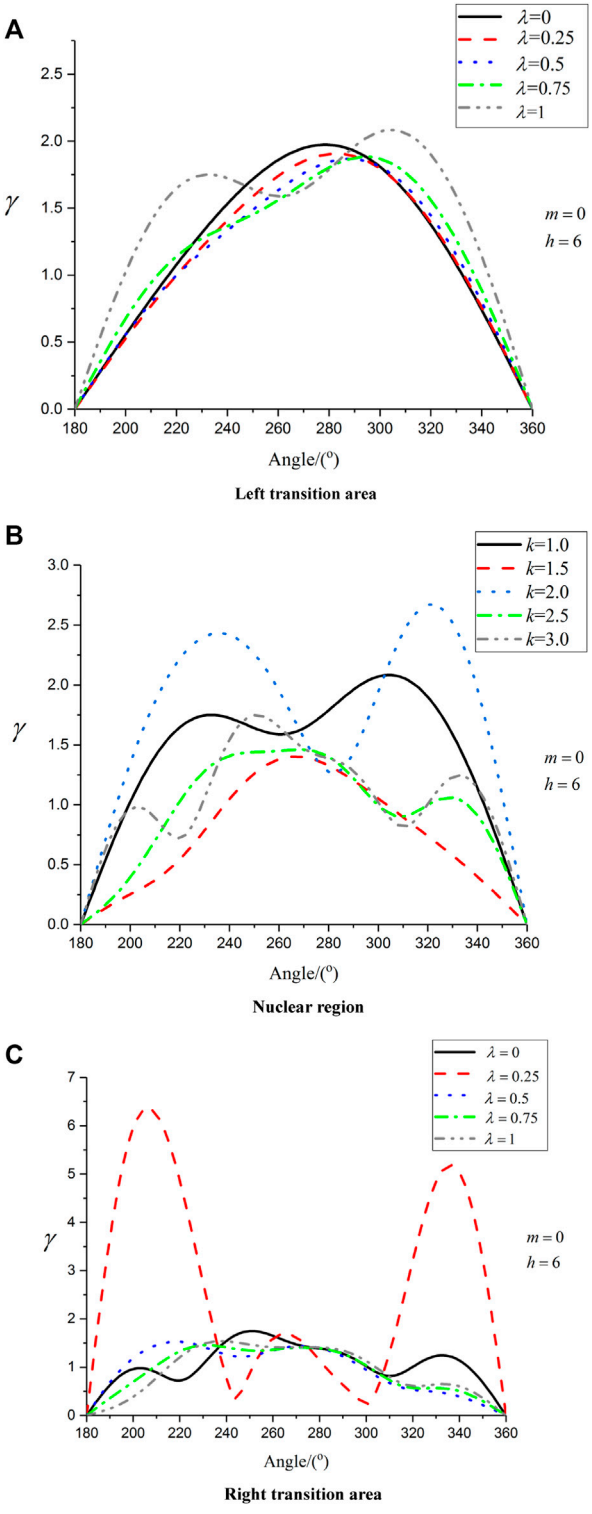

FIGURE 4
Distribution of hoop dynamic stress concentration factor of semi-circular depression when the thickness of the ribbon domain is h = 6. **(A–C)** represent the results of these three subsets: Left transition area, Nuclear region and Right transition area.

3 Examples and analysis

3.1 Analysis of fuzzy example 1

There are several fuzzy parameters in this problem including wave amplitude, frequency, and wave speed in the plane of perturbation which may all be fuzzy numbers. As can be seen from reference [20], the different affiliation curves are treated according to trapezoidal segments. It is assumed that the ambiguity membership function of the wavenumber is $\mu_k(x)$ and the trapezoidal distribution is shown in Figure 2. According to the method of fuzzy cut set, the interval under a certain degree of membership is obtained. The points in this interval actually have different degrees of membership, so that the fuzzy cutest set is not exactly the same as the general interval number. Since the subtraction and division of the four arithmetic operations of interval numbers are not reversible, it is difficult to deal with fuzzy numbers, and at most an enlarged interval solution can be obtained. According to the corresponding relationship between points and membership degrees, different membership degree curves are processed in segments.

The related membership relationship can be expressed as:

$$\mu_k(x) = \begin{cases} 0; & x \le a - a_2 \\ \dfrac{a_2 + x - a}{a_2 - a_1}; & a - a_2 < x \le a - a_1 \\ 1 \quad ; a - a_1 < x < a + a_1 \\ \dfrac{a_2 - x + a}{a_2 - a_1}; & a + a_1 \le x < a + a_2 \\ 0; & x \ge a + a_2 \end{cases}$$

The analysis only needs to consider a range of $a - a_2 < x \le a + a_2$ divided into three segments. Order $\mu_k(x) = \lambda$.

When $x = k \in (a - a_2, a - a_1)$, $k = (a_2 - a_1)\lambda + a - a_2$;

When $x = k \in (a - a_1, a + a_1)$, $\lambda \equiv 1$;

When $x = k \in (a + a_1, a + a_2)$, $k = a_2 + a - \lambda(a_2 - a_1)$;

Let $a = 2$, $a_2 = 1.5$, $a_1 = 1$, $r = 1$. By considering the different thicknesses $h = 3$, $h = 6$, $h = 10$ and $h = 20$ in the strip domain and substituting different affiliation relations, the cyclic dynamic stress concentration factor at the semi-circular depression are further obtained at different levels of affiliation.

Figure 3 shows the distribution of the hoop dynamic stress concentration factor of the semicircular depression in different sections when the thickness of the belt domain is $h = 3$. The left transition region of the membership function curve is the low wave number region, and the dynamic stress concentration factor is significantly higher than that of the core region and the right transition region (high wave number region). The angle of the left transition zone is 180^0–270^0 for the front wave and 270^0-360^0 for the back wave. The front wave front in the left transition region oscillates more obviously than the back wave front, because the front wave first arrives when the incident wave hits the inside of the band. The core area is a non-empty and non-single element interval. Although the membership degree of points in the core area is $\lambda = 1$, due to the difference in the numerical value of specific points, the dynamic stress concentration factor of the core area exhibits irregular oscillations, which is caused by fuzzy uncertainty.

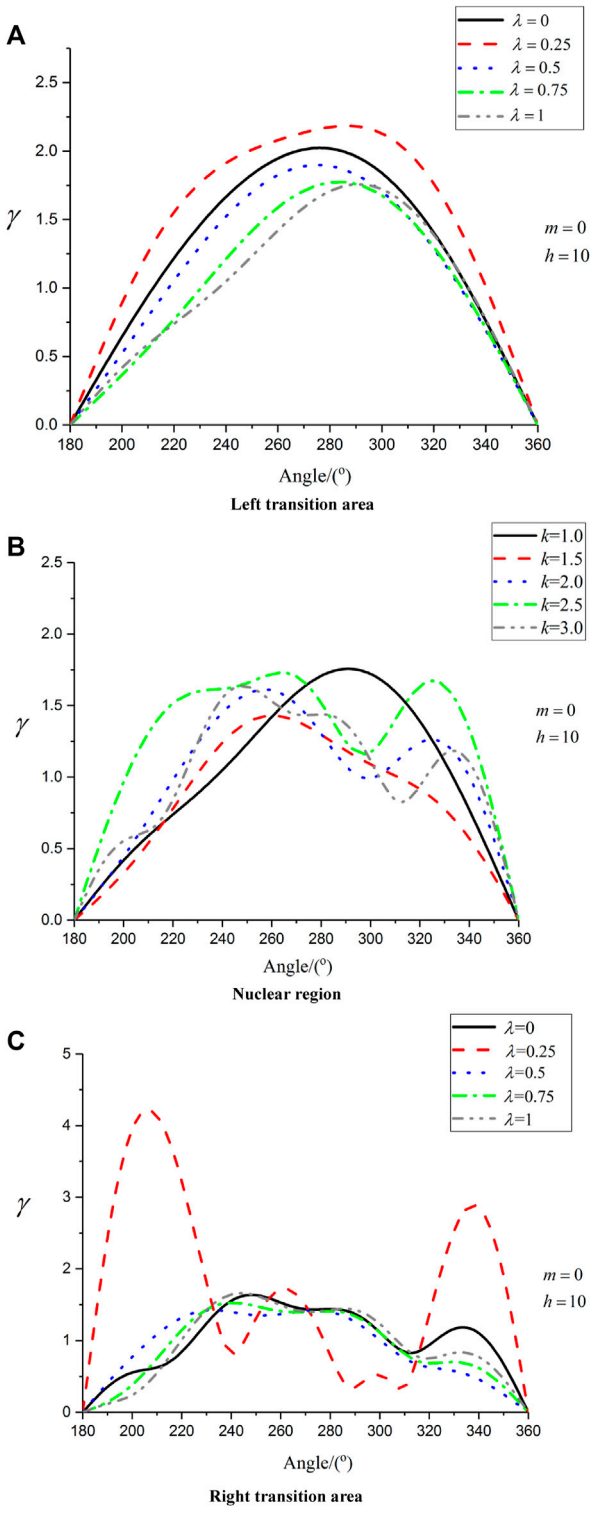

FIGURE 5
Distribution of hoop dynamic stress concentration factor of semi-circular depression when the thickness of the ribbon domain is $h = 10$. **(A–C)** represent the results of these three subsets: Left transition area, Nuclear region and Right transition area.

As can be seen from Figure 4, the left transition area of the membership function curve is a low wave number area, the maximum value of dynamic stress concentration factor

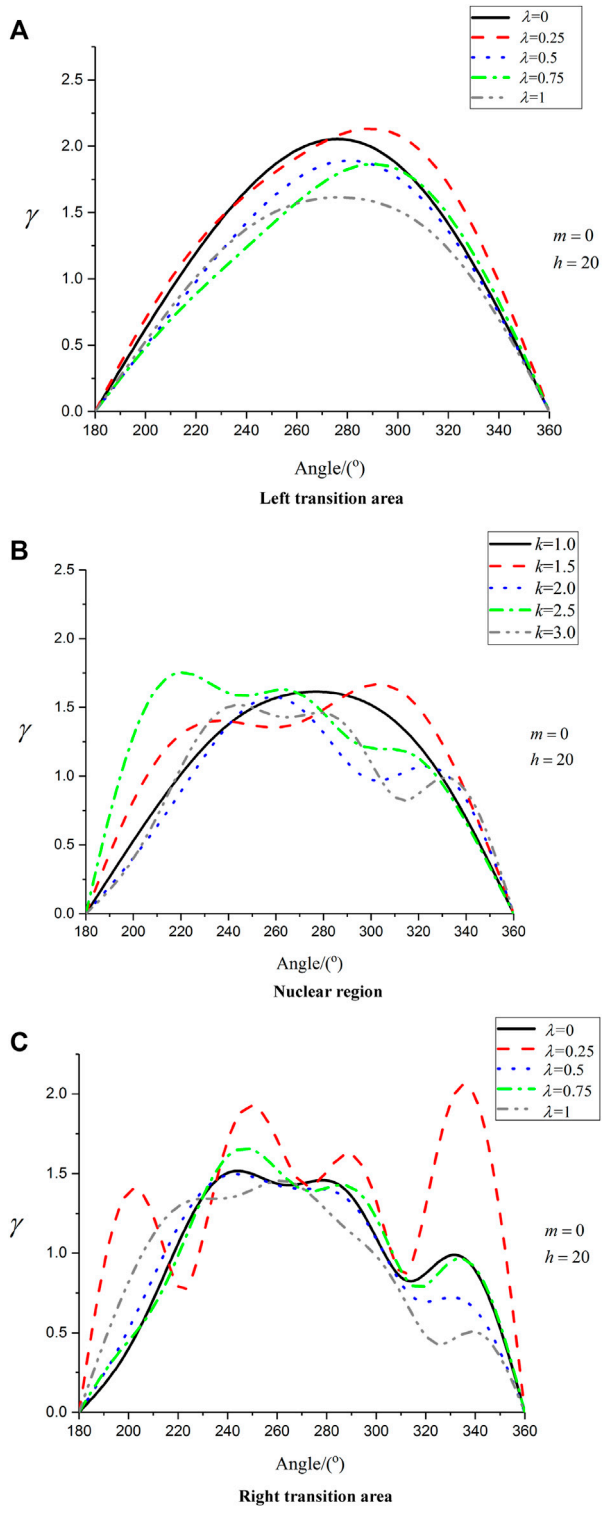

FIGURE 6
Distribution of hoop dynamic stress concentration factor of semi-circular depression when the thickness of the ribbon domain is $h = 20$. **(A–C)** represent the results of these three subsets: Left transition area, Nuclear region and Right transition area.

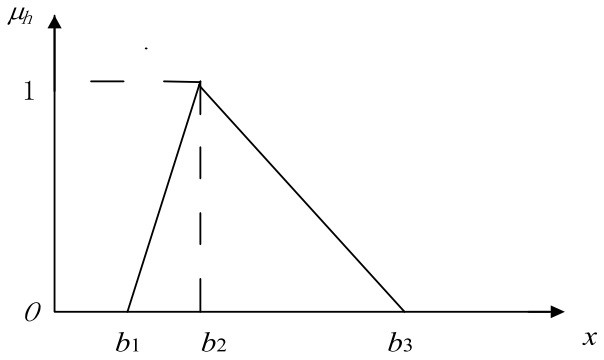

FIGURE 7
Triangular distribution.

appears on the membership degree $\lambda = 1$ curve, and the peak value of the core area appears on the membership degree $k = 2.0$ curve, while the peak value of the right transition area appears on the membership degree $\lambda = 0.5$ curve. The peaks of membership degrees appear on the curves of different membership degrees, which is obviously caused by fuzzy uncertainty. The change of the stress concentration factor curve in the right transition region is more complicated than that in the left transition region, which indicates that the high wave number region has a more serious influence than the low wave number region.

From Figure 5, the thickness $h = 10$ of the band-shaped domain shows the distribution of the hoop dynamic stress concentration factor of the semicircular depression. The left transition area of the membership function curve is the low wave number area, and the dynamic stress concentration factor curve is not obviously oscillated, and the core area and the right transition area are the medium wave number area and the high wave number area, respectively. When the membership degree of the left transition zone is $\lambda = 0.25$, the maximum value of the peak appears. The membership degrees of the core area are all $\lambda = 1$, but the maximum value of the wave peak appears at k = 1.0, and the maximum value of the peak of the dynamic stress concentration factor in the right transition area appears at $\lambda = 0.25$. Due to the influence of fuzzy and uncertain factors, the positions of the peaks in different sections of the membership curve are different. It can be seen from the figure that the number of wave peaks in the right transition area is significantly more than that in the nuclear area and the left transition area, and the right transition area oscillates more violently.

It can be seen from Figure 6 that the dynamic stress concentration factor in the left transition area of the membership function curve is significantly higher than that in the core area and the right transition area, and the curve of the stress concentration factor in the left transition area changes gently. With the increase of wave number, the curve has obvious oscillation, and the change is more obvious in the right transition region (high wave number region). The maximum value of the wave crest in the left transition area appears at the position of membership degree $\lambda = 0.25$, and although the membership degree of the core area is $\lambda = 1$, the maximum value of the wave crest appears at $k = 2.5$. The peak value of the right transition area appears at $\lambda = 0.25$. The transition regions of

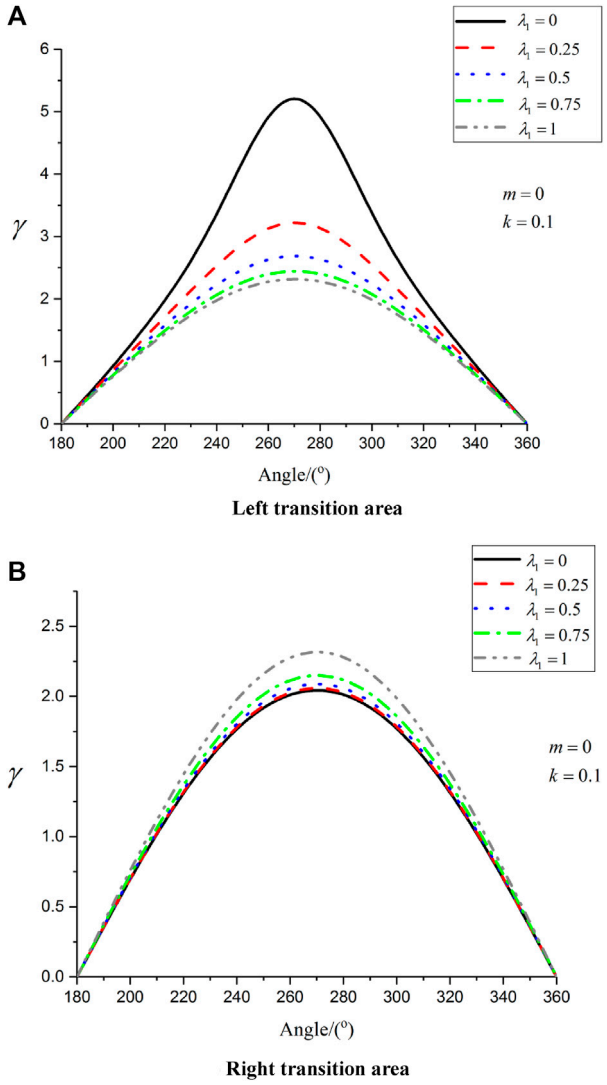

FIGURE 8
Distribution of hoop dynamic stress concentration factor with $k = 0.1$ at semicircular depressions. **(A,B)** represent the results of these two subsets: Left transition area and Right transition area.

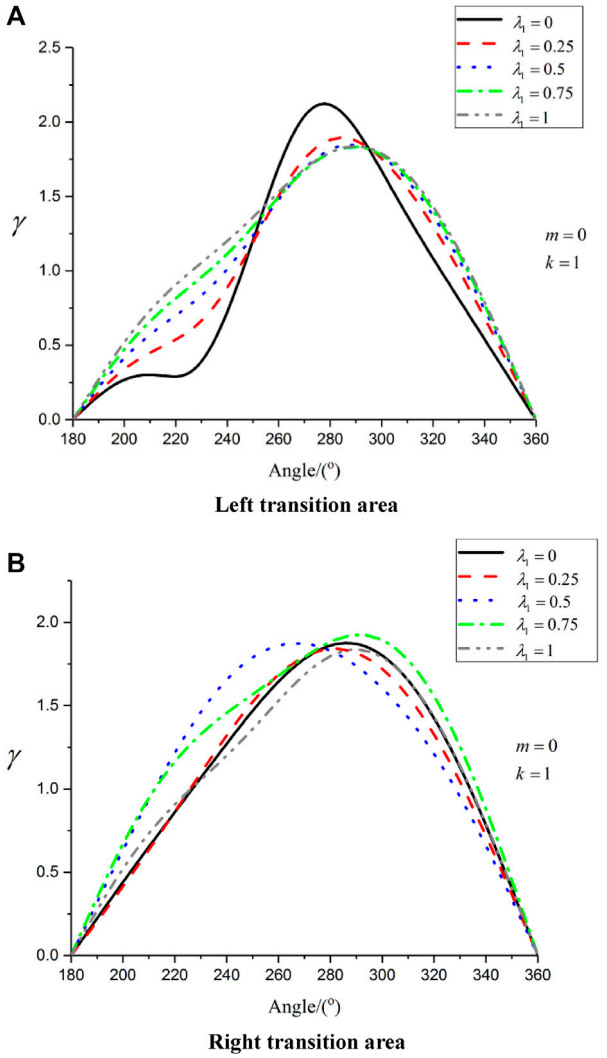

FIGURE 9
Distribution of hoop dynamic stress concentration factor with $k = 1$ at semicircular depressions. **(A,B)** represent the results of these two subsets: Left transition area and Right transition area.

different segments show different correlations, which also lead to the maximum value of the peaks appearing on the curves of different membership degrees.

3.2 Analysis of fuzzy example 2

As can be seen from reference [21], the different affiliation curves are treated according to triangular segments. Assuming that the fuzzy membership function of the thickness h of the elastic plate in the belt domain is $\mu_h(x)$, it is a triangular distribution as shown in Figure 7. According to the method of fuzzy cut set, the interval under a certain degree of membership is obtained. The points in this interval actually have different degrees of membership, so that the fuzzy cut set is not exactly the same as the general interval number. Since the subtraction and division of the four arithmetic operations of interval numbers are not reversible, it is difficult to deal with fuzzy numbers, and at most an enlarged interval solution can be obtained. According to the corresponding relationship between points and membership degrees, different membership degree curves are processed in segments.

$$\mu_h(x) = \begin{cases} 0\,; x < b_1 \\ \dfrac{1}{b_2 - b_1}x - \dfrac{b_1}{b_2 - b_1}\,;\ b_1 \le x < b_2 \\ -\dfrac{1}{b_3 - b_2}x + \dfrac{b_3}{b_3 - b_2}; b_2 \le x < b_3 \\ 0\,; b_3 \le x \end{cases}$$

In this analysis, only $b_1 < x \le b_3$ is considered and divided into two sections. Order $\mu_h(x) = \lambda_1$. When $x = h \in (b_1, b_2)$, $h = (b_2 - b_1)\lambda_1 + b_1$. When $x = h \in (b_2, b_3)$, $h = b_3 - \lambda_1(b_3 - b_2)$.

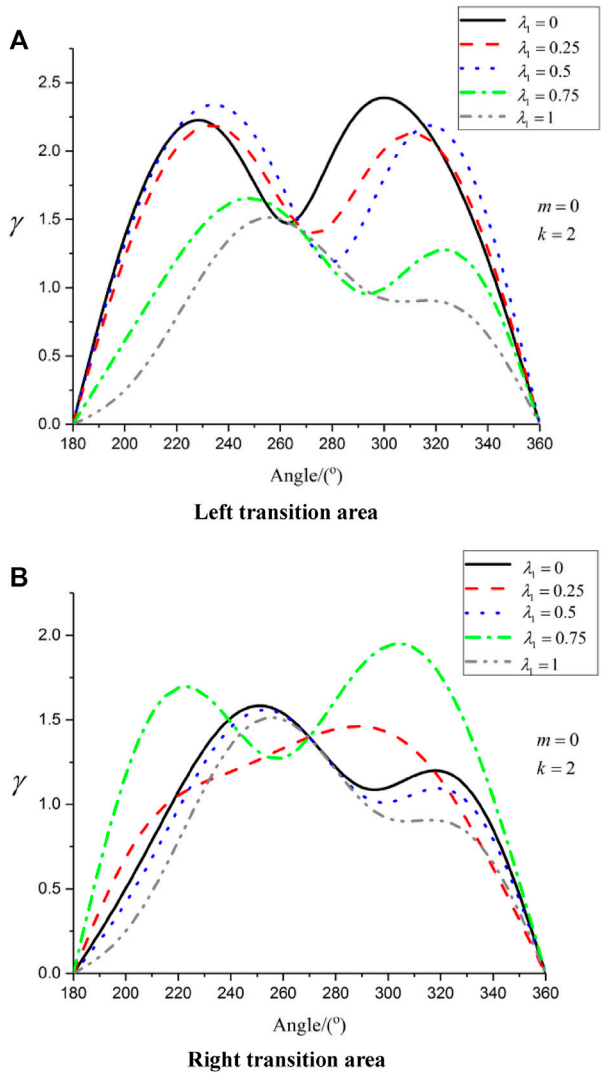

FIGURE 10
Distribution of hoop dynamic stress concentration factor with $k = 2$ at semicircular depressions. **(A,B)** represent the results of these two subsets: Left transition area and Right transition area.

Let $b_1 = 1$, $b_2 = 2$, $b_3 = 5$, $r = 0.8$ and consider the hoop dynamic stress concentration factor curve at the semicircular depression under different membership levels under the condition of $k = 0.1$, $k = 1$ and $k = 2$.

It can be seen from Figure 8 that when $m = 0$, k = 0.1 is a phenomenon of low-frequency quasi-static incidence of SH guided waves. Whether it is the left transition region or the right transition region, the dynamic stress concentration factor curve exhibits a position symmetry about 270^0. The variation law of the dynamic stress concentration factor of the membership function is very similar, and when the membership degree is $\lambda = 0$, the peak of the dynamic stress concentration factor is the largest. The changing law of the dynamic stress concentration factor in the right transition zone is also very similar in the case of different membership relationships, but the maximum value of the wave peak appears at the position of $\lambda = 1$. Due to the uncertainty of the fuzzy wave number, the positions of the peaks in the left and right transition regions are different.

It can be seen from Figure 9 that when $k = 1$ corresponds to the incident situation of the intermediate frequency SH guided wave. From the curves of the left and right transition regions, it can be seen that the dynamic stress concentration factor of the front wave surface is more obvious than the fluctuation stress concentration factor of the back side. The maximum value of the wave crest in the left transition area appears at the position of membership degree $\lambda = 0$, while the maximum value of the wave peak in the right transition area appears at the position of membership degree $\lambda = 0.75$. The values of different membership degrees are different, and the changes of the dynamic stress concentration factor in the left and right transition regions are also different.

It can be seen from Figure 10 that when $k = 2$ corresponds to the incident case of high-frequency SH guided waves. The values of different membership degrees in the left and right transition regions are different, and the variant rules of the dynamic stress concentration factor are also different. However, it can be clearly seen that the variation law of the dynamic stress concentration factor curve in the left and right transition zones basically appears in the form of two peaks. The peak maximum value in the left transition area appears on the $\lambda = 0$ curve, while the peak maximum value in the right transition area appears on the $\lambda = 0.75$ curve. From this, it can be concluded that the fuzzy relationship is uncertain, and different fuzzy membership relationships lead to different positions of wave crests.

4 Conclusion

The solution to the elastic wave scattering problem is often a non-linear function of various parameters, and there is no mature and unified method to obtain the explicit expression of the fuzzy parameters. Even if the inverse function is reached, it is mostly a multi-valued function. Various parameters are often ambiguous, and the membership function of fuzzy response is not always solved by using the membership function of known fuzzy parameters, and the irreversibility of interval algorithm also brings many difficulties in solving fuzzy response problem. In this paper, the correspondence between the subordinate function and the fuzzy quantity pairs is exploited to segment the subordinate function so that each segment corresponds to the fuzzy quantity. This method can effectively avoid the process of interval calculation and does not violate the decomposition process of fuzzy numbers. Two different affiliation curves are given for the trapezoidal and triangular distributions. We solve the multi-source fuzzy scattering problem for wave number and band shape domain thickness, respectively. The calculation example results show the feasibility of the algorithm, and provide theoretical basis and reference value for the application of fuzzy mathematics to earthquake engineering.

Data availability statement

The raw data supporting the conclusion of this article will be made available by the authors, without undue reservation.

Author contributions

EQ and HQ contributed to the conception and design of the study. EQ performed the statistical analysis and wrote the first draft of the manuscript. JG wrote sections of the manuscript. All authors contributed to manuscript revision, read, and approved the submitted version.

Funding

This work was supported by the Heilongjiang Provincial Undergraduate Universities Basic Scientific Research Business Young Innovative Talents Project (145209209).

Conflict of interest

The authors declare that the research was conducted in the absence of any commercial or financial relationships that could be construed as a potential conflict of interest.

Publisher's note

References

1. Tong S, Min X, Li Y. Observer-based adaptive fuzzy tracking control for strict-feedback nonlinear systems with unknown control gain functions. *IEEE Trans Cybernetics* (2020) 50(9):3903–13. doi:10.1109/TCYB.2020.2977175

2. Shi K, Wang J, Tang Y, Zhong S. Reliable asynchronous sampled-data filtering of T–S fuzzy uncertain delayed neural networks with stochastic switched topologies. *Fuzzy Sets Syst* (2020) 381:1–25. doi:10.1016/j.fss.2018.11.017

3. Zhao X, Wang X, Ma L, Zong G. Fuzzy approximation based asymptotic tracking control for a class of uncertain switched nonlinear systems. *IEEE Trans Fuzzy Syst* (2019) 28(4):632–44. doi:10.1109/TFUZZ.2019.2912138

4. Shi K, Wang J, Zhong S, Tang Y, Cheng J. Non-fragile memory filtering of T-S fuzzy delayed neural networks based on switched fuzzy sampled-data control. *Fuzzy Sets Syst* (2020) 394:40–64. https://doi .org/10.1016/j.fss.2019.09.001.

5. Liu P, Chen SM, Wang P. Multiple-attribute group decision-making based on q-rung orthopair fuzzy power maclaurin symmetric mean operators. *IEEE Trans Syst Man, Cybernetics: Syst* (2018) 50(10):3741–16. doi:10.1109/TSMC.2018.2852948

6. Sun K, Liu L, Qiu J, et al. Fuzzy adaptive finite-time fault-tolerant control for strict-feedback nonlinear systems[J]. *IEEE Trans Fuzzy Syst* (2020) 29(4):786–96. doi:10.11009/TFUZZ.2020.2965890

7. Hu M, Zhong Y, Xie S, Lv H, Lv Z. Fuzzy system based medical image processing for brain disease prediction. *Front Neurosci* (2021) 15:714318. doi:10.3389/fnins.2021.714318

8. Zhu Z, Pan Y, Zhou Q, Lu C. Event-triggered adaptive fuzzy control for stochastic nonlinear systems with unmeasured states and unknown backlash-like hysteresis. *IEEE Trans Fuzzy Syst* (2020) 29(5):1273–83. doi:10.1109/TFUZZ.2020.2973950

9. Lin M, Huang C, Xu Z. MULTIMOORA based MCDM model for site selection of car sharing station under picture fuzzy environment. *Sustain cities Soc* (2020) 53:101873. doi:10.1016/j.scs.2019.101873

10. Zhang L, Lam HK, Sun Y, Liang H. fault detection for fuzzy semi-markov jump systems based on interval type-2 fuzzy approach. *IEEE Trans Fuzzy Syst* (2019) 28(10):2375–88. doi:10.1109/TFUZZ.2019.2936333

11. Wang Y, Jiang B, Wu ZG, Xie S, Peng Y. Adaptive sliding mode fault-tolerant fuzzy tracking control with application to unmanned marine vehicles. *IEEE Trans Syst Man, Cybernetics: Syst* (2020) 51(11):6691–700. doi:10.1109/TSMC.2020.2964808

12. Garg H, Kumar K. A novel exponential distance and its based TOPSIS method for interval-valued intuitionistic fuzzy sets using connection number of SPA theory. *Artif Intelligence Rev* (2020) 53(1):595–624. doi:10.1007/s10462-018-9668-5

13. Pan Y, Zhang L, Li ZW, Ding L. Improved fuzzy bayesian network-based risk analysis with interval-valued fuzzy sets and D–S evidence theory. *IEEE Trans Fuzzy Syst* (2019) 28(9):2063–77. doi:10.1109/TFUZZ.2019.2929024

14. Mahariq I, Giden IH, Alboon S, Fouad Aly WH, Youssef A, Kurt H. Investigation and analysis of acoustojets by spectral element method[J]. *Mathematics* (2022) 10(17):3415. https://www.mdpi.com/2227-7390/10/23/4516.

15. Mahariq I, Kuzuoğlu M, Tarman IH, Kurt H. Photonic nanojet analysis by spectral element method[J]. *IEEE Photonics J.* (2014) 6(5):1–14. doi:10.1109/JPHOT.2014.2361615

16. Mahariq I, Kurt H. On-and off-optical-resonance dynamics of dielectric microcylinders under plane wave illumination[J]. *JOSA B* (2015) 32(6):1022–1030. doi:10.1364/JOSAB.32.001022

17. Mahariq I, Astratov VN, Kurt H. Persistence of photonic nanojet formation under the deformation of circular boundary[J]. *JOSA B* (2016) 33(4):535–542. doi:10.1364/JOSAB.33.000535

18. Qu EX, Qi H, Guo J, Wang L. Dynamic response analysis of SH-guided waves in a strip-shaped elastic medium for a semi-cylindrical depression[J]. *Arch. Appl. Mech.* (2023) 93(3):1241–1258. doi:10.1007/s00419-022-02325-9

19. Liu D, Gai B, Tao G. Applications of the method of complex functions to dynamic stress concentrations[J]. *Wave motion* (1982) 4(3):293–304. doi:10.1016/0165-2125(82)90025-7

20. Shi WP, Fang SJ, Zhang CP, Yang HL. Fuzzy response of semicircular concave boundaries in half space to SH wave scattering [J]. *Mech. strength* (2011) 33(03):373–378. doi:10.16579/j.issn.1001.9669.2011.03.012

21. Liu YW, Shi WP. Fuzzy scattering of steady-state incident plane SH waves by circular elastic inclusions in a right-angle plane[J]. *Mech. strength* (2012) 34(03):371–378. doi:10.16579/j.issn.1001.9669.2012.03.003

frontiers | Frontiers in Physics

TYPE Original Research
PUBLISHED 25 May 2023
DOI 10.3389/fphy.2023.1205060

OPEN ACCESS

EDITED BY
Gangwei Wang,
Hebei University of Economics and Business, China

REVIEWED BY
Xinyue Li,
Shandong University of Science and Technology, China
Junchao Chen,
Lishui University, China

*CORRESPONDENCE
Wen-Xiu Ma,
wma@usf.edu
Imran Siddique,
imransmsrazi@gmail.com

RECEIVED 13 April 2023
ACCEPTED 05 May 2023
PUBLISHED 25 May 2023

CITATION
Zulqarnain RM, Ma W-X, Mehdi KB, Siddique I, Hassan AM and Askar S (2023), Physically significant solitary wave solutions to the space-time fractional Landau–Ginsburg–Higgs equation via three consistent methods.
Front. Phys. 11:1205060.
doi: 10.3389/fphy.2023.1205060

Physically significant solitary wave solutions to the space-time fractional Landau–Ginsburg–Higgs equation via three consistent methods

Rana Muhammad Zulqarnain[1], Wen-Xiu Ma[1,2,3]*, Khush Bukht Mehdi[4], Imran Siddique[4]*, Ahmed M. Hassan[5] and Sameh Askar[6]

[1]School of Mathematical Sciences, Zhejiang Normal University, Jinhua, Zhejiang, China, [2]Department of Mathematics and Statistics, University of South Florida, Tampa, FL, United States, [3]School of Mathematical and Statistical Sciences, North-West University, Mmabatho, South Africa, [4]Department of Mathematics, University of Management and Technology, Lahore, Pakistan, [5]Faculty of Engineering, Future University in Egypt, Cairo, Egypt, [6]Department of Statistics and Operations Research, College of Science, King Saud University, Riyadh, Saudi Arabia

The Landau–Ginzburg–Higgs equation (LGHE) is a mathematical model used to describe nonlinear waves that exhibit weak scattering and long-range connections in the tropical and mid-latitude troposphere as interactions between equatorial and mid-latitude Rossby waves. This study assessed the fractional Landau–Ginzburg–Higgs model, previously introduced in truncated M-fractional derivatives utilizing the $(G'/G, 1/G)$, modified (G'/G^2), and new auxiliary equation methods. Using these techniques, different solutions, including unknown parameters, were obtained in trigonometric, hyperbolic, and exponential functions. This study investigated how varying values of the fractional parameter affected the deeds of the solutions obtained for the given conditions. The predicted solutions, obtained under restricted conditions, were visualized through 2D, 3D, and contour plots using appropriate parameter values. The attained results were confirmed for the aforementioned equations using symbolic soft computations. Moreover, the outcomes confirmed that the methods used in this study were effective mathematical tools for discovering exact solitary wave solutions to nonlinear models encountered in various areas of science and engineering.

KEYWORDS

Ginzburg–Higgs equation, truncated M-fractional derivative, the (G′/G,1/G)-expansion method, modified (G′/G²)-expansion method, new auxiliary equation method, exact solitary wave solutions

1 Introduction

Non-linear partial differential equations (NLPDEs) play significant roles in physics, mathematical engineering, and other phenomena such as heat flow, plasma physics, wave propagation, shallow water waves, chemically dispersed electricity, quantum mechanics, fluid dynamics, and reactive materials. NLPDEs also play substantial roles in nonlinear optical fibers

and quantum fields, such as nonlinear wave equations, Monge–Ampere equations, Burgers equations, Liouville equations, Fisher equations, and Kolmogorov–Petrovskii–Piskunov equations [1–4]. These equations assist in the implementation of essential parts of the soliton solution. The soliton is stimulated during diffusion by eliminating the effects of diffusion. Now, soliton assessment is very common [5]. Solitons are solutions to large, weakly detached partial differential equations (PDEs) for physical structures. Nowadays, many models are considered for computing the soliton solutions (SS) [6–8]. Among these, the Landau–Ginzburg–Higgs (LGH) model [9, 10] is one of the most considered in recent years, as follows:

$$\frac{\partial^2 v}{\partial t^2} - \frac{\partial^2 v}{\partial x^2} - g^2 v + h^2 v^3 = 0, \tag{1}$$

where $v = v(x,t)$ is the ion-cyclotron wave electrostatic potential g and h are real parameters and x,t indicate the nonlinearized spatial and temporal coordinates. Lev Davidovich Landau and Vitaly Lazarevich Ginzburg designed the LGHE (1) to describe superconductivity and drift cyclotron waves in radially inhomogeneous plasmas of integrated ion cyclotrons [11]. Numerous methods have been used to determine the distinctive SS of the integrable nonlinear evolution equation (NLEE) (1). Bekir and Unsal [12] provided exponential function solutions by using the first integral method for NLEE (1). Iftikhar et al. [13] utilized the $(G'/G, 1/G)$-expansion method and inspected a variety of analytical solutions for NLEE (1). They also determined general and kinked shape soliton solutions for different parameter selections. Barman et al. [14, 15] obtained various analytical solutions using the Kudryashov technique comprising the undisclosed parameters of Eq. 1. In addition, they employed the tanh function to create solutions with soliton-like shapes, such as dark solitons, bright solitons, peakons, compactons, and periodic solutions, among others. These solutions can be utilized to investigate the propagation of various waves, such as tidal and tsunami waves, ion-acoustic waves, and magneto-sound waves in plasma. Islam and Akbar [16] used the IBSEF and presented innumerable stable solutions. The results provided several soliton shapes, which considered one-way wave propagation with diffuse systems in nonlinear science.

For two centuries, fractional calculus has fascinated many intellectuals' curiosity. Use them to develop many nonlinear aspects, inclosing bioprocesses, chemical processes, fluid mechanics, etc. In the traditional integer order, the fractional-order PDEs are used to generalize PDEs. Several definitions of the fractional derivative exist in the literature, such as Riemann–Liouville [17], Caputo [18], Caputo–Fabrizio [19], conformable fractional derivative (FD) [20], and beta-derivative [21] to solve non-integer-order models. Studies have shown that these definitions of FD do not meet some of the basic assets of derivatives, such as product and chain rules. Sousa and Oliveira [22] developed a novel truncated-M fractional derivative that meets numerous properties considered to be the FD' boundary. This derivative has interesting results in different areas, such as chaos theory, biological modeling, circuit analysis, optical physics, and disease analysis.

The core aim of this study was to explore the space-time fractional LGH model [23], symbolized as

$$D_{M,t}^{2\alpha,\beta} v - D_{M,x}^{2\alpha,\beta} v - g^2 v + h^2 v^3 = 0, 0 < \alpha < 1, \beta > 0, \tag{2}$$

where α and β are the fractional parameters representing the fractional time derivative's order.

The fundamental consideration of this exploration was to take advantage of the novel indication of fractional-order derivatives, called truncated truncated-M fractional derivatives [22, 24, 25], for space-time fractional LGHE [23], and to use the $(G'/G, 1/G)$, modified (G'/G^2), and new auxiliary equation methods (NAEMs) [23, 26, 27] to obtain new inclusive solitary solutions in the form of solutions of bright, dark, single solitons, and periodic isolated waves. Up to now, the results have different corporate and diverse forms, which have not been reported previously [23].

Moreover, the planned technique has been used to solve various models. For instance, Hafiz [28] employed the $(G'/G, 1/G)$-expansion method to determine the closed-form solutions of the generalized fractional reaction Duffing model and the density-dependent fractional diffusion-reaction equation. Li et al. [29] discovered the traveling wave solutions of the Zakharov equation, and Zayed et al. [30] established solutions to the nonlinear Kdv–mKdv equation. Uddin [31] and Wazwaz [32] provided general solutions for the fifth-order NLEEs and the Burger KP-equation, respectively. Sirisubtawee [33] found exact traveling wave solutions for nonlinear fractional evolution equations. Traveling wave solutions for the nonlinear Schrodinger equation with third-order dispersion were obtained using the modified (G'/G^2)-expansion model [34]. The Fokas–Lenells equations were solved using this technique to regulate different traveling wave solutions [35]. Aljahdaly [36] extended the NLEEs and described the general exact traveling wave solutions. Dragon and Donmez [37] discovered solutions in the form of traveling waves for the Gardner equation and then used these solutions to address different plasma-related issues. The Sharma–Tasso–Olver (STO) equations were also solved, and exact nonlinear and super nonlinear traveling wave solutions were obtained [38]. Jhangeer et al. [39] used the new auxiliary equations method to find innovative soliton solutions for the fractional Caudrey–Dodd–Gibbon–Sawada–Kotera equation. Raza et al. [40] obtained the new optical solitary wave solitons of the three-dimensional Fractional Wazwaz–Benjamin–Bona–Mahony (WBBM) equation. Furthermore, Riaz et al. [41] scrutinized the various forms of solitary wave solutions for the modified equal-width wave equation.

This work is structured into six sections. Section 2 presents the truncated M-fractional derivative and its properties, which is the foundation of the proposed methods. The methodologies of the three proposed approaches are discussed in Section 3, where we explain how to use the truncated M-fractional derivative to solve mathematical models. Section 4 involves a mathematical examination of the models we have presented and the solutions we have obtained using the proposed methods. We compare them with existing methods in the literature. Section 5 provides a graphical representation of the obtained solutions for each analyzed model. Finally, Section 6 provides the study conclusion by summarizing the key findings and their implications.

2 Truncated M-fractional derivative and its properties

The following section will discuss the truncated M-fractional derivative (TMFD) of order α with its properties.

Definition 2.1. Let f: $(0,\infty) \to R$, then, the TMFD of a function f of order α is determined as

$$D_M^{\alpha,\beta} f(t) = \lim_{\varepsilon \to 0} \frac{f\left(t\epsilon_\beta\left(\varepsilon t^{1-\alpha}\right)\right) - f(t)}{\varepsilon}, \text{for all } t > 0, 0 < \alpha < 1, \beta > 0,$$

where $\alpha\epsilon_\beta(\cdot)$ is a truncated Mittag–Leffler function of one parameter [22].

Properties 2.2. Let $\alpha \in (0,1], \beta > 0$ and $f = f(t), g = g(t)$ be α-differentiable at a point $t > 0$, then:

1. $D_M^{\alpha,\beta}(af + bg) = aD_M^{\alpha,\beta} f + bD_M^{\alpha,\beta} g, \forall\ a, b \in R.$
2. $D_M^{\alpha,\beta}(c) = 0$, where $f(t) = c$, is a constant.
3. $D_M^{\alpha,\beta}(f \cdot g) = D_M^{\alpha,\beta} f + D_M^{\alpha,\beta} g.$
4. $D_M^{\alpha,\beta}\left(\frac{f}{g}\right) = \frac{gD_M^{\alpha,\beta} f - fD_M^{\alpha,\beta} g}{g^2}.$
5. If f is differentiable, then

$$D_M^{\alpha,\beta} f(t) = \frac{t^{1-\alpha}}{\Gamma(\beta+1)} \frac{df}{dt}. \tag{3}$$

6. $D_M^{\alpha,\beta}(f \circ g)(t) = f'(g(t)) D_M^{\alpha,\beta} g(t)$, for f differentiable at $g(t)$.

3 General form of the methods

3.1 $(G'/G, 1/G)$-expansion method

The core steps of the $(G'/G, 1/G)$-expansion model [24, 28] for discovering traveling wave solutions to nonlinear evolution equations are outlined in this section. We begin by examining the second-order linear ordinary differential equation (ODE):

$$G''(\eta) + \lambda G(\eta) = \mu, \tag{4}$$

where $\phi = G'/G$ and $\psi = 1/G$, then

$$\phi' = -\phi^2 + \mu\psi - \lambda, \psi' = -\phi\psi. \tag{5}$$

Case 1: When $\lambda < 0$, the general solutions of Eq. 4 is given as

$$G(\eta) = A_1 \sinh\left(\sqrt{-\lambda}\,\eta\right) + A_2 \cosh\left(\sqrt{-\lambda}\,\eta\right) + \frac{\mu}{\lambda}, \tag{6}$$

and we have

$$\psi^2 = \frac{-\lambda}{\lambda^2\sigma + \mu^2}\left(\phi^2 - 2\mu\psi + \lambda\right), \tag{7}$$

where A_1 and A_2 are arbitrary integration constants and $\sigma = {A_1}^2 - {A_2}^2$.

Case 2: When $\lambda > 0$, the general solution of Eq. 4 is clearly

$$G(\eta) = A_1 \sin\left(\sqrt{\lambda}\,\eta\right) + A_2 \cos\left(\sqrt{\lambda}\,\eta\right) + \frac{\mu}{\lambda}, \tag{8}$$

and we have

$$\psi^2 = \frac{\lambda}{\lambda^2\sigma - \mu^2}\left(\phi^2 - 2\mu\psi + \lambda\right), \tag{9}$$

where A_1 and A_2 are arbitrary integration constants and $\sigma = {A_1}^2 + {A_2}^2$.

Case 3: When $\lambda = 0$, the general solutions of Eq. 4 is

$$G(\eta) = \frac{\mu}{2}\eta^2 + A_1\eta + A_2, \tag{10}$$

and we have

$$\psi^2 = \frac{1}{{A_1}^2 - 2\mu A_2}\left(\phi^2 - 2\mu\psi\right), \tag{11}$$

where A_1 and A_2 are arbitrary integration constants.

Consider the NLPDE, such as

$$Q(u, u_t, u_x, u_{tt}, u_{xt}, u_{xx}, \ldots) = 0. \tag{12}$$

The unfamiliar function $u = u(x,t)$ is represented by a Q polynomial of the variable and its partial derivatives. The key phases involved in the $(G'/G, 1/G)$-expansion model are as follows:

Step 1: By coordinate transformation

$$\eta = x - ct, u(x,t) = v(\eta). \tag{13}$$

where c is the speed of the traveling wave.

The wave variable allows us to reduce Eq. 12 into a nonlinear ODE for $v = v(\eta)$:

$$R\left(v, v', v'', v''', \ldots\right) = 0, \tag{14}$$

where R is a polynomial of $v(\eta)$ and its total derivatives concerning η.

Step 2: Assume that a polynomial can express the solutions of Eq. 14 in two variables ϕ and ψ as

$$v(\eta) = \sum_{i=0}^{m} a_i \phi^i + \sum_{i=0}^{m} b_i \phi^{i-1}\psi. \tag{15}$$

To determine the values of the constants $a_i\,(i = 0, 1, \ldots, m)$ and $b_i\,(i = 1, \ldots, m)$ and the positive integer m, a homogenous imbalance is used among the highest-order derivatives and the nonlinear terms in the given ODE Eq. 14.

Step 3: Substitute Eq. 15 into Eq. 14 along with Eqs 5 and 7, reducing the left-hand side of the ODE into a polynomial in terms of ϕ and ψ, with a maximum degree of 1 for ψ. A system of algebraic equations is obtained by setting each coefficient of the polynomial to zero, which can be solved with the aid of Mathematica software to obtain the values for $a_i\,(i = 0, 1, \ldots, m), b_i\,(i = 1, \ldots, m), c, \mu, \lambda\,(\lambda < 0), A_1$ and A_2.

Step 4: Substitute the values obtained for $a_i\,(i = 0, 1, \ldots, m)$, $b_i\,(i = 1, \ldots, m)$, $c, \mu, \lambda(\lambda{<}0)$, A_1 and A_2 in Eq. 15 to determine the traveling wave solutions in terms of hyperbolic functions, as expressed in Eq. 14.

Step 5: Similarly, substitute Eq. 15 into Eq. 14 along with Eq. 5 and either Eq. 9 or Eq. 11 to obtain exact traveling wave solutions expressed in terms of trigonometric or rational functions, respectively.

3.2 The modified (G'/G^2)-expansion method

We outline the fundamental steps of the modified (G'/G^2)-expansion method [24, 29] as follows:

Step 1: Start by considering Eqs 12–14.

Step 2: Extend the solutions to Eq. 14 as follows:

$$v(\eta) = \sum_{i=0}^{m} a_i \left(\frac{G'}{G^2}\right)^i, \tag{16}$$

where $a_i\,(i = 0, 1, 2, 3, \ldots, m)$ are constants and found later. It is important that $a_i \neq 0$.

The function $G = G(\eta)$ satisfies the following Riccati equation:

$$\left(\frac{G'}{G^2}\right)' = \lambda_1 \left(\frac{G'}{G^2}\right)^2 + \lambda_0, \tag{17}$$

where λ_0 and λ_1 are constants.

We can obtain the following solutions to Eq. 17 under different conditions λ_0:

When $\lambda_0\lambda_1 < 0$,

$$\left(\frac{G'}{G^2}\right) = -\frac{\sqrt{|\lambda_0\lambda_1|}}{\lambda_1} + \frac{\sqrt{|\lambda_0\lambda_1|}}{2}\left[\frac{C_1 \sinh\left(\sqrt{\lambda_0\lambda_1}\,\eta\right) + C_2 \cosh\left(\sqrt{\lambda_0\lambda_1}\,\eta\right)}{C_1 \cosh\left(\sqrt{\lambda_0\lambda_1}\,\eta\right) + C_2 \sinh\left(\sqrt{\lambda_0\lambda_1}\,\eta\right)}\right]. \tag{18}$$

When $\lambda_0\lambda_1 > 0$,

$$\left(\frac{G'}{G^2}\right) = \sqrt{\frac{\lambda_0}{\lambda_1}}\left[\frac{C_1 \cos\left(\sqrt{\lambda_0\lambda_1}\,\eta\right) + C_2 \sin\left(\sqrt{\lambda_0\lambda_1}\,\eta\right)}{C_1 \sin\left(\sqrt{\lambda_0\lambda_1}\,\eta\right) - C_2 \sin\left(\sqrt{\lambda_0\lambda_1}\,\eta\right)}\right]. \tag{19}$$

When $\lambda_0 = 0$ and $\lambda_1 \neq 0$,

$$\left(\frac{G'}{G^2}\right) = -\frac{C_1}{\lambda_1 (C_1\eta + C_2)}, \tag{20}$$

where C_1 and C_2 are arbitrary constants.

Step 3: If we substitute Eq. 16 and Eq. 17 into Eq. 14 and equate the coefficients of each power of $(\frac{G'}{G^2})^i$ to zero, a set of algebraic equations can be obtained. These equations can then be solved to determine the values of $a_i, \lambda_0, \lambda_1, c$, and other parameters.

Step 4: Replacing Eq. 16 of which α_i, c, and other parameters are found in step 3 in Eq. 13, we obtain the solutions for Eq. 12.

3.3 The new auxiliary equation method

Now, we will designate the elementary steps of the new auxiliary equation method [39, 40].

Step 1: Consider Eqs 12–14.

Step 2: Subsequently determine the solutions of Eq. 14:

$$v(\eta) = \sum_{i=0}^{m} a_i \gamma^{if(\eta)}, \tag{21}$$

which satisfies the auxiliary equation:

$$f'(\eta) = \frac{1}{\ln(\gamma)}\left(\mu\gamma^{-f(\eta)} + \lambda + \zeta\gamma^{f(\eta)}\right), \tag{22}$$

where $a_0, a_1, a_2, \ldots, a_m$ are coefficients to be solved such that $a_m \neq 0$. We then utilized the balancing principle to obtain the value of m, which states that we can find m by equating the nonlinear term of Eq. 14 with the highest-order derivative.

For Eq. 22, the family of solutions can be attained as follows:

Family-1 When $\lambda^2 - 4\mu\zeta < 0$ and $\zeta \neq 0$,

$$\gamma^{f(\eta)} = \frac{-\lambda}{2\zeta} + \frac{\sqrt{4\mu\zeta - \lambda^2}}{2\zeta}\tan\left(\frac{\sqrt{4\mu\zeta - \lambda^2}}{2}\eta\right),$$

$$\gamma^{f(\eta)} = \frac{-\lambda}{2\zeta} - \frac{\sqrt{4\mu\zeta - \lambda^2}}{2\zeta}\cot\left(\frac{\sqrt{4\mu\zeta - \lambda^2}}{2}\eta\right).$$

Family-2 When $\lambda^2 - 4\mu\zeta > 0$ and $\zeta \neq 0$,

$$\gamma^{f(\eta)} = \frac{-\lambda}{2\zeta} - \frac{\sqrt{\lambda^2 - 4\mu\zeta}}{2\zeta}\tanh\left(\frac{\sqrt{\lambda^2 - 4\mu\zeta}}{2}\eta\right),$$

$$\gamma^{f(\eta)} = \frac{-\lambda}{2\zeta} - \frac{\sqrt{\lambda^2 - 4\mu\zeta}}{2\zeta}\coth\left(\frac{\sqrt{\lambda^2 - 4\mu\zeta}}{2}\eta\right).$$

Family-3 When $\lambda^2 + 4\mu^2 < 0, \zeta \neq 0$ and $\zeta = -\mu$,

$$\gamma^{f(\eta)} = \frac{\lambda}{2\mu} - \frac{\sqrt{-4\mu^2 - \lambda^2}}{2\mu}\tan\left(\frac{\sqrt{-4\mu^2 - \lambda^2}}{2}\eta\right),$$

$$\gamma^{f(\eta)} = \frac{\lambda}{2\mu} + \frac{\sqrt{-4\mu^2 - \lambda^2}}{2\mu}\cot\left(\frac{\sqrt{-4\mu^2 - \lambda^2}}{2}\eta\right).$$

Family-4 When $\lambda^2 + 4\mu^2 > 0, \zeta \neq 0$ and $\zeta = -\mu$,

$$\gamma^{f(\eta)} = \frac{\lambda}{2\mu} + \frac{\sqrt{4\mu^2 + \lambda^2}}{2\mu}\tanh\left(\frac{\sqrt{4\mu^2 + \lambda^2}}{2}\eta\right),$$

$$\gamma^{f(\eta)} = \frac{\lambda}{2\mu} + \frac{\sqrt{4\mu^2 + \lambda^2}}{2\mu}\coth\left(\frac{\sqrt{4\mu^2 + \lambda^2}}{2}\eta\right).$$

Family-5 When $\lambda^2 - 4\mu^2 < 0$ and $\zeta = \mu$,

$$\gamma^{f(\eta)} = \frac{-\lambda}{2\mu} + \frac{\sqrt{4\mu^2 - \lambda^2}}{2\mu}\tan\left(\frac{\sqrt{4\mu^2 - \lambda^2}}{2}\eta\right),$$

$$\gamma^{f(\eta)} = \frac{-\lambda}{2\mu} - \frac{\sqrt{4\mu^2 - \lambda^2}}{2\mu}\cot\left(\frac{\sqrt{4\mu^2 - \lambda^2}}{2}\eta\right).$$

Family-6 When $\lambda^2 - 4\mu^2 > 0$ and $\zeta = \mu$,

$$\gamma^{f(\eta)} = \frac{-\lambda}{2\mu} - \frac{\sqrt{-4\mu^2 + \lambda^2}}{2\mu}\tanh\left(\frac{\sqrt{-4\mu^2 + \lambda^2}}{2}\eta\right),$$

$$\gamma^{f(\eta)} = \frac{-\lambda}{2\mu} - \frac{\sqrt{-4\mu^2 + \lambda^2}}{2\mu}\coth\left(\frac{\sqrt{-4\mu^2 + \lambda^2}}{2}\eta\right).$$

Family-7 When $\lambda^2 = 4\mu\zeta$,

$$\gamma^{f(\eta)} = -\frac{2 + \lambda\eta}{2\zeta\eta}.$$

Family-8 When $\mu\zeta < 0, \lambda = 0$ and $\zeta \neq 0$,

$$\gamma^f(\eta) = -\sqrt{\frac{-\mu}{\zeta}}\tanh\left(\sqrt{-\mu\zeta}\,\eta\right),$$

$$\gamma^f(\eta) = -\sqrt{\frac{-\mu}{\zeta}}\coth\left(\sqrt{-\mu\zeta}\,\eta\right).$$

Family-9 When $\lambda = 0$ and $\mu = -\zeta$,

$$\gamma^f(\eta) = \frac{1 + e^{-2\zeta\eta}}{-1 + e^{-2\zeta\eta}}.$$

Family-10 When $\mu = \zeta = 0$,

$$\gamma^f(\eta) = \cosh(\lambda\eta) + \sinh(\lambda\eta).$$

Family-11 When $\mu = \lambda = K$ and $\zeta = 0$,

$$\gamma^f(\eta) = e^{K\eta} - 1.$$

Family-12 When $\zeta = \lambda = K$ and $\mu = 0$,

$$\gamma^f(\eta) = \frac{e^{K\eta}}{1 - e^{K\eta}}.$$

Family-13 When $\lambda = \mu + \zeta$,

$$\gamma^f(\eta) = -\frac{1 - \mu e^{(\mu-\zeta)\eta}}{1 - \zeta e^{(\mu-\zeta)\eta}}.$$

Family-14 When $\lambda = -(\mu + \zeta)$,

$$\gamma^f(\eta) = \frac{\mu - e^{(\mu-\zeta)\eta}}{\zeta - e^{(\mu-\zeta)\eta}}.$$

Family-15 When $\mu = 0$,

$$\gamma^f(\eta) = \frac{\lambda e^{\lambda\eta}}{1 - \zeta e^{\lambda\eta}}.$$

Family-16 When $\lambda = \mu = \zeta \neq 0$,

$$\gamma^f(\eta) = \frac{1}{2}\left[\sqrt{3}\,\tan\left(\frac{\sqrt{3}}{2}\mu\eta\right) - 1\right].$$

Family-17 When $\lambda = \zeta = 0$,

$$\gamma^f(\eta) = \mu\eta.$$

Family-18 When $\lambda = \mu = 0$,

$$\gamma^f(\eta) = -\frac{1}{\zeta\eta}.$$

Family-19 When $\mu = \zeta$ and $\lambda = 0$,

$$\gamma^f(\eta) = \tan(\mu\eta).$$

Family-20 When $\zeta = 0$,

$$\gamma^f(\eta) = e^{\lambda\eta} - \frac{m}{n}.$$

4 Mathematical analyses of the models and their solutions

Assuming the transformations:

$$v(x,t) = v(\eta), \eta = \frac{\Gamma(\beta+1)}{\alpha}(kx^\alpha - ct^\alpha), \tag{23}$$

where k and c are constants. Using Eq. 8 in Eq. 2, we acquire the subsequent ODE

$$(c^2 - k^2)v'' - g^2 v + h^2 v^3 = 0. \tag{24}$$

The subsequent sections employ the planned techniques to obtain the desired solutions.

4.1 Solutions with the $(G'/G, 1/G)$-expansion method

Using the homogenous balance technique to the highest-order derivative with the nonlinear term in Eq. 24, we get $m = 1$. For $m = 1$, Eq. 15 has the form:

$$v(\eta) = a_0 + a_1\phi(\eta) + b_1\psi(\eta), \tag{25}$$

where a_0, a_1 and b_1 are unknown parameters.

Case 1: The obtained Eq. 25 is substituted into Eq. 24 with the use of Eqs 5 and 7 to result in a polynomial equation. A system of algebraic equations is obtained by setting each polynomial coefficient to zero $a_0, a_1, b_1, \mu, \sigma, \lambda, c$, and k. This system of algebraic equations can be solved using symbolic computation software such as MATHEMATICA, which provides the following results:

$$a_0 = 0, a_1 = \frac{\sqrt{k^2 - c^2}}{\sqrt{2}h}, b_1 = \frac{\sqrt{k^2 - c^2}\sqrt{\lambda}\sqrt{\sigma}}{\sqrt{2}h}, g = \frac{\sqrt{c^2 - k^2}\sqrt{\lambda}}{\sqrt{2}}, \mu = 0. \tag{26}$$

The hyperbolic traveling wave solutions of Eq. 24 can be obtained by substituting Eq. 26 into Eq. 25:

$$v(x,t) = \frac{\sqrt{k^2 - c^2}}{\sqrt{2}h}\left(\frac{A_1\sqrt{-\lambda}\cosh\left(\sqrt{-\lambda}\,\eta\right) + A_2\sqrt{-\lambda}\sinh\left(\sqrt{-\lambda}\,\eta\right)}{A_1\sinh\left(\sqrt{-\lambda}\,\eta\right) + A_2\cosh\left(\sqrt{-\lambda}\,\eta\right) + \frac{\mu}{\lambda}}\right),$$
$$+\frac{\sqrt{k^2 - c^2}\sqrt{\lambda\sigma}}{\sqrt{2}h}\left(\frac{1}{A_1\sinh\left(\sqrt{-\lambda}\,\eta\right) + A_2\cosh\left(\sqrt{-\lambda}\,\eta\right) + \frac{\mu}{\lambda}}\right), \tag{27}$$

where $\sigma = {A_1}^2 - {A_2}^2$.

Family 1.1: If $A_1 = 0, A_2 \neq 0$, and $\mu = 0$ in Eq. 27, then we obtain the subsequent hyperbolic traveling wave solution:

$$v(x,t) = -\frac{\sqrt{c^2 - k^2}\sqrt{\lambda}}{\sqrt{2}h}\left(\tanh\left(\sqrt{-\lambda}\,\eta\right) - \sqrt{\sigma}\ \frac{1}{A_2}\mathrm{sech}\left(\sqrt{-\lambda}\,\eta\right)\right). \tag{28}$$

Family 1.2: If $A_1 \neq 0, A_2 = 0$and $\mu = 0$ in Eq. 27, we obtain the following hyperbolic traveling wave solution:

$$v(x,t) = -\frac{\sqrt{c^2-k^2}\sqrt{\lambda}}{\sqrt{2}h}\left(\coth\left(\sqrt{-\lambda}\,\eta\right) - \sqrt{\sigma}\ \frac{1}{A_1}\operatorname{cosech}\left(\sqrt{-\lambda}\,\eta\right)\right). \tag{29}$$

Case 2: By substituting Eq. 25 into Eq. 24 along with Eqs 5 and 9 for $\lambda > 0$, we can obtain a polynomial equation. Setting each polynomial coefficient to zero generates a system of algebraic equations for $a_0, a_1, b_1, \mu, \sigma, \lambda, c,$ and k. By solving this system of algebraic equations using software such as Mathematica, we can obtain the following outcomes:

$$a_0 = 0, a_1 = \frac{\sqrt{k^2-c^2}}{\sqrt{2}h}, b_1 = -\frac{\sqrt{k^2-c^2}\sqrt{\lambda}\sqrt{\sigma}}{\sqrt{2}h}, g = \frac{\sqrt{c^2-k^2}\sqrt{\lambda}}{\sqrt{2}}, \quad \mu = 0. \tag{30}$$

The periodic trigonometric traveling wave solution of Eq. 24 can be obtained by substituting Eq. 30 into Eq. 25, as follows:

$$v(x,t) = \frac{\sqrt{k^2-c^2}}{\sqrt{2}h}\left(\frac{A_1\sqrt{\lambda}\,\cos\left(\sqrt{\lambda}\,\eta\right) - A_2\sqrt{\lambda}\,\sin\left(\sqrt{\lambda}\,\eta\right)}{A_1\sin\left(\sqrt{\lambda}\,\eta\right) + A_2\cos\left(\sqrt{\lambda}\,\eta\right) + \frac{\mu}{\lambda}}\right), \\ -\frac{\sqrt{k^2-c^2}\sqrt{\lambda\sigma}}{\sqrt{2}h}\left(\frac{1}{A_1\sin\left(\sqrt{\lambda}\,\eta\right) + A_2\cos\left(\sqrt{\lambda}\,\eta\right) + \frac{\mu}{\lambda}}\right), \tag{31}$$

where $\sigma = {A_1}^2 + {A_2}^2$.

Family 2.1: If $A_1 = 0, A_2 \neq 0,$ and $\mu = 0$ in Eq. 31, we obtain the following trigonometric traveling wave solution:

$$v(x,t) = -\frac{\sqrt{k^2-c^2}\sqrt{\lambda}}{\sqrt{2}h}\left(\tan\left(\sqrt{\lambda}\,\eta\right) - \sqrt{\sigma}\ \frac{1}{A_2}sec\left(\sqrt{\lambda}\,\eta\right)\right), \tag{32}$$

$$v(x,t) = \frac{\sqrt{k^2-c^2}\sqrt{\lambda}}{\sqrt{2}h}\left(\cot\left(\sqrt{\lambda}\,\eta\right) - \sqrt{\sigma}\ \frac{1}{A_1}\cos ec\left(\sqrt{\lambda}\,\eta\right)\right). \tag{33}$$

4.2 Solutions with the modified (G'/G^2)-expansion method

Using the homogenous balance technique to the highest order derivatives with the nonlinear term in Eq. 24, we get $m = 1$. For $m = 1$, Eq. 16 has the form:

$$v(\eta) = a_0 + a_1\left(\frac{G'}{G^2}\right), \tag{34}$$

where a_0 and a_1 are unknown parameters. We can then substitute Eq. 34 and Eq. 17 into Eq. 24 and sum all coefficients of the same order. (G'/G^2) yields a set of algebraic equations involving $a_0, a_1,$ and other parameters. The set of algebraic equations is then solved using the symbolic computation software Mathematica, resulting in specific values for the unknown parameters:

$$a_0 = 0, a_1 = \pm\frac{ig\sqrt{\lambda_1}}{h\sqrt{\lambda_0}}, k = \pm\frac{\sqrt{-g^2+2c^2\lambda_0\lambda_1}}{\sqrt{2\lambda_0\lambda_1}}. \tag{35}$$

By substituting Eqs 35, 18, and 19 into Eq. 34 and considering the following cases, if $\lambda_1 < 0$, then

$$v_1(x,t) = -\frac{ig\sqrt{|\lambda_0\lambda_1|}}{h\sqrt{\lambda_0\lambda_1}} \left(1 - \frac{\lambda_1}{2}\left[\frac{C_1\sinh\left(\sqrt{\lambda_0\lambda_1}\,\eta\right) + C_2\cosh\left(\sqrt{\lambda_0\lambda_1}\,\eta\right)}{C_1\cosh\left(\sqrt{\lambda_0\lambda_1}\,\eta\right) + C_2\sinh\left(\sqrt{\lambda_0\lambda_1}\,\eta\right)}\right]\right), \tag{36}$$

$$v_2(x,t) = \frac{ig}{h}\left(\frac{C_1\sinh\left(\sqrt{\lambda_0\lambda_1}\,\eta\right) + C_2\cosh\left(\sqrt{\lambda_0\lambda_1}\,\eta\right)}{C_1\cosh\left(\sqrt{\lambda_0\lambda_1}\,\eta\right) + C_2\sinh\left(\sqrt{\lambda_0\lambda_1}\,\eta\right)}\right). \tag{37}$$

4.3 Solutions with the new auxiliary equation method

Using the homogenous balance technique to the highest order derivative with the nonlinear term in Eq. 24, we obtain $m = 1$. For $m = 1$, Eq. 24 has the form:

$$v(\eta) = a_0 + a_1\gamma^{f(\eta)}, \tag{38}$$

where a_0 and a_1 are unknown parameters.

Switching Eq. 10 into Eq. 24 with Eq. 22, we obtain the algebraic equations involving $a_0, a_1,$ and other parameters by equating all coefficients of different powers $\gamma^{f(\eta)}$ to zero:

$$\begin{aligned} &f^0(\eta):\ -a_0g^2 + {a_0}^3h^2 - a_1k^2\lambda\mu + a_1c^2\lambda\mu = 0,\\ &f^1(\eta):\ -a_1g^2 + 3{a_0}^2a_1h^2 - a_1k^2\lambda^2 + a_1c^2\lambda^2 - 2a_1k^2\zeta\mu + 2a_1c^2\zeta\mu = 0,\\ &f^2(\eta):\ 3a_0{a_1}^2h^2 - 3a_1k^2\zeta\lambda + 3a_1c^2\zeta\lambda = 0,\\ &f^3(\eta):\ {a_1}^3h^2 - 2a_1k^2\zeta^2 + 2a_1c^2\nu^2 = 0. \end{aligned} \tag{39}$$

Using mathematical software (Mathematica) to solve the aforementioned system of algebraic equations, we obtain the subsequent solution:

$$a_0 = \lambda\Lambda, a_1 = 2\zeta\,\Lambda, g = -\frac{\sqrt{k^2-c^2}\sqrt{\lambda^2-4\nu\mu}}{\sqrt{2}}, \tag{40}$$

where $\Lambda = \frac{\sqrt{k^2-c^2}}{\sqrt{2}\,h}$.

Substituting the attained solution Eq. 40 into Eq. 38, we obtain the following:

$$v(\eta) = \Lambda\left\{\lambda + 2\zeta\gamma^{f(\eta)}\right\}. \tag{41}$$

Substituting the solution stated by Eq. 22 into Eq. 41, the solutions regained are:

For Family 1: When $\lambda^2 - 4\mu\zeta < 0$ and $\zeta \neq 0$,

$$v_{1,1}(x,t) = \Lambda\left[\sqrt{4\mu\zeta-\lambda^2}\,\tan\left(\frac{\sqrt{4\mu\zeta-\lambda^2}}{2}\eta\right)\right], \tag{42}$$

$$v_{1,2}(x,t) = -\Lambda\left[\sqrt{4\mu\zeta-\lambda^2}\,\cot\left(\frac{\sqrt{4\mu\zeta-\lambda^2}}{2}\eta\right)\right]. \tag{43}$$

For Family 2: When $\lambda^2 - 4\mu\zeta > 0$ and $\zeta \neq 0$,

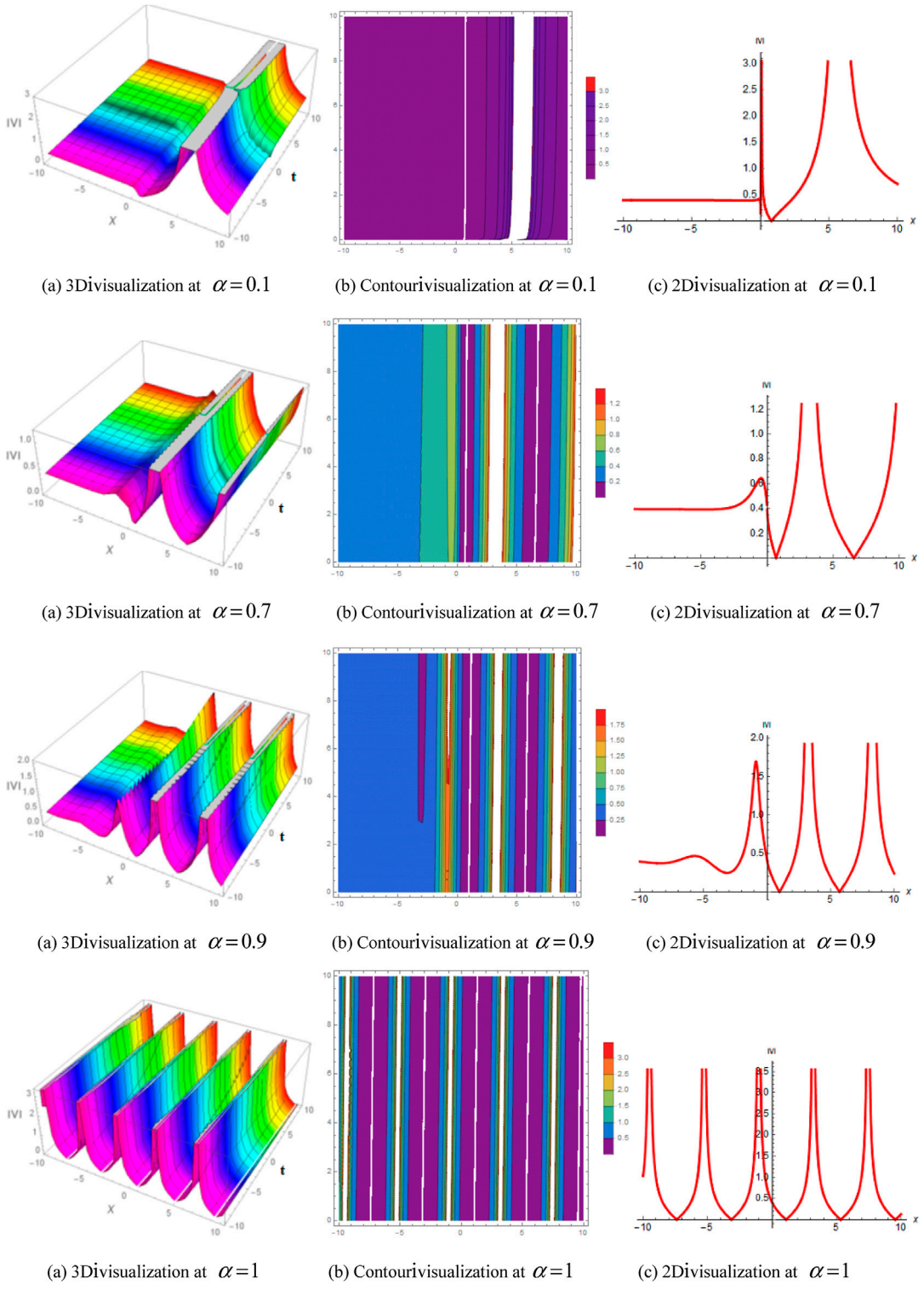

FIGURE 1
Influence of fractional order by 2D, 3D, and corresponding contours of Eq. 32 for $k = 2, h = 0.6, \lambda = 0.3, \beta = 0.5, A_2 = 2, \sigma = 4, c = 0.05, t = 1$. **Family 2.2:** If $A_1 \neq 0, A_2 = 0$ and $\mu = 0$ in Eq. 31, we obtain the following trigonometric traveling wave solution.

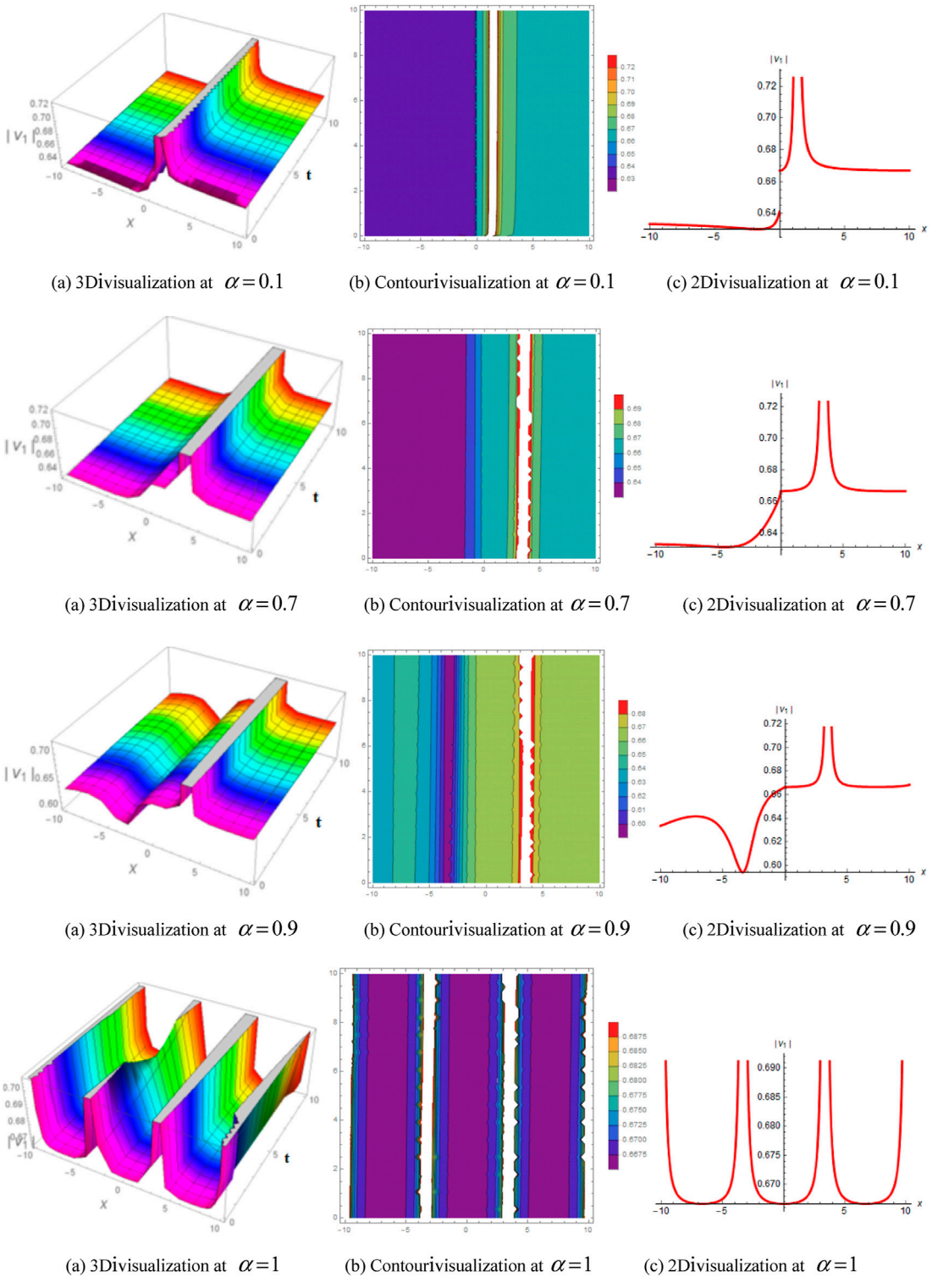

FIGURE 2
Influence of fractional order by 2D, 3D, and corresponding contours of Eq. 36 for $k = 2, h = 0.6, \lambda_0 = 0.4, \lambda_1 = -0.2, \beta = 0.5, c = 0.05, t = 1$. If $\lambda_0\lambda_1 > 0$, then

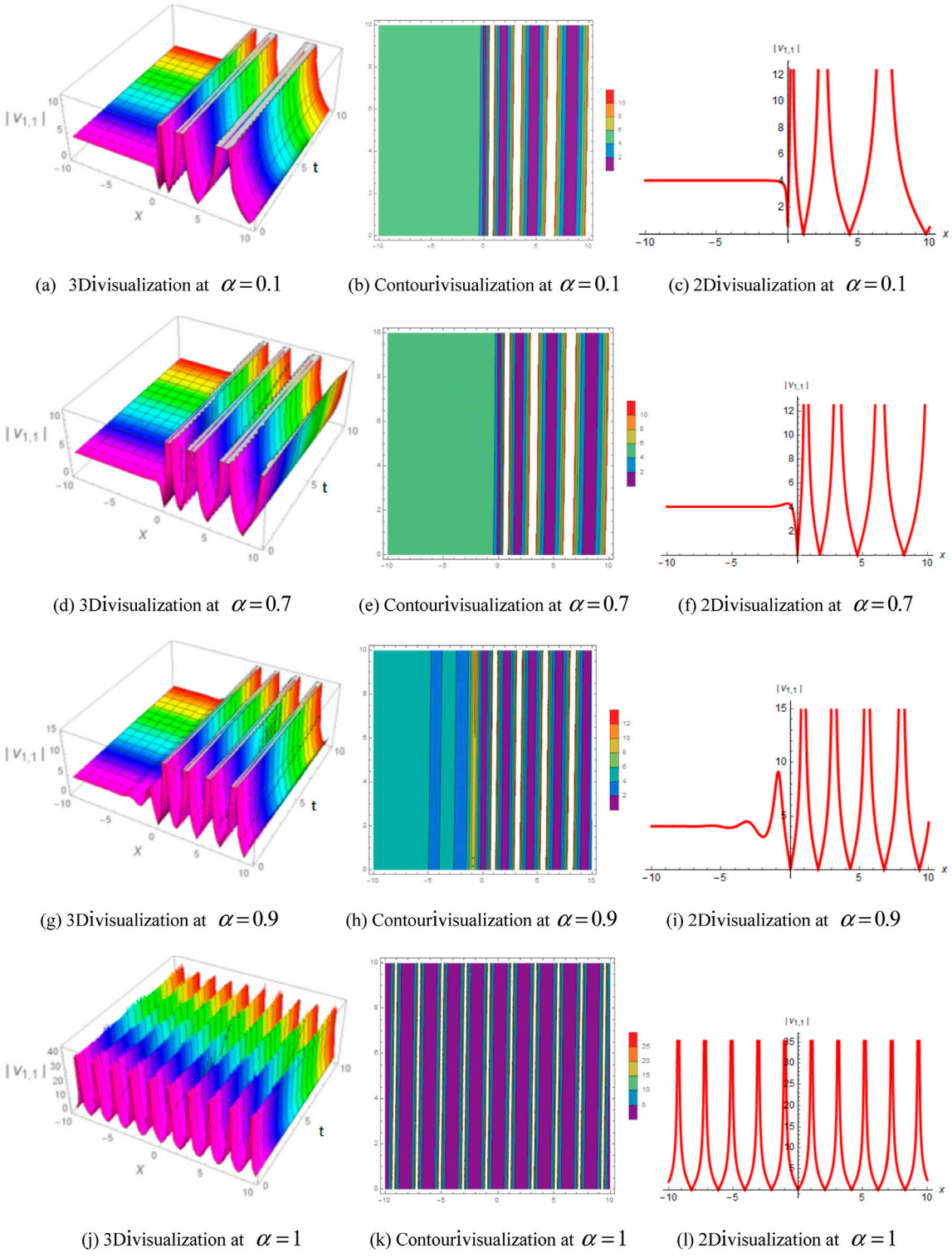

FIGURE 3
Influence of fractional order by 2D, 3D, and corresponding contours of Eq. 42 for $k = 2, h = 0.6, \lambda = 0.5, \beta = 0.5, \mu = 0.8, \zeta = 1, c = 0.05, t = 1$.

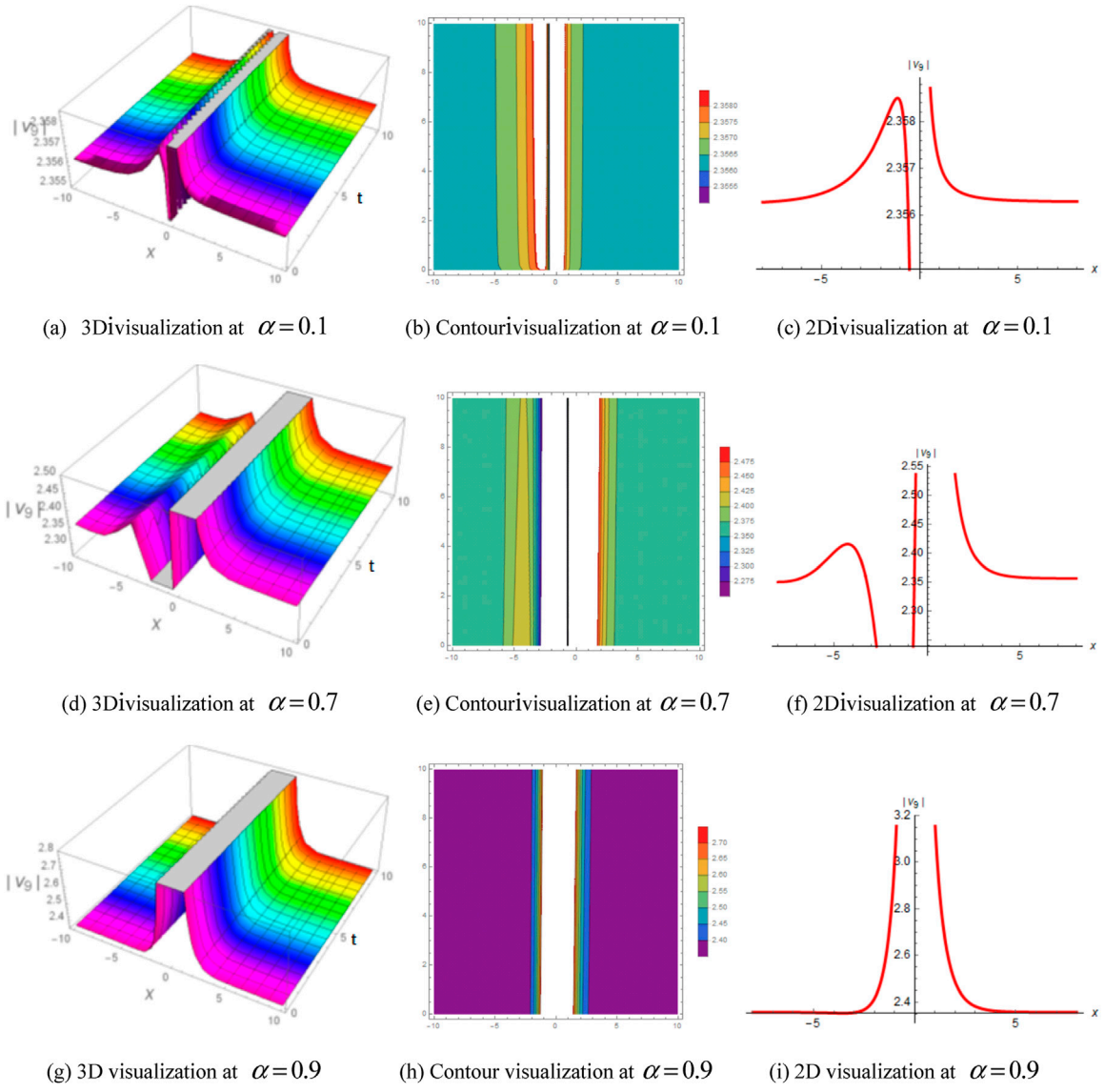

FIGURE 4
Influence of fractional order by 2D, 3D, and corresponding contours of Eq. 57 for $k = 2, h = 0.6, \lambda = 0.5, \beta = 0.5, \mu = 0.8, \zeta = 1, c = 0.05, t = 1$. For Family 12: When $\zeta = \lambda = K$ and $\mu = 0$,

$$v_{2,1}(x,t) = -\Lambda\left[\sqrt{\lambda^2 - 4\mu\zeta}\tanh\left(\frac{\sqrt{\lambda^2 - 4\mu\zeta}}{2}\eta\right)\right], \quad (44)$$

$$v_{2,2}(x,t) = -\Lambda\left[\sqrt{\lambda^2 - 4\mu\zeta}\coth\left(\frac{\sqrt{\lambda^2 - 4\mu\zeta}}{2}\eta\right)\right]. \quad (45)$$

For Family 3: When $\lambda^2 + 4\mu^2 < 0, \zeta \neq 0$ and $\zeta = -\mu$,

$$v_{3,1}(x,t) = \Lambda\left[\sqrt{-4\mu^2 - \lambda^2}\tan\left(\frac{\sqrt{-4\mu^2 - \lambda^2}}{2}\eta\right)\right], \quad (46)$$

$$v_{3,2}(x,t) = -\Lambda\left[\sqrt{-4\mu^2 - \lambda^2}\cot\left(\frac{\sqrt{-4\mu^2 - \lambda^2}}{2}\eta\right)\right]. \quad (47)$$

For Family 4: When $\lambda^2 + 4\mu^2 > 0, \zeta \neq 0$ and $\zeta = -\mu$,

$$v_{4,1}(x,t) = -\Lambda\left[\sqrt{4\mu^2 + \lambda^2}\tanh\left(\frac{\sqrt{4\mu^2 + \lambda^2}}{2}\eta\right)\right], \quad (48)$$

$$v_{4,2}(x,t) = -\Lambda\left[\sqrt{4\mu^2 + \lambda^2}\coth\left(\frac{\sqrt{4\mu^2 + \lambda^2}}{2}\eta\right)\right]. \quad (49)$$

For Family 5: When $\lambda^2 - 4\mu^2 < 0$ and $\zeta = \mu$,

$$v_{5,1}(x,t) = \Lambda\left[\sqrt{4\mu^2 - \lambda^2}\tan\left(\frac{\sqrt{4\mu^2 - \lambda^2}}{2}\eta\right)\right], \quad (50)$$

$$v_{5,2}(x,t) = -\Lambda\left[\sqrt{4\mu^2 - \lambda^2}\cot\left(\frac{\sqrt{4\mu^2 - \lambda^2}}{2}\eta\right)\right]. \quad (51)$$

For Family 6: When $\lambda^2 - 4\mu^2 > 0$ and $\zeta = \mu$,

$$v_{6,1}(x,t) = -\Lambda\left[\sqrt{\lambda^2 - 4\mu^2}\tanh\left(\frac{\sqrt{\lambda^2 - 4\mu^2}}{2}\eta\right)\right], \quad (52)$$

$$v_{6,2}(x,t) = -\Lambda\left[\sqrt{\lambda^2 - 4\mu^2}\coth\left(\frac{\sqrt{\lambda^2 - 4\mu^2}}{2}\eta\right)\right]. \quad (53)$$

For Family 7: When $\lambda^2 = 4\mu\zeta$,

$$v_7(x,t) = \frac{-2\Lambda}{\eta}. \quad (54)$$

For Family 8: When $\mu\zeta < 0, \lambda = 0$ and $\zeta \neq 0$,

$$v_{8,1}(x,t) = -\Lambda\left[2\sqrt{-\mu\zeta}\tanh\left(\sqrt{-\mu\zeta}\,\eta\right)\right], \quad (55)$$

$$v_{8,2}(x,t) = -\Lambda\left[2\zeta\sqrt{-\mu\zeta}\coth\left(\sqrt{-\mu\zeta}\,\eta\right)\right]. \quad (56)$$

For Family 9: When $\lambda = 0$ and $\mu = -\zeta$,

$$v_9(x,t) = \Lambda\left[2\zeta\left(\frac{e^{-2\zeta\eta}+1}{e^{-2\zeta\eta}-1}\right)\right], \quad (57)$$

$$v_{12}(x,t) = \Lambda\left[K + 2K\left(\frac{e^{K\eta}}{1-e^{K\eta}}\right)\right]. \quad (58)$$

For Family 13: When $\lambda = \mu + \zeta$,

$$v_{13}(x,t) = \Lambda\left[\mu + \zeta - 2\zeta\left(\frac{1-\mu e^{(\mu-\zeta)\eta}}{1-\zeta e^{(\mu-\zeta)\eta}}\right)\right]. \quad (59)$$

For Family 14: When $\lambda = -(\mu + \zeta)$,

$$v_{14}(x,t) = -\Lambda\left[\mu + \zeta - 2\zeta\left(\frac{\mu - e^{(\mu-\zeta)\eta}}{\zeta - e^{(\mu-\zeta)\eta}}\right)\right]. \quad (60)$$

For Family 15: When $\mu = 0$,

$$v_{15}(x,t) = \Lambda\left[\lambda + 2\zeta\left(\frac{\lambda e^{\lambda\eta}}{1-\zeta e^{\lambda\eta}}\right)\right]. \quad (61)$$

For Family 16: When $\lambda = \mu = \zeta \neq 0$,

$$v_{16}(x,t) = \Lambda\left[\lambda + \zeta\left(\sqrt{3}\,\tan\left(\frac{\sqrt{3}}{2}\mu\eta\right) - 1\right)\right]. \quad (62)$$

For Family 18: When $\lambda = \mu = 0$,

$$v_{18}(x,t) = -\frac{2\Lambda}{\eta}. \quad (63)$$

For Family 19: When $\mu = \zeta$ and $\lambda = 0$,

$$v_{19}(x,t) = 2\zeta\Lambda\tan(\mu\eta). \quad (64)$$

5 Graphical demonstration and explanation

To demonstrate the dynamics and behavior of our solutions, we used Eqs 32, 36, 42, and 17 to graphically represent the solutions in 3D, 2D, and contour graphs, which are shown in Figures 1–4. To illustrate the variation over time or to compare multiple wave items, 3D plots are often used. In this study, the wave points were arranged in a series with evenly spaced breaks and connected by a line to emphasize their relationships. In contrast, 2D line plots demonstrate very high and low frequency and amplitude. The authors note that the plots show the different natures of the solutions, such as periodic, singular-kink type, singular-bell shaped, and bright singular wave solutions. Furthermore, the authors emphasize that the correct physical description of the solutions can be generated by choosing distinct values for the fractional parameter α.

6 Conclusion

In this work, we applied the $(G'/G, 1/G)$-expansion, modified the (G'/G^2)-expansion, and provided new auxiliary equations methods in a satisfactory way to determine the novel soliton solutions of the space-time fractional LGHE by considering the truncated M-fractional derivative. These methods restored the periodic, singular-kink type, singular-bell shaped, and bright singular wave solutions dark, bright-singular, exponential, trigonometric, and rational solitons. Mathematica was utilized to perform the algebraic computations and generate graphical representations of the obtained solutions at different parameter values. Compared with other works [10, 23], our solutions have not been reported in the previous literature. These techniques are highly effective and robust for discovering soliton solutions for nonlinear fractional differential equations. Furthermore, the solutions obtained can provide deeper insights into the nonlinear dynamics of optical soliton propagation.

Data availability statement

The original contributions presented in the study are included in the article/Supplementary Material. Further inquiries can be directed to the corresponding author.

Author contributions

RZ, W-XM, SA, and IS contributed to the study conception and design. IS and AH organized the database. AH and SA performed the statistical analysis. RZ and KM wrote the first draft of the manuscript. W-XM, IS, and AH wrote sections of the manuscript. SA and AH writing-review and editing. SA is the project administrative. All authors contributed to the article and approved the submitted version.

Funding

This Project is funded by King Saud University, Riyadh, Saudi Arabia.

Acknowledgments

Research Supporting Project number (RSP2023R167), King Saud University, Riyadh, Saudi Arabia.

Conflict of interest

The authors declare that the research was conducted in the absence of any commercial or financial relationships that could be construed as a potential conflict of interest.

Publisher's note

References

1. Wazwaz. *Partial differential equations and solitary wave theory*. Berlin, Germany: Springer (2009).

2. Whitham GB. *Linear and nonlinear waves*. New York: Wiley (1972).

3. Wazwaz AM. The extended tanh method for abundant solitary wave solutions of nonlinear wave equations. *Appl Math Comput* (2007) 187:1131–42. doi:10.1016/j.amc.2006.09.013

4. Raza N, Zubair A. Bright, dark and dark-singular soliton solutions of nonlinear Schrödinger's equation with spatio-temporal dispersion. *J Mod Opt* (2018) 65:1975–82. doi:10.1080/09500340.2018.1480066

5. Seadawy AR. Two-dimensional interaction of a shear flow with a free surface in a stratified fluid and its solitary-wave solutions via mathematical methods. *Eur Phys J Plus* (2017) 132:518. doi:10.1140/epjp/i2017-11755-6

6. Hosseini K, Sadri K, Mirzazadeh M, Chu YM, Ahmadian A, Pansera BA, et al. A high-order nonlinear Schrödinger equation with the weak non-local nonlinearity and its optical solitons. *Results Phys* (2021) 23:104035. doi:10.1016/j.rinp.2021.104035

7. Hoan LVC, Owyed S, Inc M, Ouahid L, Abdou MA, Chu YM. New explicit optical solitons of fractional nonlinear evolution equation via three different methods. *Phys* (2020) 18:103209. doi:10.1016/j.rinp.2020.103209

8. Rezazadeh H, Ullah N, Akinyemi L, Shah A, Alizamin SMM, Chu YM, et al. Optical soliton solutions of the generalized non-autonomous nonlinear Schrödinger equations by the new Kudryashov's method. *Phys* (2021) 24:104179. doi:10.1016/j.rinp.2021.104179

9. Hu WP, Deng ZC, Han SM, Fa W. Multi-symplectic Runge-Kutta methods for Landau-Ginzburg-Higgs equation. *Appl Math Mech* (2009) 30(8):1027–34. doi:10.1007/s10483-009-0809-x

10. Bekir1 A, Unsal O. Exact solutions for a class of nonlinear wave equations by using First Integral Method. *Int J Nonlinear Sci* (2013) 15(2):99–110.

11. Cyrot M. Ginzburg-Landau theory for superconductors. *Rep Prog Phys* (1973) 36(2):103–58. doi:10.1088/0034-4885/36/2/001

12. Bekir A, Unsal O. Exact solutions for a class of nonlinear wave equations by using the first integral method. *Int J Nonlinear Sci* (2013) 15(2):99–110.

13. Iftikhar A, Ghafoor A, Jubair T, Firdous S, Mohyud-Din ST. The expansion method for travelling wave solutions of (2+1)-dimensional generalized KdV, sine Gordon and Landau-Ginzburg-Higgs equation. *Sci Res Essays* (2013) 8:1349–859.

14. Barman HK, Akbar MA, Osman MS, Nisar KS, Zakarya M, Abdel-Aty AH, et al. Solutions to the Konopelchenko-Dubrovsky equation and the Landau-Ginzburg-Higgs equation via the generalized Kudryashov technique. *Results Phys* (2021) 24:104092. doi:10.1016/j.rinp.2021.104092

15. Barman HK, Aktar MS, Uddin MH, Akbar MA, Baleanu D, Osman MS. Physically significant wave solutions to the Riemann wave equations and the Landau-Ginsburg-Higgs equation. *Results Phys* (2021) 27:104517. doi:10.1016/j.rinp.2021.104517

16. Islam ME, Akbar MA. Stable wave solutions to the Landau-Ginzburg-Higgs equation and the modified equal width wave equation using the IBSEF method. *Arab J Basic Appl Sci* (2020) 27(1):270–8. doi:10.1080/25765299.2020.1791466

17. Kilbas AA, Srivastava HM, Trujillo JJ. *Theory and applications of fractional differential equations*. Amsterdam: Elsevier (2006).

18. Miller S, Ross B. *An introduction to the fractional calculus and fractional differential equations*. New York, NY: Wiley (1993).

19. Caputo M, Fabrizio M. A new definition of Fractional differential without singular kernel. *Prog Fract Differ Appl* (2015) 1(2):1–13.

20. Khalil R, Horani MA, Yousef A, Sababheh M. A new definition of fractional derivativefinition of fractional derivative. *J Compu Appl Math* (2014) 264:65–70. doi:10.1016/j.cam.2014.01.002

21. Atangana A, Baleanu D, Alsaedi A. Analysis of time-fractional hunter-saxton equation: A model of neumatic liquid crystal. *Open Phys* (2016) 14:145–9. doi:10.1515/phys-2016-0010

22. Vanterler D, Sousa JC, Capelas deOliveira E. A new truncated M-fractional derivative type unifying some fractional derivative types with classical properties. *Int J Anal Appli* (2018) 16(1):83–96.

23. Deng SX, Ge XX. Analytical solution to local fractional Landau-Ginzburg-Higgs equation on fractal media. *Therm Sci* (2021) 25(6B):4449–55. doi:10.2298/tsci2106449d

24. Siddique I, Zafar A, Bukht Mehdi K, Osman M, Jaradat A, Zafar KB, et al. Exact traveling wave solutions for two prolific conformable M-Fractional differential equations via three diverse approaches. *Results Phys* (2021) 28:104557. doi:10.1016/j.rinp.2021.104557

25. Siddique I, Mehdi KB, Jaradat MMM, Zafar A, Elbrolosy ME, Elmandouh AA, et al. Bifurcation of some new traveling wave solutions for the time–space M-fractional MEW equation via three altered methods. *Results Phys* (2022) 41:105896. doi:10.1016/j.rinp.2022.105896

26. Sirendaoreji S. Auxiliary equation method and new solutions of Klein–Gordon equations. *Chaos Solitons Fractals* (2007) 31(4):943–50. doi:10.1016/j.chaos.2005.10.048

27. Rezazadeh H, Adel W, Tebue ET, Yao SW, Inc M. Bright and singular soliton solutions to the Atangana-Baleanu fractional system of equations for the ISALWs. *J King Saud Univ – Sci* (2021) 33:101420. doi:10.1016/j.jksus.2021.101420

28. Zayed EME, Abdelaziz MAM. The two variable G'G, 1G-expansion method for solving the nonlinear KdVmKdV equation. *Math Prob Engr., ID* (2012) 725061:14.

29. Zhang Y, Zhang L, pang J. Application of G'G2expansion method for solving Schrodinger's equation with three-order dispersion. *Adv Appl Math* (2017) 6(2):212–7.

30. Demiray S, Unsal O, Bekir A. New exact solutions for boussinesq type equations by using (G'/G, 1/G) and (1/G')-Expansion MethodsG'G, 1Gand 1G'expansion method. *Acta Phys Pol A* (2014) 125(5):1093–8. doi:10.12693/aphyspola.125.1093

31. Hafiz Uddin M. Close form solutions of the fractional generalized reaction duffing model and the density dependent fractional diffusion reaction equation. *Fractional Diffusion React Equation* (2017) 6(4):177–84. doi:10.11648/j.acm.20170604.13

32. Wazwaz AM. Couplings of a fifth order nonlinear integrable equation: Multiple kink solutions. *Comput Fluids* (2013) 84:97–9. doi:10.1016/j.compfluid.2013.05.020

33. Wazwaz AM. Kink solutions for three new fifth-order nonlinear equations. *Appl Math Model* (2014) 38:110–8. doi:10.1016/j.apm.2013.06.009

34. Sirisubtawee S, Koonprasert S, Sungnul S. Some applications of the (G′/G,1/G)-Expansion method for finding exact traveling wave solutions of nonlinear fractional evolution EquationsG'G,1Gexpansion method for finding exact traveling wave solutions of nonlinear fractional evolution equations. *Symmetry* (2019) 11:952. doi:10.3390/sym11080952

35. Mahak N, Akram G. Exact solitary wave solutions of the (1+1)-dimensional Fokas-Lenells equation. *Optik* (2020) 208:164459. doi:10.1016/j.ijleo.2020.164459

36. Noufe Aljahdaly H. Some applications of the modified G'G2expansion method in mathematical physics. *Results Phys* (2019) 13:102272. doi:10.1016/j.rinp.2019.102272

37. Daghan D, Donmez O. Exact solutions of the gardner equation and their applications to the different physical plasmas. *Braz J Phys* (2016) 46:321–33. doi:10.1007/s13538-016-0420-9

38. Ali MN, Husnine SM, Saha A, Bhowmik SK, Dhawan S, Ak T. Exact solutions, conservation laws, bifurcation of nonlinear and super nonlinear traveling waves for Sharma-Tasso-Olver equation. *Nonlinear Dyn* (2018) 94:1791–801. doi:10.1007/s11071-018-4457-x

39. Jhangeer A, Almusawa H, Rahman RU. Fractional derivative-based performance analysis to caudrey–dodd–gibbon–sawada–kotera equation. *Results Phys* (2022) 36:105356. doi:10.1016/j.rinp.2022.105356

40. Raza N, Jhangeer A, Rahman R, Butt AR, Chu YM. Sensitive visualization of the fractional wazwaz-benjamin-bona-mahony equation with fractional derivatives: A comparative analysis. *Results Phys* (2021) 25:104171. doi:10.1016/j.rinp.2021.104171

41. Riaz MB, Wojciechowski A, Oros GI, Rahman R. Soliton solutions and sensitive analysis of ModifiedEqual-width equation using fractional operators. *Symmetry* (2022) 14:1731. doi:10.3390/sym14081731

frontiers | Frontiers in Physics

TYPE Original Research
PUBLISHED 03 July 2023
DOI 10.3389/fphy.2023.1237805

OPEN ACCESS

EDITED BY
Xiangpeng Xin,
Liaocheng University, China

REVIEWED BY
Yongshuai Zhang,
Zhejiang University of Science and Technology, China
Biao Li,
Ningbo University, China

*CORRESPONDENCE
Bo Ren,
renbosemail@163.com

RECEIVED 10 June 2023
ACCEPTED 15 June 2023
PUBLISHED 03 July 2023

CITATION
Lyu J, Shi K, Ren B and Jin Y (2023), New symmetry reduction method for (1+1)-dimensional differential-difference equations.
Front. Phys. 11:1237805.
doi: 10.3389/fphy.2023.1237805

New symmetry reduction method for (1+1)-dimensional differential-difference equations

Jielin Lyu[1], Kaizhong Shi[2], Bo Ren[2]* and Yongyang Jin[2]

[1]School of Continuing Education, Zhejiang Business College, Hangzhou, China, [2]Department of Applied Mathematics, Zhejiang University of Technology, Hangzhou, China

We propose a new symmetry reduction method for (1+1)-dimensional differential-difference equations (DDEs), namely, the λ-symmetry reduction method of solving ordinary differential equations is generalized to DDEs. Order-reduction processes are a consequence of the invariance of the given DDE under vector fields of the new class. These vector fields satisfy a new prolongation formula. A simple example of order-reduction is provided to illustrate the application.

KEYWORDS

λ-symmetry, differential-difference equation, order-reduction, vector field, reduction method

1 Introduction

Symmetry is closely related to the integrability of the nonlinear evolution equations (NLEEs) in various specific meanings. For example, the existence of infinite Lie-Bäcklund symmetry is a criterion for the integrability of NLEEs, so the study of symmetry of NLEEs is particularly important. The symmetry of the NLEEs is studied systematically by Lie point symmetry theory [1–3]. Although the Lie point symmetry method has relatively mature theories, it also has great limitations [1–10]. When a given NLEE does not allow enough non-trivial Lie point symmetries, this method cannot be applied. Therefore, it is necessary to extend the classical Lie point symmetry concept from various angles [11–20]. For example, if the infinitesimal also depends on the higher derivative, the corresponding Lie-Bäcklund symmetry is obtained [21, 22].

The concept of λ-symmetry proposed by Muriel and Romero [23], aims to show that many of the known order-reduction processes can be explained by the invariance of the equation under some special vector fields that are neither Lie symmetries nor Lie-Bäcklund symmetries. The λ-symmetry reduction method for ordinary differential equations (ODEs) has attracted the attention of more and more scientists [24]. For example, Levi and Rodriguez successfully extended this method to the case of difference equations [25]. Again, the μ-symmetry reduction method is used to deal with partial differential equations (PDEs) [26–30].

For the sake of readability, we will briefly introduce the λ-symmetry reduction method for ODEs in Section 2. Then we extend the λ-symmetry reduction method to the case of (1+1)-dimensional differential-difference equations (DDEs) in Section 3. The last section is devoted to conclusions and discussions.

2 The λ-symmetry reduction method of ODEs

In this section we briefly review the λ-symmetry reduction method of ODEs. For a given mth-order ODE

$$\Delta_1 \equiv \Delta\left(x, u^{(0)}, u^{(1)}, \ldots, u^{(m)}\right) = 0, \tag{1}$$

we can set a vector field

$$v = X(x,u)\frac{\partial}{\partial x} + U(x,u)\frac{\partial}{\partial u}, \tag{2}$$

where $u^{(i)} = \frac{\mathrm{d}^i u(x)}{\mathrm{d}x^i}$, $(i = 0, 1, \ldots, m)$ means the ith-order derivative with respect to the independent variable x. Thus we can construct high-order infinitesimal prolongation vector field

$$v^{[(m)]} = v + \sum_{i=1}^{m} U^{[(i)]}\frac{\partial}{\partial u^{(i)}}, \tag{3}$$

where

$$\begin{aligned} U^{[(0)]} &= U, \\ U^{[(i+1)]} &= D_x U^{[(i)]} - u^{(i+1)} D_x X, \qquad i = 0, 1, \ldots, m. \end{aligned} \tag{4}$$

Here D_x means the total derivative with respect to x. So the invariance of Eq. 1 needs

$$v^{[(m)]}(\Delta_1)\big|_{\Delta_1=0} = 0. \tag{5}$$

Solving this equation, the expressions for X and U can be derived. For complex high-order ODEs or systems, we need to use symbolic computing software to calculate X and U. Theoretically, all of the similarity variables be derived by solving the following characteristic equation

$$\frac{\mathrm{d}x}{X} = \frac{\mathrm{d}u}{U}, \tag{6}$$

and then we can reduce and solve Eq. 1.

The above method is the Lie point symmetry method, also known as the classical symmetry reduction method. In Ref. [23], authors have introduced a new class of symmetries, that strictly includes Lie point symmetries, for which there exists an algorithm that lets us reduce the order of a given ODE. This method is now called the λ-symmetry reduction method. The key step of this generalized method is that the infinitesimal prolongation is modified to the following form

$$\begin{aligned} U^{[\lambda,(i)]}\left(x,u^{(i)}\right) = {} & D_x\left(U^{[\lambda,(i-1)]}\left(x,u^{(i-1)}\right)\right) - D_x\left(X(x,u)\right)u^{(i)} \\ & + \lambda\left(U^{[\lambda,(i-1)]}\left(x,u^{(i-1)}\right) - X(x,u)u^{(i)}\right), \end{aligned} \tag{7}$$

where λ is a smooth function that is determined simultaneously with the coefficients of the infinitesimal generators X and U. Thus the infinitesimal prolongation vector field is modified to

$$v^{[\lambda,(m)]} = X(x,u)\frac{\partial}{\partial x} + \sum_{i=0}^{m} U^{[\lambda,(i)]}\left(x,u^{(i)}\right)\frac{\partial}{\partial u^{(i)}}. \tag{8}$$

The following theorem that is important for the λ-symmetry reduction method, which is first obtained by Muriel and Romero [23].

Theorem 1. (Muriel, Romero [23]). *Let us suppose that, for some smooth functions λ, the vector field v is a λ-symmetry of the following ODE*

$$u^{(m)} = F\left(x, u^{(0)}, u^{(1)}, \ldots, u^{(m-1)}\right). \tag{9}$$

Then

$$\left[v^{[\lambda,(m-1)]}, A\right] = \lambda \cdot v^{[\lambda,(m-1)]} + \mu \cdot A, \tag{10}$$

for some smooth functions μ. Here A is the vector field of Eq. 9,

$$A = \frac{\partial}{\partial x} + u^{(1)}\frac{\partial}{\partial u} + \cdots + F\left(x, u^{(0)}, u^{(1)}, \ldots, u^{(m-1)}\right)\frac{\partial}{\partial u^{(m-1)}}. \tag{11}$$

Conversely, if

$$K = X(x,u)\frac{\partial}{\partial x} + U^{(0)}(x,u)\frac{\partial}{\partial u} + \sum_{i=1}^{m-1} U^{(i)}\left(x,u^{(i)}\right)\frac{\partial}{\partial u_i}, \tag{12}$$

is a vector field such that

$$[K, A] = \lambda \cdot K + \mu \cdot A, \tag{13}$$

for some smooth functions λ, μ, then the vector field

$$v = X(x,u)\frac{\partial}{\partial x} + U^{(0)}(x,u)\frac{\partial}{\partial u}, \tag{14}$$

is a λ-symmetry of Eq. 9 *and $K = v^{[\lambda,(m-1)]}$.*

3 The λ-symmetry reduction method of DDEs

In this section, we extend the λ-symmetry reduction method to the case of (1+1)-dimensional DDEs.

Definition 1. *For the following (1+1)-dimensional DDE with a discrete variable n and a continuous variable x,*

$$\Delta_2 \equiv \Delta\left(x, u_{n-1}^{(0)}, u_n^{(0)}, u_{n+1}^{(0)}, \ldots, u_{n-1}^{(m)}, u_n^{(m)}, u_{n+1}^{(m)}\right) = 0, \tag{15}$$

where $u_n^{(i)} = \frac{\mathrm{d}^i u_n(x)}{\mathrm{d}x^i}$, the vector field

$$\begin{aligned} v = {} & X(x,u_n)\frac{\partial}{\partial x} + U_{n-1}(x,u_{n-1})\frac{\partial}{\partial u_{n-1}} + U_n(x,u_n)\frac{\partial}{\partial u_n} \\ & + U_{n+1}(x,u_{n+1})\frac{\partial}{\partial u_{n+1}} \end{aligned}$$

is said to be λ-symmetry for this equation if there exists a differential function λ such that the mth λ-prolongation of the vector field satisfies.

$$v^{[\lambda,(m)]}(\Delta_2)\big|_{\Delta_2=0} = 0. \tag{16}$$

Particularly, for the following (1+1)-dimensional DDE

$$u_n^{(m)} = F_n\left(x, u_{n-1}^{(m-1)}, u_n^{(m-1)}, u_{n+1}^{(m-1)}\right), \tag{17}$$

we can set a vector field

$$\begin{aligned} A = {} & \frac{d}{dx} + \sum_{n=-1}^{1} u_{n+k}^{(1)}\frac{d}{du_{n+k}} + \cdots \\ & + \sum_{k=-1}^{1} F_{n+k}\left(\lambda, u_{n+k-1}^{(m-1)}, u_{n+k}^{(m-1)}, u_{n+k+1}^{(m-1)}\right)\frac{\partial}{u_{n+k}^{(m-1)}}. \end{aligned} \tag{18}$$

Here $F_n(x, u_{n-1}^{(m-1)}, u_n^{(m-1)}, u_{n+1}^{(m-1)}) = F_n(x, u_{n-1}^{(0)}, u_n^{(0)}, u_{n+1}^{(0)}, \ldots, u_{n-1}^{(m-1)}, u_n^{(m-1)}, u_{n+1}^{(m-1)})$ is for ease of writing. So we have Theorem 2.

Theorem 2. *Let us suppose that, for some differential functions λ, the vector field v is a λ-symmetry of the following DDE*

$$u_n^{(m)} = F_n\left(x, u_{n-1}^{(m-1)}, u_n^{(m-1)}, u_{n+1}^{(m-1)}\right), \tag{19}$$

Then

$$\left[v^{[\lambda,(m-1)]}, A\right] = \lambda \cdot v^{[\lambda,(m-1)]} + \mu \cdot A. \tag{20}$$

for some differential functions μ. Here A is the vector field of Eq. 19,

$$A = \frac{d}{dx} + \sum_{n=-1}^{1} u_{n+k}^{(1)} \frac{d}{du_{n+k}} + \cdots + \sum_{k=-1}^{1} F_{n+k}\left(\lambda, u_{n+k-1}^{(m-1)}, u_{n+k}^{(m-1)}, u_{n+k+1}^{(m-1)}\right) \frac{\partial}{u_{n+k}^{(m-1)}}. \tag{21}$$

Conversely, if

$$K = X(x, u_n)\frac{\partial}{\partial x} + \sum_{k=-1}^{1}\sum_{i=0}^{m-1} U_{n+k}^{(i)}\left(x, u_{n+k}^{(i)}\right)\frac{\partial}{\partial u_{n+k}^{(i)}}, \tag{22}$$

is a vector field such that

$$[K, A] = \lambda \cdot K + \mu \cdot A, \tag{23}$$

for some differential functions λ and μ, then the vector field

$$v = X(x,u)\frac{\partial}{\partial x} + U_{n-1}^{(0)}(x,u)\frac{\partial}{\partial u_{n-1}} + U_n^{(0)}(x,u)\frac{\partial}{\partial u_n} + U_{n+1}^{(0)}(x,u)\frac{\partial}{\partial u_{n+1}}, \tag{24}$$

is a λ-symmetry of Eq. 19 *and* $K = v^{[\lambda,(m-1)]}$.

Proof. Compute $[v^{[\lambda,(m-1)]}, A]$ as a function of $\{x, u_{n-1}, u_n, u_{n+1}, \ldots, u_{n-1}^{(m-1)}, u_n^{(m-1)}, u_{n+1}^{(m-1)}\}$ at each lattice point, with

$$\begin{aligned}
\left[v^{[\lambda,(m-1)]}, A\right](x) &= -A(X(x)),\\
\left[v^{[\lambda,(m-1)]}, A\right](u_{n+k}) &= U_{n+k}^{[\lambda,(1)]}\left(x, u_{n+k}^{(1)}\right) - A\left(U_{n+k}^{[\lambda,(0)]}(x, u_{n+k})\right)\\
&= -A(X(x))u_{n+k}^{(1)} + \lambda\left(U_{n+k}^{[\lambda,(0)]}(x, u_{n+k}) - X(x)u_{n+k}^{(1)}\right),\\
\left[v^{[\lambda,(m-1)]}, A\right]\left(u_{n+k}^{(1)}\right) &= U_{n+k}^{[\lambda,(2)]}\left(x, u_{n+k}^{(2)}\right) - A\left(U_{n+k}^{[\lambda,(1)]}\left(x, u_{n+k}^{(1)}\right)\right)\\
&= -A(X(x))u_{n+k}^{(2)} + \lambda\left(U_{n+k}^{[\lambda,(1)]}\left(x, u_{n+k}^{(1)}\right) - X(x)u_{n+k}^{(2)}\right),\\
&\vdots\\
\left[v^{[\lambda,(m-1)]}, A\right]\left(u_{n+k}^{(i)}\right) &= U_{n+k}^{[\lambda,(i+1)]}\left(x, u_{n+k}^{(i+1)}\right) - A\left(U_{n+k}^{[\lambda,(i)]}\left(x, u_{n+k}^{(i)}\right)\right)\\
&= -A(X(x))u_{n+k}^{(i+1)} + \lambda\left(U_{n+k}^{[\lambda,(i)]}\left(x, u_{n+k}^{(i)}\right) - X(x)u_{n+k}^{(i+1)}\right),\\
&\vdots\\
\left[v^{[\lambda,(m-1)]}, A\right]\left(u_{n+k}^{(m-1)}\right) &= v^{[\lambda,(m-1)]}\left(F_{n+k}\left(\lambda, u_{n+k-1}^{(m-1)}, u_{n+k}^{(m-1)}, u_{n+k+1}^{(m-1)}\right)\right)\\
&\quad - A\left(U_{n+k}^{[\lambda,(n-1)]}\left(x, u_{n+k}^{(m-1)}\right)\right),
\end{aligned} \tag{25}$$

and

$$v^{[\lambda,(m)]}\left(u_{n+k}^{(m)}\right) = D_x\left(U_{n+k}^{[\lambda,(m-1)]}\left(x, u_{n+k}^{(m-1)}\right)\right) - D_x(X(x))u_{n+k}^{(m)} + \lambda\left(U_{n+k}^{[\lambda,(m-1)]}\left(x, u_{n+k}^{(m-1)}\right)\right) - \lambda(X(x))u_{n+k}^{(m)}. \tag{26}$$

Since v is a λ-symmetry,

$$v^{[\lambda,(m-1)]}\left(F_{n+k}\left(\lambda, u_{n+k-1}^{(m-1)}, u_{n+k}^{(m-1)}, u_{n+k+1}^{(m-1)}\right)\right) = A\left(U_{n+k}^{[\lambda,(m-1)]}\left(x, u_{n+k}^{(m-1)}\right)\right) - A(X(x))u_{n+k}^{(m)} + \lambda\left(U_{n+k}^{[\lambda,(m-1)]}\left(x, u_{n+k}^{(m-1)}\right)\right) - \lambda(X(x))u_{n+k}^{(m)}. \tag{27}$$

Hence, if $u_n^{(m)} = F_n(x, u_{n-1}^{(m-1)}, u_n^{(m-1)}, u_{n+1}^{(m-1)})$, Eq. 26 says that

$$[\lambda, (m-1)]\left(F_{n+k}\left(\lambda, u_{n+k-1}^{(m-1)}, u_{n+k}^{(m-1)}, u_{n+k+1}^{(m-1)}\right)\right) = A\left(U_{n+k}^{[\lambda,(m-1)]}\left(x, u_{n+k}^{(m-1)}\right)\right) - A(X(x))u_{n+k}^{(m)} + \lambda\left(U_{n+k}^{[\lambda,(m-1)]}\left(x, u_{n+k}^{(m-1)}\right)\right) - \lambda(X(x))u_{n+k}^{(m)}. \tag{28}$$

If we set $\mu = -A(X(x)) - \lambda X(x)$, then we can write

$$\begin{aligned}
\left[v^{[\lambda,(m-1)]}, A\right](x) &= \lambda X(x) + \mu,\\
\left[v^{[\lambda,(m-1)]}, A\right](u_{n+k}) &= \lambda U_{n+k}^{[\lambda,(0)]}(x, u_{n+k}) + \mu u_{n+k}^{(1)},\\
\left[v^{[\lambda,(m-1)]}, A\right]\left(u_{n+k}^{(1)}\right) &= \lambda U_{n+k}^{[\lambda,(1)]}\left(x, u_{n+k}^{(1)}\right) + \mu u_{n+k}^{(2)},\\
&\vdots\\
\left[v^{[\lambda,(m-1)]}, A\right]\left(u_{n+k}^{(i)}\right) &= \lambda U_{n+k}^{[\lambda,(i)]}\left(x, u_{n+k}^{(i)}\right) + \mu u_{n+k}^{(i+1)},\\
&\vdots\\
\left[v^{[\lambda,(m-1)]}, A\right]\left(u_{n+k}^{(m-1)}\right) &= \lambda U_{n+k}^{[\lambda,(m-1)]}\left(x, u_{n+k}^{(m-1)}\right) + \mu u_{n+k}^{(m)}
\end{aligned} \tag{29}$$

Therefore, we conclude that $[v^{[\lambda,(m-1)]}, A] = \lambda \cdot v^{[\lambda,(m-1)]} + \mu \cdot A$. The vector field

$$K = X(x, u_n)\frac{\partial}{\partial x} + \sum_{k=-1}^{1}\sum_{i=0}^{m-1} U_{n+k}^{(i)}\left(x, u_{n+k}^{(i)}\right)\frac{\partial}{\partial u_{n+k}^{(i)}}, \tag{30}$$

depends on three lattice points with $n-1$, n and $n+1$. If we apply both elements of this equation to each coordinate function, we obtain

$$\mu = -A(X(x,u)) - \lambda X(x,u), \tag{31}$$

and, for $0 \le i \le m-2$, the coordinate $U_{n+k}^{(i)}(x, u_{n+k}^{(i)})$ of K must satisfy

$$U_{n+k}^{[\lambda,(i+1)]}\left(x, u_{n+k}^{(i+1)}\right) = D_x\left(U_{n+k}^{[\lambda,(i)]}\left(x, u_{n+k}^{(i)}\right)\right) - D_x(X(x))u_{n+k}^{(i+1)} + \lambda\left(U_{n+k}^{[\lambda,(i)]}\left(x, u_{n+k}^{(i)}\right)\right) - \lambda(X(x))u_{n+k}^{(i+1)}. \tag{32}$$

Hence

$$K = v^{[\lambda,(m-1)]}. \tag{33}$$

Then we apply both elements of $[K, A] = \lambda K + \mu A$, to the coordinate function $u_{n-1}^{(m-1)}$, $u_n^{(m-1)}$ and $u_{n+1}^{(m-1)}$, we obtain

$$\begin{aligned}
[K, A]\left(u_{n+k}^{(m-1)}\right) &= K\left(F_{n+k}\left(\lambda, u_{n+k-1}^{(m-1)}, u_{n+k}^{(m-1)}, u_{n+k+1}^{(m-1)}\right)\right) - A\left(U_n^{[\lambda,(m-1)]}\left(x, u_{n+k}^{(m-1)}\right)\right)\\
&= \lambda U_{n+k}^{[\lambda,(m-1)]}\left(x, u_{n+k}^{(m-1)}\right)\\
&\quad -(A(X(x)) + \lambda X(x)) \cdot \left(F_{n+k}\left(\lambda, u_{n+k-1}^{(m-1)}, u_{n+k}^{(m-1)}, u_{n+k+1}^{(m-1)}\right)\right),
\end{aligned} \tag{34}$$

where $k = -1, 0, 1$. The above equation yields

$$\begin{aligned}
&K\left(F_{n+k}\left(\lambda, u_{n+k-1}^{(m-1)}, u_{n+k}^{(m-1)}, u_{n+k+1}^{(m-1)}\right)\right)\\
&= A\left(U_{n+k}^{[\lambda,(m-1)]}\left(x, u_{n+k}^{(m-1)}\right)\right) + \lambda U_{n+k}^{[\lambda,(m-1)]}\left(x, u_{n+k}^{(m-1)}\right)\\
&\quad -(A(X(x)) + \lambda X(x)) \cdot \left(F_{n+k}\left(\lambda, u_{n+k-1}^{(m-1)}, u_{n+k}^{(m-1)}, u_{n+k+1}^{(m-1)}\right)\right).
\end{aligned} \tag{35}$$

Calculate

$$\begin{aligned}
&v^{[\lambda,(m)]}\left(u_{n+k}^{(m)} - F_{n+k}\left(x, u_{n+k-1}^{(m-1)}, u_{n+k}^{(m-1)}, u_{n+k+1}^{(m-1)}\right)\right)\\
&= D_x\left(U_{n+k}^{[\lambda,(m-1)]}\left(x, u_{n+k}^{(m-1)}\right)\right) - D_x(X(x))u_{n+k}^{(m)}\\
&\quad + \lambda\left(U_{n+k}^{[\lambda,(m-1)]}\left(x, u_{n+k}^{(m-1)}\right) - X(x)u_{n+k}^{(m)}\right)\\
&\quad -K\left(F_{n+k}\left(x, u_{n+k-1}^{(m-1)}, u_{n+k}^{(m-1)}, u_{n+k+1}^{(m-1)}\right)\right)
\end{aligned} \tag{36}$$

when $u_n^{(m)} = F_n(x, u_{n-1}^{(m-1)}, u_n^{(m-1)}, u_{n+1}^{(m-1)})$, we obtain, by Eq. 35, that

$$v^{[\lambda,(m)]}\left(\Delta\left(x, u_{n-1}^{(0)}, u_n^{(0)}, u_{n+1}^{(0)}, \ldots, u_{n-1}^{(m)}, u_n^{(m)}, u_{n+1}^{(m)}\right)\right) = 0, \quad \text{when} \quad u_{n+k}^{(m)} = F_{n+k}\left(\lambda, u_{n+k-1}^{(m-1)}, u_{n+k}^{(m-1)}, u_{n+k+1}^{(m-1)}\right). \tag{37}$$

Therefore v is a λ-symmetry of Eq. 19.

In order to reduce the mth-order DDEs to $(m-1)$th-order DDEs and first-order DDEs, we can determine invariants for the λ-prolongation of v by deriving invariants of lower order. This can be achieved through the application of the main tools, Theorem 2.

Theorem 3. *Let v be a vector field defined on M and let λ is a differential function, If*

$$\alpha = \alpha\left(x, u_{n-1}^{(k)}, u_n^{(k)}, u_{n+1}^{(k)}\right), \quad \beta = \beta\left(x, u_{n-1}^{(k)}, u_n^{(k)}, u_{n+1}^{(k)}\right), \tag{38}$$

are such that

$$v^{[\lambda,(k)]}\left(\alpha\left(x, u_{n-1}^{(k)}, u_n^{(k)}, u_{n+1}^{(k)}\right)\right) = v^{[\lambda,(k)]}\left(\beta\left(x, u_{n-1}^{(k)}, u_n^{(k)}, u_{n+1}^{(k)}\right)\right) = 0, \tag{39}$$

then

$$v^{[\lambda,(k+1)]}\left(\frac{D_x\alpha\left(x, u_{n-1}^{(k)}, u_n^{(k)}, u_{n+1}^{(k)}\right)}{D_x\beta\left(x, u_{n-1}^{(k)}, u_n^{(k)}, u_{n+1}^{(k)}\right)}\right) = 0. \tag{40}$$

Proof 3. By Theorem 2, we have

$$\left[v^{[\lambda,(k+1)]}, D_x\right] = \lambda v^{[\lambda,(k+1)]} + \mu D_x, \tag{41}$$

where $\mu = -D_x(v(x)) - \lambda v(x)$. Therefore,

$$\begin{aligned} v^{[\lambda,(k+1)]}\left(\frac{D_x\alpha}{D_x\beta}\right) &= \frac{1}{(D_x\beta)^2}\left(D_x\beta \cdot v^{[\lambda,(k+1)]}(D_x\alpha) - D_x\alpha \cdot v^{[\lambda,(k+1)]}(D_x\beta)\right) \\ &= \frac{1}{(D_x\beta)^2}\left(D_x\beta \cdot \left[v^{[\lambda,(k+1)]}, D_x\right](\alpha) - D_x\alpha \cdot \left[v^{[\lambda,(k+1)]}, D_x\right](\beta)\right) \\ &= \frac{1}{(D_x\beta)^2}\left(D_x\beta \cdot (\mu \cdot D_x\alpha) - D_x\alpha \cdot (\mu \cdot D_x\beta)\right) = 0. \end{aligned} \tag{42}$$

Proposition 1. *Let v be a λ-symmetry. Let*

$$y = y\left(x, u_{n-1}, u_n, u_{n+1}\right) \quad \text{and} \quad w = w\left(x, u_{n-1}, u_n, u_{n+1}, u_{n-1}^{(1)}, u_n^{(1)}, u_{n+1}^{(1)}\right)$$

be two functionally independent first-order invariants of $v^{[\lambda,(m)]}$. By solving an equation of $\Delta_r\left(y, w^{(m-1)}\right) = 0$ and an auxiliary equation $w = w\left(x, u_{n-1}, u_n, u_{n+1}, u_{n-1}^{(1)}, u_n^{(1)}, u_{n+1}^{(1)}\right)$, the general solution of the equation can be obtained.

With the help of independent first-order invariant, we demonstrate a simple application of λ-symmetry. Considering a (1+1)-dimensional DDE

$$u_n^{(2)} = \left[(x + x^2)e^{u_{n+1}}\right]_x, \tag{43}$$

Eq. 43 has the from

$$u_n^{(2)} = D_x\left(F_n\left(x, u_{n+1}\right)\right), \tag{44}$$

which admits the obvious order reduction

$$u_n^{(1)} = F_n\left(x, u_{n+1}\right) + C, \quad C \in \mathbb{R}. \tag{45}$$

Letting $X(x) = 0$, $U_{n-1}(x, u_{n-1}) = 1$, $U_n(x, u_n) = 1$, $U_{n+1}(x, u_{n+1}) = 1$ and $\lambda = F_{n,u_{n+1}}\left(x, u_{n+1}\right)$, we have the following λ-prolongation vector field

$$\begin{aligned} v^{[\lambda,(2)]} = &\frac{\partial}{\partial u_{n-1}} + \frac{\partial}{\partial u_n} + \frac{\partial}{\partial u_{n+1}} + F_{n,u_{n+1}}\left(\frac{\partial}{\partial u_{n-1}^{(1)}} + \frac{\partial}{\partial u_n^{(1)}} + \frac{\partial}{\partial u_{n+1}^{(1)}}\right) \\ &+\left(F_{n,u_{n+1}}^2 + u_{n+1}^{(1)}F_{n,u_{n+1}u_{n+1}} + F_{n,xu_{n+1}}\right)\left(\frac{\partial}{\partial u_{n-1}^{(2)}} + \frac{\partial}{\partial u_n^{(2)}} + \frac{\partial}{\partial u_{n+1}^{(2)}}\right), \end{aligned} \tag{46}$$

We can easily prove that the vector field v is the λ-symmetry of Eq. 43. The λ-symmetry generator has two obvious invariants $z = x$, $w = u_n^{(1)} - F_n\left(x, u_{n+1}\right)$. Furthermore, the differential invariant $w_z = \frac{D_x w}{D_x Z} = u_n^{(2)} - D_x\left(F_n\left(x, u_{n+1}\right)\right)$. Therefore, Eq. 43 can be reduced to Eq. 45.

4 Conclusion

λ-symmetry reduction method is useful in establishing effective alternative methods analyze ODEs without using Lie point symmetries. At present, there is no programmatic algorithm package to solve λ-symmetry directly. Therefore, it is difficult to determine the general form of λ.

There are many examples of DDEs, without Lie point symmetries, that can be completely integrated. So we have to study the reduction of these DDEs. In this paper, we have extended the λ-symmetry reduction method to the case of (1+1)-dimensional DDEs. We have obtained some theorems Theorem 2, 3 and Proposition 1 which can be used to reduce and solve DDEs in Section 3. By comparison, DDEs can be more complex. Here we have just listed a simple example to illustrate the method. How to combine the integrating factor method and the λ-symmetry reduction method of DDEs to construct more effective examples will be the next work.

Data availability statement

The raw data supporting the conclusion of this article will be made available by the authors, without undue reservation.

Author contributions

JL: Methodology, software, formal analysis, writing-original draft. KS: Investigation, formal analysis, writing-original draft. BR: software, formal analysis. YJ: Conceptualization, funding acquisition, resources, supervision, writing-review and editing. All authors contributed to the article and approved the submitted version.

Acknowledgments

The authors thank Prof. S.F. Shen for their helpful discussions.

Conflict of interest

The authors declare that the research was conducted in the absence of any commercial or financial relationships that could be construed as a potential conflict of interest.

Publisher's note

References

1. Li B, Ye WC, Chen Y. Symmetry, full symmetry groups, and some exact solutions to a generalized Davey–Stewartson system. *J Math Phys* (2008) 49:103503. doi:10.1063/1.2993975

2. Cheng WG, Li B, Chen Y. Nonlocal symmetry and exact solutions of the (2+1)-dimensional breaking soliton equation. *Commun Nonlinear Sci Numer Simul* (2015) 29:198–207. doi:10.1016/j.cnsns.2015.05.007

3. Rahioui M, El Kinani EH, Ouhadan A. Lie symmetry analysis and conservation laws for the time fractional generalized advection–diffusion equation. *Comput Appl Math* (2023) 42:50. doi:10.1007/s40314-023-02186-0

4. Olver PJ. *Applications of Lie groups to diferential equations*. New York, NY: Springer-Verlag (1986).

5. Bluman GW, Kumei S. *Symmetries and diferential equations*. New York, NY: Springer-Verlag (1989).

6. Anderson IM, Fels ME, Torre CG. Group invariant solutions without transversality. *Commun Math Phys* (2000) 212:653–86. doi:10.1007/s002200000215

7. Eastwood M. Higher symmetries of the laplacian. *Ann Math* (2005) 161:1645–65. doi:10.4007/annals.2005.161.1645

8. Zhdanov RZ, Lahno VI. Group classification of heat conductivity equations with a nonlinear source. *J Phys A: Math Gen* (1999) 32:7405–18. doi:10.1088/0305-4470/32/42/312

9. Zhdanov RZ, Lahno VI, Fushchych WI. On covariant realizations of the Euclid group. *Commun Math Phys* (2000) 212:535–56. doi:10.1007/s002200000222

10. Lahno VI, Zhdanov RZ. Group classification of nonlinear wave equations. *J Math Phys* (2005) 46:053301–3337. doi:10.1063/1.1884886

11. Molati M, Mahomed FM. A group classification of the general second-order coupled diffusion system. *J Phys A: Math Theor* (2010) 43:415203. doi:10.1088/1751-8113/43/41/415203

12. Pucci E, Saccomandi G. Contact symmetries and solutions by reduction of partial differential equations. *J Phys A: Math Gen* (1994) 27:177–84. doi:10.1088/0305-4470/27/1/011

13. Momoniat E, Mahomed FM. The existence of contact transformations for evolution-type equations. *J Phys A: Math Gen* (1999) 32:8721–30. doi:10.1088/0305-4470/32/49/312

14. Ibragimov NH, Khabirov SV. Contact transformation group classification of nonlinear wave equations. *Nonlinear Dynam* (2000) 22:61–71. doi:10.1023/a:1008309626744

15. Khabirov SV. A property of the defining equations for the Lie algebra in the group classification problem for wave equations. *Sib Math J* (2009) 50:515–32. doi:10.1007/s11202-009-0058-8

16. Zhdanov RZ. On Lie group characterization of quasi-local symmetries of nonlinear evolution equations. *J Lie Theor* (2010) 20:375–92.

17. Popovych RO, Kunzinger M, Ivanova NM. Conservation laws and potential symmetries of linear parabolic equations. *Acta Appl Math* (2008) 100:113–85. doi:10.1007/s10440-007-9178-y

18. Craddock M, Platen E. Symmetry group methods for fundamental solutions. *J Differential Equations* (2004) 207:285–302. doi:10.1016/j.jde.2004.07.026

19. Craddock M, Lennox KA. Lie group symmetries as integral transforms of fundamental solutions. *J Differential Equations* (2007) 232:652–74. doi:10.1016/j.jde.2006.07.011

20. Craddock M, Lennox KA. The calculation of expectations for classes of diffusion processes by Lie symmetry methods. *Ann Appl Prob* (2009) 19:127–57. doi:10.1214/08-aap534

21. Craddock M, Lennox KA. Lie symmetry methods for multi-dimensional parabolic PDEs and diffusions. *J Differential Equations* (2012) 252:56–90. doi:10.1016/j.jde.2011.09.024

22. Craddock M. Fourier type transforms on Lie symmetry groups. *J Math Phys* (2015) 56:091501. doi:10.1063/1.4929653

23. Muriel C, Romero JL. New methods of reduction for ordinary differential equations. *IMA J Appl Math* (2001) 66:111–25. doi:10.1093/imamat/66.2.111

24. Muriel C, Romero JL. The λ-symmetry reduction method and Jacobi last multipliers[J]. *Commun Nonlinear Sci Numer Simul* (2014) 19:807–20. doi:10.1016/j.cnsns.2013.07.027

25. Levi D, Rodriguez MA. λ-symmetries for discrete equations. *J Phys A Math Theor* (2010) 43:292001–1860. doi:10.1088/1751-8113/43/29/292001

26. Cicogna G, Gaet G. Noether theorem for μ-symmetries. *J Phys A: Math Theor* (2007) 40:11899–921. doi:10.1088/1751-8113/40/39/013

27. Gaeta GA. gauge-theoretic description of μ-prolongations, and μ-symmetries of differential equations. *J Geom Phys* (2009) 59:519–39. doi:10.1016/j.geomphys.2009.01.004

28. Pashayi S, Shahmorad S, Hashemi MS, Inc M. Lie symmetry analysis of two dimensional weakly singular integral equations. *J Geom Phys* (2021) 170:104385. doi:10.1016/j.geomphys.2021.104385

29. Servan AR, Patino MCM. Variational lambda-symmetries and exact solutions to Euler-Lagrange equations lacking standard symmetries. *Math Meth Appl Sci* (2022) 45:10946–58. doi:10.1002/mma.8430

30. Pan-Collantes AJ, Ruiz A, Muriel C, Romero JL. C-infinity-symmetries of distributions and integrability. *J Differential Equations* (2023) 348:126–53. doi:10.1016/j.jde.2022.11.051

frontiers | Frontiers in Physics

TYPE Original Research
PUBLISHED 03 July 2023
DOI 10.3389/fphy.2023.1207381

OPEN ACCESS

EDITED BY
Samir A. El-Tantawy,
Port Said University, Egypt

REVIEWED BY
Zhiwei Ji,
Nanjing Agricultural University, China
Xiaojun Chang,
University of Technology Sydney, Australia

*CORRESPONDENCE
Saleem Riaz,
saleemriaznwpu@mail.nwpu.edu.cn

RECEIVED 17 April 2023
ACCEPTED 14 June 2023
PUBLISHED 03 July 2023

CITATION
Lei T, Hu J and Riaz S (2023), An innovative approach based on meta-learning for real-time modal fault diagnosis with small sample learning. *Front. Phys.* 11:1207381. doi: 10.3389/fphy.2023.1207381

An innovative approach based on meta-learning for real-time modal fault diagnosis with small sample learning

Tongfei Lei[1], Jiabei Hu[2] and Saleem Riaz[3]*

[1]School of Mechanical Engineering, Xijing University, Xi'an, China, [2]Xi'an Aeronautical Computing Technique Research Institute, Xi'an, China, [3]School of Automation, Northwestern Polytechnical University, Xi'an, China

The actual multimodal process data usually exhibit non-linear time correlation and non-Gaussian distribution accompanied by new modes. Existing fault diagnosis methods have difficulty adapting to the complex nature of new modalities and are unable to train models based on small samples. Therefore, this paper proposes a new modal fault diagnosis method based on meta-learning (ML) and neural architecture search (NAS), MetaNAS. Specifically, the best performing network model of the existing modal is first automatically obtained using NAS, and then, the fault diagnosis model design is learned from the NAS of the existing model using ML. Finally, when generating new modalities, the gradient is updated based on the learned design experience, i.e., new modal fault diagnosis models are quickly generated under small sample conditions. The effectiveness and feasibility of the proposed method are fully verified by the numerical system and simulation experiments of the Tennessee Eastman (TE) chemical process.

KEYWORDS

new modal fault diagnosis, meta-learning, neural architecture search, small samples, artificial intelligence

1 Introduction

With the development of many sensors and industrial networks, modern chemical industry is moving toward large-scale, hierarchical, information integration and strong interaction, leading to frequent failures and unstable product quality in chemical production processes, and chemical process troubleshooting is one of the effective techniques to ensure product quality and efficient production operation [1, 2]. In the actual chemical production process, the adjustment of the product grade or index, the fluctuation of material quality, and the imbalance of feed ratio all lead to the multimodal characteristics of the chemical process [3]. Therefore, multimodal characteristics are widely present in modern manufacturing industries [4, 5]. Compared with unimodal processes, the multimodal process data are more complex, usually manifested as non-linear time correlation and non-Gaussian distribution accompanied by new modes [6]. If deep learning is directly applied to multimodal chemical processes, it will be difficult to adapt to complex characteristics such as new modes and to construct accurate fault diagnosis models under small samples [7, 8]. Therefore, the deep learning-based fault diagnosis method for new modes in small samples is of research value.

Existing multimodal chemical process fault diagnosis methods can be classified into statistical learning, machine learning, and deep learning methods, among which statistical learning and machine learning methods have been studied previously. For example, Zhao

et al. studied a local modal fault diagnosis method using multiple local PCA statistical models [9], but the method requires the use of accurate modal information in the offline modeling stage. To address the problem of incomplete modal prior knowledge, Tan et al. applied the clustering method to the multimodal chemical process and effectively improved the accuracy of fault diagnosis [10]. Wang et al. proposed a stable and transitional modal fault diagnosis method based on the transition probabilities between different modes [11]. Natarajan et al. gave the minimum distance from the test data to the training data center by calculating the selection of the locally optimal PCA model criterion [12]. Deep learning has made important progress in many fields in recent years, but there are relatively few studies on deep learning for multimodal chemical process fault diagnosis. In addition, the training of deep learning fault diagnosis models usually requires a large amount of labeled data, but new modes often have only a small amount of data [13–16]. How to make full use of multimodal process characteristics and model design experience of the existing modes under small-sample conditions to rapidly construct new modal fault diagnosis models based on deep learning is of great importance to ensure the safety and product quality of the actual chemical processes.

Existing small-sample data learning methods can be divided into three categories: data augmentation-based methods, model improvement-based methods, and algorithm optimization-based methods [17, 18]. Data augmentation-based methods achieve the purpose of expanding the dataset by generating new data [19], but the manipulation of data is not universal and requires the designer to have sufficient knowledge of the relevant domain. Model improvement-based approaches model small data by limiting the model complexity, reducing the hypothesis space, and reducing VC dimension [20] but require *a priori* knowledge and extensive experience of the designer, and the aforementioned two approaches cannot effectively utilize the design experience of existing modes. Algorithm-based optimization methods search for suitable solutions faster by improving the optimization algorithm [21, 22], and meta-learning is an improved optimization algorithm. The proposed meta-learning method provides research ideas to solve the problems such as inadequate utilization of model design experience of the existing modes and small samples [23]. For example, Finn et al. proposed the model-agnostic meta-learning (MAML) method, which first trains a set of initialization parameters and then performs one or more steps of gradient adjustment to achieve rapid adaptation to new tasks with only a small amount of data [24, 25]. However, MAML is very sensitive to the neural network structure and requires time-consuming hyperparameter search to stabilize the training and improve the model generalization power [26]. To address these problems, Antoniou et al. optimized MAML in terms of robustness, training stability, automatic learning of inner-loop hyperparameters, and computational efficiency during inference and training, which significantly improved the generalization performance of MAML [27] but at the expense of computation and memory. Nichol et al. replaced the process of computing second-order differentiation in MAML with the one in which each task is performed using the stochastic gradient descent (SGD) in a standard form without expanding the computational graph or computing arbitrary second-order derivatives, reducing the amount of computation and memory required by MAML [28]. However, the aforementioned methods have a single network structure and cannot transform the network structure as the task changes, and meta-learning faces problems such as cumbersome network structure design and time-consuming parameter search.

In the field of machine learning and artificial intelligence, several state-of-the-art (SOTA) algorithms have been developed to tackle various tasks. Although these algorithms have their own advantages, they also come with certain limitations. Here is a summary of the advantages and limitations to the existing SOTA algorithms in this area. The advantages are as follows: high accuracy: SOTA algorithms often achieve remarkable accuracy in solving complex problems; robustness: many SOTA algorithms exhibit robustness in handling noisy or incomplete data; generalization: SOTA algorithms often possess excellent generalization capabilities; and scalability: several SOTA algorithms are designed to handle large-scale datasets efficiently. The limitations are as follows: computational complexity: many SOTA algorithms, particularly those based on deep learning architecture, require significant computational resources to train and deploy; interpretability: while SOTA algorithms often achieve impressive performance, they can be black-box models, meaning they lack interpretability; data dependency: SOTA algorithms heavily rely on large and diverse datasets for training; and overfitting: some SOTA algorithms are susceptible to overfitting, especially when dealing with small datasets.

To solve the aforementioned problems, this paper proposes a new modal fault diagnosis method, MetaNAS, which uses meta-learning to find the optimal initial parameters, and the new modal can find the network structure with optimal performance by only a few steps of gradient update based on the optimal initial parameters. The optimal initial parameters are to be learned so that the fault diagnosis model is obtained by performing a few steps of updates based on the optimal initial parameters under a small sample of the new mode. MetaNAS solves the limitations to fault diagnosis by NAS, such as underutilization of the existing modal design experience and difficulty in training models under small samples.

The main contributions of this paper are as follows [1]: the proposed MetaNAS method can automatically design fault diagnosis network models and realize automatic fault diagnosis under small samples of new modes [2]. To address the problems of underutilization of the existing modal design experience and difficulty in training models under small samples, meta-learning is used to learn the model design experience of existing models and obtain the optimal initial parameters so that the new modal can obtain the fault diagnosis model with only a few steps of gradient update under small samples [3]. Continuous relaxation optimization converts the discrete channel selection process into a continuous optimization process, making NAS more efficient and convenient.

2 Manuscript formatting

2.1 Model-agnostic meta-learning

The entire dataset, training set, and test set are denoted by D, $D_{meta-train}$, and $D_{meta-test}$, respectively, and in meta-learning, a series of tasks T is sampled according to the distribution $p(T)$ of $D_{meta-train}$, where there are N categories in the i_{th} task, and each category has K samples, calling the problem an N-class K-sample problem [19]. The data in each N-class K-sample problem are further divided into a

training set and a test set, and in order not to be confused, the training set in T_i is called the support set and the test set is called the query set, denoted as T_i^s and T_i^q, respectively. The core idea of MAML is to learn an optimal initial parameter $\tilde{\omega}$ in all tasks T such that $D_{meta-test}$ to perform one or more steps of gradient adjustment based on $\tilde{\omega}$ to achieve the goal of fast adaptation to new tasks and good performance with only a small amount of data. The optimal initial parameters are learned according to the following rules:

$$\omega_i^{m+1} = \omega_i^m - \chi_{inner}\frac{\partial L\left(T_i^s; \omega_i^m\right)}{\partial \omega_i^{m+1}}, \tag{1}$$

where χ_{inner} is the internal learning rate of parameter ω, m is the update step in each task T, f is the parameterization function of the network weight ω, and L is the loss function. During the internal learning process, T_i^s is used to calculate the loss of task T_i and let the parameter ω be updated from ω_i^m to ω_i^{m+1}, where $\omega_i^0 = \omega$. After M steps, $L(f(T_i^q; \omega_i^M))$ in T_i^q is used to update the optimal initial parameters, which can be expressed as follows:

$$\tilde{\omega} = \tilde{\omega} - \chi_{outer}\frac{\partial \sum_{T_i^q \sim p(T)} L\left(f\left(T_i^q; \omega_i^M\right)\right)}{\partial \tilde{\omega}}, \tag{2}$$

where χ_{outer} is the external learning rate of parameter $\tilde{\omega}$, and eventually, when the model converges, the optimal initial parameter $\tilde{\omega}$ is obtained. This makes the initial parameters so sensitive that a better model can be obtained in only a few steps of updating on $D_{meta-test}$.

2.2 Automatic fault diagnosis

The core idea of the automatic fault diagnosis (AutoFD) method is to continue the discrete network search process by continuous relaxation optimization, assigning weights to all candidate operations separately, then optimizing the operation weights and network parameters by gradient descent, and then using the operation weight parameters to select the corresponding operations to form the final network model [29, 30].

Let O be the candidate operation set, each candidate operation is denoted as o; given the input x, the operation output $\bar{o}(x)$ after continuous relaxation optimization is as follows:

$$\bar{o}(x) = \sum_{o \in O} \frac{\exp(\alpha_o)}{\sum_{o' \in O} \exp(\alpha_{o'})} o(x), \tag{3}$$

where α represents the operation weight vector, which represents the importance of different candidate operations in the corresponding edge. After the training is completed, the operation corresponding to the largest weight is selected according to the operation weight parameter as the final result.

Through continuous relaxation optimization, the NAS problem is transformed into a double optimization problem, which can be solved by using the two-step update algorithm.

$$\alpha = \alpha - \delta\frac{\partial L\left(\omega - \xi\frac{\partial L(\omega,\alpha)}{\partial \omega}\right)}{\partial \alpha}, \tag{4}$$

$$\omega = \omega - \chi\frac{\partial L(\omega, \alpha)}{\partial \omega}, \tag{5}$$

where L denotes the loss function and ξ means the internal learning rate.

3 The proposed method

The MetaNAS method is proposed to address the problems of existing methods that do not fully utilize the model design experience of the previous modes and require a large amount of feature data, and the overall flow chart of the method is shown in Figure 1. MetaNAS first assigns weights to the candidate channels and transforms the discrete channel selection process into a continuous optimization process by optimizing the continuous weights instead of the channel selection process. Then, MAML is used to learn the optimal initial parameters of the required learning parameters in NAS, and when a new mode appears, a better fault diagnosis model for the new mode is obtained with only a few steps of updates based on the optimal initial parameters when only a small amount of data is available for the new mode.

3.1 Channel weight parameters

AutoFD uses multi-channel convolution to enhance the performance of the network, but the selection of convolutional channels is very time-consuming. In order to make NAS more efficient, this paper uses continuous relaxation optimization to make the discrete convolutional channel selection process continuous. The candidate channels are denoted by $C = \{C_1, C_2, \cdots, C_n\}$ to denote the set of candidate channels, which are used as the candidate input channels of the network, i.e., $I = \{I_1, I_2, \cdots, I_n\}$, the selection process of these candidate input channels is discrete, the channels are assigned weights $\beta = \{\beta_1, \beta_2, \cdots, \beta_n\}$, and these weights are transformed by the Softmax function to mix all the channels in the candidate channel set to obtain a mixed input.

$$\text{Input} = \sum \frac{\exp(\beta)}{\sum_{i' \in I} \exp\left(\beta_{i'}\right)} i. \tag{6}$$

Thus, each channel C is associated with a weight coefficient β corresponding to it, and continuous relaxation optimization uses a continuous weight coefficient to represent the discrete candidate channels. This continuous weight coefficient indicates the importance of the corresponding channel in the network input, so the performance of the network on the validation set can be updated quickly by using gradient descent for each operation, effectively avoiding the time-consuming process of training all network inputs and selecting the well-performing inputs. After the search is completed, the channel corresponding to the top three values of the weight coefficient is selected as the final operation convolution channel. By the aforementioned method, the NAS problem is transformed into a two-layer optimization problem of learning the smallest values of operation weight α^*, network weight ω^*, and channel weight β^* with the loss function.

$$\text{Lval}\left(\omega^*, \alpha^*, \beta^*\right), \tag{7}$$

$$\min_{\alpha} \text{Lval}\left(\omega^* | (\alpha, \beta), \alpha, \beta\right), \tag{8}$$

$$\text{s.t.}\omega^*(\alpha) = \arg\min_{\omega} \text{Ltrain}(\omega, \alpha), \tag{9}$$

$$\omega^*(\beta) = \arg\min_{\omega} \text{Ltrain}(\omega, \beta). \tag{10}$$

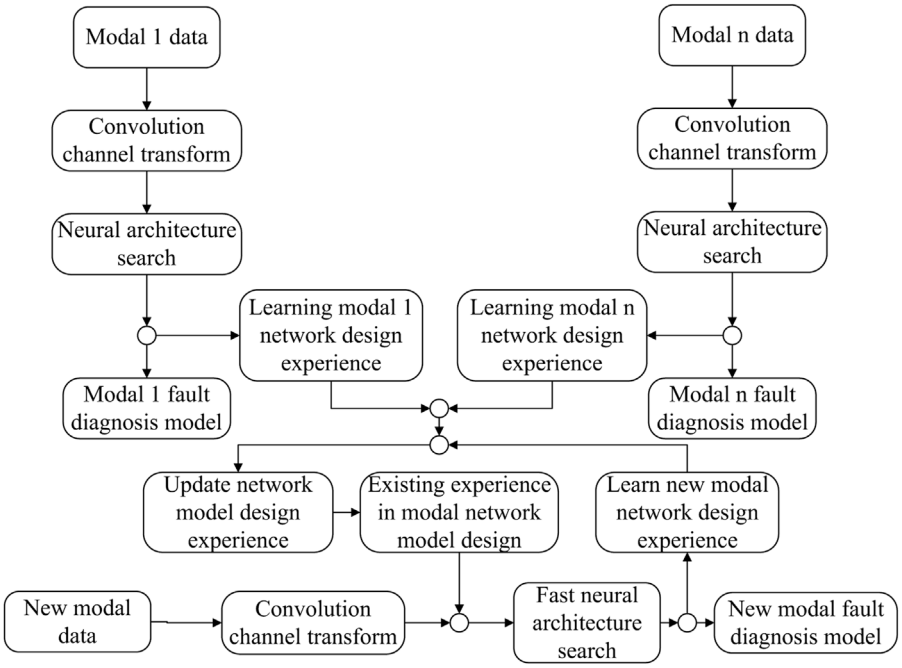

FIGURE 1
Flowchart of the proposed MetaNAS method.

3.2 The proposed method

In order to make the NAS process of the new modal fault diagnosis more efficient, this paper uses MAML to learn the design experience of previous modes and NAS, the new modal chemical process based on the learned design experience. In Subsection 3.1, MAML is trained on the training set to obtain the optimal initial parameters $\tilde{\omega}$ for fast adaptation in the new task. Similarly, the optimal network initial parameter $\tilde{\omega}$, operation weight initial parameter $\tilde{\alpha}$, and channel weight initial parameter $\tilde{\beta}$ are learned using the training set data in MetaNAS, which enables MetaNAS to quickly obtain a better model with a few steps of the gradient update on the new task, where the parameters $\tilde{\omega}$, $\tilde{\alpha}$, and $\tilde{\beta}$ are the NAS parameters defined in Subsection 2.1 and Subsection 3.1.

In order to learn the previous modal NAS design experience, this paper is based on the MAML strategy to learn the optimal NAS initial parameters $\tilde{\omega}$, $\tilde{\alpha}$, and $\tilde{\beta}$. Similar to AutoFD, the operation weight parameter α, network parameter ω, and channel weight parameter β cannot be trained independently, so the initial parameters $\tilde{\omega}$, $\tilde{\alpha}$, and $\tilde{\beta}$ also need to be jointly optimized. In MetaNAS, the initial parameters $\tilde{\omega}$, $\tilde{\alpha}$, and $\tilde{\beta}$ are also solved by joint optimization. Eqs 1, 2 are used in subsection 2.1 to update the optimal initial parameters $\tilde{\omega}$, where Eq. 1 is used to update the internal parameters and Eq. 2 is used to update the external initial parameters, and similarly, MetaNAS contains two parts: internal parameter update and external initial parameter update. In the internal parameter update part, the NAS parameters ω, α, and β are jointly optimized in a specific task T_i^s according to the following equations:

$$\omega_i^{m+1} = \omega_i^m - \chi_{inner}\frac{\partial L\left(g\left(T_i^s;\alpha_i^m,\beta_i^m,\omega_i^m\right)\right)}{\partial \omega_i^m}, \tag{11}$$

$$\alpha_i^{m+1} = \alpha_i^m - \delta_{inner}\frac{\partial L\left(g\left(T_i^s;\alpha_i^m,\beta_i^m,\omega_i^m\right)\right)}{\partial \alpha_i^m}, \tag{12}$$

$$\beta_i^{m+1} = \beta_i^m - \varepsilon_{inner}\frac{\partial L\left(g\left(T_i^s;\alpha_i^m,\beta_i^m,\omega_i^m\right)\right)}{\partial \beta_i^m}, \tag{13}$$

where χ_{inner} is the internal learning rate of the network parameter ω, δ_{inner} is the internal learning rate of the operational weight parameter α, ε_{inner} is the internal learning rate of the channel weight parameter β, and g is the parameterization function of ω, α, and β; initially, $(\omega_i^0 = \tilde{\omega}, \alpha_i^0 = \tilde{\alpha}, \beta_i^0 = \tilde{\beta})$. In the external parameter update, in order to obtain an optimal initial point, after M steps, the loss function $L(g(T_i^s;\alpha_i^m,\beta_i^m,\omega_i^m))$ in task T_i^q is calculated to jointly optimize the parameters $\tilde{\omega}$, $\tilde{\alpha}$, and $\tilde{\beta}$ according to the following equation:

$$\tilde{\omega} = \tilde{\omega} - \chi_{outer}\frac{\partial \sum_{T_i^q\sim p(T)} L\left(g\left(T_i^q;\alpha_i^M,\beta_i^M,\omega_i^M\right)\right)}{\partial \tilde{\omega}}, \tag{14}$$

$$\tilde{\alpha} = \tilde{\alpha} - \delta_{outer}\frac{\partial \sum_{T_i^q\sim p(T)} L\left(g\left(T_i^q;\alpha_i^M,\beta_i^M,\omega_i^M\right)\right)}{\partial \tilde{\alpha}}, \tag{15}$$

$$\tilde{\beta} = \tilde{\beta} - \varepsilon_{outer}\frac{\partial \sum_{T_i^q\sim p(T)} L\left(g\left(T_i^q;\alpha_i^M,\beta_i^M,\omega_i^M\right)\right)}{\partial \tilde{\beta}}, \tag{16}$$

where χ_{outer} is the external learning rate of the network parameter $\tilde{\omega}$, δ_{outer} is the external learning rate of the operational weight parameter $\tilde{\alpha}$, and ε_{outer} is the external learning rate of the channel weight parameter $\tilde{\beta}$. When the results converge, the optimal initial parameters $\tilde{\omega}$, $\tilde{\alpha}$, and $\tilde{\beta}$ are obtained, and the new

task is updated on the basis of the parameters $\tilde{\omega}$, $\tilde{\alpha}$, and $\tilde{\beta}$ to obtain better results quickly.

3.3 New modal fault online diagnosis steps

The new modal chemical process fault diagnosis algorithm proposed in this paper can be divided into four steps, namely, model construction, search phase, training and optimization phase, and real-time diagnosis, which are as follows:

Step 1: Model construction. The network model is a two-way branch linked by several convolutional neural network units, the network units within the branch and between the branches are linked by edge operations, the data to be processed are input at the beginning of the two branches, the fully connected layer for outputting fault diagnosis results is also connected at the end of the two branches, the said network units also include edge operations and nodes, the input within the unit is also divided into two ways, and the output is one way, the same as the network model in the AutoFD method.

Step 2: Search phase.

Step 2.1: The raw chemical production process data on multiple modes are normalized and dimensionally preprocessed to make data dimensions that satisfy the structural search of the meta-learning network.

Step 2.2: The pre-processed data are manipulated to form candidate channels for multi-channel convolution and are stitched with the preprocessed data to generate inputs for the network search phase.

Step 2.3: The candidate input channels are individually assigned weights to further obtain the mixed inputs.

Step 2.4: The set of candidate operations are defined, and a weight is assigned to each operation.

Step 2.5: Iterating steps 2.3 and 2.4 repeatedly, the Adam/SGD optimizer is chosen to adjust the network parameters, channel weight parameters, and operation weight parameters by using the cross-entropy loss function and backpropagation so as to obtain the optimal network initial parameters, channel optimal initial parameters, and operation optimal initial parameters as the initial parameters of the new mode.

Step 3: Training and optimization phase.

Step 3.1: Normalization and dimensional preprocessing are performed for the new modal chemical production process data so that the input data dimensions satisfy the meta-learning network structure search.

Step 3.2: The optimal network initial parameter $\tilde{\omega}$, optimal channel weight initial parameter $\tilde{\beta}$, and optimal operation weight initial parameter $\tilde{\alpha}$ are used as initial parameters to train the new modal chemical production process data into the network, and the optimized network parameter ω^*, channel weight parameter β^*, and operation weight parameter α^* are obtained after training.

Step 3.3: The channel weight parameter β^* and operation weight parameter α^* obtained by the aforementioned optimization are used to filter the selected convolutional channels and convolutional operations in the network, and obtain the fault diagnosis network model corresponding to the new mode.

Step 4: Real-time diagnosis. The data obtained in real time are normalized and preprocessed so that the input data dimensions of the network are satisfied. Then, the data are input into the obtained diagnosis network for real-time diagnosis.

4 Experimental verifications

For all datasets, in the network search phase, the same candidate operations, candidate convolution channels, and the structure of the network are used as in AutoFD, with candidate convolution channels. The network in the empirical phase of the learning design is determined by the operation weight parameter $\tilde{\alpha}$ and the channel weight parameter $\tilde{\beta}$. The candidate operations are as follows: 3 × 3 separable convolution, 5 × 5 separable convolution, 3 × 3 null convolution, 5 × 5 null convolution, 3 × 3 maximum pooling, 3 × 3 average pooling, keep the original input, and clear the original input. When there is a new task, the optimal network structures α_i^* and β_i^* can be obtained by updating on the basis of the original network structure parameters.

The dataset is first divided into validation and test sets, and then, the training set is subdivided into training and validation sets, and the test set is subdivided into training and test sets, and the aforementioned four sets are noted as the training set in the training phase, validation set in the training phase, training set in the test phase, and test set in the test phase for easy distinction [31, 32].

First, in the training set of the training phase, K data are randomly selected from the selected N class samples as a task T. Then, in the validation set of the training phase, 10 data are randomly selected from each category sample as the test data in the training phase, so there should be N*(K+10) data in task T. In the NAS process, let the network training epoch be E1, and each time, first, S1 independent tasks are randomly selected, and then, the search training of the network is performed with these S1 tasks. In the internal search phase, the ordinary SGD is chosen to optimize the parameters of the network, the operation weight parameters, and the channel weight parameters, and the internal learning rates are set to χ_{inner}, δ_{inner}, and ε_{inner} in the internal sojourn phase, and the accuracy and efficiency of the network are weighed by adjusting the internal step size M. In the external search phase, the Adam optimizer is chosen to optimize the initial parameters of the network, the initial parameters of the operation weights, and the initial parameters of the channel weights, and the external learning rates are set to χ_{outer}, δ_{outer}, and ε_{outer}. In the validation phase, first, K data are randomly selected from the samples of N classes as task T in the training set of the testing phase, so there should be N*(K + Q) data in task T. Let the network

training epoch be E2 times, and each time, S2 independent tasks are randomly selected first, and the final accuracy is the average diagnostic accuracy of S2 independent tasks.

All training and verification experiments are completed on a PC equipped with Inteli7-10875H 2.30 GHz, 16 GB DDR4, WDC PCSN730, and NVIDIA GeForce RTX 2060. All Python codes are completed under the PyTorch framework, using the parallel acceleration capabilities provided by CUDA and cuDNN to achieve fast training and diagnostic tasks.

4.1 New modal fault online diagnosis steps

In this paper, a typical multimodal numerical simulation model proposed by Ge et al. [25] is taken for testing, which has been adopted by many scholars to verify the effectiveness of multimodal algorithms, and the specific structure of the model is denoted as follows:

$$\begin{aligned} x_1 &= 0.5678s_1 + 0.3766s_2 + e_1, \\ x_2 &= 0.7382s_1 + 0.0566s_2 + e_2, \\ x_3 &= 0.8291s_1 + 0.4009s_2 + e_3, \\ x_4 &= 0.6519s_1 + 0.2070s_2 + e_4, \\ x_5 &= 0.3792s_1 + 0.8045s_2 + e_5, \end{aligned} \tag{17}$$

where five variables x_1, x_2, x_3, x_4, and x_5 have different distributions of s_1 and s_2. e_1, e_2, e_3, e_4, and e_5 are five mutually independent noises that obey the Gaussian distribution with mean 0 and standard deviation 0.01. According to the two different distributions of s_1 and s_2, the model has two different modes, mode 1 (mode1) and mode 2 (mode2), which are represented as follows [26]:

$$\begin{aligned} &\text{model1 } s_1\colon U(-10, 7), s_2\colon N(-15, 1), \\ &\text{model1 } s_1\colon U(2, 5), s_2\colon N(7, 1), \end{aligned} \tag{18}$$

where U denotes uniform distribution and N denotes Gaussian distribution; each measured data contain five moments of data $[d_1, d_2, d_3, d_4, d_5]$, and d_i is $[x_1, x_2, x_3, x_4, x_5]$ for each moment; each data have 25 features; for each mode, first 1,000 normal samples are generated, followed by the next 1,000 samples generated as fault data, and the fault data are generated according to the following rules.

Fault 1: Addition of a step signal of amplitude 4 at the beginning of the 1001st sample.

Fault 2: Adding a ramp signal of 0.02 (i-400) at the beginning of the 1001st sample.

Fault 3: A sinusoidal signal with amplitude, offset, and frequency of 1 is added at the beginning of the 1001st sample.

Here, 1,000 data were generated for each mode of normal and fault 1, 2, and 3, respectively, where 4,000 data of mode1 were used as the training set and the data were divided into training and validation sets in the ratio of 7:3 to learn the optimal initial parameters. mode2 also contained 4,000 data, and the data were divided into training and test sets in the ratio of 7:3.

The dataset is divided according to the category $N = 4$; the number of data items $K = 10, 50, 100$, and 150; the network training epoch is $E_1 = 10$; the number of randomly selected independent tasks $S_1 = 100$; the internal learning rate $\chi_{innner} = 0.05$, $\delta_{innner} = 15$, and $\varepsilon_{innner} = 15$; the internal step size $M = 4$; the external learning rate $\chi_{outer} = 10^{-3}$, $\delta_{outer} = 10^{-3}$, and $\varepsilon_{outer} = 10^{-3}$; test data size $Q =$ 150 for the validation phase; $E_2 = 5$ for the network training epoch; and the number of randomly selected independent tasks $S_2 = 80$. The results of the numerical system multi-fault experiments are shown in Table 1 and Figure 2.

It can be seen that as the training set size increases on mode2 data, the amount of knowledge learned by each method from the data increases accordingly and the diagnostic accuracy of MetaNAS, MAML++ [21], Reptile [22], and MAML [19] also increases. The diagnostic accuracy of MetaNAS with a training set size of 3 × 10 was as high as 74%, while the highest of the compared methods was 68.17% for MAML++. The diagnostic accuracy of MetaNAS with a training set size of 3 × 50 was 85.27%, and none of the compared methods exceeded 76%. The diagnostic accuracy of MetaNAS with a training set size of 3 × 100 was 86.35%, and all the compared methods exceeded 80%. At a training set size of 3 × 150, the diagnostic accuracy of MetaNAS was 88.34%, and all the compared methods exceeded 84%. MetaNAS achieved the highest diagnostic accuracy in each category of the training set size.

4.2 TE multi-modal simulation

The TE chemical process is a standard experimental simulation platform. This paper adopts the TE simulation platform provided by http://depts.washington.edu/control/LARRY/TE/download.html. The TE process is presented in Figure 3. In the multimodal process fault diagnosis experimental study, the TE process simulation platform is set up with six G/H product ratios to obtain the process data under normal and fault conditions in six modes as mentioned in Table 2 and verify the performance of MetaNAS through multimodal TE process fault diagnosis experiments. In each mode normal operating condition, simulation for 72 h with a sampling interval of 3 min, 1,440 normal samples were obtained. In total, 15 kinds of faults were set when collecting fault samples, including seven step change faults (faults 1–7), five random change faults (faults 8–12), one slow drift fault (fault 13), and two blockage faults (faults 14 and 15); faults were introduced after 10 h of simulation in the normal operating condition, and the simulation was continued for 62 h with a sampling interval of 3 min, i.e., 200 normal samples and 1,220 fault samples were collected each time during the simulation of collecting fault samples.

In the multimodal process fault diagnosis experiment, for the six modal process data obtained, 1,000 normal samples (6,000 normal samples) and 1,000 samples for each fault (i.e., 6,000 samples for each fault) are selected to form the dataset to be used; each data contains 12 operational variables and 41 process variables, and the variable dimension of each data is 53, which is filled with 0 at the end of the data and then converted into an 8 × 8 two-dimensional matrix as the candidate input of the network.

The data on modes 1, 2, 3, 4, and 5 were used as the training set, and the data on mode 6 were used as the test set. First, single-fault diagnosis experiments are performed on the multimodal dataset with the division $N = 2$; the number of data entries $K = 10, 50, 100$, and 150; $E_1 = 12$ for the network training epoch; the number of randomly selected independent tasks $S_1 = 200$; the internal learning rate $\chi_{inner} = 0.05$, $\delta_{inner} = 15$, and $\varepsilon_{inner} = 15$; the internal step size $M = 4$; the external learning rate $\chi_{outer} = 10^{-3}$, $\delta_{outer} = 10^{-3}$, and $\varepsilon_{outer} = 10^{-3}$; the test data

TABLE 1 Multi-fault diagnosis accuracy of numerical simulation with different training set sizes.

Training set	Test set	MetaNAS (%)	MAML++	Reptile	MAML
4*10	4*150	**74.00**	68.17%	64.54%	62.75%
4*50	4*150	**85.27**	75.53%	73.25%	71.95%
4*100	4*150	**86.35**	79.16%	77.39%	74.98%
4*150	4*150	**88.34**	81.69%	83.96%	84.93%

That the bold values indicates the results of our proposed MetaNAS method.

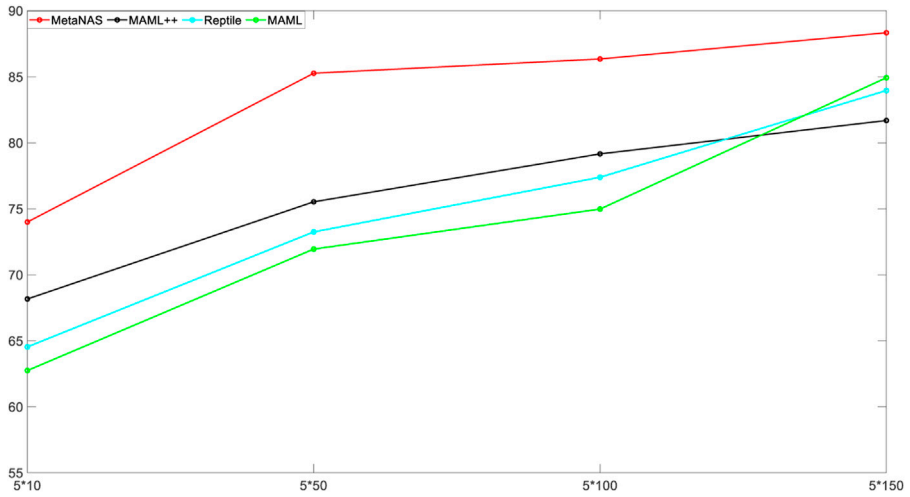

FIGURE 2
Multi-fault diagnosis accuracy of numerical simulation with different training set sizes.

TABLE 2 TE operation mode single-fault description.

Fault condition	Serial number	Process variation	Interference type
Fault 1	1	A/C material feeding ratio perturbed and B unchanged	Step interference
Fault 2	2	B changes, and the A/C feed ratio remains the same	Step interference
Fault 3	3	Feed temperature variation of D (stream 2)	Step interference
Fault 4	4	Condenser cooling water inlet temperature	Step interference
Fault 5	5	Reactor cooling water inlet temperature	Step interference
Fault 6	6	A feed loss (stream 1)	Step interference
Fault 7	7	Component C pressure drop disturbance	Step interference
Fault 8	8	A, B, and C feed ingredients (stream 4)	Random interference
Fault 9	9	Feed temperature of D (stream 2)	Random interference
Fault 10	10	Feed temperature of C (stream 4)	Random interference
Fault 11	11	Condenser cooling water inlet temperature	Random interference
Fault 12	12	Reactor cooling water inlet temperature	Random interference
Fault 13	13	Reaction dynamics	Drift interference
Fault 14	14	Reactor cooling water valve	Blocking interference
Fault 15	15	Condenser cooling water valve	Blocking interference

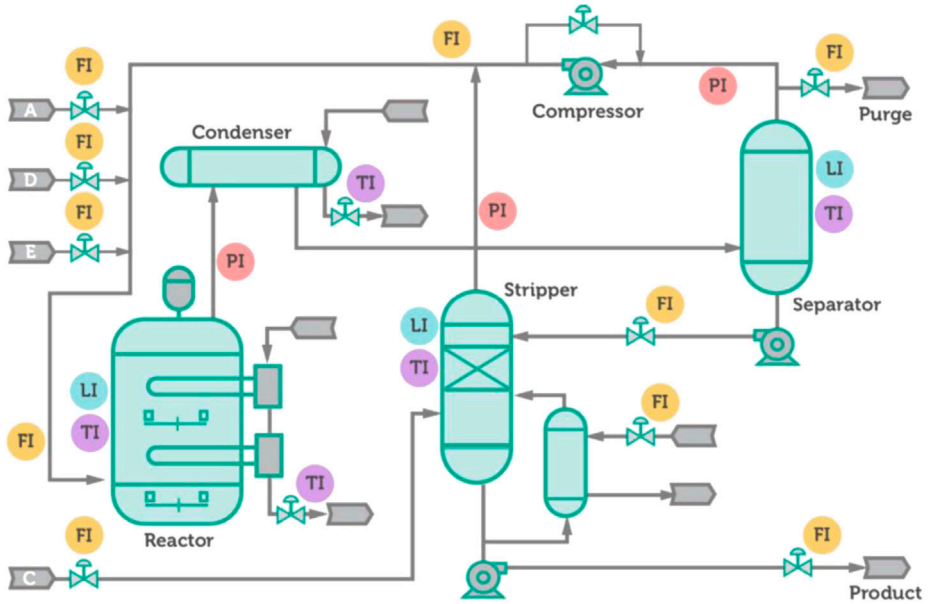

FIGURE 3
Tennessee Eastman process.

TABLE 3 TE single-fault diagnosis accuracy with different training set sizes.

Fault	Training set 2 × 10 test set 2*150				Training set 2 × 100 test set 2 × 150			
	MetaNAS	MAML++	Reptile	MAML	MetaNAS	MAML++	Reptile	MAML
1	**96.70%**	94.30%	88.33%	85.45%	**100.00%**	96.70%	**100.00%**	93.00%
2	**93.30%**	83.35%	80.00%	63.33%	**100.00%**	96.70%	88.67%	88.33%
3	73.34%	**76.66%**	66.55%	67.00%	79.00%	**86.67%**	73.34%	74.66%
4	96.70%	**97.30%**	96.00%	93.30%	**100.00%**	98.34%	**100.00%**	94.00%
5	**93.30%**	75.70%	88.67%	90.00%	**96.70%**	90.67%	90.67%	93.30%
6	**100.00%**	**100.00%**	99.00%	97.66%	**100.00%**	**100.00%**	**100.00%**	**100.00%**
7	**100.00%**	96.00%	**100.00%**	98.00%	**100.00%**	99.30%	**100.00%**	98.34%
8	**100.00%**	**100.00%**	96.34%	93.00%	**100.00%**	**100.00%**	97.66%	97.30%
9	**76.66%**	73.34%	69.34%	73.34%	**80.00%**	76.66%	80.00%	75.00%
10	**83.35%**	63.00%	80.00%	73.00%	**93.60%**	82.00%	93.30%	78.30%
11	73.34%	64.65%	76.66%	69.70%	**85.35%**	81.70%	78.65%	83.35%
12	**100.00%**	73.00%	**100.00%**	89.00%	**100.00%**	90.33%	**100.00%**	92.70%
13	96.70%	**100.00%**	90.67%	81.00%	**100.00%**	**100.00%**	91.00%	95.00%
14	76.66%	60.35%	**80.00%**	72.30%	**84.67%**	82.67%	82.00%	81.23%
15	76.66%	**80.00%**	69.70%	61.00%	**84.35%**	83.35%	73.34%	75.34%
Top	9	6	4	0	14	4	6	1

It can be seen that MetaNAS achieves the highest diagnostic accuracy for nine faults when the training size is 2 × 10, which is better than six faults for MAML++, four faults for Reptile, and zero faults for MAML. As the training size increases, MetaNAS achieves the highest diagnostic accuracy for 14 out of 15 faults when the training size is 2 × 100, compared to four faults for MAML++, six faults for Reptile, and one fault for MAML. Moreover, MetaNAS achieves 100% diagnostic accuracy on faults 1, 2, 4, 6, 7, 8, 12, and 13 when the training set size is 2 × 100.
That the bold values indicates the results of our proposed MetaNAS method.

TABLE 4 TE multi-fault diagnosis accuracy with different training set sizes.

Training set	Test set	MetaNAS	MAML++	Reptile	MAML
5 × 10	5 × 150	72.35%	57.07%	53.14%	51.25%
5 × 50	5 × 150	80.47%	65.50%	64.36%	62.65%
5 × 100	5 × 150	84.29%	74.10%	75.29%	72.18%
5 × 150	5 × 150	85.34%	73.60%	76.64%	74.63%

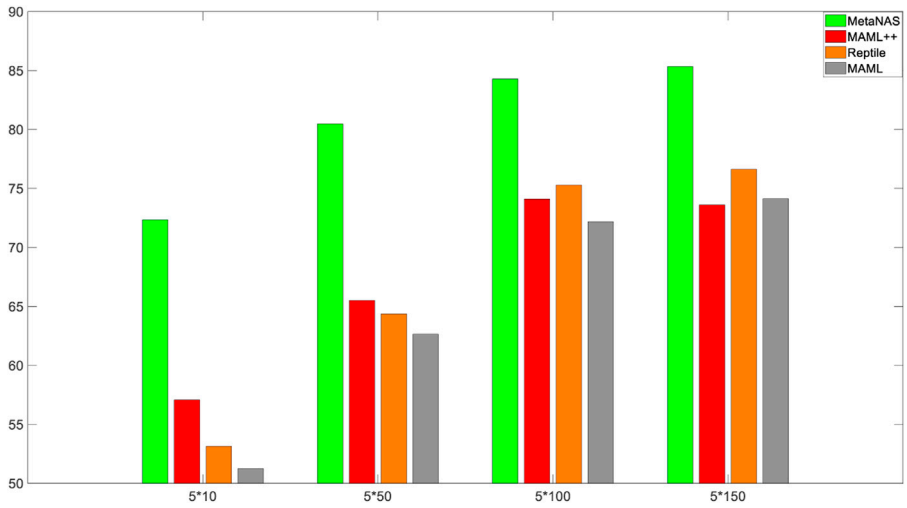

FIGURE 4
TE multi-fault diagnosis accuracy with different training set sizes.

size Q = 150 in the validation phase; $E_2 = 6$ in the network training epoch, and the number of randomly selected independent tasks $S_2 = 90$; the results of the single-fault diagnosis are shown in Table 3.

Then, the multimodal dataset is subjected to multiple fault diagnosis experiments, and a total of five operating conditions, normal 0, fault 1, fault 8, fault 13, and fault 15, are selected as the study objects, covering common step disturbances, random disturbances, drift disturbances, blocking disturbances, and other faults. The division of the dataset $N = 5$; the number of data entries $K = 10$, 50, 100, and 150; the training epoch $E_1 = 10$; the number of randomly selected independent tasks $S_1 = 500$; the internal learning rate $\chi_{inner} = 0.1$, $\delta_{inner} = 30$, and $\varepsilon_{inner} = 30$; the internal step size $M = 5$; the external learning rate $\chi_{outer} = 10^{-3}$, $\delta_{outer} = 10^{-3}$, and $\varepsilon_{outer} = 10^{-3}$; the test data size $Q = 150$ in the validation phase; the training epoch $E_2 = 10$; and the number of randomly selected independent tasks $S_2 = 100$; the multi-fault diagnosis results are shown in Table 4 and Figure 4.

It can be seen that the diagnostic accuracy of MetaNAS, MAML++, Reptile, and MAML increases as the size of the mode6 training set increases. The diagnostic accuracy of MetaNAS with a training set size of 5 × 10 is 72.35%, while the highest diagnostic accuracy of the comparison method is 57.07% for MAML++. The diagnostic accuracy of MetaNAS with a training set size of 5 × 50 is 80.47%, while the comparison method does not exceed 66%. The diagnostic accuracy of MetaNAS with a training set size of 5 × 100 is 84.29%, and the comparison methods are all over 76%. The diagnostic accuracy of MetaNAS with a training set size of 5 × 150 is 85.34%, and all the comparison methods exceed 77%. MetaNAS achieves the highest diagnostic accuracy in each category of the training set size.

Because MetaNAS has the advantage of using design experience to design a unique network structure for new modes, unlike MAML++, Reptile, and MAML, which use fixed network models, it usually requires additional time overhead for network model generation. During TE multi-fault experiments, the number of model parameters of MetaNAS, MAML, MAML++, and Reptile are 2.4 megabytes, 3.2 megabytes, 3.2 megabytes, 3.2 megabytes, and 3.2 megabytes, respectively, and MetaNAS takes about 1.5 s more than MAML for network model generation in each batch during the validation phase, where the number of model parameters is calculated by the thop.profile () function and the model runtime is calculated by the time.time () function.

Summarizing the aforementioned three experiments, it can be concluded that the diagnostic accuracy of MetaNAS is higher than that of the compared MAML++, Reptile, and MAML methods in most faults. MetaNAS uses AutoFD for NAS based on MAML, which provides a rich candidate network structure for MAML and solves the problem of a single meta-learning network structure, and MetaNAS's network model does not require a complex and time-consuming design process. Comparing the results of MetaNAS and MAML in the three experimental results, we can see that the

diagnostic results of MetaNAS are higher than those of the base method MAML in the case of different training set sizes of the same dataset, which indicates that MetaNAS can obtain better fault diagnosis capability after adding AutoFD because the network model structure can be learned, and the fault diagnosis results of MetaNAS in many faults are better than those of MAML++ and the Reptile algorithm, which are improved on the basis of MAML, proving the effectiveness of the MetaNAS method.

5 Conclusion

The MetaNAS method is proposed to find the optimal initial parameters to be learned in NAS by meta-learning, and the new mode can find the best performing network structure with only a few gradient updates based on the optimal initial parameters. MetaNAS uses NAS to provide a rich learnable network architecture for meta-learning method so that the network structure of meta-learning is no single. It also automates the network design, making it possible to quickly obtain fault diagnosis models with better performance even for new modes with small samples. MetaNAS solves the limitations to fault diagnosis through NAS, such as underutilization of the existing modal design experience and difficulty in training models with small samples. The effectiveness and superiority of the proposed method in fault diagnosis under the small samples of new models are demonstrated by numerical system and TE process simulations. However, the existing model design experiences are obtained from different modes of the same chemical process, and the learning of different industrial process model design experiences is lacking. The next work will focus on the study of learning algorithms about different industrial process model design experiences and NAS algorithms on unbalanced datasets.

Moving forward, there are several potential avenues for future research and improvement. First, expanding the application of MetaNAS to different fault diagnosis domains and datasets would provide a broader evaluation of its effectiveness and generalizability. Second, investigating the integration of additional data sources or modalities could enhance the diagnostic capabilities of MetaNAS. Furthermore, exploring the interpretability of the MetaNAS approach is an important direction for future research. Last, considering the scalability of the MetaNAS approach to handle larger and more complex fault diagnosis tasks would be valuable. By pursuing these future research directions, we can further advance the field of real-time fault diagnosis with small sample learning and continue to improve the performance, applicability, and interpretability of the MetaNAS approach.

Data availability statement

The datasets presented in this study can be found in online repositories. The names of the repository/repositories and accession number(s) can be found in the article/Supplementary Material.

Author contributions

Conceptualization, TL; software, JH; methodology, SR. All authors contributed to the article and approved the submitted version.

Funding

The study was supported by Shaanxi Provincial Science and Technology Department: 2023-JC-YB-547.

Conflict of interest

The authors declare that the research was conducted in the absence of any commercial or financial relationships that could be construed as a potential conflict of interest.

Publisher's note

References

1. Zhao K, Hu J, Shao H, Hu J. Federated multi-source domain adversarial adaptation framework for machinery fault diagnosis with data privacy. *Reliability Eng Syst Saf* (2023) 236:109246. doi:10.1016/j.ress.2023.109246

2. Liu Y, Zeng J, Bao J, Xie L. A unified probabilistic monitoring framework for multimode processes based on probabilistic linear discriminant analysis. *IEEE Trans Ind Inform* (2020) 16(10):6291–300. doi:10.1109/tii.2020.2966707

3. Zhang J, Zhou D, Chen M. Monitoring multimode processes: A modified PCA algorithm with continual learning ability. *J Process Control* (2021) 103:76–86. doi:10.1016/j.jprocont.2021.05.007

4. Dong J, Zhang C, Peng K. A new multimode process monitoring method based on a hierarchical Dirichlet process—hidden semi-markov model with application to the hot steel strip mill process. *Control Eng Pract* (2021) 110:104767. doi:10.1016/j.conengprac.2021.104767

5. Jin B, Cruz L, Gonçalves N. Pseudo RGB-D face recognition. *IEEE Sensors J* (2022) 22(22):21780–94. doi:10.1109/jsen.2022.3197235

6. Jiang Q, Yan X. Multimode process monitoring using variational Bayesian inference and canonical correlation analysis. *IEEE Trans Automation Sci Eng* (2019) 16(4):1814–24. doi:10.1109/tase.2019.2897477

7. Yang C, Zhou L, Huang K, Ji H, Long C, Chen X, et al. Multimode process monitoring based on robust dictionary learning with application to aluminium electrolysis process. *Neurocomputing* (2019) 332:305–19. doi:10.1016/j.neucom.2018.12.024

8. Zhao K, Jiang H, Wang K, Pei Z. Joint distribution adaptation network with adversarial learning for rolling bearing fault diagnosis. *Knowledge-Based Syst* (2021) 222:106974. doi:10.1016/j.knosys.2021.106974

9. Zhao SJ, Zhang J, Xu YM. Performance monitoring of processes with multiple operating modes through multiple PLS models. *J process Control* (2006) 16(7):763–72. doi:10.1016/j.jprocont.2005.12.002

10. Jin B, Cruz L, Gonçalves N. Deep facial diagnosis: Deep transfer learning from face recognition to facial diagnosis. *IEEE Access* (2020) 8:123649–61. doi:10.1109/access.2020.3005687

11. Wang F, Tan S, Peng J, Chang Y. Process monitoring based on mode identification for multi-mode process with transitions. *Chemometrics Intell Lab Syst* (2012) 110(1): 144–55. doi:10.1016/j.chemolab.2011.10.013

12. Zhao K, Jiang H, Liu C, Wang Y, Zhu K. A new data generation approach with modified Wasserstein auto-encoder for rotating machinery fault diagnosis with limited fault data. *Knowledge-Based Syst* (2022) 238:107892. doi:10.1016/j.knosys.2021.107892

13. Yao R, Jiang H, Li X, Cao J. Bearing incipient fault feature extraction using adaptive period matching enhanced sparse representation. *Mech Syst Signal Process* (2022) 166:108467. doi:10.1016/j.ymssp.2021.108467

14. Wang Y, Yao Q, Kwok JT, Ni LM. Generalizing from a few examples: A survey on few-shot learning. *ACM Comput Surv (Csur)* (2020) 53(3):1–34. doi:10.1145/3386252

15. Benaim S, Wolf L. One-shot unsupervised cross domain translation. *Adv Neural Inf Process Syst* (2018) 31. doi:10.48550/arXiv.1806.06029

16. Riaz S, Qi R, Tutsoy O, Iqbal J. A novel adaptive PD-type iterative learning control of the PMSM servo system with the friction uncertainty in low speeds. *PloS one* (2023) 18(1):e0279253. doi:10.1371/journal.pone.0279253

17. Bertinetto L, Henriques JF, Valmadre J, Torr P, Vedaldi A. Learning feed-forward one-shot learners. *Adv Neural Inf Process Syst* (2016) 29. doi:10.48550/arXiv.1606.05233

18. Riaz S, Lin H, Waqas M, Afzal F, Wang K, Saeed N. An accelerated error convergence design criterion and implementation of lebesgue-p norm ILC control topology for linear position control systems. *Math Probl Eng* (2021) 2021:1–12. doi:10.1155/2021/5975158

19. Zhao K, Jia F, Shao H. A novel conditional weighting transfer Wasserstein auto-encoder for rolling bearing fault diagnosis with multi-source domains. *Knowledge-Based Syst* (2023) 262:110203. doi:10.1016/j.knosys.2022.110203

20. Hariharan B, Girshick R. Low-shot visual recognition by shrinking and hallucinating features. In: Proceedings of the IEEE international conference on computer vision; 22-29 Oct. 2017; Venice, Italy (2017).

21. Finn C, Abbeel P, Levine S. Model-agnostic meta-learning for fast adaptation of deep networks. In: International conference on machine learning; August 6th to August 11th, 2017; Sydney, Australia (2017).

22. Riaz S, Lin H, Elahi H. A novel fast error convergence approach for an optimal iterative learning controller. *Integrated Ferroelectrics* (2020) 213(1):103–15. doi:10.1080/10584587.2020.1859828

23. Al-Shedivat M, Bansal T, Burda Y, Sutskever I, Mordatch I, Abbeel P. *Continuous adaptation via meta-learning in nonstationary and competitive environments*. (2017) arXiv preprint arXiv:171003641 2017.

24. Antoniou A, Storkey AJ. Learning to learn by self-critique. *Adv Neural Inf Process Syst* (2019) 32. doi:10.48550/arXiv.1905.10295

25. Riaz S, Lin H, Mahsud M, Afzal D, Alsinai A, Cancan M. An improved fast error convergence topology for PDα-type fractional-order ILC. *J Interdiscip Math* (2021) 24(7):2005–19. doi:10.1080/09720502.2021.1984567

26. Nichol A, Achiam J, Schulman J. *On first-order meta-learning algorithms*. (2018) arXiv preprint arXiv:180302999 2018.

27. Yan K, Ji Z, Shen W. Online fault detection methods for chillers combining extended kalman filter and recursive one-class SVM. *Neurocomputing* (2017) 228: 205–12. doi:10.1016/j.neucom.2016.09.076

28. Yan K, Ji Z, Lu H, Huang J, Shen W, Xue Y. Fast and accurate classification of time series data using extended ELM: Application in fault diagnosis of air handling units. *IEEE Trans Syst Man, Cybernetics: Syst* (2017) 49(7):1349–56. doi:10.1109/tsmc.2017.2691774

29. Yan C, Chang X, Li Z, Guan W, Ge Z, Zhu L, et al. Zeronas: Differentiable generative adversarial networks search for zero-shot learning. *IEEE Trans pattern Anal machine intelligence* (2021) 44(12):9733–40. doi:10.1109/tpami.2021.3127346

30. Li M, Huang P-Y, Chang X, Hu J, Yang Y, Hauptmann A. Video pivoting unsupervised multi-modal machine translation. *IEEE Trans Pattern Anal Machine Intelligence* (2022) 45:3918. doi:10.1109/TPAMI.2022.3181116

31. Zhang L, Chang X, Liu J, Luo M, Li Z, Yao L, et al. TN-ZSTAD: Transferable network for zero-shot temporal activity detection. *IEEE Trans Pattern Anal Machine Intelligence* (2022) 45:3848–61. doi:10.1109/tpami.2022.3183586

32. Chang X, Ren P, Xu P, Li Z, Chen X, Hauptmann A. A comprehensive survey of scene graphs: Generation and application. *IEEE Trans Pattern Anal Machine Intelligence* (2021) 45(1):1–26. doi:10.1109/tpami.2021.3137605

frontiers | Frontiers in Physics

TYPE Original Research
PUBLISHED 06 July 2023
DOI 10.3389/fphy.2023.1169548

OPEN ACCESS

EDITED BY
Gangwei Wang,
Hebei University of Economics and Business, China

REVIEWED BY
Amin Jajarmi,
University of Bojnord, Iran
Roman Ullah,
Higher Colleges of Technology, United Arab Emirates

*CORRESPONDENCE
Rasool Shah,
rasoolshahawkum@gmail.com

†These authors have contributed equally to this work

RECEIVED 19 February 2023
ACCEPTED 14 June 2023
PUBLISHED 06 July 2023

CITATION
Shah MA, Yasmin H, Ghani F, Abdullah S, Khan I and Shah R (2023), Fuzzy fractional Gardner and Cahn–Hilliard equations with the Atangana–Baleanu operator. *Front. Phys.* 11:1169548. doi: 10.3389/fphy.2023.1169548

Fuzzy fractional Gardner and Cahn–Hilliard equations with the Atangana–Baleanu operator

Manzoor Ali Shah[1†], Humaira Yasmin[2†], Fazal Ghani[1†], Saleem Abdullah[1†], Imran Khan[3†] and Rasool Shah[1*†]

[1]Department of Mathematics, Abdul Wali Khan University, Mardan, Pakistan, [2]Department of Basic Sciences, Preparatory Year Deanship, King Faisal University, Al-Ahsa, Saudi Arabia, [3]Department of Mathematics and Statistics, Bacha Khan University Charsadda, Charsadda, Pakistan

This article focuses on the investigation and computation of solutions to fuzzy fractional-order Cahn–Hilliard and Gardner equations. The study hybridizes the fuzzy Gardner and Cahn–Hilliard equation into two equations using hybrid techniques and the concept of a parametric fuzzy number. To explore these equations, a combination of a novel iterative approach and the Shehu transformation is employed. The article presents detailed procedures for computing a series of solutions to the fractional-order Cahn–Hilliard and Gardner problem. The applied techniques not only offer precision, simplicity, and efficacy but also outperform other existing technologies. Additionally, several examples are solved to validate the proposed theoretical solution.

KEYWORDS

iterative transform method, fractional fuzzy Gardner and Cahn–Hilliard equations, analytical solution, Atangana–Baleanu operator, fractional calculus

Introduction

In mathematics, fractional calculus is a useful tool for dealing with ambiguity, recognizing emotional or confusing circumstances, and providing more general answers. Physical models of real-world occurrences may contain significant uncertainty due to a variety of variables. It appears that fuzzy sets can be used to replicate the uncertainty caused by imprecision and ambiguity. If data involve uncertainty, we use it in the medical, environmental, economic, physical, and social sciences. Zadeh investigated these concerns when he contributed fuzziness to set theory in 1965. Fractional calculus has risen in popularity over the last 20 years as a result of its numerous applications in practical research [1–4]. In the behavior of the aforementioned system processes, there are numerous examples of fuzzy uncertainty as opposed to stochastic uncertainty. Many authors have focused on the theoretical foundations of fuzzy problems in recent years. Fractional fuzzy differential equations can be used in civil engineering, population models, electro-hydraulics models, and weapon systems, among others. Fractional fuzzy differential equations are also studied in real-world contexts such as medicine [6], practical systems [7], the golden mean [5], gravity, quantum optics [8], and engineering phenomena. Zadeh [9] became familiar with fuzzy set theory for the first time. The idea of a fuzzy number and its use in fuzzy controls [10] and approximation reasoning problems [11] then became the subjects of research. It is challenging to effectively represent a variety of circumstances using real numbers in data analysis. Later, the fundamentals of fuzzy number arithmetic were specified by Mizumoto and

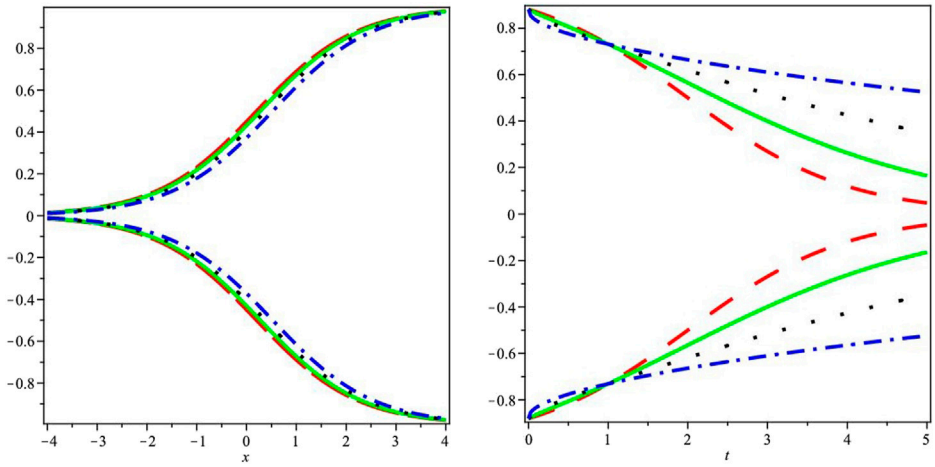

FIGURE 1
The first graph demonstrates the two-dimensional fuzzy lower and upper branch graphs for the analytical series solution, while the second graph illustrates the fractional-order differences between the two different series.

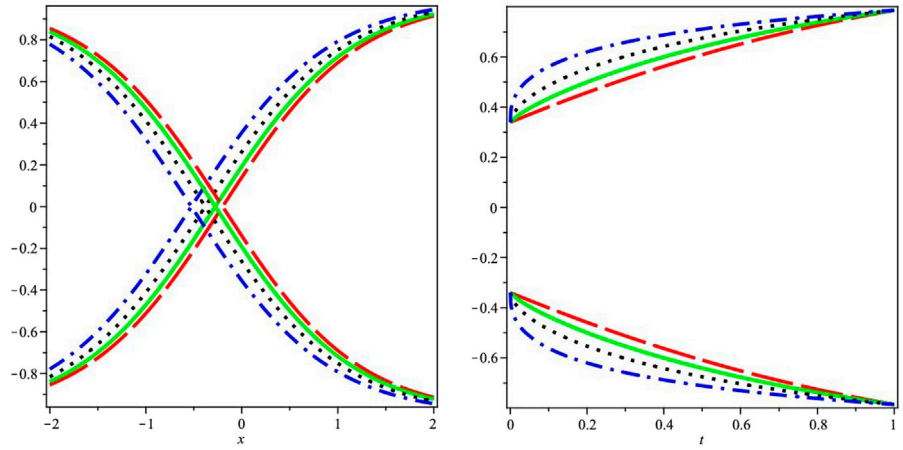

FIGURE 2
The first graph demonstrates the two-dimensional fuzzy lower and upper branch graphs for the analytical series solution, while the second graph illustrates the fractional-order differences between the two different series.

Tanaka [12, 13], Dubois and Prade [14, 15], Nahmias [17], and Ralescu [16]. They used a variety of intervals, such as ϱ-levels, $0 < \varrho \leq 1$, [18], to compute the fuzzy number. It contains information on fuzzy differential equations as well as the fundamental concepts of non-crisp sets. Equations of differential generalization are the recommended notions. Numerous academics have shown interest in this novel idea. Applications of fractional-order differential equations in real-world scenarios are significant; they may be found in fields like engineering, chemistry, and physics. The fractional differential equation is a helpful tool for representing non-linear events in scientific and engineering models. In applied mathematics and engineering, partial differential equations (PDEs), particularly non-linear PDEs, have been utilized to simulate a wide range of scientific phenomena.

Fractional differential equations have received an immense attention in the last two decades because of their ability to mimic a wide range of occurrences in a variety of academic domains and practical applications. Many physical applications in engineering and science can be described using fractional differential equations, which are particularly useful for a wide range of physical challenges. Because these equations are represented by fractional linear and non-linear PDEs, fractional differential equations must be solved [19–21]. The most significant processes occurring in the world are described by non-linear equations. Non-linear partial differential equations remain a challenging topic in both applied mathematics and physics, requiring the employment of a variety of methods to arrive at creative approximations or precise solutions [22–25]. Fractional differential equations have been solved using a variety of numerical and approximation methods. There have been several

innovative ways for solving fractional differential equations recently, some of which include the following: the iterative Laplace transform method (ILTM) [27], differential transform method (FDTM) [26], Adomain decomposition technique [29], variational iteration transform technique [30], fractional Adomian decomposition method (FADM) [28], natural decomposition technique [32], and fractional homotopy perturbation technique [31]. The primary goal of this article is to use the natural decomposition technique, one of the most efficient approaches, to solve non-linear fractional Cahn–Hilliard and Gardner equations. Natural decomposition methods do not need discretization, linearization, perturbation, or prescriptive assumptions to prevent round-off errors. The KdV and modified KdV equations were combined to create the Gardner equation [33], which is used to explain internal solitary waves in shallow water. In physics, Gardner's equation is often applied in fields including quantum field theory, fluid physics, and plasma physics [34, 35]. It also covers a variety of wave events in solid and plasma states [36]. We quickly review the fractional Gardner (FG) equation of the form

$$D_{\varepsilon}^{\beta}\nu(\wp,\varepsilon)+6\left(\nu-\Upsilon^{2}\nu^{2}\right)\frac{\partial\nu}{\partial\wp}+\frac{\partial\nu^{3}}{\partial\wp^{3}}=0,\qquad 0<\beta\leq 1,\qquad (1)$$

where Υ is a real constant. The wave function $\nu(\wp, \varepsilon)$ has the scaling variables space ($\wp$) and time (ε), the terms $\nu\frac{\partial\nu}{\partial\wp}$ and $\nu^{2}\frac{\partial\nu}{\partial\wp}$ represent non-linear wave steepen, and $\frac{\partial\nu^{3}}{\partial\wp^{3}}$ represents the wave dispersive effect.

In 1958, Cahn and Hilliard [37] developed the Cahn–Hilliard equation to represent the phase separation of a binary alloy at the critical temperature. This equation is essential to several outstanding scientific phenomena, such as phase separation, phase-ordering dynamics, and spinodal decomposition. In this context, the fractional Cahn–Hilliard (FCH) equation is expressed as follows:

$$D_{\varepsilon}^{\beta}\nu(\psi,\varepsilon)-\frac{\partial\nu}{\partial\psi}-6\nu\frac{\partial\nu^{2}}{\partial\psi}-\left(3\nu^{2}-1\right)\frac{\partial^{2}\nu}{\partial\psi^{2}}+\frac{\partial^{4}\nu}{\partial\psi^{4}}=0,\qquad 0<\beta\leq 1.\qquad (2)$$

Several techniques are applied to analyze the Cahn–Hilliard and Gardner equations, such as the Adomian decomposition method [38], modified Kudryashov method [39], reduced differential transform technique [40], residual power series technique [41], and homotopy perturbation method [42].

The article is organized as follows: theBasic definitionsection provides the basic definition of a fractional fuzzy set. Methodology of the iterative transform method is described in the Roadmap of the suggested techniquesection. The Implementation section describes the application of numerical fuzzy problems, which is followed by the conclusion.

Basic definitions

Definition 2.1. If $\varpi: \mathbb{R} \mapsto [0,1]$ denotes a fuzzy set, it is understood to be a fuzzy set if the following main requirements hold true [43–46]:

1. ϖ is normal (for some $\eta_0 \in \mathbb{R}; \varpi(\vartheta_0) = 1$);
2. ϖ is upper semi-continuous;
3. $\varpi(\vartheta_1\omega + (1-\omega)\vartheta_2) \geq (\varpi(\vartheta_1) \wedge \varpi(\vartheta_2)) \forall \omega \in [0,1], \vartheta_1, \vartheta_2 \in \mathbb{R}$, i.e., ϖ is convex;
4. $cl\{\vartheta \in \mathbb{R}, \varpi(\vartheta) > 0\}$ is compact.

Definition 2.2. The fuzzy number ϖ is a r-level set expressed as [43–46]

$$[\varpi]^{r} = \{\nu \in \mathbb{R}: \varpi(\nu) \geq 1\},$$

where $r \in [0, 1]$ and $\nu \in \mathbb{R}$.

Definition 2.3. A fuzzy number's parameterized variant is represented as $[\underline{\varpi}(r), \bar{\varpi}(r)]$ such that $r \in [0, 1]$ fulfills the following assumptions [43–46]:

1. $\varpi(r)$ is left continuous, left continuous at zero, non-decreasing, and over bounded (0,1];
2. $\varpi(r)$ is right continuous, right continuous at zero, non-increasing, and over bounded (0,1];
3. $\underline{\varpi}(r) \leq \bar{\varpi}(r)$.

Definition 2.4. Suppose that there are fuzzy set numbers $r \in [0, 1]$ and Y [43–46] $\tilde{\rho_1} = (\underline{\rho_1}, \overline{\rho_1}), \tilde{\rho_2} = (\underline{\rho_2}, \overline{\rho_2})$, then the additions, subtractions, and multiplications, consequently, are defined as follows:

1. $\tilde{\rho_1} \oplus \tilde{\rho_2} = (\underline{\rho_1}(r) + \underline{\rho_2}(r), \overline{\rho_1}(r) + \overline{\rho_2}(r))$;
2. $\tilde{\rho_1} \ominus \tilde{\rho_2} = (\overline{\rho_1}(r) - \overline{\rho_2}(r), \overline{\rho_1}(r) - \overline{\rho_2}(r))$;
3. $\mathrm{Y} \odot \tilde{\rho_1} = \begin{cases} (\mathrm{Y}\underline{\rho_1}, \mathrm{Y}\overline{\rho_1})\mathrm{Y} \geq 0, \\ (\mathrm{Y}\overline{\rho_1}, \mathrm{Y}\underline{\rho_1})\mathrm{Y} < 0. \end{cases}$

Definition 2.5. the fuzzy mappings Θ: $\tilde{E} \times \tilde{E} \mapsto \mathbb{R}$ have fuzzy two sets [43–46] $\tilde{\rho_1} = (\underline{\rho_1}, \overline{\rho_1}), \tilde{\rho_2} = (\underline{\rho_2}, \overline{\rho_2})$, then Θ-distances between $\tilde{\rho_1}$ and $\tilde{\rho_2}$ is defined as

$$\Theta(\tilde{\rho_1}, \tilde{\rho_2}) = \sup_{r\in[0,1]}\left[\max\left\{|\underline{\rho_1}(r) - \underline{\rho_2}(r)|, |\overline{\rho_1}(r) - \overline{\rho_2}(r)|\right\}\right].$$

Theorem 2.1. *Consider a fuzzy valued function* $\mathbf{E}$: $\mathbb{R} \mapsto \tilde{E}$ *such that* $\mathbf{E}(\gamma_0; r) = [\underline{\mathbf{E}}(\gamma_0; r), \bar{\mathbf{E}}(\gamma_0; r)]$ *and* $r \in [0, 1]$. *Then* [43–46],

1. $(\gamma_0; r)$ *and* $\mathbf{E}(\gamma_0; r)$ *are differentiable functions, if* $\mathbf{E}$ *is a (1)-differentiable* function *and*

$$[\mathbf{E}'(\gamma_0)]^{r} = [\underline{\mathbf{E}}'(\gamma_0; r), \bar{\mathbf{E}}'(\gamma_0; r)].$$

11. $\underline{\mathbf{E}}(\gamma_0; r)$ *and* $\bar{\mathbf{E}}(\gamma_0; r)$ *are differentiable functions, if* $\mathbf{E}$ *is a (2)-differentiable function and*

$$[\mathbf{E}'(\gamma_0)]^{r} = [\bar{\mathbf{E}}'(\gamma_0; r), \underline{\mathbf{E}}'(\gamma_0; r)].$$

Definition 2.6. Assume that a fuzzy mapping $\nu_{g\mathcal{H}}^{(r)} = \nu^{(r)} \in \mathbb{C}^{F}[0, s] \cap \mathbb{L}^{F}[0, s]$. The fuzzy $g\mathcal{H}$-fractional differentiability Caputo of the fuzzy value mappings *nu* is thus written as [43–46]

$$\left(g\mathcal{H}\mathcal{D}^{\beta}\nu\right)(\varepsilon) = \mathcal{J}_{a_1}^{r-\beta} \odot \left(\nu^{(r)}\right)(\gamma) = \frac{1}{\Gamma(r-\beta)} \odot \int_{a_1}^{\varepsilon} (\varepsilon_1 - \vartheta)^{r-\beta-1} \odot \nu^{(r)}(\vartheta)d\vartheta, \quad \beta \in (r-1, r], r \in \mathbb{N}, \varepsilon > a_1.$$

The parametric values of $\nu = [\underline{\nu}_r(\varepsilon), \bar{\nu}_r(\varepsilon)], r \in [0, 1]$ and $\varepsilon_{10} \in (0, s)$, and Caputo fractional differential in the presence of fuzzy are expressed as

$$\left[\mathcal{D}^{\beta}_{(i)-g\mathcal{H}}\nu(\varepsilon_{10})\right]_r = \left[\mathcal{D}^{\beta}_{(i)-g\mathcal{H}}\underline{\nu}(\varepsilon_{10}), \mathcal{D}^{\theta}_{(i)-g\mathcal{H}}\bar{\nu}(\varepsilon_{10})\right], r \in [0, 1],$$

where $r = [r]$

$$\left[\mathcal{D}^{\beta}_{(i)-g\mathcal{H}}\underline{\nu}(\varepsilon_{10})\right] = \frac{1}{\Gamma(r-\beta)}\left[\int_0^{\varepsilon} (\varepsilon - \mathbf{x})^{r-\beta-1}\frac{d^r}{d\mathbf{x}^r}\underline{\nu}_{(i)-g\mathcal{H}}(\mathbf{x})d\mathbf{x}\right]_{\varepsilon=\varepsilon_{10}},$$
$$\left[\mathcal{D}^{\theta}_{(i)-g\mathcal{H}}\bar{\nu}(\varepsilon_{10})\right] = \frac{1}{\Gamma(r-\beta)}\left[\int_0^{t_1} (\varepsilon - \mathbf{x})^{r-\beta-1}\frac{d^r}{d\mathbf{x}^r}\bar{\nu}_{(i)-g\mathcal{H}}(\mathbf{x})d\mathbf{x}\right]_{\varepsilon=\varepsilon_{10}}.$$

Definition 2.7. Suppose that fuzzy mappings $\tilde{\nu}(\varepsilon) \in \tilde{\mathbb{H}}^1(0, T)$ and $\beta \in [0, 1]$, then the fuzzy $g\mathcal{H}$-fractional differentiability Atangana–Baleanu of fuzzy value mappings is expressed as

$$\left(g\mathcal{H}\mathcal{D}^{\beta}\nu\right)(\varepsilon) = \frac{\mathbb{B}(\beta)}{1-\beta} \odot \left[\int_0^{t_1} \underline{\nu}'(\mathbf{x}) \odot E_{\beta}\left[\frac{-\beta(\varepsilon-\mathbf{x})^{\beta}}{1-\beta}\right]d\mathbf{x}\right].$$

Thus, the parameterized formulation of $\nu = [\underline{\nu}_r(\varepsilon), \bar{\nu}_r(\varepsilon)], r \in [0, 1]$ and $\varepsilon_0 \in (0, s)$, and the fuzzy Atangana–Baleanu operator is defined by

$$\left[{}^{ABC}\mathcal{D}^{\beta}_{(i)-g\mathcal{H}}\tilde{\nu}(\varepsilon_0; r)\right] = \left[{}^{ABC}\mathcal{D}^{\beta}_{(i)-g\mathcal{H}}\underline{\nu}(\varepsilon_0; r), {}^{ABC}\mathcal{D}^{\theta}_{(i)-g\mathcal{H}}\nu(\varepsilon_0; r)\right], \quad r \in [0, 1],$$

where

$${}^{ABC}\mathcal{D}^{\theta}_{(i)-g\mathcal{H}}\underline{\nu}(\varepsilon_0; r) = \frac{\mathbb{B}(\beta)}{1-\beta}\left[\int_0^{t_1} \underline{\nu}'_{(i)-g\mathcal{H}}(\mathbf{x})E_{\theta}\left[\frac{-\beta(\varepsilon-\mathbf{x})^{\theta}}{1-\beta}\right]d\mathbf{x}\right]_{\varepsilon=\varepsilon_0},$$
$${}^{ABC}\mathcal{D}^{\theta}_{(i)-g\mathcal{H}}\bar{\nu}(\varepsilon_0; r) = \frac{\mathbb{B}(\beta)}{1-\beta}\left[\int_0^{t_1} \bar{\nu}'_{(i)-g\mathcal{H}}(\mathbf{x})E_{\theta}\left[\frac{-\beta(\varepsilon-\mathbf{x})^{\theta}}{1-\beta}\right]d\mathbf{x}\right]_{\varepsilon=\varepsilon_0},$$

where $\mathbb{B}(\beta)$ represents the function of normalization which is equal to 1 when β is supposed to be 0 and 1. Moreover, we assume that form (i) $-g\mathcal{H}$ exists. Now, there is no requirement to consider the differentiability of (ii) $-g\mathcal{H}$.

Definition 2.8. Suggest a continuous real-value mapping Ψ, and there is an inappropriate Riemann fuzzy integrable mappings $\exp(\frac{-\omega}{\sigma}) \odot \tilde{\nu}(\varepsilon)$ on $[0, +\infty)$. Then, the integral $\int 0^{+\infty} \exp(-\frac{\omega}{\sigma}) \odot \tilde{\nu}(\varepsilon)d\varepsilon$ is recognized to be the Shehu fuzzy transformation, and it is noted over the set of mapping [43–46]as follows:

$$\mathcal{S} = \left\{\tilde{\nu}(\mathbf{g}): \exists \mathcal{A}, p_1, p_2 > 0, |\tilde{\nu}(\varepsilon)| < \mathcal{A}\exp\left(\frac{|\varepsilon|}{\psi_j}\right), \text{if } \varepsilon \in (-1)^{\mathrm{J}} \times [0, +\infty)\right\},$$

as

$$\mathbf{S}[\tilde{\nu}(\varepsilon)] = \mathcal{S}(\omega, \sigma) = \int_0^{+\infty} \exp\left(\frac{-\omega}{\sigma}\varepsilon\right) \odot \tilde{\nu}(\varepsilon)d\varepsilon, \quad \omega, \sigma > 0.$$

Remark 1

In Equation 14, $\tilde{\nu}$ satisfies the expectation of the reducing diameter $\underline{\nu}$, diameter $\bar{\nu}$ of a mapping of fuzzy ν. If $\sigma = 1$, then fuzzy Shehu transform is reduced to * Laplace transform [43–46].

$$\int_0^{+\infty} \exp\left(\frac{-\omega}{\sigma}\varepsilon\right) \odot \tilde{\nu}(\varepsilon)d\varepsilon = \left(\int_0^{+\infty} \exp\left(\frac{-\omega}{\sigma}\varepsilon\right)\underline{\nu}(\varepsilon; r)d\varepsilon, \int_0^{+\infty} \exp\left(\frac{-\omega}{\sigma}\varepsilon\right)\bar{\nu}(\varepsilon; r)d\varepsilon\right).$$

Moreover, by analyzing the traditional Shehu transformation [43–46], we achieve

$$\mathbb{S}[\underline{\nu}(\varepsilon; r)] = \int_0^{+\infty} \exp\left(\frac{-\omega}{\sigma}\varepsilon\right)\underline{\nu}(\varepsilon; r)d\varepsilon,$$

and

$$\mathbb{S}[\bar{\nu}(\varepsilon; r)] = \int_0^{+\infty} \exp\left(\frac{-\omega}{\sigma}\varepsilon\right)\bar{\nu}(\varepsilon; r)d\varepsilon.$$

The aforementioned expression can then be expressed as

$$\mathbf{S}[\tilde{\nu}(\varepsilon)] = (\mathbb{S}[\underline{\nu}(\varepsilon; r)], \mathbb{S}[\bar{\nu}(\varepsilon; r)]) = (\underline{\mathcal{S}}(\omega, \sigma), \bar{\mathcal{S}}(\omega, \sigma)).$$

Then, we shall define the Caputo generalized Hukuhara derivative's fuzzy Shehu transformation as ${}^{c}_{g\mathscr{H}}\mathcal{D}^{\ominus}_{\varepsilon}\nu(\varepsilon)$.

Definition 2.9. Suppose there is a fuzzy integrable value mapping ${}^{c}_{g\mathscr{H}}\mathcal{D}^{\beta}_{\varepsilon}\tilde{\nu}(\varepsilon)$, and $\nu(\varepsilon)$ is the primitive of ${}^{c}_{g\mathscr{H}}\mathcal{D}^{\beta}_{\varepsilon}\tilde{\nu}(\varepsilon)$ on $[0, +\infty)$, then the CFD of order β is expressed as [43–46]

$$\mathbf{S}\left[{}^{c}_{g\mathscr{H}}\mathcal{D}^{\beta}_{\varepsilon}\tilde{\nu}(\varepsilon)\right] = \left(\frac{\omega}{\sigma}\right)^{\beta} \odot \mathbf{S}[\tilde{\nu}(\varepsilon)] \ominus \sum_{\mathrm{J}=0}^{r-1}\left(\frac{\omega}{\sigma}\right)^{\beta-\mathrm{J}-1} \odot \tilde{\nu}^{(\mathrm{J})}(0), \quad \beta \in (r-1, r],$$

$$\left(\frac{\omega}{\sigma}\right)^{\beta} \odot \mathbf{S}[\tilde{\nu}(\varepsilon)] \ominus \sum_{\mathrm{J}=0}^{r-1}\left(\frac{\omega}{\sigma}\right)^{\beta-\mathrm{J}-1} \odot \tilde{f}^{(\mathrm{J})}(0) = \left(\left(\frac{\omega}{\sigma}\right)^{\beta}\mathbf{S}[\underline{\nu}(\varepsilon; r)] - \sum_{\mathrm{J}=0}^{r-1}\left(\frac{\omega}{\sigma}\right)^{\beta-\mathrm{J}-1} \odot \underline{\nu}^{(\mathrm{J})}(0; r), \left(\frac{\omega}{\sigma}\right)^{\beta}\mathbf{S}[\bar{\nu}(\varepsilon; r)] - \sum_{\mathrm{J}=0}^{r-1}\left(\frac{\omega}{\sigma}\right)^{\beta-\mathrm{J}-1}\bar{\nu}^{(\mathrm{J})}(0; r)\right).$$

Bokhari et al. defined the ABC operator's fractional derivative in terms of the Shehu transform. Additionally, we extend the concept of fuzzy ABC fractional derivative in the context of a fuzzy Shehu transform as follows:

Definition 2.10. Consider $\nu \in \mathbb{C}^F[0, s] \cap \mathbb{L}^F[0, s]$ such that $\tilde{\nu}(\varepsilon) = [\underline{\nu}(\varepsilon, r), \bar{\nu}(\varepsilon, r)]$, $r \in [0, 1]$; then, the Shehu transformation of the fuzzy *ABC* of order $\beta \in [0, 1]$ is defined as follows:

$$\mathbf{S}\left[g\mathcal{H}\mathcal{D}^{\beta}_{\varepsilon}\tilde{\nu}(\varepsilon)\right] = \frac{\mathbb{B}(\beta)}{1-\beta+\beta\left(\frac{\sigma}{\omega}\right)^{\beta}} \odot \left(\tilde{\mathbf{V}}(\sigma, \omega) \ominus \frac{\sigma}{\omega}\tilde{\nu}(0)\right).$$

Moreover, by applying the fact of Salahshour et al. [45], we obtain

$$\frac{\mathbb{B}(\beta)}{1-\beta+\beta\left(\frac{\sigma}{\tilde{\omega}}\right)^{\beta}}\odot\left(\tilde{\mathbf{V}}(\sigma,\omega)\ominus\frac{\omega}{\sigma}\tilde{\nu}(0)\right)$$
$$=\left(\frac{\mathbb{B}(\beta)}{1-\beta+\beta\left(\frac{\sigma}{\tilde{\omega}}\right)^{\beta}}\left(\underline{\mathbf{V}}(\sigma,\omega;r)-\frac{\sigma}{\omega}\nu(0;r)\right),\right.$$
$$\left.\frac{\mathbb{B}(\beta)}{1-\beta+\beta\left(\frac{\sigma}{\psi}\right)^{\theta}}\left(\bar{\mathbf{V}}(\sigma,\omega;r)-\frac{\sigma}{\tilde{\omega}}\bar{\nu}(0;r)\right)\right).$$

Road map of the suggested technique

Consider the fractional fuzzy partial differential equation

$$\mathcal{S}\left[{}^{ABC}D_{\varepsilon}^{\beta}\tilde{\nu}(\psi,\varepsilon)\right]=\mathcal{S}\left[D_{\psi}^{2}\tilde{\nu}(\psi,\varepsilon)+D_{\psi}^{3}\tilde{\nu}(\psi,\varepsilon)+\tilde{k}(r)\mathcal{F}(\psi,\varepsilon)\right],\quad(3)$$

where $\beta\in(0,1]$; therefore, the Shehu transform of Equation 3 is

$$\frac{\mathbb{B}(\beta)}{1-\beta+\beta\left(\frac{\sigma}{\omega}\right)^{\beta}}\mathcal{S}[\tilde{\nu}(\psi,\varepsilon)]-\frac{\mathbb{B}(\beta)}{1-\beta+\beta\left(\frac{\sigma}{\omega}\right)^{\beta}}\left(\frac{\nu}{\omega}\right)\tilde{\nu}(\psi,\xi,0)$$
$$=\mathcal{S}\left[D_{\psi}^{2}\tilde{\nu}(\psi,\varepsilon)+D_{\psi}^{3}\tilde{\nu}(\psi,\varepsilon)+\tilde{k}(r)\mathcal{F}(\psi,\varepsilon)\right].$$

On using the initial condition, we obtain

$$\mathcal{S}[\tilde{\nu}(\psi,\varepsilon)]=\frac{g(\psi,\xi)}{\omega}+\frac{1-\beta+\beta\left(\frac{\sigma}{\omega}\right)^{\beta}}{\mathbb{B}(\beta)}\mathcal{S}\left[D_{\psi}^{2}\tilde{\nu}(\psi,\varepsilon)+D_{\psi}^{3}\tilde{\nu}(\psi,\varepsilon)+\tilde{k}(r)\mathcal{F}(\psi,\varepsilon)\right].\quad(4)$$

Decomposing the solution as $\tilde{\nu}(\psi,\varepsilon)=\sum_{n=0}^{\infty}\tilde{\nu}_n(\psi,\varepsilon)$, then (4) implies

$$\mathcal{S}\sum_{n=0}^{\infty}\tilde{\nu}_n(\psi,\varepsilon)=\frac{g(\psi,\xi)}{\omega}+\frac{1-\beta+\beta\left(\frac{\sigma}{\omega}\right)^{\beta}}{\mathbb{B}(\beta)}\mathcal{S}\left[D_{\psi}^{2}\sum_{n=0}^{\infty}\tilde{\nu}_n(\psi,\varepsilon)+D_{\psi}^{3}\sum_{n=0}^{\infty}\tilde{\nu}_n(\psi,\varepsilon)+\tilde{k}(r)\mathcal{F}(\psi,\varepsilon)\right].\quad(5)$$

Taking parts of the solution by the choice of comparison, we obtain

$$\begin{aligned}
\mathcal{S}[\tilde{\nu}_0(\psi,\varepsilon)]&=\frac{g(\psi,\xi)}{\omega}+\frac{1-\beta+\beta\left(\frac{\sigma}{\omega}\right)^{\beta}}{\mathbb{B}(\beta)}\mathcal{S}\left[\tilde{k}(r)\mathcal{F}(\psi,\varepsilon)\right].\\
\mathcal{S}[\tilde{\nu}_1(\psi,\varepsilon)]&=\frac{1-\beta+\beta\left(\frac{\sigma}{\omega}\right)^{\beta}}{\mathbb{B}(\beta)}\mathcal{S}\left[D_{\psi}^{2}\tilde{\nu}_0(\psi,\varepsilon)+D_{\psi}^{3}\tilde{\nu}_0(\psi,\varepsilon)\right].\\
\mathcal{S}[\tilde{\nu}_2(\psi,\varepsilon)]&=\frac{1-\beta+\beta\left(\frac{\sigma}{\omega}\right)^{\beta}}{\mathbb{B}(\beta)}\mathcal{S}\left[D_{\psi}^{2}\tilde{\nu}_1(\psi,\varepsilon)+D_{\psi}^{3}\tilde{\nu}_1(\psi,\varepsilon)\right].\\
&\vdots\\
\mathcal{S}[\tilde{\nu}_{n+1}(\psi,\varepsilon)]&=\frac{1-\beta+\beta\left(\frac{\sigma}{\omega}\right)^{\beta}}{\mathbb{B}(\beta)}\mathcal{S}\left[D_{\psi}^{2}\tilde{\nu}_n(\psi,\varepsilon)+D_{\psi}^{3}\tilde{\nu}_n(\psi,\varepsilon)\right].
\end{aligned}\quad(6)$$

Taking the inverse Shehu transform, we obtain

$$\begin{aligned}
\underline{\nu}_0(\psi,\varepsilon)&=g(\psi,\xi)+\mathcal{S}^{-1}\left[\frac{1-\beta+\beta\left(\frac{\sigma}{\omega}\right)^{\beta}}{\mathbb{B}(\beta)}\mathcal{S}[\underline{k}(r)\mathcal{F}(\psi,\varepsilon)]\right],\\
\bar{\nu}_0(\psi,\varepsilon)&=g(\psi,\xi)+\mathcal{S}^{-1}\left[\frac{1-\beta+\beta\left(\frac{\sigma}{\omega}\right)^{\beta}}{\mathbb{B}(\beta)}\mathcal{S}[\bar{k}(r)\mathcal{F}(\psi,\varepsilon)]\right],\\
\underline{\nu}_1(\psi,\varepsilon)&=\mathcal{S}^{-1}\left[\frac{1-\beta+\beta\left(\frac{\sigma}{\omega}\right)^{\beta}}{\mathbb{B}(\beta)}\mathcal{S}\left[D_{\psi}^{2}\underline{\nu}_0(\psi,\varepsilon)+D_{\psi}^{3}\underline{\nu}_0(\psi,\varepsilon)\right]\right],\\
\bar{\nu}_1(\psi,\varepsilon)&=\mathcal{S}^{-1}\left[\frac{1-\beta+\beta\left(\frac{\sigma}{\omega}\right)^{\beta}}{\mathbb{B}(\beta)}\mathcal{S}\left[D_{\psi}^{2}\bar{\nu}_0(\psi,\varepsilon)+D_{\psi}^{3}\bar{\nu}_0(\psi,\varepsilon)\right]\right],\\
\underline{\nu}_2(\psi,\varepsilon)&=\mathcal{S}^{-1}\left[\frac{1-\beta+\beta\left(\frac{\sigma}{\omega}\right)^{\beta}}{\mathbb{B}(\beta)}\mathcal{S}\left[D_{\psi}^{2}\underline{\nu}_1(\psi,\varepsilon)+D_{\psi}^{3}\underline{\nu}_1(\psi,\varepsilon)\right]\right],\\
\bar{\nu}_2(\psi,\varepsilon)&=\mathcal{S}^{-1}\left[\frac{1-\beta+\beta\left(\frac{\sigma}{\omega}\right)^{\beta}}{\mathbb{B}(\beta)}\mathcal{S}\left[D_{\psi}^{2}\bar{\nu}_1(\psi,\varepsilon)+D_{\psi}^{3}\bar{\nu}_1(\psi,\varepsilon)\right]\right],\\
&\vdots\\
\underline{\nu}_{n+1}(\psi,\varepsilon)&=\mathcal{S}^{-1}\left[\frac{1-\beta+\beta\left(\frac{\sigma}{\omega}\right)^{\beta}}{\mathbb{B}(\beta)}\mathcal{S}\left[D_{\psi}^{2}\underline{\nu}_n(\psi,\varepsilon)+D_{\psi}^{3}\underline{\nu}_n(\psi,\varepsilon)\right]\right],\\
\bar{\nu}_{n+1}(\psi,\varepsilon)&=\mathcal{S}^{-1}\left[\frac{1-\beta+\beta\left(\frac{\sigma}{\omega}\right)^{\beta}}{\mathbb{B}(\beta)}\mathcal{S}\left[D_{\psi}^{2}\bar{\nu}_n(\psi,\varepsilon)+D_{\psi}^{3}\bar{\nu}_n(\psi,\varepsilon)\right]\right].
\end{aligned}\quad(7)$$

Thus, the solution becomes

$$\begin{aligned}
\underline{\nu}(\psi,\varepsilon)&=\underline{\nu}_0(\psi,\varepsilon)+\underline{\nu}_1(\psi,\varepsilon)+\underline{\nu}_2(\psi,\varepsilon)+\cdots,\\
\bar{\nu}(\psi,\varepsilon)&=\bar{\nu}_0(\psi,\varepsilon)+\bar{\nu}_1(\psi,\varepsilon)+\bar{\nu}_2(\psi,\varepsilon)+\cdots.
\end{aligned}\quad(8)$$

Equation 8 is the solution in series form.

Implementation

Example 4.1. Consider the fractional fuzzy Gardner equation as follows:

$${}^{ABC}D_{\varepsilon}^{\beta}\tilde{\nu}(\psi,\varepsilon)+6\left(\tilde{\nu}(\psi,\varepsilon)-\Upsilon^{2}\tilde{\nu}^{2}(\psi,\varepsilon)\right)\frac{\partial\tilde{\nu}(\psi,\varepsilon)}{\partial\psi}+\frac{\partial\tilde{\nu}^{3}(\psi,\varepsilon)}{\partial\psi^{3}}=0,\quad 0<\beta\le 1,\quad(9)$$

with the fuzzy initial condition

$$\tilde{\nu}(\psi,0)=\tilde{k}\left(\frac{1}{2}+\frac{1}{2}\tanh\left(\frac{\psi}{2}\right)\right).\quad(10)$$

Applying the proposed Equation 7, we achieve

$$\begin{aligned}
\underline{\nu}_0(\psi,\varepsilon) &= \underline{k}(r)\left(\frac{1}{2}+\frac{1}{2}\tanh\left(\frac{\psi}{2}\right)\right),\\
\bar{\nu}_0(\psi,\varepsilon) &= \bar{k}(r)\left(\frac{1}{2}+\frac{1}{2}\tanh\left(\frac{\psi}{2}\right)\right),\\
\underline{\nu}_1(\psi,\varepsilon) &= \underline{k}(r)\frac{\operatorname{sech}^2\left(\frac{\psi}{2}\right)\left(-1+\left(-4+3\Upsilon^2\right)\cosh(\psi)+3\left(-1+\Upsilon^2\right)\sinh(\psi)\right)}{8}\\
&\quad\times\frac{1}{\mathbb{B}(\beta)}\left\{\frac{\beta\varepsilon^{\beta}}{\Gamma(\beta+1)}+(1-\beta)\right\},\\
\bar{\nu}_1(\psi,\varepsilon) &= \bar{k}(r)\frac{\operatorname{sech}^2\left(\frac{\psi}{2}\right)\left(-1+\left(-4+3\Upsilon^2\right)\cosh(\psi)+3\left(-1+\Upsilon^2\right)\sinh(\psi)\right)}{8}\\
&\quad\times\frac{1}{\mathbb{B}(\beta)}\left\{\frac{\beta\varepsilon^{\beta}}{\Gamma(\beta+1)}+(1-\beta)\right\},
\end{aligned}\tag{11}$$

$$\begin{aligned}
\underline{\nu}_2(\psi,\varepsilon) &= \underline{k}(r)\frac{-\operatorname{sech}^7\left(\frac{\psi}{2}\right)}{64}\left(-24\left(-1+\Upsilon^2\right)\cosh\left(\frac{\psi}{2}\right)-6\left(22-37\Upsilon^2+15\Upsilon^4\right)\right.\\
&\quad\times\cosh\left(\frac{3\psi}{2}\right)+6\left(4-7\Upsilon^2+3\Upsilon^4\right)\cosh\left(\frac{5\psi}{2}\right)+2\left(103-102\Upsilon^2\right)\sinh\left(\frac{\psi}{2}\right)\\
&\quad\left.-3\left(43-74\Upsilon^2+30\Upsilon^4\right)\sinh\left(\frac{3\psi}{2}\right)+\left(25-42\Upsilon^2+18\Upsilon^4\right)\sinh\left(\frac{5\psi}{2}\right)\right)\\
&\quad\times\frac{1}{\mathbb{B}^2(\beta)}\left\{\frac{\beta^2\varepsilon^{2\beta}}{\Gamma(2\beta+1)}+2\beta(1-\beta)\frac{\varepsilon^{\beta}}{\Gamma(\beta+1)}+(1-\beta)^2\right\},\\
\bar{\nu}_2(\psi,\varepsilon) &= \bar{k}(r)\frac{-\operatorname{sech}^7\left(\frac{\psi}{2}\right)}{64}\left(-24\left(-1+\Upsilon^2\right)\cosh\left(\frac{\psi}{2}\right)-6\left(22-37\Upsilon^2+15\Upsilon^4\right)\right.\\
&\quad\times\cosh\left(\frac{3\psi}{2}\right)+6\left(4-7\Upsilon^2+3\Upsilon^4\right)\cosh\left(\frac{5\psi}{2}\right)+2\left(103-102\Upsilon^2\right)\sinh\left(\frac{\psi}{2}\right)\\
&\quad\left.-3\left(43-74\Upsilon^2+30\Upsilon^4\right)\sinh\left(\frac{3\psi}{2}\right)+\left(25-42\Upsilon^2+18\Upsilon^4\right)\sinh\left(\frac{5\psi}{2}\right)\right)\\
&\quad\times\frac{1}{\mathbb{B}^2(\beta)}\left\{\frac{\beta^2\varepsilon^{2\beta}}{\Gamma(2\beta+1)}+2\beta(1-\beta)\frac{\varepsilon^{\beta}}{\Gamma(\beta+1)}+(1-\beta)^2\right\}.
\end{aligned}\tag{12}$$

The higher terms can also be obtained in a similar manner. Equation 8 provides solution in series form; consequently, we write

$$\tilde{\nu}(\psi,\varepsilon)=\tilde{\nu}_0(\psi,\varepsilon)+\tilde{\nu}_1(\psi,\varepsilon)+\tilde{\nu}_2(\psi,\varepsilon)+\tilde{\nu}_3(\psi,\varepsilon)+\tilde{\nu}_4(\psi,\varepsilon)+\cdots,\tag{13}$$

while, in lower and upper portion types, it is, respectively, written as

$$\begin{aligned}
\underline{\nu}(\psi,\varepsilon) &= \underline{\nu}_0(\psi,\varepsilon)+\underline{\nu}_1(\psi,\varepsilon)+\underline{\nu}_2(\psi,\varepsilon)+\underline{\nu}_3(\psi,\varepsilon)+\underline{\nu}_4(\psi,\varepsilon)+\cdots,\\
\bar{\nu}(\psi,\varepsilon) &= \bar{\nu}_0(\psi,\varepsilon)+\bar{\nu}_1(\psi,\varepsilon)+\bar{\nu}_2(\psi,\varepsilon)+\bar{\nu}_3(\psi,\varepsilon)+\bar{\nu}_4(\psi,\varepsilon)+\cdots.
\end{aligned}\tag{14}$$

$$\begin{aligned}
&\underline{\nu}(\psi,\varepsilon)=\underline{k}(r)\left(\frac{1}{2}+\frac{1}{2}\tanh\left(\frac{\psi}{2}\right)\right)\\
&+\underline{k}(r)\frac{\operatorname{sech}^2\left(\frac{\psi}{2}\right)\left(-1+\left(-4+3\Upsilon^2\right)\cosh(\psi)+3\left(-1+\Upsilon^2\right)\sinh(\psi)\right)}{8}\\
&\quad\frac{1}{\mathbb{B}(\beta)}\left\{\frac{\beta\varepsilon^{\beta}}{\Gamma(\beta+1)}+(1-\beta)\right\}\\
&\quad+\underline{k}(r)\frac{-\operatorname{sech}^7\left(\frac{\psi}{2}\right)}{64}\left(-24\left(-1+\Upsilon^2\right)\cosh\left(\frac{\psi}{2}\right)-6\left(22-37\Upsilon^2+15\Upsilon^4\right)\right.\\
&\cosh\left(\frac{3\psi}{2}\right)+6\left(4-7\Upsilon^2+3\Upsilon^4\right)\cosh\left(\frac{5\psi}{2}\right)+2\left(103-102\Upsilon^2\right)\sinh\left(\frac{\psi}{2}\right)\\
&\quad\left.-3\left(43-74\Upsilon^2+30\Upsilon^4\right)\sinh\left(\frac{3\psi}{2}\right)+\left(25-42\Upsilon^2+18\Upsilon^4\right)\sinh\left(\frac{5\psi}{2}\right)\right)\\
&\frac{1}{\mathbb{B}^2(\beta)}\left\{\frac{\beta^2\varepsilon^{2\beta}}{\Gamma(2\beta+1)}+2\beta(1-\beta)\frac{\varepsilon^{\beta}}{\Gamma(\beta+1)}+(1-\beta)^2\right\}+\cdots\bar{\nu}(\psi,\varepsilon)\\
&=\bar{k}(r)\left(\frac{1}{2}+\frac{1}{2}\tanh\left(\frac{\psi}{2}\right)\right)\\
&\quad+\bar{k}(r)\frac{\operatorname{sech}^2\left(\frac{\psi}{2}\right)\left(-1+\left(-4+3\Upsilon^2\right)\cosh(\psi)+3\left(-1+\Upsilon^2\right)\sinh(\psi)\right)}{8}\\
&\quad\frac{1}{\mathbb{B}(\beta)}\left\{\frac{\beta\varepsilon^{\beta}}{\Gamma(\beta+1)}+(1-\beta)\right\}+\bar{k}(r)\frac{-\operatorname{sech}^7\left(\frac{\psi}{2}\right)}{64}\left(-24\left(-1+\Upsilon^2\right)\cosh\left(\frac{\psi}{2}\right)\right.\\
&\quad-6\left(22-37\Upsilon^2+15\Upsilon^4\right)\cosh\left(\frac{3\psi}{2}\right)+6\left(4-7\Upsilon^2+3\Upsilon^4\right)\cosh\left(\frac{5\psi}{2}\right)\\
&\quad+2\left(103-102\Upsilon^2\right)\sinh\left(\frac{\psi}{2}\right)\\
&\quad\left.-3\left(43-74\Upsilon^2+30\Upsilon^4\right)\sinh\left(\frac{3\psi}{2}\right)+\left(25-42\Upsilon^2+18\Upsilon^4\right)\sinh\left(\frac{5\psi}{2}\right)\right)\\
&\frac{1}{\mathbb{B}^2(\beta)}\left\{\frac{\beta^2\varepsilon^{2\beta}}{\Gamma(2\beta+1)}+2\beta(1-\beta)\frac{\varepsilon^{\beta}}{\Gamma(\beta+1)}+(1-\beta)^2\right\}+\cdots.
\end{aligned}\tag{15}$$

The exact result is given as

$$\tilde{\nu}(\psi,\varepsilon)=\tilde{k}\left(\frac{1}{2}+\frac{1}{2}\tanh\left(\frac{\psi-\varepsilon}{2}\right)\right).\tag{16}$$

Example 4.2. Consider the fractional fuzzy Cahn–Hilliard equation as follows:

$$\begin{aligned}
&D_{\varepsilon}^{\beta}\tilde{\nu}(\psi,\varepsilon)-\frac{\partial\tilde{\nu}(\psi,\varepsilon)}{\partial\psi}-6\tilde{\nu}(\psi,\varepsilon)\frac{\partial\tilde{\nu}^2(\psi,\varepsilon)}{\partial\psi}\\
&-\left(3\tilde{\nu}^2(\psi,\varepsilon)-1\right)\frac{\partial^2\tilde{\nu}(\psi,\varepsilon)}{\partial\psi^2}+\frac{\partial^4\tilde{\nu}(\psi,\varepsilon)}{\partial\psi^4}=0,\qquad 0<\beta\le 1,
\end{aligned}\tag{17}$$

with the fuzzy initial condition

$$\tilde{\nu}(\psi,0)=\tilde{k}\tanh\left(\frac{\psi}{\sqrt{2}}\right).\tag{18}$$

Applying the system of Equation 7, we achieve

$$\begin{aligned}
\underline{\nu}_0(\psi,\varepsilon) &= \underline{k}(r)\tanh\left(\frac{\psi}{\sqrt{2}}\right),\\
\bar{\nu}_0(\psi,\varepsilon) &= \bar{k}(r)\tanh\left(\frac{\psi}{\sqrt{2}}\right),\\
\underline{\nu}_1(\psi,\varepsilon) &= \underline{k}(r)\operatorname{sech}^2\frac{\left(\frac{\psi}{\sqrt{2}}\right)}{\sqrt{2}}\frac{1}{\mathbb{B}(\beta)}\left\{\frac{\beta\varepsilon^{\beta}}{\Gamma(\beta+1)}+(1-\beta)\right\},\\
\bar{\nu}_1(\psi,\varepsilon) &= \bar{k}(r)\operatorname{sech}^2\frac{\left(\frac{\psi}{\sqrt{2}}\right)}{\sqrt{2}}\frac{1}{\mathbb{B}(\beta)}\left\{\frac{\beta\varepsilon^{\beta}}{\Gamma(\beta+1)}+(1-\beta)\right\},
\end{aligned}\tag{19}$$

$$\begin{aligned}
\underline{\nu}_2(\psi,\varepsilon) &= -\underline{k}(r)\operatorname{sech}^2\left(\frac{\psi}{\sqrt{2}}\right)\tanh\left(\frac{\psi}{\sqrt{2}}\right)\frac{1}{\mathbb{B}^2(\beta)}\\
&\quad\times\left\{\frac{\beta^2\varepsilon^{2\beta}}{\Gamma(2\beta+1)}+2\beta(1-\beta)\frac{\varepsilon^{\beta}}{\Gamma(\beta+1)}+(1-\beta)^2\right\},\\
\bar{\nu}_2(\psi,\varepsilon) &= -\bar{k}(r)\operatorname{sech}^2\left(\frac{\psi}{\sqrt{2}}\right)\tanh\left(\frac{\psi}{\sqrt{2}}\right)\frac{1}{\mathbb{B}^2(\beta)}\\
&\quad\times\left\{\frac{\beta^2\varepsilon^{2\beta}}{\Gamma(2\beta+1)}+2\beta(1-\beta)\frac{\varepsilon^{\beta}}{\Gamma(\beta+1)}+(1-\beta)^2\right\}.
\end{aligned}\tag{20}$$

The higher terms can also be obtained in a similar manner. Equation 8 provides solution in series form; consequently, we write

$$\tilde{\nu}(\psi,\varepsilon)=\tilde{\nu}_0(\psi,\varepsilon)+\tilde{\nu}_1(\psi,\varepsilon)+\tilde{\nu}_2(\psi,\varepsilon)+\tilde{\nu}_3(\psi,\varepsilon)+\tilde{\nu}_4(\psi,\varepsilon)+\cdots.\tag{21}$$

In the lower and upper portion types, it is, respectively, written as

$$\underline{\nu}(\psi,\varepsilon) = \underline{\nu}_0(\psi,\varepsilon) + \underline{\nu}_1(\psi,\varepsilon) + \underline{\nu}_2(\psi,\varepsilon) + \underline{\nu}_3(\psi,\varepsilon) + \underline{\nu}_4(\psi,\varepsilon) + \cdots,$$
$$\bar{\nu}(\psi,\varepsilon) = \bar{\nu}_0(\psi,\varepsilon) + \bar{\nu}_1(\psi,\varepsilon) + \bar{\nu}_2(\psi,\varepsilon) + \bar{\nu}_3(\psi,\varepsilon) + \bar{\nu}_4(\psi,\varepsilon) + \cdots. \tag{22}$$

$$\begin{aligned}\underline{\nu}(\psi,\varepsilon) &= \underline{k}(r)\tanh\left(\frac{\psi}{\sqrt{2}}\right) + \underline{k}(r)\operatorname{sech}^2\frac{\left(\frac{\psi}{\sqrt{2}}\right)}{\sqrt{2}}\frac{1}{\mathbb{B}(\beta)}\left\{\frac{\beta\varepsilon^{\beta}}{\Gamma(\beta+1)} + (1-\beta)\right\}\\ &\quad - \underline{k}(r)\operatorname{sech}^2\left(\frac{\psi}{\sqrt{2}}\right)\tanh\left(\frac{\psi}{\sqrt{2}}\right)\frac{1}{\mathbb{B}^2(\beta)}\\ &\quad \times\left\{\frac{\beta^2\varepsilon^{2\beta}}{\Gamma(2\beta+1)} + 2\beta(1-\beta)\frac{\varepsilon^{\beta}}{\Gamma(\beta+1)} + (1-\beta)^2\right\} + \cdots,\\ \bar{\nu}(\psi,\varepsilon) &= \bar{k}(r)\tanh\left(\frac{\psi}{\sqrt{2}}\right) + \bar{k}(r)\operatorname{sech}^2\frac{\left(\frac{\psi}{\sqrt{2}}\right)}{\sqrt{2}}\frac{1}{\mathbb{B}(\beta)}\left\{\frac{\beta\varepsilon^{\beta}}{\Gamma(\beta+1)} + (1-\beta)\right\}\\ &\quad - \bar{k}(r)\operatorname{sech}^2\left(\frac{\psi}{\sqrt{2}}\right)\tanh\left(\frac{\psi}{\sqrt{2}}\right)\frac{1}{\mathbb{B}^2(\beta)}\\ &\quad \times\left\{\frac{\beta^2\varepsilon^{2\beta}}{\Gamma(2\beta+1)} + 2\beta(1-\beta)\frac{\varepsilon^{\beta}}{\Gamma(\beta+1)} + (1-\beta)^2\right\} + \cdots.\end{aligned} \tag{23}$$

The exact result is

$$\tilde{\nu}(\psi,\varepsilon) = \tilde{k}\tanh\left(\frac{\psi+\varepsilon}{\sqrt{2}}\right). \tag{24}$$

Discussion of results

In Figure 1, the first graph presents the two-dimensional fuzzy lower and upper branch graphs showcasing the analytical series solution. This graph visually represents the behavior and characteristics of the solution in a two-dimensional space. The second graph in Figure 1 illustrates the fractional-order differences between the two different series of Example 1. This graph highlights the variations and disparities between the fractional-order components of the series, providing insights into the impact of fractional-order differences on the overall solution.

Moving on to Figure 2, similar to Figure 1, the first graph displays the two-dimensional fuzzy lower and upper branch graphs representing the analytical series solution. This visualization offers a comprehensive view of the solution's behavior and properties. The second graph in Figure 2 focuses on the fractional-order differences between the two different series of Example 2. By examining this graph, one can observe and analyze the variations and discrepancies in the fractional-order components, gaining a deeper understanding of their influence on the overall solution.

Overall, the graphical discussion presented in Figure 1 and Figure 2 provides a visual representation of the analytical series solutions, allowing for a better comprehension of the fuzzy lower and upper branch graphs as well as the fractional-order differences in the respective examples. These graphical analyses enhance the interpretation and interpretation of the results obtained in the study, contributing to a more comprehensive understanding of the investigated phenomena.

Conclusion

The Atangana–Baleanu operator is used in this work to attempt a semi-analytic solution to the fuzzy fractional Gardner and Cahn–Hilliard equations. As a result, in this case, fuzzy operators are better suited to describe the physical phenomena. Using a fuzzy method that takes into account the starting condition's uncertainty, we computed the solutions to the Gardner and Cahn–Hilliard equations. This study generalized the fuzzy fractional of the Gardner and Cahn–Hilliard equations. Next, we created the approximate parametric formulation of the suggested problem using a novel iterative transform technique. We demonstrated many examples that supported the methodology's intended use and created a parametric solution for each case. Last but not least, solving a wide variety of fuzzy fractional partial differential equations analytically is not an easy task.

Data availability statement

The raw data supporting the conclusion of this article will be made available by the authors, without undue reservation.

Author contributions

All authors listed have made a substantial, direct, and intellectual contribution to the work and approved it for publication.

Funding

This work was supported by the Deanship of Scientific Research, the Vice Presidency for Graduate Studies and Scientific Research, King Faisal University, Saudi Arabia (Grant No. 3661).

Conflict of interest

The authors declare that the research was conducted in the absence of any commercial or financial relationships that could be construed as a potential conflict of interest.

Publisher's note

References

1 Baleanu D, Jajarmi A, Mohammadi H, Rezapour S. A new study on the mathematical modelling of human liver with Caputo-Fabrizio fractional derivative. *Chaos, Solitons and Fractals* (2020) 134:109705. doi:10.1016/j.chaos.2020.109705

2 Attia N, Akgul A, Seba D, Nour A, Asad J. A novel method for fractal-fractional differential equations. *Alexandria Eng J* (2022) 61(12):9733–48. doi:10.1016/j.aej.2022.02.004

3 Baleanu D, Ghassabzade FA, Nieto JJ, Jajarmi A. On a new and generalized fractional model for a real cholera outbreak. *Alexandria Eng J* (2022) 61(11):9175–86. doi:10.1016/j.aej.2022.02.054

4 Asjad MI, Usman M, Kaleem MM, Akgul A. Numerical solutions of fractional Oldroyd-B hybrid nanofluid through a porous medium for a vertical surface. *Waves in Random and Complex Media* (2022) 1–21. doi:10.1080/17455030.2022.2128233

5 Datta DP. The golden mean, scale free extension of real number system, fuzzy sets and 1/f spectrum in physics and biology. *Chaos, Solitons and Fractals* (2003) 17(4):781–8. doi:10.1016/s0960-0779(02)00531-3

6 Haq EU, Hassan QMU, Ahmad J, Ehsan K. Fuzzy solution of system of fuzzy fractional problems using a reliable method. *Alexandria Eng J* (2022) 61(4):3051–8. doi:10.1016/j.aej.2021.08.034

7 El Naschie MS. On a fuzzy Kahler-like manifold which is consistent with the two slit experiment. *Int J Nonlinear Sci Numer Simulation* (2005) 6(2):95–8. doi:10.1515/ijnsns.2005.6.2.95

8 El Naschie MS. From experimental quantum optics to quantum gravity via a fuzzy Kahler manifold. *Chaos, Solitons and Fractals* (2005) 25(5):969–77. doi:10.1016/j.chaos.2005.02.028

9 Zadeh LA. Fuzzy sets. In: *Fuzzy sets, fuzzy logic, and fuzzy systems: Selected papers by lotfi A zadeh*. Singapore: World Scientific Publishing Co. Inc (1996). p. 394–432.

10 Chang SS, Zadeh LA. On fuzzy mapping and control. In: *Fuzzy sets, fuzzy logic, and fuzzy systems: Selected papers by lotfi A zadeh*. Singapore: World Scientific Publishing Co. Inc (1996). p. 180–4.

11 Zadeh LA. Linguistic variables, approximate reasoning and dispositions. *Med Inform* (1983) 8(3):173–86. doi:10.3109/14639238309016081

12 Mizumoto M, Tanaka K. The four operations of arithmetic on fuzzy numbers. *Syst Comput Controls* (1976) 7(5):73–81.

13 Mizumoto M, Tanaka K. Some properties of fuzzy sets of type 2. *Inf Control* (1976) 31(4):312–40. doi:10.1016/s0019-9958(76)80011-3

14 Dubois DJ. *Fuzzy sets and systems: Theory and applications*. New York, NY: Academic Press (1980).

15 Dubois D, Prade H. Operations on fuzzy numbers. *Int J Syst Sci* (1978) 9(6):613–26. doi:10.1080/00207727808941724

16 Ralescu D. A survey of the representation of fuzzy concepts and its applications. In: *Advances in fuzzy set theory and applications*. Amsterdam: North Holland (1979). p. 77–91.

17 Nahmias S. Fuzzy variables. *Fuzzy sets Syst* (1978) 1(2):97–110. doi:10.1016/0165-0114(78)90011-8

18 Negoita CV, Ralecu DA. *Applications of fuzzy sets to system analysis*. New York, NY: John Wiley and Sons (1975).

19 Caputo M. Linear models of dissipation whose Q is almost frequency independent. Part II. *Ann Geophys* (1966) 19(4):383–93. doi:10.1111/j.1365-246X.1967.tb02303.x

20 Marin M, Marinescu C. Thermoelasticity of initially stressed bodies, asymptotic equipartition of energies. *Int J Eng Sci* (1998) 36(1):73–86. doi:10.1016/s0020-7225(97)00019-0

21 Marin M. A domain of influence theorem for microstretch elastic materials. *Nonlinear Anal Real World Appl* (2010) 11(5):3446–52. doi:10.1016/j.nonrwa.2009.12.005

22 Miller KS, Ross B. *An introduction to the fractional calculus and differential equations*. New York, NY: John Wiley (1993).

23 Podlubny I. *Fractional differential equations: An introduction to fractional derivatives, fractional differential equations, to methods of their solution and some of their applications*. San Diego, CA: Academic Press (1998).

24 Rawashdeh SM. An efficient approach for time-fractional damped Burger and time-sharma-tasso-Olver equations using the FRDTM. *Appl Math Inf Sci* (2015) 9(3):1239–46. doi:10.12785/amis/090317

25 Rawashdeh MS, Al-Jammal H. Numerical solutions for systems of nonlinear fractional ordinary differential equations using the FNDM. *Mediterr J Math* (2016) 13(6):4661–77. doi:10.1007/s00009-016-0768-7

26 Arikoglu A, Ozkol I. Solution of fractional differential equations by using differential transform method. *Chaos, Solitons* and *Fractals* (2007) 34(5):1473–81. doi:10.1016/j.chaos.2006.09.004

27 Khan H, Khan A, Al-Qurashi M, Shah R, Baleanu D. Modified modelling for heat like equations within Caputo operator. *Energies* (2020) 13(8):2002. doi:10.3390/en13082002

28 Momani S, Odibat Z. Analytical solution of a time-fractional Navier-Stokes equation by Adomian decomposition method. *Appl Math Comput* (2006) 177(2):488–94. doi:10.1016/j.amc.2005.11.025

29 Khan H, Khan A, Kumam P, Baleanu D, Arif M. A case report of absolute thrombocytopenia with ticagrelor. *Adv Difference Equations* (2020) 2020(1):1–5. doi:10.1093/ehjcr/ytaa169

30 Wu GC. A fractional variational iteration method for solving fractional nonlinear differential equations. *Comput Math Appl* (2011) 61(8):2186–90. doi:10.1016/j.camwa.2010.09.010

31 Qin Y, Khan A, Ali I, Al Qurashi M, Khan H, Shah R, et al. An efficient analytical approach for the solution of certain fractional-order dynamical systems. *Energies* (2020) 13(11):2725. doi:10.3390/en13112725

32 Rawashdeh MS. The fractional natural decomposition method: Theories and applications. *Math Methods Appl Sci* (2017) 40(7):2362–76. doi:10.1002/mma.4144

33 Gardner GHF, Gardner LW, Gregory AR. Formation velocity and density-the diagnostic basics for stratigraphic traps. *Geophysics* (1974) 39(6):770–80. doi:10.1190/1.1440465

34 Fu Z, Liu S, Liu S. New kinds of solutions to Gardner equation. *Chaos Solit Fractals* (2004) 20(2):301–9. doi:10.1016/s0960-0779(03)00383-7

35 Xu GQ, Li ZB, Liu YP. Exact solutions to a large class of nonlinear evolution equations. *Chin J Phys* (2003) 41(3):232–41.

36 Kuo CK. New solitary solutions of the Gardner equation and Whitham-Broer-Kaup equations by the modified simplest equation method. *Optik* (2017) 147:128–35. doi:10.1016/j.ijleo.2017.08.048

37 Cahn JW, Hilliard JE. Free energy of a nonuniform system. I. Interfacial free energy. *J Chem Phys* (1958) 28(2):258–67. doi:10.1063/1.1744102

38 Dahmani Z, Benbachir M. Solutions of the Cahn-Hilliard equation with time- and space-fractional derivatives. *Int J Nonlinear Sci* (2009) 8(1):19–26. doi:10.1007/3-540-32371-6_3

39 Hosseini K, Bekir A, Ansari R. New exact solutions of the conformable time-fractional Cahn-Allen and Cahn-Hilliard equations using the modified Kudryashov method. *Optik* (2017) 132:203–9. doi:10.1016/j.ijleo.2016.12.032

40 Rawashdeh MS, Obeidat NA. Applying the reduced differential transform method to solve the telegraph and Cahn-Hilliard equations. *Thai J Math* (2015) 13(1):153–63.

41 Arafa A, Elmahdy G. Application of residual power series method to fractional coupled physical equations arising in fluids flow. *Int J Differ Equ* (2018) 2018:1–10. doi:10.1155/2018/7692849

42 Bouhassoun A, Cherif MH. Homotopy perturbation method for solving the fractional Cahn-Hilliard equation. *J Interdiscip Math* (2015) 18(5):513–24. doi:10.1080/10288457.2013.867627

43 Allahviranloo T. *Fuzzy fractional differential operators and equation studies in fuzziness and soft computing*. Berlin, Germany: Springer (2021).

44 Gottwald S. *Fuzzy set theory and its applications*. Dordrecht: Kluwer Academic Publishers (1992).

45 Allahviranloo T, Ahmadi MB. Fuzzy laplace transforms. *Soft Comput* (2010) 14(3):235–43. doi:10.1007/s00500-008-0397-6

46 Maitama S, Zhao W. Homotopy analysis Shehu transform method for solving fuzzy differential equations of fractional and integer order derivatives. *Comput Appl Math* (2021) 40(3):86–30. doi:10.1007/s40314-021-01476-9

frontiers | Frontiers in Physics

TYPE Original Research
PUBLISHED 10 July 2023
DOI 10.3389/fphy.2023.1148306

OPEN ACCESS

EDITED BY
Snezhana I. Abarzhi,
University of Western Australia, Australia

REVIEWED BY
Naveed Anjum,
Government College University, Pakistan
Roman Ullah,
Higher Colleges of Technology, United Arab Emirates

*CORRESPONDENCE
Samir A. El-Tantawy,
tantawy@sci.psu.edu.eg

RECEIVED 19 January 2023
ACCEPTED 22 June 2023
PUBLISHED 10 July 2023

CITATION
Hammad MA, Alrowaily AW, Shah R, Ismaeel SME and A. El-Tantawy S (2023), Analytical analysis of fractional nonlinear Jaulent-Miodek system with energy-dependent Schrödinger potential. *Front. Phys.* 11:1148306. doi: 10.3389/fphy.2023.1148306

Analytical analysis of fractional nonlinear Jaulent-Miodek system with energy-dependent Schrödinger potential

Ma'mon Abu Hammad[1], Albandari W. Alrowaily[2], Rasool Shah[3], Sherif M. E. Ismaeel[4,5] and Samir A. El-Tantawy[6,7]*

[1]Department of Mathematics, Al-Zaytoonah University of Jordan, Amman, Jordan, [2]Department of Physics, College of Science, Princess Nourah bint Abdulrahman University, Riyadh, Saudi Arabia, [3]Department of Mathematics, Abdul Wali Khan University Mardan, Mardan, Pakistan, [4]Department of Physics, College of Science and Humanities in Al-Kharj, Prince Sattam Bin Abdulaziz University, Riyadh, Saudi Arabia, [5]Department of Physics, Faculty of Science, Ain Shams University, Cairo, Egypt, [6]Department of Physics, Faculty of Science, Port Said University, Port Said, Egypt, [7]Research Center for Physics (RCP), Department of Physics, Faculty of Science and Arts, Al-Baha University, Al Baha, Saudi Arabia

In this work, a novel technique is considered for analyzing the fractional-order Jaulent-Miodek system. The suggested approach is based on the use of the residual power series technique in conjunction with the Laplace transform and Caputo operator to solve the system of equations. The Caputo derivative is applied to express the fractional operator, which is more suitable for modeling real-world phenomena with memory effects. As a real example, the proposed technique is implemented for analyzing the Jaulent-Miodek equation under suitable initial conditions. Additionally, the proposed technique's validity (accuracy and effectiveness) is examined by studying some numerical examples. The obtained solutions show that the suggested technique can provide a reliable solution for the fractional-order Jaulent-Miodek system, making it a helpful tool for researchers in different areas, including engineering, physics, and mathematics. We also analyze the absolute error between the derived approximations and the analytical solutions to check the validation and accuracy of the obtained approximations. Many researchers can benefit from both the obtained approximations and the suggested method in analyzing many complicated nonlinear systems in plasma physics and nonlinear optics, and many others.

KEYWORDS

Fractional-order Jaulent-Miodek system, Residual power series, Laplace transform, Caputo operator, Fractional calculus

1 Introduction

Fractional differential equations (DEs) are types of DEs that involve fractional derivatives (FDs). Unlike ordinary DEs, where the order of the derivative is a positive integer, fractional DEs (FDEs) involve operators of non-integer orders. These equations are applied to model various physical and biological phenomena, such as anomalous diffusion, viscoelasticity, and fractal growth [1–3]. FDEs have several unique properties that differentiate them from ordinary DEs, such as non-locality and memory effects. Solving the FDEs requires specialized techniques, such as fractional calculus and numerical methods [4–8]. These equations have become an active area of research in recent decades due to their potential application in various fields of science [9–12].

Fractional nonlinear systems of partial DEs (PDEs) are mathematics model that describes the behavior of complex models in different areas, such as chemistry, biology, physics, engineering, and finance [13–15]. These systems are characterized by the presence of FDs, which are generalizations of the classical integer-order derivatives. FDs describe the system's memory and long-range interactions and allow for modeling anomalous diffusion, power-law behavior, and other non-local effects that classical models cannot capture. Nonlinearities are another essential feature of fractional systems, as they can lead to the emergence of rich and diverse phenomena, such as chaos, bifurcations, solitons, and patterns. Nonlinear systems are ubiquitous in nature and technology, and understanding their dynamics is crucial for predicting and controlling their behavior [16–23].

Fractional nonlinear systems of PDEs are challenging to study due to their non-locality, nonlinearity, and complexity. They require developing new analytical and numerical tools, such as fractional calculus (FC), dynamical systems theory, and computer simulations [24–26]. Despite the difficulties, fractional nonlinear systems of PDEs have attracted increasing attention in recent years due to their relevance in many applications. They provide a powerful framework for modeling and understanding complex phenomena and offer new opportunities for scientific and technological advances [27, 28].

It has been found that FDEs describe real-world problems more precisely than integral order DEs. The study of coupled systems of FDEs is also quite interesting. Because mathematical models of many phenomena in bio-mathematics, physics, psychology, and other fields are coupled systems of DEs [29, 30]. Among such coupled systems of fractional PDEs (FPDEs), we have the coupled Jaulent-Miodek models with Schrodinger energy-dependent potential. This type of equation system is widely applied as a model for the solution of several real worlds problems in the areas of applied sciences [31, 32]. Extensive analysis of nonlinear coupled fractional-order Jaulent-Miodek models a key role in many areas fields of science, such as plasma physics [33], condensed matter physics [34, 35]. There are a variety of techniques applied in achieving analytic and numeric results to linear and nonlinear FPDE, such as the homotopy perturbation technique (HPT) [36–39], the variational iteration technique [40], the q-homotopy analysis transformation technique [41], the fractional natural decomposition technique [42], the fractional multi-step differential transform technique [43], the new iterative technique [44, 45] and the homotopy analysis technique [46, 47], Residual power series technique [48].

The suggested method is called Laplace residual power series method (LRPSM) which was introduced recently to address nonlinear DEs (NLDEs) with fractional orders [49, 50]. This method is a combination between Laplace transform (LT) and RPSM which provides a more accurate solution, requiring less time and simpler calculations than other analytical methods. Unlike other methods, LRPSM does not involve differentiation or linearization and only utilizes the LT, followed by taking the limit at infinity. Thus, the current work aims to apply an innovative analytical technique (LRPSM) to obtain highly accurate estimated fractional solutions to the Jaulent-Miodek equation in the Caputo sense subject to suitable initial conditions. Also, the outcomes of the LRPSM will be compared with the precise answer by creating graphs and tables for the numerical problem. The suggested technique has been used to make exact results for emerging realistic models of physical phenomena by using fast convergent power series. This method succeeded because it is straightforward and handles different kinds of initial conditions directly. Also, it doesn't need linearization or restrictive assumptions, doesn't need a lot of computing power, takes less time, and is more accurate.

The framework of this study is detailed as follows: Section 2 reviews certain essential concepts, properties, and theorems related to FC, LT, and Laplace fractional expansion. The general methodology of LRPSM for the proposed model is presented in Section 3. Fractional solution Jaulent-Miodek equations are provided applying the LRPSM in Section 4. Section 5 contains the result and discussion. Finally, the conclusion is given in Section 6.

2 Basic definitions

Definition 1. *For at least n time differentiable function, the fractional Caputo derivative of order ρ reads [51]*

$$ {}^{C}D_{\tau}^{\rho}\psi(\gamma,\tau) = \begin{cases} \int_0^{\tau} \frac{(\tau-w)^{n-\rho-1}\psi(\eta,w)}{\Gamma(n-\rho)}dw, & n-1<\rho\le n, \\ \frac{\partial^n \psi(\eta,\tau)}{\partial\tau^n}, & n=\rho, \end{cases} \tag{1} $$

where $n \in N$ and the fractional Riemann–Liouville (RL) of $\Omega(\gamma,\tau)$ of order κ becomes

$$ J_{\tau}^{\rho}\psi(\eta,\tau) = \frac{1}{\Gamma(\rho)}\int_0^{\tau}(\tau-w)^{\rho-1}\psi(\eta,w)dw, \tag{2} $$

assuming that the given integral exists.

Lemma 1. *For $n-1<\rho\le n$, $q>-1$, $\tau\ge 0$ and $\lambda \in R$, we have [52]:*

1. $D_{\tau}^{\rho}\tau^{q} = \frac{\Gamma(q+1)}{\Gamma(q-\rho+1)}\tau^{q-\rho}$,
2. $D_{\tau}^{\rho}\lambda = 0$,
3. $D_{\tau}^{\rho}I_{\tau}^{\rho}\psi(\eta,\tau) = \psi(\eta,\tau)$,
4. $I_{\tau}^{\rho}D_{\tau}^{\rho}\psi(\eta,t) = \psi(\eta,\tau) - \sum_{j=0}^{n-1}\partial^{j}\psi(\eta,0)\frac{\tau^{j}}{j!}$.

Definition 2. *The function of LT $\psi(\eta,\tau)$ is given as [52]*

$$ \psi(\eta,s) = \mathcal{L}_{\tau}[\psi(\eta,\tau)] = \int_0^{\infty} e^{-s\tau}\psi(\eta,\tau)d\tau, \quad s>\mu. \tag{3} $$

The expression for the inverse of LT reads

$$ \psi(\eta,\tau) = \mathcal{L}_{\tau}^{-1}[\psi(\eta,s)] = \int_{l-i\infty}^{l+i\infty} e^{s\tau}\psi(\eta,s)ds, \quad l = Re(s) > l_0, \tag{4} $$

where l_0 is in the right half-plane of absolute convergence the Laplace integral's.

Lemma 2. *Assuming that $\psi(\eta,\tau)$ is a piecewise continuous function with exponential-order δ, we can obtain $\psi(\eta,s) = \mathcal{L}_{\tau}[\psi(\eta,\tau)]$ by taking the LT of $\psi(\eta,\tau)$.*

1. $\mathcal{L}_{\tau}[J_{\tau}^{\rho}\psi(\eta,\tau)] = \frac{\psi(\eta,s)}{s^{\rho}}, \quad \kappa>0$.

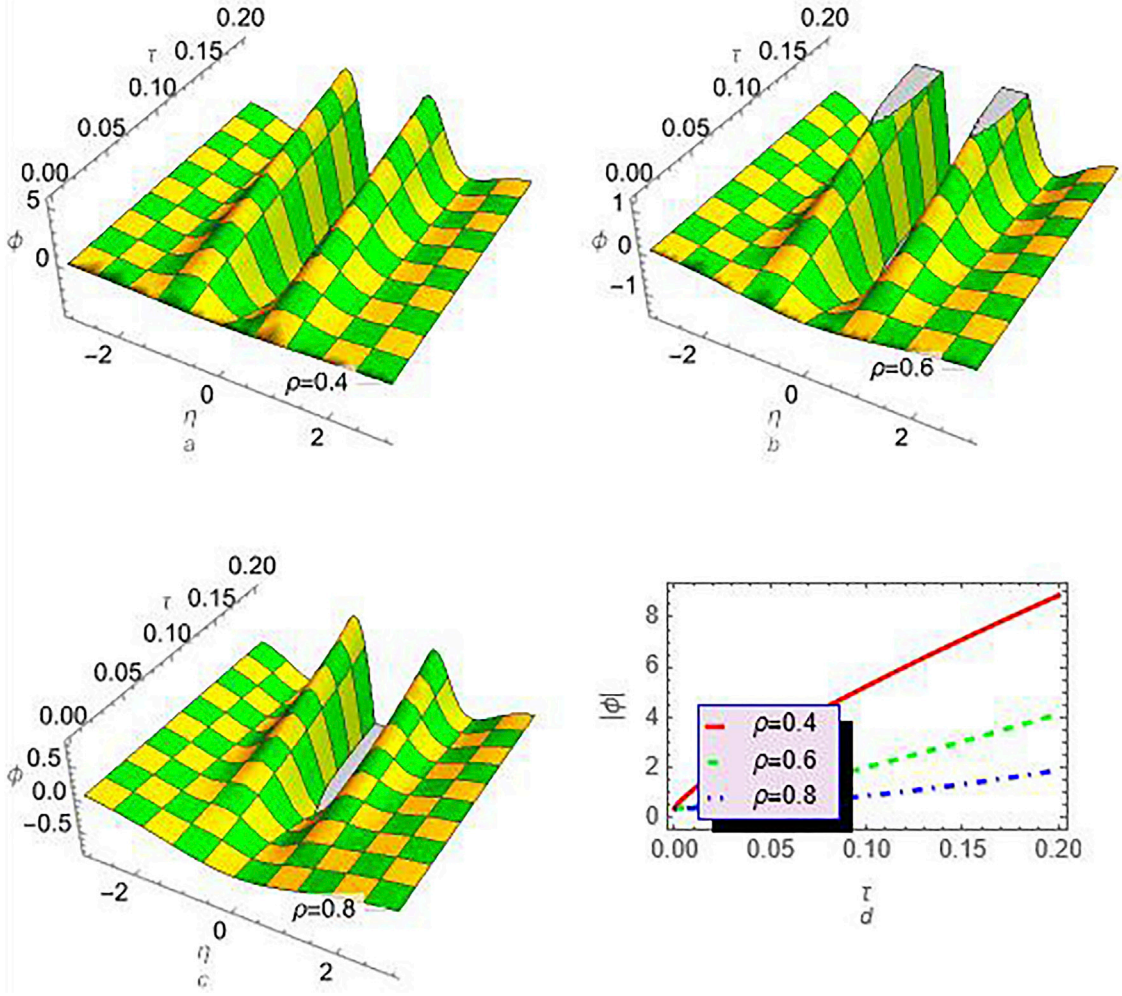

FIGURE 1
The profile of the approximation $\phi(\eta, \tau)$ (24) is plotted at different values of ρ and with $\lambda = 1$: **(A)** $\rho = 0.4$, **(B)** $\rho = 0.6$, **(C)** $\rho = 0.8$., and **(D)** the comparison between different values of ρ at $x = 0$.

2. $\mathcal{L}_\tau[D_\tau^\rho \psi(\eta,\tau)] = s^\rho \psi(\eta,s) - \sum_{k=0}^{m-1} s^{\rho-k-1}\psi^k(\eta,0),\ m-1<\rho\le m.$
3. $\mathcal{L}_\tau[D_\tau^{n\rho} \psi(\eta,\tau)] = s^{n\rho} \psi(\eta,s) - \sum_{k=0}^{n-1} s^{(n-k)\rho-1} D_\tau^{k\rho}\psi(\eta,0),$
$0<\rho\le 1.$

Theorem 1. *Consider a function $\Omega(\gamma, \tau)$ that is continuous and piecewise-defined over the interval $I \times [0, \infty)$ and has an exponential order of ζ. Let us define the term $\Omega(\gamma, s)$ as the Laplace transform of $\Omega(\gamma, \tau)$ with respect to τ. It is worth noting that $\Omega(\gamma, s)$ has a fractional expansion.*

$$\Omega(\gamma,s) = \sum_{n=0}^{\infty} \frac{f_n(\gamma)}{s^{1+n\mu}}, 0<\mu\le 1, \gamma\in I, s>\zeta. \tag{5}$$

Then, $f_n(\gamma) = D_\tau^{n\mu}\Omega(\gamma,0)$.

3 General implementation laplace residual power series method

Consider the general FPDE

$$D_\tau^\rho \psi(\eta,\tau) + N[\psi(\eta,\tau)] + A[\psi(\eta,\tau)] = 0, \quad \text{where} \quad 0<\rho\le 1, \tag{6}$$

subject to initial condition:

$$\psi(\eta,\tau) = f_0(\eta). \tag{7}$$

The function $d\psi(\eta, \tau)$ is unknown and depends on the independent variables η and τ, where the operator A is linear and N is nonlinear.Applying LT to Eq. 6 and making use of Eq. 7 we get

$$\psi(\eta,s) - \frac{f_0(\eta,s)}{s} + \frac{1}{s^\rho}\mathcal{L}_\tau[N[\mathcal{L}_\tau^{-1}[\psi(\eta,s)]] + A[\psi(\eta,\tau)]] = 0. \tag{8}$$

The result of Eq. 8 is given as

$$\psi(\xi,s) = \sum_{n=0}^{\infty} \frac{f_n(\xi,s)}{s^{n\rho+1}}, \tag{9}$$

the kth-truncate terms series are

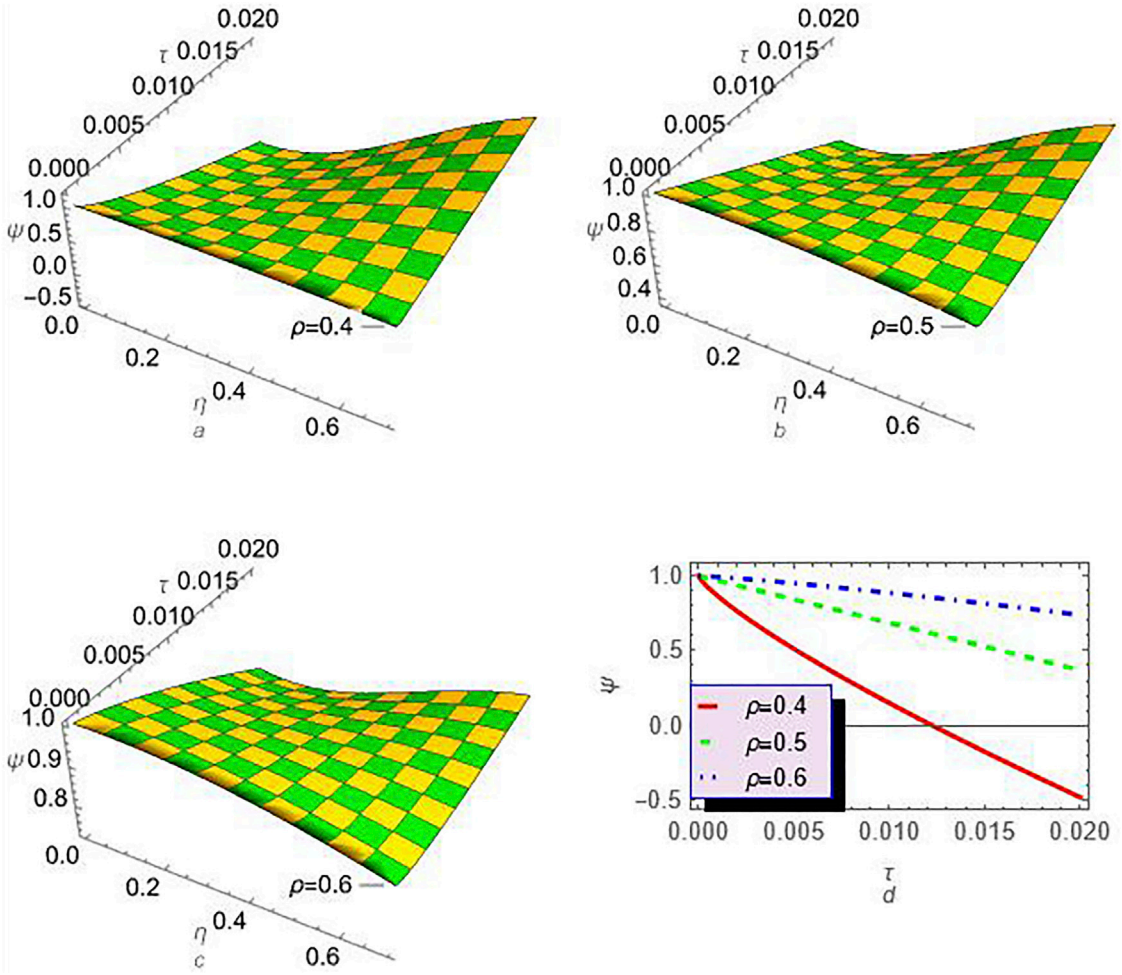

FIGURE 2
The profile of the approximation $\psi(\eta, \tau)$ (25) is plotted at different values of ρ and with $\lambda = 1$: **(A)** $\rho = 0.4$, **(B)** $\rho = 0.5$, **(C)** $\rho = 0.6$., and **(D)** the comparison between different values of ρ at $x = 0$.

$$\psi(\eta, s) = \frac{f_0(x, s)}{s} + \sum_{n=1}^{k} \frac{f_n(\eta, s)}{s^{n\rho+1}}, \quad n = 1, 2, 3, 4\cdots \tag{10}$$

The residual Laplace function reads [53].

$$\mathcal{L}_\tau Res(\eta, s) = \psi(\eta, s) - \frac{f_0(\eta, s)}{s} + \frac{1}{s^\rho}\mathcal{L}_\tau\Big[N[\mathcal{L}_\tau^{-1}[\psi(\eta, s)]] + A[\psi(\eta, \tau)]\Big]. \tag{11}$$

And the kth-LRFs as:

$$\mathcal{L}_\tau Res_k(\eta, s) = \psi_k(\eta, s) - \frac{f_0(\eta, s)}{s} + \frac{1}{s^\rho}\mathcal{L}_\tau\Big[N[\mathcal{L}_\tau^{-1}[\psi_k(\eta, s)]] + A[\psi_k(\eta, \tau)]\Big]. \tag{12}$$

The few properties of the LRPSM [53], is expressed as.

- $\mathcal{L}_\tau Res(\eta, s) = 0$ and $\lim_{j\to\infty}\mathcal{L}_\tau Res_k(\eta, s) = \mathcal{L}_\tau Res_\psi(\eta, s)$ for each $s > 0$,
- $\lim_{s\to\infty} s\mathcal{L}_\tau Res_\psi(\eta, s) = 0 \Rightarrow \lim_{s\to\infty} s\mathcal{L}_\tau Res_{\psi,k}(\eta, s) = 0$,
- $\lim_{s\to\infty} s^{k\rho+1}\mathcal{L}_\tau Res_{\psi,k}(\eta, s) = \lim_{s\to\infty} s^{k\rho+1}\mathcal{L}_\tau Res_{\psi,k}(\eta, s) = 0, \quad 0 < \rho \le 1, \quad k = 1, 2, 3, \cdots$.

To investigate the coefficient $f_n(\eta, s)$ and $g_n(\eta, s)$, we find the solution of the following system

$$\lim_{s\to\infty} s^{k\rho+1}\mathcal{L}_\tau Res_{\psi,k}(\eta, s) = 0, \quad \lim_{s\to\infty} s^{k\rho+1}\mathcal{L}_\tau Res_{\phi,k}(\eta, s) = 0, \quad k = 1, 2, \cdots. \tag{13}$$

Finally, we apply the inverse of the LT to Eq. 9, to get the k^{th} analytical solution of $\psi_k(\eta, \tau)$ and $\phi_k(\eta, \tau)$.

4 Numerical problem

Consider the coupled fractional-order Jaulent-Miodek equations:

TABLE 1 The approximate solution $\phi(\eta, \tau)$ (24) is considered at different values ρ and with ($\tau = 0.0099$, $\lambda = 0.2$). Also, the absolute error of $\phi(\eta, \tau)$ (24) at $\rho = 1$ as compared to the exact solution (26) is estimated.

η	$\rho = 0.5$	$\rho = 0.7$	$\rho = 0.8$	LRPSM ($\rho = 1$)	*exact*	*Abs.error*
0.1	−0.01	−0.0150	−0.0150	−0.0150	−0.0150	8.67132×10^{-8}
0.2	−0.01	−0.01499	−0.01499	−0.01499	−0.01499	1.69551×10^{-7}
0.3	−0.01	−0.01498	−0.01498	−0.01498	−0.01498	2.51868×10^{-7}
0.4	−0.01	−0.01497	−0.01497	−0.01497	−0.01497	3.33415×10^{-7}
0.5	−0.01	−0.01495	−0.01495	−0.01495	−0.01495	4.1395×10^{-7}
0.6	−0.01	−0.01493	−0.01493	−0.01493	−0.01493	4.93232×10^{-7}
0.7	−0.01	−0.0149	−0.0149	−0.0149	−0.0149	5.71027×10^{-7}
0.8	−0.01	−0.01488	−0.01487	−0.01487	−0.01487	6.47109×10^{-7}
0.9	−0.01	−0.01484	−0.01484	−0.01484	−0.01484	7.21256×10^{-7}
1	−0.01	−0.0148	−0.0148	−0.0148	−0.0148	7.93258×10^{-7}
1.1	−0.01	−0.01476	−0.01476	−0.01476	−0.01476	8.62914×10^{-7}
1.2	−0.01	−0.01472	−0.01472	−0.01472	−0.01471	9.30033×10^{-7}
1.3	−0.01	−0.01467	−0.01467	−0.01467	−0.01467	9.94433×10^{-7}
1.4	−0.01	−0.01462	−0.01462	−0.01461	−0.01461	1.05595×10^{-6}
1.5	−0.01	−0.01456	−0.01456	−0.01456	−0.01456	1.11442×10^{-6}
1.6	−0.01	−0.0145	−0.0145	−0.0145	−0.0145	1.16971×10^{-6}
1.7	−0.01	−0.01444	−0.01444	−0.01443	−0.01443	1.22168×10^{-6}
1.8	−0.01	−0.01437	−0.01437	−0.01437	−0.01437	1.27022×10^{-6}
1.9	−0.01	−0.0143	−0.0143	−0.0143	−0.01429	1.31522×10^{-6}
2	−0.01	−0.01423	−0.01422	−0.01422	−0.01422	1.35661×10^{-6}

$$
\begin{aligned}
&D_\tau^\rho \phi(\eta,\tau) + \frac{\partial^3 \phi(\eta,\tau)}{\partial \eta^3} + \frac{3}{2}\psi(\eta,\tau)\frac{\partial^3 \psi(\eta,\tau)}{\partial \eta^3} + \frac{9}{2}\frac{\partial \psi(\eta,\tau)}{\partial \eta}\frac{\partial^2 \psi(\eta,\tau)}{\partial \eta^2} \\
&\quad - 6\phi(\eta,\tau)\frac{\partial \phi(\eta,\tau)}{\partial \eta} - 6\phi(\eta,\tau)\psi(\eta,\tau)\frac{\partial \psi(\eta,\tau)}{\partial \eta} \\
&\quad - \frac{3}{2}\psi^2(\eta,\tau)\frac{\partial \phi(\eta,\tau)}{\partial \eta} = 0, \\
&D_\tau^\rho \psi(\eta,\tau) + \frac{\partial^3 \psi(\eta,\tau)}{\partial \eta^3} - 6\frac{\partial \phi(\eta,\tau)}{\partial \eta}\psi(\eta,\tau) - 6\phi(\eta,\tau)\frac{\partial \psi(\eta,\tau)}{\partial \eta} \\
&\quad - \frac{15}{2}\frac{\partial \psi(\eta,\tau)}{\partial \eta}\psi^2(\eta,\tau) = 0,
\end{aligned}
$$

where $0 < \rho \le 1$, (14)

with the initial conditions (ICs)

$$
\begin{cases}
\phi(\eta,0) = \dfrac{\lambda^2}{8}\left(1 - Sech^2\left(\dfrac{\lambda\eta}{2}\right)\right), \\
\psi(\eta,0) = \lambda Sech^2\left(\dfrac{\lambda\eta}{2}\right).
\end{cases} \tag{15}
$$

By utilizing Eq. 14 and taking advantage of Eq. 15, we get

$$
\begin{aligned}
&\phi(\eta,s) - \frac{\phi(\eta,0)}{s} + \frac{1}{s^\rho}\frac{\partial^3 \phi(\eta,s)}{\partial \eta^3} + \frac{3}{2s^\rho}\mathcal{L}_\tau\left[\mathcal{L}_\tau^{-1}\psi(\eta,s)\mathcal{L}_\tau^{-1}\frac{\partial^3 \psi(\eta,s)}{\partial \eta^3}\right] \\
&\quad + \frac{9}{2s^\rho}\mathcal{L}_\tau\left[\mathcal{L}_\tau^{-1}\frac{\partial \psi(\eta,s)}{\partial \eta}\mathcal{L}_\tau^{-1}\frac{\partial^2 \psi(\eta,s)}{\partial \eta^2}\right] \\
&\quad - \frac{6}{s^\rho}\mathcal{L}_\tau\left[\mathcal{L}_\tau^{-1}\phi(\eta,s)\mathcal{L}_\tau^{-1}\frac{\partial \phi(\eta,s)}{\partial \eta}\right] \\
&\quad - \frac{6}{s^\rho}\mathcal{L}_\tau\left[\mathcal{L}_\tau^{-1}\phi(\eta,s)\mathcal{L}_\tau^{-1}\psi(\eta,s)\mathcal{L}_\tau^{-1}\frac{\partial \psi(\eta,s)}{\partial \eta}\right] \\
&\quad - \frac{3}{2s^\rho}\mathcal{L}_\tau\left[\left(\mathcal{L}_\tau^{-1}\psi(\eta,s)\right)^2\mathcal{L}_\tau^{-1}\frac{\partial \phi(\eta,s)}{\partial \eta}\right] = 0, \\
&\psi(\eta,s) - \frac{\phi(\eta,0)}{s} + \frac{1}{s^\rho}\frac{\partial^3 \psi(\eta,s)}{\partial \eta^3} - \frac{6}{s^\rho}\mathcal{L}_\tau\left[\mathcal{L}_\tau^{-1}\frac{\partial \phi(\eta,s)}{\partial \eta}\mathcal{L}_\tau^{-1}\psi(\eta,s)\right] \\
&\quad - \frac{6}{s^\rho}\mathcal{L}_\tau\left[\mathcal{L}_\tau^{-1}\phi(\eta,s)\mathcal{L}_\tau^{-1}\frac{\partial \psi(\eta,s)}{\partial \eta}\right] \\
&\quad - \frac{15}{2s^\rho}\mathcal{L}_\tau\left[\mathcal{L}_\tau^{-1}\frac{\partial \psi(\eta,s)}{\partial \eta}\left(\mathcal{L}_\tau^{-1}\psi(\eta,s)\right)^2\right] = 0.
\end{aligned} \tag{16}
$$

By applying the ICs, we get

10.3389/fphy.2023.1148306

$$\begin{aligned}
&\phi(\eta,s)-\frac{\frac{\lambda^2}{8}\left(1-Sech^2\left(\frac{\lambda\eta}{2}\right)\right)}{s}+\frac{1}{s^{\rho}}\frac{\partial^3\phi(\eta,s)}{\partial\eta^3}\\
&\quad+\frac{3}{2s^{\rho}}\mathcal{L}_{\tau}\left[\mathcal{L}_{\tau}^{-1}\psi(\eta,s)\mathcal{L}_{\tau}^{-1}\frac{\partial^3\psi(\eta,s)}{\partial\eta^3}\right]\\
&\quad+\frac{9}{2s^{\rho}}\mathcal{L}_{\tau}\left[\mathcal{L}_{\tau}^{-1}\frac{\partial\psi(\eta,s)}{\partial\eta}\mathcal{L}_{\tau}^{-1}\frac{\partial^2\psi(\eta,s)}{\partial\eta^2}\right]\\
&\quad-\frac{6}{s^{\rho}}\mathcal{L}_{\tau}\left[\mathcal{L}_{\tau}^{-1}\phi(\eta,s)\mathcal{L}_{\tau}^{-1}\frac{\partial\phi(\eta,s)}{\partial\eta}\right]\\
&\quad-\frac{6}{s^{\rho}}\mathcal{L}_{\tau}\left[\mathcal{L}_{\tau}^{-1}\phi(\eta,s)\mathcal{L}_{\tau}^{-1}\psi(\eta,s)\mathcal{L}_{\tau}^{-1}\frac{\partial\psi(\eta,s)}{\partial\eta}\right]\\
&\quad-\frac{3}{2s^{\rho}}\mathcal{L}_{\tau}\left[\left(\mathcal{L}_{\tau}^{-1}\psi(\eta,s)\right)^2\mathcal{L}_{\tau}^{-1}\frac{\partial\phi(\eta,s)}{\partial\eta}\right]=0,\\
&\psi(\eta,s)-\frac{\lambda Sech^2\left(\frac{\lambda\eta}{2}\right)}{s}+\frac{1}{s^{\rho}}\frac{\partial^3\psi(\eta,s)}{\partial\eta^3}\\
&\quad-\frac{6}{s^{\rho}}\mathcal{L}_{\tau}\left[\mathcal{L}_{\tau}^{-1}\frac{\partial\phi(\eta,s)}{\partial\eta}\mathcal{L}_{\tau}^{-1}\psi(\eta,s)\right]\\
&\quad-\frac{6}{s^{\rho}}\mathcal{L}_{\tau}\left[\mathcal{L}_{\tau}^{-1}\phi(\eta,s)\mathcal{L}_{\tau}^{-1}\frac{\partial\psi(\eta,s)}{\partial\eta}\right]\\
&\quad-\frac{15}{2s^{\rho}}\mathcal{L}_{\tau}\left[\mathcal{L}_{\tau}^{-1}\frac{\partial\psi(\eta,s)}{\partial\eta}\left(\mathcal{L}_{\tau}^{-1}\psi(\eta,s)\right)^2\right]=0.
\end{aligned}\tag{17}$$

The kth-truncated term series reads

$$\begin{aligned}
&\phi(\eta,s)=\frac{\frac{\lambda^2}{8}\left(1-Sech^2\left(\frac{\lambda\eta}{2}\right)\right)}{s}+\sum_{n=1}^{k}\frac{f_n(\eta,s)}{s^{n\rho+1}},\\
&\psi(\eta,s)=\frac{\lambda Sech^2\left(\frac{\lambda\eta}{2}\right)}{s}+\sum_{n=1}^{k}\frac{f_n(\eta,s)}{s^{n\rho+1}},\\
&n=1,2,3,4\cdots.
\end{aligned}\tag{18}$$

The Laplace residual functions (LRFs) reads

$$\begin{aligned}
&\mathcal{L}_{\tau}Res(\eta,s)=\phi(\eta,s)-\frac{\frac{\lambda^2}{8}\left(1-Sech^2\left(\frac{\lambda\eta}{2}\right)\right)}{s}+\frac{1}{s^{\rho}}\frac{\partial^3\phi(\eta,s)}{\partial\eta^3}\\
&\quad+\frac{3}{2s^{\rho}}\mathcal{L}_{\tau}\left[\mathcal{L}_{\tau}^{-1}\psi(\eta,s)\mathcal{L}_{\tau}^{-1}\frac{\partial^3\psi(\eta,s)}{\partial\eta^3}\right]\\
&\quad+\frac{9}{2s^{\rho}}\mathcal{L}_{\tau}\left[\mathcal{L}_{\tau}^{-1}\frac{\partial\psi(\eta,s)}{\partial\eta}\mathcal{L}_{\tau}^{-1}\frac{\partial^2\psi(\eta,s)}{\partial\eta^2}\right]\\
&\quad-\frac{6}{s^{\rho}}\mathcal{L}_{\tau}\left[\mathcal{L}_{\tau}^{-1}\phi(\eta,s)\mathcal{L}_{\tau}^{-1}\frac{\partial\phi(\eta,s)}{\partial\eta}\right]\\
&\quad-\frac{6}{s^{\rho}}\mathcal{L}_{\tau}\left[\mathcal{L}_{\tau}^{-1}\phi(\eta,s)\mathcal{L}_{\tau}^{-1}\psi(\eta,s)\mathcal{L}_{\tau}^{-1}\frac{\partial\psi(\eta,s)}{\partial\eta}\right]\\
&\quad-\frac{3}{2s^{\rho}}\mathcal{L}_{\tau}\left[\left(\mathcal{L}_{\tau}^{-1}\psi(\eta,s)\right)^2\mathcal{L}_{\tau}^{-1}\frac{\partial\phi(\eta,s)}{\partial\eta}\right],\\
&\mathcal{L}_{\tau}Res(\eta,s)=\psi(\eta,s)-\frac{\lambda Sech^2\left(\frac{\lambda\eta}{2}\right)}{s}+\frac{1}{s^{\rho}}\frac{\partial^3\psi(\eta,s)}{\partial\eta^3}\\
&\quad-\frac{6}{s^{\rho}}\mathcal{L}_{\tau}\left[\mathcal{L}_{\tau}^{-1}\frac{\partial\phi(\eta,s)}{\partial\eta}\mathcal{L}_{\tau}^{-1}\psi(\eta,s)\right]\\
&\quad-\frac{6}{s^{\rho}}\mathcal{L}_{\tau}\left[\mathcal{L}_{\tau}^{-1}\phi(\eta,s)\mathcal{L}_{\tau}^{-1}\frac{\partial\psi(\eta,s)}{\partial\eta}\right]\\
&\quad-\frac{15}{2s^{\rho}}\mathcal{L}_{\ell}\left[\mathcal{L}_{\tau}^{-1}\frac{\partial\psi(\eta,s)}{\partial\eta}\left(\mathcal{L}_{\tau}^{-1}\psi(\eta,s)\right)^2\right].
\end{aligned}\tag{19}$$

The kth-LRFs are given by

$$\begin{aligned}
&\mathcal{L}_{\tau}Res_k(\eta,s)=\phi_k(\eta,s)-\frac{\frac{\lambda^2}{8}\left(1-Sech^2\left(\frac{\lambda\eta}{2}\right)\right)}{s}+\frac{1}{s^{\rho}}\frac{\partial^3\phi_k(\eta,s)}{\partial\eta^3}\\
&\quad+\frac{3}{2s^{\rho}}\mathcal{L}_{\tau}\left[\mathcal{L}_{\tau}^{-1}\psi_k(\eta,s)\mathcal{L}_{\tau}^{-1}\frac{\partial^3\psi_k(\eta,s)}{\partial\eta^3}\right]\\
&\quad+\frac{9}{2s^{\rho}}\mathcal{L}_{\tau}\left[\mathcal{L}_{\tau}^{-1}\frac{\partial\psi_k(\eta,s)}{\partial\eta}\mathcal{L}_{\tau}^{-1}\frac{\partial^2\psi_k(\eta,s)}{\partial\eta^2}\right]\\
&\quad-\frac{6}{s^{\rho}}\mathcal{L}_{\tau}\left[\mathcal{L}_{\tau}^{-1}\phi_k(\eta,s)\mathcal{L}_{\tau}^{-1}\frac{\partial\phi_k(\eta,s)}{\partial\eta}\right]\\
&\quad-\frac{6}{s^{\rho}}\mathcal{L}_{\tau}\left[\mathcal{L}_{\tau}^{-1}\phi_k(\eta,s)\mathcal{L}_{\tau}^{-1}\psi_k(\eta,s)\mathcal{L}_{\tau}^{-1}\frac{\partial\psi_k(\eta,s)}{\partial\eta}\right]\\
&\quad-\frac{3}{2s^{\rho}}\mathcal{L}_{\tau}\left[\left(\mathcal{L}_{\tau}^{-1}\psi_k(\eta,s)\right)^2\mathcal{L}_{\tau}^{-1}\frac{\partial\phi_k(\eta,s)}{\partial\eta}\right],\\
&\mathcal{L}_{\tau}Res_k(\eta,s)=\psi_k(\eta,s)-\frac{\lambda Sech^2\left(\frac{\lambda\eta}{2}\right)}{s}+\frac{1}{s^{\rho}}\frac{\partial^3\psi_k(\eta,s)}{\partial\eta^3}\\
&\quad-\frac{6}{s^{\rho}}\mathcal{L}_{\tau}\left[\mathcal{L}_{\tau}^{-1}\frac{\partial\phi_k(\eta,s)}{\partial\eta}\mathcal{L}_{\tau}^{-1}\psi_k(\eta,s)\right]\\
&\quad-\frac{6}{s^{\rho}}\mathcal{L}_{\tau}\left[\mathcal{L}_{\tau}^{-1}\phi_k(\eta,s)\mathcal{L}_{\tau}^{-1}\frac{\partial\psi_k(\eta,s)}{\partial\eta}\right]\\
&\quad-\frac{15}{2s^{\rho}}\mathcal{L}_{\tau}\left[\mathcal{L}_{\tau}^{-1}\frac{\partial\psi_k(\eta,s)}{\partial\eta}\left(\mathcal{L}_{\tau}^{-1}\psi_k(\eta,s)\right)^2\right].
\end{aligned}\tag{20}$$

To compute $f_k(\eta,s)$ and $g_k(\eta,s)$ for $k=1,2,3,\ldots,$ we can use Eq. 18 which gives the nth-truncated series, and substitute it into Eq. 20, which gives the nth-Laplace residual term. Then, we can multiply the solution of the equation by $s^{n\rho+1}$ and solve the relation recursively for $\lim_{s\to\infty}(s^{n\rho+1}\mathcal{L}\tau Res\phi,n(\eta,s))=0$ and $\lim_{s\to\infty}(s^{n\rho+1}\mathcal{L}\tau Res\psi,n(\eta,s))=0$ for $n=1,2,3,\cdots$. The following are the first few terms:

$$\begin{aligned}
&f_0=\frac{\lambda^2}{8}\left(1-Sech^2\left(\frac{\lambda\eta}{2}\right)\right),g_0=\lambda Sech^2\left(\frac{\lambda\eta}{2}\right),\\
&f_1=-\frac{1}{128}\lambda^5Sech^7\left(\frac{\lambda\eta}{2}\right)\left(794Sinh\left(\frac{\lambda\eta}{2}\right)-165Sinh\left(\frac{3\lambda\eta}{2}\right)+\sinh\left(\frac{5\lambda\eta}{2}\right)\right)\\
&g_1=-\frac{1}{32}\lambda^4\left(-189+52Cosh(\lambda\eta)+Cosh(2\lambda\eta)\right)Sech^6\left(\frac{\lambda\eta}{2}\right)Tanh\left(\frac{\lambda\eta}{2}\right),\\
&f_2=\frac{\lambda^8}{16384}\left(10003020-11000862Cosh(\lambda\eta)\right.\\
&\quad\left.+1410960Cosh(2\eta\lambda)\right)Sech^{12}\left(\frac{\lambda\eta}{2}\right)\\
&\quad+\frac{\lambda^8}{16384}\left(61341Cosh(3\lambda\eta)\right.\\
&\quad\left.-4700Cosh(4\lambda\eta)+Cosh(5\lambda\eta)\right)Sech^{12}\left(\frac{\lambda\eta}{2}\right),\\
&g_2=\frac{\lambda^7}{8192}\left(-1713684+1217538Cosh(\lambda\eta)315984Cosh(2\lambda\eta)\right)Sech^{12}\left(\frac{\lambda\eta}{2}\right)\\
&\quad+\frac{\lambda^7}{8192}\left(-79491Cosh(3\lambda\eta)+1348Cosh(4\lambda\eta)\right.\\
&\quad\left.+Cosh(5\lambda\eta)\right)Sech^{12}\left(\frac{\lambda\eta}{2}\right),
\end{aligned}\tag{21}$$

Now, by using the values of $f_k(\eta)$, $k=1,2,3,\ldots,$ we get

TABLE 2 The approximate solution $\psi(\eta, \tau)$ (25) is considered at different values ρ and with ($\tau = 0.0095$, $\lambda = 0.02$). Also, the absolute error of $\psi(\eta, \tau)$ (25) at $\rho = 1$ as compared to the exact solution (276) is estimated.

η	$\rho = 0.56$	$\rho = 0.78$	$\rho = 0.85$	LRPSM ($\rho = 1$)	*exact*	*Abs.error*
0.1	0.0200	0.0200	0.0200	0.0200	0.0200	1.00061×10^{-8}
0.2	0.0200	0.0200	0.0200	0.0200	0.0200	4.0012×10^{-8}
0.3	0.0200	0.0200	0.0200	0.0200	0.0200	9.00175×10^{-8}
0.4	0.0200	0.0200	0.0200	0.0200	0.0200	1.60022×10^{-7}
0.5	0.020	0.0200	0.0200	0.0200	0.0200	2.50025×10^{-7}
0.6	0.019999	0.019999	0.019999	0.019999	0.02000	3.60025×10^{-7}
0.7	0.019999	0.019999	0.019999	0.019999	0.02000	4.9002110×10^{-7}
0.8	0.019999	0.019999	0.019999	0.019999	0.019999	6.40011×10^{-7}
0.9	0.019998	0.019998	0.019998	0.019998	0.019999	8.09995×10^{-7}
1	0.019998	0.019998	0.019998	0.019998	0.019999	9.99969×10^{-7}
1.1	0.019998	0.019998	0.019998	0.019998	0.019999	1.20993×10^{-6}
1.2	0.019997	0.019997	0.019997	0.019997	0.019999	1.43988×10^{-6}
1.3	0.019997	0.019997	0.019997	0.019997	0.019998	1.68982×10^{-6}
1.4	0.019996	0.019996	0.019996	0.019996	0.019998	1.95973×10^{-6}
1.5	0.019996	0.019996	0.019996	0.019996	0.019998	2.24963×10^{-6}
1.6	0.019995	0.019995	0.019995	0.019995	0.019997	2.5595×10^{-6}
1.7	0.019994	0.019994	0.019994	0.019994	0.019997	2.88934×10^{-6}
1.8	0.019994	0.019994	0.019994	0.019994	0.019997	3.23915×10^{-6}
1.9	0.019993	0.019993	0.019993	0.019993	0.019996	3.60892×10^{-6}
2	0.019992	0.019992	0.019992	0.019992	0.019996	3.99866×10^{-6}

$$\phi(\eta,s)=\frac{\frac{\lambda^2}{8}\left(1-Sech^2\left(\frac{\lambda\eta}{2}\right)\right)}{s}-\frac{\frac{1}{128}\lambda^5 Sech^7\left(\frac{\lambda\eta}{2}\right)\left(794Sinh\left(\frac{\lambda\eta}{2}\right)-165Sinh\left(\frac{3\lambda\eta}{2}\right)+sinh\left(\frac{5\lambda\eta}{2}\right)\right)}{s^{\kappa+1}}+\frac{\frac{\lambda^8}{16384}\left(10003020-11000862Cosh(\lambda\eta)+1410960Cosh(2\eta\lambda)\right)Sech^{12}\left(\frac{\lambda\eta}{2}\right)}{s^{2\kappa+1}}+\frac{\frac{\lambda^8}{16384}\left(61341Cosh(3\lambda\eta)-4700Cosh(4\lambda\eta)+Cosh(5\lambda\eta)\right)Sech^{12}\left(\frac{\lambda\eta}{2}\right)}{s^{2\kappa+1}}+\cdots, \tag{22}$$

$$\psi(\eta,s)=\frac{\lambda Sech^2\left(\frac{\lambda\eta}{2}\right)\Big)}{s}-\frac{\frac{1}{32}\lambda^4\left(-189+52Cosh(\lambda\eta)+Cosh(2\lambda\eta)\right)Sech^6\left(\frac{\lambda\eta}{2}\right)Tanh\left(\frac{\lambda\eta}{2}\right)}{s^{\kappa+1}}+\frac{\frac{\lambda^7}{8192}\left(-1713684+1217538Cosh(\lambda\eta)315984Cosh(2\lambda\eta)\right)Sech^{12}\left(\frac{\lambda\eta}{2}\right)}{s^{2\kappa+1}}+\frac{\frac{\lambda^7}{8192}\left(-79491Cosh(3\lambda\eta)+1348Cosh(4\lambda\eta)+Cosh(5\lambda\eta)\right)Sech^{12}\left(\frac{\lambda\eta}{2}\right)}{s^{2\kappa+1}}+\cdots. \tag{23}$$

Applying the inverse of LT, we get

$$\phi(\eta,\rho)=\frac{\lambda^2}{8}\left(1-Sech^2\left(\frac{\lambda\eta}{2}\right)\right)-\frac{\frac{1}{128}\lambda^5 Sech^7\left(\frac{\lambda\eta}{2}\right)\left(794Sinh\left(\frac{\lambda\eta}{2}\right)-165Sinh\left(\frac{3\lambda\eta}{2}\right)+sinh\left(\frac{5\lambda\eta}{2}\right)\right)}{\Gamma(\rho+1)}\tau^{\rho}+\frac{\frac{\lambda^8}{16384}\left(10003020-11000862Cosh(\lambda\eta)+1410960Cosh(2\eta\lambda)\right)Sech^{12}\left(\frac{\lambda\eta}{2}\right)}{\Gamma(2\rho+1)}\tau^{2\rho}+\frac{\frac{\lambda^8}{16384}\left(61341Cosh(3\lambda\eta)-4700Cosh(4\lambda\eta)+Cosh(5\lambda\eta)\right)Sech^{12}\left(\frac{\lambda\eta}{2}\right)}{\Gamma(2\rho+1)}\tau^{2\rho}+\cdots, \tag{24}$$

$$\psi(\eta,\rho)=\lambda Sech^2\left(\frac{\lambda\eta}{2}\right)\Big)-\frac{\frac{1}{32}\lambda^4\left(-189+52Cosh(\lambda\eta)+Cosh(2\lambda\eta)\right)Sech^6\left(\frac{\lambda\eta}{2}\right)Tanh\left(\frac{\lambda\eta}{2}\right)}{\Gamma(\rho+1)}\tau^{\rho}+\frac{\frac{\lambda^7}{8192}\left(-1713684+1217538Cosh(\lambda\eta)315984Cosh(2\lambda\eta)\right)Sech^{12}\left(\frac{\lambda\eta}{2}\right)}{\Gamma(2\rho+1)}\tau^{2\rho}+\frac{\frac{\lambda^7}{8192}\left(-79491Cosh(3\lambda\eta)+1348Cosh(4\lambda\eta)+Cosh(5\lambda\eta)\right)Sech^{12}\left(\frac{\lambda\eta}{2}\right)}{\Gamma(2\rho+1)}\tau^{2\rho}+\cdots. \tag{25}$$

The exact solutions of $\phi(\eta, \tau)$ and $\psi(\eta, \tau)$ are, respectively, given by

$$\phi(\eta,\tau)=\frac{\lambda^2}{8}\left(1-Sech^2\left(\frac{\lambda}{2}\left(\eta+\frac{\lambda^2\tau}{2}\right)\right)\right), \tag{26}$$

$$\psi(\eta,\tau)=\lambda Sech\left(\frac{\lambda}{2}\left(\eta+\frac{\lambda^2\tau}{2}\right)\right). \tag{27}$$

In the results section, we will discuss the profile of the obtained solutions as well as will make a comparison with the exact solutions and the other literature approximations.

5 Results and discussion

Figures 1, 2 represent both two- and three-dimensional graphs for the approximations (24) and (25), respectively, using the LRPSM at different values of fractional order derivative ρ. It is clear that the absolute amplitude of the approximation $\phi(\eta, \tau)$ decreases with the enhancement of ρ while the amplitude of the approximation $\psi(\eta, \tau)$ has an opposite behavior, i.e., its amplitude increases with increasing ρ. Moreover, the two approximations are presented in Tables 1, 2 at different values of ρ and discrete values for η and τ. Furthermore, the absolute error for the approximations $\phi(\eta, \tau)$ and $\phi(\eta, \tau)$ at $\rho = 1$ as compared to the exact solutions is estimated in Tables 1, 2, respectively. After analyzing the obtained results, we can conclude that the obtained approximations using the proposed technique are closely aligned with the exact solutions, indicating a strong level of agreement. We have applied the proposed method to the fractional-order Jaulent-Miodek system to analyze it, and this is not the only example, and it can be applied to a wide range of complicated systems related to nonlinear mediums such as plasma physics and optical fibers.

6 Conclusion

In conclusion, the fractional-order Jaulent-Miodek system has been solved using a novel technique, called the residual power series method with the help of the Laplace transform (LT) in the sense of the Caputo operator. The LT, in conjunction with the Caputo operator, has been used to transform the fractional differential equation into an algebraic equation, which can then be solved using the residual power series method. The suggested method (Laplace residual power series method (LRPSM)) involves using a truncated power series to approximate the solution, and the residual error is minimized by adjusting the power series coefficients. The study of fractional-order systems has gained significant attention in recent years due to their ability to model complex phenomena in various fields of science and engineering. For instance, the Jaulent-Miodek system is a well-known example of such a fractional system, and its solution has been a topic of interest for many researchers. Accordingly, the LRPSM has been applied for derived high accurate approximations for the fractional-order Jaulent-Miodek system. The derived approximations have been compared with the analytical solutions. It was found great harmony and agreement with a very small absolute error between both the approximate solutions and the analytical solutions. This method has proven to be an effective tool for solving fractional-order systems, as it can provide accurate and efficient solutions. The findings of this study may be helpful in different areas of applied sciences where fractional-order systems are commonly encountered.

Data availability statement

The original contributions presented in the study are included in the article/supplementary material, further inquiries can be directed to the corresponding author.

Author contributions

MH: conceptualization (equal), formal analysis (equal), investigation (equal), and methodology (equal). AA: conceptualization (equal), formal analysis (equal), investigation (equal), and methodology (equal). RS: conceptualization (equal), formal analysis (equal), investigation (equal), and methodology (equal). SI: validation (equal), formal analysis (equal), investigation (equal), data curation (equal). SA-T: methodology (equal), writing—review and editing (equal), visualization (equal), supervision (equal). All authors contributed to the article and approved the submitted version.

Funding

This study is supported via funding from Prince Sattam bin Abdulaziz University project number (PSAU/2023/R/1444).

Acknowledgments

The authors express their gratitude to Princess Nourah bint Abdulrahman University Researchers Supporting Project number (PNURSP2023R378), Princess Nourah bint Abdulrahman University, Riyadh, Saudi Arabia.

Conflict of interest

The authors declare that the research was conducted in the absence of any commercial or financial relationships that could be construed as a potential conflict of interest.

Publisher's note

References

1. Oldham K, Spanier J. *The fractional calculus theory and applications of differentiation and integration to arbitrary order*. Elsevier (1974).

2. Kumar S. A numerical study for the solution of time fractional nonlinear shallow water equation in oceans. *Z Naturforsch A* (2013) 68:547–53. doi:10.5560/zna.2013-0036

3. Yao JJ, Kumar A, Kumar S. A fractional model to describe the Brownian motion of particles and its analytical solution. *Adv Mech Eng* (2015) 7:168781401561887. doi:10.1177/1687814015618874

4. Dahmani Z, Anber A, Gouari Y, Kaid M, Jebril I. Extension of a method for solving nonlinear evolution equations via conformable fractional approach. In: 2021 International Conference on Information Technology, ICIT 2021 - Proceedings, 2021. p. 38–42. doi:10.1109/ICIT52682.2021.9491735

5. Hammad MA. Conformable fractional martingales and some convergence theorems. *Mathematics* (2021) 6:6. doi:10.3390/math10010006

6. Hammad MA, Alsharif S, Shmasnah A, Khalil R. Fractional Bessel differential equation and fractional Bessel functions. *Ital J Pure Appl Math* 47(2022):521–31.

7. Hammad MA, Horani MA, Shmasenh A, Khalil R. Ruduction of order of fractional differential equations. *J Math Comput Sci* (2018) 8(6):683–8.

8. Yasmin H, Hammad MA, Shah R, M Alotaibi B, Ismaeel SME, El-Tantawy SA. On the solutions of the fractional-order sawada–kotera–ito equation and modeling nonlinear structures in fluid mediums. *Symmetry* (2023) 15(3):605. doi:10.3390/sym15030605

9. Ain QT, Anjum N, Din A, Zeb A, Djilali S, Khan ZA. On the analysis of Caputo fractional order dynamics of Middle East Lungs Coronavirus (MERS-CoV) model. *Alexandria Eng J* (2022) 61(7):5123–31. doi:10.1016/j.aej.2021.10.016

10. Anjum N, He CH, He JH. Two-scale fractal theory for the population dynamics. *Fractals* (2021) 29(07):2150182. doi:10.1142/s0218348x21501826

11. Atangana A, Gomez-Aguilar J. Numerical approximation of riemann-liouville definition of fractional derivative: From riemann-liouville to atangana-baleanu. *Numer Methods Partial Differ Equations* (2018) 34:1502–23. doi:10.1002/num.22195

12. Anjum N, Ain QT, Li XX. Two-scale mathematical model for tsunami wave. *GEM-Int J Geomathematics* (2021) 12(1):10. doi:10.1007/s13137-021-00177-z

13. Chen H, Xiong Y, Li S, Song Z, Hu Z, Liu F. Multi-sensor data driven with PARAFAC-IPSO-PNN for identification of mechanical nonstationary multi-fault mode. *Machines* (2022) 10:155. doi:10.3390/machines10020155

14. Chen H, Li S. Multi-sensor fusion by CWT-PARAFAC-IPSO-SVM for intelligent mechanical fault diagnosis. *Sensors* (2022) 22:3647. doi:10.3390/s22103647

15. Sun L, Hou J, Xing C, Fang Z. A robust hammerstein-wiener model identification method for highly nonlinear systems. *Processes* (2022) 10:2664. doi:10.3390/pr10122664

16. Alharbey RA, Alrefae WR, Malaikah H, Tag-Eldin E, El-Tantawy SA. Novel approximate analytical solutions to the nonplanar modified kawahara equation and modeling nonlinear structures in electronegative plasmas. *Symmetry* (2023) 15:97. doi:10.3390/sym15010097

17. Ismaeel SM, Wazwaz AM, Tag-Eldin E, El-Tantawy SA. Simulation studies on the dissipative modified kawahara solitons in a complex plasma. *Symmetry* (2023) 15:57. doi:10.3390/sym15010057

18. Khattak MY, Masood W, Jahangir R, Siddiq M, Alyousef HA, El-Tantawy S. Interaction of ion-acoustic solitons for multi-dimensional Zakharov Kuznetsov equation in Van Allen radiation belts. *Chaos, Solitons & Fractals* (2022) 161:112265. doi:10.1016/j.chaos.2022.112265

19. Ain QT, Anjum N, He CH. An analysis of time-fractional heat transfer problem using two-scale approach. *GEM-Int J Geomathematics* (2021) 12:18–0. doi:10.1007/s13137-021-00187-x

20. Shohaib M, Masood W, Siddiq M, Alyousef HA, El-Tantawy SA. Formation of electrostatic solitary and periodic waves in dusty plasmas in the light of Voyager 1 and 2 spacecraft and Freja satellite observations. *J Low Frequency Noise, Vib Active Control* (2022) 41:896–909. doi:10.1177/14613484221091340

21. Wazwaz AM, Alatawi NS, Albalawi W, El-Tantawy S. Painleve analysis for a new (3+ 1)-dimensional KP equation: Multiple-soliton and lump solutions. *Europhys Lett* (2022) 140:52002. doi:10.1209/0295-5075/aca49f

22. El-Tantawy S, Bakry A, Alhejaili W, Wazwaz AM. On the analytical approximations to the nonplanar damped Kawahara equation: Cnoidal and solitary waves and their energy. *Phys Fluids* (2022) 34:113103. doi:10.1063/5.0119630

23. El-Tantawy S, Salas AH, Alharthi M. On the analytical and numerical solutions of the linear damped NLSE for modeling dissipative freak waves and breathers in nonlinear and dispersive mediums: An application to a pair-ion plasma. *Front Phys* (2021) 9:580224. doi:10.3389/fphy.2021.580224

24. Liu L, Li Z, Fu X, Liu X, Li Z, Zheng W. Impact of power on uneven development: Evaluating built-up area changes in chengdu based on NPP-VIIRS images (2015-2019). *Land* (2022) 11:489. doi:10.3390/land11040489

25. Liu X, Tong D, Huang J, Zheng W, Kong M, Zhou G. What matters in the e-commerce era? Modelling and mapping shop rents in guangzhou, China. *Land Use Policy* (2022) 123:106430. doi:10.1016/j.landusepol.2022.106430

26. Qin X, Liu Z, Liu Y, Liu S, Yang B, Yin L, et al. User OCEAN personality model construction method using a BP neural network. *Electronics* (2022) 11:3022. doi:10.3390/electronics11193022

27. Guechi S, Dhayal R, Debbouche A, Malik M. Analysis and optimal control of φ-Hilfer fractional semilinear equations involving nonlocal impulsive conditions. *Symmetry* (2021) 13:2084. doi:10.3390/sym13112084

28. Sultana M, Arshad U, Ali AH, Bazighifan O, Al-Moneef AA, Nonlaopon K. New efficient computations with symmetrical and dynamic analysis for solving higher-order fractional partial differential equations. *Symmetry* (2022) 14:1653. doi:10.3390/sym14081653

29. Alyousef HA, Shah R, Shah NA, Chung JD, Ismaeel SM, El-Tantawy SA. The fractional analysis of a nonlinear mKdV equation with Caputo operator. *Fractal Fractional* (2023) 7(3):259. doi:10.3390/fractalfract7030259

30. Albalawi W, Shah R, Shah NA, Chung JD, Ismaeel SM, El-Tantawy SA. Analyzing both fractional porous media and heat transfer equations via some novel techniques. *Mathematics* (2023) 11(6):1350. doi:10.3390/math11061350

31. Atangana A, Alabaraoye E. Solving a system of fractional partial differential equations arising in the model of HIV infection of CD4+ cells and attractor one-dimensional Keller-Segel equations. *Adv Differ Equations* (2013) 2013:94–14. doi:10.1186/1687-1847-2013-94

32. Atangana A, Kilicman A. Analytical solutions of the space-time fractional derivative of advection dispersion equation. *Math Probl Eng* (2013) 2013:1–9. doi:10.1155/2013/853127

33. Naeem M, Yasmin H, Shah NA, Nonlaopon K. Investigation of fractional nonlinear regularized long-wave models via novel techniques. *Symmetry* (2023) 15(1):220. doi:10.3390/sym15010220

34. Tao H, Yu-Zhu W, Yun-Sheng H. Bogoliubov quasiparticles carried by dark solitonic excitations in nonuniform Bose-Einstein condensates. *Chin Phys Lett* (1998) 15:550–2. doi:10.1088/0256-307x/15/8/002

35. Ma WX, Li CX, He J. A second Wronskian formulation of the Boussinesq equation. *Nonlinear Anal Theor Methods Appl* (2009) 70:4245–58. doi:10.1016/j.na.2008.09.010

36. El-Tantawy S, Shan SA, Mustafa N, Alshehri MH, Duraihem FZ, Turki NB. Homotopy perturbation and Adomian decomposition methods for modeling the nonplanar structures in a bi-ion ionospheric superthermal plasma. *The Eur Phys J Plus* (2021) 136:561–16. doi:10.1140/epjp/s13360-021-01494-w

37. Kashkari BS, El-Tantawy S. Homotopy perturbation method for modeling electrostatic structures in collisional plasmas. *Eur Phys J Plus* (2021) 136:121–3. doi:10.1140/epjp/s13360-021-01120-9

38. Kashkari BS, El-Tantawy S, Salas AH, El-Sherif L. Homotopy perturbation method for studying dissipative nonplanar solitons in an electronegative complex plasma. *Chaos, Solitons Fractals* (2020) 130:109457. doi:10.1016/j.chaos.2019.109457

39. Abdulaziz O, Hashim I, Momani S. Solving systems of fractional differential equations by homotopy-perturbation method. *Phys Lett A* (2008) 372:451–9. doi:10.1016/j.physleta.2007.07.059

40. Neamaty A, Agheli B, Darzi R. Variational iteration method and He's polynomials for time-fractional partial differential equations. *Prog Fractional Differ Appl* (2015) 1:47–55.

41. Naeem M, Yasmin H, Shah R, Shah NA, Chung JD. A comparative study of fractional partial differential equations with the help of yang transform. *Symmetry* (2023) 15(1):146. doi:10.3390/sym15010146

42. Prakasha DG, Veeresha P, Rawashdeh MS. Numerical solution for (2+ 1)-dimensional time-fractional coupled Burger equations using fractional natural decomposition method. *Math Methods Appl Sci* (2019) 42:3409–27. doi:10.1002/mma.5533

43. Alshehry AS, Ullah R, Shah NA, Nonlaopon K. Implementation of Yang residual power series method to solve fractional non-linear systems. *AIMS Math* (2023) 8:8294–309. doi:10.3934/math.2023418

44. Daftardar-Gejji V, Bhalekar S. Solving fractional boundary value problems with Dirichlet boundary conditions using a new iterative method. *Comput Math Appl* (2010) 59:1801–9. doi:10.1016/j.camwa.2009.08.018

45. Akinyemi L, Iyiola OS, Akpan U. Iterative methods for solving fourth-and sixth-order time-fractional Cahn-Hillard equation. *Math Methods Appl Sci* (2020) 43:mma.6173–4074. doi:10.1002/mma.6173

46. Abdulaziz O, Hashim I, Saif A. Series solutions of time-fractional PDEs by homotopy analysis method. *Differ Equations Nonlinear Mech* (2009) 2008:1–16. doi:10.1155/2008/686512

47. Rashidi M, Domairry G, Dinarvand S. The homotopy analysis method for explicit analytical solutions of Jaulent-Miodek equations. *Numer Methods Partial Differ Equations: Int J* (2009) 25:430–9. doi:10.1002/num.20358

48. El-Ajou A, Al-Smadi M, Moa'ath NO, Momani S, Hadid S. Smooth expansion to solve high-order linear conformable fractional PDEs via residual power series method: Applications to physical and engineering equations. *Ain Shams Eng J* (2020) 11: 1243–54. doi:10.1016/j.asej.2020.03.016

49. Burqan A, El-Ajou A, Saadeh R, Al-Smadi M. A new efficient technique using Laplace transforms and smooth expansions to construct a series solution to the time-fractional Navier-Stokes equations. *Alexandria Eng J* (2022) 61:1069–77. doi:10.1016/j.aej.2021.07.020

50. Alderremy AA, Shah R, Iqbal N, Aly S, Nonlaopon K. Fractional series solution construction for nonlinear fractional reaction-diffusion brusselator model utilizing Laplace residual power series. *Symmetry* (2022) 14:1944. doi:10.3390/sym14091944

51. Caputo M. *Elasticita e Dissipazione*. Bologna: Zani-Chelli (1969).

52. El-Ajou A. Adapting the Laplace transform to create solitary solutions for the nonlinear time-fractional dispersive PDEs via a new approach. *Eur Phys J Plus* (2021) 136:229–2. doi:10.1140/epjp/s13360-020-01061-9

53. Areshi M, Khan A, Shah R, Nonlaopon K. Analytical investigation of fractional-order Newell-Whitehead-Segel equations via a novel transform. *AIMS Math* (2022) 7: 6936–58. doi:10.3934/math.2022385

frontiers | Frontiers in Physics

TYPE Original Research
PUBLISHED 27 July 2023
DOI 10.3389/fphy.2023.1221720

OPEN ACCESS

EDITED BY
Samir A. El-Tantawy,
Port Said University, Egypt

REVIEWED BY
Nehad Ali Shah,
Sejong University, Republic of Korea
Gaston Tiofack,
University of Maroua, Cameroon

*CORRESPONDENCE
Huda Alsaud,
halsaud@ksu.edu.sa
Mansoor H. Alshehri,
mhalshehri@ksu.edu.sa

RECEIVED 12 May 2023
ACCEPTED 13 July 2023
PUBLISHED 27 July 2023

CITATION
Alsaud H and Alshehri MH (2023), Continuum modeling for lithium storage inside nanotubes.
Front. Phys. 11:1221720.
doi: 10.3389/fphy.2023.1221720

Continuum modeling for lithium storage inside nanotubes

Huda Alsaud* and Mansoor H. Alshehri*

Department of Mathematics, College of Science, King Saud University, Riyadh, Saudi Arabia

Lithium storage and capture are of particular importance for the development of new technology in electric vehicles and portable electronics. Nanotubes (NTs) are among many porous nanomaterials offered as potential candidates for lithium storage. In this paper, we adopt a continuum approach together with the Lennard–Jones function to determine the minimum interaction energies for lithium atoms in boron nitride nanotubes (BNNTs) and carbon nanotubes (CNTs). By minimizing the interaction energies, we may obtain the preferred type and size of the nanotubes to encapsulate the lithium atoms. The results showed that BNNTs and CNTs are attractive candidates for lithium atom encapsulation, and the optimal nanotube to enclose lithium is the BNNT with a radius equal to 3.4 Å, and corresponding (5, 5) armchair nanotubes and (9, 0) zigzag nanotubes, where the minimum energy is obtained. The present computations observed that both nanotubes are promising candidates for lithium intercalation materials suitable for battery applications.

KEYWORDS

lithium, nanotube, continuum approach, Lennard–Jones potential, mathematical physics equations

1 Introduction

Recently, with the rapid development of nanotechnology, nanomaterials represent a high level of importance in many applications, such as pharmaceuticals, electronic technology, energy applications, the biomedical sector, and environmental applications. They are used, for example, but not limited to the new generation of computer chips, harder and more durable cutting tools, removal of pollutants, very efficient batteries, magnets with high power, sensors with high sensitivity, automobiles, aerospace components, weapon platforms, long-lasting medical implants, and electrochromic display devices [1–3]. One of the most well-known and widely studied nanostructures in science is nanotubes (NTs), including boron nitride nanotubes (BNNTs) and carbon nanotubes (CNTs). Due to the distinctive structures and exceptional properties of nanotubes, they have attracted more interest in research and developing nanotechnology, and they are expected to be used in many new applications. CNTs have gained a wide range of theoretical and experimental research since their discovery in the 1990s [4]. They show a variety of captivating qualities, including exceptional electronic sensitivity, good mechanical strength, high surface area to volume ratios, high levels of flexibility, and exceptionally strong electro-catalytic activities, which enable them to find practical use in sensors, actuators, energy storage devices, etc. [5]. Until now, this field is still active and attractive to the interest of many researchers, and many distinguished and important applications of CNTs have emerged since their discovery. There are numerous studies on CNTs, and some authors highlight their applications in the field of electronics, sensing, and composite [6, 7].

Studies and research paid significant attention to the new material, BNNTs. Numerous accomplishments have allowed access to this material, and several applications have been

implemented in this field since Chopra et al.'s invention of BNNTs in 1995. Both BNNTs and CNTs share some basic properties like outstanding mechanical properties and high heat conductivity. This is because of the similarity between the structures of BNNTs and CNTs, where boron and nitrogen atoms in BNNTs are replaced by carbon atoms in CNTs [8]. One exceptional physical feature of BNNTs is that they are an excellent insulator with a wide bandgap (5–6 eV), while CNTs are semiconducting materials. Moreover, they are not sensitive to the chirality and morphology of the tubes. BNNTs also have distinct characteristics such as high-temperature stability and neutron radiation shielding capability, which make them essential for use in sensors and devices in extreme environments [8]. The chiral vector $C = ia_1 + ja_2$ is used to classify the structure of the nanotubes, where a_1 and a_2 are the basis vectors of a hexagonal unit cell on layered inorganic sheets [such as hexagonal boron nitride (h-BN) and graphene (GRA)], and i and j are integers. Alternatively, the chiral vector may be indicated by (i, j), and the radii of the corresponding nanotubes are then given by $r = \ell\sqrt{3(i^2 + j^2 + ij)}/2\pi$, where ℓ denotes the bond length [3]. Although BNNTs and CNTs have structural similarities, the two nanotubes differ in some properties, which cause different behaviors for each. For example, the bond lengths of C–C bonds and B–N bonds are approximately 1.42 and 1.45 Å, respectively [9, 10].

The energy demand is increasing dramatically recently, and energy storage has become one of the major interests in technology and science. Due to climate change caused by global warming, researchers focus on developing systems of generating renewable energy and using electric motors in vehicles instead of the known engines [11, 12]. Sources of renewable energy like solar power generators also need batteries to store energy for later use [11, 12]. Therefore, improving battery technology requires materials with the ability to charge and recharge with high efficiency in order to be able to use energy resources successfully [11]. Owing to their advantages of excellent cyclic stability, lightweight, high capacity density, and high efficiency, lithium (Li) batteries have received considerable attention in many applications, such as electric vehicles, electric power grids, and portable electronics [12, 13].

One of the scientific challenges facing lithium batteries is their safety, which needs to be ensured before they can be widely used in everyday portable devices, and the most important factor that threatens the safety of the battery is the overheating of the cell, which results from a short circuit under a high temperature and high current environment. Since the separator plays an important role in avoiding short circuits, it is important that the separator be thermally stable [14]. Nanotubes can play an important role in energy storage systems, including the lithium battery, and they may protect against thermal shrinkage at high temperatures and high current operation, which improves the stability of the temperature in the polyolefin separator and then prevents battery short-circuits [12, 14]. Lithium batteries have offered great success for mobile electronics because of the progress in cell design and the manufacturing of lithium batteries with more efficient electrochemical performances regarding power densities and energy [15]. Further studies are required to improve the progress of these materials with the lithium battery technology. Moreover, nanomaterials, including nanotubes, might provide long-lasting separation of electron charges, and supramolecular nanoclusters can be supported, increasing the photoelectrochemical performance of photovoltaic cells [16]. Many experimental studies have worked on determining the lithium adsorption energetics in NTs. Theoretical studies have concentrated on the intercalation of Li atoms in nanotubes and the calculation of energy barriers for the entry and diffusion of Li inside the tubes.

Song et al. examined the intercalation and diffusion of Li ions in CNTs and found that lithium intercalation may cause deformation of CNTs [17]. Khantha et al. used density functional theory (DFT) to study the interaction of a single Li atom inside a (5, 5) CNT and reported that the lithium insertion capacities are dependent on the chirality and the equilibrium position of the Li atom on the tube axis, which provides strong binding energy, and is about 1.46 Å [18]. Zhong-Heng et al. used *ab initio* molecular dynamics (AIMD) simulations and first-principle calculations to probe the Li transport mechanism in armchair and zigzag CNTs, and their results showed a fast Li transport with an ultralow activation energy in the CNTs with a diameter of 5.5 Å, corresponding to (4, 4) and (7, 0) CNTs [19]. Meunier et al. found an equilibrium distance of 1.29 Å using *ab initio* simulations for Li inside the (5, 5) and (8, 0) CNTs [20]. Yanhong and Junwei have applied the DFT to investigate the adsorption of Li atoms in different CNTs [21]. Their results showed that a Li atom is steadily adsorbed inside the CNTs, and the strongest adsorption energy of the Li atom is obtained in the (6, 0) CNTs.

In addition, Rahman et al. presented a new separator coated by BNNTs with a thermal stability of up to 150°C for the safer operation of lithium batteries. Kim et al. investigated BNNT-based separators in lithium–sulfur batteries and showed the comparison of the electrochemical behavior of lithium–sulfur batteries with BNNTs and those without BNNTs [11]. They found that the BNNT-loaded polypropylene separator prevents the formation of dendrite on the Li metal anode, helps the ions move easily through the separator, and reduces the shuttle effect at the cathode compared to the ordinary polypropylene separator. Zhong et al. used the DFT method to investigate the interaction between (5, 0) BNNTs and lithium atoms, which is located near the open end of the tube [22]. Their results showed that the interaction between the lithium atom and the edge of BNNTs is around −30.05 (kcal/mol). Seif et al. performed the DFT method to study the effects of lithium doping on the properties of the electronic structure of (4, 4) BNNTs, and their results showed a heterogeneous electrostatic environment along the tube [23].

The investigation of the adsorption and encapsulation of lithium in different nanotubes is still active to improve the performance of lithium batteries. Experiments can be performed directly, but they are time-consuming and expensive. Mathematical modeling and simulation may be used as an alternative, complementary, and guiding method. Calculating the interaction energy between non-bonded atoms and molecules is usually performed by either the discrete method, which calculates the force for every non-bonded atom as a pair using molecular dynamics, or the continuum method, which approximates these atoms using geometric representation. Here, we apply the continuum approach with the Lennard–Jones (LJ) potential to calculate the van der Waals energies and the interaction between atoms and molecules. In this method, some simple geometric shapes with rotational symmetry are used to represent the molecular structures and the distance between

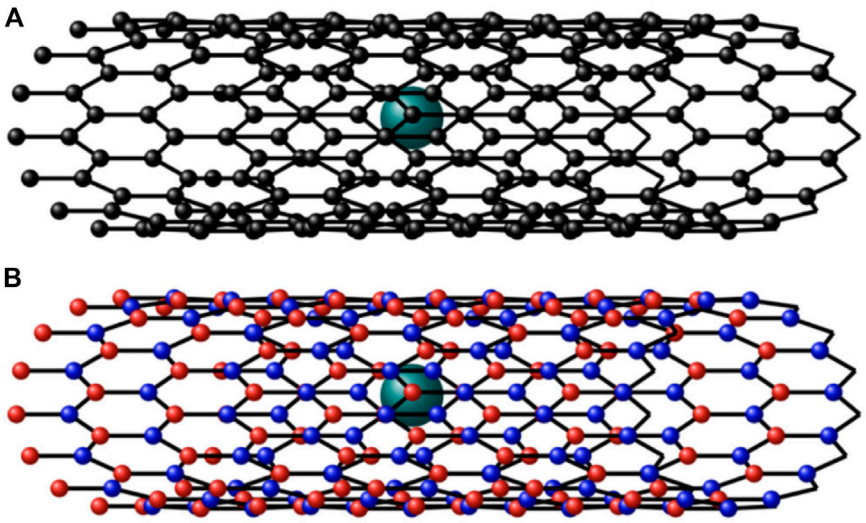

FIGURE 1
Geometrical diagram of **(A)** Li in CNTs and **(B)** BNNTs.

TABLE 1 Values of the well depth and van der Waals diameter used in this study.

Atom type	C	B	N	Li
ε (kcal/mol)	0.105	0.180	0.069	0.025
σ Å	3.851	4.083	3.660	2.451

them. These geometric shapes, like points and cylinders, with this geometric property are useful to simplify interaction expressions. In particular, we use this approach to determine the minimum interaction energies for lithium in two different nanotubes, namely, BNNTs and CNTs, as shown in Figure 1. By minimizing the interaction energies, we may obtain the preferred type and size of the nanotubes to encapsulate the lithium atoms.

2 Modeling approach

In this section, the interactions between Li atoms inside BNNTs and CNNTs are modeled. Predominantly, van der Waals forces are the forces present in physisorption, so we may use the Lennard–Jones potential to determine the interaction between lithium atoms and nanotubes, and it is given as

$$P(\varrho) = -T\varrho^{-6} + R\varrho^{-12},$$

which evaluates the potential energy between two atoms at distance ϱ apart. The coefficients T and R are the attractive and repulsive parameters of the interaction, respectively, and their values might be obtained by applying the Lorentz–Berthelot mixing rule [24], where $T = 4\varepsilon\sigma^6$ and $R = 4\varepsilon\sigma^{12}$. Furthermore, σ is the van der Waals diameter and ε is the well depth for Li, B, N, and C atoms, and their values are taken from Rappi et al. [25], as shown in Table 1. For two different atoms, they

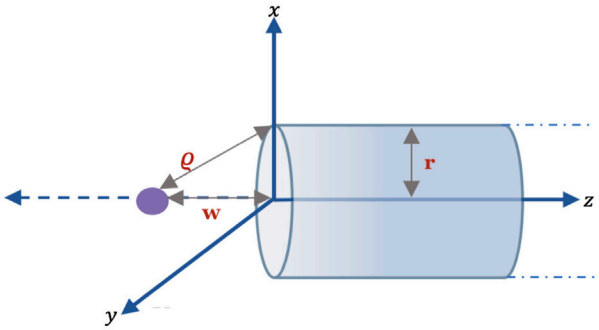

FIGURE 2
Li atom entering the nanotube.

might be computed using $\sigma_{12} = (\sigma_1 + \sigma_2)/2$ and $\varepsilon_{12} = \sqrt{\varepsilon_1\varepsilon_2}$. As the nanotubes have cylindrical structures, we approximate them as continuum surfaces, where their atoms are uniformly distributed over their entire surfaces, and they are modeled continuously over their atoms by employing a typical surface element, dA. For such a problem, the hybrid discrete–continuum approach is used to obtain the interaction of an atom (i.e., a point) with the surface A (the cylinder), and it is given as

$$E = \sum_i \varpi_j \int P(\varrho i)\, dA, \tag{1}$$

where $P(\varrho i)$ is the potential function, ϱ is the distance between an atom (point i) and the surface of nanotubes (BNNT and CNT), and ϖ_j ($j \in \{B, C\}$) is the atomic surface density of NTs, and their values are given by $\varpi_B = 0.3661$ and $\varpi_C = 0.3812$ Å^{-2} [26, 27]. In the following subsections, we considered two factors affecting the interaction energies of lithium atoms and nanotubes.

2.1 Li atom entering nanotubes

Here, we considered the entry of a Li atom in the nanotube, and the atom is assumed to be outside the tube. Figure 2 shows the Li atom as it enters an open-ended semi-infinite tube with the radius r. Thus, the NTs can be modeled as a cylinder, and their coordinates are $(r\cos u, r\sin u, z)$, where $-\pi \le u \le \pi$ and $0 < z < \infty$, and the parametric equation of the atom is denoted by $(0, 0, w)$, where w is the distance between the atom and the open end of the tube on the z-axis of the tube. The distance ϱ between the surface of the nanotube and the entering atom is given by

$$\varrho^2 = r^2\cos^2 u + r^2\sin^2 u + (z-w)^2 = r^2 + (z-w)^2,$$

and the total interaction between the nanotube and the atom is given by

$$E^{tot} = r\varpi_j \int_{-\pi}^{\pi}\int_{0}^{\infty} \left(-T\varrho^{-6} + R\varrho^{-12}\right) dz\, du. \tag{2}$$

This integral may be rewritten as follows:

$$E^{tot} = r\varpi_j\left(-TQ_3 + RQ_6\right). \tag{3}$$

The integral Q_n $(n = 3, 6)$ can be evaluated as follows:

$$\begin{aligned} Q_n &= r\int_{-\pi}^{\pi}\int_{0}^{\infty} \frac{1}{\left[r^2 + (z-w)^2\right]^n}\, dzdu \\ &= 2\pi r\int_{0}^{\infty} \frac{1}{\left[r^2 + (z-w)^2\right]^n}\, dz. \end{aligned}$$

By using the change of variables $t = z - w$ and the substitution $t = r\tan\phi$, we have

$$\begin{aligned} Q_n &= 2\pi r^{2-2n}\int_{\arctan(-w/r)}^{\pi/2} \sec^{2-2n}\phi\, d\phi \\ &= 2\pi r^{2-2n}\int_{\arctan(-w/c)}^{\pi/2} \cos^{2n-2}\phi\, d\phi. \end{aligned}$$

Now, using the formula, we obtain [∮2.512(2)] [28]. For $n = 3$ and 6, the integral, Q_n, is given by

$$Q_3 = \pi r^{-5}\left[\frac{3\pi}{8} + \frac{3}{4}\arctan\left(\frac{w}{r}\right) + \frac{3wr}{4\left(r^2+w^2\right)} + \frac{wr^3}{2\left(r^2+w^2\right)^2}\right], \tag{4}$$

and

$$\begin{aligned} Q_6 = \pi r^{-11}\Bigg[&\frac{9\pi}{3840} + \frac{3}{640}\arctan\left(\frac{w}{r}\right) + \frac{wr^9}{5\left(r^2+w^2\right)^5} + \frac{9wr^7}{40\left(r^2+w^2\right)^4} \\ &+ \frac{7wr^5}{60\left(r^2+w^2\right)^3} + \frac{wr^3}{16\left(r^2+w^2\right)^2} + \frac{3wr}{80\left(r^2+w^2\right)}\Bigg], \end{aligned} \tag{5}$$

and these expressions are completed (Eq. 3).

2.2 Preferred position of a Li atom inside nanotubes

For a specific size nanotube, the preferred position of the Li atom inside the nanotube is determined with respect to the cross section of the tube, as shown in Figure 3. The atom is located at $(\alpha, 0, 0)$, where α is the distance of the offset atom (on the x-axis of the tube) from the central axis of the nanotube (z-axis), and the nanotubes are assumed to be of infinite length with a parametric equation, $(r\cos u, r\sin u, z)$, where $-\pi \le u \le \pi$ and $-\infty < z < \infty$. In this case, the distance ϱ is given by

$$\begin{aligned} \varrho^2 &= (r\cos u - \alpha)^2 + r^2\sin^2 u + z^2 \\ &= \alpha^2 + r^2 - 2\alpha r\cos u + z^2 \\ &= (r-\alpha)^2 + 4r\alpha\sin^2(u/2) + z^2, \end{aligned}$$

and the total interaction of the Li atom in the nanotube is given by

$$E^{tot} = r\varpi_j\int_{-\pi}^{\pi}\int_{-\infty}^{\infty} \left(-T\varrho^{-6} + R\varrho^{-12}\right) dzdu. \tag{6}$$

Again, these integrals can be written as

$$E = r\varpi_j\left(-TW_3 + RW_6\right), \tag{7}$$

where W_n is given by

$$W_n = r\int_{-\pi}^{\pi}\int_{-\infty}^{\infty} \frac{1}{\left[(r-\alpha)^2 + 4r\alpha\sin^2(u/2) + z^2\right]^n}\, dzdu. \tag{8}$$

Here, these integrals can be solved by letting $\gamma^2 = (r-\alpha)^2 + 4r\alpha\sin^2(u/2)$, and using the substitution $z = \gamma\tan\theta$, we obtain

$$\begin{aligned} W_n &= r\int_{-\pi/2}^{\pi/2}\cos^{2n-2}\theta\, d\theta\int_{-\pi}^{\pi}\frac{1}{\gamma^{2n-1}}\, du. \\ &= r\mathbf{B}\left(n-1/2, 1/2\right)\int_{-\pi}^{\pi}\frac{1}{\gamma^{2n-1}}\, du, \end{aligned}$$

where $\mathbf{B}(i^*, j^*)$ is the beta function. By following the steps performed by Cox et al. in this work [29], the integral W_n became

$$\begin{aligned} W_n = &\frac{2\pi r}{(r-\alpha)^{2n-1}}\mathbf{B}\left(n-1/2, 1/2\right) \\ &\times F\left(n-1/2, 1/2; 1/2; 1; 4r\alpha/(r-\alpha)^2\right), \end{aligned}$$

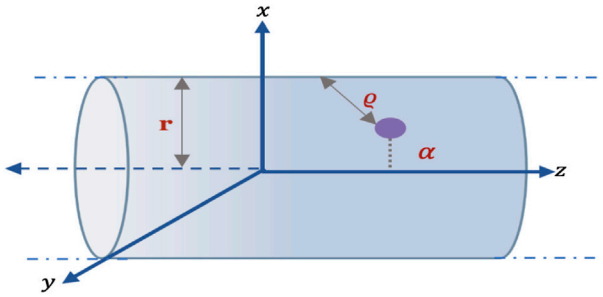

FIGURE 3
Offset distance of the Li atom in the nanotube.

TABLE 2 Constants utilized in this study.

Mean surface density of BNNT ϖ_B (Å^{-2})	0.3682
Mean surface density of CNT ϖ_C (Å^{-2})	0.3412
Attractive constant of T_{B-Li} (kcal mol^{-1} Å^6)	210.402
Attractive constant of T_{C-Li} (kcal mol^{-1} Å^6)	200.592
Repulsive constant of R_{B-Li} (kcal mol^{-1} Å^{12})	210092.098
Repulsive constant of R_{C-Li} (kcal mol^{-1} Å^{12})	196338.506

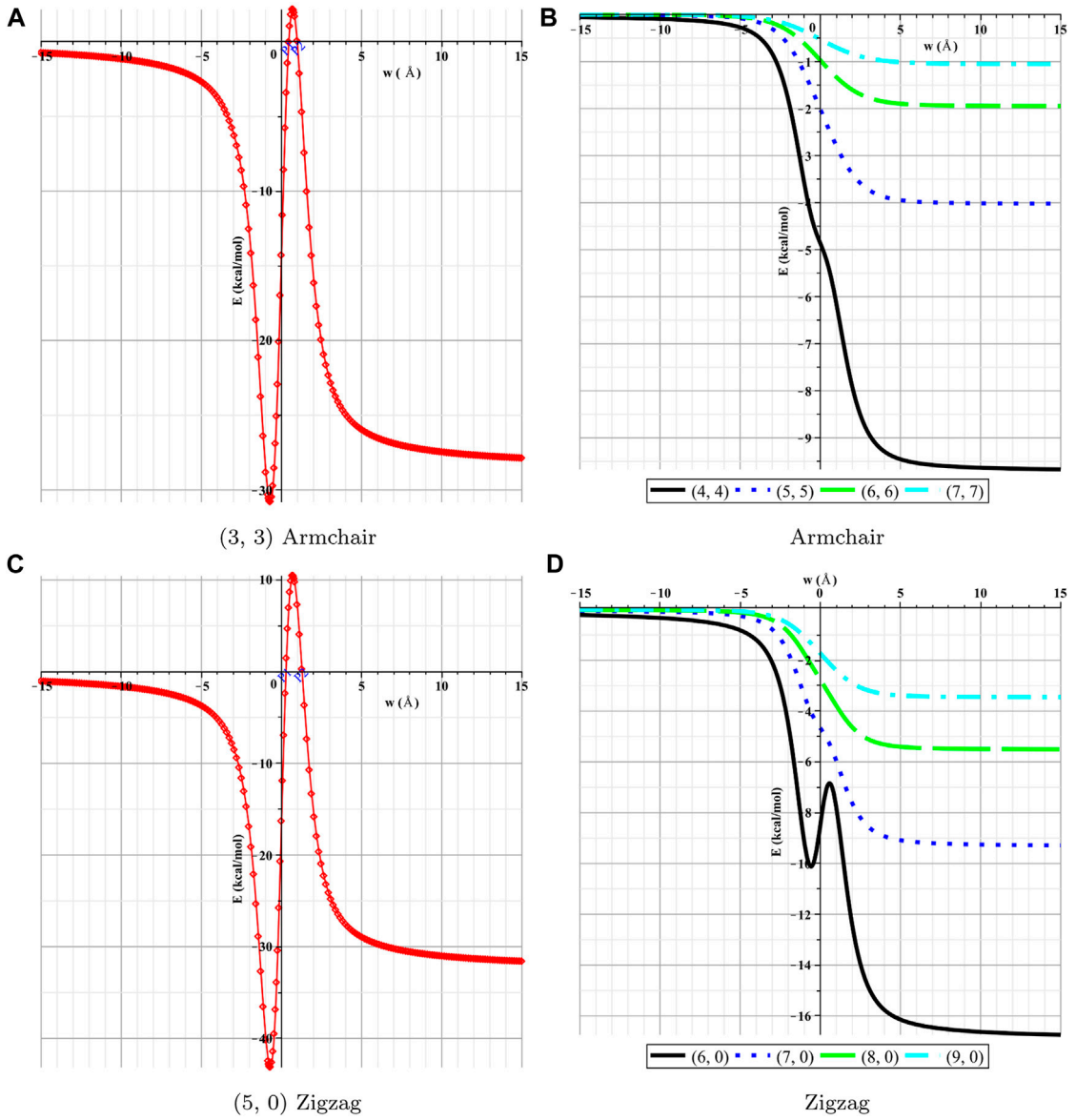

FIGURE 4
Interactions of Li and BNNTs with respect to *w*. **(A)** (3, 3) armchair, **(B)** armchair, **(C)** (5, 0) zigzag, and **(D)** zigzag.

where $F(a^{\star}, b^{\star}; c^{\star}, z^{\star})$ indicates the usual hypergeometric function. Then, this expression is substituted in Eq. 7) in the cases of $n = 3$ and $n = 6$.

3 Numerical results

In this section, the interactions between the lithium atom and the nanotubes are presented numerically for various types of nanotubes by using the numerical values for the parameters associated with Li and nanotubes, which are given in Table 2. First, we determine the numerical solutions of the interactions of the Li atom entering various types of NTs. Figures 4, 5 show the results of the entry of the Li atom in CNTs and BNNTs. Moreover, by using the algebraic computer package Maple, in particular with optimization and then minimization, the minimal interaction energy values are obtained, as shown in Table 3. We comment that when the energies are lower in the $+w$ tube side (i.e., inside the nanotube) than those in the $-w$ tube side (i.e., outside the nanotube), Li is inserted in the tube. The results indicate that for both BNNTs and CNTs, the Li atom is accepted in all tubes except (3, 3) armchair and (5, 0) zigzag nanotubes. The results show that the interaction energies of the Li atom at the open end of the CNTs and BNNTs with a radius less than ≈ 2.2 Å are highly positive, indicating that Li insertion is not feasible energetically due to the energy barrier. Moreover, Figures 4 and 5show that both tubes would not accept the Li atom from the rest because the suction energy is not sufficient to outdo the barrier energy at the opening of these tubes. Therefore, the interactions can exhibit two peaks [positive in the range (P_1, P_2) and

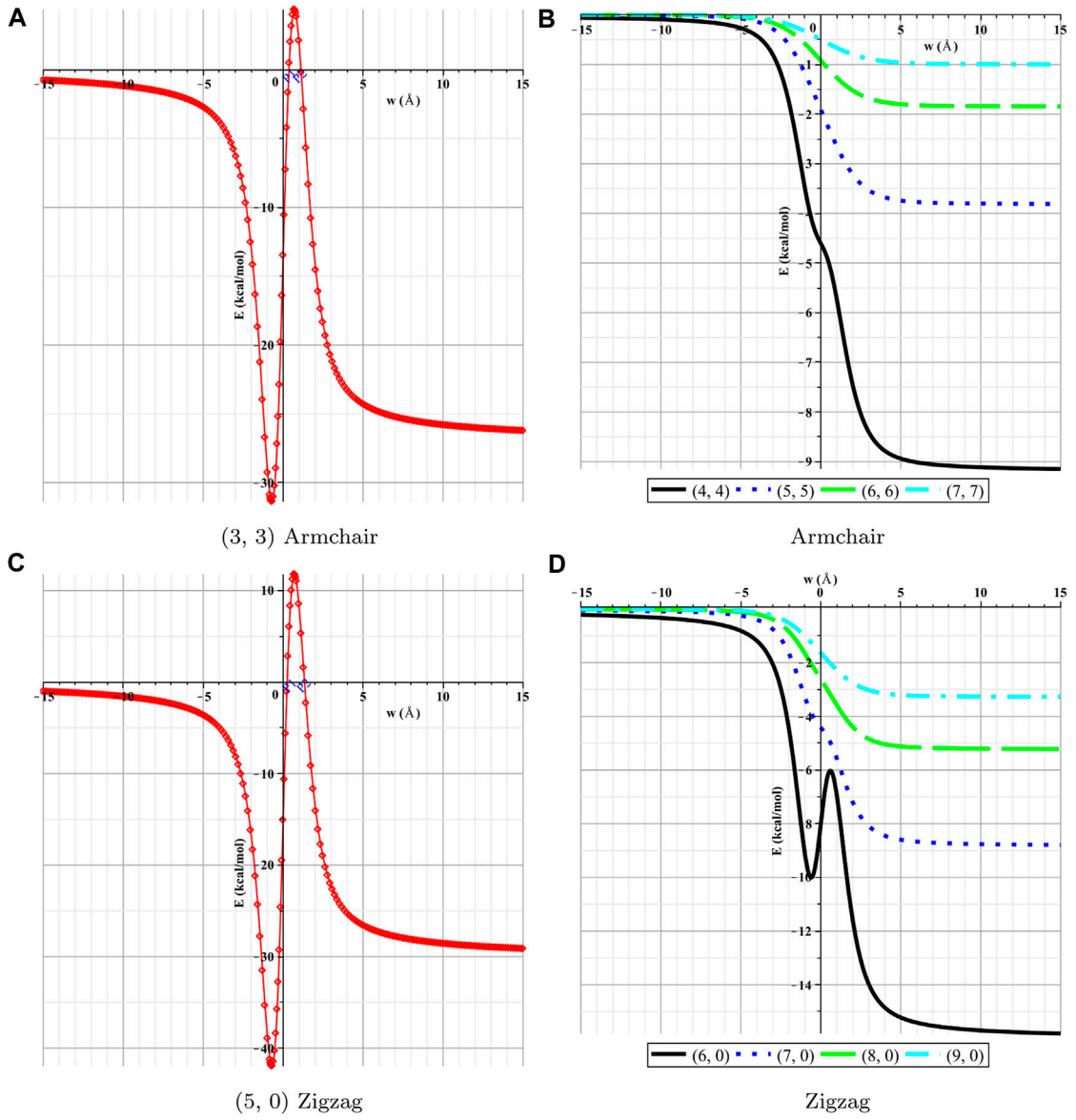

FIGURE 5
Interactions of Li and CNNTs with respect to *w*. **(A)** (3, 3) armchair, **(B)** armchair, **(C)** (5, 0) zigzag, and **(D)** zigzag.

negative in the range (P_2, ∞)], where it is possible for the Li atom to be inside these tubes when the curve of the energy crosses the horizontal axis at *P*2 as some additional energies are required. Our results for the interactions of Li with CNTs and BNNTs are in excellent agreement with the results given in [18–20] for the interactions of Li with CNTs and with those given in [22] for the interactions of Li with BNNTs. In addition, Table 4 summarizes the results for the relationship between the interaction energies and the offset position for Li inside (5, 5), (6, 6), (7, 7), (8, 8), and (9, 9) nanotubes. Our results show that the lowest energies for all CNTs and BNNTs considered in this study are obtained for the (5, 5) NTs with an equilibrium distance of 0 Å from the tube axis, assuming that the Li atom remains on the tube axis. These results differ from [18, 20], who used the *ab initio* simulations and the DFT method, and they showed that the equilibrium distance was between 1.29 and 1.46 Å inside the (5, 5) CNT. It is observed that the discrepancy between our results and these results may be attributed to the parameters which we have adopted here. In addition, our results are in excellent agreement with those performed by Yanhong and Junwei [21] using the DFT method, where their results showed that the strongest adsorption energy of the Li atom is obtained in the (6, 0) CNT. Finally, Figure 6 shows the preferred radii of both BNNTs and CNTs to encapsulate a Li atom, and the results show that the optimal radii are about 3.433 and 3.422 Å, corresponding to energies −2.476 and −2.217 kcal/mol, respectively. Our methods and results that are presented in this work yield the theoretical design of the interaction of a lithium atom stored in various types of nanotubes; moreover, further research should study the interaction

TABLE 3 Main results of the interactions of Li atoms with NTs.

Tube type	Tube radius (Å)		Interaction (kcal mol^{-1})		Position of Li	
	BNNT	CNT	Li-BNNT	Li-CNT	Li-BNNT	Li-CNT
(3, 3)	2.072	2.034	−30.814	−31.382	Outside	Outside
(4, 4)	2.761	2.713	−9.720	−9.199	Inside	Inside
(5, 5)	3.451	3.391	−4.027	−3.816	Inside	Inside
(6, 6)	4.142	4.069	−1.946	−1.845	Inside	Inside
(7, 7)	4.832	4.747	−1.0514	−0.997	Inside	Inside
(5, 0)	1.993	1.968	−43.193	−41.989	Outside	Outside
(6, 0)	2.391	2.349	−16.928	−16.002	Inside	Inside
(7, 0)	2.790	2.741	−9.331	−8.838	Inside	Inside
(8, 0)	3.188	3.132	−5.516	−5.228	Inside	Inside
(9, 0)	3.587	3.524	−3.453	−2.1523	Inside	Inside

TABLE 4 Interaction energies of an offset Li atom inside NTs.

Tube type		(5, 5)	(6, 6)	(7, 7)	(8, 8)	(9, 9)
BNNTs	E^{tot} (kcal mol^{-1})	−2.4	−1.8	−1.4	−1.2	−1.1
	α (Å)	0	0.7	1.6	2.3	3
CNTs	E^{tot} (kcal mol^{-1})	−2.2	−1.6	−1.3	−1.1	−1.0
	α (Å)	0	0.7	1.5	2.2	2.9

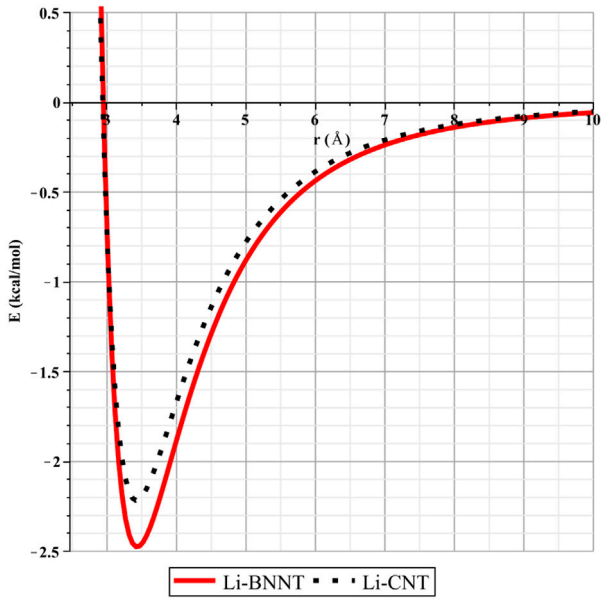

FIGURE 6
Interactions between the Li atom and nanotube as the function of tube radius *r*.

energies and the changes in the electronic structure of the interaction configurations for lithium atoms interacting with nanotubes. In conclusion, the results are obvious that the BNNT and CNT are attractive candidates for Li atom encapsulation, and the best nanotubes are the BNNTs as the interaction between the Li atom and BNNT is slightly stronger than that between the Li atom and CNTs as the former gives the lowest minimum energy. We note that our approach can be used to investigate the interactions between the metal atoms with different types of nanotubes and nanomaterials such as fullerenes (see, for example, [30]).

4 Summary

In this study, the Lennard–Jones potential, in conjunction with continuum modeling, has been used to investigate the interactions between a lithium atom and BNNTs and CNTs. First, calculations of the insertion of a Li atom at an open edge of nanotubes show that a lithium atom is attracted to the entrance open end of the tubes that have a radius larger than 2.2 Å. In addition, our results for (3, 3) and (5, 0) nanotubes showed that the lithium atom confronted a large energy barrier at the open end of these tubes, consequently, for the

lithium atom to be enclosed into the nanotube with a radius less than 2.2 Å; some additional energy is also needed. Moreover, when the lithium atom is assumed to be inside the tube, our results indicate that the equilibrium distance from the tube axis depends on the size of the tube; as the radius gets larger, the position of the Li atom tends to be closer to the wall of the tube. By minimizing the interaction energy, we predicted that the preferred radii of both BNNTs and CNTs to encapsulate the Li atom are about 3.433 and 3.422 Å, respectively, with corresponding (5, 5) armchair nanotubes and (9, 0) zigzag nanotubes. Our results observed that both tubes are attractive candidates for Li atom encapsulation, and by minimizing the interaction energies, we obtained that the interaction between the Li atom and BNNTs is slightly stronger than that between the Li atom and CNTs. Overall, nanostructures, including CNTs and BNNTs, might offer a well-suited playground for optimizing rate performance nanomaterials and capacity for Li storage as an anode material in lithium batteries. Future work could involve a calculation on other nanotubes to enclose the lithium atoms as the particular architecture of nanotubes can offer a useful design idea for the electrode of next-generation lithium batteries.

Data availability statement

The original contributions presented in the study are included in the article/Supplementary Material; further inquiries can be directed to the corresponding authors.

Author contributions

All authors listed have made a substantial, direct, and intellectual contribution to the work and approved it for publication.

Funding

This project was supported by the Researchers Supporting Project number (RSP2023R411), King Saud University, Riyadh, Saudi Arabia.

Conflict of interest

The authors declare that the research was conducted in the absence of any commercial or financial relationships that could be construed as a potential conflict of interest.

Publisher's note

All claims expressed in this article are solely those of the authors and do not necessarily represent those of their affiliated organizations, or those of the publisher, the editors, and the reviewers. Any product that may be evaluated in this article, or claim that may be made by its manufacturer, is not guaranteed or endorsed by the publisher.

References

1. Sharma VP, Sharma U, Chattopadhyay M, Shukla V. Advance applications of nanomaterials: A review. *Mater Today Proc* (2018) 5:6376–80. doi:10.1016/j.matpr.2017.12.248

2. Alshehri MH. Continuum modelling for encapsulation of anticancer drugs inside nanotubes. *Mathematics* (2021) 9:2469. doi:10.3390/math9192469

3. Baowan D, Cox BJ, Hilder TA, Hill JM, Thamwattana N. *Modelling and mechanics of carbon-based nanostructured materials*. 1st ed. Norwich, NY, USA: William Andrew (2017).

4. Iijima S. Helical microtubules of graphitic carbon. *Nature* (1991) 354:56–8. doi:10.1038/354056a0

5. Zheng B, Dong H, Zhu J, Wang Y. Molecular dynamics study of lithium intercalation into -oh functionalized carbon nanotube bundle. *Res Square* (2022) 2022. doi:10.21203/rs.3.rs-1326366/v1

6. Dresselhaus MS, Dresselhaus G, Avouris P. *Carbon nanotubes: Synthesis, structure, properties, and applications*. Berlin, Germany: Springer-Verlag (2000).

7. Coleman JN, Khan U, Blau WJ, Gun'ko YK. Small but strong: A review of the mechanical properties of carbon nanotube-polymer composites. *Carbon* (2006) 44(9): 1624–52. doi:10.1016/j.carbon.2006.02.038

8. Kim JH, Pham TV, Hwang JH, Kim CS, Kim MJ. Boron nitride nanotubes: Synthesis and applications. *Nano Convergence* (2018) 5:17. doi:10.1186/s40580-018-0149-y

9. Alshehri MH, Duraihema FZ, Aba Oud MA. Instability and translocation through nanopores of DNA interacting with single-layer materials. *RSC Adv* (2020) 10: 36962–70. doi:10.1039/D0RA06359B

10. Vovusha H, Sanyal B. Adsorption of nucleobases on 2D transition-metal dichalcogenides and graphene sheet: A first principles density functional theory study. *RSC Adv* (2015) 5:67427–34. doi:10.1039/C5RA14664J

11. Kim HS, Kang HJ, Lim H, Hwang HJ, Park JW, Lee TG, et al. Boron nitride nanotube-based separator for high-performance lithium-sulfur batteries. *Nanomaterials* (2022) 12:11. doi:10.3390/nano12010011

12. Yang F, Feng X, Glans PA, Guo J. MoS2 for beyond lithium-ion batteries. *APL Mater* (2021) 9:050903. doi:10.1063/5.0050118

13. Landi BJ, Ganter MJ, Cress CD, DiLeoa RA, Raffaelle RP. Carbon nanotubes for lithium ion batteries. *Energy Environ. Sci.* (2009) 2:638–54. doi:10.1039/B904116H

14. Rahman MM, Mateti S, Cai Q, Sultana I, Fan Y, Wang X, et al. High temperature and high rate lithium-ion batteries with boron nitride nanotubes coated polypropylene separators. *Energ Storage Mater* (2019) 19:352–9. doi:10.1016/j.ensm.2019.03.027

15. Zhili X, Young SY, Hyoung-Joon J. Applications of carbon nanotubes for lithium ion battery anodes. *Materials* (2013) 6:1138–58. doi:10.3390/ma6031138

16. Ohkubo K, Kawashima Y, Fukuzumi S. Strong supramolecular binding of Li+@C60 with sulfonated meso-tetraphenylporphyrins and long-lived photoinduced charge separation. *Chem Commun* (2012) 48:4314–6. doi:10.1039/C2CC31186K

17. Song B, Yang JW, Zhao JJ, Fang HP. Intercalation and diffusion of lithium ions in a carbon nanotube bundle by *ab initio* molecular dynamics simulations. *Energ Environ. Sci.* (2011) 4:1379–84. doi:10.1039/C0EE00473A

18. Khantha M, Cordero NA, Alonso JA, Cawkwell M, Girifalco LA. Interaction and concerted diffusion of lithium in a (5,5) carbon nanotube. *Phys Rev B* (2008) 78:115430. doi:10.1103/PhysRevB.78.115430

19. Zhong-Heng F, Xiang C, Nan Y, Le-Geng Y, Xin S, Shaochen S, et al. Diameter-dependent ultrafast lithium-ion transport in carbon nanotubes. *J Chem Phys* (2023) 158: 014702. doi:10.1063/5.0131408

20. Meunier V, Kephart J, Roland C, Bernholc J. *Ab initio* investigations of lithium diffusion in carbon nanotube systems. *Phys Rev Lett* (2002) 88:075506. doi:10.1103/PhysRevLett.88.075506

21. Yanhong Y, Junwei Y. Density functional theory study of lithium atom adsorbing in the interior and exterior of a series of carbon nanotubes. *Adv Mater Res* (2014) 1053: 150–6. doi:10.4028/www.scientific.net/AMR.1053.150

22. Rong-Lin Z, Hong-Liang X, Zhong-Min S. The interaction between Boron-carbon-nitride heteronanotubes and lithium atoms: Role of composition proportion. *Chem Phys Lett* (2016) 658:230–3. doi:10.1016/j.cplett.2016.06.054

23. Seif A, Boshra A, Seif M. Lithium-doped (4,4) Boron nitride nanotube: Density functional theory study of N and B nuclear magnetic shielding and electric field gradient tensors. *J Mol Struct THEOCHEM* (2009) 895:82–5. doi:10.1016/j.theochem.2008.10.028

24. Maitland GC, Rigby M, Smith EB, Wakeham WA. *Intermolecular forces–their origin and determination*. Oxford, UK: Clarendon Press (1981).

25. Rappi AK, Casewit CJ, Colwell KS, Goddard WA, III, SkidUFF WM. A full periodic table force field formolecular mechanics and molecular dynamics simulations. *J Am Chem Soc* (1992) 114:10024–35. doi:10.1021/ja00051a040

26. Hilder TA, Hill JM. Modelling the encapsulation of the anticancer drug cisplatin into carbon nanotubes. *Nanotechnology* (2007) 18:275704. doi:10.1088/0957-4484/18/27/275704

27. Hilder TA, Hill JM. Theoretical comparison of nanotube materials for drug delivery. *Micro Nano Lett* (2008) 3:18–24. doi:10.1049/mnl:20070070

28. Gradshteyn IS, Ryzhik IM. *Table of integrals, series and products*. 6th ed. San Diego, USA: Academic Press (2000).

29. Barry JC, Ngamta T, James MH. Mechanics of atoms and fullerenes in single-walled carbon nanotubes. I. Acceptance and suction energies. *Proc R Soc A* (2007) 2007:463. doi:10.1098/rspa.2006.1771

30. Alshehri MH. An analytical model for lithium storage in spherical fullerenes. *Energies* (2022) 15:7154. doi:10.3390/en15197154

frontiers | Frontiers in Physics

TYPE Original Research
PUBLISHED 24 November 2023
DOI 10.3389/fphy.2023.1150457

OPEN ACCESS

EDITED BY
Samir A. El-Tantawy,
Port Said University, Egypt

REVIEWED BY
Nepal Chandra Roy,
University of Dhaka, Bangladesh
Aurang Zaib,
Federal Urdu University of Arts, Sciences and Technology Islamabad, Pakistan
A. M. Rashad,
Aswan University, Egypt

*CORRESPONDENCE
Sadia Asad,
sadia.k@mu.edu.sa

RECEIVED 24 January 2023
ACCEPTED 30 October 2023
PUBLISHED 24 November 2023

CITATION
Asad S (2023), Nonlinear stretched flow of a radiative MHD Prandtl fluid with entropy generation and mixed convection.
Front. Phys. 11:1150457.
doi: 10.3389/fphy.2023.1150457

Nonlinear stretched flow of a radiative MHD Prandtl fluid with entropy generation and mixed convection

Sadia Asad*

Department of Architecture and Interior Design, College of Engineering, Majmaah University, Al-Majmaah, Saudi Arabia

This paper examines the analysis of entropy generation in the flow of an MHD Prandtl fluid over a nonlinear stretching sheet. Heat transfer is developed through a convectively heated sheet. The impacts of nonlinear radiation and nonlinear mixed convection are considered. The resulting nonlinear systems are computed for the unique solutions of velocity and temperature profiles. Effects of thermal radiation, the Prandtl number, Prandtl fluid parameters, and the Biot number are discussed. Results for the Nusselt number and skin friction coefficient are analyzed. The impact of the radiation parameter is to improve the rate of heat transport to the flow region. It is stated that temperature distribution increases for greater values of θ_f. We state that the fluid temperature decreases with the increasing importance of the Prandtl number Pr. Growth in the Prandtl number decreases the rate of thermal diffusion. It shows that the magnitude of drag forces decreases for larger values of Prandtl fluid parameters. Furthermore, curvature and mixed convection parameters boost the flow and heat transfer rate near the cylinder wall. The entropy generation grew up rapidly with larger values of magnetic and Brinkman numbers. The temperature ratio parameter and Prandtl fluid parameters reduce the entropy generation rate. These parameters are also used to control the entropy generation process.

KEYWORDS

Prandtl fluid, entropy generation, MHD, nonlinear thermal radiation, nonlinear mixed convection, convective condition

1 Introduction

In recent years, non-Newtonian fluid with boundary layer approximation over the moving surface has gained considerable attention due to its extensive applications. In [1], the Couette flow of a viscoelastic fluid with thermal convection was studied. In [2], the micropolar fluid flow in a channel was analytically investigated. In [3], the flow and heat transfer of a viscoelastic electrically conducting fluid over a stretching/shrinking sheet was reported. In [4], the exact solution of a rate-type fluid in a circular duct was developed. Coupled flow and heat transfer of a Maxwell fluid over a stretching sheet was discussed in [5, 6], where the mixed convection flow of power-law fluids past an inclined sheet was explored. The effects of shear flow and power-law viscosity on the temperature field were also considered. MHD boundary layer stagnation point flow of a Jeffrey fluid over a moving sheet was analyzed in [7].

TABLE 1 Homotopic convergence for various orders of approximations when a =0.4, θ_f =1.03, R =0.2, Pr=1.0, Bi =0.3, h_f =−0.9, and h_θ =−1.7.

Order of approximation	$-f''0)$	$-\theta'0)$
1	1.1525	0.1889
5	1.2043	0.1683
10	1.2046	0.1620
15	1.2047	0.1596
20	1.2047	0.1587
25	1.2047	0.1583
30	1.2047	0.1581
35	1.2047	0.1581

Convective heat transfer has great interest among researchers, both theoretical and practical, and also has many applications in engineering and geophysical fields. Initially, in [8], the convective heat transfer flow over a moving sheet was reported. In [9], the convective heat transfer over a stretching/shrinking surface was numerically examined. In [10], the steady flow of double-diffusive mixed convection boundary layer flow through convective boundary conditions was numerically reported. The flow of a Maxwell fluid due to constantly moving radiative surfaces with the convective condition was reported in [11, 12],where numerical analysis over a continuous stretching sheet with nonlinear thermal radiation was performed. In [13], the flow of a nanofluid in the existence of nonlinear thermal radiation was numerically analyzed. In [14], the three-dimensional flow of a Jeffrey nanofluid subject to thermal radiation effects was explored. In [15], the analysis of MHD flow and heat transfer with nonlinear radiation in a viscoelastic fluid was performed. The study of three-dimensional magnetohydrodynamics with thermophoresis and Brownian motion aspects was extended in [16].

In the present study, we explore the entropy generation in the flow of an MHD Prandtl fluid with nonlinear thermal radiation. Although the stretching problems are explored extensively for linear thermal radiation, much less emphasis has been given to the flow problems with nonlinear thermal radiation. Such information is further scarce when heat transfer through convective conditions is considered. The radiation effect in the flow of a pseudo-plastic nanofluid was examined in [17]. The MHD stretched flow of a nanofluid in the presence of buoyancy and thermal radiation was analyzed in [18]. A salient feature of radiation in nanofluid flow over an unsteady stretching sheet was reported in [19, 20],where the thermal radiation effect in time-dependent MHD flow with variable viscosity was analyzed. The hydromagnetic flow of a second-grade fluid in the presence of thermal radiation was examined in [21]. The effect of thermal radiation in the flow of a micropolar fluid was considered in [22, 23],where entropy generation in nonlinear radiative flow in the direction of a variable thick surface was reported. A mathematical model for entropy generation with variable fluid properties was examined in [24]. The impact of mixed convection and nonlinear radiation was further considered. The results of surface drag forces, entropy generation rate, heat/mass transfer, and the Bejan number were presented numerically in [25], where the entropy generation in an MHD micropolar nanofluid was analyzed using a nonlinear stretching sheet.

We explore the nonlinear effects of radiation, mixed convection, and stretching sheet with an MHD [26–31] Prandtl fluid and heat transfer on entropy generation. The first objective of the current article is to venture further into the regime of the nonlinear stretched flow of the Prandtl fluid with convective heat transfer [32–41] effects. Thus, the Prandtl fluid dealt with the nonlinear flow of thermal radiation. Our second objective is to consider the nonlinear mixed convection in the entropy generation by nonlinear stretching. Having such an incentive in mind, the reason here is to model first the appropriate problem and then compute it. Nonlinear radiation properties are also incorporated. Governing differential systems are solved for the unique solution of velocity and temperature fields. Velocity, temperature, and entropy generation are sketched and examined for different emerging parameters. The local Nusselt number and skin friction coefficient are studied by graphical illustrations and tabular values.

2 Mathematical construction

We consider the 2D flow of an MHD Prandtl fluid over a stretching sheet. The flow is induced by using a nonlinear stretching sheet. The x- and y-axis are taken along and perpendicular correspondingly. Furthermore, the effects of nonlinear radiation, mixed convection, and convective condition are considered. The Cauchy stress tensor for the Prandtl fluid is given by

$$S = \frac{A \sin^{-1}\left\{\frac{1}{C}\left[\left(\frac{\partial u_i}{\partial x_j}\right)^2 + \left(\frac{\partial u_j}{\partial x_i}\right)^2\right]^{\frac{1}{2}}\right\}}{\left[\left(\frac{\partial u_i}{\partial x_j}\right)^2 + \left(\frac{\partial u_j}{\partial x_i}\right)^2\right]^{\frac{1}{2}}} A_1, \tag{1}$$

where A and C are the material parameters and A_1 is the first Rivlin–Erickson tensor. The boundary layer equations containing the stability of mass, linear momentum, and energy can be written as follows:

$$\frac{\partial u}{\partial x} + \frac{\partial v}{\partial y} = 0, \tag{2}$$

$$u\frac{\partial u}{\partial x} + v\frac{\partial u}{\partial y} = \left(\frac{A}{C}\right)\frac{\partial^2 u}{\partial y^2} + \frac{A}{2C^3}\left(\frac{\partial u}{\partial y}\right)^2\frac{\partial^2 u}{\partial y^2} - \frac{\sigma B_0}{\rho}u + g\{\wedge_1 (T - T_\infty) + \wedge_2 (T - T_\infty)^2\}, \tag{3}$$

$$u\frac{\partial T}{\partial x} + v\frac{\partial T}{\partial y} = \frac{\partial}{\partial y}\left\{\alpha + \frac{16\sigma^* T^3}{3\rho c_p k^*}\right\}\frac{\partial T}{\partial y} + \frac{1}{\rho c_p}\left[\frac{A}{C}\left(\frac{\partial u}{\partial y}\right)^2 + \frac{A}{6C^3}\left(\frac{\partial u}{\partial y}\right)^4\right] + \sigma B_0 u^2, \tag{4}$$

with the subjected boundary conditions

$$U_w(x) = \frac{\nu}{L^{\frac{1}{3}}}x^{\frac{1}{3}},\ v = 0,\ -k\frac{\partial T}{\partial y} = h\left(T_f - T\right) \text{ at } y = 0,$$
$$u \to 0,\ T \to T_\infty \text{ as } y \to \infty. \tag{5}$$

In the aforementioned expressions, $\nu = (\mu/\rho)$ is the kinematic viscosity, μ is the dynamic viscosity, k is the thermal conductivity of

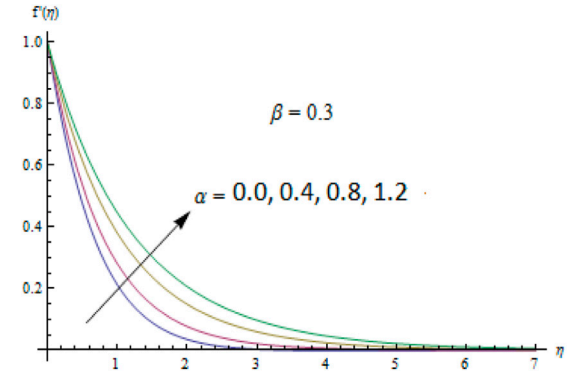

FIGURE 1
$f'(\eta)$ versus α.

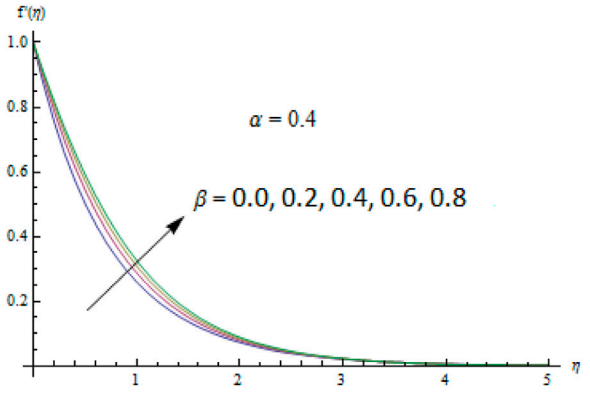

FIGURE 2
$f'(\eta)$ versus β.

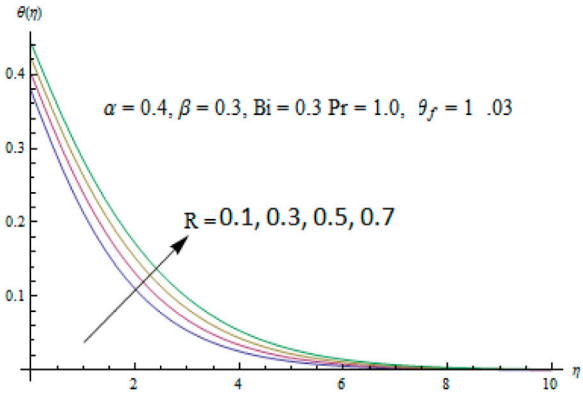

FIGURE 3
$f'(\eta)$ versus R.

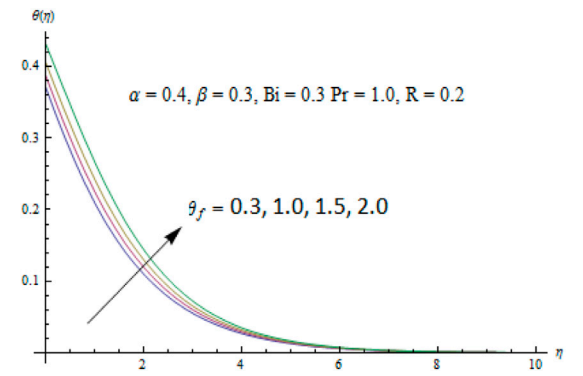

FIGURE 4
$f'(\eta)$ versus θ_f.

the fluid, ρ is the fluid density, T is the fluid temperature, c_p is the specific heat, $q_r = -\frac{16\sigma^* T^3}{3k^*}\frac{\partial T}{\partial y}$ is the radiative heat flux, k^* is the mean absorption coefficient, σ^* is the Stefan–Boltzmann constant, and Bi is the Biot number.

Setting

$$u = \frac{v}{L^{\frac{4}{3}}}x^{\frac{1}{3}}f'(\eta),\ v = -\frac{v}{L^{\frac{2}{3}}}x^{-\frac{1}{3}}\frac{(2f-\eta f)}{3},$$
$$\theta = \frac{T-T_\infty}{T_f-T_\infty},\ \eta = y\frac{x^{\frac{-1}{3}}}{L^{\frac{2}{3}}}, \theta_f = \frac{T_f}{T_\infty}, \tag{6}$$

equation 2 is identically satisfied, and Eqs.3–5) give

$$\alpha f''' - f'^2 + \frac{2}{3}ff'' - \beta f''^2 f'''' - Mf' + \lambda(1+\beta_t\theta)\theta = 0, \tag{7}$$

$$(1+R)\theta'' + R(\theta_f-1)\left\{\theta''\theta^3(\theta_f-1)^2 + 3\theta''\theta^2(\theta_f-1) + 3\theta\theta''\right\},$$
$$+3R(\theta_f-1)\left\{\theta'^2 + \theta^2\theta'^2(\theta_f-1)^2 + 2\theta'^2\theta(\theta_f-1)\right\} + \frac{2}{3}\Pr f\theta'$$
$$+\Pr Ec\left(\alpha f'' + \frac{\beta}{3}f''^4\right) + \Pr EcMf'^2 = 0, \tag{8}$$

$$f = 0,\ f' = 1,\ \theta' = -Bi(1-\theta)\text{ at }\eta = 0,$$
$$f' \to 0,\ \theta \to 0\text{ as }\eta \to \infty, \tag{9}$$

where prime denotes the differentiation with respect to η, f is the dimensionless stream function, θ is the dimensionless temperature, and θ_f is the temperature ratio parameter; the dimensionless numbers are

$$\alpha = \frac{A}{\mu C}, R = \frac{16\sigma^* T_\infty^3}{3kk^*}, \beta = \frac{Av}{2\rho L^4 C^3}, Bi = \frac{h}{k}, \Pr = \frac{\mu c_p}{k},$$
$$E_k = \frac{U_w(x)}{c_p(T_f - T_\infty)}. \tag{10}$$

Here, α and β are the dimensionless Prandtl parameters, R is the radiation parameter, Bi is the Biot number, and Pr is the Prandtl number.

The local Nusselt number Nu_x and skin friction coefficient C_f are defined as follows:

$$Nu_x = \frac{xq_w}{k(T_f - T_\infty)},\ C_f = \frac{\tau_w}{\rho U_w^2}, \tag{11}$$

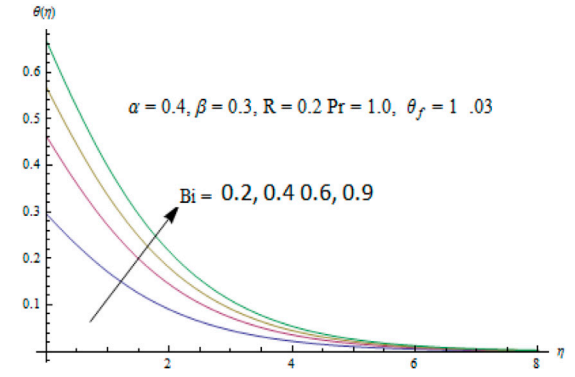

FIGURE 5
θ(η) *versus* Bi.

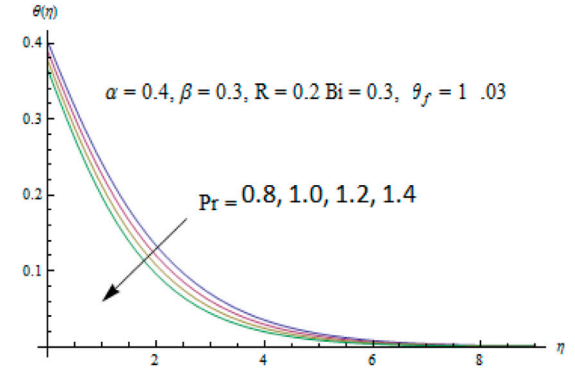

FIGURE 6
θ(η) *versus* Pr.

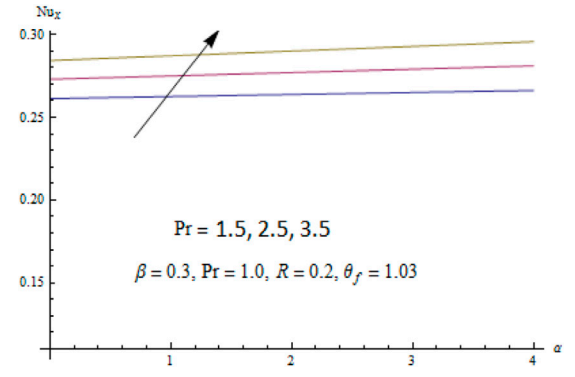

FIGURE 7
Nusselt number *versus* Pr.

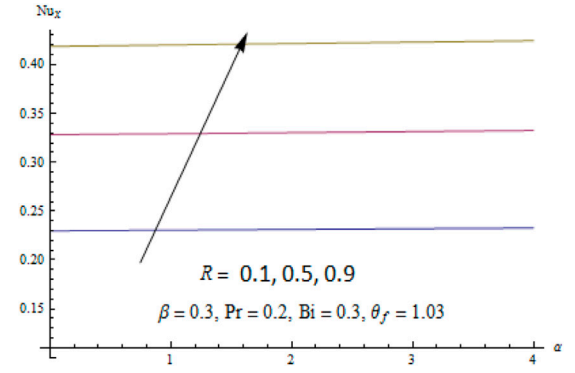

FIGURE 8
Nusselt number *versus* R.

where ρ is the fluid density, τ_w is the surface shear stress, and q_w is the surface heat flux. These quantities are defined by

$$q_w = -k\left(\frac{\partial T}{\partial y}\right)_{y=0} + (q_r)_w, \quad \tau_w = \frac{A}{C}\frac{\partial u}{\partial y} + \frac{A}{6C^3}\left(\frac{\partial u}{\partial y}\right)^3. \tag{12}$$

The dimensionless Nusselt number and skin friction coefficient are

$$\mathrm{Re}_x^{1/2} Nu_x = -\left(1 + R\theta_f^3\right)\theta'(0), \tag{13}$$

$$\mathrm{Re}xC_f = \alpha f''(0) + \frac{\beta}{3}\left(f''(0)\right)^3, \tag{14}$$

where $\mathrm{Re}_x = \frac{U_w(x)L}{\upsilon}$ is the local Reynolds number.

3 Entropy generation

This sector is associated with the influence of the MHD Prandtl fluid with heat transfer on entropy generation. The local volumetric rate of entropy generation is defined as

$$S'''_{gen} = \frac{k}{T_\infty^2}\left[\left(\frac{\partial T}{\partial y}\right)^2 + \frac{16\sigma^* T_\infty^3}{3k^*}\left(\frac{\partial T}{\partial y}\right)^2\right] + \frac{\sigma B_0^2 u^2}{T_\infty} + \frac{\mu}{T_\infty}\left[\frac{A}{C}\left(\frac{\partial u}{\partial y}\right)^2 + \frac{A}{6C^3}\left(\frac{\partial u}{\partial y}\right)^4\right]. \tag{15}$$

The aforementioned equation is the combination of three different phenomena. The first is heat transfer, the second is due to the magnetic field, and the third one is due to viscous dissipation of Walter's B fluid. The characteristic entropy generation rate is defined as

$$\dot{S}_0''' = \frac{k(\Delta T)^2}{l^2 T_\infty^2}. \tag{16}$$

Thus, the dimensionless form of entropy generation is obtained by taking a ratio of Eqs 21 and 22.

$$N_G = \frac{S'''_{gen}}{\dot{S}_0'''} = \mathrm{Re}\left[(1+R)\theta'' + R\left(\theta_f - 1\right)\left\{\theta''\theta^3\left(\theta_f - 1\right)^2 + 3\theta''\theta^2\left(\theta_f - 1\right) + 3\theta\theta''\right\}\right] + \frac{1}{\theta_f^2}\mathrm{Re}BrMf'^2 - \frac{1}{\theta_f^2}\mathrm{Re}Br\left[\alpha f''^2 + \beta f''^4\right], \tag{17}$$

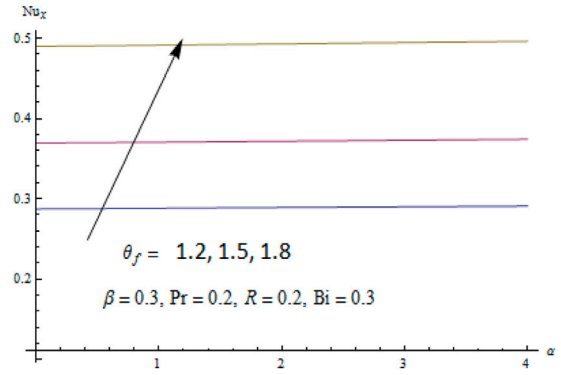

FIGURE 9
Nusselt number *versus* θ_f.

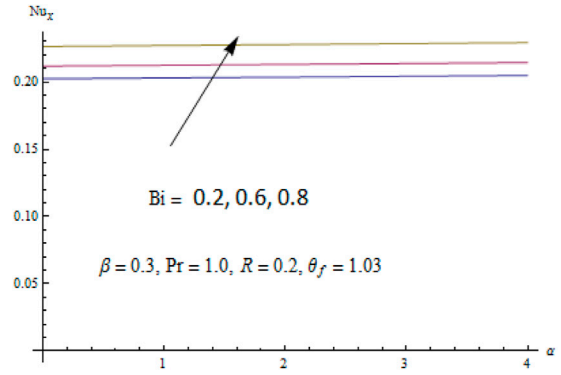

FIGURE 10
Nusselt number *versus* Bi.

TABLE 2 Values of drag forces for various fluid parameters.

α	β	$-f''(0)$
0.4	0.3	1.3133
0.5		1.4265
0.6		1.5341
0.4	0.3	1.3133
	0.2	1.2789
	0.1	1.2381

where $\mathrm{Re} = \frac{U_w(x)x}{\upsilon}$, $Br = \frac{\mu(U_w(x))^2}{k\Delta T}$, and $\theta_f = \frac{\Delta T}{T_\infty}$.

4 Convergent series solutions

Convergent series solutions depend on the non-zero auxiliary parameters. The convergence of solution is checked by drawing the h-curves for the velocity and temperature distributions. Figures (a and b) show the *h*-curves of velocity and temperature profiles for fixed values of other physical parameters. The admissible ranges are h_f and h_θ, respectively. It is observed that the solutions converge for the complete region. Table 1 illustrates the convergence of solutions for various orders of approximations. Tabular values elucidate that 15th and 30th order of approximations are enough for the convergence of series solutions of momentum and energy equations, respectively.

Figures a and b show the ħ-curves for velocity and temperature profiles.

TABLE 3 Comparison of the Nusselt number at the wall for the present results and those of Ishak [42] and Aziz [43] for Pr and Biot number *Bi*.

Pr	*Bi*	Present	[42]	[43]
0.1	0.05	0.03731	0.036844	0.0373
	0.10	0.05951	0.058338	0.0594
	0.20	0.0823	0.082363	0.0848
0.72	0.05	0.04110	0.042767	0.0428
	0.10	0.07053	0.074724	0.0747
	0.20	0.1125	0.119,295	0.1193
	0.40	0.1638	0.169,994	0.1700

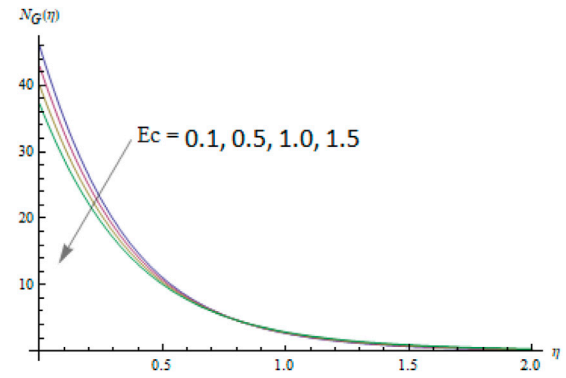

FIGURE 11
Entropy generation *versus* Ec.

5 Results and discussion

To analyze the physical aspects of the considered problem, we discuss the effects of dimensionless parameters α, β, R,θ_f, Bi, and Pr on the velocity $f'\eta$) and temperature $\theta(\eta)$ distributions. The influence of Prandtl fluid parameters α and β on the velocity profile is presented in Figures 1, 2. It is inspected that the velocity profile increases for greater α and β. The increment in velocity for larger values of β is smaller when compared with α. The effect of thermal radiation parameter R on the temperature profile is displayed in Figure 3. It represents the increasing behavior of thermal radiation parameters when $\alpha = 0.4$, $\beta = 0.3$, Bi = 0.3, Pr = 1.0, and $\theta_f = 1.03$. There is heat transfer from the flow region to the wall, indicating that the boundary layer thickness increases throughout the region. Physically, the effect of the

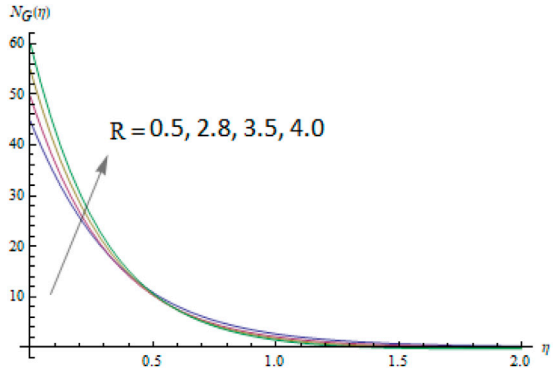

FIGURE 12
Entropy generation *versus R*.

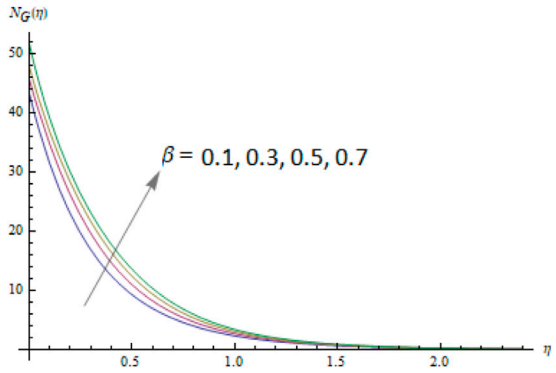

FIGURE 13
Entropy generation *versus* β.

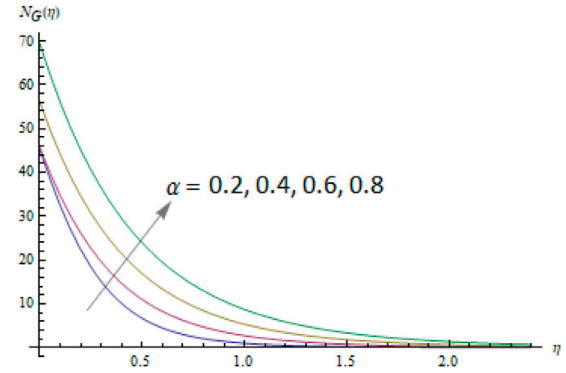

FIGURE 14
Entropy generation *versus* α.

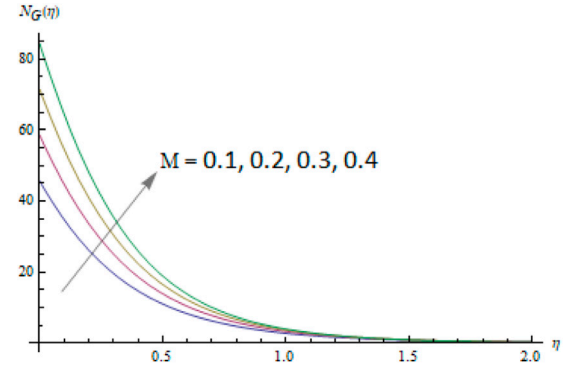

FIGURE 15
Entropy generation *versus M*.

radiation parameter is to increase the rate of heat transport to the flow region. Figure 4 illustrates the behavior of ratio parameter θ_f on the thermal profile. It is observed that temperature distribution increases for greater values of θ_f. Figure 5 shows the effect of the Biot number on the temperature field. A larger Biot number *Bi* boosts the temperature profile. Here, a gradual increase in *Bi* results in the larger convection at the stretching sheet which increases the temperature. This outcome leads to the conclusion that the heat transfer rate at the sheet is enhanced by increasing the velocity of the stretching sheet. Figure 6 depicts the temperature distribution for different values of the Prandtl number. We observe that the fluid temperature decreases with the increase in the value of the Prandtl number Pr. Growth in the Prandtl number decreases the rate of thermal diffusion. Consequently, the boundary layer thickness becomes thinner due to the reduction in thermal conductivity. The Nusselt number characterizes the heat flux from a solid surface to a fluid. Here, we see graphical effects of radiation parameter R, Prandtl number Pr, and Prandtl fluid parameters on the Nusselt number. Figures 7–10 reveal the influences of emerging parameters on the Nusselt number. Figure 7 describes the variation of the Nusselt number. Physically, a larger-Prandtl number fluid has a relatively lower thermal conductivity; thus, an increase in Pr decreases conduction and,

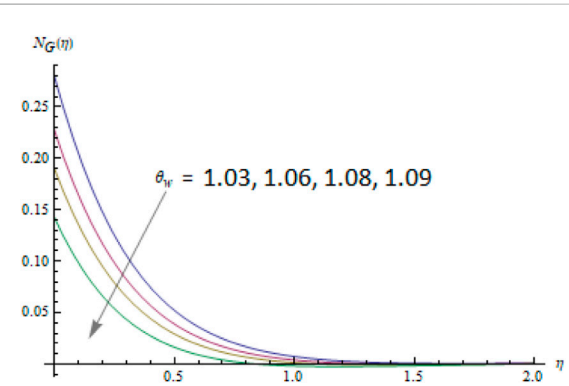

FIGURE 16
Entropy generation *versus* θ_f.

thereby, increases the variations of thermal characteristics. This results in the reduction of the thermal boundary layer thickness and an increase in the heat transfer rate at the bounding surface. We can see that the heat transfer rate increases for greater values of α and Pr. Figure 8 depicts that the Nusselt number increases for

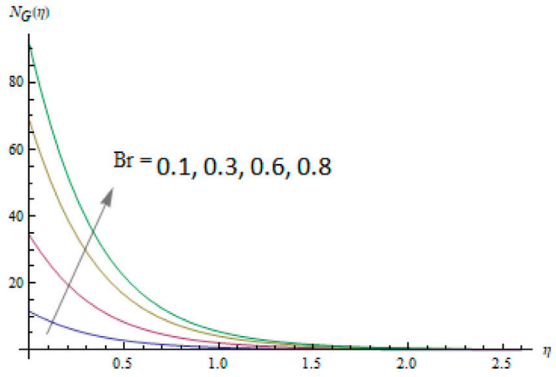

FIGURE 17
Entropy generation *versus* Br.

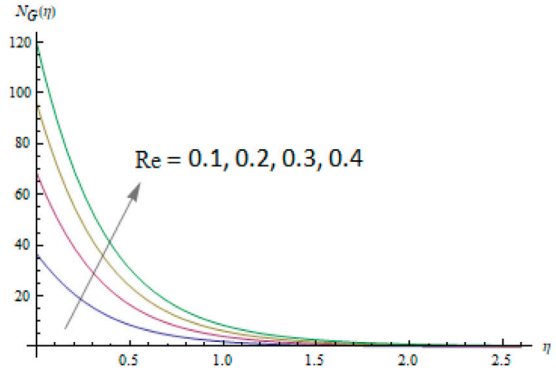

FIGURE 18
Entropy generation *versus* Re.

radiation parameter R. An increase in R enhances the heat flux from the sheet which increases the fluid's velocity and temperature. Figure 9 depicts that the Nusselt number increases for a larger temperature ratio parameter. Figure 10 shows that the Nusselt number increases with an increase in the Biot number. The values of drag forces are given in Table 2. It shows that the magnitude of drag forces decreases for larger values of Prandtl fluid parameters. Table 3 shows the validation of the method, and we found good agreement with the published work.

Deviation of entropy generation with η is represented in Figure 11 for different values of Eckert's number. Growth in Eckert's number leads to a decrease in entropy generation. It is also observed that near-the-surface variation is almost negligible. Figure 12 shows the dual behavior of the radiation parameter: a small increase is displayed near the wall, but far away from the wall, entropy generation increases rapidly. Figures 13,14 exhibit the influence of fluid parameters α and β which boost the entropy generation. The distribution of the magnetic framework on entropy generation is displayed in Figure 15. The magnetic parameter persuades Lorentz force which boosts the entropy generation. The effect of the temperature ratio framework on entropy generation is shown in Figure 16. From this figure, it can be seen that entropy generation decreases when the temperature ratio parameter increases. The effect of the Brickman number is discussed in Figure 17. The Brickman number produces heat transport by viscous heating, which leads to the development in entropy generation. The variation of entropy generation with the Reynolds number is discussed in Figure 18. It is distinguished that entropy generation increases with a larger Reynolds number because a larger Reynolds number corresponds to a larger inertia and smaller viscous force.

6 Conclusion

Important features of the heat transfer flow of an MHD Prandtl fluid past a stretching are investigated. Important points are mentioned as follows.

- By increasing α and β, the velocity field increases.
- Larger values of radiation parameter enhance the temperature distribution.
- The temperature field decreases by increasing the Prandtl number.
- Larger Biot number enhances the temperature and thermal boundary thickness.
- The effect of fluid parameters α and β on the magnitude of the skin friction coefficient is quite the opposite.
- Entropy generation develops with the magnetic parameter, Reynolds number, curvature parameter, and Brinkman number, while contrary behavior is detected for larger values of the temperature ratio parameter.
- Nusselt number enhances when R and Bi are enhanced.

Data availability statement

The original contributions presented in the study are included in the article/Supplementary Material; further inquiries can be directed to the corresponding author.

Author contributions

The author confirms being the sole contributor of this work and has approved it for publication.

Acknowledgments

The author would like to thank Deanship of Scientific Research at Majmaah University for supporting this work under Project Number (R-2023-787).

Conflict of interest

The author declares that the research was conducted in the absence of any commercial or financial relationships that could be construed as a potential conflict of interest.

Publisher's note

References

1. Yin C, Niu J, Fu C, Tan W, Thermal convection of viscoelastic fluid in porous system subjected to horizontal plane Couette flow. *Int J Heat Fluid Flow* (2013) 44, 711 – 8. doi:10.1016/j.ijheatfluidflow.2013.10.002

2. Sheikholeslami M, Ashorynejad HR, Ganji DD, Rashidi MM, Heat and mass transfer of a micropolar fluid in a porous channel. *Commun Numer Anal* (2014) 2014, 1 – 20. doi:10.5899/2014/CNA-00166

3. Turkyilmazoglu M, Three dimensional MHD flow and heat transfer over a stretching/shrinking surface in viscoelastic fluid with various physical effects. *Int J Heat Mass Transfer* (2014) 78, 150 – 5. doi:10.1016/j.ijheatmasstransfer.2014.06.052

4. Fetecau C, Rana M, Nigar N, Fetecau C, First exact solutions for flows of rate type fluids in a circular duct that applies a constant couple to the fluid. *Z Naturforschung Section A J Phys Sci* (2014) 69, 232 – 8. doi:10.5560/zna.2014-0022

5. Han S, Zheng L, Li C, Zhang X. Coupled flow and heat transfer in viscoelastic fluid with Cattaneo-Christov heat flux model. *Appllied Maths Lett* (2014) 38:87–93. doi:10.1016/j.aml.2014.07.013

6. Sui J, Zheng L, Zheng X, Chen G, Mixed convection heat transfer in power law fluids over a moving conveyor along an inclined plate. *Int J Heat Mass Transfer* (2015) 85, 1023 – 33. doi:10.1016/j.ijheatmasstransfer.2015.02.014

7. Hayat T, Sad S, Mustafa M, Alsaedi A, MHD stagnation point flow of Jeffrey fluid over convectively heated stretching sheet. *Comput Fluids* (2015) 108, 179 – 85. doi:10.1016/j.compfluid.2014.11.016

8. Ishak A. Similarity solutions for flow and heat transfer over a permeable stretching surface with convective boundary condition. *Appllied Maths Compution* (2010) 217: 837–42. doi:10.1016/j.amc.2010.06.026

9. Bachok N, Ishak A, Pop I, Stagnation point flow toward a stretching/shrinking sheet with a convective surface boundary condition. *J Franklin Inst* (2013) 350, 2736 – 44. doi:10.1016/j.jfranklin.2013.07.002

10. Patil PM, Omoniat E, Roy S, Influence of convective boundary condition on double diffusive mixed convection flow from a permeable vertical surface. *Int J Heat Mass Transfer* (2014) 70, 313 – 21. doi:10.1016/j.ijheatmasstransfer.2013.11.021

11. Mustafa M, Khan JA, Hayat T, Alsaedi A. Sakiadis flow of Maxwell fluid considering magnetic field and convective boundary conditions. *AIP Adv* (2015) 5. doi:10.1063/1.4907927.027106

12. Cortell R, Fluid flow and radiative nonlinear heat transfer over stretching sheet. *J King Saud University-Science* (2013) 26, 161 – 7. doi:10.1016/j.ijheatmasstransfer.2013.11.021

13. Mushtaq A, Mustafa M, Hayat T, Alsaedi A. Nonlinear radiative heat transfer in the flow of nanofluid due to solar energy: a numerical study. *J Taiwan Inst Chem. Eng* (2014) 45:1176–83. doi:10.1016/j.jtice.2013.11.008.1176-1183

14. Shehzad SA, Hayat T, Alsaedi A, Obid MA, Nonlinear thermal radiation in three-dimensional flow of Jeffrey nanofluid: a model for solar energy. *Appllied Maths Compution* (2014) 248. 273 – 86. doi:10.1016/j.amc.2014.09.091(2014)

15. Cortell R. MHD (magneto-hydrodynamic) flow and radiative nonlinear heat transfer of a viscoelastic fluid over a stretching sheet with heat generation/absorption. *Energy* (2014) 74:896–905. doi:10.1016/j.energy.2014.07.069. 896-905

16. Hayat T, Muhammad T, Alsaedi A, Alhuthali MS, Magnetohydrodynamic three-dimensional flow of viscoelastic nanofluid in the presence of nonlinear thermal radiation. *J Magnetism Magn Mater* (2015) 385, 222 – 9. doi:10.1016/j.jmmm.2015.02.046(2015)

17. Lin Y, Zheng L, Zhang X. Radiation effects on Marangoni convection flow and heat transfer in pseudo-plastic non-Newtonian nanofluids with variable thermal conductivity. *Int J Heat Mass Transfer* (2014) 77:708–16. doi:10.1016/j.ijheatmasstransfer.2014.06.028

18. Rashidi MM, Ganesh NV, Hakeem AKA, Ganga B. Buoyancy effect on MHD flow of nanofluid over a stretching sheet in the presence of thermal radiation. *J Mol Liquids* (2014) 198:234–8. doi:10.1016/j.molliq.2014.06.037

19. Das K, Duari PR, Kundu PK. Nanofluid flow over an unsteady stretching surface in presence of thermal radiation. *Alexandria Eng J* (2014) 53:737–45. doi:10.1016/j.aej.2014.05.002

20. Turkyilmazoglu M. Thermal radiation effects on the time-dependent MHD permeable flow having variable viscosity. *Int J Therm Sci* (2011) 50:88–96. doi:10.1016/j.ijthermalsci.2010.08.016

21. Olajuwon BI. Convection heat and mass transfer in a hydromagnetic flow of a second grade fluid in the presence of thermal radiation and thermal diffusion. *Int Commun Heat Mass Transfer* (2011) 38:377–82. doi:10.1016/j.icheatmasstransfer.2010.11.006

22. Bhattacharyya K, Mukhopadhyay S, Layek GC, Pop I. Effects of thermal radiation on micropolar fluid flow and heat transfer over a porous shrinking sheet. *Int J Heat Mass Transfer* (2012) 55:2945–52. doi:10.1016/j.ijheatmasstransfer.2012.01.051

23. Hayat T, Khan MWA, Khan MI, Alsaedi A. Nonlinear radiative heat flux and heat source/sink on entropy generation minimization rate. *Phys B: Condensed Matter* (2018) 538:95–103. doi:10.1016/j.physb.2018.01.054

24. Khan MI, Hayat T, Khan MI, Waqas M, Alsaedi A. Numerical simulation of hydromagnetic mixed convective radiative slip flow with variable fluid properties: a mathematical model for entropy generation. *J Phys Chem Sol* (2019) 125:153–64. doi:10.1016/j.jpcs.2018.10.015

25. Almakki M, Mondal H, Sibanda P. Entropy generation in magneto nanofluid flow with Joule heating and thermal radiation. *World J Eng* (2020) 17:1–11. doi:10.1108/wje-06-2019-0166

26. Devi SPA, Kumar PS. Effect of magnetic field on Blasius and Sakiadis flow of nanofluids past on inclined plate. *J Taibah Univ Sci* (2017) 11:1275–88. doi:10.1016/j.jtusci.2017.03.004

27. Disu AB, Dada MS. Rynolds model viscosity of radiative MHD flow in porous medium between two vertical wavy walls. *J Taibah Univ Sci* (2017) 11:548–65. doi:10.1016/j.jtusci.2015.12.001

28. Ganga B, Ansari SMY, Ganesh NV, Hakeem AKA. Hydromagnetic flow and radiative heat transfer of nanofluid past a vertical plate. *J Taibah Univ Sci* (2017) 11: 1200–13. doi:10.1016/j.jtusci.2015.12.005

29. Waqas M, Shehzad SA, Hayat T, Ijaz Khan M, Alsaedi A. Simulation of magnetohydrodynamics and radiative heat transport in convectively heated stratified flow of Jeffrey nanofluid. *J Phys Chem Sol* (2019) 133:45–51. doi:10.1016/j.jpcs.2019.03.031

30. Waqas M, Khan M, Farooq M, Alsaedi A, Hayat T, Yasmeen T. Magnetohydrodynamic (MHD) mixed convection flow of micropolar liquid due to nonlinear stretching sheet with convective condition. *Int J Heat Mass Transfer* (2016) 102:766–72. doi:10.1016/j.ijheatmasstransfer.2016.05.142

31. Asad S. Radiative analysis of entropy generation on MHD Walters-B fluid with heat and mass transfer. Int J *Bulgarian Chem Commun* (2021) 53:343–54. doi:10.34049/bcc.53.3.5390.343

32. Alharbi SO, Khan U, Zaib A, Ishak A, Raizah Z, Ishak S, et al. Heat transfer analysis of buoyancy opposing radiated flow of alumina nanoparticles scattered in water-based fluid past a vertical cylinder. *Scientific Rep* (2023) 13:10725. doi:10.1038/s41598-023-37973-6

33. Khan U, Zaib A, Ishak A, ElSHERIF SM, Sarris IE, Eldin SM, et al. Analysis of assisting and opposing flows of the Eyring-Powell fluid on the wall jet nanoparticles with significant impacts of irregular heat source/sink. *Case Stud Therm Eng* (2023) 49: 103209. doi:10.1016/j.csite.2023.103209

34. Khan U, Zaib A, Madhukesh JK, Elattar S, Eldin SM, Ishak A, et al. Features of radiative mixed convective heat transfer on the slip flow of nanofluid past a stretching bended sheet with activation energy and binary reaction. *Energies* (2022) 15:7613. doi:10.3390/en15207613

35. Khan U, Zaib A, Ishak A, Eldin SM, Alotaibi AM, Raizah Z, et al. Features of hybridized AA7072 and AA7075 alloys nanomaterials with melting heat transfer past a movable cylinder with Thompson and Troian slip effect. *Arabian J Chem* (2023) 16: 104503. doi:10.1016/j.arabjc.2022.104503

36. Roy NC, Pop I. Dual solutions of a nanofluid flow past a convectively heated nonlinearly shrinking sheet. *Chin J Phys* (2023) 82:31–40. doi:10.1016/j.cjph.2022.12.008

37. Roy NC, Pop I. Dual solutions of magnetohydrodynamic mixed convection flow of an Oldroyd-B nanofluid over a shrinking sheet with heat source/sink. *Alexandria Eng J* (2022) 61:5939–48. doi:10.1016/j.aej.2021.11.021

38. Roy NC, Hossain A, Pop I. Flow and heat transfer of MHD dusty hybrid nanofluids over a shrinking sheet. *Chin J Phys* (2022) 77:1342–56. doi:10.1016/j.cjph.2021.12.012

39. Roy NC, Pop I. Exact solutions of Stokes' second problem for hybrid nanofluid flow with a heat source. *Phys Fluids* (2021) 33:063603. doi:10.1063/5.0054576

40. Roy NC, Pop I. Unsteady magnetohydrodynamic stagnation point flow of a nanofluid past a permeable shrinking sheet. *Chin J Phys* (2022) 75:109–19. doi:10.1016/j.cjph.2021.12.018

41. Roy NC, Pop I. Heat and mass transfer of a hybrid nanofluid flow with binary chemical reaction over a permeable shrinking surface. *Chin J Phys* (2022) 76:283–98. doi:10.1016/j.cjph.2021.10.041

42. Ishak A. Similarity solutions for flow and heat transfer over a permeable surface with convective boundary condition. *Appl Maths Comput* (2010) 217:837–42. doi:10.1016/j.amc.2010.06.026

43. Aziz A. A similarity solution for laminar thermal boundary layer over a flat plate with a convective surface boundary condition. *Commun Nonlinearsci Numer Simul* (2009) 14:1064–8. doi:10.1016/j.cnsns.2008.05.003

Nomenclature

u, v	Velocity components	h	Heat transfer coefficient
x, y	Space coordinates	A and C	Material parameters
T	Fluid temperature	σ^*	Stefan–Boltzmann constant
T_∞	Ambient temperature	k^*	Mean absorption coefficient
L	Length	η	Dimensionless space variable
$\wedge_1$	Linear thermal expansion coefficient	f	Dimensionless velocity
$\wedge_2$	Nonlinear thermal expansion coefficient	θ	Dimensionless temperature
U_w	Stretching velocity	ϕ	Dimensionless concentration
B_0	Free stream velocity	ψ	Stream function
ρ	Fluid density	α&β	Fluid parameters
ν	Kinematic viscosity	M	Magnetic parameter
μ	Dynamic viscosity	Br	Brinkman number
c_p	Specific heat	g	Mixed convection
σ	Electrical conductivity	Bi	Biot number
ρ_f	Fluid density	R	Radiation parameter
$(c_p)_f$	Fluid heat capacity	Pr	Prandtl number

Frontiers in Physics

Investigates complex questions in physics to understand the nature of the physical world

Addresses the biggest questions in physics, from macro to micro, and from theoretical to experimental and applied physics.

Discover the latest Research Topics

See more →

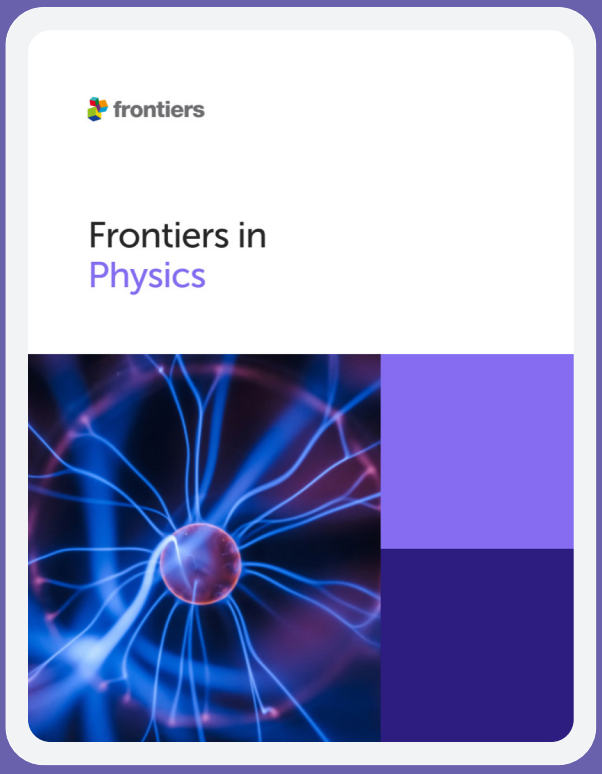

Frontiers

Avenue du Tribunal-Fédéral 34
1005 Lausanne, Switzerland
frontiersin.org

Contact us

+41 (0)21 510 17 00
frontiersin.org/about/contact